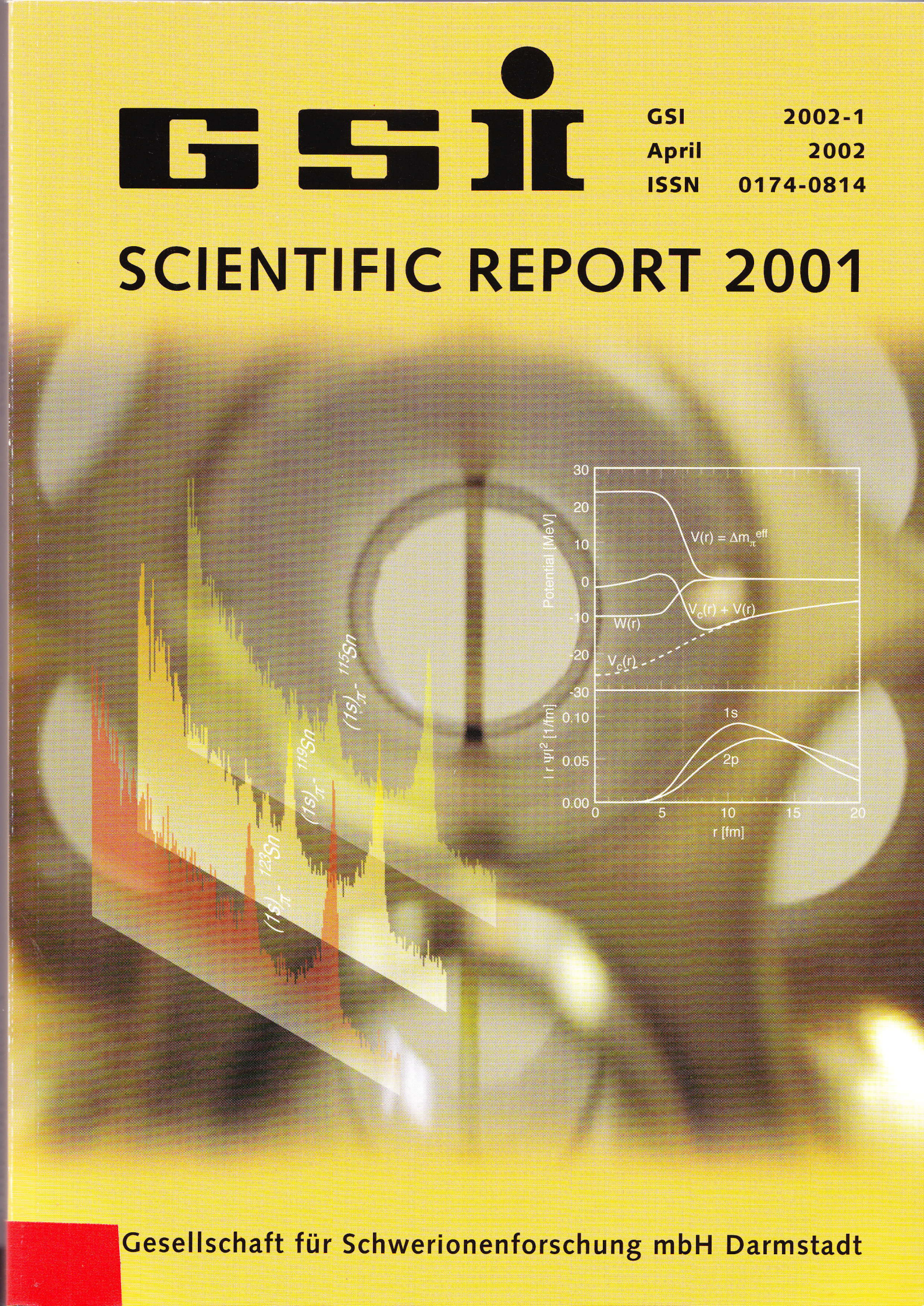
GSI

GSI 2002-1
April 2002
ISSN 0174-0814

SCIENTIFIC REPORT 2001



Gesellschaft für Schwerionenforschung mbH Darmstadt

Cover Picture:
Deeply-bound pionic states of heavy atoms were discovered by a japanese-german group at the fragment separator FRS. Recently, this new spectroscopic tool was applied to study the 1s pionic state in a series of Sn isotopes. Well-resolved peaks of the pionic 1s states were observed and their binding energies and widths were precisely determined. These measurements will reveal how the pion mass as well as the pion decay constant are modified in nuclear media due to quantum chromodynamics effects.
The front cover shows the measured spectra, calculated interaction potentials and a close-up view of the FRS target ladder with the used thin stripes of Sn targets carefully prepared by the GSI target laboratory for this high-resolution experiment.

SCIENTIFIC REPORT
2001

(URL: http://www.gsi.de/annrep2001)

Publisher: **Gesellschaft für Schwerionenforschung (GSI)**

Address: GSI
Planckstr. 1
D-64291 Darmstadt
Germany

Editor: U. Grundinger, Scientific Information and Documentation
Tel.: 06159 71-2610
FAX: 06159 71-3049
E-mail address: U.Grundinger@GSI.de

Print: Schmidt & more Drucktechnik GmbH
Ginsheim-Gustavsburg

C O N T E N T S

PREFACE

NUCLEAR HEAVY ION PHYSICS
- Nuclear Structure
  - Synthesis and Studies of Heavy and Superheavy Elements 1
  - Nuclei far off Stability 4
  - Secondary Beams and Nuclear Collective Modes 16
  - Theory 25

- Nuclear Matter
  - Multifragmentation 31
  - Highly Excited Hadron Matter 34
  - Nucleus-Nucleus Collisions at Ultrarelativistic Energies 43
  - Theory 52

ATOMIC HEAVY ION PHYSICS
- Experiments 85
- Developments 105
- Theory 116

HEAVY ION RESEARCH IN OTHER FIELDS
- Plasma Physics 127
- Heavy Ion Induced Effects in Solids 137
- Biophysics with Highly Ionizing Beams 151
- Chemistry 179

ACCELERATOR-EXPERIMENTS AND -DEVELOPMENT 189

NEW INSTRUMENTS AND METHODS 205

ANNEX

- Publications 225
- GSI-Reports and -Preprints 248
- Invited Talks at Conferences, Sympos., Workshops 251
- Invited Talks at other Institutes 257
- Lectures and Courses 261
- Seminars, Workshops at GSI 263
- Thesis, Diploma 270
- Beamtime at GSI 271
- Collaborations 274

- Author Index
- Internal Organisation

Foreword

This document gives the detailed yearly status report of the research activities at GSI. But the situation is perhaps somewhat different for 2001, in that a major activity that took place during the year is not explicitly described here. This is the preparation of the conceptual design report (CDR) for the future GSI facility, which was prepared last year with the help of the international science community. The work resulted in a 700-page report, 'An International Accelerator Facility for Beams of Ions and Antiprotons', that was submitted last October to the Wissenschaftsrat, the highest scientific advisory committee to the federal government in Germany, for evaluation.

The document concluded a process that had been ongoing for a number of years with extensive discussions, workshops and planning activities by the international science community. I would like to take this opportunity to express our sincerest thanks to the large number of scientists both from inside GSI and from the many universities and research groups worldwide, that have contributed to this important activity for GSI. The report, which has been widely distributed, attempts at the end to list all the individuals involved in this activity. The report itself may be downloaded from the GSI Website (http://www.gsi.de/GSI-Future/cdr/) or can be requested as a CD. Due to the volume of the report and the large range of science discussions and technical concepts presented, we decided not to repeat its content in this annual report (except for some specific ongoing technical developments) but rather refer the interested reader to the full CDR document.

Despite the intense work for the CDR, the ongoing research program went ahead full steam. It took advantage of the improved beam intensities now available from the recent upgrade and from further developments in instrumentation. This is described in the various contributions to the present document. Some selected highlights follow.

In the heavy-element work the most interesting development is perhaps the first chemical study of element 108, hassium. In addition new isotopes of curium, rutherfordium and hassium were discovered. SHIPTRAP, the ion trap after the recoil separator to collect, identify and study heavy nuclei was completed and first on-line tests with stable beams successfully performed.

The study of nuclei far from stability involved a broad range of both, on-line decay studies as well as experiments with energetic radioactive beams. A breakthrough was achieved at the on-line mass separator for the selective and fast ISOL (isotope separation on-line) extraction of tin and germanium isotopes. This is expected to provide novel opportunities for the study of nuclei at and around the doubly-magic ^{100}Sn. A radioactive beam experiment that drew some attention in the form of a Physical Review front page figure was the study of the spin-orbit splitting in the neutron-rich helium-7 isotope.

In the area of hadron physics two very successful experiments were performed that may have considerable impact on the understanding of hadron properties in nuclear matter. First, by a clever scheme of acceleration, stripping of all electrons, cooling of the resulting poor beam in the ESR, and then reinjection and reacceleration to the highest energy, it was possible to prepare beams of gold ions of 1.5 GeV per nucleon. This allowed for a key study of kaon production in nucleus-nucleus collisions and the related question of the mass shift of kaons in the nuclear medium. Second, in a direct reaction experiment, pionic K-shell atoms were

produced and measured for medium-mass tin isotopes. From these measurements one expects precise and seminal information on the s-wave pion-nucleus potential.

In the atomic physics program precision measurements were successfully made, ranging from 1s and two-electron Lamb shifts to a new determination of the electron's mass. For PHELIX, the peta-watt high-energy laser for heavy-ion experiments which is constructed together with the plasma physics group at GSI, a major milestone was reached with the demonstration of the performance requirements for the femto-second front-end.

The broad program of applying ion beams to plasma physics, materials research, and to biophysics and radiation therapy was successfully continued. Highlights from this research are: proton radiography measurements with laser generated high-quality proton beams, applications of ion induced nanopores as model channels of biomembranes or as templates for submicron-sized metal wires, and the observation of a localized protein response to individual particles traversing a cell nucleus. In heavy-ion therapy well over 120 patients have been successfully treated. This corresponds to 250 days of therapy operation and more than 1500 fractions, i.e. radiation treatments.

A wide range of technical developments is underway, aimed at both the short- and mid-term research programs with the present facility and at the long-term program that we hope will be carried out at the future facility discussed above.

Finally, in 2001 a major change was introduced in the funding process for the Helmholtz-Gemeinschaft, the organization of research centers to which GSI belongs. Funding is being changed from institutional to program-oriented funding. In this new scheme program presentation and evaluation will happen on a strategic level every five years. This implies presentation of the GSI research activities in a broader scheme along major research program lines. We intend, nevertheless, to provide the annual status of the detailed research activities in the form of this traditional annual report. Please let us know your views and comments about this.



NUCLEAR HEAVY ION PHYSICS

Nuclear Structure

- Synthesis and Studies of Heavy and Superheavy Elements 1
- Nuclei Far Off Stability 4
- Secondary Beams and Nuclear Collective Modes 16
- Theory 25

Nuclear Matter

- Multifragmentation 31
- Highly Excited Hadron Matter 34
- Nucleus-Nucleus Collisions at Ultrarelativistic Energies 43
- Theory 52

Results included here are progress reports of research projects and therefore should be considered as preliminary communications.

Several university projects were funded by the Federal Ministry of Education, Science, Research and Technology (BMBF); they are marked with a 'B' after the title. In addition GSI supported external groups with certain resources for development of methods and facilities which are of general interest, this is indicated by a 'G' in the title.

Nuclear Structure

Synthesis and Studies of Heavy and Superheavy Elements

Decay Properties of ^{269}Hs and Evidence for the new Nuclide ^{270}Hs 1
A. Türler, Ch.E. Düllmann, H.W. Gäggeler, S. Soverna, R. Dressler, B. Eichler, F. Glaus, D.T. Jost, D. Piguet, T.N. Ginter, K.E. Gregorich, U. Kirbach, D.M. Lee, R. Sudowe, D.C. Hoffman, H. Nitsche, J.B. Patin, P. Zielinski, W. Brüchle, R. Eichler, E. Jäger, V. Pershina, M. Schädel, B. Schausten, E. Schimpf, H.-J. Schött, G. Wirth, S.N. Timokhin, A.B. Yakushev, K. Eberhardt, P. Thörle, N. Trautmann, Z. Qin, A. Vahle

An EC-Branch in the Decay of 27-s ^{263}Db: Evidence for the new Isotope ^{263}Rf 2
J.V. Kratz, A. Nähler, U. Rieth, A. Kronenberg, B. Kuczewski, E. Strub, W. Brüchle, M. Schädel, B. Schausten, A. Türler, H. Gäggeler, C.Laue, R. Sudowe, P.A. Wilk

Alpha - Gamma - Decay Studies of ^{253}No 3
F.P. Heßberger, S. Hofmann, D. Ackermann, A.G. Popeko, S. Saro, A.V. Yeremin

Nuclear Far Off Stability

Decay Study of ^{50}Ni 4
C. Mazzocchi, C. Bingham, B. Blank, M. Chartier, H. Geissel, J. Giovinazzo, E. Grodner, R. Grzywacz, M. Hellström, Z. Janas, J. Kurcewicz, A.S. Lalleman, I. Mukha, M. Pfützner, C. Plettner, E. Roeckl, K. Rykaczewski, K. Schmidt, M. Stanoiu, J.-C. Thomas

Decay Spectroscopy of the N=Z+1 Odd-Mass Nucleus ^{79}Y 5
J. Döring, S.L. Tabor, L. Batist, R. Borcea, H. Grawe, Z. Janas, M. Kavatsyuk, R. Kirchner, C. Mazzocchi, I. Mukha, J.R. Pavan, C. Plettner, A. Plochocki, E. Roeckl, B. Salvachúa, M. Wiedeking

High-Spin ß Decay of ^{94}Ag 6
C. Plettner, M. La Commara, K. Schmidt, H. Grawe, J. Döring, R. Borcea, S. Galanopoulos, M. Górska, S. Harrisopulos, M. Hellström, Z. Janas, R. Kirchner, C. Mazzocchi, A. Ostrowski, G. Rainovski, E. Roeckl

Gamov Teller Decay of Nuclei near ^{100}Sn 7
A. Stolz, T. Fästermann, R. Schneider, K. Sümmerer, E. Wefers, J. Friese, H. Geissel, J. Gerl, M. Hellström, P. Kienle, H.-J. Körner, M.N. Mineva, M. Münch, G. Münzenberg, C. Schlegel, R.S. Simon, P. Thirolf, H. Weick, K. Zeitelhack

Total Absorption Spectroscopy of the ß-Decay of ^{148}Tb (2^- and 9^+) 8
E. Nácher, A. Algora, B. Rubio, D. Cano-Ott, J. L. Tain, A. Gadea, L. Batist, R. Collatz, H. Grawe, M. Hellström, Z. Hu, Z. Janas, M. Karny, R. Kirchner, P. Kleinheinz, F. Moroz, E. Roeckl, K. Rykaczewski, V. Wittman

Recent TAS Experiments Carried out at the On-line Mass-Separator in the Rare Earth Region 9
B. Rubio, A. Algora, E. Nácher, D. Cano-Ott, J.L. Tain, A. Gadea, L. Batist, A. Blazhev, J. Döring, M. Gierlik, H. Grawe, R. Kirchner, P. Kleinheinz, I. Mukha,C. Plettner, E. Roeckl, J.J. Valiente

Mass and Half-life Measurements of Stored Exotic Nuclei 10
Yu.A. Litvinov, J. Stadlmann, F. Attallah, K. Beckert, P. Beller, F. Bosch, D. Boutin, H. Eickhoff, M. Falch, B. Franczak, B. Franzke, H. Geissel, M. Hausmann, E. Kaza, Th. Kerscher, O. Klepper, H.-J. Kluge, C. Kozhuharov, K.E.G. Löbner, M. Matos, G. Münzenberg, N. Nankov, F. Nolden, Yu.N. Novikov, Z. Patyk, W. Quint, T. Radon, H. Reich, H. Schatz, C. Scheidenberger, M. Steck, Z. Sun, L. Vermeeren, H. Weick, M. Winkler, T. Winkler, H. Wollnik

Alpha - Decay Studies of ^{217g}Pa and ^{217m}Pa 12
F.P. Heßberger, S. Hofmann, I. Kojouharov, D. Ackermann, S. Antalic, P. Cagarda, B. Kindler, B. Lommel, R. Mann, A.G. Popeko, S. Saro, J. Uusitalo, A.V. Yeremin

Isomer and ß Decay Studies in n-Rich A~180 Nuclei 13
S.D. Al-Garni, P.H. Regan, P.M. Walker, H.M. El-Masri, J. Garces Narro, C.J. Pearson, E. Roeckl, R. Kirchner, M. La Commara, C. Mazzocchi, H. Grawe, R. Borcea, J.Döring, S.C. Wooding, K. Schmidt, D.M. Cullen, C. Wheldon, W.D. Schmidt-Ott, R. Wood, L. Batist, I. Mukha, C. Plettner, A. Blazhev, Y. Shimbara

Fine Structure in the Alpha Decay of Neutron-Deficient Polonium Isotopes 14
K. Van de Vel, A.N. Andreyev, D. Ackermann, S. Antalic, H.J. Boardman, P. Cagarda, J. Gerl, F.P. Hessberger, S. Hofmann, M. Huyse, D. Karlgren, B. Kindler,I. Kozhoukharov, M. Leino, B. Lommel, G. Münzenberg, C. Moore, R.D. Page, C. Schlegel, P. Van Duppen

New Isotopes ^{233}Cm and ^{234}Cm 15
P. Cagarda, S. Antalic, D. Ackermann, F.P. Heßberger, S. Hofmann, B. Kindler, J. Kojouharova, B. Lommel, R. Mann, A.G. Popeko, S. Saro, J. Uusitalo, A.V. Yeremin

Secondary Beams and Nuclear Collective Modes

New Deeply Bound Pionic States in Sn Isotopes 16
M.Fujita, H.Geissel, H.Gilg, A. Gillitzer, R.S.Hayano, S.Hirenzaki, K.Itahashi, M.Iwasaki, P.Kienle, L.Maier, M.Matos, G.Muünzenberg, T.Ohtsubo, M.Sato, M.Shindo, K.Suzuki, T.Suzuki, H.Weick, M.Winkler, T.Yamazaki, T.Yoneyama

Reaction Studies and Continuum Spectroscopy with Exotic Neutron-Rich Nuclei 17
H.Simon, D. Aleksandrov, T. Aumann, L. Axelsson, T. Baumann, M.J.G. Borge, D. Cortina-Gil, L.V. Chulkov, W. Dostal, B. Eberlein, Th.W. Elze, H. Emling, C. Forssén, H. Geissel, M. Hellström, B. Jonson, J.V. Kratz, R. Kulessa, Y. Leifels,K. Markenroth, M. Meister, G. Münzenberg, T. Nilsson, G. Nyman, M. Pfützner, A. Richter, K. Riisager, Ch. Scheidenberger, G. Schrieder, O. Tengblad, M.V. Zhukov

Coulomb Dissociation of ^{8}B: Determination of the E2 Component 18
F. Schümann, F. Hammache, S. Typel, Z. Sun, F. Uhlig, K. Sümmerer, S233 Coll.

Coulomb Breakup of the One-Neutron Halo Nucleus ^{11}Be 19
R. Palit, T. Aumann, K. Boretzky, D. Cortina, U. Datta Pramanik,Th.W. Elze, H. Emling, H. Geissel, A. Grünschloß, M. Hellström, S. Ilievski, N. Iwasa, K.L. Jones, J.V. Kratz, R. Kulessa, Y. Leifels, A. Leistenschneider, E. Lubkiewicz, G. Münzenberg, P. Reiter, C. Scheidenberger, H. Simon, K. Sümmerer, E. Wajda, W. Walus

Fragmentation of Unstable Neutron-Rich Oxygen Beams 20
A. Leistenschneider, T. Aumann, K. Boretzky, L.F. Canto, B.V. Carlson, D. Cortina,
U. Datta Pramanik, Th.W. Elze, H. Emling, H. Geissel, A. Grünschloss, K. Helariutta,
M. Hellström, M.S. Hussein, S. Ilievski, K.L. Jones, J.V. Kratz, R. Kulessa, Le Hong Khiem,
E. Lubkiewicz, G. Münzenberg, R. Palit, P. Reiter, C. Scheidenberger, K.-H. Schimdt,
H. Simon, K. Sümmerer, E. Wajda, W. Walus

Production of Light Nuclides in 1 GeV Proton-Induced Fission of ^{238}U 21
M.V. Ricciardi, K. -H. Schmidt, O.Yordanov, P. Armbruster, J. Benlliure, M. Bernas,
A. Boudard, S. Czajkowski, T. Enqvist, R. Legrain, S. Leray, B. Mustapha, M. Pravikoff,
F. Rejmund, C. Stéphan, L. Tassan-Got, C. Volant

Isotopic Production Cross Sections of Fragmentation Residues in Reactions Induced by ^{238}U (1 AGeV) in Deuterium 22
P. Armbruster, J. Benlliure, M. Bernas, A. Boudard, E. Casarejos, S.Czajkowski, T. Enqvist,
R. Legrain, S. Leray, B. Mustapha, M. Pravikoff, F. Rejmund, K.-H. Schmidt, C. Stephan,
J. Taieb, L. Tassan-Got, C. Volant, W.Wlazlo

Determination of the Freeze-Out Temperature with the Isospin Thermometer 23
K.-H. Schmidt, M.V. Ricciardi, A. Botvina, T. Enqvist

Effects of Dissipation and Simultaneous Break-Up on Fission at High Excitation Energies 24
B. Jurado, K.-H. Schmidt, A. R. Junghans, J. Benlliure

Theory

Low Momentum Nucleon-Nucleon Interaction and Fermi Liquid Theory 25
A. Schwenk, G.E. Brown, B. Friman

Short-Range Repulsive and Tensor Correlations in Nuclei 26
T. Neff, H. Feldmeier

Two- and Three-Body Halos in Helium and Lithium Isotopes 27
M. Tomaselli, S. Fritzsche, A. Dax, H.-J. Kluge, T. Kühl, L.C. Liu, D. Marx, M. Mutterer,
S.R. Neumaier, W. Nörtershäuser, I. Tanihata, H. Wang

A Nuclear Point-Coupling Model and its Applications 28
T. Bürvenich, T. Cornelius, A. Sulaksono, P.-G. Reinhard, J. A. Maruhn, D.G. Madland,
W. Greiner

Self-Consistent Calculations of Surface Vibrations 29
T. Cornelius, M. Bender, T. Bürvenich, P. Fleischer, P.-G. Reinhard, J.A. Maruhn,
W. Greiner

Entrance-Channel Potentials in the Syntheses of the Heaviest Nuclei 30
V.Yu. Denisov, W. Nörenberg

Nuclear Matter

Multifragmentation

Transverse Velocity Scaling in Au+Au Midrapidity Emissions 31
J. Lukasik, W. Trautmann, INDIRA-ALADIN Coll.

Statistical Multifragmentation of Non-Spherical Sources in Au+Au 32
A. Le Fèvre, INDRA-ALADIN Coll.

Mechanisms Behind the Rise and Fall of Sideflow at SIS Energies 33
W. Reisdorf, A. Andronic, A. Devismes, Ch. Finck, A. Gobbi, O. N. Hartmann, N. Herrmann, K. D. Hildenbrand, Y. J. Kim, T. Kress, Y. Leifels, Z. Tyminski, FOPI Coll.

Highly Excited Hadron Matter

Flow Intensity Fields in Heavy Ion Collisions 34
W. Reisdorf, A. Andronic, A. Devismes, Ch. Finck, A. Gobbi, O. N. Hartmann, N. Herrmann, K. D. Hildenbrand, Y. J. Kim, T. Kress, Y. Leifels, Z. Tyminski, FOPI Coll.

Pion Production at SIS Energies 35
M.R. Stockmeier, W. Reisdorf, N. Herrmann, M. Merschmeyer, D. Pelte, K. Wisniewski, FOPI Coll.

First Measurements of Antikaons in Proton-Nucleus Collisions at SIS Energies 36
W. Scheinast, I. Böttcher, M. Debowski, F. Dohrmann, A. Förster, E. Grosse, B. Kamys, P. Koczon, B. Kohlmeyer, F. Laue, M. Menzel, L. Naumann, H. Oeschler, F. Pühlhofer, Ch. Schneider, E. Schwab, P. Senger, Y. Shin, H. Ströbele, Ch. Sturm, G. Surowka, F. Uhlig, KaoS Coll.

Kaon and Antikaon Production in Au + Au Collisions at 1.5 AGeV 37
A. Förster, I. Böttcher, E. Grosse, P. Koczon, B. Kohlmeyer, S. Lang, M. Menzel, L. Naumann, H. Oeschler, M. Ploskon, F. Pühlhofer, W. Scheinast, A. Schmah, T. Schuck, E. Schwab, P. Senger, Y. Shin, H. Ströbele, C. Sturm, F. Uhlig, A. Wagner, W. Walus, KaoS Coll.

Progress Report from the Commissioning of HADES 39
HADES Coll.

Nucleus-Nucleus Collisions at Ultrarelativistic Energies

Results on Particle Yields, Fluctuations, and Correlations from NA49 43
C. Blume, R.Bramm, P. Buncic, P. Dinkelaker, M. Gazdzicki, T. Kolleger, I. Kraus, A. Mischke, R. Renfordt, A. Sandoval, H. Sann, R. Stock, H. Stroebele, A. Wetzler, J. Zaranek, NA 49 Coll.

Bose-Einstein Correlations of Charged Kaons in Central Pb+Pb Collisions at 158 AGeV 47
I.-K. Yoo, C. Blume, R. Bramm, P. Buncic, P. Dinkelaker, M. Gazdzicki, T. Kolleger, I. Kraus, A. Mischke, R. Renfordt, A. Sandoval, H. Sann, R. Stock, H. Stroebele, A. Wetzler, J. Zaranek, NA49 Collaboration

CBM Future: A Detector for Antiproton Physics 48
Q.X. Hartmann. U. Lynen, H. Orth, C.Schwarz, S. Ganzhur, V. Hejny, H. Koch, K. Peters, **H.L. Roman.** U. Wiedner

Measuring Jets with ALICE 51
D. Miskowiec. P. Braun-Munzinger

Theory

Stability and Instability of a Hot and Dilute Nuclear Droplet: Dissipative Isoscalar Modes 52
W. Nörenberg, G. Papp, P. Rozmej

Isoscaling and its Statistical Interpretation 53
A.S. Botvina, W. Trautmann

Signatures of the Liquid-Gas Phase Transition in Multifragmentation 54
Al. H. Raduta, Ad. R. Raduta

Chiral Dynamics of Nuclear Matter 55
S. Fritsch, N. Kaiser, W. Weise

Determination of the Equation of State of Dense Matter 56
P. Danielewicz, R. Lacey, W.G. Lynch

Remarks on Delta Radiative and Dalitz Decays 57
M.I. Krivoruchenko, A. Faessler

Dilepton Production in Heavy Ion Collisions at Intermediate Energies 58
K. Shekhter, A. Faessler, C. Fuchs, M. Krivoruchenko, B. Martemyanov

Quasiparticles in QCD Thermodynamics and Dilepton Radiation 59
R.A. Schneider, T. Renk, W. Weise

π N -> ω N in a Coupled-Channel Approach 60
G. Penner, U. Mosel

Finite Momentum of the π π-Pair in the A(π, 2π) Reaction 61
C. Isselhorst, Z. Aouissat, J. Wambach

Scattering of Photons and Vector Mesons off Nucleons 62
M.F.M. Lutz, Gy. Wolf, B. Friman

The χ-BS(3) Approach 63
M.F.M. Lutz, E.E. Kolomeitsev

Self Consistent Propagation of Hyperons and Antikaons in Nuclear Matter Based on Relativistic Chiral SU(3) Dynamics 64
M.F.M Lutz, C.L. Korpa

Strange Particle Production in Heavy Ion Collisions 65
P. Braun-Munzinger, J. Cleymans, H. Oeschler, K. Redlich

What Determines the K^- Multiplicities at Energies Around 1-2 AGeV? 66
Ch. Hartnack, J. Aichelin, H. Oeschler

Extracting Information on the Nuclear Equation of State from K^+ Production in Heavy Ion Collisions 67
C. Fuchs, A. Faessler, E. Zabrodin

Phi Meson Propagation in a Hot Hadronic Gas 68
L. Alvarez-Ruso, V. Koch

Off-Shell Pions in the BUU Transport Theory 69
A.B. Larionov, S. Leupold, U. Mosel

Equal-Time Formulation for Off-Shell Transport Theory 70
R.A. Ionescu, H.H. Wolter

Renormalization of Self-Consistent Schwinger-Dyson Equations at Finite Temperature 71
H. van Hees, J. Knoll

Non-Equilibrium Time Evolution of Φ^4-Theory in 2+1 Dimensions 72
S. Juchem, W. Cassing

Boson Expansion for Quantum Field Theory 73
Z. Aouissat, J.Wambach

Finite-Temperature Gluon Condensate with Renormalization Group Flow Equations 74
B.-J. Schäfer, O. Bohr, J. Wambach

Cooling of Neutron Stars with Superconducting Quark Matter Cores 75
D. Blaschke, H. Grigorian, D.N. Voskresensky

Understanding Nuclear Effects with QCD 76
J. Hüfner, B.Z. Kopeliovich, A. Schäfer, A.V. Tarasov

Contribution of rho-Mesons to Charge Fluctuations 79
M. Döring, V. Koch

Spectral Function of Quarks in Quark Matter 80
F. Frömel, S. Leupold, U. Mosel

Nonequilibrium Quark Dynamics in Ultrarelativistic Heavy Ion Collisions 81
S. Scherer, M. Hofmann, M. Bleicher, L. Neise, H. Stöcker, W. Greiner

Parton Production Scenarios 82
D.D. Dietrich, G.C. Nayak, W. Greiner

Partonic Scattering in the Pre-equilibrium Stage of the Gluonic Minijet Plasma 83
J. Ruppert, D.D. Dietrich, G.C. Nayak, H. Stöcker, W. Greiner

Decay properties of ^{269}Hs and evidence for the new nuclide ^{270}Hs

A. Türler, Ch.E. Düllmann, H.W. Gäggeler, S. Soverna (Univ. Bern & PSI), R. Dressler, B. Eichler, F. Glaus, D.T. Jost, D. Piguet (PSI), T.N. Ginter, K.E. Gregorich, U. Kirbach, D.M. Lee, R. Sudowe, (LBNL), D.C. Hoffman, H. Nitsche, J.B. Patin, P. Zielinski (UC Berkeley & LBNL), W. Brüchle, R. Eichler, E. Jäger, V. Pershina, M. Schädel, B. Schausten, E. Schimpf, H.-J. Schött, G. Wirth (GSI), S.N. Timokhin, A.B. Yakushev (FLNR), K. Eberhardt, P. Thörle, N. Trautmann (Univ. Mainz), Z. Qin (IMP Lanzhou), A. Vahle (FZ Rossendorf)

Three decays of the nuclide ^{269}Hs were observed by Hofmann et al. [1,2] as grand daughter of ^{277}112. The deduced relatively long half-life of about 10 s makes ^{269}Hs an ideal candidate for first chemical experiments with hassium (element 108). ^{269}Hs can be produced directly in the reaction ^{248}Cm(^{26}Mg, 5n). In the 4n de-excitation channel, the new nuclide ^{270}Hs is produced, which was predicted to be the next heavier "doubly-magic" nucleus after ^{208}Pb [3]. Its decay properties are of great interest to nuclear physics.

In order to investigate the chemical properties of Hs, the gas chromatographic separation system IVO (In situ Volatilization and On-line detection) [4] and the cryo on-line detector (COLD) [5] were set up at the rotating target- and window irradiation facility of the UNILAC at GSI Darmstadt. Hs is expected to belong to group 8 of the periodic table of the elements and should thus form very volatile HsO_4 molecules. Test experiments with short-lived Os isotopes, the lighter homologue element of Hs, showed that OsO_4 molecules were formed when the recoiling Os nuclei were stopped in a mixture of He and O_2.

In the course of the experiment, data was collected during 64.2 h and a beam integral of 1.0×10^{18} ^{26}Mg ions was accumulated. The count rate in all detectors was very low. Only the nuclides ^{219}Rn, ^{220}Rn, ^{211}At and their decay products were identified after chemical separation. While ^{211}At (and its decay product ^{211}Po) was deposited mainly in the first two detectors, ^{219}Rn and ^{220}Rn and their decay products accumulated in the last three detectors, where the temperature was low enough to condense Rn. Due to a defect, one side of detector sandwich 1 was not operating and was therefore excluded from the data analysis. The average count rate per detector pair was 0.6 h^{-1} in the relevant α-decay energy window E_α=8.0-9.5 MeV in detectors 2 through 9.

The data analysis revealed one four-member- and 4 three-member decay chains (Fig. 1) which all occurred within a time period of less than 70 s and which all have random probabilities of less than 7×10^{-5}. Since only about 77% of the inner surface of the COLD channel consisted of active detector surface, detection of a few incomplete decay sequences is expected. Two α–SF correlations were observed in detectors 3 and 4 that still have a rather low random probability, but could not be assigned with certainty to ^{269}Hs or ^{270}Hs. Also, 4 uncorrelated SF decays with fragment energies >50 MeV were registered in detectors 2, 3, and 4. Only for one SF both fragments were observed. All other detectors 5 through 12 registered zero SF events. The 4-member and the 3-member α-decay chains were attributed to the decay of the nuclide ^{269}Hs, since these almost perfectly match the decay properties observed previously by Hoffman et al. [1] (except for the low α-decay energy of ^{269}Hs in the three member decay chain). Three decay chains were terminated by spontaneous fission. From the previously known decay data such a signature would be expected only for the decay of the new nuclide ^{270}Hs. But, one of the terminating SF events had a rather long life-time of 7.9 s, which is not very likely for ^{262}Rf with a half-life of 2.1 s. A similar decay sequence has also been observed in one of the decay chains assigned to ^{277}112 [2]. Therefore, this chain was attributed to ^{269}Hs. Noteworthy are the very unusual decay properties of ^{261}Rf [6]. We tentatively assigned the remaining two decay chains to the new nuclide ^{270}Hs. From the measured E_α=9.16±0.03 MeV an α-decay half-life of 2-7 s was estimated.

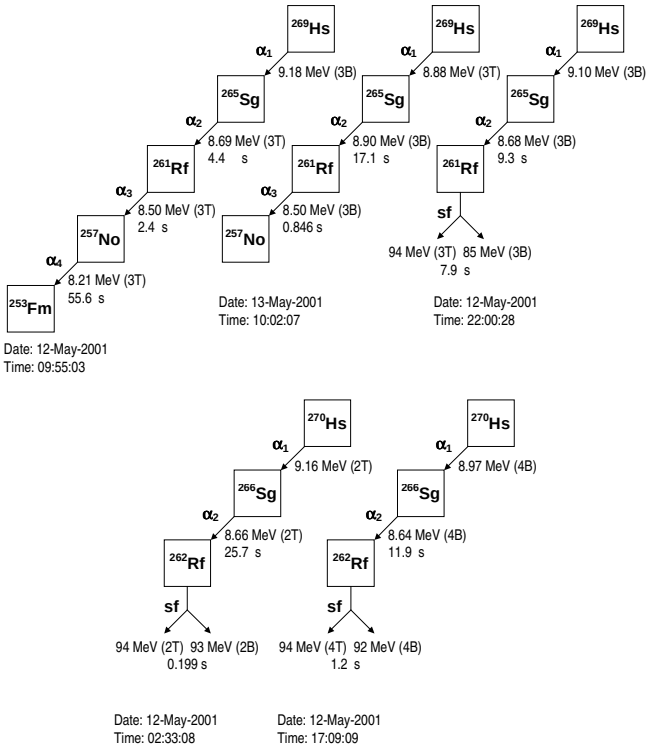


Fig. 1: Decay chains attributed to the decay of Hs-nuclides.

References

[1] S. Hofmann et al., Z. Phys. **A354,** 229 (1996).

[2] S. Hofmann et al., Rev. Mod. Phys. **72,** 733 (2000).

[3] Z. Patyk et al., Nucl. Phys. **A533,** 132 (1991).

[4] Ch.E. Düllmann et al., Nucl. Instrum. Meth. **A479**, 631 (2002)

[5] Ch.E. Düllmann et al., this Annual Report

[6] R. Dressler et al., PSI Scientific Report 2001, Vol. I (2002).

An EC-branch in the decay of 27-s ^{263}Db: Evidence for the new isotope ^{263}Rf

J.V. Kratz[1], A. Nähler[1], U. Rieth[1], A. Kronenberg[1], B. Kuczewski[1], E. Strub[1], W. Brüchle[2], M. Schädel[2], B. Schausten[2], A. Türler[3], H. Gäggeler[3], C. Laue[4], R. Sudowe[4], P.A. Wilk[4]
[1]Institut für Kernchemie, Johannes Gutenberg-Universität Mainz, 55099 Mainz, Germany
[2]Gesellschaft für Schwerionenforschung, 64291 Darmstadt, Germany
[3]Paul Scherrer Institut, 5232 Villigen, Switzerland
[4]Lawrence Berkeley National Laboratory, Berkeley, CA 94720, USA

The first hint for ^{263}Rf was reported by Czerwinski et al. who detected 7 spontaneous fission (SF) events with a half life of 500^{+300}_{-200} s in rutherfordium fractions separated by manual TTA extractions from the ^{248}Cm(^{18}O, 3n) reaction at 92.5 MeV [1]. No α events could be attributed to ^{263}Rf.

In 1990, we discovered the new isotope 27-s ^{263}Db in the ^{249}Bk(^{18}O, 4n) reaction at 93 MeV by eluting element 105 from cation exchange columns in unbuffered 0.05 M α-HiB [2].

In 1993, a rutherfordium fraction was milked from ^{263}Db, and 22 SF events were registered in that fraction. Of these, 8.8 events had to be assigned to a contamination by ^{256}Fm. A two-component decay curve with the ^{256}Fm fixed gave a half life of 10^{+5}_{-3} min for the isotope ^{263}Rf [3]. Based on the effective production cross section, an EC-branch in ^{263}Db on the order of 5% was deduced [3]. Two α particles at 7.9 MeV were discussed as possibly being associated with the decay of ^{263}Rf giving an upper limit for the α-decay branch of 30%.

A search for ^{263}Rf in the ^{248}Cm(^{22}Ne, α3n) reaction at 122 MeV by Dressler et al. [4] involving a chemical separation of Rf as the volatile tetrachloride yielded two α particles at 7.8 and 7.9 MeV and four SF events with very long life times. Another search using the same reaction and aqueous chemistry with fluoride complexes of Rf [5] yielded two α events near 7.9 MeV with unusually long life times. This was not considered to present conclusive evidence for ^{263}Rf [4],[5].

We have attempted to add further evidence for an EC-branch in the decay of ^{263}Db and for ^{263}Rf in an experiment at the Paul Scherrer Institute (PSI), Switzerland, producing again ^{263}Db in the ^{249}Bk(^{18}O, 4n) reaction at 93 MeV. The activity was transported by a He/KCl jet and collected for 15 min on a Ta disc. It was dissolved in 2 x 20 µl of unbuffered 0.5 M α-HiB and added on top of a 3 x 50 mm cation-exchange column (AG 50Wx8). The α-HiB solution contained ^{88}Zr tracer for the determination of the chemical yield for group-4 elements. These were eluted from the column with 1 ml 0.5 M α-HiB. The eluate was mixed with 3 ml 12 M HCl yielding a solution being 9 M in HCl. This was subject to liquid-liquid extraction with 200 µl of 20 vol% TBP/Cyclohexane which, after phase separation, was evaporated to dryness on a Ta disc. The Ta discs were assayed for α and SF activity starting about 8 min after the end of collection. The He/KCl jet efficiency was about 50%, the chemical yields were 70% on the average. The decontamination factor for Fm was on the order of 10^4.

In some 200 experiments, a total of 9 SF events was registered of which 2 have to be considered a long-lived background. The life times are consistent with a half life of ^{263}Rf of about 22 min with an uncertainty of ±5 min. Relative to the measured cross section for production of ^{263}Db in the ^{249}Bk(^{18}O, 4n) reaction at 93 MeV, 10±6 nb [2], the new experiments give an EC-branch in the decay of ^{263}Db of

$$3^{+4}_{-1}\%$$

and provide additional evidence for the new isotope ^{263}Rf. The latter decays predominantly by spontaneous fission with a long half life of tens of minutes. In principle, the observation of α particles from the α-decay daugther of ^{263}Rf, ^{259}No (7.472 – 7.689 MeV), could help to fix the α-decay branch in the decay of ^{263}Rf. However, this part of the spectrum is masked by a contamination with the naturally occuring ^{214}Po (7.687 MeV). The picture that consistently emerges from [3] and the present work is shown in Fig.1.

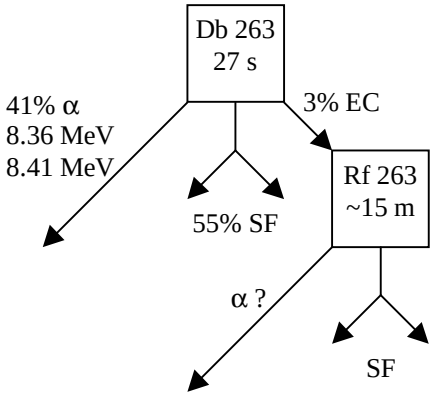


Fig.1 Decay scheme for ^{263}Db and ^{263}Rf

References

[1] K.R. Czerwinski et al., Annual Report 1991 LBL-32855, p.54

[2] J.V. Kratz et al., Phys.Rev. C45, 1064 (1992)

[3] K.E.Gregorich et al., GSI Scientific Report 1994, GSI 94-1, p.14

[4] R. Dressler, Doctoral thesis, Universität Bern 1999

[5] D. Schumann et al., PSI Annual Report 1999, p.7

α - γ - decay studies of ^{253}No

F.P.Heßberger[1], S. Hofmann[1], D. Ackermann[1,2], A.G. Popeko[3], S. Saro[4], A.V. Yeremin[4] .

[1]GSI, Darmstadt, Germany, [2]Johannes Gutenberg - Universität, Mainz, Germany,
[3]FLNR JINR, Dubna, Russia, [4]Comenius University, Bratislava, Slovakia

In a previous decay study of ^{257}Rf at SHIP [1] we also performed α-γ - coincidence measurements for the daughter nucleus ^{253}No. This isotope was recently studied at the RITU - separator in Jyväskylä using the reaction ^{207}Pb(^{48}Ca,2n)^{253}No [2]. Three γ - lines of 152, 222 and 280 keV were observed in coincidence to α - decays attributed to ^{253}No [2]. Although our rate of nuclei was considerably lower we observed few α-γ-coincidences which confirmed the results of [2] (Fig.1 and Tab.1).

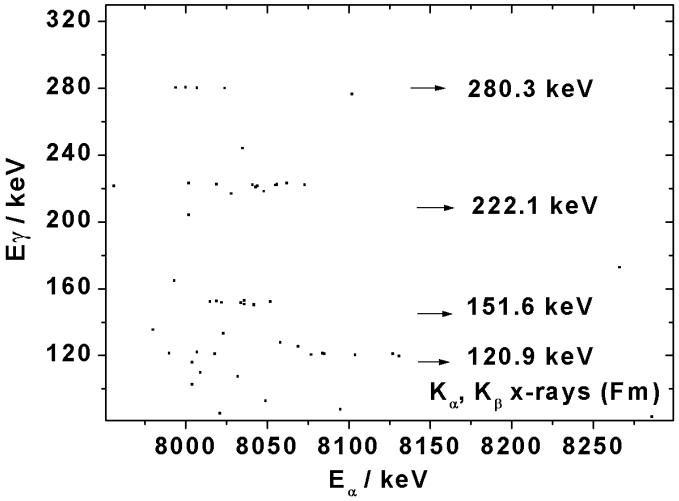


Figure 1: α-γ-coincidences assigned to the decay of ^{253}No.

The line at 120.9 keV is close to the value of 121.058 keV [3] expected for the $K_{\alpha 1}$ x-rays of Fm. Thus we interpret this line as x-rays emitted after K- conversion, while the other three lines are attributed to γ - transitions from one or several nuclear levels populated by the α - decay.

E_γ / keV	E_α / keV	events
280.3 ± 0.2	8006 ± 13	4
222.1 ± 0.7	8054 ± 11	8
	8010 ± 12	2
	7956	1
	7785	1
151.6 ± 0.6	8040 ± 7	6
	8019 ± 4	3
120.9 ± 0.6	8121 ± 15	3
	8082 ± 4	3
	8005 ± 14	3

Table 1: Summary of α - γ - coincidences for ^{253}No

The energy of the α - decays from ^{253}No is essentially located in a broad distribution at E_α = (7990-8080) keV with ΔE (FWHM) = 71 keV[1] at a detector resolution of 20 keV (FWHM), indicating a strong influence due to energy summing with conversion electrons. This broad distribution was divided into three lines in [1] (see Tab. 2), which roughly agree with those coincident to the γ - rays. The hindrance factors are small, indicating favoured transitions. So, tentatively, we assign the γ - lines to the decay into the ground state band of ^{249}Fm from a level which is populated by the favoured α - transition from ^{253}No (see Fig. 2).

E_α / keV	i_{rel}	$T_{1/2}$ / s	$T_{\alpha,calc}$ /s	HF
8033 (average)	0.92 ± 0.02	77 ± 5	53	1.5
8011	0.33 ± 0.03	80 ± 9	62	3.9
8038	0.31 ± 0.03	74 ± 9	49	4.8
8063	0.28 ± 0.03	72 ± 8	29	9.6
8114	0.08 ± 0.02	83 +24/-15		

Table 2: α - decay energies assigned to ^{253}No [1].

Using level assignments 9/2$^-$[734] and 7/2$^+$[624] known for ground states of the lighter N = 151 (^{251}Fm, ^{249}Cf, ^{247}Cm) and N = 149 (^{247}Cd, ^{245}Cm, ^{243}Pu) isotones, respectively [3], we obtain the decay scheme shown in Fig. 2.

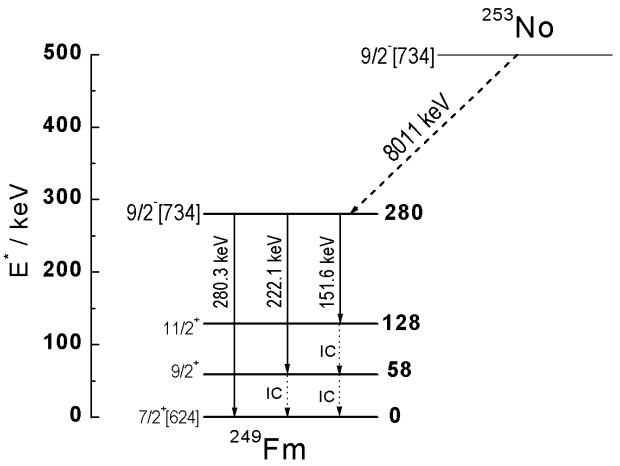


Figure 2: Tentative decay scheme of ^{253}No

This assignment is preliminary since a) measurements of conversion electrons [2] cannot exclude the multipolarity E2 for the 280.3 keV γ-transition, which is in conflict with E1 expected for a 9/2$^-$ → 7/2$^+$ - transition, b) the measured sum energy, obtained from few events, of the α - particles and conversion electrons coincident to E_γ = 151.6 keV is lower than of those coincident to E_γ = 222.1 keV. However, according to Fig. 2 we would expect just the opposite result. Thus more sensitive measurements are necessary for a final assignment.

References

[1] F.P. Heßberger et al. Z. Phys. A 359, 415 (1997)
[2] R.-D. Herzberg, private communication, 2001
[3] R.B. Firestone et al. Table of Isotopes, Wiley & Sons Inc. New York, Chicester, Brisbane, Toronto, Singapore 1996

Decay study of ^{50}Ni

C. Mazzocchi[a,b], C. Bingham[c], B. Blank[d], M. Chartier[e], H. Geissel[a], J. Giovinazzo[d], E. Grodner[a], R. Grzywacz[f], M. Hellström[a], Z. Janas[f], J. Kurcewicz[f], A.S. Lalleman[d], I. Mukha[a], M. Pfützner[f], C. Plettner[a], E. Roeckl[a], K. Rykaczewski[g], K. Schmidt[h], M. Stanoiu[i], J.-C. Thomas[d]

[a]GSI, [b]Univ. Milano, [c]Univ. Tennesee, [d]CENBG Bordeaux, [e]Univ. Liverpool, [f]Univ. Warsaw, [g]ORNL, [h]Univ. Edinburgh, [i]GANIL

A few years ago, the very neutron-deficient isotope ^{50}Ni ($T_Z = -3$) has first been identified as a product of a fragmentation reaction and a lower limit of about 200ns was determined for its half-life [1]. This implies that the isotope is either stable against proton emission or has a very small Q value for this decay mode. Its production cross section was determined to be $(6.1^{+3.3}_{-3.0})\cdot 10^{-8}$ mb for the reaction induced by a 650A MeV ^{58}Ni beam on a ^{9}Be target, but no spectroscopic information could be gained. Based on these results, ^{50}Ni is expected to disintegrate mainly by β^+/EC decay, with a Q_{EC} value estimated to be 13400 keV [2] or 14600 keV [3]. Since its β-decay daughter ^{50}Co is predicted to be proton unbound by 90 keV [2], all ^{50}Co levels populated in β decay of ^{50}Ni should promptly emit a proton. From a comparison with the mirror nucleus ^{50}V [4], the spin and parity of ^{50}Co ground-state can be tentatively estimated to be (6^+). Thus, one expects the population of the ^{50}Co ground-state in ^{50}Ni (0^+) decay to be weak and the branching ratio for β-delayed protons (βp) to be of the order of 100 %.

In this contribution we report on preliminary results from a first spectroscopic investigation of ^{50}Ni. This isotope was produced in the fragmentation reaction of a ^{58}Ni beam at 650A MeV on a 4 g/cm^2 thick ^{9}Be target, and separated by means of the FRS at GSI. The average beam intensity ammounted to about $3\cdot 10^8$ ^{58}Ni ions per SIS spill. The identification of the fragments was accomplished on the basis of the scatter plot Z versus A/q. In order to get an unambiguos identification, i.e. to suppress background events originating from reaction products closer to the β-stability line, the time-of-flight was measured between the third and fourth focal plane of the FRS, additionally to determining it in the normal way, i.e. between the second and fourth focal planes. At the final FRS focus, the fragments were implanted into a telescope of 8 silicon surface-barrier detectors, each 300 μm thick. The energy resolution amounted to 250 keV for 1.9 MeV βp. Out of a total of 77 ^{50}Ni ions identified at the final FRS focus during the measurement time of 36 hours, 41 were implanted in the telescope. The implantation of such energetic ions leads to saturation of standard preamplifiers for a few hundreds of μs. In order to overcome this problem, a new type of preamplifier has been developed at GSI [5]. They are "blocked" for 2 μs at the beginning of the implantation. In this way the large charge generated by the implantation does not overload the preamplifier which thus can still have the large amplification required for spectroscopy studies.

The preliminary βp energy spectrum of ^{50}Ni, as shown in Figure 1, was obtained by requiring that a low-energy signal was recorded within 100 ms after the implantation of a ^{50}Ni ion. The group of protons that are concentrated around 3−4 MeV could be emitted from the isobaric analog state (I^π=0^+, T=3) and neighboring 1^+ levels in ^{50}Co. By assuming an efficiency of (84±8) % for βp detection and by taking into account the 26 βp events recorded and the 41 ^{50}Ni ions implanted, a branching ratio of (75±20) % was tentatively estimated.

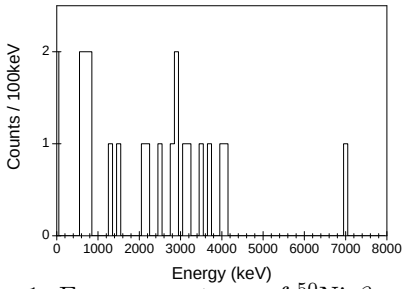


Figure 1: Energy spectrum of ^{50}Ni βp events.

The time distribution of the ^{50}Ni βp data was obtained by evaluating the time difference between the implanted ^{50}Ni ion and the subsequent βp event. The highest rate was 1 event per hour; this is perfectly compatible with the correlation technique applied for half-lives in the 1-100 ms range. The preliminary time spectrum obtained in this way is displayed as Figure 2. The mean life was obtained by applying the maximum likelihood method to an exponential distribution [6]. The best estimate of the mean life is in this case given by the arithmetic average of the time intervals and the uncertainties were estimated according to [6] for an exponential distribution. Its preliminary value was to be $12^{+3.1}_{-2.1}$ ms corresponding to $T_{1/2}$=$8.7^{+2.1}_{-1.5}$ ms.

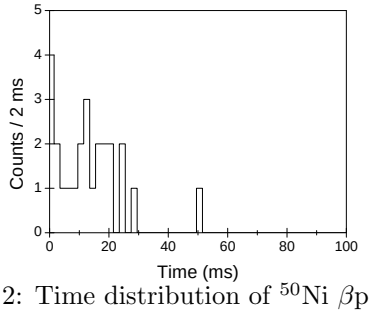


Figure 2: Time distribution of ^{50}Ni βp events.

References

[1] B. Blank et al., Phys. Rev. C **50** (1994) 2398
[2] G. Audi et al., Nucl Phys. A **624** (1997) 1
[3] P. Möller et al., ADNDT **66** (1997) 131
[4] R. Firestone, Table of Isotopes, J. Wiley & Sons, 1996
[5] E. Badura, private communication
[6] K.-H. Schmidt et al., Z. Phys. A **316** (1984) 19

Decay spectroscopy of the N=Z+1 odd-mass nucleus ^{79}Y

J. Döring[1], S.L. Tabor[2], L. Batist[3], R. Borcea[1], H. Grawe[1], Z. Janas[1,4], M. Kavatsyuk[1], R. Kirchner[1], C. Mazzocchi[1,5], I. Mukha[1], J.R. Pavan[2], C. Plettner[1,6], A. Płochocki[4], E. Roeckl[1], B. Salvachúa[1], M. Wiedeking[2]

[1]GSI, D-64291 Darmstadt, [2]Florida State Uni., FL-32306 Tallahassee, [3]PNPI, RU-188-350 Gatchina, [4]Warsaw Uni., PL-00681 Warsaw, [5]Uni. of Milan, I-20133 Milan, [6]FZR, D-01314 Dresden

The proton-rich odd-mass strontium ($Z = 38$) and yttrium ($Z = 39$) nuclei are well known to exhibit a large prolate-deformed nuclear shape [1] due to the occupation of the intruder orbitals from the $d_{5/2}$ and the high-j $g_{9/2}$ subshells by the unpaired proton and/or neutron. The deformed shapes are well-stabilized by the $Z = 38$ gap in the single-particle energies. This gives rise to low-lying states which may form bandheads of rotational-like collective structures. Over the last decade, many of such collective bands of positive and negative parity built on low-lying prolate-deformed states have been identified in ^{79,81}Sr from in-beam work, see e.g., Ref. [2]. One of them, a highly-deformed band originating from the $1/2^+[431]$ Nilsson orbital, has been observed only in ^{81}Sr at a bandhead energy of 120 keV [3]. This band exhibits a quadrupole deformation of $\beta_2 \approx 0.4$ which translates into a transition quadrupole moment of $Q_t = 3.5$ eb.

The $1/2^+[431]$ bandhead state is expected in ^{79}Sr at a somewhat higher excitation energy as extrapolated from the single-particle energies for $N = 41$ at large prolate deformation. However, this band has been neither observed in previous in-beam γ-ray experiments to ^{79}Sr nor in ^{79}Y$\rightarrow$^{79}Sr [4, 5] β decay. So far, only preliminary evidence has been presented for a high-spin band built on a $(1/2^+)$ level at 375 keV in ^{79}Sr [6].

Thus, we searched for non-yrast low-lying states in ^{79}Sr populated in the β decay of ^{79}Y by measuring of β-γ and β-γ-γ coincidences on mass-separated sources which, to our knowledge, has not been done so far. Our decay study was carried out at the GSI on-line mass separator by using the ^{46}Ti(^{40}Ca,$\alpha p2n$)^{79}Y fusion-evaporation reaction at 5.3 MeV/nucleon. In order to enhance the separation efficiency of the catcher-ion-source system for yttrium isotopes, the CF_4-fluorination technique was applied [7]. Small addition (partial pressure of 10^{-4} mbar) of CF_4 gas stimulated the production of $^{79}YF_2^+$ molecules at mass 79+38 which were efficiently separated from other reaction products leading to almost chemically pure mass-separated yttrium sources. In order to suppress the longer-lived ^{79}Sr daughter decays ($T_{1/2} = 2.3$ min), the mass-separated ^{79}Y activity ($T_{1/2} = 14.8$ s) was implanted into a tape at rest, measured (grow-in method) and subsequently removed from the measuring position with a cycle time of 64 s. The experimental setup included a plastic scintillator as β detector with an efficiency of about 80% and 15 Ge crystals for detection of γ radiation. An absolute γ-ray efficiency of about 4.5% was obtained for 1.33 MeV γ rays.

Besides the 511 keV annihilation line and the known decay lines at 153, 178 and 1106 keV, many new γ rays were observed. Most of the new transitions have been placed in a much extended decay scheme, see Fig. 1. In this way, a low-lying level structure in ^{79}Sr involving the 375, 443, 597, and 751 keV levels have been firmly established. Spin and positive-parity assignments are based on the apparent β feeding and the observed depopulation pattern.

The nucleus ^{79}Sr is known to show an excitation spectrum of a highly-deformed nuclear ellipsoid. Thus, particle-triaxial-rotor calculations [8] have been performed to further explore the evolution of the nuclear shape and the composition of the wave function to discuss the experimental properties of the low-lying states.

The $3/2^-$ ground state of ^{79}Sr and the $5/2^+$ state at 178 keV are interpreted to originate from the $3/2^-[301]$ and $5/2^+[422]$ Nilsson configurations, respectively, at a well-deformed prolate shape with a quadrupole deformation of $\beta_2 \approx 0.37$ [2]. Based on our model calculations, the $(1/2^+)$ state at 375 keV can be well interpreted as the bandhead of the $1/2^+[431]$ Nilsson orbital, with the levels at 443 and 597 keV being the $3/2^+$ and $5/2^+$ collective band members, respectively. There is only little level mixing between the $1/2^+[431]$ and the $5/2^+[422]$ configurations in the wave functions. Thus, the relatively weak population of the $1/2^+[431]$ band in ^{79}Sr via the β decay from the $5/2^+[422]$ ground state in ^{79}Y requires a $\Delta K = 2$ decay which seems to be retarded.

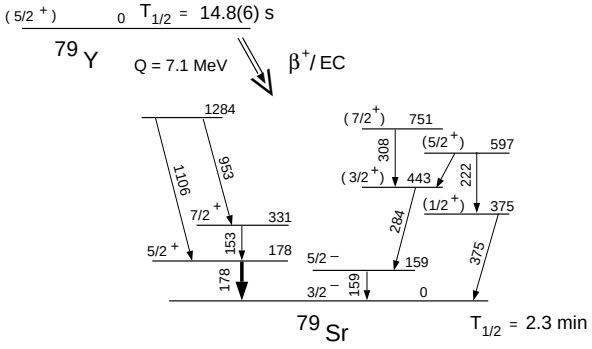


Figure 1: Partial ^{79}Y$\rightarrow$^{79}Sr decay scheme.

The authors appreciate technical support from the GSI mass-separator group, the GSI VEGA group, the FZ Rossendorf and the company ORTEC.

References

[1] C.J. Lister et al., Phys. Rev. Lett. **49**, 308 (1982).
[2] J. Heese et al., Phys. Rev. C **41**, 603 (1990).
[3] E.F. Moore et al., Phys. Lett. B **211**, 14 (1988); Phys. Rev. C **38**, 696 (1988).
[4] H. Grawe et al., Z. Phys. A **341**, 247 (1992).
[5] J. Mukai et al., Z. Phys. A **342**, 393 (1992).
[6] S. Suematsu et al., Kyushu University, Tandem Acc. Lab. Report 1991-1992, p. 72.
[7] R. Kirchner, Nucl. Instrum. Methods in Phys. Res. B **126**, 135 (1997).
[8] I. Ragnarsson and P.B. Semmes, Hyperfine Interac. **43**, 425 (1988).

High-spin β decay of ^{94}Ag

C. Plettner[a], M. La Commara[b], K. Schmidt[a], H. Grawe[a], J. Döring[a], R. Borcea[a], S. Galanopoulos[c], M. Górska[a], S. Harissopulos[c], M. Hellström[a], Z. Janas[a,d], R. Kirchner[a], C. Mazzocchi[a], A. Ostrowski[e], G. Rainovski[f], E. Roeckl[a]

[a]GSI, [b] Univ. and INFN Napoli, [c] N.C.S.R. Demokritos, Athen, [d]Warsaw Univ., [e] Univ. Edinburgh, [f]FZ Rossendorf

The structure of the $N = Z$ nucleus ^{94}Ag, presumably the lightest proton-bound silver isotope, provides information about the proton-neutron interaction in identical orbitals and on possible high-spin isomers if the nucleons couple in stretched configurations. An analogous case is known in ^{52}Fe, one major shell lower than ^{94}Ag, where a 12^+ state originating from the maximum aligned $\pi(1f_{7/2})^{-2}\nu(1f_{7/2})^{-2}$ configuration receives an extra-binding energy which makes it isomeric and thus undergoing β and E4 decay [1].

^{94}Ag has previously been studied at the GSI ISOL by Schmidt et al. [2], who measured a half-life of 0.42(5) s for a β-delayed proton activity. This was assigned to a low-lying isomer. The tentative $J^\pi = (7-9)^+$ assignment for this isomer is one of the topics addressed in the present study. Following the fusion-evaporation reaction

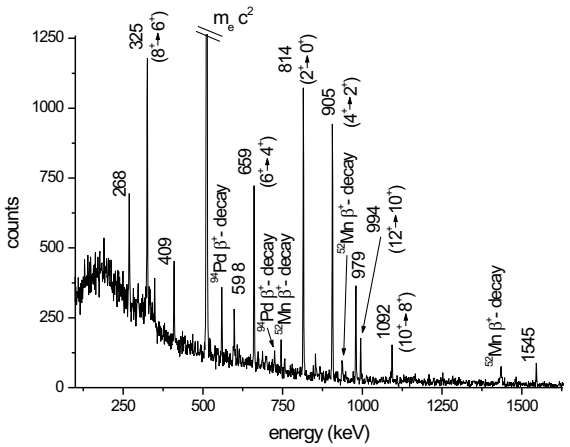


Figure 1: Gamma-ray spectrum in coincidence with positrons at mass $A = 94$. The ^{52}Mn lines represent a contaminant from a previous experiment. The γ rays assigned to the ^{94}Ag decay are marked by transition energies.

^{58}Ni(^{40}Ca,p3n)^{94}Ag, the reaction products were stopped in the hot graphite catcher inside the GSI ISOL ion source. The ^{94}Ag activity was implanted into a tape at rest which moved every 2.4 s. The implantation position was viewed by a $\beta\gamma$ detector set-up. The β-delayed γ rays were registered by a high-resolution Ge array comprising a Super-Clover, a Cluster and a single-crystal Ge detector, yielding a photopeak efficiency of 3.5 % at 1.3 MeV γ-ray energy. To detect β radiation, a plastic scintillator with an efficiency of 85 % was employed. The total measuring time was 14 hours. The intensity of the ^{94}Ag secondary beam at the collection point was estimated to be about 2 atoms/s.

The β-gated γ spectrum is presented in Fig. 1. One can clearly see feeding of the medium spin $J^\pi = (6-8)^+$ states in the daughter ^{94}Pd from the known $J^\pi = (7-9)^+$ isomer. From the strong apparent feeding of the (6^+) and (8^+) states in ^{94}Pd, we assign the parent spin of the β decaying state to be (7^+). The surprising feature of the $\beta\gamma$ spectrum is, however, that states with spins higher than 8^+ were observed. On the basis of $\beta\gamma\gamma$ coincidences we were able to extend the known level scheme of the daughter ^{94}Pd. In addition, half-life information has been deduced by fitting a single-component exponential grow-in function to the data. From the time analysis of all the $\beta\gamma$ lines observed, an average half-life of 0.36(3) s was obtained. This is assigned to ^{94}Ag and is in good agreement with the previous result of 0.42(5) s. If only γ rays deexciting states with $J^\pi \geq 8$ are considered, i.e. transitions possibly originating from the second isomer decay, an average of 0.3(2) s is determined [3]. This is not significantly different from the value of 0.36(3) s, but improved measurements of this type may allow us to identify the higher-lying high-spin isomer.

To understand the microscopic structure of ^{94}Pd, shell-model calculations have been performed in the $1p_{1/2}, 0g_{9/2}$ model space using an empirical interaction. The resulting predictions are compared with the experimental data in Fig. 2. The spin-parity assignment of the potential ^{94}Ag isomer with $J^\pi \geq 15$, not predicted by the shell-model calculations, is the subject of future experiments at ISOL.

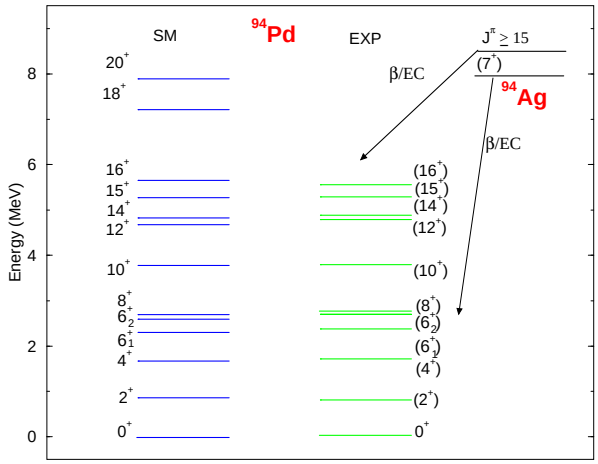


Figure 2: Shell-model calculations for excited ^{94}Pd states in comparison with the corresponding experimental data. The isomeric parent states in ^{94}Ag are also indicated.

References

[1] A. Gadea et al., Proc. Pingst 2000, LUIP 0003, printed by Bloms i Lund, Lund 2000, p 118.
[2] K. Schmidt et al., Z. Phys. A 350 (1994) 99.
[3] M. La Commara et al., to be published.

Gamov-Teller Decay of Nuclei Near ^{100}Sn

A. Stolz[1], T. Faestermann[1], R. Schneider[1], K. Sümmerer[2], E. Wefers[1], J. Friese[1], H. Geissel[2], J. Gerl[2], M. Hellström[2,3], P. Kienle[1], H.-J. Körner[1], M. N. Mineva[3], M. Münch[1], G. Münzenberg[2], C. Schlegel[2], R. S. Simon[2], P. Thirolf[4], H. Weick[2] and K. Zeitelhack[1]

[1]TU München, [2]GSI, [3] University of Lund, [4] LMU München

Neutron deficient nuclei near ^{100}Sn have been produced by fragmentation of a 1 A·GeV ^{112}Sn beam in a beryllium target, separated in the FRS and unambiguously identified. The ions were stopped in the center of a stack of highly segmented silicon strip detectors placed at the final focal plane. This 4π implantation detector measured the total energy of emitted β^+-particles with high efficiency. For measuring γ-radiation the implantation detector was surrounded by a 6-fold segmented NaI detector covering 2π and a Germanium clover detector in close geometry. We determined the half-lives and the positron energies for each implanted nuclide with a maximum likelihood method taking into account three decay generations as well as background events during a fixed correlation time after the implantation. Half-life results for $N \approx Z < 50$ nuclei were already reported [1].

During a run of 60 hours a single ^{100}Sn nucleus could be identified resulting in a production cross section of $\sigma = 1.8$ pb. The decay data of this event together with 6 events observed [2] in 1994 (with ^{124}Xe fragmentation) result in a half-life of $T_{1/2} = 1.0^{+0.54}_{-0.26}$ s and a β end-point energy of $E_{\beta_0} = 3.8^{+0.7}_{-0.3}$ MeV. Due to the low statistics a meaningful comparison between the experimental Gamov-Teller strength and theoretical values is not yet possible.

With the implantation of 2800 ^{102}Sn nuclei we were able to study this nuclide in decay spectroscopy for the first time. Analyzing the correlated β-decay events with a maximum likelihood method the ^{102}Sn half-life was determined as $T_{1/2} = 3.8 \pm 0.2$ s. With the knowledge of the half-life it is possible to calculate the probability that an observed event in a decay chain can be assigned to a decay of the mother istope. Using only decay events with a probability $p > 0.70$ for a ^{102}Sn decay, 8 γ-transitions could be identified that follow the ^{102}Sn $\rightarrow$ ^{102}In decay (see Fig. 1). In the case of electron-capture decay it was possible to observe a 150 keV sum line from conversion electrons of the low energy transitions in the silicon detector (Fig. 1). Considering this additional information and guided by theoretical expectations [3] it is possible to construct a decay scheme which is consistent with all experimental observations: the β-decay feeds two 1^+ states at 1598 keV and 1964 keV with an intensity ratio 70:30. From these states γ cascades lead down to the (7^+) ground state.

The measured β^+ spectrum (Fig. 1) was fitted with two components to levels 366 keV apart and with the relative feeding observed in the γ decay. This determined the endpoint energies to these two levels and also the ground-state decay Q-value as $Q_{\rm EC} = 5760 \pm 90 \pm 50$ keV. The first error is that of the endpoint energy, the second is estimated to take care of the uncertainty in the low energy level scheme of ^{102}In. The summed Gamov-Teller strength of the two individual transitions observed for the ^{102}Sn decay is $B_{\rm GT} = 4.0 \pm 0.6$. This value is among the largest observed in the nuclear chart. The reference strength value, expected for the $\pi g_{9/2} \rightarrow \nu g_{7/2}$ decay of ^{102}Sn on the basis of the extreme single-particle shell model, is $B^{\rm ref}_{\rm GT} = 17.8$, thus leading to a hindrance factor $h = B^{\rm ref}_{\rm GT}/B_{\rm GT} = 4.5$.

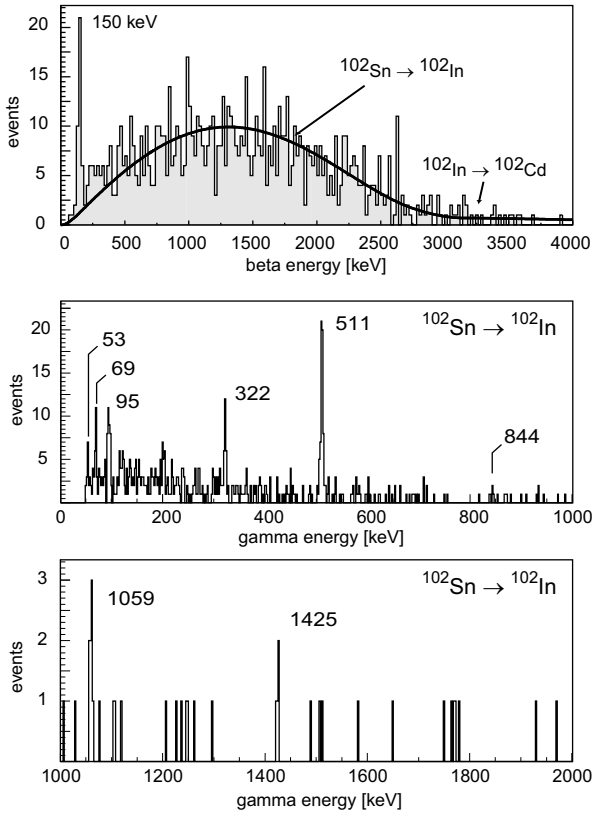


Figure 1: Measured β and γ spectra for the ^{102}Sn decay. Only decay events wich can be assigned to a decay of ^{102}Sn with a probability $p > 0.7$ are shown. In the β spectrum also a line from conversion electrons shows up.

Using the same experimental techniques it was possible to measure the Q-value of ^{98}Cd with high precision ($Q_{\rm EC} = 5430 \pm 40$ keV). Together with the already known decay data [4] the summed Gamov-Teller strength for the four observed transitions results in $B_{\rm GT} = 2.9 \pm 0.2$. This result is in agreement with the published value of $B_{\rm GT} = 3.5^{+0.8}_{-0.7}$ [4].

This work was supported by BMBF (06TM872 TPI) and SFB 375.

References

[1] E. Wefers et al., GSI Scientific Report 2000, p.10
[2] R. Schneider et al., Z. Phys. A348 (1994) 241
[3] B.A. Brown, private communication, 2000
[4] A. Plochocki et al., Z. Phys. A342 (1992) 43

Total Absorption Spectroscopy of the β-decay of ^{148}Tb (2^- and 9^+)

E. Nácher[1], A. Algora[1], B. Rubio[1], D. Cano-Ott[1], J. L. Tain[1], A. Gadea[1], L. Batist[2], R. Collatz[3], H. Grawe[3], M. Hellström[3], Z. Hu[3], Z. Janas[4], M. Karny[4], R. Kirchner[3], P. Kleinheinz[1], F. Moroz[2], E. Roeckl[3], K. Rykaczewski[4], V. Wittman[2]

[1] *IFIC, Valencia (Spain)*, [2] *NPI, St Petersburg (Russia)*, [3] *GSI, Darmstadt (Germany)*, [4] *IEP, Warsaw (Poland)*

There are few examples in the nuclide chart where the Gamow-Teller β-decay can be studied in detail. Among them, the neutron deficient rare-earth region is privileged for several reasons: firstly, most of the Gamow-Teller strength (B_{GT}) is expected inside the Q_{EC} window, secondly, the nuclei are easily accessible through fusion evaporation reactions, and thirdly, the combination of the UNILAC, the On-line Mass-separator and the Total Absorption Spectrometer (TAS) at GSI [1] provides the best experimental conditions to perform this kind of studies. In particular the TAS has shown to be an excellent experimental tool to measure the B_{GT} distribution along the energy window up to Q_{EC} value [2].

A few years ago we reported on studies for the B_{GT} of the 2^- and 9^+ isomers in the nucleus ^{150}Ho (upper part of Fig. 1, and Ref. [3] [4]). Here we present the B_{GT} data for the 2^- and 9^+ isomers in ^{148}Tb, a nucleus with two protons less than ^{150}Ho. In Fig. 1 the resulting B_{GT} observed in the four decays is presented. In the decay of the 2^- and 9^+ isomers of ^{150}Ho we observed a narrow resonance located at $\approx$4.5 MeV in the daughter nucleus (upper part of Fig. 1). This was interpreted as the decay of the $(h_{11/2})^2_{0+}$ pair present in the parent state.

In ^{148}Tb, with only one valence proton (and one valence neutron) outside the ^{146}Gd core, we do not expect to have proton 0^+ pairs with high probability, but a fraction of them could be present due to the scattering of proton pairs across the Z=64 gap. Our observation in the decay of the 9^+ isomer is in good agreement with these expectations. We see a narrow resonance at 4.4 MeV in the daughter nucleus but with less strength than in the ^{150}Ho case: 0.58 $g^2/4\pi$ in the decay of ^{150}Ho(9^+) and only 0.14 $g^2/4\pi$ in the decay of ^{148}Tb(9^+).

One expects the decay of the ^{148}Tb(2^-) isomer to be of similar characteristics, however we did not detect any sizable strength at 4.5 MeV in the daughter nucleus in this case. We observe some strength one MeV higher in excitation energy and very close to the Q_{EC}. The reason for this difference is not yet understood.

Finally, in the decay of the ^{148}Tb(9^+) we observe the decay to the 8^+ two-quasiparticle state in the daughter. The feeding to this state is due to the decay of the valence $\pi h_{11/2}$ present in the parent state. This state is similar to the 8^+ level observed in ^{150}Dy at 2403 keV.

References

[1] M. Karny et al., Nucl. Instr. and Meth. B 126 (1997) 411

[2] A. Algora et al., Nucl. Phys. A654 (1999) 727c

[3] D. Cano-Ott et al., Workshop on *The beta decay, from weak interaction to nuclear structure* (1999) 175, Eds. Ph. Dessagne, A. Michalon and C. Miehe.

[4] D. Cano-Ott, PhD Thesis, Universidad de Valencia (2000)

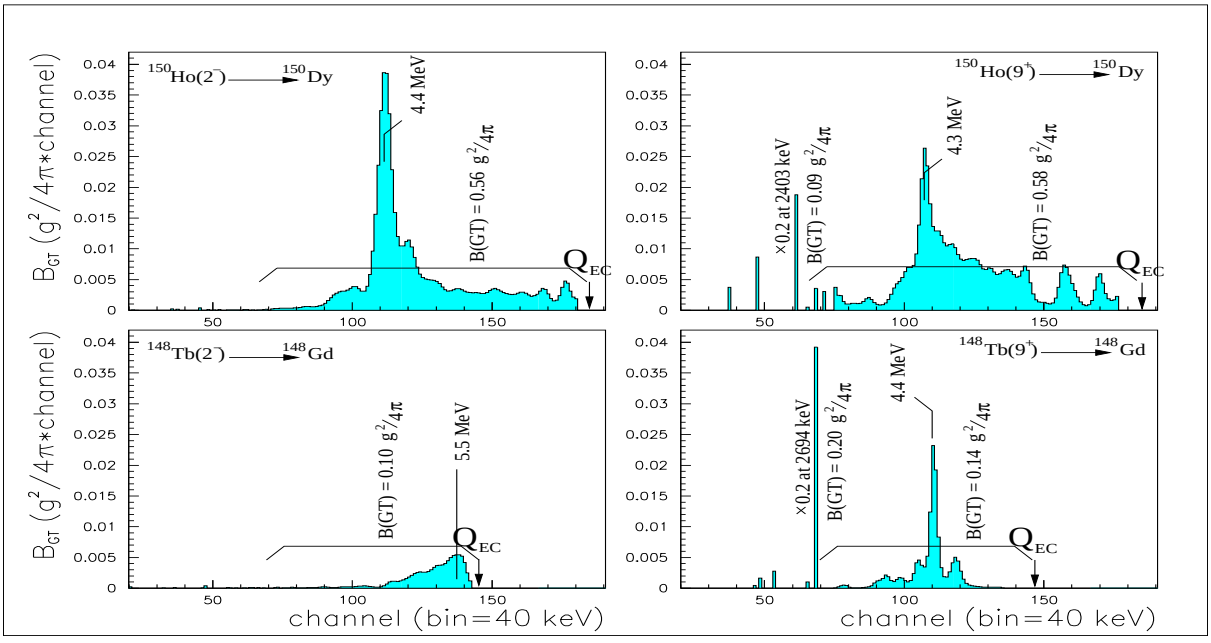


Fig. 1 *Upper panels: Decay of ^{150}Ho (2^- and 9^+) into ^{150}Dy. The resonance at $\approx$4.5 MeV corresponds to the four q.p. excitations in ^{150}Dy. Lower panels: New results on the decay of ^{148}Tb (2^- and 9^+). The reaction to produce the low spin isomer was ^{93}Nb(^{58}Ni,3pβ^+)^{148}Tb(2^-), whereas for the high spin isomer it was ^{94}Zr(^{58}Ni,3pn)^{148}Tb(2^- and 9^+).*

Recent TAS experiments carried out at the On-line Mass-separator in the Rare Earth Region

B. Rubio[1], A. Algora[1], E. Nácher[1], D. Cano-Ott[2], J. L. Tain[1], A. Gadea[3], L. Batist[4], A. Blazhev[5], J. Döring[5], M. Gierlik[6], H. Grawe[5], R. Kirchner[5], P. Kleinheinz[1], I. Mukha[5], C. Plettner[5], E. Roeckl[5], J. J. Valiente[7]

[1] *IFIC, Valencia (Spain)* [2] *CIEMAT, Madrid (Spain)* [3] *LNL INFN, Legnaro, (Italy)* [4] *NPI, St Petersburg (Russia)*

[5] *GSI, Darmstadt (Germany)* [6] *IEP, Warsaw (Poland)* [7] *Surrey Univ., Guildford (UK)*

Following the motivation outlined in our previous contribution [1] we have performed measurements of the $\beta-$decays of the ^{152}Tm and ^{147}Dy by using the Total Absorption Spectrometer at the On-line Mass-separator of GSI. ^{152}Tm, with 2^- and 9^+ $\beta-$decaying isomers, has two more protons compared with the very well studied ^{150}Ho [2]. In a first-order approximation one expects the same Gamow-Teller (GT) strength for the $\pi h_{11/2} \rightarrow \nu h_{9/2}$ transition to the 8^+ 2-quasiparticle state in the daughter nucleus and double as much in the $(\pi h_{11/2})^2_{0^+} \rightarrow (\pi h_{11/2} \nu h_{9/2})_{1^+}$ transition to the 4-quasiparticle states in the daughter as compared with the ^{150}Ho case. In Figure 1 we show the raw TAS spectra obtained for the ^{152}Tm 9^+ and ^{150}Ho 9^+ decays gated on the daughter X-rays. In a "perfect" total absorption spectrometer with 100% efficiency these spectra would directly show the EC-feeding as a function of excitation energy in the daughter nucleus. The real data have to be evaluated but the raw spectra give a rough impression about the direct $\beta-$feeding. The data show indeed that there is more GT strength in the decay to the 4-quasiparticle states (pair decay) in the ^{152}Tm than in the ^{150}Ho case as compared with the decay to the 2-quasiparticle state (at 2.2 and 2.4 MeV in the two daughter nuclei respectively).

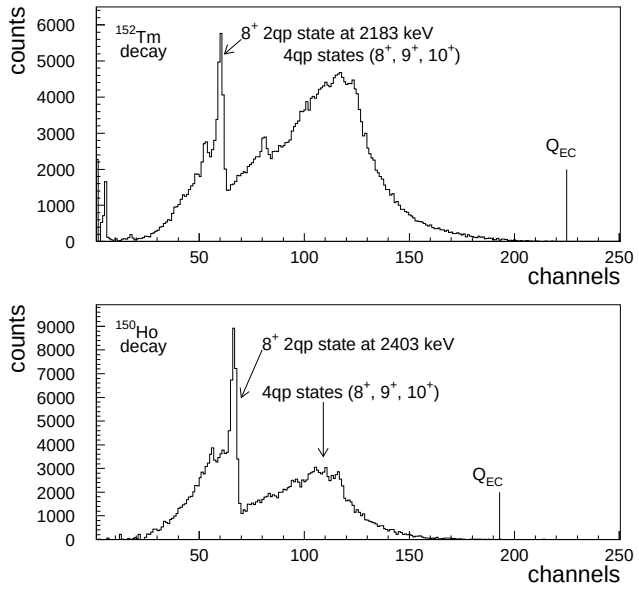


Figure 1: Total absorption EC-spectra obtained for the ^{152}Tm 9^+ and ^{150}Ho 9^+ decays. The nuclei were produced in the $^{102}Pd(^{58}Ni, \alpha 3pn)^{152}Tm(9^+)$ and $^{95}Mo(^{58}Ni, 3p)^{150}Ho(9^+)$ respectively. The contribution of the 2^- decay has been subtracted in both cases.

We also studied the decay of the $1/2^+$ and $11/2^-$ isomers of the N=81 nucleus ^{147}Dy. Most of the decay in these two cases proceeds through the ground-state to ground-state transitions, but some of the GT strength is also expected at high excitation energy in the daughter. These two cases have previously been studied by Collatz *et al.* using Ge detectors [3]. In their work the decay of the proton pair present in the ground state configuration $((\pi h_{11/2})^2_{0^+}(\nu^{-1}s_{1/2}$ or $\nu^{-1}h_{11/2}))$ to 3-quasiparticle states $((\pi h_{11/2}\nu h_{9/2})(\nu^{-1}s_{1/2}$ or $\nu^{-1}h_{11/2}))$ at 3.5 to 5.5 MeV excitation energy in the daughter was observed. Surprisingly the GT strength observed in the decay of the $11/2^-$ isomer was smaller by more than a factor of four than the strength observed in the decay of the $1/2^+$ isomer. It is still unclear if this result reflects the problems inherent to high-resolution techniques. In ref. [3] the authors argue that the problem could be due to the higher level density of ^{147}Tb states with spin $9/2, 11/2$ and $13/2$ and consequently to a higher fragmentation of the GT strength.

Here we present the raw spectrum of the same two decays, but using the powerful total absorption technique. The two resonances, previously observed in ref. [3] are clearly seen in these data (see Figure 2.). The aim of this experiment is to detect and compare the full strength for both decays.

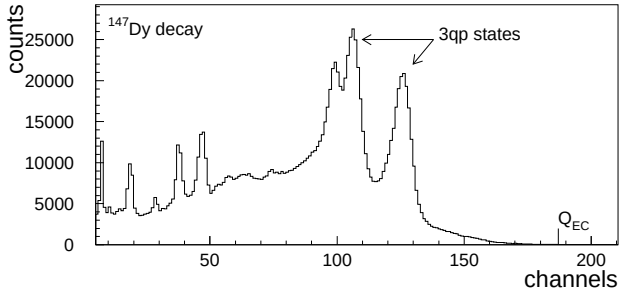


Figure 2: Total absorption EC-spectra obtained for the ^{147}Dy decay. The nucleus was produced through the reaction $^{93}Mo(^{58}Ni, 3pn)^{147}Dy$.

The sorting of these experimental data is being carried out using the new methods developed at GSI, named Go4, which has been adapted to the analysis of the data taken at the On-line Mass Separator. The authors would like to acknowledge the invaluable help of J. Adamczewski in this part of the work.

References

[1] E. Nácher et al., contribution to this annual report
[2] D. Cano-Ott, PhD Thesis, Univ. Valencia, 2000
[3] R. Collatz *et al.*, Z. Phys. A 358 (1997) 241.

Mass and Half-Life Measurements of Stored Exotic Nuclei

Yu.A. Litvinov[1,2], J. Stadlmann[1,3], F. Attallah[1], K. Beckert[1], P. Beller[1], F. Bosch[1], D. Boutin[1], H. Eickhoff[1], M. Falch[4], B. Franczak[1], B. Franzke[1], H. Geissel[1,3], M. Hausmann[1], E. Kaza[1], Th. Kerscher[4], O. Klepper[1], H.-J. Kluge[1], C. Kozhuharov[1], K.E.G. Löbner[4], M. Matoš[1], G. Münzenberg[1], N. Nankov[1], F. Nolden[1], Yu.N. Novikov[1,2], Z. Patyk[1,5], W. Quint[1], T. Radon[1], H. Reich[1], H. Schatz[1], C. Scheidenberger[1], M. Steck[1], Z. Sun[1], L. Vermeeren[1], H. Weick[1], M. Winkler[1], T. Winkler[1], H. Wollnik[3]

[1] GSI, Darmstadt, Germany, [2] State University and PNPI, St. Petersburg, Russia, [3] JLU, Giessen, Germany, [4] LMU, München, Germany, [5] Soltan INS, Warsaw, Poland

1 Time-resolved Schottky Mass Spectrometry

Time-resolved Schottky Mass Spectrometry (SMS) [1, 2, 3] has been applied for direct mass and half-life measurements on neutron-deficient ^{209}Bi fragments, which were separated with the FRS and stored and cooled in the ESR. In this experiment the Schottky noise of the stored ions is recorded continuously. This allows in an off-line FFT analysis to generate frequency spectra which are subsequent in time. In order to achieve a compromise between sufficiently high signal-to-noise ratio and time resolution, each spectrum comprises 30 seconds of measurement time. The mass resolution amounts to $1.5 \cdot 10^{-6}$ (FWHM). The spectra cover the whole acceptance of the ESR, and ultimate sensitivity is reached, i. e., even single ions can be observed. Time-resolved Schottky beam noise analysis can not only be used for mass spectrometry, but it is ideally suited to study dynamic processes in the ESR such as radioactive decays [4]. In particular the decay of mother and the creation of daughter nuclei can be studied, as is illustrated in Fig. 1.

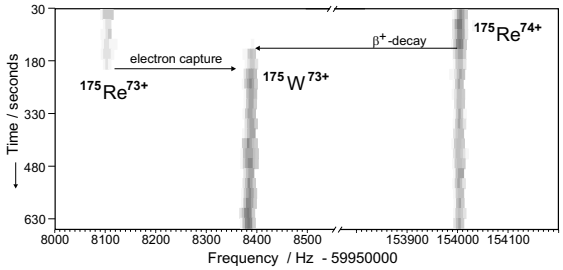


Figure 1: Consecutive 30 s Schottky-noise frequency spectra from top to bottom. The Schottky-noise power density is indicated by the grey-scale. The β^+ decay of a ^{175}Re^{74+} ion is visible, and, 60 seconds later, the electron capture of a single ^{175}Re^{73+} ion to the same daughter nuclide ^{175}W^{73+}.

The noise power of a frequency peak is proportional to the number of ions. This fact allows us to use time-resolved SMS for half-life measurements. Pioneering experiments on the modification of half-lives for bare ions as compared to neutral atoms have been carried out at the ESR [5]. Here we report on so far unobserved half-life modifications of bare isomers: when an isomeric transition is highly converted, the corresponding decay rate will change drastically when the isomer is fully stripped. An example is the isomeric state in the bare ^{151}Er^{68+}, whose measured decay curve is shown in Fig. 2. In the neutral atom this isomeric state ($T_{1/2} = 0.58$ s) decays mainly via internal conversion, because the total conversion coefficient $\alpha_{\rm tot} \simeq 1250$. In the absence of the atomic electron cloud internal conversion is impossible. The theoretically expected half-life for bare ^{151m}Er^{68+} amounts to (16±10) s [6], which is in agreement with the experimentally determined value of (29±14) s in the rest frame of the ion. This value is obtained from the observed decay curve in the laboratory frame (Fig. 2) taking into account charge-changing processes in the residual gas and in the electron cooler and the transformation from the laboratory frame to the rest frame of the ion.

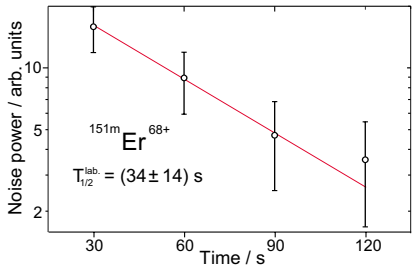


Figure 2: Decay curve of the isomeric state of bare ^{151}Er. The straight solid line is an exponential fit to the data.

The evaluation of half-lives can yield useful information for the proper identification of nuclides, for instance in those few cases, where the assignment from the frequency alone is ambiguous. Another example is shown in Fig. 3, where a single ^{192}Tl^{81+} ion is produced by electron capture of ^{192}Pb^{81+}. The ^{192}Tl has a long-lived isomeric state with an excitation energy $E^* = (160 \pm 50)$ keV, which cannot be resolved. However, the decay scheme [7] shows that ^{192}Pb^{81+} decays with a probability of 99.9943 % to the ground state. Therefore one can safely assign the observed line in Fig. 3 to the ground state of ^{192}Tl.

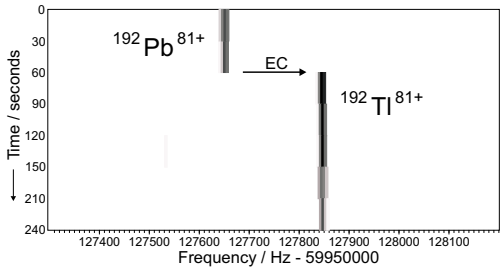


Figure 3: Electron-capture decay of a single stored ^{192}Pb^{81+} ion to ^{192}Tl^{81+}.

Meanwhile all raw data have been analyzed and in the experimental spectra about 194000 lines have been identified finding more than 500 different ion species, more than 200 of them having unknown masses [8].

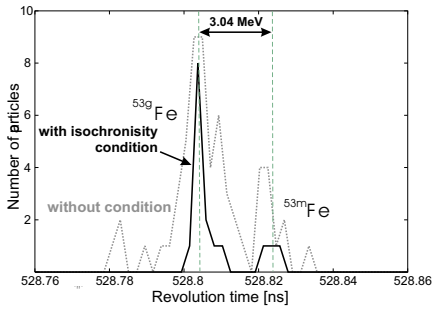


Figure 4: The revolution time spectra of ^{53}Fe illustrate the effect of the isochronicity condition in the data analysis: without this filter a broad and poorly shaped distribution is obtained (dotted line), whereas the application of the filter leads to a clear structure and a distinct separation of the ground and isomeric states(solid line).

2 Isochronous Mass Spectrometry

The masses of neutron-deficient nuclides produced by projectile fragmentation of a 445 MeV/u ^{84}Kr beam in a beryllium target have been measured [9, 10, 11] using isochronous mass spectrometry (IMS) [12, 9]. In this mode cooling is not required, and the ions can be observed for typically 200 μs corresponding to approximately 400 revolutions. The best performance is reached when those particles are rejected from the analysis, whose motion in the ESR is not isochronous thus exhibiting a strong variation of the revolution time, as is illustrated in Fig. 4. The remaining particles fulfill the isochronicity condition [9] very well and for instance the ground and isomeric state of ^{53}Fe are clearly separated. The application of this condition leads to a mass resolving power m/Δm = 110000 (FWHM). The masses of four short-lived nuclides (^{41}Ti,^{44}V,^{45}Cr,^{48}Mn) with half-lives down to values as low as 50 ms have been measured for the first time [10, 11]. In Fig. 5 the new mass values are compared with the values predicted by several mass models, which deviate from the experimental results by up to 2.8 MeV. These new data contribute to put rp-process model calculations for stellar nucleosynthesis on a solid basis, but more measurements in this area are imperative.

Finally, an interesting observation has been made when comparing the present results to literature values for nuclides with known mass [8]. All data are in agreement except for ^{43}Ti, where a clear deviation of almost 300 keV is observed (upper panel of Fig. 6). Looking at the revolution time spectrum and comparing the line shape of ^{43}Ti to that of the other nuclides, significant differences become visible (lower panel of Fig. 6). Since the identification is unambiguous, we interprete this observation as an indication that some of the analyzed 24 particles are in an isomeric state of ^{43}Ti, which is characterized by an excitation energy $E^* = 313$ keV and a half-life of 12.6 μs [17]. This shows that IMS is applicable even to such rapidly decaying nuclides.

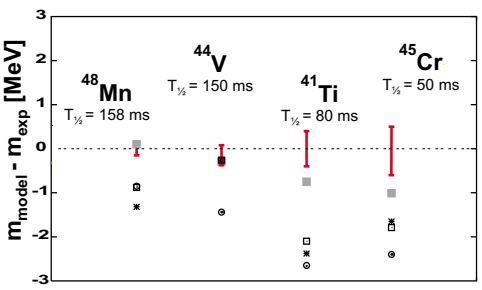


Figure 5: Comparison of new mass values with the predictions of different mass models: ETFSI with SkSc18 (crosses) [13]; HF BCS with MSk7 (open rectangles) [14]; Mac-Mic TF Modell (filled rectangles) [15]; Mac-Mic FRLDM (circles) [16].

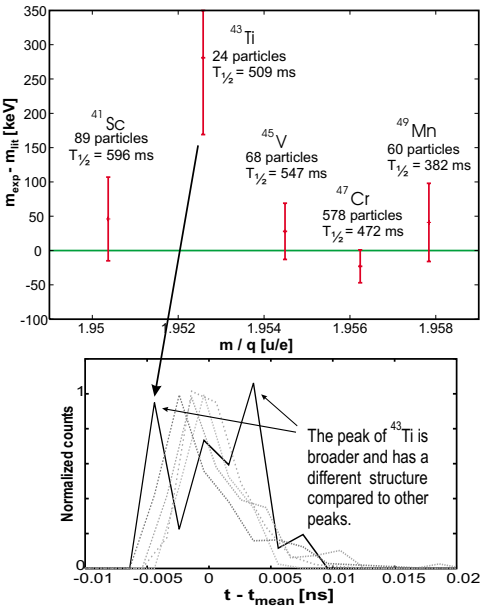


Figure 6: The comparison of the results from IMS to the literature [8] shows good agreement (top panel) except for ^{43}Ti. The bottom panel illustrates that the revolution time peak of this nuclide is broader than similar neighboring lines (in this representation all lines are overlayed by shifting them to the same mean revolution time t_{mean}). Both observations indicate a contamination with an isomeric state.

References

[1] M. Falch, Thesis, LMU München (2000).
[2] T. Radon *et al.*, Nucl. Phys. **A 677** (2000) 75.
[3] Yu.A. Litvinov *et al.*, GSI Rep. 2001-1 (2001) 16.
[4] Yu.A. Litvinov *et al.*, Hyp. Int. **132** (2001) 283.
[5] M. Jung *et al.*, Phys. Rev. Lett. **69** (1992) 2164, H. Irnich *et al.*, Phys. Rev. Lett. **75** (1995) 4182.
[6] Yu.A. Litvinov *et al.*, publication in preparation.
[7] R. Firestone, V. Shirley, *Table of Isotopes*, 8th ed., J. Wiley & Sons (1999).
[8] G. Audi *et al.*, Nucl. Phys. **A624** (1997), 1.
[9] M. Hausmann *et al.*, Hyp. Int. **132** (2001) 289.
[10] J. Stadlmann, Thesis, JLU Giessen (2002).
[11] J. Stadlmann *et al.*, publication in preparation.
[12] M. Hausmann *et al.*, NIM **A446** (2000) 569.
[13] Y. Aboussir *et al.*, ADNDT **61** (1995) 127.
[14] S. Goriely *et al.*, ADNDT **77** (2001) 311.
[15] W.D. Myers *et al.*, Nucl.Phys. **A601** (1996) 141.
[16] P. Moeller *et al.*, ADNDT **59** (1995) 185.
[17] J.A. Cameron *et al.*, NDS **92** (2001) 882.

α - decay studies of ^{217g}Pa and ^{217m}Pa

F.P.Heßberger[1], S.Hofmann[1], I.Kojouharov[1], D.Ackermann[1,2], S.Antalic[3], P.Cagarda[3], B.Kindler[1], B.Lommel[1], R.Mann[1], A.G.Popeko[4], S.Saro[3], J.Uusitalo[5], A.V.Yeremin[4]

[1]GSI Darmstadt, Germany, [2]Johannes Gutenberg - Universität, Mainz, Germany, [3]Comenius University, Bratislava, Slovakia, [4]FLNR JINR, Dubna, Russia, [5]University of Jyväskylä, Jyväskylä, Finland

More than twenty years ago an isomeric state at $E^* \approx 1854$ keV decaying by α - emission of $E_\alpha = 10.16$ MeV was identified in ^{217}Pa by Schmidt et al. [1]. Recently Ikuta et al. [2] observed an α-line with an energy of 9.54 MeV which they attributed to a second isomeric state. This line was reproduced in an experiment at SHIP, but it was rather interpreted as fine structure in the decay of the known isomeric state especially since an additional weak line at 9694 keV was observed [3]. To settle the decay of ^{217m}Pa we performed a new experiment also aiming to measure α-γ- and α-γ-γ- coincidences using a four-fold segmented clover detector. The isotope was produced by the reaction ^{181}Ta(^{40}Ar,4n)^{217}Pa using beam currents of up to 2.2 pμA. The results of our measurement are shown in Fig. 1 and Tab. 1.

Isotope	E_α / keV	i_α	$T_{1/2}$ / ms	E_γ / keV
^{217m}Pa	10157 ± 5	0.72±0.04	1.08 ± 0.02	
	9697 ± 5	0.02±0.01	0.95 ± 0.05	466.5 ± 0.2
	9552 ± 5	0.09±0.01	0.94 ± 0.09	613.0 ± 0.2
	9533 ± 5	0.06±0.01	1.11 ± 0.20	634.3 ± 0.1
	8306 ± 5	0.11± 0.02	0.68 ± 0.05	450.4 ± 0.1 612.7 ± 0.1 820.8 ± 0.2
^{217g}Pa	8337 ± 5	0.99 ± 0.01	3.8 ± 0.2	
	7873 ± 10	0.004±0.002		466.1 ± 2.0
	7728 ± 10	0.003±0.002		612.5 ± 0.8
	7710 ± 10	0.003±0.002		634.3 ± 1.1

Table 1: Summary of α - γ decay data for ^{217}Pa

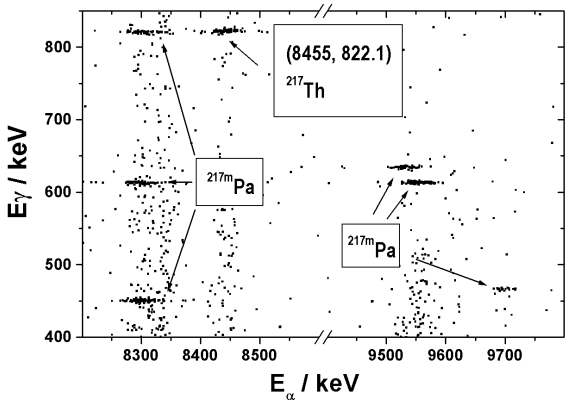


Figure 1: α-γ- coincidence spectrum observed in a bombardment of ^{181}Ta with ^{40}Ar using a detector setup behind SHIP.

The new results fully confirm our previous interpretation of fine structure in the α - decay of ^{217}Pa. The sum $E_\alpha + E_\gamma$ amounts to the energy of the previously known decay, which further indicates that the 10157 keV - α transition represents the decay into the groundstate of ^{213}Ac. The α - γ - coincidence measurements identified the line at 9.55 MeV as a doublet not resolved in the single α - spectra. In addition we observed a line of low energy at $E_\alpha = 8306$ keV, populating a level at $E^* = 1884$ keV, which decays by emission of a series of three γ - events. The latter was verified by measuring γ - γ - coincidences. It is seen in Fig. 2 that each two lines occur in coincidence to the third one.

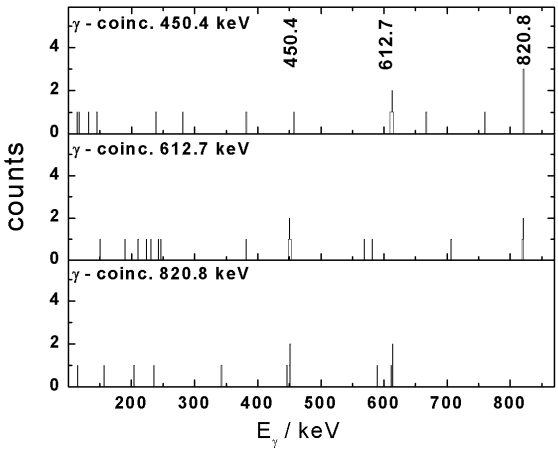


Figure.2: γ-spectra coincident to α - particles of (8250-8350) keV and to γ-transitions of 450, 613 and 821 keV, respectively.

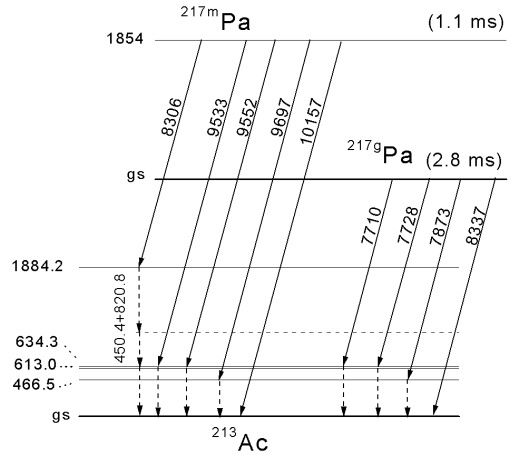


Figure 3: Decay scheme of ^{217m,217g}Pa. All energies are in keV

Knowing the decay- pattern of ^{217m}Pa we searched for fine structure in the α-decay of ^{217g}Pa. Three weak lines attributed to the decay into the levels at 466.5, 613.0, and 634.3 keV were identified by α - α - correlation to the daughter ^{213}Ac (see Fig. 3); also a few α - γ - coincidences were observed (Tab.1). No α - lines were observed that could be attributed to decays into other levels of ^{213}Ac.

References

[1] K.-H. Schmidt et al. Nucl. Phys. A318, 243 (1979)

[2] Ikuta et al. Phys. Rev. C R2804 (1998)

[3] F.P.Heßberger et al. EPJ A8, 521 (2000)

Isomer and β Decay Studies in Neutron-Rich A$\sim$180 Nuclei

S.D. Al-Garni[1], P.H. Regan[1], P.M. Walker[1], H.M. El-Masri[1], J. Garces Narro[1], C.J. Pearson[1], E. Roeckl[2], R. Kirchner[2], M. La Commara[2], C. Mazzocchi[2], H. Grawe[2], R. Borcea[2], J. Döring[2], S.C. Wooding[1,2], K. Schmidt[2], D.M. Cullen[3], C. Wheldon[3], W.D. Schmidt-Ott[4], R. Wood[1], L. Batist[2], I. Mukha[2], C. Plettner[2], A. Blazhev[2], Y. Shimbara[5]

1. *Dept. of Physics, University of Surrey, Guildford, GU2 7XH, UK*
2. *GSI, Gesellschaft für Schwerionenforschung mbH, Darmstadt,Germany*
3. *Dept. of Physics, University of Liverpool, Liverpool, L69 3BX, UK*
4. *Dept. of Physics, University of Göttingen, Germany*
5. *Dept. of Physics, Osaka University, 1-1 Machikaneyama Toyonaka, Osaka 560-0043, Japan*

Deep-inelastic collisions of ^{136}Xe ions with tantalum and tungsten targets have been used to study β-decays and high-spin isomers in neutron-rich A$\approx$180 nuclei at the GSI on-line mass separator. Reaction products were extracted from the thermal ion source (TIS), accelerated to 55 keV, mass separated with a dipole magnet, and transported to a β/γ counting station. The implanted activity was periodically removed, with periods 160 s, 1600 s and 16000 s. Electron-gamma coincident events were written to magnetic tape in list mode, so that they could be analysed with respect to the half-lives invloved.

Gamma-rays associated with the decay of the well known $K^\pi = \frac{37}{2}^-$, 51.4 min isomer in ^{177}Hf were observed with an unexpectedly high yield as shown in Fig. 1.

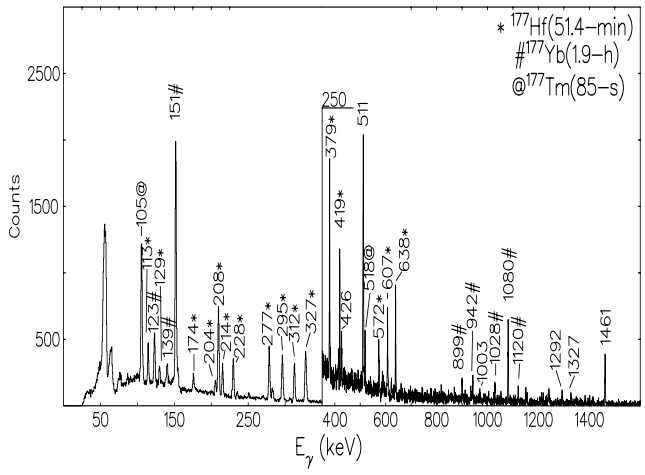


Figure 1: Gamma-ray spectrum for A=177 with a tantalum target.

The single-component grow-in analysis, for the sum of lines depopulating the $K^\pi = \frac{37}{2}^-$ isomer, gives a half-life of 76.4^{+16}_{-9} minutes which is distinctly longer than the previous measurements for this decay of $t_{1/2} = 51.4$ min [1]. Other half-lives are well reproduced in the same A=177 data set.

One possible explanation is that the $K^\pi = \frac{37}{2}^-$ decay in ^{177}Hf is due to the production of a theoretically predicted $K^\pi = \frac{39}{2}^-$, isomeric state in ^{177}Lu, which β decays (after extraction from the ion source) to ^{177}Hf.

A two component grow-in analysis for the observed decays from the $K^\pi = \frac{37}{2}^-$ isomer in ^{177}Hf gives a first component of 6^{+3}_{-2} min, when the second component is fixed to the published value of $t_{1/2} = 51.4$ min, as shown in Fig. 2. If this interpretation is correct, this would constitute the highest-spin beta-decaying state yet identified.

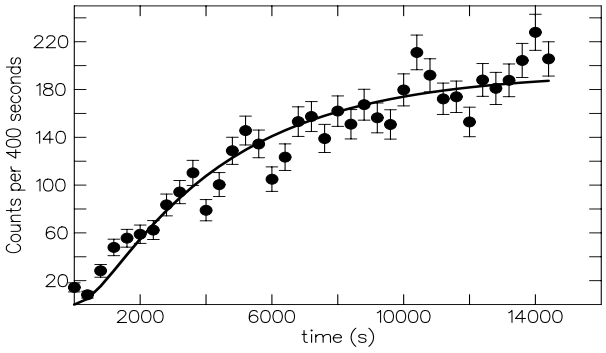


Figure 2: Two-parameter grow-in fit for the $K^\pi = 37/2^-$ isomer in ^{177}Hf (assuming the half-life for the ^{177}Hf isomer is 51.4 minutes).

A follow-up experiment has been performed at the GSI mass separator, using the total absorption spectrometer (TAS) which comprises a silicon detector, and a germanium crystal for X-ray, γ-ray and β-spectroscopy, inside a large NaI(Tl) γ-ray detector [2], operated in both coincidence and anticoincidence modes. Preliminary analysis has shown, at A=182, well resolved ytterbium (Z=70) X-rays in association with a new γ-ray transition at 102 keV, proposed as the $2^+ \rightarrow 0^+$ transition in ^{182}Yb, which lies just above the 98 keV $2^+ \rightarrow 0^+$ transition of ^{182}Hf [1]. This is the first observational evidence for ^{182}Yb and its excited states. Apart from this new result, it is hoped that the TAS data will clarify the decay of high-K isomers at A=177.

References

[1] R.B. Firestone and V.S. Shirley, Table of Isotopes, **8th ed.** J. Wiley and Sons, New York (1996)

[2] M. Karny *et al.*, Nuclear Instruments and Methods **B126**, 411 (1997)

Fine structure in the alpha decay of neutron-deficient polonium isotopes

K. Van de Vel[1], A.N. Andreyev[2], D. Ackermann[3], S. Antalic[4], H.J. Boardman[2], P. Cagarda[3], J. Gerl[3], F.P. Heßberger[3], S. Hofmann[3], M. Huyse[1], D. Karlgren[1,5], B. Kindler[3], I. Kozhoukharov[3], M. Leino[6], B. Lommel[3], G. Münzenberg[3], C. Moore[2], R.D. Page[2], C. Schlegel[3], P. Van Duppen[1]

[1]Instituut voor Kern- en Stralingsfysica, University of Leuven, Belgium; [2]Oliver Lodge Laboratory, University of Liverpool, UK; [3]GSI Darmstadt; [4]Comenius University of Bratislava, Slovakia;

[5]Royal Institute of Technology, Stockholm, Sweden; [6]JYFL, University of Jyväskylä, Finland

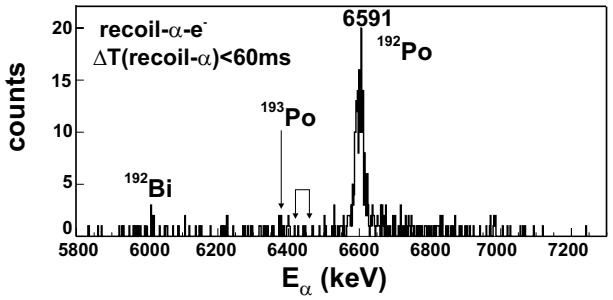


Figure 1: Spectum of α particles, correlated with evaporation residues within 60 ms, and in prompt coincidence with conversion electrons.

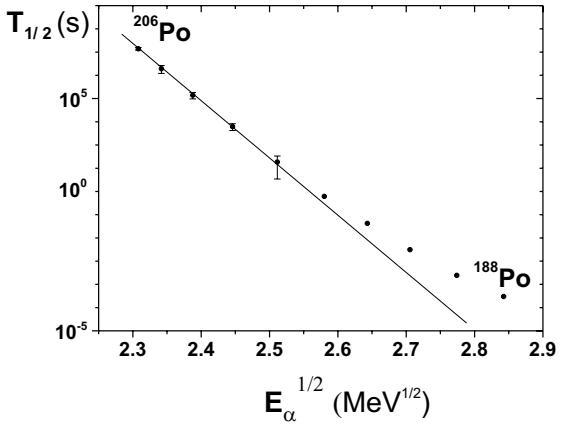


Figure 2: Geiger-Nuttall plot of the even-mass Po isotopes below A=206. The half-life is given in seconds, the energy in MeV.

Shape coexistence is a well-studied phenomenon in nuclei around the closed Z=82 proton shell [1]. One of the best studied cases to date is ^{186}Pb, where three differently shaped (spherical-oblate-prolate) 0^+ states were observed in a recent experiment at the SHIP [2]. In ^{188}Pb an oblate 0^+ state was earlier observed in three experiments [3, 4, 5], while two different candidates for the position of a prolate 0^+ state were suggested: at 767(12) keV [4] or at 725(2) keV [5]. In the present experiment at the SHIP, the α decay of light $^{188-192}$Po and $^{186-190}$Bi nuclei was re-studied. The experimental set-up used was described in [2]. We present preliminary results for fine structure (f.s.) in the α decay of ^{192}Po, to clarify the data on the prolate 0^+ state in ^{188}Pb. The nuclei of interest were produced in the ^{142}Nd(^{52}Cr,2n)^{192}Po reaction. Fig 1. shows an α-particle spectrum, recorded in the silicon stop detector within 60 ms after implantation of the evaporation residue, and in prompt coincidence with conversion electrons, detected in the backward silicon detector array. The peak at 6591(20) keV (after correction for α-electron summing in the stop detector) corresponds to the α decay of ^{192}Po to the oblate 0^+ state at 588 keV in ^{188}Pb, in agreement with the results of [3, 4, 5]. The α decay to the prolate 0^+ state in ^{188}Pb, either at 767 keV or at 725 keV from [4, 5], respectively, corresponds to α-particle energies of 6416 keV and 6457 keV, respectively (indicated with arrows in Fig. 1). An upper limit of 3 % for the intensity of the α decay to the suggested prolate 0^+ states in ^{188}Pb, relative to the decay to the oblate state has been deduced. This brings into question the presence of the prolate state at 767 keV, identified in [4] as the intensity of the decay to the prolate state obtained in their work was 51 %, relative to the intensity of the decay to the oblate state. The population of the prolate state at 725 keV, suggested in [5], might be smaller in the present reaction.

By using the ^{142}Nd(^{50}Cr,4n)^{188}Po reaction, improved data for the ground state→ground state (g.s.) decay of ^{188}Po were obtained: E_α=7908(15) keV, $T_{1/2}$=300(50)μs, in agreement with [6]. In Fig. 2 a Geiger-Nuttall plot is shown for the g.s.→g.s. decay of the even-mass Po nuclei with A$\leq$206. From mass 196 onwards the log($T_{1/2}$) values start to deviate from the linear behaviour described by the Geiger-Nuttall law, the half-life of the α decay to the g.s. in the Pb daughter nucleus being considerably longer than expected. This can be explained by the gradual change in the g.s. configuration of Po from a spherical one close to N=126, to a mixed spherical-oblate configuration for A$\leq$196. In ^{188}Po the prolate configuration probably becomes lowest in energy [6]. As the ground state of the daughter Pb isotopes remains mainly spherical, the strength of the α decay from the g.s. of Po to the spherical ground state of the corresponding Pb isotopes decreases, while the α decay to the deformed excited 0^+ states in Pb is enhanced when moving towards N=104, the neutron mid-shell.

References

[1] R. Julin *et al.*, J. Phys. G **27**, R109 (2001).
[2] A.N. Andreyev *et al.*, Nature, **405**, 430 (2000).
[3] N. Bijnens *et al.*, Z. Phys. A **356**, 3 (1996).
[4] R.G. Allatt *et al.*, Phys. Lett. B **437**, 29 (1998).
[5] Y. Le Coz *et al.*, EPJdirect **A3**, 1 (1999),
[6] A.N. Andreyev *et al.*, Eur. Phys. J. **A6**, 381 (1999).

New isotopes ^{233}Cm and ^{234}Cm

P.Cagarda[1], S.Antalic[1], D.Ackermann[2], F.P.Heßberger[2], S.Hofmann[2], B.Kindler[2], J.Kojouharova[2], B.Lommel[2], R.Mann[2], A.G.Popeko[3], Š.Šáro[1], J.Uusitalo[4], A.V.Yeremin[3]

[1]Comenius University, Bratislava, Slovakia, [2]GSI Darmstadt, Germany, [3]FLNR JINR, Dubna, Russia, [4]University of Jyväskylä, Finland

In a study of neutron deficient isotopes of curium we were aiming to produce isotopes beyond the known ^{238}Cm [1] and to investigate the decay of their daughter products. The experiment was performed at SHIP in April and August 2001. Two new curium isotopes, ^{233}Cm and ^{234}Cm were produced using the reaction ^{198}Pt (^{40}Ar,xn) $^{238-x}$Cm, x = 4,5 at average beam currents of 1 pμA. An isotopically enriched (95.7 %) self-supporting ^{198}Pt target, (1.36 - 1.42) mg/cm^2 thick, was mounted on a rotating target wheel.

Both isotopes were identified using the method of α - α - correlation. The result of the measurement using a time window of 1500 s and a position window of 1 mm is shown in Fig. 1. To minimize the number of accidental coincidences one of the α events had to occur in the pause between the beam pulses. A previously unknown α-activity with an energy of (7239 ± 10) keV was detected as mother activity of an α - decay chain characterized by the sequence $E_{\alpha1}$(7239 keV) → $E_{\alpha2}$(7057 keV) → $E_{\alpha3}$(7560 keV) → $E_{\alpha4}$ (7979 keV) → $E_{\alpha5}$(17470 keV). $E_{\alpha1}$ is attributed to ^{234}Cm, since $E_{\alpha2}$, $E_{\alpha3}$, $E_{\alpha4}$ are in perfect agreement with the α particle energies of ^{230}Pu, ^{226}U and ^{222}Th reported in literature [1,2] and $E_{\alpha4}$ corresponds to the sum of the α energies of ^{218}Ra and the fast decaying ^{214}Rn.

A total amount of 175 chains of this type were observed. In addition 26 spontaneous fission events were recorded and tentatively attributed to ^{234}Cm resulting in a α/fission ratio of 0.94 ± 0.09. A half-life of $T_{1/2}$ = (51 ± 12) s was measured for ^{234}Cm which is in good agreement with predictions. Calculated values of EC decay half-lives (240 s [3] and 138 s [4]) suggest an EC branch of about 50 %. Taking into account the measured α to fission ratio a spontaneous fission half-life of about 1500 s is determined for ^{234}Cm.

Five different beam energies of E_{lab} = 184, 192, 196, 200 and 208 MeV were used to measure the excitation function of the 4n-reaction channel. A maximum value of (1.3 ± 0.1) nb was measured for the yield of α particles from the ^{234}Cm decay at an excitation energy 45 MeV in the centre of the target.

Twelve α-decay chains measured at E_{lab} = 208 MeV were attributed to the decay of ^{233}Cm. An alpha energy of E_α = (7340 ± 10) keV was measured. The half-life could not be determined using the correlation method because of the high background rate in the energy region, where the recoils were expected.

New and improved data for the decay of ^{229}Pu and ^{230}Pu were obtained. Half-life values of (102 ± 10) s for ^{230}Pu and (90^{+71}_{-27}) s for ^{239}Pu were determined.

The measured decay properties are summarized in Tab. 1.

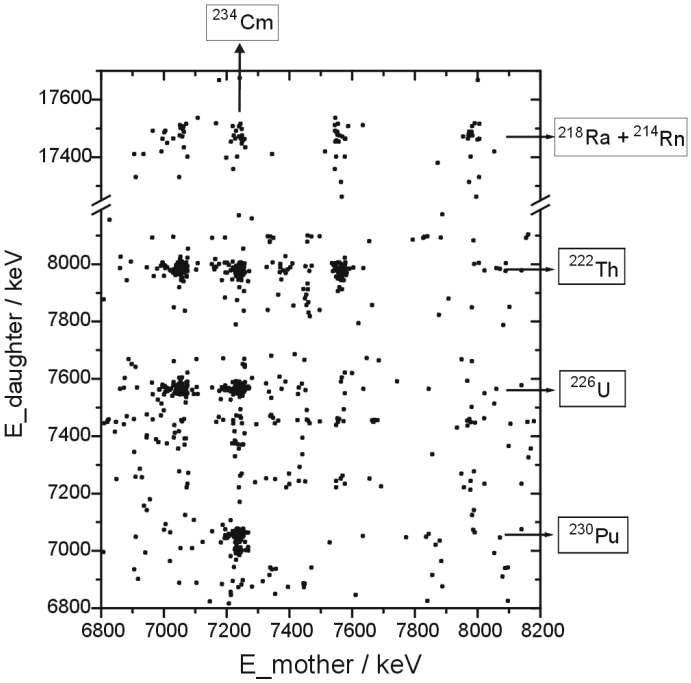


Fig. 1: α - α correlation plot for the decays of ^{234}Cm → ^{230}Pu → ^{226}U → ^{222}Th → (^{218}Ra + ^{214}Rn) (see text for details)

Isotope	E_α [keV]	i_α	$T_{1/2}$ [s]
^{234}Cm	7239 ± 10		51 ± 12
^{233}Cm	7340 ± 10		
^{230}Pu	7057 ± 10	0.81 ± 0.04	102 ± 10
	6999 ± 15	0.19 ± 0.04	
^{229}Pu	7465 ± 10		90^{+71}_{-27}
^{226}U	7560 ±10	0.86 ± 0.03	0.258 ± 0.013
	7384 ± 20	0.14 ± 0.03	

Table 1: Summary of measured decay properties.

References

[1] R.B. Firestone, V.S. Shirley (Editors), Table of Isotopes, 8th edition (J. Wiley and Sons, New York, 1996)

[2] P.T. Greenlees et al. Eur. Phys. J A6, 269 (1999)

[3] T.Takahashi et al. At.Data Nucl.Data Tables, 101 (1973)

[4] N.N.Kolesnikov et al. JINR Preprint, P6-9421 (1976)

New deeply bound pionic states in Sn isotopes

M. Fujita[1], H. Geissel[2], H. Gilg[3], A. Gillitzer[4], R.S. Hayano[5], S. Hirenzaki[1], K. Itahashi[6], M. Iwasaki[6], P. Kienle[3], L. Maier[3], M. Matos[2], G. Münzenberg[2], T. Ohtsubo[7], M. Sato[6], M. Shindo[5], K. Suzuki[5], T. Suzuki[5], H. Weick[2], M. Winkler[2], T. Yamazaki[8], T. Yoneyama[6]

[1]Nara Women's University, [2]GSI Darmstadt, [3]Technische Universität München, [4]Forschungszentrum Jülich [5]University of Tokyo, [6]Tokyo Institute of Technology, [7]Niigata University, [8]RI Beam Science Lab., RIKEN

An experimental study of the ^{208}Pb(d,^{3}He) reaction at the Fragment Separator (FRS) had led to the discovery of the deeply bound pionic states $2p$ and $1s$ in ^{207}Pb [1]. In a following experiment pionic states in ^{205}Pb were populated in the ^{206}Pb(d,^{3}He) reaction. The better suited neutron hole excitation spectrum of ^{205}Pb together with an improved energy resolution of $\sim$ 300keV allowed for a clear separation of the pionic $1s$ state from the $2p$ state in the excitation energy spectrum. The data analysis of this experiment was completed, and final values for the pionic binding energies and widths for both $1s$ state and $2p$ state were determined [2]. From the pionic $1s$ binding energy and width, which is almost exclusively determined by the s-wave pion-nucleus potential, the central potential V_0 could be deduced to be $\sim$ 27MeV (repulsive) [2], which indicates a significant additional repulsion as compared to the value obtained with the free πN scattering lengths. The experiment does however not allow to decide whether this additional repulsion is due to the isoscalar or the isovector part of the interaction.

In order to experimentally separate both parts, one has to compare deeply bound pionic states in nuclei with different neutron to proton number ratio. In this respect the study of pionic states in Sn isotopes was considered particularly promising, an expectation which was supported by theoretical studies [3]. Sn has the advantage of having both a long chain of stable isotopes ranging from $A = 112$ to $A = 124$ and a well-suited neutron level scheme with low-lying $3s_{1/2}$ neutrons. This opens the possibility of populating quasi-substitutional configurations where the $s_{1/2}$ neutron is replaced by a negative pion in the $1s$ state. These configurations are preferentially formed at vanishing momentum transfer, a condition which is achieved in (d,^{3}He) transfer reactions at a deuteron incident kinetic energy close to 500 MeV.

In a beam time in May 2001 the population of deeply bound pionic states in Sn isotopes was studied at the FRS in the (d,^{3}He) reaction. The Sn isotopes $A = 112, 116, 120, 124$ were irradiated with a d beam at $T_d = 503.388$ MeV. One of the prerequisites for the experiment was a high quality of the d beam, which was delivered from SIS with an intensity of $1.5{\cdot}10^{11}$ per spill (average intensity $\sim 0.5 \cdot 10^{11}$/s), a momentum spread $\delta p/p = 3 \cdot 10^{-4}$, and a horizontal beam spot $\delta x \simeq$ 1mm. In order to achieve the aspired energy resolution of 300 keV, thin strip targets of 1.5 mm width and 20 mg/cm^2 were used. The ^{3}He energy at the FRS focal plane was calibrated by using the non-pionic ^{112,116,120,124}Sn(d,^{3}He)^{111,115,119,123}In$_{(g.s.)}$ reactions, and independently by using the $p(d,^3\mathrm{He})\pi^0$ reaction from a thin mylar layer attached to the downstream surfaces of the Sn targets. Fig. 1 shows the observed energy spectra (acceptance corrected) of ^{3}He in the ^{116,120,124}Sn(d,^{3}He) reactions. The three distinct peaks in the middle part correspond to the $1s$ states in ^{115,119,123}Sn, respectively. The large skewed peaks close to 371 MeV arise from the $p(d,^3\mathrm{He})\pi^0$ reaction, and are subject to a large kinematical shift and broadening. They not only assured that there was no long term drift in the experiment but also provided an independent energy calibration which turned out to be consistent with the calibration with the Sn(d,^{3}He)In reactions. Further analyses to deduce the binding energies, widths, isotope shifts and cross sections are in progress.

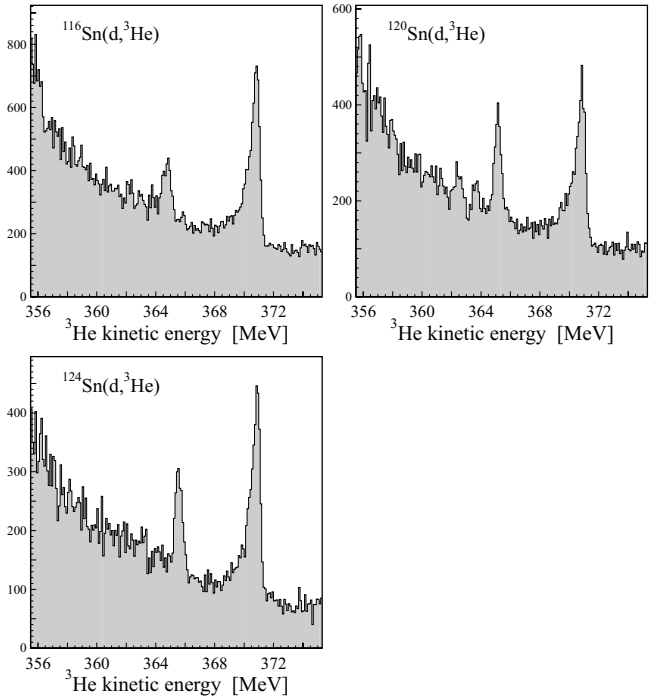


Figure 1: Acceptance corrected ^{3}He kinetic energy spectra measured in ^{116,120,124}Sn(d,^{3}He) reactions at $T_d = 503.388$ MeV. See text for further explanation.

References

[1] T. Yamazaki *et al.*, Z. Phys. **A355** (1996) 219; H. Gilg *et al.*, Phys. Rev. C **62** (2000) 025201; K. Itahashi *et al.*, Phys. Rev. C **62** (2000) 025202.

[2] H. Geissel *et al.*, GSI Scientific Report 2000, p.20; H. Geissel *et al.*, accepted by Phys. Rev. Lett.

[3] Y. Umemoto, S. Hirenzaki, K. Kume and H. Toki, Phys. Rev. C **62** (2000) 024606.

Reaction Studies and Continuum Spectroscopy with Exotic Neutron-Rich Nuclei [B,G]

H. Simon[1], D. Aleksandrov[2], T. Aumann[3], L. Axelsson[4], T. Baumann[3], M.J.G. Borge[5], D. Cortina-Gil[3], L.V. Chulkov[2,3], W. Dostal[6], B. Eberlein[3,6], Th.W. Elze[7], H. Emling[3], C. Forssén[4], H. Geissel[3], M. Hellström[3], B. Jonson[4], J.V. Kratz[6], R. Kulessa[8], Y. Leifels[3], K. Markenroth[4], M. Meister[1,4], G. Münzenberg[3], T. Nilsson[4], G. Nyman[4], M. Pfützner[3], A. Richter[1], K. Riisager[9], C. Scheidenberger[3], G. Schrieder[1], O. Tengblad[5], M.V. Zhukov[4]

[1]TU Darmstadt, [2]Kurchatov Institute, Moscow, [3]GSI Darmstadt, [4]CTH Göteborg, [5]CSIC Madrid, [6]Univ. Mainz, [7]Univ. Frankfurt, [8]Univ. Kraków, [9]Univ. Aarhus

Break-up reactions of neutron-rich ^{6,8}He isotopes have been studied at energies of 240 and 226 MeV/u respectively. The one neutron knockout channel provides essential information about the nuclear structure of the projectile and intermediate unbound resonance states, populated in the reactions.

For the ^{6}He reactions, the ^{5}He invariant mass, $\alpha - n$ angular correlation spectra, the ^{5}He-fragment momentum distributions and one-neutron knockout cross sections have been compared for hydrogen, carbon and lead targets detecting one neutron in coincidence with the α in the exit channel. While the ^{5}He invariant mass spectra do not reveal target dependence, the ^{5}He momentum distribution becomes wider for lighter targets. The neutron knockout model in the sudden approximation reproduces satisfactorily the experimental observables. The difference in momentum distributions is explained by a smooth dependence of the cut-off parameter R_{cut} on the target size. It is introduced to assure fragment survival in the reaction and thus reflects the effective size of the ^{5}He subsystem inside ^{6}He. The R_{cut} parameter is therefore as well directly connected with the neutron knock-out cross section:

$$\sigma_{-1n} = \sigma_T < n > P(R_{cut}) \qquad (1)$$

where the cross section σ_T for free neutron-target interaction was taken from published experimental data, R_{cut} is obtained from the fit to the measured momentum distribution of the ^{5}He fragments, $P(R_{cut})$ is the probability to find a $p_{3/2}$ neutron in the projectile outside a cylindrical cut through the ^{6}He nuclear matter density distribution, and $< n >$ is the mean number of neutrons in the $p_{3/2}$ shell. $P(R_{cut})$ was obtained by integration of the squared single-neutron wave function $|\psi(r)|^2$. The $\psi(r)$ functions were calculated by solving Schrödinger equations with Gaussian-shaped potentials. The radial parameter of the potential was fixed by the known r.m.s. radii of ^{6}He ($< r^2 >^{1/2} = 2.48 \pm 0.03$) while the potential depths were chosen to reproduce the known one-neutron binding energy (1.87 MeV for ^{6}He $\rightarrow$ ^{5}He+n). The good agreement between calculated and measured values shown in Table 1 gives evidence that the neutron knockout mechanism remains important even for heavy targets.

Table 1: Calculated and experimental one-neutron knockout cross sections, including the parameters used in the calculations.

^{6}He 240 MeV/u				
Target	R_{cut}	$P_n(R_{cut})$	σ_{-1n}^{calc} (mb)	σ_{-1n}^{exp} (mb)
^{1}H	2.6	0.298	22.6	30 ± 13
^{12}C	3.1	0.202	111	127 ± 14
^{208}Pb	3.95	0.105	358	320 ± 90

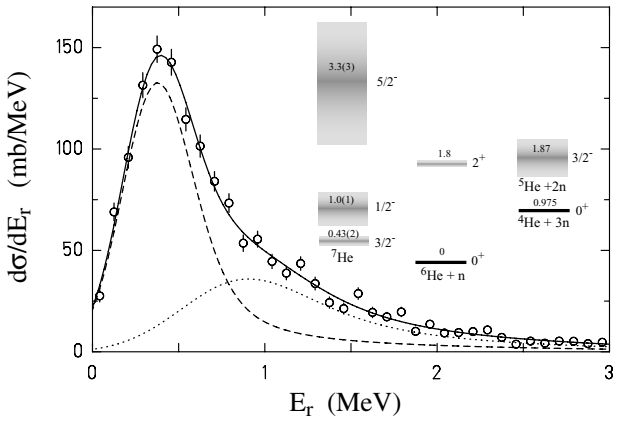


Figure 1: Coincidence cross section of the ^{6}He-n system after breakup of 227 MeV/u ^{8}He on a carbon target as function of the relative energy E_r. The lines show the decomposition of a fit to the data (solid) into the groundstate (dashed) and the proposed first excited state (dotted), using a R-Matrix expression folded with the experimental acceptance and response. The inset shows the proposed level scheme with the new $1/2^-$ state in ^{7}He.

While the measured invariant mass spectrum for the unbound ^{5}He shows dominantly a contribution from the known ground state, for ^{7}He a similarly simple description fails [1]. The invariant mass spectrum of ^{7}He displayed in Figure 1 shows a structure near the threshold, which can only be interpreted in a consistent way, if an overlap of the known ^{7}He $J^\pi = 3/2^-$ ground state resonance with an excited state at 1.0(1) MeV and of a width $\Gamma = 0.75(8)$ MeV is assumed. We assign this new resonance to the $J^\pi = 1/2^-$ spin orbit partner. A profound statistical analysis has been applied to prove that (i) the observed structure cannot be described as a single resonance and (ii) the known ground state properties are consistently reproduced in a free parameter fit. The spin assignment is supported by an independent measurement of an angular correlation function for which the anisotropy was found to be reduced by a factor of two compared with the ^{5}He case where only a small admixture of the first $1/2^-$ excited state was observed. Theoretical models result in a wide spread for the spin-orbit splitting for ^{7}He to be between about 0.9 and 3.0 MeV. The current observation is good agreement with the lowest value obtained in recent many-body quantum Monte-Carlo calculations [2].

References

[1] M. Meister, K. Markenroth et al., accepted for publication in Phys. Rev. Lett.

[2] B.S. Pudliner et al., Phys. Rev. **C56**(1997)1720, R.B. Wiringa et al., Phys. Rev. **C62**(2000)014001

Coulomb dissociation of ^{8}B: determination of the E2 component

F. Schümann[1], F. Hammache[2], S. Typel[3], Z. Sun[2], F. Uhlig[4], K. Sümmerer[2], and the S223 Collaboration
[1]Ruhr-Universität Bochum, [2]GSI Darmstadt, [3]MSU East Lansing, [4]TU Darmstadt

Recently, the solar fusion reaction ^{7}Be(p,γ)^{8}B has received renewed interest: on one hand, it represents the source of the high-energy neutrinos that have been measured in the SNO and Super-Kamiokande experiments to pin down neutrino oscillations; the zero-energy S_{17}-factor is directly proportional to the predicted solar neutrino flux to be compared to the SNO and Super-K experiments. On the other hand, new discrepancies in the most recent direct capture experiments [1,2] have made it desirable to check their results by an independent measurement.

One indirect method is Coulomb dissociation (CD) of ^{8}B. We have previously performed such an experiment [3]. The analysis that allows to extract the zero-energy S-factor $S_{17}(0)$ from CD experiments requires a precise knowledge of the multipolarity contributions. Here, discrepancies among different CD experiments were observed: The GSI and a similar RIKEN experiment [4] concluded from their angular distributions that the multipolarity in CD was predominantly E1, whereas a MSU experiment [5] found evidence for a finite E2 contribution from an analysis of ^{7}Be longitudinal momentum spectra..

We have repeated the CD experiment at GSI with an improved setup. A 254 A MeV ^{8}B beam was produced and purified at the FRS; the breakup was measured in complete kinematics at KaoS. The new setup allowed to track the incident ^{8}B beam at the ^{208}Pb breakup target with good angular resolution (≈0.5 mrad). Downstream from the target, the breakup products, p and ^{7}Be, were tracked with two pairs of small-pitch (100 μm) Si strip detectors. This allowed to measure the angular correlations of the breakup products both in the reaction plane and perpendicular to it.

Fig.1 shows in the top panel the distribution of the breakup angles, Φ, of the p-^{7}Be system relative to the incoming ^{8}B beam and transverse to the reaction plane. The bottom panel shows the transverse momenta in the reaction plane, p_t^{in}. Both distributions can be well approximated with pure E1 multipolarity. The theoretical curves shown in Fig.1 have been calculated with E1 plus 10% of the theoretical E2 multipolarity, this gives roughly an upper limit to the E2 amplitude that is compatible with the data. The in-plane angles, θ, (not shown) are symmetric around 90 degrees and are also compatible with this theoretical description, even though the data show a somewhat larger anisotropy.

These findings confirm the analyses of the earlier GSI and RIKEN experiments [3,4], which were done under the assumption of pure E1 multipolarity. The preliminary result for $S_{17}(0)$ from the present experiment is 19.7 ± 1.2 eV b, in good agreement with our previous experiment [3] and with the direct measurements of Ref.[1]. We cannot confirm, however, the higher value published by Junghans *et al.* [2].

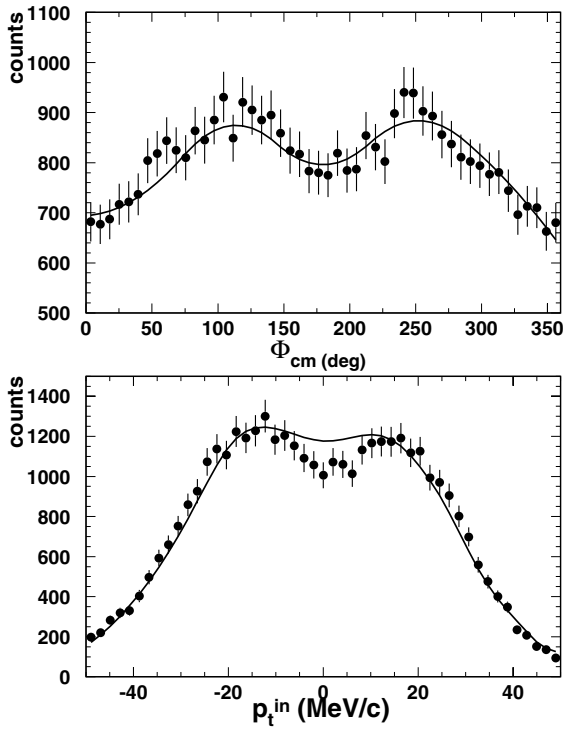


Figure 1: Angular distributions of the p-^{7}Be breakup vector with respect to the ^{8}B beam. Top: out-of-plane angles Φ; bottom: in-plane transverse momenta, p_t^{in}. The smooth curves represent theoretical calculations using 1.order perturbation theory; they include the full E1 and 10% of the E2-amplitude from a single-particle model.

References

[1] F. Hammache *et al.*, Phys.Rev.Lett. **86**, 3985 (2001).
[2] A. Junghans *et al.*, Phys.Rev.Lett. **88**, 041101 (2001).
[3] N. Iwasa *et al.*, Phys.Rev.Lett. **83**, 2910 (1999).
[4] T. Kikuchi *et al.*, Eur.Phys.J. A **3**, 213 (1998).
[5] B. Davids *et al.*, Phys.Rev.C **63**, 065806 (2001).

Coulomb Breakup of the One-Neutron Halo Nucleus ^{11}Be

R.Palit[a], T.Aumann[b], K.Boretzky[c], D.Cortina[b], U.Datta Pramanik[b], Th.W.Elze[a], H.Emling[b], H.Geissel[b], A.Grünschloß[a], M.Hellström[b], S.Ilievski[a,b], N.Iwasa[b], K.L.Jones[b], J.V.Kratz[c], R.Kulessa[d], Y.Leifels[b], A.Leistenschneider[a], E.Lubkiewicz[d], G.Münzenberg[b], P.Reiter[e], C.Scheidenberger[b], H.Simon[f], K.Sümmerer[b], E.Wajda[d], W.Walus[d]

[a]Univ. Frankfurt, [b]GSI Darmstadt, [c]Univ. Mainz, [d]Univ. Kraków, [e]LMU Garching, [f]TU Darmstadt

One-neutron-removal reactions have been proven to be very useful to study the reaction mechanism and the structure of exotic nuclei. In the present work, the electromagnetic and nuclear contributions to the breakup of ^{11}Be have been investigated with a secondary beam of ^{11}Be (520 MeV/u) on lead and carbon targets.

The secondary beam of ^{11}Be ions was produced by fragmentation of a primary ^{40}Ar beam delivered by the synchrotron SIS at GSI and was separated by the Fragment Separator (FRS). The projectiles were identified uniquely by means of energy loss and time of flight measurements. Behind the target, the fragments were deflected by a large-gap dipole magnet (ALADIN). By using energy-loss and time-of-flight measurements as well as position measurements before and after the dipole magnet, the charge, velocity, scattering angle and the mass of the fragments were determined. Neutrons and γ-rays were detected by the LAND and the 4π- Crystal Ball spectrometer, respectively. The γ-spectra show that the 0^+, 2^+, 1^- and 2^- levels of ^{10}Be were populated in one-neutron-removal reactions, both with the carbon target and with the lead target (see Fig. 1). The detector response functions corresponding to the individual γ-rays were generated with the Monte Carlo code GEANT in a simulation procedure that took into account the Doppler shift. The calculated line shapes, together with a smooth background, were fitted to the measured spectra and thus determine the relative population of excited states and ground state of the ^{10}Be core.

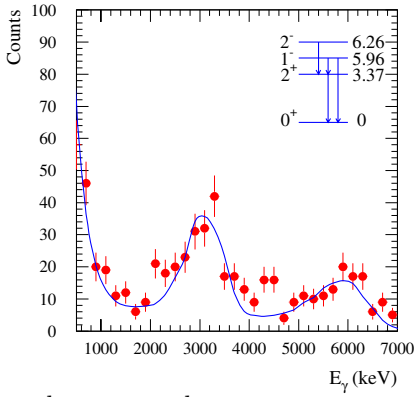


Figure 1: Doppler corrected γ-energy spectrum measured with the Crystal Ball in coincidence with ^{10}Be and one neutron (Pb target). The fitted spectrum is shown by solid line.

The observed γ-spectrum from the ^{10}Be fragment indicates that not only the halo neutron, but also neutrons from the core are removed. For the further analysis, the excitation energy spectrum of ^{11}Be was reconstructed from the measured momenta of the ^{10}Be fragment and the emitted neutron. These spectra were differentiated according to the ground state or the excited states in the ^{10}Be fragment. By comparing these differential cross sections in case of electromagnetic excitation (Pb-target) with the cross sections calculated on the basis of the direct-breakup model, one can deduce information about the ground state structure [1]. The ground state of ^{11}Be with spin $I^\pi = 1/2^+$ can be represented as $|^{11}Be> = \sqrt{S_1}|2s_{1/2}\nu \otimes 0^+ > + \sqrt{S_2}|1d_{5/2}\nu \otimes 2^+ > + ...$, where S_1 and S_2 represent the spectroscopic factors for the two configurations with neutrons in the $2s_{1/2}$ and $1d_{5/2}$ orbits, respectively.

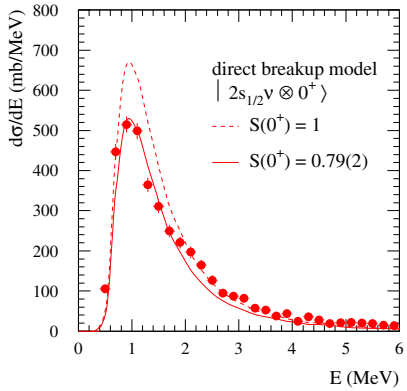


Figure 2: Excitation energy spectrum of ^{11}Be obtained with the Pb target requiring the ^{10}Be fragment to be in its ground state. Calculations within the direct breakup model are also shown.

By subtracting contributions of the excited states as well as nuclear contributions from the measured differential cross section obtained with Pb target, we extract the decay spectrum explicitly for the $2s_{1/2}$ neutron coupled to the ^{10}Be ground state as shown in Fig. 2. By comparing to the direct breakup model we obtain a spectroscopic factor of 0.79(2) for the $2s_{1/2}$ neutron halo configuration, which is consistent with the previous measurements of knockout reactions [2], transfer reactions [3] and with shell model calculations [4].

The excited-state partial cross sections for pure Coulomb and nuclear processes were determined. While in the case of Coulomb dissociation only a few percent of the total breakup cross section is accounted for the ^{10}Be excited state population, about 20% of the nuclear cross section is due to population of the excited states. This is understood due to the strong dependence of the Coulomb breakup cross section on the spatial extension of the neutron wave function.

References

[1] T. Nakamura *et al.* Phys. Lett. B **331** (1994) 296.
[2] T. Aumann *et al.* Phys. Rev. Lett. **84** (2000) 35.
[3] S. Fortier *et al.* Phys. Lett. B 461, (1999) 22.
[4] E. K. Warburton and B. A. Brown, Phys. Rev. C **46** (1992) 923.

Fragmentation of Unstable Neutron-Rich Oxygen Beams

A. Leistenschneider[1], T. Aumann[2], K. Boretzky[3], L.F. Canto[7], B.V. Carlson[8], D. Cortina[2], U. Datta Pramanik[2], Th.W. Elze[1], H. Emling[2], H. Geissel[2], A. Grünschloß[1], K. Helariutta[2], M. Hellström[2], M.S. Hussein[9], S. Ilievski[1,2], K.L. Jones[2], J.V. Kratz[3], R. Kulessa[5], Le Hong Khiem[3], E. Lubkiewicz[5], G. Münzenberg[2], R. Palit[1], P. Reiter[6], C. Scheidenberger[2], K.-H. Schmidt[2], H. Simon[4], K. Sümmerer[2], E. Wajda[5], W. Walús[5]

[1]Universität Frankfurt, Germany; [2]GSI Darmstadt, Germany; [3]Universität Mainz, Germany; [4]Technische Universität Darmstadt, Germany; [5]Uniwersytet Kraków, Poland; [6]Ludwig-Maximilians-Universität, Múnchen, Germany; [7]Universidade Federal do Rio de Janeiro, Brazil; [8]CTA Sao Jose dos Campos, Brazil; [9]Universidade de Sao Paulo, Brazil

Fragmentation of energetic heavy-ion beams is widely used to produce secondary beams of exotic nuclei far from stability. Recently, two-step fragmentation processes were discussed in the context of an efficient production of very neutron-rich isotopes at next-generation exotic nuclear beam facilities. This process involves an unstable neutron-rich fragment as an intermediate product which undergoes fragmentation again, yielding the final nucleus of interest. So far, the influence of the neutron-to-proton ratio of the projectile on the projectile fragment distributions (the "memory effect") was studied in a very narrow range of isospin only, since stable projectiles were used.

In this measurement [1], fragmentation of the unstable neutron-rich nuclei ^{19,20,21}O, together with that of the stable ^{17,18}O isotopes was studied. Secondary beams of $^{17-21}$O ions were produced in a fragmentation reaction of a primary ^{40}Ar beam (720 MeV/u) delivered by the synchrotron SIS at GSI. Secondary oxygen beams with kinetic energies around 600 MeV/u were subsequently separated in the Fragment Separator FRS and transported to the LAND experimental area. Both the incident projectiles and their fragments produced in interactions with carbon and lead targets were identified with regard to mass and charge number and the fragment angular distributions were measured; for experimental details see [1]. Fragment production cross sections could be determined for $^{17-21}$O projectiles and carbon, nitrogen, and oxygen fragments which include both stable and neutron-rich isotopes. The results obtained for the carbon target are shown in Fig. 1. The data are compared with fragment production cross sections obtained from the empirical EPAX parameterization [2] and with those obtained from two different abrasion-ablation models [3, 4], which are based on a microscopic description of the fragmentation process. As seen in Fig. 1, the EPAX parameterization seems to reproduce the general trend of the data rather well. Though the EPAX formula was obtained by adjusting to fragmentation data of stable beams only, the good, almost quantitative description indicates that the parameterization of the "memory effect" is valid also for unstable projectiles as neutron-rich as ^{21}O ($A/Z = 2.625$). An obvious deficiency of the EPAX parameterization, however, is the fact that the odd-even effects, observed in the experimental data particularly for the nitrogen fragments, cannot be reproduced. This is expected since the EPAX parameterization does not contain any physical description and no attempt has been made to parameterize the odd-even effects.

The experimental data show that isotopes with even neutron numbers, especially ^{15}N with a closed N=8 shell, are more abundantly produced than their neighbors with odd neutron numbers. It is likely that the large difference in neutron separation energy between unpaired and paired neutrons is responsible for the odd-even staggering in the production cross sections. This is illustrated by quoting the one-neutron separation energies of the ^{15,16,17,18}N isotopes which amount to 10.8, 2.5, 5.9 and 2.8 MeV, respectively. The unpaired neutron in ^{16}N or in ^{18}N is thus easily removed at the end of the evaporation chain, explaining their lower production cross sections in comparison to ^{15}N or ^{17}N, respectively. Odd-even effects in the production cross sections are predicted by both formulations of the abrasion-ablation model as seen from Fig. 1. Apparently, both calculations, however, overestimate the effects. Nevertheless, the results, in general, agree with the experimental data within roughly a factor of two.

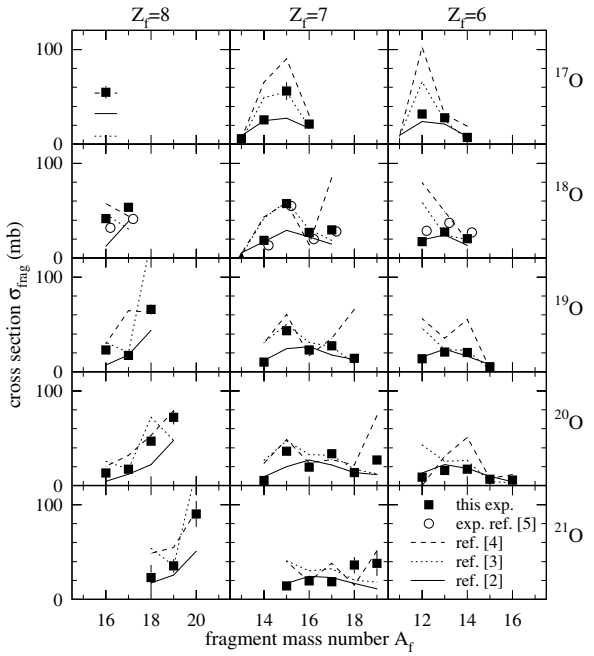


Figure 1: Production cross sections of fragments of $^{17-21}$O beams (carbon target).

References

[1] A. Leistenschneider *et al.*, submitted to Phys. Rev. C
[2] K. Sümmerer *et al.*, Phys. Rev. **C42**, 2546 (1990); K. Sümmerer and B. Blank, Phys. Rev. **C61**, 034607 (2000)
[3] J.J. Gaimard and K.-H. Schmidt, Nucl. Phys. **A531**, 709 (1991)
[4] B.V. Carlson, M.S. Hussein and R.C. Mastroleo, Phys. Rev. C **46**, R30 (1992); B.V. Carlson, Phys. Rev. **C51**, 252 (1995)
[5] D.L. Olson *et al.*, Phys. Rev. **C24**, 1529 (1981); Phys. Rev. **C28**, 1602 (1983)

Production of light nuclides in 1 GeV proton-induced fission of ^{238}U

M. V. Ricciardi[(1)], K. -H. Schmidt[(1)], O.Yordanov [(1)],
P. Armbruster[(1)], J. Benlliure[(2)], M. Bernas[(3)], A. Boudard[(4)], S. Czajkowski[(5)], T. Enqvist[(1)], R. Legrain[(4)],
S. Leray[(4)], B. Mustapha[(3)], M. Pravikoff[(5)], F. Rejmund[(3)], C. Stéphan[(3)], L. Tassan-Got[(3)], C. Volant[(4)]

(1) GSI – Planckstr. 1 – D-64291 Darmstadt - Germany
(2) Univ. Santiago de Compostela – E-15706 Santiago de Compostela - Spain
(3) IPN Orsay – IN2P3, F-91406 Orsay - France
(4) CEA Saclay – F-91191 Gif sur Yvette - France
(5) CEN Bordeaux-Gradignan – F-33175 Gradignan - France

A dedicated experimental program, devoted to reaching a full comprehension of the proton-induced spallation reactions, started in 1996 at the GSI. The accurate knowledge of these reactions is relevant both for the development of methods of incineration of radioactive waste [1] and for the production of secondary beams [2]. Within this program, the first ever complete survey on nuclide production cross sections in ^{197}Au + ^{1}H [3, 4] and ^{208}Pb + $^{1, 2}$H [5, 6] at around 1 GeV per nucleon was obtained. Experiments on other systems in the energy range 0.5-1.5 GeV per nucleon are still being analyzed or in preparation (^{238}U + ^{1,2}H [7, 8], ^{56}Fe + ^{1,2}H and ^{136}Xe + ^{1}H [9]). Two methods can be used for the production of residual nuclides in nuclear reactions: the target fragmentation ("direct kinematics") and the projectile fragmentation ("inverse kinematics"). The above quoted experiments were performed in inverse kinematics at relativistic energies. In these experimental conditions the fragment escapes the target and is detected in-flight prior to its β decay.

In this report, we present new results on the formation of light fission fragments produced in the reaction ^{238}U + ^{1}H at 1 *A* GeV. The 1 *A* GeV ^{238}U beam impinged on a liquid hydrogen target of 87.3 mg/cm thickness, which was enclosed in a thin titanium casing [10]. The fully stripped reaction products were identified at the FRS [11] by detecting their nuclear charge, Z, with a ionization chamber and their mass, A, from the A/Z ratio deduced from the magnetic rigidity and from the time-of-flight between the mid plane and the exit of the spectrometer. Once the nuclides were identified, so A and Z were integer numbers, their velocity was precisely evaluated by the magnetic rigidity.

As described in ref. [12] the ratio of transmitted reaction residues can be calculated. By the known beam intensities, target properties and transmission ratios the production cross sections were calculated on the basis of the measured yields. The measured velocity spectra allowed deducing the reaction mechanism in which the residues were formed. In this way, fission events, mostly originating from reactions with hydrogen, could be disentangled from the fragmentation ones, produced in the titanium windows. The results for the fission cross sections in the ^{238}U + ^{1}H reaction are shown on figure 1. The lower part of the complete nuclide distribution of this reaction, measured in our experiment is presented.

This reaction has been the basis for the production, in direct kinematics, of long isotopic chains of a few elements at ISOLDE [13] (see fig. 1). A direct measure of the production cross sections and of the kinematics of the reaction mechanism does not exist in this case, since the production and identification of the residues are separated by the intermediate extraction process. Our experiment provides the normalization factors to determine the extraction efficiency of the ISOL-target-ion-system. Although with the uranium beam intensities used in our survey experiment it was not possible to observe the extremely neutron-rich isotopes that were detected at ISOLDE, our experiment revealed the continuity in the production of all these light elements in the high-energy fission processes. Our experiment reveals that all these nuclides could be made available at ISOL facilities with a high-energy proton driver by developing appropriate extraction methods.

Financial supports by the European commission in the frame of the HINDAS [1] and EURISOL [2] projects and by the EC-HPRI-CT-1999-00001 program are gratefully acknowledged.

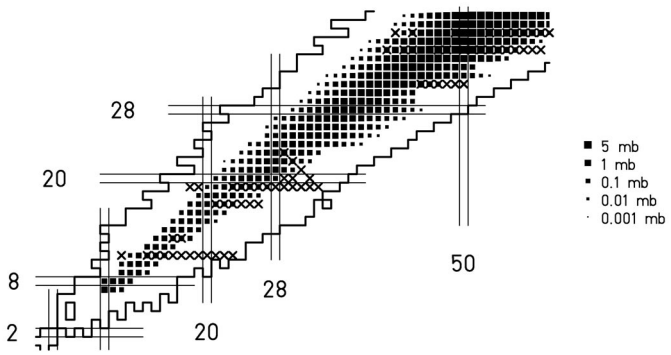


Figure 1: Measured nuclide cross sections from the reaction ^{238}U (1 A GeV) + ^{1}H. The crosses indicate nuclides observed at ISOLDE [13].

References

[1] http://www.fynu.ucl.ac.be/collaborations/hindas/
[2] http://www.ganil.fr/eurisol/index.html
[3] F. Rejmund et al., Nucl. Phys. A683 (2001) 540.
[4] J. Benlliure et al., Nucl. Phys. A683 (2001) 513.
[5] T. Enqvist et al., Nucl. Phys. A 686 (2001) 481.
[6] T.Enqvist et al., Nucl. Phys., accepected.
[7] J. Taieb, PhD thesis, INP Orsay, 2000.
[8] E. Casarejos, PhD thesis, Univ. Sant. de Compostela, 2001.
[9] Experiment proposals S184 and S248.
[10] P. Chesny et al., GSI 97.-1 (1997) 190.
[11] H. Geissel et al., Nucl. Instr. Meth. A 313 (1992) 377.
[12] J. Benlliure et al., Nucl. Instr. Meth. A, accepted.
[13] ISOLDE user's guide, H.-J. Kluge ed., CERN 86-05.

Isotopic production cross sections of fragmentation residues in reactions induced by $^{238}U(1A \cdot GeV)$ in deuterium

P. Armbruster[a], J. Benlliure[b], M. Bernas[c], A. Boudard[d], E. Casarejos[b], S. Czajkowski[e], T. Enqvist[a], R. Legrain[d], S. Leray[d], B. Mustapha[c], M. Pravikoff[e], F. Rejmund[c], K.-H. Schmidt[a], C. Stephan[c], J. Taieb[c], L. Tassan-Got[c], C. Volant[d], W. Wlazlo[a]

[a] GSI D-64291 Darmstadt, Germany [b] Univ. de Santiago de Compostela, E-15782 Santiago, Spain

[c]IPN F-91406 Orsay cedex, France [d] DAPNIA/SPhN, CEA/Saclay, F-91191 Gif sur Yvette cedex, France

[e] CENBG , F-33175 Gradignan cedex, France

The production cross sections of more than 500 fragmentation residues produced in the interaction of $^{238}U(1\ A \cdot GeV)$ with deuterium have been measured [1] within an European collaboration at GSI started in 1996. The aim of this work is to provide fundamental data for spallation sources (e.g. accelerator-driven systems). These data are also relevant to investigate the production of radioactive nuclear beams. The goal of this experimental program is to provide a large benchmark data collection which will help to better understand the reaction mechanisms involved in the residue production in spallation reactions. In this program, the spallation of ^{197}Au [2,3], ^{208}Pb [4], and ^{238}U [5,1] has been measured so far. The quality and quantity of the data now available, allow to study the differences among the reactions investigated.

The present experiment was performed by shooting a U-beam accelerated in the SIS synchrotron, into a cryogenic liquid-deuterium target. The use of *inverse kinematics* allows to investigate the produced residual nuclei in mass and atomic numbers while flying forward, using the **FRS** as an achromatic energy-loss spectrometer. Only a few extremely short-lived alpha-emitters with 128 neutrons, having half-lives around 100 ns, partly decayed inside the spectrometer. For all other nuclides, the production cross sections were determined prior to their radioactive decay. With this procedure we demonstrated that the isotopic identification is unambiguous, a challenge for nuclides with Z above 70 at this energy. To define the cross sections we had to correct the counting rates for the effects inherent to our method. The resulting uncertainty of the cross-section values was 12-19%, higher for lower masses.

In Fig. 1 we show the cross-section values measured in the ^{238}U induced reactions on proton [4] (upper panel) and deuteron [5] (lower panel), plotted in grey-scale on top of a chart of nuclides. We can see that the length of the fragmentation corridor is larger in the case of the deuteron. This effect is due to the additional available excitation energy in the system, just after the collision. The de-excitation can proceed further, reaching lighter residues. We also observed that the production of heavy residues in the reactions induced by protons and deuterons are rather similar. The heaviest residues result from the most peripheral collisions. Due to the large spatial distribution of the deuteron, many of the impacts involve a single nucleon. Thus both reactions, with deuteron and proton, result in the same production. No differences between neutron and proton impacts were found. We also compared the productions of residues in the reactions induced by ^{208}Pb and ^{238}U on deuteron. As known from other reactions [4], the

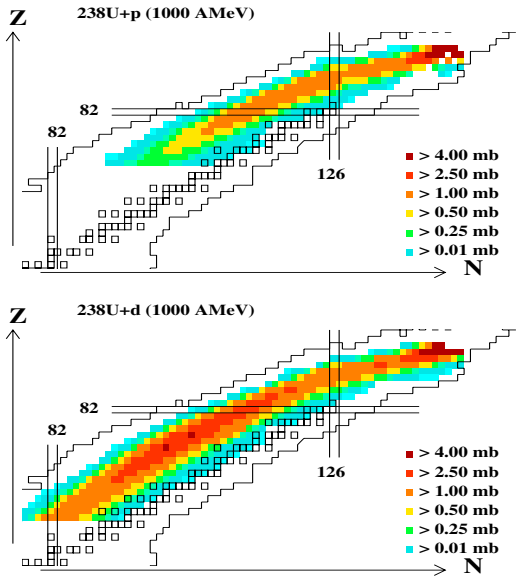


Figure 1: Production cross-sections measured in the ^{238}U induced reactions on proton (upper panel) and deuteron (lower panel) at $1A \cdot GeV$, plotted in grey-scale on top of a chart of nuclides.

results are expected to be similar, just scaled by the ratio of the total reaction cross sections. However large differences in the production of heavy residues were observed, due to the fission channel. This channel largely dominates the reaction mechanism in the neighborhood of the projectile ^{238}U, populating medium-mass residues.

The comparison of the results from proton and deuteron induced reactions will allow to improve the description of the impact of several nucleons, since the deuteron is the simplest extension after the collision of a single nucleon. The difference in energy deposition between nucleon and ion collisions can also be investigated [6]. The comparisons of reactions involving ions with very different fissilities, help to determine the accuracy of the description of the fission to particle-emission competition. All these results are essential in order to improve the models that describe the reactions mechanisms.

This work was supported by EC-HPRI-CT-1999-00001.

[1] E. Casarejos, PhD thesis, USC Santiago, 2001 [2] J. Benlliure et al., Nucl. Phys. A 683 (2001) 513 [3] F. Rejmund et al., Nucl. Phys. A 683 (2001) 540 [4] T. Enqvist et al., Nucl. Phys. A 686 (2001) 481 [5] J. Taieb, PhD thesis, IPN Orsay, 2000 [6] K.-H. Schmidt et al., this report.

Determination of the freeze-out temperature with the isospin thermometer

K.-H. Schmidt, M. V. Ricciardi, A. Botvina[(1)] , T. Enqvist[(2)]

GSI Darmstadt
[(1)] Permanent address: Inst. for Nuclear Research, Russian Academy of Sciences, 117312 Moscow, Russia
[(2)] Present address: University of Jyväskylä, 40351 Jyväskylä, Finland

As a prominent signature of instabilities of highly excited nuclei, the *multifragmentation* process, i.e. the formation of several clusters in a simultaneous break-up, has extensively been studied. Efforts are being made to deduce information on the liquid-gas-type phase transition of nuclear matter [1].

In this report we describe our efforts to obtain complementary information on thermal instabilities of nuclei from an alternative approach, by measuring nuclide cross sections of heavy residues in the fragmentation of ^{238}U in a lead target [2]. The experiment was performed in inverse kinematics with the fragment separator (FRS) at GSI. With the FRS the residual nuclei can be fully identified, and their velocities can be precisely evaluated from their magnetic rigidities. In this way, fission events could be discriminated and non-fission data were used to construct the fragmentation isotopic distribution of every observed element.

In figure 1, the so-obtained values of the mean *N*-over-*Z* ratio of the fragmentation products are presented as a function of the nuclear charge, *Z*. The experimental results are compared with two "reference" lines, the position of the beta-stability valley and the expectation of EPAX [3], a semi-empirical code based on the idea that fragmentation products result from long, *sequential* evaporation chains. Surprisingly enough, the experimental data show larger mean values, with a tendency to even cross the stability line for products with nuclear charge below ≈ 28. Lighter residues obviously experienced an evaporation cascade that was too short to reach the evaporation corridor. *More violent collisions seem to introduce lower excitation energies.* These apparently contradictory results can be explained assuming that the residues are formed in a *simultaneous* break-up process. This has two essential characteristics. Firstly, most of the energy acquired in the collision is consumed in the break-up stage and the remaining excitation energy is shared among the clusters. Secondly, the *N*-over-*Z* ratio of these clusters is expected to be close to the one of total decaying system. Indeed, the data can be explained assuming that the freeze-out temperature, i.e. the temperature of the clusters, at which the evaporation process starts, has a well-defined value, and it represents a limiting temperature above which no fully equilibrated compound nucleus can exist.

This idea is the basis of the *isospin thermometer* [4], a specific method used to deduce the temperature of nuclear systems from the isotopic distributions of the residues. The method consists of applying an evaporation code, with the quite well known ingredients of the statistical model, in order to deduce the temperature at the beginning of the evaporation cascade. For this purpose we have used the statistical multifragmentation model, SMM [5]. Within this model, a microcanonical ensemble of all break-up channels composed of nucleons and excited fragments of different masses is considered. It is assumed that an excited nucleus expands to a certain volume and then breaks up into nucleons and hot fragments. All possible break-up channels are considered. It is also assumed that at the break-up time the nucleus is in thermal equilibrium characterised by the channel temperature *T*. After break-up of the system, the fragments propagate independently in their mutual Coulomb fields and undergo secondary decays (evaporation-fission or Fermi break-up). In figure 1, the mean *N*-over-*Z* ratio of the isotopic distributions that results from these calculations, starting from different freeze-out temperatures, is compared to the experimental values. With increasing temperature, the mean neutron excess approaches the evaporation-residue corridor, marked by EPAX. There is a remarkable agreement found with the data when a freeze-out temperature close to 5 MeV is assumed. A similar conclusion has also been deduced from light charged particles emitted from intermediate-mass fragments in the range from Z = 2 to Z = 30 produced in central collisions of ^{129}Xe + ^{nat}Sn at 50 A MeV [6]. Thus, heavy-ion collisions in very different energy regimes show signatures of the same phenomenon.

By the use of a high-resolution spectrometer, we have revealed a new experimental signature of thermal instabilities of nuclei. A possible information on the liquid-gas like phase transition from this signature is clearly related to the liquid phase.

This work is supported by EC-HPRI-CT-1999-00001.

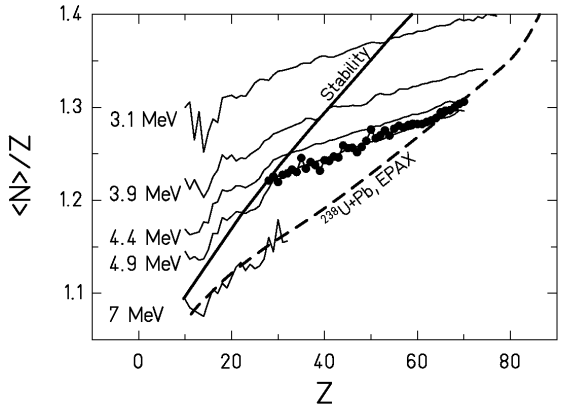


Figure 1: Experimental mean *N*-over-*Z* ratio of the fragmentation residues produced in the reaction ^{238}U on lead at 1·*A* GeV (full points), compared to the valley of beta stability and the prediction of EPAX. Fission events are not included. Mean neutron excess of the isotopic distributions of heavy residues obtained with SMM with different values of the freeze-out temperature show that there is a remarkable agreement with the data when a freeze-out temperature of about 5 MeV is assumed.

[1] W. Trautmann, Nucl. Phys. **A 685** (2001) 233.

[2] T. Enqvist et al., Nucl. Phys. **A 658** (1999) 47.

[3] K. Sümmerer, B. Blank, Phys. Rev. C 61 (2000) 034607

[4] K.-H. Schmidt et al., submitted to Nucl. Phys. A.

[5] J. P. Bondorf et al., Phys. Rep. **257** (1995) 133.

[6] N. Marie et al., Phys. Rev. **C 58** (1998) 256.

Effects of dissipation and simultaneous break-up on fission at high excitation energies

B. Jurado, K.-H. Schmidt, A. R. Junghans, GSI Darmstadt, Germany
J. Benlliure, Univ. Santiago de Compostela, Spain

The time a nucleus needs to populate its deformation space is ruled by dissipation, that is, the transfer of energy between intrinsic and collective degrees of freedom. The study of fission allows for gaining information on the strength of dissipation within a broad range of deformation. For small deformations, the hindrance of fission caused by dissipation starts to be remarkable only at high nuclear temperatures, when the statistical decay time is shorter than the dynamical delay. On the other hand, as shown in [1], thermal instabilities arise when nuclear temperatures larger than 5 MeV are reached. The aim of this work is to investigate the effects of dissipation and thermal instabilities on fission at high temperatures.

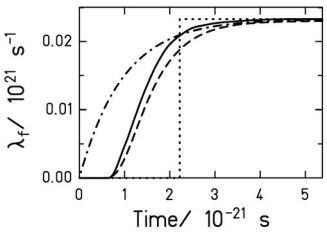


Figure 1: Time-dependent fission rate $\lambda_f(t) = \Gamma_f(t)/\hbar$ for A = 248, T = 3 MeV, and $\beta = 5 \cdot 10^{21}$ s^{-1}. The full line is the numerical solution of the FPE [3]. The dashed line is the result of including eq. (1) and (2) in eq. (3). The dotted line represents the step function and the dashed-dotted line the exponential-like function [2].

To obtain reliable conclusions, a realistic description of the effects of dissipation in fission by means of a time-dependent fission width $\Gamma_f(t)$ is mandatory. In our previous contributions [2], we have discussed the two most widely used approximations for $\Gamma_f(t)$, a step function and an exponential-like in-growth function. Comparing to the numerical solution of the FPE obtained in reference [3] for the fission rate, full line in figure 1, these two approximations appear to be considerably crude. For this reason, we have implemented in our model a highly realistic description based on the analytical solution of the Fokker-Planck equation (FPE) when the nuclear potential is approximated by a parabola [4]. Solving the FPE under these conditions gives the time dependence of the probability distribution W at the saddle point deformation x_b

$$W(x_b,t) = \frac{1}{\sqrt{2\pi\sigma}} \cdot \exp\left(-\frac{x_b^2}{2\sigma^2}\right) \quad (1)$$

where σ^2 is a time-dependent function of the form: $\sigma^2 =$

$$\frac{kT}{\mu\omega_1^2}\left\{1-e^{(-\beta\cdot t)}\left[\frac{2\beta^2}{\beta_1^2}\sinh^2\left(\frac{1}{2}\beta_1 t\right)+\frac{\beta}{\beta_1}\sinh(\beta_1 t)+1\right]\right\} \quad (2)$$

where k is Boltzmann´s constant, T is the nuclear temperature, μ is the reduced mass associated to the deformation degree of freedom, ω_1 describes the curvature of the potential at the ground state, and $\beta_1 = (\beta^2 - 4\omega_1^2)^{1/2}$.
In the overdamped regime ($\beta > 2\omega_1$) and for the case of a parabolic potential, the fission width can be approximated by

$$\Gamma_f(t) = \hbar\lambda_f \approx \frac{W(x_b,t)}{W(x_b,t\to\infty)} \cdot \Gamma_f^K \quad (3)$$

Implementing equations (1) and (2) in equation (3), we find an analytical expression that represents a very adequate description of $\Gamma_f(t)$, see dashed line in figure 1, especially at the onset of the fission rate, which is particularly important.
Two calculations with this new description of $\Gamma_f(t)$ have been performed in order to study the reaction of ^{238}U at 1 A GeV on lead. In one case, the simultaneous break-up stage, explained in [1], that results from the thermal instabilities at high temperatures has been considered and in the other case not. The simultaneous break-up has an influence on the deduced value of the dissipation coefficient β. In fact, to reproduce the total nuclear cross section of ^{238}U at 1 A GeV + Pb when the model without break-up is used a value of $\beta = 3.5 \cdot 10^{21}$ s^{-1} is needed, while for the calculation with the break-up stage the value of β has to be decreased to $\beta = 2 \cdot 10^{21}$ s^{-1}. In figure 2 the excitation energy at fission is plotted against the initial excitation energy for the two calculations with and without the break-up stage and $\beta = 2 \cdot 10^{21}$ s^{-1}. The 45-degree straight lines depicted in these spectra represent the upper limit for the excitation energy at fission. This line starts to be depopulated at initial excitation energies of around 150 MeV, indicating that above these excitation energies the transient time is longer than the decay time for particle emission. On the other extreme, comparing figure 2a) and 2b) one realises that the break-up process suppresses fission of nuclei produced with initial excitation energies E^*_0 over 800 MeV. Consequently, the data investigated in the present work are sensitive to the value of β at initial excitation energies E^*_0 between 150 MeV and about 800 MeV.

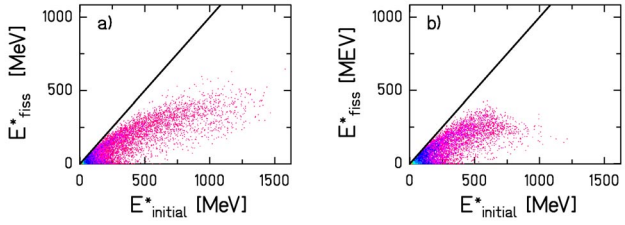


Figure 2: Calculations performed with $\beta = 2 \cdot 10^{21}$ s^{-1} and $\hbar\omega_1$ = 1MeV without including the break-up stage a) and including it b). They represent the excitation energy at fission versus the excitation energy of the prefragment for the fission events obtained in the reaction of 1·A GeV ^{238}U on a lead target.

This work has been supported by EC-HPRI-CT-1999-00002

References

[1] K.-H. Schmidt et al. GSI Ann. Rep. (2001)
[2] B. Jurado et al. GSI Ann. Rep. (2000) 27.
[3] K.-H. Bhatt, et al., Phys. Rev. C 33 (1986) 954.
[4] S. Chandrasekhar, Rev. Mod. Phys. 15 (1943) 1.

Low Momentum Nucleon-Nucleon Interaction and Fermi Liquid Theory[G]

Achim Schwenk, Gerald E. Brown (Stony Brook) and Bengt Friman (GSI/TUD)

Bogner, Kuo et al. [1] have constructed a low momentum nucleon-nucleon potential $V_{\rm low\,k}$ using folded-diagram techniques. Starting from a realistic nucleon-nucleon interaction, the hard momenta larger than a cutoff Λ are integrated out and renormalize an effective interaction $V_{\rm low\,k}$, such that the physical amplitudes at relative momenta smaller than Λ are preserved. For $\Lambda \lesssim 2\,{\rm fm}^{-1}$, they find that $V_{\rm low\,k}$ is unique, i.e. independent of the different short distance parts of the traditional potentials, and depends only weakly on the cutoff.

In normal Fermi systems, the low momentum quasiparticle interaction, which is characterized by the Fermi liquid parameters, is determined by a renormalization group (RG) fixed point. In this paper [2], we derive two novel relations between the Fermi liquid parameters of nuclear matter and the unique low momentum nucleon-nucleon interaction at $\Lambda = k_{\rm F}$. These relations connect the fixed point of the quasiparticle interaction to $V_{\rm low\,k}$ in the region where it depends only weakly on the cutoff.

The quasiparticle interaction, $\mathcal{F}$, parameterized in terms of Landau parameters F_l, etc., is given by

$$\mathcal{F}(\theta) = \sum_l (F_l + F_l'\,\boldsymbol{\tau}\cdot\boldsymbol{\tau}' + G_l\,\boldsymbol{\sigma}\cdot\boldsymbol{\sigma}' + G_l'\,\boldsymbol{\tau}\cdot\boldsymbol{\tau}'\,\boldsymbol{\sigma}\cdot\boldsymbol{\sigma}')P_l(\cos\theta)\,, \quad (1)$$

where for brevity we have omitted the tensor terms and θ denotes the angle between the quasiparticles on the Fermi surface. The quasiparticle interaction is dimensionless in units of the density of states at the Fermi surface. The forward scattering amplitude, $\mathcal{A}$, is then obtained by solving the quasiparticle scattering equation. This sums all quasiparticle-quasihole reducible diagrams in the zero sound channel and one finds

$$\mathcal{A}(\theta) = \sum_l (B_l + B_l'\,\boldsymbol{\tau}\cdot\boldsymbol{\tau}' + C_l\,\boldsymbol{\sigma}\cdot\boldsymbol{\sigma}' + C_l'\,\boldsymbol{\tau}\cdot\boldsymbol{\tau}'\,\boldsymbol{\sigma}\cdot\boldsymbol{\sigma}')P_l(\cos\theta)\,, \quad (2)$$

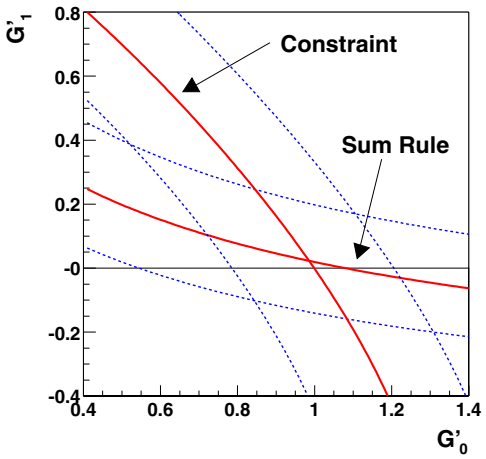
where $B_l = F_l/(1+F_l/(2l+1))$, etc. The Pauli principle requires that the forward scattering amplitude vanishes in singlet-odd and triplet-odd states for zero relative momentum, i.e., $\theta = 0$. This leads to the Pauli principle sum rules [3, 4]

$$\sum_l (B_l + B_l' + C_l + C_l') = 0 \quad (3)$$

$$\sum_l (B_l - 3\,B_l' - 3\,C_l + 9\,C_l') = 0. \quad (4)$$

The sum rules provide constraints on empirically determined Fermi liquid parameters. In an RG approach to Fermi liquids, they define an invariant under the decimation to the Fermi surface, which we show explicitly by deriving the RG equations in the particle-hole channels from the induced interaction.

Using the induced interaction of Babu and Brown [5], we derive two additional RG invariant constraints, which relate the Fermi liquid parameters of nuclear matter to the low momentum interaction in vacuum. We find in the singlet-even and triplet-even states [2]



$$\sum_l \{2F_l - B_l + 2F_l' - B_l' - 3\,(2G_l - C_l) - 3\,(2G_l' - C_l')\} = \mathcal{F}_{\rm driving}\,(S=0, T=1) \quad (5)$$

$$\sum_l \{2F_l - B_l - 3\,(2F_l' - B_l') + 2G_l - C_l - 3\,(2G_l' - C_l')\} = \mathcal{F}_{\rm driving}\,(S=1, T=0), \quad (6)$$

where the driving term $\mathcal{F}_{\rm driving}$ is given by the s-wave matrix elements of $V_{\rm low\,k}$ at $\theta = 0$.

Using these new constraints together with the Pauli principle sum rules, we can compute the large spin-dependent parameters, given the empirical values for the spin-independent parameters, F_0, F_1 and F_0'. In the figure we show the results for the spin-isospin parameters G_0' and G_1'. The dashed bands reflect the estimated errors in the constraints, due to the omitted parameters of higher l and errors in the input parameters. The resulting parameters are in fair agreement with empirical values as well as with microscopic calculations. Finally, the inclusion of tensor parameters into the analysis shows that these must be treated self-consistently in the induced interaction.

References

[1] S.K. Bogner, T.T.S. Kuo, and L. Coraggio, [nucl-th/9912056]; S.K. Bogner, T.T.S. Kuo, A. Schwenk, D.R. Entem, and R. Machleidt, [nucl-th/0108041].

[2] A. Schwenk, G.E. Brown, and B. Friman, Nucl. Phys. **A** in press, [nucl-th/0109059].

[3] L.D. Landau, Sov. Phys. JETP **3** (1957) 920; ibid. **5** (1957) 101; ibid. **8** (1959) 70.

[4] B. Friman and A.K. Dhar, Phys. Lett. **B85** (1979) 1.

[5] S. Babu and G.E. Brown, Ann. Phys. **78** (1973) 1.

Short-Range Repulsive and Tensor Correlations in Nuclei

T. Neff and H. Feldmeier (GSI)

It is a central challenge of nuclear physics to explain the properties of nuclear many-body systems in terms of realistic nuclear interactions that reproduce the phase shifts. Only recently it became possible to perform quasi-exact ab initio calculations of the nuclei up to $A = 8-12$ with realistic interactions [1,2]. For bigger nuclei these calculations become exceedingly difficult.

Our aim is to perform approximate ab initio calculations of larger nuclei where the short-range central and tensor correlations induced by the realistic forces are explicitly introduced into the many-body state. For that we construct a unitary correlation operator C as a product of a radial correlator C_r and a tensor correlator C_Ω.

$$C = C_\Omega C_r \tag{1}$$

The correlated state $\big|\,\hat{\Psi}\,\big\rangle = C\big|\,\Psi\,\big\rangle = C_\Omega C_r\big|\,\Psi\,\big\rangle$ is obtained by a unitary mapping of the uncorrelated $\big|\,\Psi\,\big\rangle$.

The unitary correlation operator defines also a correlated interaction $\hat{H} = C^\dagger H C$, that can be considered as an effective interaction. Other observables can be correlated as well and the physical implications of the short-range correlations, for example on the nucleon momentum distributions, can be evaluated.

The radial correlator C_r [3], which shifts a pair of particles in the radial direction away from each other, uses as generator the radial momentum operator p_r together with a shift function $s(r)$ that depends on the distance of the two nucleons.

$$C_r = \exp\left\{-i\sum_{i<j}\frac{1}{2}\Big(s(r_{ij})\;p_{r\,ij} + h.a.\Big)\right\} \tag{2}$$

The shift will be strong at short distances and will vanish at large distances.

The tensor force in the $S=1$ channels depends on the spins and the spatial orientation $\vec{r} = (\vec{r}_1 - \vec{r}_2)/(|\vec{r}_1 - \vec{r}_2|)$ of the nucleons via the tensor operator

$$S_{12}(\vec{r},\vec{r}) = 3(\vec{\sigma}_1\cdot\vec{r})(\vec{\sigma}_2\cdot\vec{r}) - (\vec{\sigma}_1\cdot\vec{\sigma}_2) = 2\left(3(\vec{S}\cdot\vec{r})^2 - \vec{S}^2\right). \tag{3}$$

An alignment of $\vec{r}$ with the direction of total spin $\vec{S} = \frac{1}{2}(\vec{\sigma}_1 + \vec{\sigma}_2)$ is favored energetically. The tensor correlator C_Ω, defined as

$$C_\Omega = \exp\left\{-i\sum_{i\neq j}\frac{3}{4}\Big(\vartheta(r_{ij})\,(\vec{\sigma}_i\vec{r}_{ij})(\vec{\sigma}_j\vec{p}_{\Omega\,ij}) + h.a.\Big)\right\}, \tag{4}$$

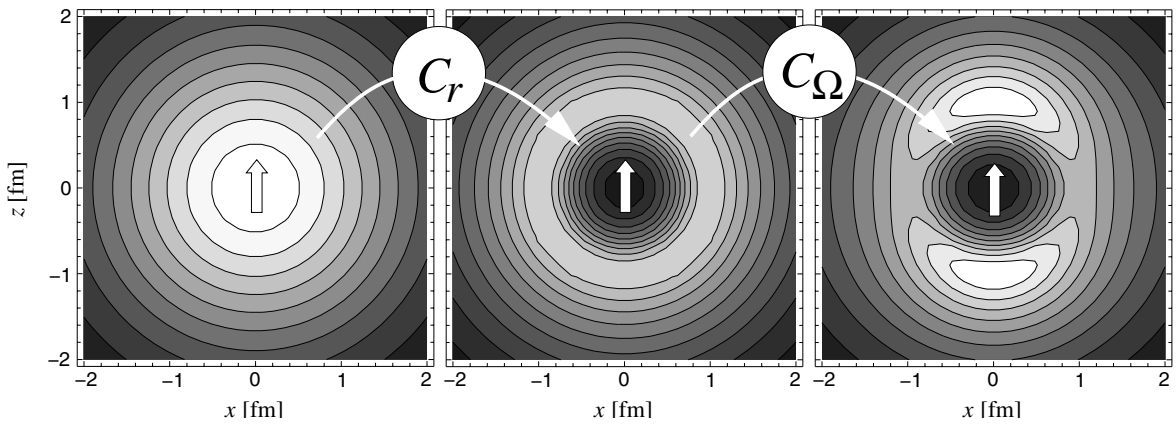
achieves this alignment by shifts perpendicular to the relative orientation $\vec{r}_{ij}$. To achieve this the generator uses a tensor operator constructed with the orbital part of the momentum operator $\vec{p}_\Omega = \vec{p} - \vec{p}_r$. The r-dependent strength of the tensor correlations is controlled by $\vartheta(r)$.

The figure illustrates the action of C_r and C_Ω in the $S=1, M_S=1; T=0$ channel of the ^{4}He two-body density $\rho^{(2)}_{S,T}(\vec{r})$. The arrow indicates the spin direction $\vec{S}$ and the correlation operator is determined for the Argonne V18 interaction. The left plot shows the density (bright areas = high densities) calculated in the uncorrelated state $\big|\,\Psi\,\big\rangle$ of four nucleons in the s-shell, here the nucleons are found with the highest probability at zero distance. The radially correlated state $C_r\big|\,\Psi\,\big\rangle$ yields the two-body density shown in the middle where a hole has been created to accommodate the repulsive core of the two-body potential.

The subsequent application of the tensor correlator $C_\Omega C_r\big|\,\Psi\,\big\rangle$ results in the correlations shown on the right. C_Ω, which acts only on the $S=1$ part of a pair, moves probability perpendicular to $\vec{r}$ from the "equator" to the "poles". The spherical distribution transforms into an axially symmetric one with enhanced probability in regions where $\vec{r}$ and $\vec{S}$ are parallel, which implies more binding from the tensor interaction.

The correlated interaction $\hat{H}$ is used successfully with simple shell model and Fermionic Molecular Dynamics Slater determinants [4]. This allows us to perform calculations for all nuclei up to about $A = 50$. Although a single Slater determinant as many-body trial state is the most simple ansatz for the uncorrelated $\big|\,\Psi\,\big\rangle$ we obtain results very close to those of the quasi-exact methods.

[1] S.C. Pieper et al., PR **C64** (2001) 014001
[2] P. Navrátil et al., PR **C62** (2000) 054311
[3] H. Feldmeier et al., NP **A632** (1998) 61
[4] T. Neff, *Short-Ranged Central and Tensor Correlations in Nuclear Many-Body Systems*, PhD thesis, 2001



Two- and three-body halos in helium and lithium isotopes

M. Tomaselli[1,2], S. Fritzsche[3], A. Dax[2], H.-J. Kluge[2], T. Kühl[2,4], L.C. Liu[5], D. Marx[2], M. Mutterer[1], S.R. Neumaier[2], W. Nörtershäuser[2,6], I. Tanihata[7], and H. Wang[2,7]
[1] TU Darmstadt, [2] GSI Darmstadt, [3] Univ. Kassel, [4] Univ. Mainz,
[5] Los Alamos National Laboratory, [6] Univ. Tübingen, [7] Univ. Tokyo

Exotic radioactive beams, which are obtained by fragmentation of heavy ions, have largely contributed to the investigation of the structure of nuclei far from stability [1]. Experiments have revealed new properties that characterize the light neutron-rich nuclei, i.e. the existence of a neutron halo which extends outwards to large radii. Theoretically this effect has been analyzed mainly in terms of the Borromean approximation. This model assumes that the halo structure of the ground states of exotic nuclei is determined only by the valence neutrons which are confined into the lowest shell, while collective excitations of the system are neglected [2]. However, according to Ref. [3] these excitations play an important role in modelling the two-body and three-body halo structure of the matter and charge distibutions of light exotic nuclei.

In order to proof the role of the collective excitations, calculations for the wave function of the ground state of ^{6}Li and for the matter distribution of ^{6}He have been performed. The DCM describes the ground states of nuclei in terms of interacting clusters: valence particles and intrinsic vacuum states. It allows a separated analysis of the valence particle and the collective excitations of the core. The amplitudes of the mixed-mode wave-functions are derived in the framework of non-perturbative solutions of the equation of motion.

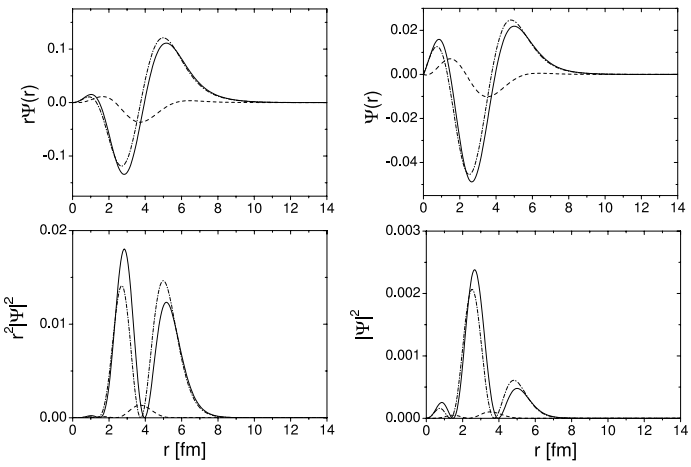


Figure 1: Calculated wave function and probablity distributions of the ground state of ^{6}Li. The dash-dotted line gives the CM result for the two particles in the shell-model approximation, the dashed line the DCM contributions, and the solid line the results for the dressed two particles.

The model spaces for the ground state of ^{6}Li and ^{6}He are constructed by allowing valence particles to be scattered to higher configuration states ($2\hbar\omega$) and to interact with the core intrinsic states formed by exciting particles from the s-shell. The single-particle states, used as input in the DCM calculations, have been approximated by harmonic oscillators with a state-dependent range introduced to reproduce the single-particle radii as calculated in a Wood-Saxon potential well. The single-particle energies are also obtained in this procedure. The two-body matrix elements are the same as used in Ref. [3].

In Fig. 1, the wave function of the dressed two particles ground state is given for ^{6}Li in terms of the shell-model (dashed-dot line) and DCM (dashed line) contributions. The core excitation terms are moving the first maximum of the ψ^2 distribution to larger r values, thus contributing to the formation of a long tail in the matter distribution. In Fig. 2 the effect of different center-of-mass (CM) components on the matter distribution of ^{6}He is shown. The dotted line has been calculated considering only the $L = 0$ center-of-mass components and has been presented previously [3], while for the dashed line all allowed CM components have been included. It should be noted that the higher-order CM components are typical for the core excitation mechanism. Finally, the solid line was calculated like the dashed line but including the $L = 0, 1, 2, 3, 4$ CM components as well and increasing the spin-orbit term of the d shells. This energy variation simulates the different shell closure postulated in Ref. [4] for the neutron-rich nuclei.

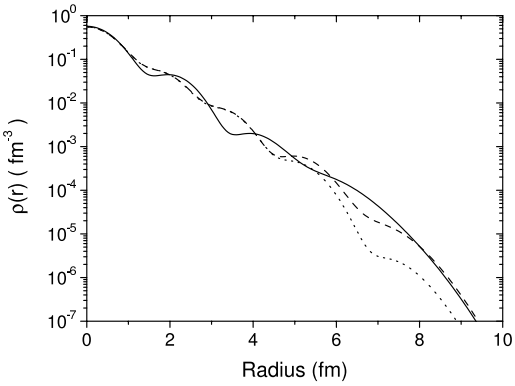


Figure 2: Calculated matter densities of ^{6}He: the dotted line included only the L=0 CM components, the dashed line was calculated considering the L=0,1,2,3,4 CM components, and the solid line distribution was calculated increasing the spin-orbit splitting of the d states.

References

[1] S.R. Neumaier *et al.*, Nucl. Phys. A, to be published; G.D. Alkhazov *et al.*, Phys. Rev. Lett. **78**, 2313 (1997)
[2] P.G. Hansen and B. Jonson, Europhys. Lett. **4**, 409 (1987)
[3] M. Tomaselli *et al.*, Phys. Rev. **C62**, 67305 (2000); M. Tomaselli *et al.*, Proc. NPBL, Lipari (2001), in press; M. Tomaselli *et al.*, Proc. DANF, Casta-Papiernicka (2001), in press
[4] R. Kanungo, I. Tanihata, and A. Ozawa, Proc. INPC, Berkeley, USA (2001), in press

A nuclear point-coupling model and its applications

T. Bürvenich[1], T. Cornelius[1], A. Sulaksono[1], P.–G. Reinhard[2],
J. A. Maruhn[1], D. G. Madland[3], W. Greiner[1]

[1] Institut für Theoretische Physik, Universität Frankfurt, Robert-Mayer-Str. 8–10, D–60325 Frankfurt am Main
[2] Institut für Theoretische Physik II, Universität Erlangen, Staudtstr. 7, D–91058 Erlangen
[3] Los Alamos National Laboratory (LANL), Los Alamos, USA

Relativistic mean field (RMF) models are quite successful in describing ground-state properties of finite nuclei and nuclear matter properties. They describe the nucleus as a system of Dirac nucleons that interact in a relativistic covariant manner via mean meson fields [1]. The meson fields produce a finite range (FR) effective interaction. An alternative is the point coupling model (RMF-PC) where nucleons are interacting directly via contact terms together with derivative terms that simulate to some extend finite-range effects [2].

One can view RMF-PC as an approach that lies in between the RMF-FR approach and the nonrelativistic Skyrme-Hartree-Fock (SHF) approach which is also a well-developed self-consistent mean-field model that performs very well (for a review see [3]). Whereas SHF is based upon density-dependent contact interactions with extensions to gradient terms, kinetic terms, and the spin-orbit interaction, RMF-FR is based upon a coupled field theory of Dirac nucleons and effective meson fields treated at the mean-field level, where density dependence is modeled by nonlinear meson self couplings and the role of gradient terms is taken over by the finite ranges of the mesons. A comparison of RMF-PC and SHF addresses the differences between in-medium Dirac and Schrödinger nucleons, whereas a comparison of RMF-PC and RMF-FR addresses the absence *vs.* presence of finite range and the different treatments of density dependence.

The elementary building blocks of the point-coupling vertices are two-fermion terms of the type

$$(\bar{\psi}\mathcal{O}_\tau\Gamma\psi) \quad , \quad \mathcal{O}_\tau \in \{1, \tau_i\} \quad , \quad \Gamma \in \{1, \gamma_0\} \qquad (1)$$

with ψ the nucleon field, τ_i the isospin matrices and Γ one of the 4x4 Dirac matrices. We use 4 fermion terms with corresponding derivative terms and higher order terms in both the scalar and vector density. The model studied here contains 9 parameters. To estimate its predictive power compared to established mean-field approaches, we performed a fit in the manner it was done to fit the RMF-FR force NL-Z2 [4]. The resulting force is called PC-F1.

In figure 1 we compare the results for the observables that were part of the fitting procedure. We see that while NL-Z2 performs a bit better for binding energies and surface thicknesses, PC-F1 is superior with respect to radii.

Comparing the predictions for isotopic and isotonic chains, density-related observables, fission barriers, spin-orbit splittings and nuclear matter [5], we find overall agreement with the predictions from the RMF-FR model. The spin-orbit splittings can be reproduced with similar quality as with the meson model, showing that the relativistic framework is superior to the SHF model in that respect. It agrees with the RMF-FR model predicting a doubly-magic superheavy nucleus $^{292}120_{172}$.

The RMF-PC will serve as a tool to understand more deeply the structures of RMF and SHF in comparison, particularly the impact of nucleon kinematics and of the density dependence.

References

[1] P.–G. Reinhard, Rep. Prog. Phys. **52** (1989) 439
[2] B. A. Nikolaus, T. Hoch, and D. G. Madland, Phys. Rev. C **46** (1992) 1757
[3] P. Quentin and H. Flocard, Ann. Rev. Nucl. Part. Sci. **21** (1978) 523
[4] M. Bender, K. Rutz, P.–G. Reinhard, J. A. Maruhn, and W. Greiner, Phys. Rev. C **60** (1999) 34304
[5] T. Bürvenich, D. G. Madland, J. A. Maruhn, and P. -G. Reinhard, nucl-th/0111012 (2001), accepted for publication in Phys. Rev. C

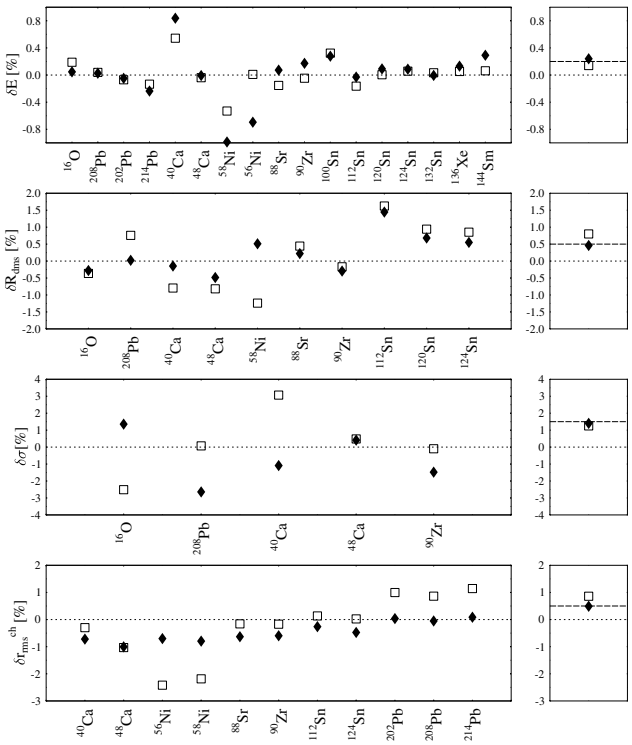


Figure 1: Errors in percent for the observables binding energy, diffraction radius, surface thickness and rms charge radius for PC–F1 (filled diamonds) and NL–Z2 (open squares) are seen on the left. The right panels show the absolute mean errors for the corresponding observables, where the dashed lines indicate the chosen relative errors ΔO in the fitting procedure.

Self-consistent calculations of surface vibrations

T. Cornelius[1], M. Bender[2], T. Bürvenich[1], P. Fleischer[3], P.–G. Reinhard[3], J. A. Maruhn[1], W. Greiner[1]

[1] Institut für Theoretische Physik, Universität Frankfurt, Robert-Mayer-Str. 8–10, D–60325 Frankfurt am Main
[2] Service de Physique Nucléaire Théorique – CP229, Université Libre de Bruxelles, B–1050 Bruxelles
[3] Institut für Theoretische Physik, Universität Erlangen, Staudtstr. 7, D–91058 Erlangen

The spectrum of low lying nuclear states is traditionally associated with the collective motion of the nuclear surface. Various empirically developed collective models (Bohr-Hamiltonian, fluid dynamics, interacting boson model) have been used for its description. The link with a microscopic description has been established on the grounds of a deformed shell model and, more recently, using constrained Skyrme-Hartree-Fock (SHF) calculations [1]. We report here result of such a fully microscopic and self-consistent calculation of low lying spectra as well as its consequences for ground state correlations.

The microscopic input is obtained in the spirit of an adiabatic picture from deformed SHF. This produces the collective path, a dense series of mean field states along which the collective motion is supposed to evolve. We deduce from these states: the potential energy surface (PES), the self-consistent cranking mass (often called ATDHF cranking), and the associated zero-point energy corrections [2]. These pieces are used to build a collective Bohr-Hamiltonian for quadrupole vibrations The rules to link the microscopic information to a collective model are deduced theroetically from dynamical generator-coordinate method augmented by appropriate consideration of the topology of the collective mode [2]. Actually, we are performing the deformed SHF calculations with axial symmetry and describe triaxial properties by interpolation. This approach is acceptable for nuclei close to sphericity or with only small defomation. The Bohr-Hamiltonian thus derived is solved numerically. The solutions provide the low lying collective spectra of the nucleus. The ground state of the collective calculation yields immediately the ground state energy of the total nucleus including the correlation energy from quadrupole vibrations.

Figure 1 shows a first result of excitation spectra for ^{186}Pb as test case. This proton rich nucleus is particularly interesting because its PES shows several isomers. As a consequence it produces an unusual spectrum where two excited 0^+ states come below the first excited 2^+. It is

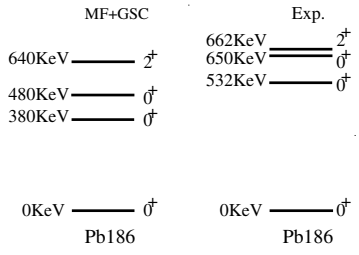


Figure 1: Spectrum of low lying excitations in ^{186}Pb. Left part: result of calculations with SHF using the force SkI3. Right part: experimental data.

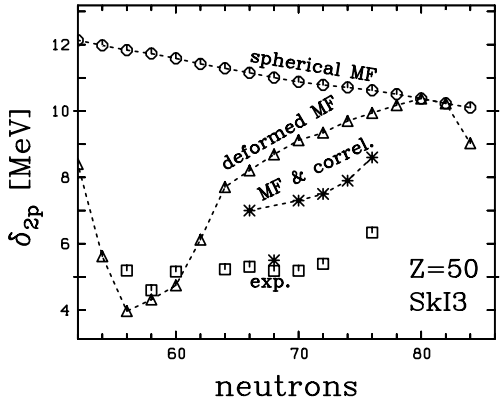


Figure 2: Two–proton shell gap δ_{2p} for Sn isotopes calculated with SHF (force SkI3) at various levels of approximation and compared with experimental data.

comforting to see that our microscopic calculation produce at once (i.e. without adjustable paremeter) these typical spectral pattern. Even the actual excitation energies are hit fairly well in view of the precision one can expect from such an involved and parameter free calculation. It is, of course, clear that one has to perform now systematic investigations. It is known that there exist a large variety of Skyrme forces with different features. One needs to check a handful of them to disentangle which features of the microscopic force are repsonsible for that (pertinent) result.

Figure 2 shows results on collective ground state correlations. Test case are the two-proton shell gaps $\delta_{2p} = E(Z-2,N) - 2E(Z,N) + E(Z+2,N)$ for the chain of Sn isotopes (Z=50). This second difference of energy is very sensitive to any correction on the ground state energy. Purely spherical SHF is clearly not enough as it even produces the wrong trends. The reason is that Sn keeps its spherical shape but the neighbours (Z=48 and 52) develop already a small deformation. Obviously, the deformed SHF improves the results, but not sufficiently. All involved nuclei with non-magic neutron numbers are rather soft and thus we obtain a visible effect from correlations, helping towards the experimental results. Correlations are obvisouly important for two-nucleon shell gaps. There remains still a discrepancy. This may be due to the actual force used. More systematic investigation for a broad selection of forces are to come.

References

[1] P. Bonche et al, Nucl.Phys. A510 (1990) 466
[2] P.-G. Reinhard, K. Goeke, Rep.Prog.Phys. **50** (1987) 1

Entrance-channel potentials in the syntheses of the heaviest nuclei

V.Yu. Denisov *, W. Nörenberg

The mechanism of compound-nucleus formation by the fusion of very heavy nuclei is an outstanding problem in the synthesis of super-heavy elements (SHEs) [1, 2]. The ultimate aim is the description of fusion as part of the quantum-mechanical scattering process between two nuclei. In such a formulation one has to consider all kinds of channels which are coupled (in general non-perturbatively) to the entrance channel of the colliding nuclei. Thus one faces the problem of describing the coupling of a large number of channels, which include inelastic excitations and transfer, quasi-fission, fusion and compound-nucleus formation. One of the crucial steps in such a description is the coupling of the entrance-channel wave function to more compact configurations. It is obvious that the energy dependence of the entrance-channel wave-function strongly affects the cross-sections for all processes including those which involve compact-shape configurations. Therefore, we are interested to understand as a first step the basic properties of the entrance channel in fusion reactions.

Since the approach of the colliding nuclei is fast compared to the relaxation process, the frozen-density approximation has been used for defining the entrance-channel potentials. Microscopic Hartree-Fock-Bogoliubov calculations are used to obtain these densities, while the Thomas-Fermi approximation, extended to include all terms up to second-order spatial derivatives [3], has been applied together with Skyrme energy densities to obtain the energy of the system as function of distance.

The results on cold-fusion systems (^{48}Ca, ^{50}Ti, ^{54}Cr, ^{58}Fe, ^{64}Ni,^{70}Zr,^{76}Ge, and ^{86}Kr on ^{208}Pb and oblate ^{198}Pt, as well as symmetric systems with $A_1 \approx A_2 \approx 120...150$) and hot-fusion systems (^{48}Ca and ^{40,42}Ca on ^{238}U, ^{244}Pu, ^{248}Cm, and ^{252}Cf, as well as ^{50}Ti, ^{54}Cr, ^{58}Fe, ^{58}Ni, ^{64}Ni, ^{68}Ni, ^{70}Zr,^{78}Ge, ^{74}Se, ^{82}Se on ^{238}U and ^{252}Cf) are reported and discussed in [4].

An example (^{70}Zr+^{208}Pb) is shown in Fig. 1. The main features of the entrance-channel potential are summarized as follows.

- The potential pocket are much shallower then for light systems (e.g. ^{58}Fe+^{64}Ni).
- The observed fusion windows (vertical thick bar in Fig. 1) lie systematically 5 to 10 MeV below our barriers, indicating the importance of subbarrier processes like transfer and collective deformations.
- With increasing masses of the projectile and target the pockets and energy difference between barrier and compound-nucleus g.s. energy decreases.

The barriers obtained with the help of different analytical expressions for nucleus-nucleus potentials introduced by Bass in 1974 [5] and in 1980 [6], by Blocki et al. (proximity 77) [7] and by Krappe-Nix-Sierk (KNS) [8] are spread over a very wide interval, as shown in Fig. 1b. The differences between the barriers evaluated in these approaches reach 25 MeV. The KNS potential is closest to our ETF potential. The results for the KNS potential is presented only up to the touching point.

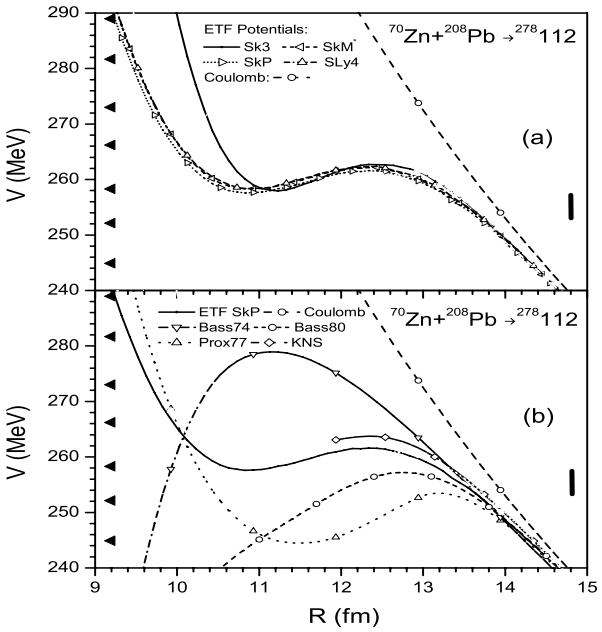


Figure 1: **(a)** The interactiion potentials for ^{70}Zr+^{208}Pb evaluated in the ETF approximation with the Skyrme forces SIII, SkM*, SkP and SLy4. For comparison also the Coulomb potential is given. The energy window for observed SHE formation range of collision energies for observed synthesis of the SHE 112 [1] is marked by vertical thick bar. The ground-state Q-value is indicated by the lowest triangle at the left vertical axis. The other 6 triangles mark, respectively, the thresholds for the emission of 1, 2, 3, 4, 5 and 6 neutrons. **(b)** The potentials for the collision system ^{70}Zr+^{208}Pb obtained in the ETF approximation with the Skyrme force SkP in relation to the proximity (1977), the Bass (1974, 1980) and the KNS potentials.

References

[1] S. Hofmann, G. Münzenberg, Rev. Mod. Phys. **72**, 733 (2000)
[2] Yu.Ts. Oganessian, et al., Eur. Phys. J. **A5**, 63 (1999)
Yu.Ts. Oganessian, et al., Phys. Rev. **C62**, 041606 (2000)
Yu.Ts. Oganessian, et al., Phys. Rev. **C63**, 011301 (2001)
[3] M. Brack, et al., Phys. Rep. **123**, 275 (1985)
[4] V.Yu. Denisov, W. Nörenberg, in preparation.
[5] R. Bass, Nucl. Phys. **A231**, 45 (1974)
[6] R. Bass, *Nuclear Reactions with Heavy Ions* (Springer-Verlag, Berlin 1980) 410
[7] J. Blocki, et al., Ann. Phys. **105**, 427 (1977)
[8] H.J. Krappe, J.R. Nix, A.J. Sierk, Phys. Rev. **C20**, 992 (1979)

* Inst. Nucl. Res., Kiev, Ukraine

Transverse Velocity Scaling in Au+Au Midrapidity Emissions

J. Łukasik and W. Trautmann for the INDRA-ALADIN Collaboration

Both, central and peripheral collisions of symmetric heavy ions at intermediate energies, despite having been studied for decades now, are still drawing attention, still provide new pieces of information, and still contain open questions. In order to study these reactions in more detail a series of experiments has been performed during the 4th INDRA Campaign carried out at the GSI. The reaction products formed using the beams delivered by the SIS synchrotron were measured with the 4π multidetector INDRA [1]. In this contribution we will focus on the Au+Au reactions at energies 40-150 A MeV (see also [2]).

In peripheral and mid-central collisions the 2 heaviest residua or their remnants remembering the entrance channel conditions, are usually accompanied by a sizable amount of particles and fragments with parallel velocities intermediate between those of the projectile and of the target [3-6]. They are often referred to as *midrapidity* (*midvelocity*) emissions. The origin of these midrapidity fragments and related reaction scenarios are still debated and their characteristics are still a matter of interest.

Inspection of transverse velocities, or energies, for different rapidity bins leads to some interesting observations.

The upper row of Fig. 1 presents invariant cross sections for Li fragments from Au+Au @ 100 A MeV reaction, as a function of transverse velocity and rapidity with the indicated rapidity cuts for different centrality selections. The middle row presents transverse velocity distributions of Li ions for different bombarding energies, and the bottom one the corresponding mean transverse energies.

At projectile rapidity and for peripheral collisions (left column) a pronounced Coulomb component is seen in the velocity spectra. The position of the peak is remarkably constant for all bombarding energies and indicates emission from the surface of the heavy primary fragment.

The Coulomb component is nearly absent or possibly spread out over a wide velocity range in the emissions at midrapidity where one can observe two different scaling behaviors for the peripheral and central collisions. In the central case (right panel), both, the mean and the width of the spectra *increase* considerably with increasing bombarding energy and with the fragment mass (see also bottom right panel). This reflects the increasing importance of flow for central collisions [7].

For peripheral reactions (middle column), a particularly intriguing behavior is observed. The shapes of the velocity spectra are between Gaussian and exponential and *invariant* with respect to the incident energy and also with respect to the mass in the range of Z indicated in the middle bottom panel. The corresponding mean transverse energies of about 28 MeV for lithium ions seem too large for a purely thermal origin and are larger than the value of 14.6 MeV temperature obtained from the Goldhaber model [8] with $p_F = 265$ MeV/c (the thick horizontal line) but may reflect the additional Coulomb potential that is generated by the two heavy residua in the neck region.

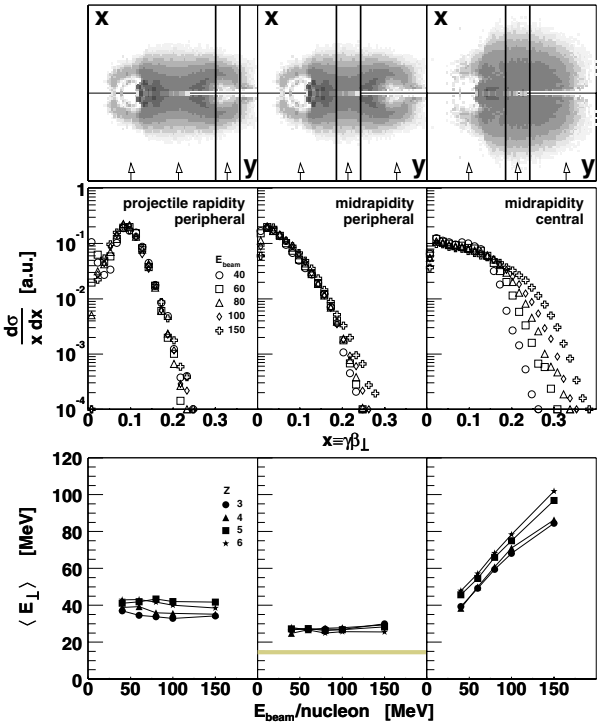


Figure 1: Top row: invariant cross sections for Z=3 fragments as a function of transverse velocity (x) and rapidity (y), for Au+Au @ 100 A MeV reaction with the indicated rapidity cuts. The arrows denote, from the left, the target, CM, and projectile rapidities, respectively. Middle row: invariant transverse velocity distributions for Z=3 at bombarding energies from 40 to 150 A MeV. Bottom row: mean transverse energies of IMFs with $3 \leq Z \leq 6$ as a function of incident energy. The thick solid line represents the Goldhaber model prediction. The 3 columns correspond to three selections in rapidity and centrality: projectile rapidity and peripheral collisions (left column), midrapidity and peripheral collisions (middle column) and midrapidity and central collisions (right column), respectively.

Simulations of nucleon-nucleon collisions imply that the Pauli blocking of the collisions can be partly responsible for this invariance. The mean transverse energies of nucleons scattered into the midrapidity region show a very weak dependence on incident energy provided Pauli blocking is effective. Otherwise, the mean transverse energies increase with the incident energy. Within a coalescence picture one might expect invariance of mean transverse energies at midrapidity also for fragments.

References

[1] J. Pouthas *et al.*, Nucl. Instr. Meth. in Phys. Res. **A357**, 418 (1995).
[2] J. Łukasik, A.S. Botvina *et al.*, GSI Sci. Rep. (2000).
[3] J.F. Dempsey *et al.*, Phys. Rev. C **54**, 1710 (1996).
[4] Y. Larochelle *et al.*, Phys. Rev. C **55**, 1869 (1997).
[5] J. Łukasik *et al.*, Phys. Rev. C **55**, 1906 (1997).
[6] E. Plagnol *et al.* Phys. Rev. C **61**, 014606 (2000).
[7] F. Lavaud, PHD Thesis, IPNO-T.01-06 (2001).
[8] A.S. Goldhaber, Phys. Lett. **53B**, 306 (1974).

Statistical Multifragmentation of Non-Spherical Sources in Au+Au

A. Le Fèvre for the INDRA-ALADIN Collaboration

From the results of previous INDRA campaigns at GANIL, it is known that central collisions of heavy symmetric systems lead to the formation of a heavy, hot and expanding composite nucleus. The break-up properties have been successfully reproduced within standard statistical approaches [1-3], except for pronounced anisotropies in the fragment yields and kinetic energies. This has motivated the extension of the standard version of the Berlin statistical multifragmentation model (MMMC, ref. [4]) to non-spherical sources [5]. Similar anisotropies have been observed in the Au+Au systems studied in the energy range of 40 to 150A.MeV [6, 7], during the 4th INDRA Campaign at GSI. The reaction products have been measured using the 4π multidetector INDRA [8]. For this contribution, we will focus on the central collisions of Au+Au at 80A.MeV, selected using the transverse energy as in [9].

Fragment mean kinetic energies as a function of Z and, for the heaviest fragment, as a function of angle are shown in Fig. 1. Fragments emitted at forward angles are much more energetic than those emitted sidewards. For the heaviest fragment, this decrease of the kinetic energies with the angle is continuous and fairly strong. This cannot result from a detector efficiency effect, since the isotropy of a MMMC-simulated spherical source is fairly well conserved through the INDRA filter. The MMMC simulation of a prolate source, elongated along the beam axis (with a size ratio 1:0.7), is able to reproduce the data, both qualitatively and quantitatively. In the simulations, the size (Z=110), the excitation energy (7A.MeV), and the collective radial flow (5A.MeV) have been adjusted such as to reproduce the experimental partitions and the total kinetic energy of fragments.

The partitions exhibit an anisotropy too, as shown in the left panel of Fig. 2. The multiplicities of heavier fragments are twice as high in the direction of the beam as in sideward direction. The angular distribution of the heaviest fragment exhibits a strong forward-backward focusing. The average size of the fragments emitted sidewards are smaller and, the heavier the fragment, the higher the probability to be emitted forward or backward. These effects are well reproduced by the MMMC simulation with a prolate source, but not with a spherical source, as illustrated in both panels. The MMMC approach explains the anisotropies of partitions and kinetic observables as due to the minimization of the Coulomb energy of the system at freeze-out, which strongly correlates the charge of the fragments with their location inside the deformed volume.

The fact that the present statistical approach explains successfully the partitions and kinetic observables along with their anisotropies demonstrates that the presence of anisotropies does not necessarily imply the absence of equilibrium in the system. It seems that, though some part of the energy has not been relaxed (in deformation and collective flow) and does not participate in the equilibrium, a sufficient degree of equilibration and opening of the phase space has been achieved in the system to validate a statistical description.

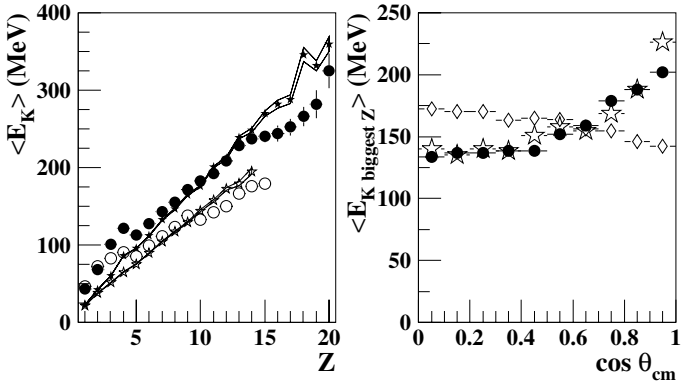


Figure 1: Left: mean kinetic energy of fragments as a function of Z in the center of mass. Circles are experimental data, stars are the MMMC-prolate source prediction. Full symbols account for forward angles (below 60° around the beam), open symbols for sideward angles (60°-90°). Right: mean kinetic energy of the biggest Z as a function of the angle. The circles are the experimental data. MMMC predictions are denoted by stars (prolate) and diamonds (sphere).

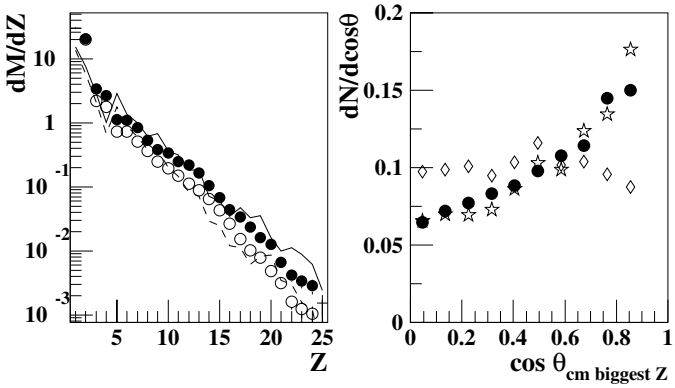


Figure 2: Left: multiplicities of charges normalized to the total solid angle. The circles represent the experimental data, and the lines are the MMMC predictions with the prolate source; like in Fig. 1, forward (full circles and line) and sideward angles (open circles and dashed line) have been separately considered. Right: angular distributions of the biggest fragment; the symbols were chosen as in Fig. 1, right panel.

References

[1] R. Bougault *et al.* (INDRA Collaboration), Proceedings of the Bormio Conference 1997.
[2] N. Marie *et al.*, Phys. Lett. **B391**, 15 (1997).
[3] A. Le Fèvre, Ph.D. thesis GANIL T9703.
[4] D.H.E. Gross, Rep. Prog. Phys. **53**, 605 (1990).
[5] A. Le Fèvre *et al.*, Phys. Rev. C **60**, 051602 (1999).
[6] J. Łukasik *et al.*, GSI Sci. Rep. (2000).
[7] F. Lavaud, PHD Thesis, IPNO-T.01-06 (2001).
[8] J. Pouthas *et al.*, Nucl. Instr. Meth. in Phys. Res. **A357**, 418 (1995).
[9] J. Łukasik *et al.*, Phys. Rev. C **55**, 1906 (1997).

Mechanisms Behind the Rise and Fall of Sideflow at SIS Energies

W. Reisdorf, A. Andronic, A. Devismes, Ch. Finck, A. Gobbi, O. N. Hartmann, N. Herrmann[1], K.D. Hildenbrand, Y.J. Kim, T. Kress, Y. Leifels, Z. Tyminski
FOPI Collaboration, GSI Darmstadt,[1] Universität Heidelberg

Studies of flow in heavy ion collisions are expected to yield information constraining the nuclear equation of state. As shown in Fig. 1, scaled directed flow observed in Au on Au collisions with the FOPI detector peaks near 400 AMeV. This remarkable rise and fall offers a unique opportunity to study the mechanisms behind this phenomenon. Besides the mean field gradients established in the evolution of the collision, several other factors can influence flow. Two aspects of our recent experimental results are shown here. In the 'rising' part of the flow, we observe a strong correlation with the increasing separation of 'spectator' and 'participant' matter. This is illustrated in Fig. 2 for Z=3 ejectiles from Au on Au collisions at 90 (top panel), 150 and 400 AMeV (the reduced impact parameter is $\hat{b} = 0.3$). In the 'falling' part of the excitation function, we observe a suggestive correlation with the scaled stopping illustrated in Fig. 3 where the observed longitudinal and transverse rapidity distributions of Z=1 ejectiles are shown for central ($\hat{b} \leq 0.15$) collisions of Au on Au at 400, 1000 and 1500 AMeV.

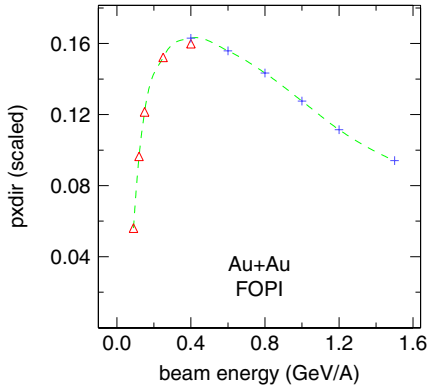


Fig. 1. Scaled directed flow in Au on Au collisions versus beam energy.

Fig. 3. Transverse and longitudinal rapidity distributions for Z=1 ejectiles at 400, 1000 and 1500 AMeV.

We find a remarkable increase of apparent transparency beyond the incident energy of 400 AMeV. Such systematic data will be useful in future confrontations with theoretical simulations.

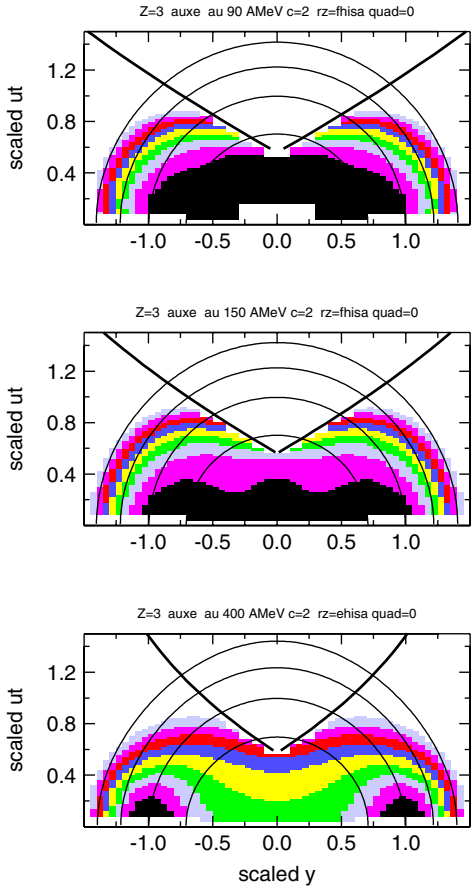
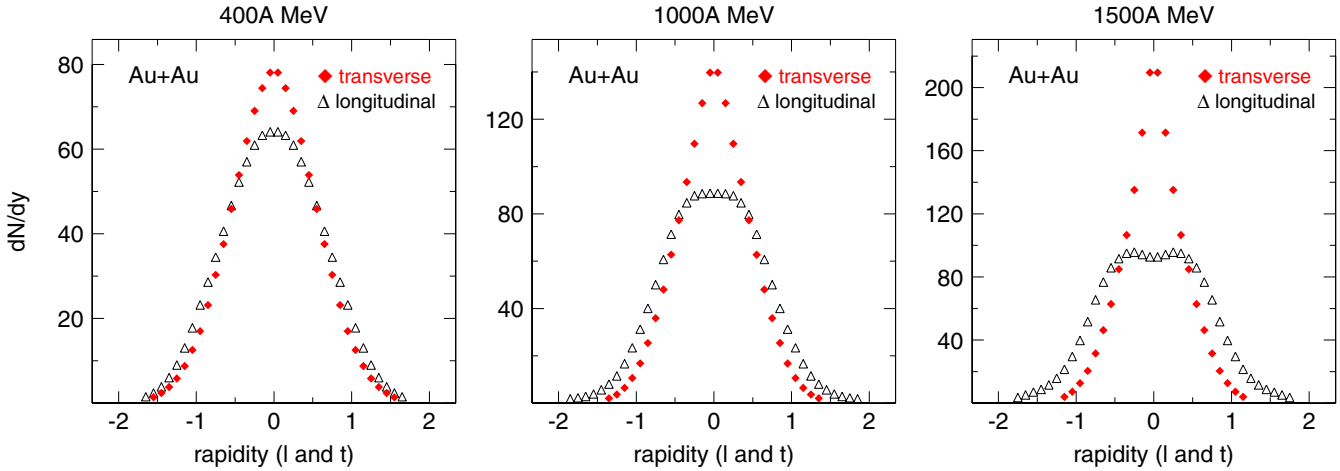


Fig. 2. Transverse 4-velocity vs rapidity contours for Z=3 ejectiles at 90, 150 and 400 AMeV.



Flow Intensity Fields in Heavy Ion Collisions

W. Reisdorf, A. Andronic, A. Devismes, Ch. Finck, A. Gobbi, O. N. Hartmann, N. Herrmann[1], K.D. Hildenbrand, Y.J. Kim, T. Kress, Y. Leifels, Z. Tyminski
FOPI Collaboration, GSI Darmstadt,[1] Universität Heidelberg

The extraction of information on the nuclear equation of state (EOS) from heavy ion collision data has proven to be a formidable task because microscopic simulations have shown that the collision dynamics depends in a complex way on the assumed density and momentum dependence of the mean fields, as well as on many (in-medium) cross sections for the ongoing elementary processes. Attempts to extract basic information from just sub-aspects of the data, such as 'sideflow' or 'elliptic flow' are plagued with ambiguities. To unravel the various only partially known aspects of the theoretical input, a complete set of experimental data should be available. This report shows the progress made by our Collaboration in the direction of obtaining the complete three-dimensional momentum distribution of all the particles emitted in heavy ion collisions in the SIS energy range. The example chosen refers to particles with charge $Z = 2$ emitted in 'half-overlap' collisions of Au on Au at 400A MeV. Emitted charged particles are known to have a momentum space distribution that can be described by $dN/u_t du_t dy d\phi = v_0\,[1+2v_1\cos(\phi)+2v_2\cos(2\phi)]$, where u_t is the transverse 4-velocity, y the rapidity and ϕ the azimuth with respect to the reaction plane. The Fourier coefficients v_0, v_1 and v_2 are 2-dim. functions $v_i(y, u_t)$, i.e. neglecting the higher order coefficients, the third dimension (ϕ) is summarized at each point (y, u_t) by just three coefficients. Technically, we extract the three $v_i(y, u_t)$ coefficient fields from measurements of particle yields in the 4 quadrants subdividing the 2π range of ϕ. After some filtering to eliminate regions of distorted measurements (such as edge effects) and correcting for efficiency, we apply a locally varying biquadratic logarithmic fitting procedure that smoothens the data and fills the gaps in the acceptance. We deduce three intensity fields which are shown in Fig. 1. While the top panel shows the familiar ϕ-integrated two-dimensional invariant cross sections contours (they differ by a factor 1.5), the middle and lower panels show the complete sideflow and the elliptic flow *intensity* fields (on a linear equally binned scale). Obviously the flow intensity fields are highly correlated with the participant/spectator structure. In the middle panel the negative sign of the flow was suppressed in the backward hemisphere, in lower panel the background colour separates regions of out-of-plane emissions (near midrapidity) from those of in-plane emission. The full three-dimensional information allows one to look at the data also in rotated frames. Fig. 2 shows the modification of the average v_2 coefficient as a function of the rotation angle around the out-of-plane (y) axis in a longitudinal (rotated) rapidity bin -0.5 to +0.5. While such rotations do not introduce new information, they reveal the known interdependence of various forms of flow (side and elliptic flow). The *simultaneous* reproduction of all three intensity fields should be a challenge to future theoretical simulations and will help to unravel the theoretical unknowns.

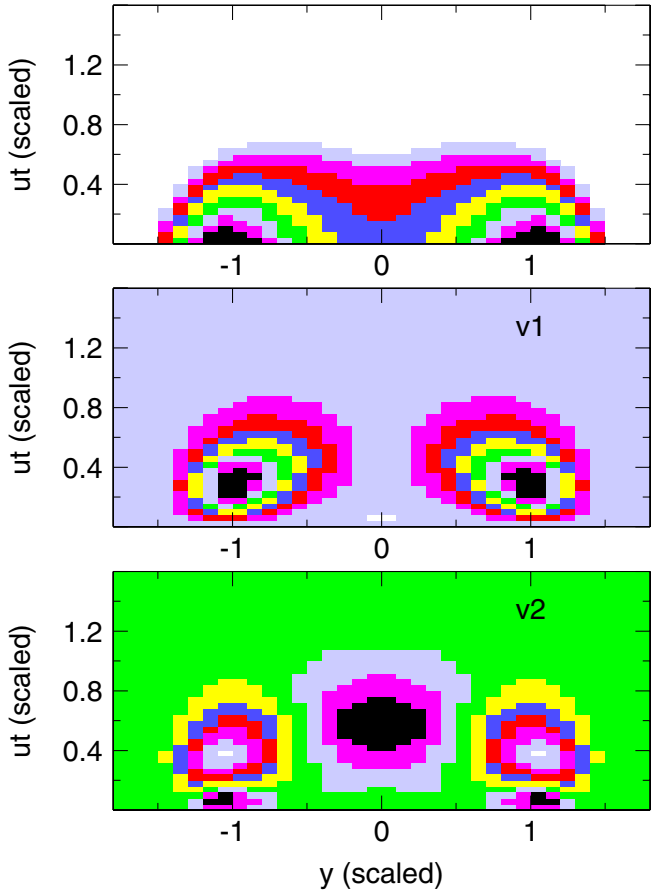


Fig. 1. Invariant cross sections for Z=2 particles emitted in semi-central collisions of Au+Au at 400 AMeV (upper panel) and the associated sideflow (middle panel) and elliptic flow intensity fields.

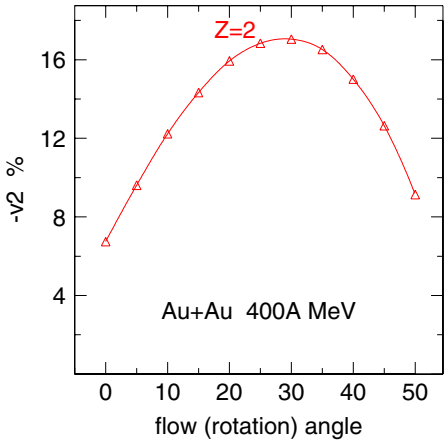


Fig. 2. Mid-rapidity elliptic flow ($-v_2$), deduced from the data in Fig.1, as function of flow axis angle.

Pion Production at SIS Energies

M.R. Stockmeier[1], W. Reisdorf[2], N. Herrmann[1], M.Merschmeyer[1], D.Pelte[1], K. Wiśniewski[1], and the FOPI collaboration. [1] Universität Heidelberg, [2] GSI Darmstadt

Pion production is the most important inelastic channel in relativistic heavy ion reactions. The yield of pions in the final state is connected, albeit through the population of intermediate nucleon resonances, to the temperature within the reaction zone. Thus, although not directly related to the Equation-of-State (EOS), pions are an integral part of the effort to determine the properties of nuclear matter. The available data on pion production in the full solid angle are sparse and partially controversial [1]. In order to improve this situation the systems $Ca+Ca$, $Ru+Ru$, and $Au+Au$ were studied at incident beam energies of 400 AMeV, 1000 AMeV and 1500 AMeV.

Pions were identified using the Central Drift Chamber (CDC) of the FOPI apparatus by combining the specific energy loss and the curvature of the tracks in the solenoidal magnetic field. For symmetric systems the acceptance covers more than 90% of the total solid angle.

The raw numbers have to be corrected for i) the geometrical acceptance ϵ_{geo} and ii) the tracking efficiency ϵ_{trk}. Both quantities were determined by means of GEANT based Monte Carlo studies employing IQMD as event generator [2]. ϵ_{geo} was found to be independent of centrality and amounts to $\epsilon_{geo} = 0.9 \pm 0.05$ slightly varying with the incident energy. ϵ_{trk} varies with centrality in the range 100%-60% for π^+ and 100%-80% for π^- and was determined for all measured systems individually. After applying the corrections a straight line was fitted to the sum of π^+ and π^- as function of A_{part}, the number of participants. The latter quantity was derived from the differential cross sections $d\sigma/dMUL$; for MUL several quantities like the forward wall multiplicity, the baryon multiplicity in the CDC acceptance and the total charged particle multiplicity were tested and gave the same results. The fit was restricted to a range $0.15 < A_{part}/A_{sys} < 0.85$ in order to avoid distortions due to the impact parameter selectivity of the apparatus.

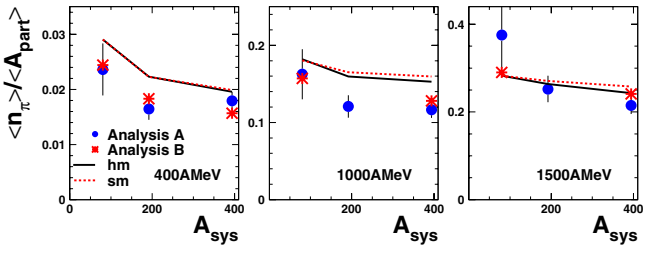


Figure 1: Total pion yield for different energies and colliding systems.

Figure 1 shows the total pion yield $< n_\pi >$ per participating nucleon, A_{part}, versus the system size, A_{sys}. An alternate, independent, analysis (B) give results in very good agreement with the first evaluation, see Fig. 1. In the alternate procedure, with a systematic error of about 10%, the effects of geometrical cuts and of transverse momentum thresholds were corrected by extrapolation of smooth fits to the measured data and the effects of track quality cuts were estimated by a systematic variation of the cuts and extrapolation to zero cuts. The relative π^-/π^+ efficiency was inferred from the data for ^{40}Ca+^{40}Ca, an isospin symmetric system. Differences between analysis A and B to former analysis [4] are currently under investigation.

At all energies a dependence of the normalized pion production with the system size is observed. Whether this decrease is connected to the system size or rather to the correlated change of the isospin content of the system is currently investigated by comparing the systems $Ru+Ru$ and $Zr+Zr$. The experimental results are compared in Fig. 1 with IQMD model calculations for different parameters of the equation of state (EOS), namely a soft (dashed line) and a hard (solid line) with the "standard" compressibilities of 200 MeV and 380 MeV, respectively. The IQMD events were analyzed with the same procedure as applied to the data. Calculating the pion production probability directly from the IQMD output allows to give a systematic error of procedure A. The results agree within 4%. The IQMD model describes the data with an accuracy of 20%. The pion yield is found to be independent from the stiffness of the EOS.

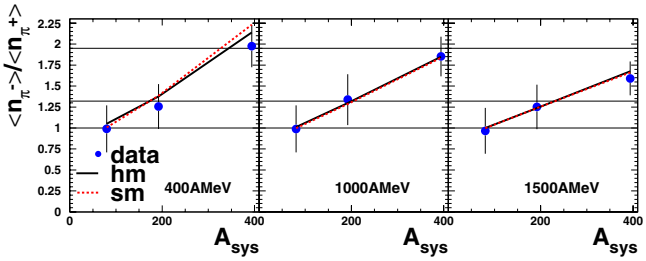


Figure 2: Ratio of charged pions for different energies and colliding systems. The lines indicate the predictions of the isobar model [3].

Figure 2 shows the π^- to π^+ ratio $R_\pi = < n_{\pi^-} > / < n_{\pi^+} >$ for the colliding systems and energies mentioned above. For the heaviest system, $Au+Au$, a strong energy dependence is observed. With rising energy the ratio, R_π, drops from 2.0 at 400 AMeV incident energy to 1.65 for the highest energy. The data are compared with the IQMD model. The measured ratios are perfectly described by the model including the observed energy dependence for the Gold system.

References

[1] P.Senger, H.Ströbele J.Phys. G25(1999),R59-R131
[2] C.Hartnack et al., Eur. Phys. J. A 1(1998),151-169
[3] R.Stock, Physics Report, 135, 5(1986),259-315
[4] D. Pelte et al., Z. Phys., A, 357(1997),215-234

First Measurements of Antikaons in Proton-Nucleus Collisions at SIS Energies[B,G]

W. Scheinast[1], I. Böttcher[4], M. Dębowski[1], F. Dohrmann[1], A. Förster[3], E. Grosse[1], B. Kamys[6], P. Koczoń[2], B. Kohlmeyer[4], F. Laue[2], M. Menzel[4], L. Naumann[1], H. Oeschler[3], F. Pühlhofer[4], Ch. Schneider[1], E. Schwab[2], P. Senger[2], Y. Shin[5], H. Ströbele[5], Ch. Sturm[3], G. Surówka[6], F. Uhlig[3], A. Wagner[1], W. Waluś[6] [1]FZ Rossendorf, [2]GSI, [3]TU Darmstadt [4]Univ. Marburg, [5]Univ. Frankfurt, [6]Univ. Cracow

The first systematic experimental investigation of K^- production in proton-nucleus collisions at SIS energies has been performed using the Kaon Spectrometer at SIS/GSI. Au and C targets were bombarded with proton beams at energies of 1.6, 2.5, and 3.5 GeV. K mesons and pions were measured at laboratory angles of 32°, 40°, 48°, and 56°. In total, 350000 K^+ and 35000 K^- have been recorded. Fig. 1 shows the inclusive invariant production cross sections for K^+ (open symbols) and K^- (full symbols) as function of transverse mass (minus rest mass).

The spectra measured at different angles can be described by a Boltzmann distribution with a normalization factor, a temperature, and a longitudinal source velocity as free parameters. By integrating the Boltzmann distribution we estimate the total production cross sections σ_K. The resulting multiplicity $M_K = \sigma_K/\sigma_R$ with σ_R the geometrical reaction cross section is shown in fig. 2.

A detailed comparison of the data to results of transport model calculations is in progress.

Fig. 2 *Multiplicity of K^+ and K^- mesons in $p+C$ and $p+Au$ collisions as function of beam energy (preliminary).*

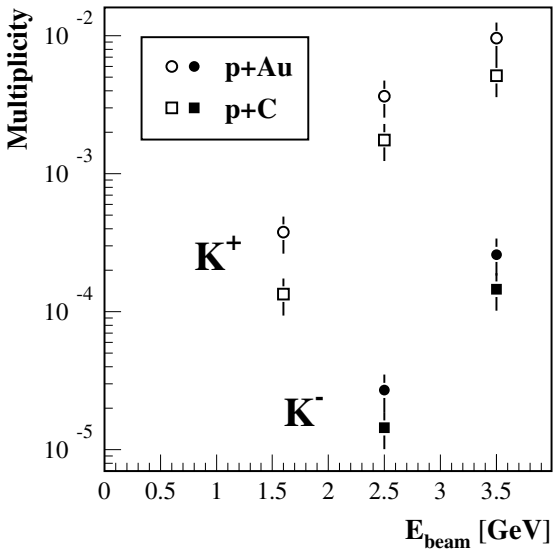
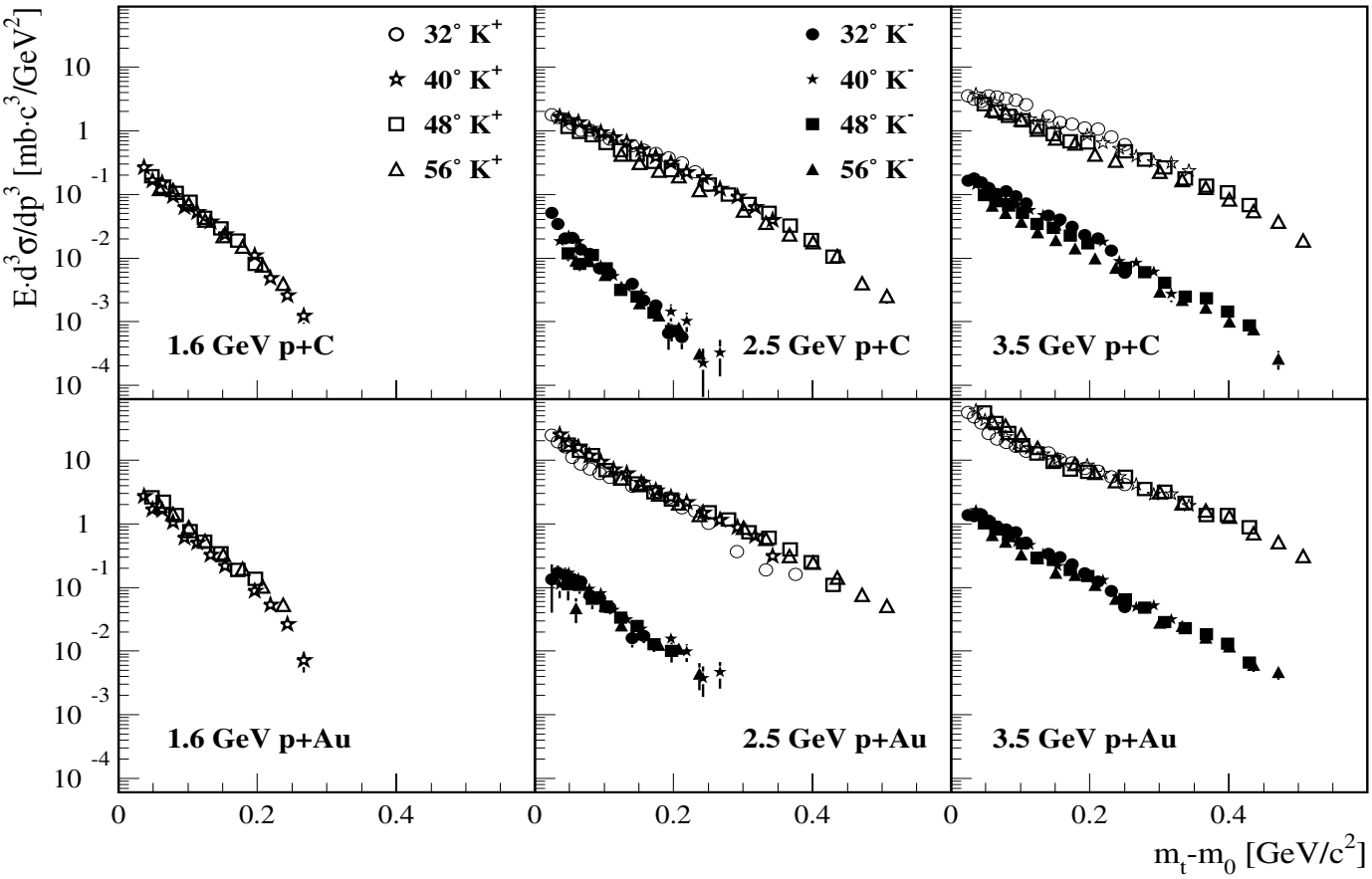


Fig. 1 *Inclusive invariant production cross sections for K^+ (open symbols) and K^- (full symbols) measured in proton-nucleus collisions (preliminary).*



Kaon and Antikaon Production in Au + Au Collisions at 1.5 AGeV[B,G]

A.Förster[1], I.Böttcher[4], E.Grosse[6,7], P.Koczoń[2], B.Kohlmeyer[4], S.Lang[1], M.Menzel[4], L.Naumann[6], H.Oeschler[1], M.Płoskon[2], F.Pühlhofer[4], W.Scheinast[6], A.Schmah[1], T.Schuck[3], E.Schwab[2], P.Senger[2], Y.Shin[3], H.Ströbele[3], C.Sturm[1], F.Uhlig[1], A.Wagner[6], W.Waluś[5]
[1]TU Darmstadt, [2]GSI, [3]Univ. Frankfurt, [4]Univ. Marburg,
[5]Univ. Cracow, [6]FZ Rossendorf, [7]TU Dresden
KaoS Collaboration

Heavy ion collisions provide the unique possibility to study strange mesons in baryonic matter at densities well above saturation density. Of special interest is their production and propagation at and below the NN-threshold [1]. Here we present data on the production of K^+ and K^- in Au + Au collisions at a beam energy of 1.5 AGeV measured recently with the Kaon Spectrometer at SIS/GSI. The acceptance in transverse momentum and rapidity covered by measuring at laboratory angles $\theta_{lab} = 32°, 40°, 48°, 60°$, and 72° and laboratory momenta p_{lab} = 280 - 1120 MeV/c is shown in figure 1.

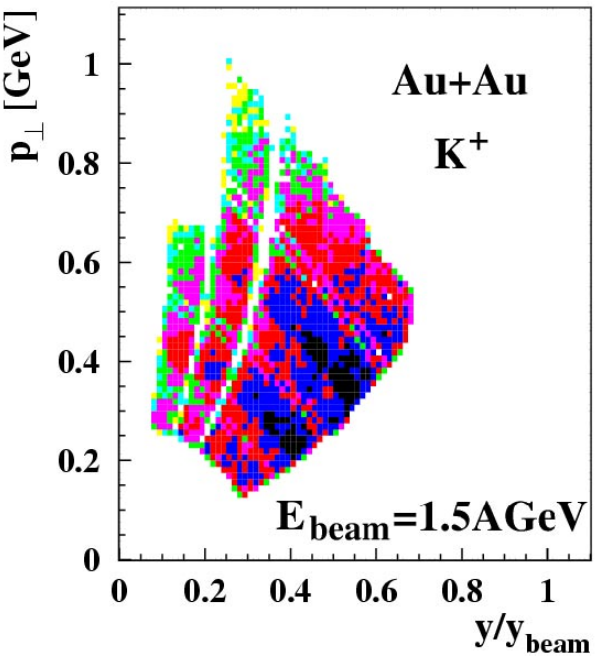


Figure 1: Transverse momentum as a function of rapidity for K^+. The different bands correspond to different spectrometer angles in the laboratory.

The resulting wide angular coverage in the center of momentum frame allows to extract information on the polar angle distribution which is expressed as the deviation of the kaon and antikaon emission from isotropy $\sigma_{inv}(\theta_{cm}) \,/\, \sigma_{inv}(90°)$. This ratio is shown in figure 2 for two centrality classes ($b > 6.3$ fm and $b < 6.3$ fm according to the geometrical model). Here the anisotropy is more pronounced for K^+ than for K^- and is decreasing with increasing centrality. Near central K^- data are isotropically distributed. Similar trends have been observed in Ni + Ni collisions at a higher beam energy of 1.93 AGeV [2]. The solid lines represent fits assuming a quadratic dependence on $\cos(\theta_{cm})$

$$\frac{d\sigma}{d\left(\cos\left(\theta_{cm}\right)\right)} \quad \sim \quad 1 + a_2 \cdot \cos^2\left(\theta_{cm}\right) \quad . \qquad (1)$$

The resulting values for a_2 are given in figure 2.

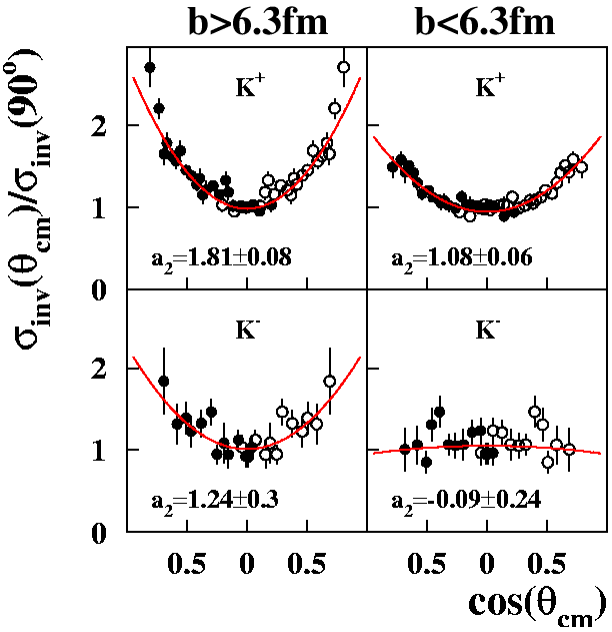


Figure 2: Preliminary polar angle distributions for K^+ and K^- in Au + Au collisions at E_{beam} = 1.5 AGeV. The left panel shows data for impact parameters $b > 6.3$ fm, the right one for $b < 6.3$ fm. The open symbols are reflected at $\theta_{cm} = 90°$.The solid lines represent a parametrization according to equation 1.

To investigate the centrality dependence of the kaon and antikaon production we have divided the data measured close to midrapidity ($\theta_{lab} = 40° \pm 4°$) into five centrality classes according to 5% (most central collisions), 15%, 15%, 25%, and 40% (most peripheral collisions) of the total reaction cross section. The upper part of figure 3 shows the energy spectra of K^+ and K^- for Au + Au collisions at E_{beam} = 1.5 AGeV for the different centrality classes. The lines represent Boltzmann distributions fitted to the data. The resulting inverse slope parameters for the K^+ spectra are about 20 MeV larger than those for the K^- spectra for all centrality classes. The lower part of figure 3 shows the corresponding spectra for π^+ and π^-.

The dependence of the particle multiplicity on the number of participating nucleons A_{part} as determined from the measured centrality by the geometrical model is found to be the same for kaons and antikaons yielding a constant K^-/K^+ ratio as a function of A_{part} (figure 4, upper part).

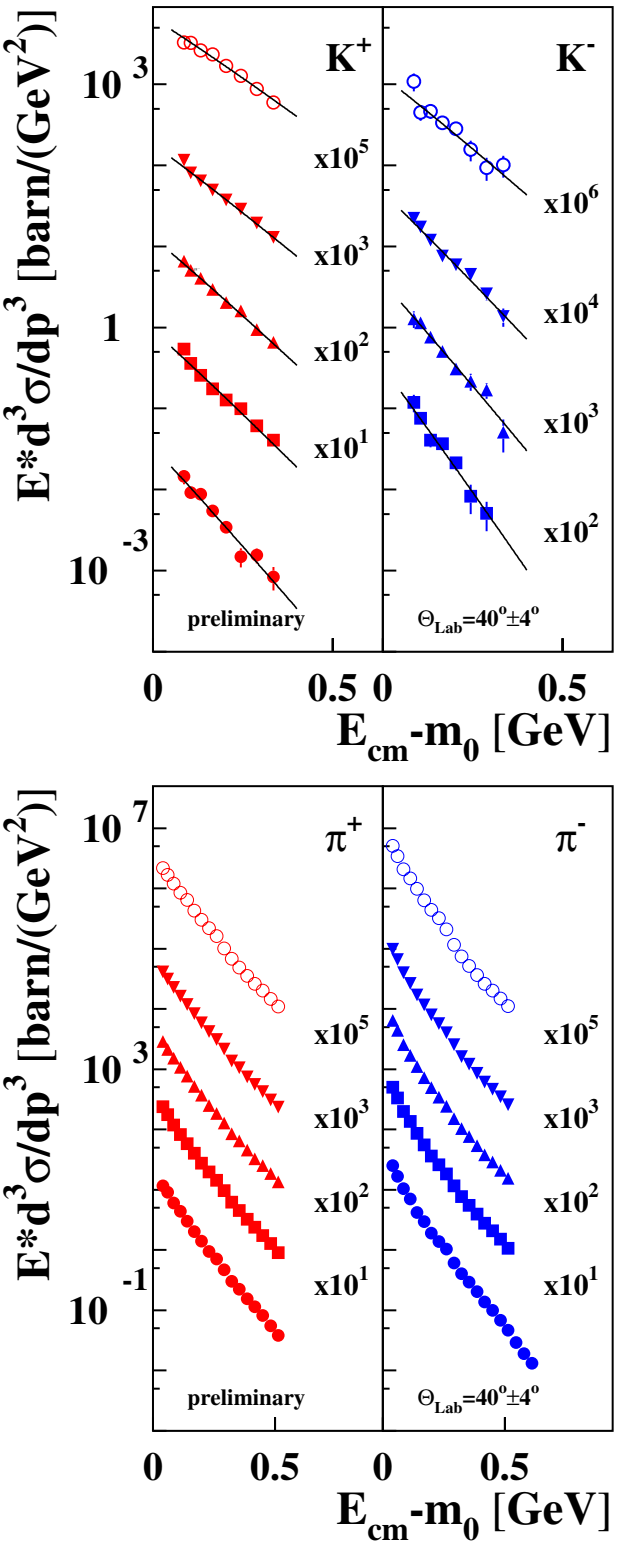


Figure 3: The upper part shows the invariant cross sections for K^+ and K^- in Au + Au collisions at E_{beam} = 1.5 AGeV for 5 centrality classes. The open circles depict the most central data with decreasing centrality from the top to the bottom of the figure. The most peripheral K^- data are not shown due to low statistics. The lower part shows the corresponding π^+ and π^- spectra.

A similar ratio is observed in Ni + Ni collisions at the same beam energy [2]. Even the absolute values of the multiplicity per A_{part} at a given A_{part} are the same for

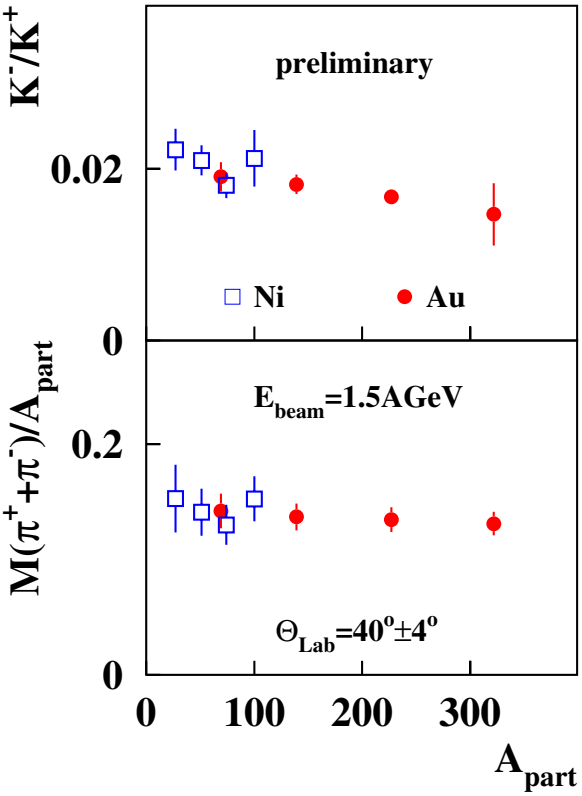


Figure 4: The upper part of this figure shows the K^-/K^+ ratio, the lower part the multiplicity of π^- and π^+ per A_{part} both as a function of A_{part}.

Au and Ni. The K^+ and K^- production seems to depend only on the number of participating nucleons. In addition the pion multiplicity per A_{part} is constant as a function of A_{part} and collision system as shown in the lower part of figure 4.

In summary the data presented shed further light on the mechanisms of kaon and antikaon production in heavy ion collisions. The observed differences in the inverse slope parameters of K^+ and K^- are at variance with the simple picture of an equilibrated source. On the other hand the K^-/K^+ ratio and the pion multiplicity per A_{part} being constant as a function of A_{part} and independent of the size of the collision system supports the idea that the antikaon production at SIS energies is dominated by the strangeness exchange reaction

$$\pi + Y \leftrightharpoons \overline{K} + N \qquad (2)$$

as suggested by recent transport calculations [3, 4].

References

[1] KaoS-Coll. (R. Barth *et al., Phys.Rev.Lett.* **78**, 4007 (1997); Y. Shin *et al., Phys.Rev.Lett.* **81**, 1576 (1998); F. Laue, C.Sturm *et al., Phys.Rev.Lett.* **82**, 1640 (1999); C. Sturm *et al., Phys.Rev.Lett.* **86**, 39 (2001))

[2] M. Menzel *et al., Phys.Lett.* **B495**, 26 (2000)

[3] W. Cassing, E. Bratkovskaya *Phys.Rep.* **308**, 65 (1999)

[4] C. Hartnack *et al., nucl-th/0109016* (2001)

Progress Report from the Commissioning of HADES

The HADES collaboration

Overview

The commissioning of the new dielectron spectrometer HADES continued throughout the past year with a strong emphasis on optimisation of detector readout speed, 2nd level trigger implementation, integration to a common data acquisition system, and software development. In addition, the installation of further detector modules went on. The inner detectors surrounding the target (Start/Veto, RICH, and 2 planes of Multiwire Drift Chambers) are now complete. In the outer region the PreShower detector, the outer Time-Of-Flight (TOF) wall and the forward Time-of-Flight paddles (Tofino) are also completed. Furthermore, five modules of the large high resolution tracking detectors (outer MDC planes) were installed. The systems for slow control, detector readout, trigger and data acquisition were continuously extended. The installed spectrometer components cover now the full geometrical acceptance as defined by the superconducting magnet (ILSE).

In altogether 4 commissioning runs with beam in parallel operation to therapy several millions of events could be recorded (see Tab. 1). Considerable progress was made in detector calibration and in the development of the ROOT based analysis package HYDRA which led to the production of data summary tapes necessary for further physics analysis. In parallel, the simulation package HGeant could be completed with refined digitizers for all detectors based on real data and allowing for quantitative comparisons between measurement and simulation.

Reaction	E/A [MeV]	Field [A]	Rec. Events	Anal. Events	DST Gen.
^{12}C+^{12}C	1000	400	$1 \cdot 10^7$	$1 \cdot 10^7$	1
^{12}C+^{12}C	1000	-	$3 \cdot 10^6$	$3 \cdot 10^6$	1
^{12}C+^{12}C	1500	-	$5 \cdot 10^5$	$5 \cdot 10^5$	5
^{12}C+^{12}C	1900	2500	$6 \cdot 10^6$	$1 \cdot 10^6$	5
^{12}C+^{12}C	2000	2500	$9 \cdot 10^7$	$6 \cdot 10^6$	1
^{52}Cr+^{27}Al	1500	-	$1 \cdot 10^6$	$5 \cdot 10^5$	2
^{52}Cr+^{27}Al	1500	2500	$2 \cdot 10^7$	$2 \cdot 10^7$	2

Table 1: Total number of events recorded for various field settings in last years commissioning runs (not ordered in time). Part of the data have been analysed to calibration and hit level and stored in consecutive generations of data summary tapes (DST) for further analysis.

The META detector

The Multiplicity and Electron Trigger array (META) consists of an electromagnetic PreShower detector combined with a Time of Flight scintillator wall with an highly segmented outer part (TOF) and a low segmented inner part (TOFino). The start signal for the time of flight and multiplicty measurement is delivered from a segmented diamond detector. All detector modules as well as the laser calibration system for the whole Time of Flight wall are complete and operational. The slow control software, in the EPICS framework, is extensively being used, along with its latest and quite useful features of alarm signaling. Considerable increase in readout speed and further improvements in DAQ integration of all components could be achieved. For the TOF wall the already existing readout chain for the timing measurement was supplemented by an additional electronics chain for signal amplitude readout consisting of suitable signal shapers followed by VME ADC's for digitization. The amplitude information allows to better equalize the PMT gain and therefore to achieve a better uniformity in terms of threshold. After proper calibration redundant particle ID for hadrons should be possible in a ΔE-ToF representation as shown in Fig. 1. From the amplitude information the light attenuation length can be evaluated for each rod. The results obtained with the November 2001 beam data are in agreement with previous measurements of cosmic rays and are shown in Fig. 2.

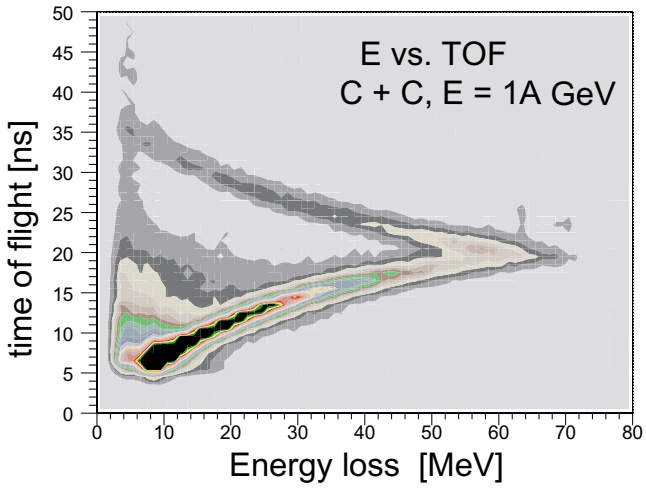


Figure 1: ΔE-ToF correlations measured in one TOF sector with 32 scintillator rods of 3x3 cm^2 cross section.

A preliminary analysis of recorded events shows a perfect correlation between the positions as measured with TOF and with the MDC tracking detectors in front. From this analysis a position resolution in the order of 2-3 cm was deduced. The timing resolution was found to be better than 130ps (σ) for the small rods and 150ps (σ) for the large rods, thus achieving the initial design goal for this subdetector. For the 24 large and conically shaped TOFino scintillator paddles placed in front of the PreShower chambers and read out by only 1 phototube an overall time resolution of about 610 ps (σ) was measured. This allows to reduce the number of hadrons misidentified as electrons in the PreShower detector.

The PreShower data were analysed to determine effi-

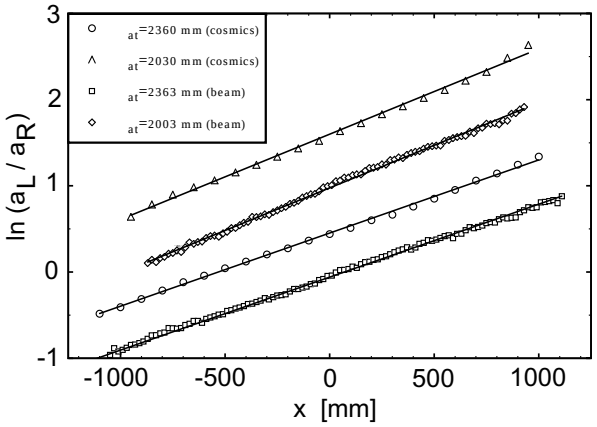


Figure 2: Photon attenuation length of sample rods measured with cosmic rays and beam (C+C, E = 1A GeV).

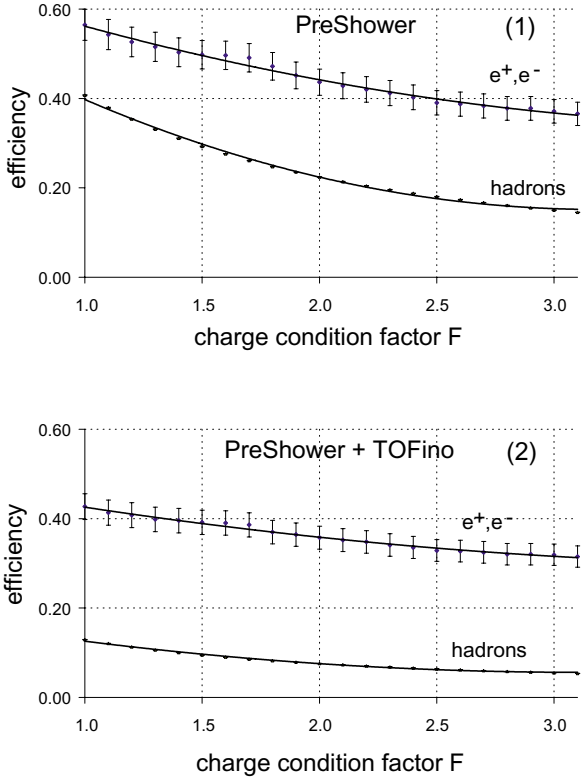


Figure 3: Efficiencies for e^+ / e^- identification and for misidentification of hadrons as electrons in the PreShower alone (1) and in the combined PreShower - Tofino detector (2) for various charge ratios F ($F = Q_{post1}/ Q_{pre}$ or Q_{post2}/Q_{pre}). The results are for C+C (E =1 A GeV) and mean lepton momenta p$\simeq$ 250 MeV/c.

ciencies for electron identification and hadron misidentification. The results presented in Fig. 3 were obtained for various ratios $F = Q_{post}/Q_{pre}$ of charges deposited in the chambers before (pre-) and behind (post-) the lead converter. The efficiency for electron identification depends on particle momentum and was determined to $\epsilon = 45\%$ at F=2.0 for p = 250 MeV/c, the average momentum of registered leptons. This result is in good agreement with simulation calculations. Extrapolation to the momenta of decaying vector mesons (p $\simeq$ 600 MeV/c) yields $\epsilon = 90\%$ (F=2.0). From a combined PreShower-TOFino analysis it was found that only 5% of protons and 15% of fast pions produce charge ratios F = 2, which are then registered as fake lepton candidates. This corresponds to a hadron rejection capability of about 95% for protons and 85% for pions.

Mini Drift Chambers

In the past year a major step towards a completion of the outer tracking section was taken. In the third tracking plane four sectors produced at FZ Rossendorf were equipped and in plane 4 the first chamber was installed. A second chamber of plane 4 was completed in November and is still being tested at IPN Orsay. Modules of the forth tracking plane are 3.2 m long and have an active area of 3.5 m^2. Figure 4 shows the installation of the outer tracking detectors in the upper sector of the spectrometer. The inner tracking section composed of chambers provided by LHE at the JINR in Dubna and by GSI was already completed in 2000.

During the commissioning runs in 2001 the chambers showed an overall stable operation. The detector system reaches an efficiency (> 98%) and resolution (100-140 μm for single drift cells) well within the design specification. A strong effort was made to tune the readout process in order to achieve stable operation at the anticipated high trigger rates. Full performance will be reached in 2002 when the current VME readout and control boards (SAM modules) will be upgraded from the prototype version to the customized version 3. The amble data taken during the commissioning runs was used to tailor calibration methods as well as on-line/off-line analysis tools. The chamber response was modeled on the basis of microscopic simulations with GARFIELD. An important aspect are corrections needed to compensate non-linearities of the drift velocities in the chambers, which result from the particular cell geometries needed to achieve the requested granularity and redundancy. In addition refined digitizers were developed to permit realistic (HGEANT) simulation of the spectrometer response. As an example, in Fig. 5 we show a comparison of the measured drift time distributions to simulation results. The non-uniform distributions with tails to long drift times are perfectly reproduced by the simulation.

RICH

With the installation of the last mirror segments and readout electronics in spring 2001 the RICH was completed and could be operated reliably in all commissioning runs. Significant improvements were achieved in the VUV transmission of the radiator gas, the noise level and rate capability of the photon detector readout, and the integration into the common DAQ system. In Fig. 6 the polar and azimuthal distributions of ring centers found in the preliminary offline analysis of data from the C+C run in

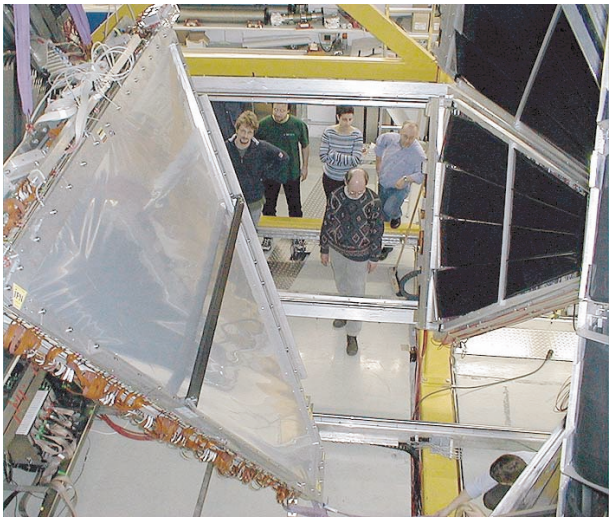


Figure 4: A pre-assembled outer tracking section is installed into the upper sector of the spectrometer. The section is composed of two chambers, a plane III module (not seen because residing on the backside) and a plane IV chamber.

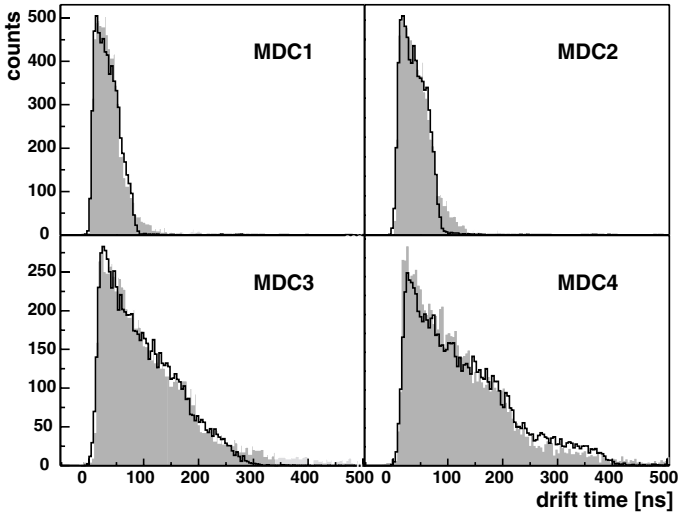


Figure 5: Comparison of measured drift time distribution (shaded histograms) to simulations (full lines) for all four chamber types. The innermost drift chambers (MDC1) have a cell size of 5 × 5 mm^2, the dimension of the cells in the outermost chambers (MDC4) is 10 × 14 mm^2.

November last year are depicted and show a smooth and homogeneous detector response. Variations in yield for different sectors are mainly attributed to noise and corresponding fake ring candidates. A detailed pulse height analysis of the photon detector response (pulseheight, pad multiplicity) to single photons was performed and led to refined digitizers for the HGEANT simulation package. As a result good agreement between measured and simulated rings is achieved. It should be noted that the distributions shown in Fig. 6 contain almost entirely lepton candidates from conversion, π^0- Dalitz decays and fake recognitions.

Presently data from both, beam and simulation runs, are analysed with the goal to identify and reject close lepton pairs from the sources mentioned above. The efficiency for this close pair rejection is of majour importance for the understanding and suppression of combinatorial background in the reconstructed dilepton invariant mass spectra. For this reason and in order to extract reliable experimental values a dedicated run with low magnetic field setting was performed (see Tab. 1). Under this condition the acceptance for low mass dilepton pair detection (with at least 1 low momentum lepton) is significantly increased as compared to the standard settings and should allow to unambiguously identify and reconstruct π^0- Dalitz decays. This analysis is still in progress.

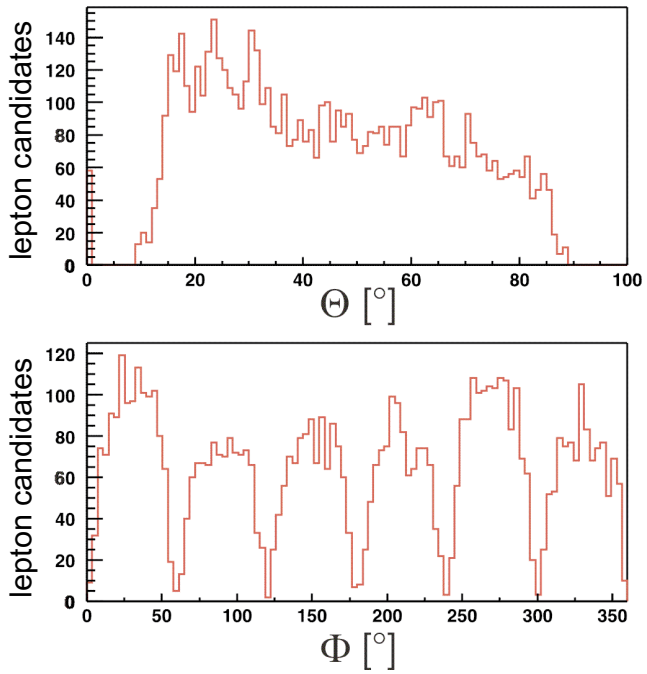


Figure 6: Polar and azimuthal distributions of ring centers identified in the RICH in C+C (E=1AGeV) reactions. The characteristic yield pattern in the lower plot reflects the sixfold spoke structure of HADES.

Trigger

The functionality of the HADES second level trigger has been examined in comparison to simulations of the algorithms used, and the results from the offline analysis.
The RICH IPU algorithm has been implemented in software: a comparison of the hardware and the software results from the November 2001 beamtime has a spatial resolution of 1 pad with less than 0.8% discrepancies, as shown in Fig.7. The TOF IPU has been recently tested with cosmics: a comparison of the hardware to the offline analysis has a resolution of 2 degrees in the azimuthal direction and less than 0.2% discrepancies. The Shower IPU has also been tested with cosmics and the first part of the pattern recognition algorithm has been compared with the equivalent in the offline analysis: this comparison has a resolution of 1 pad and less than 2.7% discrepancies. The Matching Unit (MU) algorithm has been implemented in software. A comparison between the MU hardware and the corre-

sponding software implementation shows full agreement. An event reduction factor of 17.5 was obtained for the system C+C at 1.5 AGeV reaction. Furthermore 93% of the lepton candidates found by the offline analysis were also found by the second level trigger.

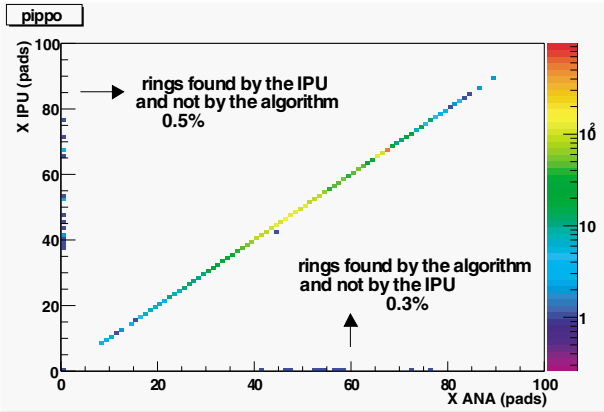


Figure 7: Azimuthal positions of ring centers found by the hardware RICH IPU (vertical axis) versus those found in all recorded data by a software implementation of the RICH IPU algorithm. The strong correlation reflects excellent agreement.)

Data Acquisition

The full implementation of the 2nd level trigger could be achieved and allows now for online rejection of events without lepton or lepton pair candidates. For C+C reactions this leads even for single lepton triggers to a possible increase of the primary event rate by more than one order of magnitude without saturating the taping speed.

Therefore considerable efforts were undertaken to increase the data transfer rates by optimising soft and hardware components within the readout chain. Operation of the whole system at larger rates unfortunately revealed stability problems mainly caused by the increased digital noise and the full asynchronous data transfer. To overcome these problems, a consolidation phase was scheduled at the end of 2001. Hardware and software providing the communication for proper event tagging were investigated systematically. The weak points are now clearly identified. Within the first half of 2002 modifications will be implemented to gain stability and getting the system more fault tolerant. First tests were successfully performed already but a full system test is still needed to prove the performance gain under in beam conditions.

Analysis and Simulation

Hand in hand with the intensive work on commissioning beam time data, the Hades analysis and simulation framework has been consolidated during the year 2001. This involved efforts on a broad front:

- Semi-automatic calibration procedures for all detectors have been developed and are used routinely now.
- The tracking software has been developed further: the parameterization of the kick plane at low momentum has been improved, demonstrating an intrinsic resolution of <1%, and track-piece fitting has been implemented. Work on reference trajectories is in progress, the final step needed for performing high-resolution momentum fits.
- Various alignment algorithms have been developed and tested. They allow to determine the location of detectors and target to better than 1 mm. This precision is absolutely mandatory to achieve the design mass resolution.
- Hit matching algorithms have been designed and implemented, based either on simple θ, ϕ cuts or on a more sophisticated principal-component analysis (PCA). This step is essential to reduce fake matches between e.g. rings in the RICH and reconstructed tracks.
- At a higher level of event reconstruction, the question of close-pair recognition has been adressed. The close pairs are mostly due to conversion of the copious neutral-pion decay photons and contribute largely to the combinatorial background in the electron pair distribution. Ongoing effort is undertaken to identify close pairs in a detailed analysis of the RICH ring properties and/or the MDC hit properties.
- The Oracle data base holding setup, geometry, calibration, and analysis parameters has been developed further. A flexible interface, as well as a versatile version management based on run numbers and contexts have been designed. Online and analysis logbooks accessible through graphical web applications have been implemented and are used routinely.
- The commissioning runs of this year allowed furthermore to gain hands-on experience with analyzing large data sets. Calibration procedures, data summary tape (DST) generation scripts and quality assessment methods have been put into operation.
- Finally, our simulation package is now fully interfaced to the analysis. Digitizers for all detector components have been refined and a comparison of simulations with real data shows now very good agreement up to hit level.

Extensive simulation work has been done in 2001, both on the carbon–carbon reaction and on pion-induced elementary reactions. The expected di-electron mass distributions have been generated for realistic assumptions on event rates and DAQ performance. They served as the basis for a first physics proposal approved in the June EA meeting. The main physics goals pursued follow two main lines of thrust: 1) investigating the excess yields observed by the DLS collaboration in light heavy-ion collisions and 2) studying rho and omega meson production and possible interference effects in π^-- and π^+-induced reactions on a liquid-hydrogen target.

Results on Particle Yields, Fluctuations, and Correlations from NA49 *

C.Blume[2],R.Bramm[1],P.Buncic[1], P. Dinkelaker[1],M.Gazdzicki[1], T.Kolleger[1],I.Kraus[1],A.Mischke[3],R.Renfordt[1], A.Sandoval[2], H.Sann[2],R.Stock[1],H.Ströbele[1],A.Wetzler[1], J.Zaranek[1] for the NA49 Collaboration.
[1]Universität Frankfurt, [2]GSI Darmstadt

Experiment NA49 at the Cern SPS uses a large acceptance detector for a systematic study of particle yields, event-by-event fluctuations, anisotropic azimuthal flow, and two particle correlations in nucleus–nucleus collisions. Preliminary results for Pb+Pb collisions at 40, 80 and 158 A·GeV beam energy are shown and compared to measurements at lower and higher energies.

The NA49 experiment [1] was designed for the investigation of hadron production in the most violent Pb+Pb interactions at the Cern SPS. The main features are large acceptance precision tracking and particle identification using time projection chambers (TPCs). The first two are located inside superconducting dipole magnets which provide the particle trajectory bending necessary for momentum determination. Charged particles in the forward hemisphere of the reaction are identified from the measurement of their energy loss dE/dx in the TPC gas (accuracy 3 –4 %).

At central rapidity the identification is further improved by measurement of the time-of-flight (resolution 60 ps) in two arrays of scintillation counter tiles (TOF-T) and strips (TOF-G). Strange particles are detected via decay topology and invariant mass measurement. The forward calorimeter VCAL measures the energy of the projectile spectators from which one can deduce the impact parameter in A+A collisions.

1 Yields of π, K, Λ and $\bar{\Lambda}$

The energy dependence of pion multiplicity (entropy) and strange particle yields is expected to be sensitive to the formation of a state of deconfined hadron constituents. In the following we describe how results on these observables were obtained with the NA49 detector. Raw K^+ and K^- yields were extracted from fits of the distributions of dE/dx and TOF (where available) in narrow bins of rapidity y and transverse momentum p_T. The resulting spectra were then corrected for geometrical acceptance, losses due to in–flight decays and reconstruction efficiency. The latter was determined from embedding simulated tracks into real events and amounted to $\approx 95\%$. Spectra of π^- mesons were derived from the acceptance corrected negatively charged particle yields in p_T and y (assuming the π mass) by subtracting the estimated contribution of K^-, $\bar{p}$ and the contamination from secondary hadron decays. The ratio π^+/π^- was determined in the region where both dE/dx and TOF are available (0.91, 0.94 and 0.97 at 40, 80 and 158 A·GeV) and was assumed to be y independent. The resulting rapidity distributions of π^- are plotted in Fig.1 (upper part). The integrated yields are 312±15, 445±22 and 610±30 at 40, 80 and 158 A·GeV respectively. The yield of pions (estimated here as $\langle\pi\rangle = 1.5 \cdot (\langle\pi^-\rangle + \langle\pi^+\rangle)$) divided by the number of wounded nucleons (participants) N_W is shown versus the Fermi energy variable $F \equiv (\sqrt{s}-2m_N)^{3/4}/\sqrt{s_{NN}}^{1/4} \approx s_{NN}^{1/4}$ in Fig.1 (lower part). While p+p data show a linear rise throughout there is a change for A+A collisions (illustrated more clearly in the inset) in the SPS energy range. Below one finds a regime of slight suppression, above a region of enhancement with a steeper linear rise than for p+p reactions.

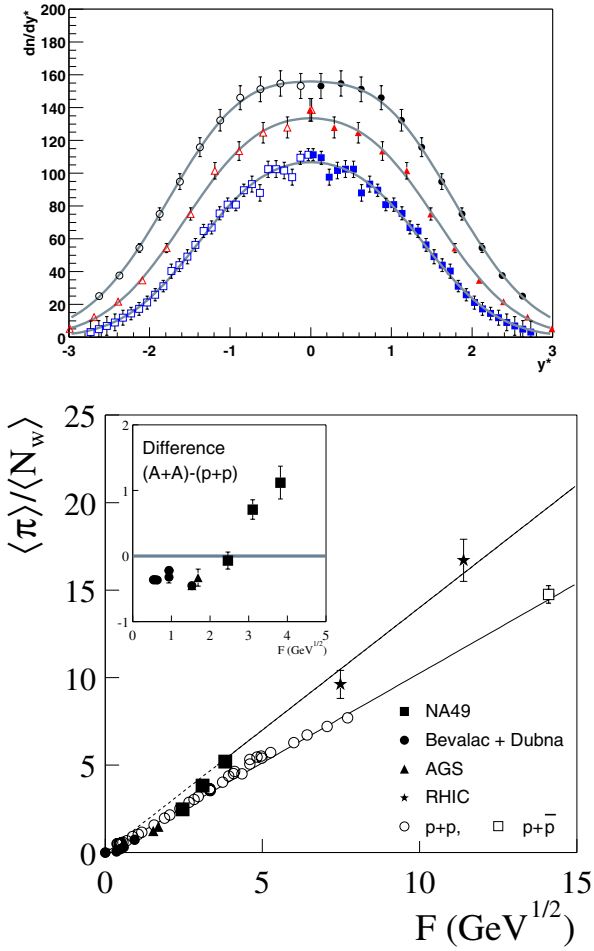


Figure 1: Upper: Rapidity distribution of π^- in central Pb+Pb collisons at 40 (squares), 80 (triangles) and 158 (dots) A·GeV. Open symbols show values reflected at $y^*=0$ (NA49 preliminary). Lower: total pion multiplicity $\langle\pi\rangle$ produced per wounded (participant) nucleon versus the Fermi energy variable $F \approx s_{NN}^{0.25}$ for p+p reactions (open symbols) and central nucleus–nucleus collisions (full symbols)

Kaons contain about 75% of the $s, \bar{s}$ quarks in the produced hadrons at SPS energies and thus their number indicates the total strangeness content of the final state. The rapidity distributions are displayed in Fig.2 and integrate

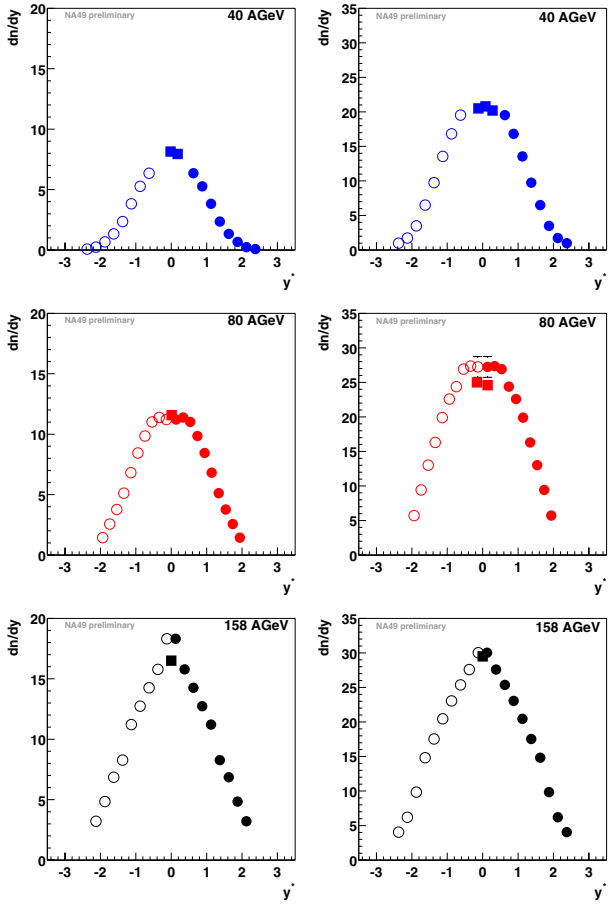


Figure 2: Rapidity distribution of K^- (left column) and K^+ (right column) from dE/dx (circles) and combined dE/dx and TOF (squares) analysis. Open symbols show values reflected at $y^\star$=0. (NA49 preliminary)

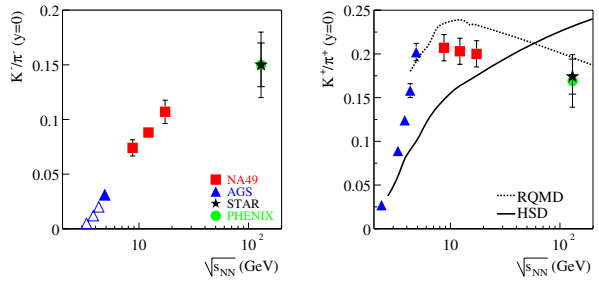


Figure 3: Midrapidity ratio of K^-/π^- (left) and K^+/π^+ (right) as function of energy from NA49 (squares, preliminary) compared to measurements at lower and higher energies. Predictions of the RQMD [2] (dotted) and HSD [3] (full curve) models are shown.

with small extrapolation to total yields of 18±1, 29±2, 50±5 for K^- and 56±3, 79±5, 95±9 for K^+ at 40, 80, 160 A·GeV respectively. In general, yields of particles increase with energy. Changes in the composition of the produced system are better characterised by particle ratios. Measurements of K^-/π^- and K^+/π^+ at midrapidity from NA49 are plotted versus energy in Fig.3 and compared to results at lower and higher energies. A continuous increase is seen for K^-/π^-. For K^+/π^+ one finds a steeper rise followed by a maximum at the lower end of the SPS energy region and a gradual decrease.

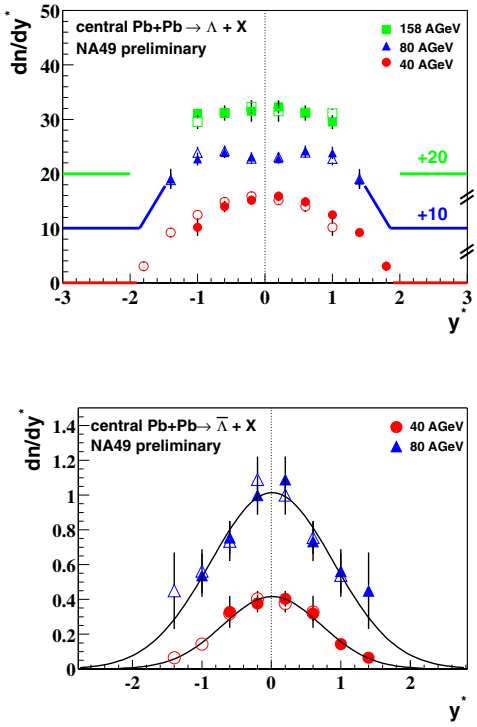


Figure 4: Rapidity distribution of Λ (upper) and $\bar{\Lambda}$ (lower). Open symbols show values reflected at $y^\star$=0. Λ yields at 80 and 158 A·GeV are displaced vertically by 10 respectively 20 units for clarity. (NA49 preliminary)

The most abundantly produced hyperons are Λ and $\bar{\Lambda}$ for which Fig.4 shows the rapidity distributions. These show a broad shape for Λ reflecting the associate production mechanism and the partially stopped participant nucleon distribution. In contrast the distribution is of narrower Gaussian type for $\bar{\Lambda}$ which are most likely produced as members of hyperon–antihyperon ($Y\bar{Y}$) pairs. The ratios $\langle\Lambda\rangle/\langle\pi\rangle$ and $\langle\bar{\Lambda}\rangle/\langle\pi\rangle$ of 4π integrated yields are displayed as a function of energy in Fig.5. One observes a steep threshold rise for the $\langle\Lambda\rangle/\langle\pi\rangle$ ratio followed by a decline the gross feature of which can be attributed to the rapidly decreasing net baryon density. The ratio $\langle\bar{\Lambda}\rangle/\langle\pi\rangle$ exhibits a continuous rise due to the high mass $Y\bar{Y}$ threshold. The ratio $\bar{\Lambda}/\Lambda$ as function of cms energy is shown in Fig.6 in the range from AGS to RHIC energies. The decrease with energy reflects the decrease in net baryon density or baryochemical potential.

2 Event-to-event charge fluctuations

Recently it was proposed that event–to–event fluctuations of the charge ratio $R=N_+/N_-$ or the net charge $Q=N_+-N_-$ may be sensitive to deconfinement in the early stage of nucleus–nucleus collisions [8, 9]. The smaller charge quanta in a partonic phase are expected to result in a reduction of such fluctuations.

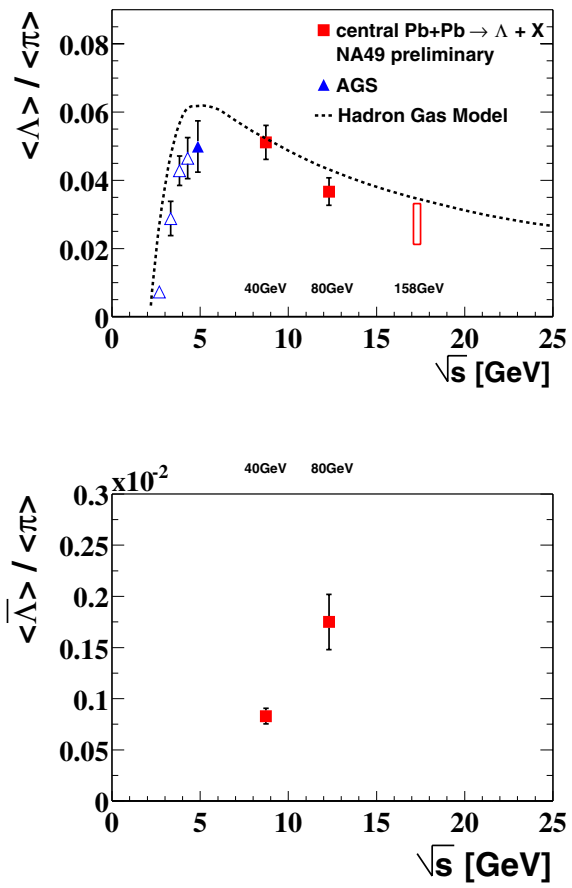


Figure 5: 4π yield ratios $\langle\Lambda\rangle/\langle\pi\rangle$ (upper) and $\langle\bar{\Lambda}\rangle/\langle\pi\rangle$ (lower) versus energy from NA49 (squares, preliminary) and lower energy AGS experiments. The dotted line shows a prediction from the extended hadron gas model [4].

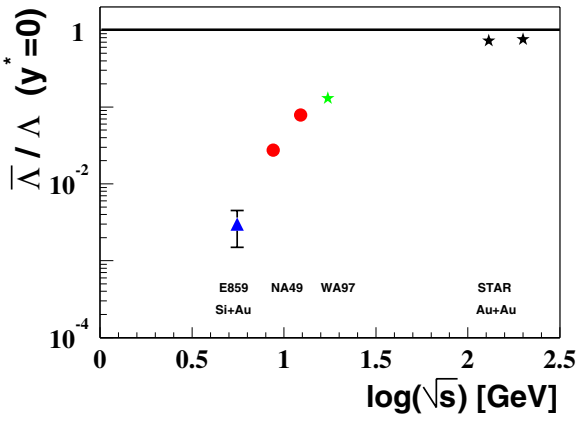


Figure 6: Ratio $\bar{\Lambda}/\Lambda$ as function of cms energy including data from AGS [5], preliminary data from NA49 at 40 and 80 A GeV, data from WA87[6] and STAR[7].

The quantity Φ_q was proposed in ref. [10] for studying fluctuations of the net charge. It is independent of the number of superimposed particle sources, has value zero for independent particle emission and -1 for local charge conservation. Preliminary NA49 measurements are plotted in Fig.7 versus the ratio $\langle N_{ch}\rangle/\langle N_{ch}\rangle_{tot}$ of the multiplicity in the acceptance window and the total multiplicity in the events. The results are close to the prediction for independent particle emission plus global charge conservation $\Phi_q^{cc} = \sqrt{1-\langle N_{ch}\rangle/\langle N_{ch}\rangle_{tot}} - 1$ (ref. [11], line in Fig.7).

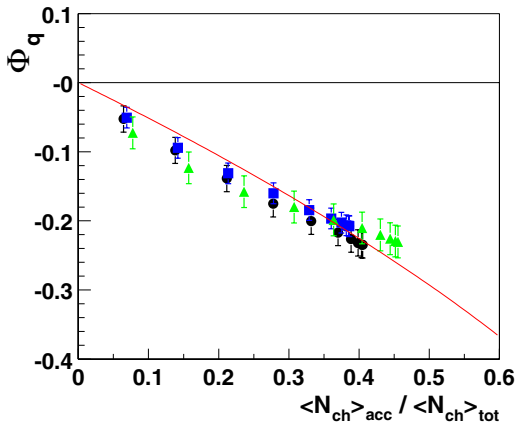


Figure 7: Measure of event-to-event charge fluctuations in central Pb+Pb collisions: Φ_q versus the ratio $\langle N_{ch}\rangle/\langle N_{ch}\rangle_{tot}$ of the multiplicity in the acceptance window and the total multiplicity in the events; the curve shows the prediction for independent particle emission plus global charge conservation (NA49 preliminary).

3 Directed and Elliptic Flow

Anisotropic flow in non-central collisions is sensitive to pressure in the early stage of the reaction, which can transform the initial space anisotropy of the reaction zone into an azimuthal anisotropy of the momentum distribution of the observed particles. The onset of deconfinement might result in a minimum of this effect [12]. Anisotropic flow is quantified by the Fourier coefficients v_n of the distribution of particle azimuthal angles Φ with respect to the reaction plane Ψ [13]:

$$v_n = \langle cos(n(\Phi_i - \Psi_n))\rangle = \sqrt{2}\langle sin(n\cdot\Phi_i)\cdot sin(n\cdot\Psi_n)\rangle$$

Corrections for reaction plane resolution, nonuniform azimuthal acceptance and momentum conservation were applied. The results for v_1 (directed flow) and v_2 (elliptic flow) for pions are plotted versus rapidity in Fig.8. The values for v_1 decrease from 40 (upper) to 158 (lower) A·GeV by a factor of 2, whereas v_2 shows a slight increase.

4 $\Lambda\Lambda$ and Λp correlations

Two particle correlations between Λ hyperons are one possibility to probe the $\Lambda\Lambda$ interaction. An attractive potential will manifest through a positive correlation at low relative momenta superimposed on the Pauli suppression for vanishing momentum difference. Confirmation of an attractive potential would support the speculation of ex-

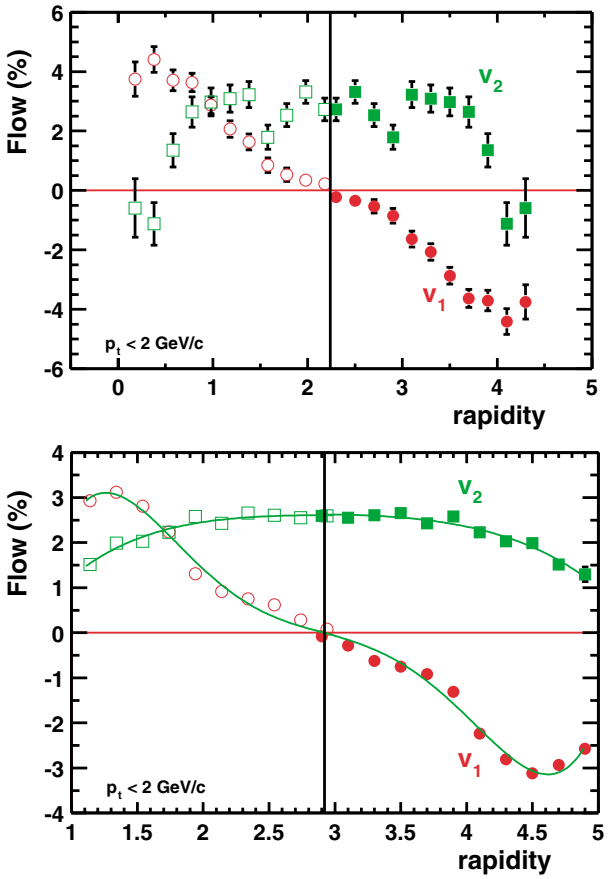


Figure 8: Fourier coefficients v_1 (directed flow) and v_2 (elliptic flow) of the azimuthal distribution of pions in min.bias Pb+Pb collisions versus the rapidity at 40 (upper) and 158 (lower) A·GeV beam energy (NA49 preliminary).

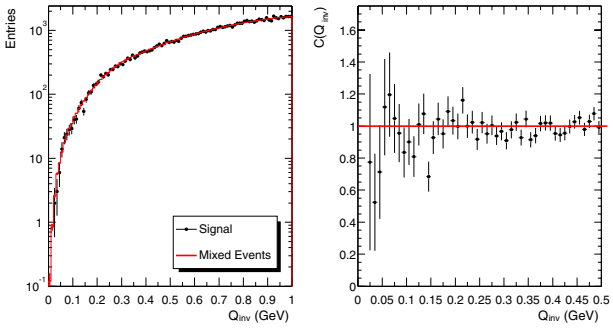


Figure 9: ΛΛ correlation function in terms the invariant momentum difference

istence of a ΛΛ dibaryon state. Na49 has extracted from 3 million central Pb+Pb collisions at 158 A GeV the ΛΛ correlation function which is shown in Fig.9. No positive correlation beyond the level of our statistical errors is visible.

A less exotic observable is the Λp correlation , is shown in Fig.10 as function of $k = 0.5 \cdot |\mathbf{p_\Lambda} - \mathbf{p_p}|$, where $\mathbf{p_\Lambda}$ and $\mathbf{p_p}$ are momenta of Λ and proton in the pair c.m. system. Here a positive correlation is clearly visible. It is the first

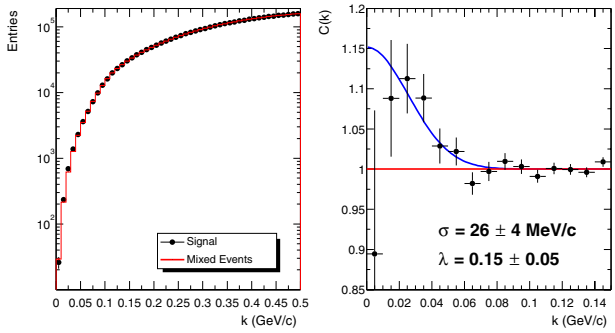


Figure 10: Λp correlation function in terms momentum difference $k = 0.5 * |p1 - p2|$

step towards an estimate of the source size responsible for hyperon production.

Acknowledgements
*gefördert vom Bundesministerium für Bildung und Forschung

References

[1] S.Afanasev et al., NIM **A430** (1999) 210.
[2] F. Wang, H. Liu, H. Sorge, N. Xu and J. Yang, Phys. Rev. **C61** (2000) 064904.
[3] W. Cassing, E.L. Bratkovskaya and S. Juchem, Nucl. Phys. **A674** (2000) 249.
[4] J. Cleymans and K. Redlich, Phys. Rev. **C60** (1999) 054908, P. Braun-Munzinger et al., Nucl. Phys. **A697** (2002) 902.
[5] B.A. Cole *et al.* E802 Coll., NPA590(1995) 179c
[6] E. Andersen et al., WA97 Coll., PLB449(1999)401
[7] H. Caines *et al.* STAR Coll., Proc. QM2001 NPA: in print
[8] S.Jeon and V.Koch, PRL **85** (2000) 2076.
[9] M.Asakawa, U.Heinz and B.Müller, Phys. Rev. Lett. **85** (2000) 2072.
[10] M.Gaździcki, Eur. Phys. J. **C8** (1999) 131.
[11] J.Zaranek, preprint hep-ph/0111228 (Nov. 2001)
[12] C.Hung and E.Shuryak, PRL **75** (1995) 4003.
[13] A.Poskanzer and S.Voloshin, PR**C58** (1998) 1671.

Bose-Einstein Correlations of Charged Kaons in Central Pb+Pb Collisions at 158 AGeV^{G,B}

In-Kwon Yoo[2],C.Blume[2],R.Bramm[1],P.Buncic[1], P. Dinkelaker[1],M.Gazdzicki[1], T.Kolleger[1],I.Kraus[1],A.Mischke[2], R.Renfordt[1],A.Sandoval[2], H.Sann[2],R.Stock[1],H.Ströbele[1], A.Wetzler[1],J.Zaranek[1] for the NA49 Collaboration.
[1]Universität Frankfurt, [2]GSI Darmstadt

We present data from an experimental study of Bose-Einstein (BE) correlations between charged kaons emitted in 780,000 Pb+Pbcollisions (5% most central) at 158 AGeV measured by the NA49 spectrometer (described in detail in [1]) at the CERN SPS. We compare the results with those from an earlier analysis of pion data for the same reaction. The combination of large-volume TPCs with a high-resolution TOF detector allows for a good kaon identification in the midrapidity region.

The distribution of relative four momenta q for charged kaons was extracted from the data and normalized to a mixed-event distribution. Assuming an expanding Gaussian source-distribution, the four momenta can be parameterized in a representation of $q_\perp = \sqrt{(\Delta p_x)^2 + (\Delta p_y)^2}$, $q_\parallel = \Delta p_z$ and $q_0 = E_1 - E_2$ given by Yano-Koonin-Podgoretskii (YKP) [2], or of q_{long} $(= q_\parallel)$ and the transverse components q_{out}, q_{side} suggested by Bertsch-Pratt (BP). The Fourier conjugates of each q-component deliver therefore the spatial or temporal extent R_i $(i = \parallel, \perp, 0$ or $i = long, out, side)$. As reference frame, the so-called fixed local center-of-mass system is taken considering the limited rapidity range $(y \in [y_{CM}, y_{CM} + 0.5])$.

The Coulomb correlation between like-sign kaons was corrected in the raw two-kaon correlation functions by using an iterative theoretical calculation suggested by [5]. The Coulomb-corrected two particle correlations are shown in Figure 1 with 3-dimensional fit to data. Since the HBT radius parameters depend on the transverse mass as a consequence of the collective expansion of the source, we show in Figure 2 the earlier pion data [3] for the same reaction together with the kaon results as well as those from the CERN experiment NA44 [4] as a function of $m_\perp$.

According to the relation : $R_\parallel = \tau_f \sqrt{\frac{T}{m_\perp}}$ based on a hydrodynamic expansion model [6], where τ_f and T are the freeze-out time and temperature of the particles ($T \simeq 120$ MeV from [3]), respectively, the freeze-out time is extracted as 9.5 ± 1.5 fm/c from its gradient (in Figure 3a), which is consistent with the previous result in [3]. Furthermore, the dependence of $R_\perp$ on $m_\perp$ is in good agreement with a model calculation applied in [3], which delivers a transverse expansion velocity $\beta_\perp$ around 0.55 (Figure 3b).

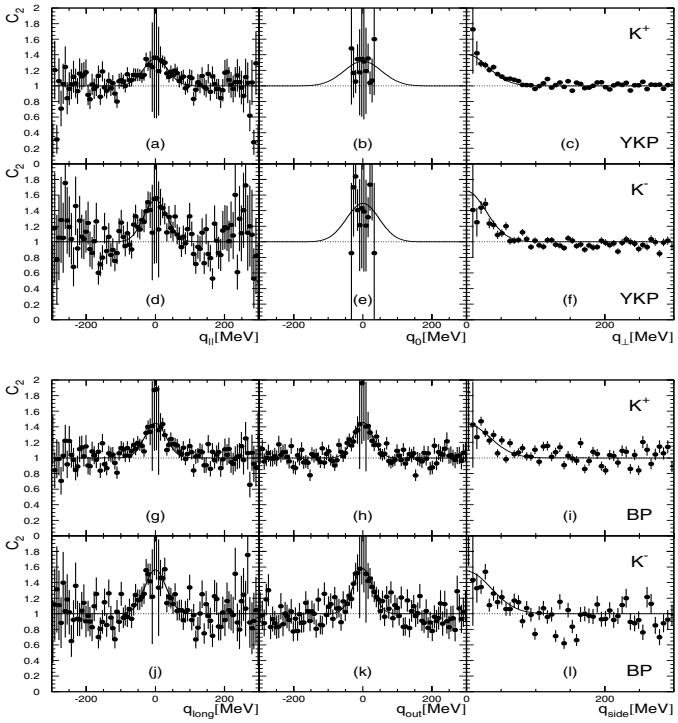


Figure 1: The Coulomb-corrected 3-dimensional correlation between like-sign kaons with $q_j \leq 30$ MeV $(j \neq i)$ in YKP (top) and BP (bottom) parameterizations.

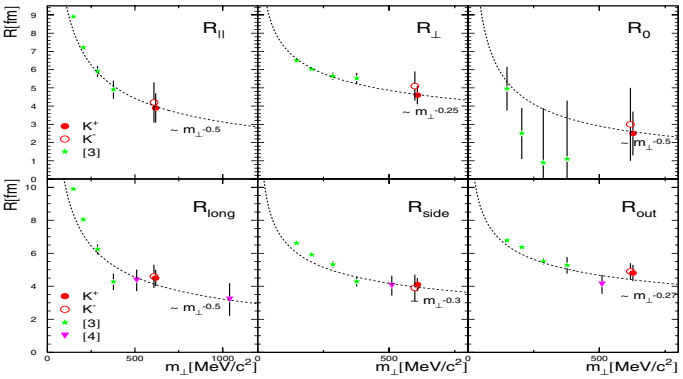


Figure 2: Comparison of HBT radii of kaons and pions as a function of $m_\perp$.

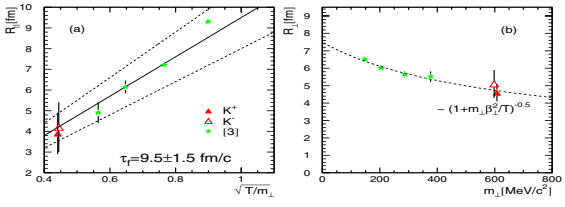


Figure 3: (a) $R_\parallel$ as a function of $\sqrt{T/m_\perp}$. (b) $R_\perp$ as a function of $m_\perp$.

References

[1] S. Afanasiev *et al.*, Nucl. Instrum. Meth. **A430** (1999) 210
[2] F. B. Yano *et al.*, Phys. Lett. **B78** (1978) 556
[3] H. Appelshäuser *et al.*, Eur. Phys. J. **C2** (1998) 661; H. Appelshäuser, Dissertation (1997) ; S. Schönfelder, Dissertation (1997)
[4] I. Bearden *et al.*, Phys. Rev. Lett **87** (2001) 112301
[5] Y. M. Sinyukov *et al.*, Phys. Lett. **B432** (1998) 248
[6] A. N. Makhlin, Z. Phys. **C39** (1988) 69

GSI Future: A Detector for Antiproton Physics

O.N. Hartmann[1], U. Lynen[1], H. Orth[1], C. Schwarz[1],
S. Ganzhur[2], V. Hejny[3], H. Koch[2], K. Peters[2], J.L. Ritman[4], U. Wiedner[5]
[1]GSI, [2]Univ. Bochum, [3]FZ Jülich, [4]Univ. Gießen, [5]Univ. Uppsala

Introduction

A major part of the GSI future project [1] is the possibility to open up a new research field in hadron spectroscopy and hadron properties in nuclear matter using cooled antiprotons in a High Energy Storage Ring (HESR). This machine will provide antiproton beams in a momentum range of 1.5 to 15 GeV/c with excellent beam quality. Internal targets in the ring are pellets of frozen H_2 or cluster jets ($\overline{p}p$ reactions) or thin wires of heavier elements ($\overline{p}A$ reactions). The main topics are precision charmonium spectroscopy, search for hybrids and glueballs, interaction of open and hidden charm with nucleons and nuclei, and (double) hypernuclei.

The Proposed Detector

To serve the many experiments proposed with the new facility a general purpose detector was conceived. Figure 1

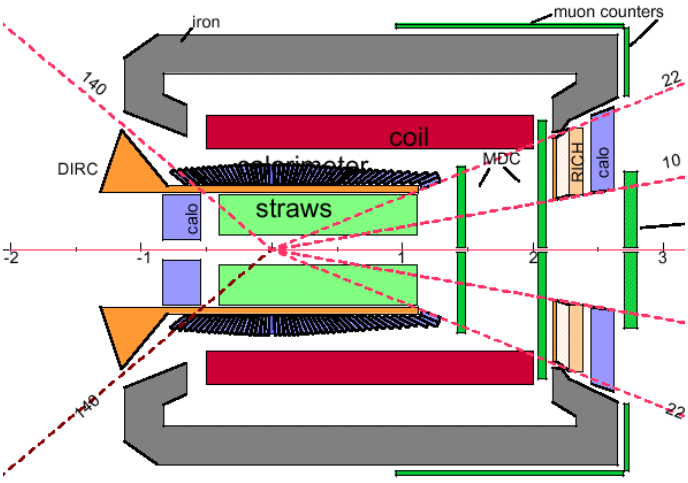


Figure 1: Top view of the proposed detector

shows a schematic view of the detector. It is comprised of a target spectrometer which uses a solenoidal magnetic field of 2 T, and a forward spectrometer, which is not shown, that uses a large dipole magnetic field of 2 Tm.
To fulfill the physics requirements the detector componenets have to handle a rate of $2{\cdot}10^7$ annihilations per second in case of maximum design luminosity ($2{\cdot}10^{32}$ $cm^{-2}s^{-1}$) experiments. While the total annihilation cross section is about 100 mb, dedicated triggers on events with nb cross sections are needed. A good particle identification and high resolution in energy and angle are necessary for charged particles as well as for photons. For precision spectroscopy with partial wave analysis of resonance states complete coverage of the solid angle is needed.

Detector Components

The innermost part of the target spectrometer is formed by a microvertex detector (MVD). It is optimized for maximum acceptance around the interaction point and is used for the determination of secondary vertices. Its concept is based on the design for LHC experiments [2, 3] consisting of radiation hard silicon pixel detectors. Here we propose a five layer barrel detector with $7.2{\cdot}10^6$ pixels of $50{\cdot}300$ μm^2. In addition there will be five detector layers perpendicular to the beam axis in the forward part ($2{\cdot}10^6$ pixels of $100{\cdot}150$ μm^2). The detector wafers have a thickness of 200 μm each. Figure 2 shows a schematic view on the MVD.

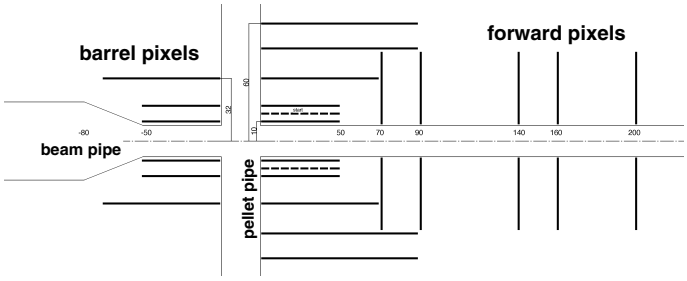


Figure 2: Layout of the microvertex detector

Outside of the MVD will be a cylindrical straw tube tracker (STT), and mini drift chambers downstream of the target. This tracking chambers will be e.g. used to detect secondary vertices which occur outside the MVD (K^0_S, Λ). For the target spectrometer three sets of six layer mini drift chambers from the HADES [4, 5] type are foreseen. The STT consists of 15 double layers, whereby the 13 inner double layers are arranged at skew angles (2-3°). The intrinsic resolution of an individual tube is 150 μm, thereby providing a position resolution along the beam axis of about 1 mm. This system provides a momentum resolution $\sigma_p/p = 1\%$ to 2% depending on polar angle and momentum. Figure 3 shows a view of the MVD and STT with an superimposed simulated $\overline{p}p \to \phi\phi$ event. Here the skew angles of the straw tubes are set to zero.

Two types of ring imaging Čerenkov counters are foreseen for particle identification (π,K in particular). For the polar angles $\vartheta \geq 22°$ the detection of internally reflected Čerenkov (DIRC) light [6] is used. The radiator will be constructed out of 1.7 cm thick quartz bars. For the smaller polar angles we plan to use proximity focussing Čerenkov counters similiar to those in STAR/ALICE [7]. An important part of the detector is the electromagnetic calorimeter. In order to realize the desired compact structure and high rate capability, scintillators of the $PbWO_4$ type are very advantageous. Experiments using phototubes for readout show that they have a small radiation length and good energy resolution for γ/e^- detection [8].

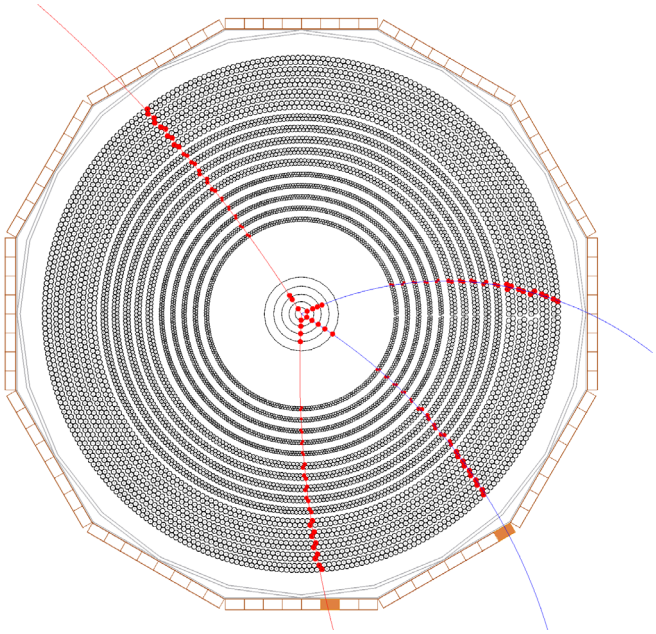


Figure 3: View of the inner tracking system

Our concept uses 15 cm long crystals (17 X_0) in a barrel and two endcaps, in total 7150 crystals, and for the readout the use of avalanche photodiodes is planned.

Finally, outside the iron yoke of the solenoid magnet, the target spectrometer has two layers of 72 scintillator strips for muon detection. They are arranged like a barrel parallel to the beam axis and in a perpendicular part on the forward edge of the magnet.
The forward spectrometer has not yet been designed in detail. This work is in progress.

Monte Carlo Simulation

The properties of the proposed detector system have been investigated extensively during the past year. All the components of the target spectrometer are implemented in a simulation package based on the GEANT4 software [9]. The analysis part uses ROOT [10], and as event generator PLUTO^{++} [11] has been chosen.
Microvertex Detector: To be able to examine reactions involving D mesons (e.g. $c\tau = 124$ μm for D^0) which are produced with a relativistic γ-factor of $\approx$2 a vertex resolution on the order of 100 μm is required. The single track resolution of the MVD has been studied using a background reaction of the type $\overline{p}p \rightarrow 2\pi^+2\pi^-$. The helix flight path of the charged particles has been fitted. Figure 4 shows the two most important fit parameters which are D0 (minimal transverse distance of the track to the z-axis) and Z0 (z-coordinate of the track at that point). Resolutions of 51 μm in transverse and 82 μm in longitudinal direction have been obtained.

The track resolution of the STT and the MDC has been investigated with the reaction $\overline{p}p \rightarrow J/\Psi + \phi$ at $\sqrt{s}$=4.4 GeV/c^2. Figure 5 shows the $\mu^{\pm}$/K$^{\pm}$ invariant mass distribution, respectively. The invariant mass spectra have been fit with Gaussian peaks of width $\sigma = 36$ and 3.6 MeV/c^2, respectively.

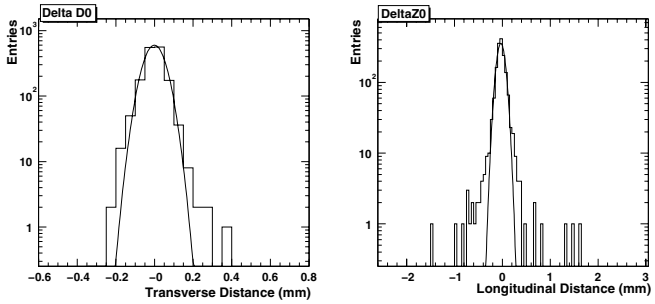


Figure 4: Spatial resolution of the MVD

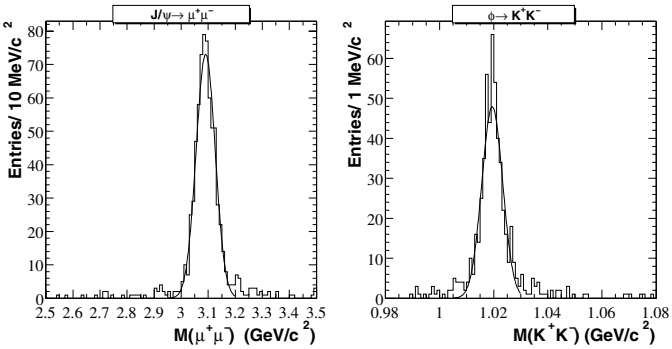


Figure 5: Invariant mass distribution

The DIRC provides an information on the velocity of a particle, and combining this with the momentum measurement from the tracking the mass of the particle can be determined. The left part of figure 6 shows the reconstructed mass, there is a well separated peak from kaons and another peak from pions. The right part of figure 6 shows the efficiency for kaon identfication (open circles) and the probability to misidentifiy a pion as a kaon (filled circles). The vertical scales are on the right/left, respectively.

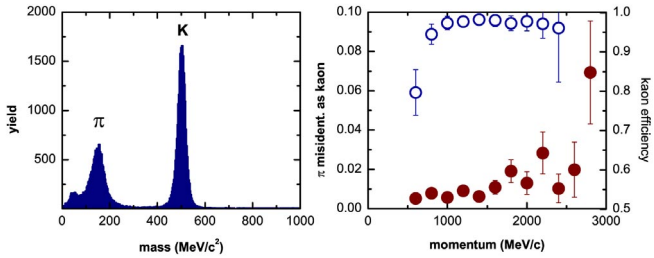


Figure 6: DIRC reconstructed mass and efficiency

Electromagnetic Calorimeter: Here the reaction $\overline{p}p \rightarrow J/\Psi + \eta$, an important annihilation channel in $\overline{p}p$, at an energy $\sqrt{s}$=4.4 GeV/c^2 has been used. The invariant mass distribution of all cluster pairs is shown in figure 7. The peak from the η meson sits on top of a combinatorial background. This peak has a width of about 20 MeV.

The electron/pion separation power of the calorimeter has been studied by analysing the distribution of the deposited energy for various momenta of electrons and

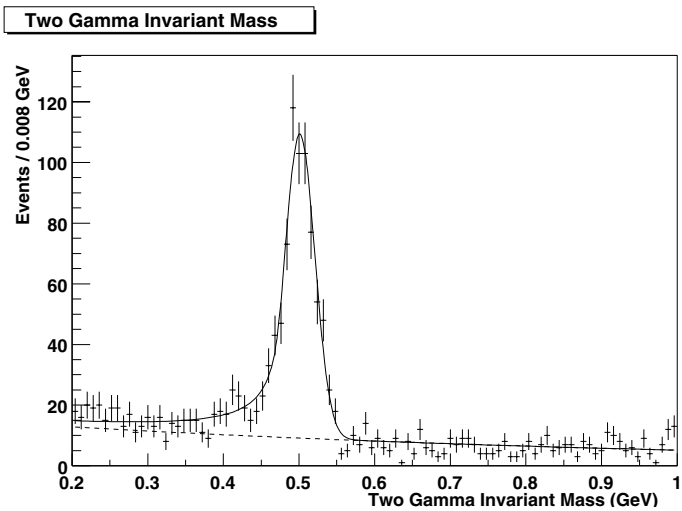


Figure 7: Invariant mass of γ pairs

pions. At momenta larger than 400 MeV/c most of the pions are no longer stopped in the crystals, whereas the electrons deposit their full kinetic energy. For leptons with momenta above about 150 MeV/c a detection efficiency of close to 100% can be achieved. Above 450 MeV/c the probability to misidentify a $\pi^{\pm}$ is on the level of 10^{-3}.

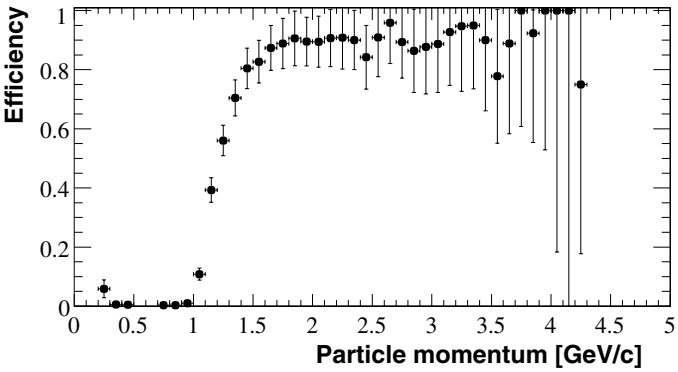


Figure 8: Efficiency of the muon counters

Figure 8 shows the integrated efficiency as a function of momentum for the Muon Counters. Muons need an initial momentum of 1.3 GeV/c to pass the iron necessary for the return yoke of the solenoid without being stopped. Above that threshold the efficiency is larger than 90%. In the most relevant momentum range the misidentification probability for pions to be registered as muons is between 1% and 2%.

The performance of the target spectrometer was tested simulating the reaction $\overline{\mathrm{p}}\mathrm{p} \to J/\Psi + \eta$ at $\sqrt{s}$=4.4 GeV/c^2. The decay of the J/Ψ was assumed to be isotropic. For each of the dilepton decay channels of the J/Ψ the geometrical acceptance times the efficiency for detection and reconstruction has been determined individually. The efficiency was determined as a function of cosine of the J/Ψ center-of-mass polar angle for the dielectron channel. Figure 9 shows the result. The flat behaviour of the acceptance is important for the partial wave analysis.

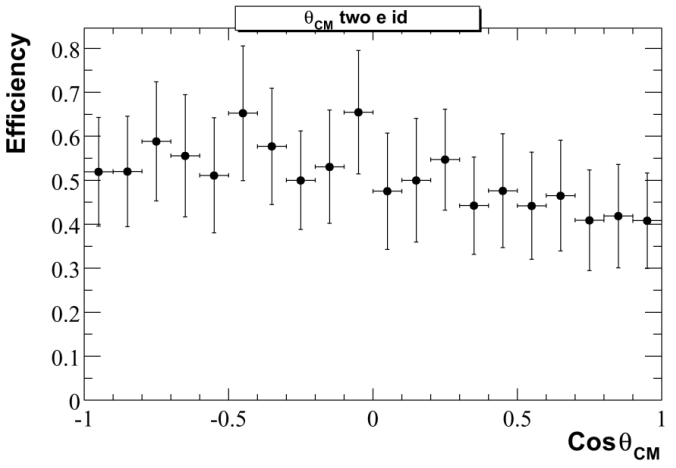


Figure 9: Efficiency to measure the reaction $\overline{\mathrm{p}}\mathrm{p} \to J/\Psi + \eta$ for the dielectron decay channel

Summary

The performed simulations of the functionality of the proprosed detector show its ability to measure electrons, muons, pions and kaons over a large phase space region. The momentum resolution is sufficient and we obtained a high power for particle identification. Combining these features with the large coverage of the solid angle which is close to 4π our system allows the application of strong kinematical constraints to the data which will serve for a high level of background suppression.

Open questions are the feasibility of a pellet target system [1, 12] and details of the proximity focussing Čerenkov counters. The forward spectrometer has to be included to perform a full simulation of the antiproton annihilation reactions.

Acknowledgements

We would like to express our thanks to all colleagues who have contributed to the workout of the conceptual design report, namely T. Barnes, D. Bettoni, R. Calabrese, W. Cassing, M. Düren, S. Ganzhur, V. Hejny, P. Kienle, H. Koch, W. Kühn, U. Lynen, V. Metag, H. Orth, S. Paul, J. Pochodzalla, J. Ritman, L. Schmitt, C. Schwarz, K. Seth, W. Weise, U. Wiedner.

References

[1] Conceptual Design Report, GSI 2001
[2] ATLAS TDR 11, CERN/LHCC 98-13
[3] CMS TDR 5, CERN/LHCC 98-6
[4] C. Müntz, Nucl. Phys. B78(1999)139
[5] C. Garabatos, NIM A412(1998)38
[6] R. Aleksan et al., NIM A397(1997)261
[7] http://consult.cern.ch/alice/Documents/1998/01/HMPID/tdr.html
[8] R. Novotny et al., IEEE Trans.Nucl.Sc. 47(2000)1499
[9] CERN http://wwwinfo.cern.ch/asd/geant4
[10] CERN http://root.cern.ch
[11] GSI http://www-hades.gsi.de
[12] C. Ekström et al., NIM A371(1996)572

Measuring jets with ALICE

D. Miśkowiec and P. Braun-Munzinger

The general-purpose heavy ion experiment ALICE at LHC has been designed to measure single- and two-particle distributions of identified mesons, leptons, and photons in central collisions of two lead ions at $\sqrt{s}$=5.5 TeV. In this note we present an estimate of the ALICE ability to measure hard QCD jets.

The rate of jets expected in ALICE was determined using PYTHIA. We first calculated the inclusive jet cross section in p$\bar{\text{p}}$ collision at $\sqrt{s}$=1.8 TeV and compared it to the data of the D0 experiment[1]. As shown in Fig. 1, the PYTHIA calculation, up-scaled by K=1.5, describes the data reasonably well. The calculation was performed in three runs differing by the value of the CKIN(50) parameter which defines the minimum momentum transfer, i.e. the "hardness" of a collision. The three curves, corresponding to CKIN(3) of 50, 100, and 200 GeV, nicely match in overlap regions. The CTEQ4HJ structure function was used.

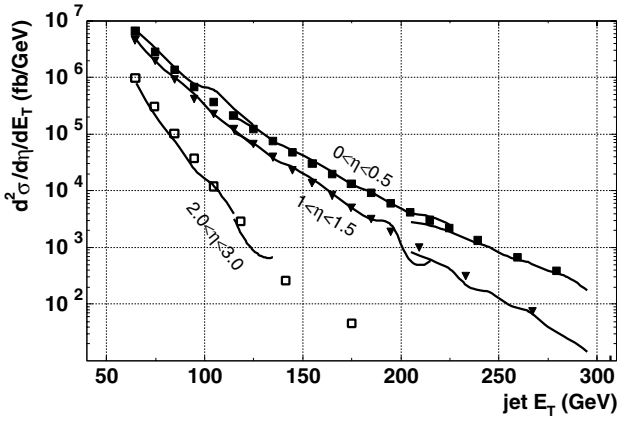


Figure 1: PYTHIA calculation of the inclusive jet cross section in p$\bar{\text{p}}$ at $\sqrt{s}$=1.8 TeV, compared to the D0 data.

Subsequently, we ran PYTHIA for pp at $\sqrt{s}$=5.5 TeV and applied the same K-factor of 1.5. The jet multiplicity in central 15% lead-lead collisions was then calculated by multiplying the obtained cross sections by 22 mb^{-1}, the nuclear overlap function T_{AB} averaged over impact parameter within the considered centrality range [2]. Assuming a rate of clean minimum bias collisions of 1000/s, and with the acceptance of the ALICE TPC of 1.8 pseudorapidity units, we arrive to the expected rate of 1 (0.01) central event with a jet of E_T>100 (250) GeV per second.

The traditional way of detecting jets is to use hadronic calorimeters. In ALICE, the Time Projection Chamber (TPC) and the readout chambers of the Transition Radiation Detector (TRD) provide an alternative access to jets via charged particles. The fraction of the jet energy carried by charged particles was estimated to be about 60-70 percent, rather independent on jet energy (Fig. 2). Furthermore, TRD can provide a trigger, needed for jets

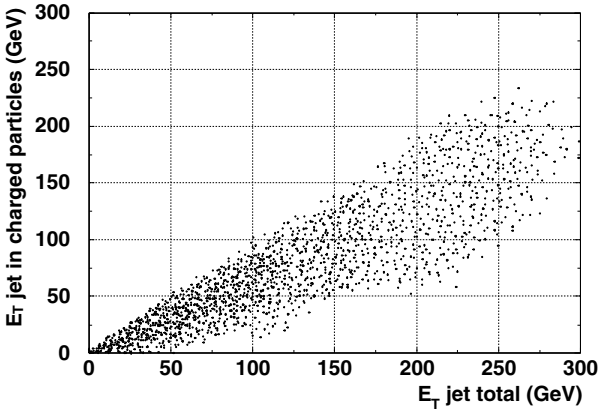


Figure 2: Fraction of jet energy carried by charged particles – PYTHIA calculation for $\sqrt{s}$=5.5 TeV.

with E_T>150 GeV. The trigger can be constructed by requiring a number of high $p_T$charged particles within a solid angle cone. The p_T is determined from the curvature of the track crossing the six planes of the TRD. The optimum size of the cone roughly coincides with the size of a TRD module, $\Delta\eta$=0.36 x $\Delta\phi$=0.35. The efficiency of such a trigger, simulated using jets from PYTHIA, was found to be sufficiently high (Fig. 3).

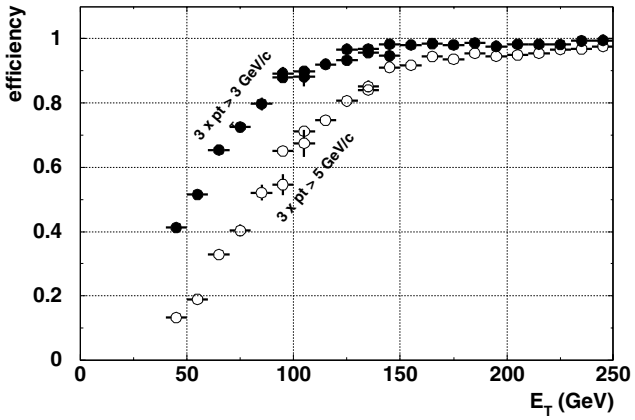


Figure 3: Efficiency of a jet trigger based on requiring three high p_T charged particles in any of the 90 TRD modules.

The jets in ALICE will be embedded in a background from soft processes. Random combinations of hard tracks lead to fake triggers. With the 3-tracks-above-5-GeV trigger (open symbols in Fig. 3) the rate of fake triggers was estimated to be below the rate of good jet events. The total rate is well within the expected data acquisition capability.

References

[1] B. Abott *et al.*, Phys. Rev. Lett. **86**, 1707 (2001).
[2] `http://www.gsi.de/~misko/overlap`

Stability and instability of a hot and dilute nuclear droplet: dissipative isoscalar modes

W. Nörenberg, G. Papp* and P. Rozmej†

In [1] we have introduced a collective model which allows to study the bulk and surface modes of a nuclear droplet as function of its density ϱ and temperature T. The description is based on the diabatic approach to dissipative collective motion and – in the local density approximation – yields equations of motion for small amplitudes, where the mass and stiffness tensors are obtained analytically. The model is suited to explore systematically characteristic properties of hot nuclear droplets as function of their densities.

In [1] we have studied isoscalar modes in the adiabatic limit, which is defined by a vanishing relaxation time ($\tau = 0$, instantaneous intrinsic equilibration). However, the adiabatic (or thermodynamic) limit is quite unrealistic for nuclear systems, because realistic values for the relaxation time are of the same order as the characteristic times of collective motion in the region of the liquid-gas phase transition. Therefore, we extend our study here to arbitrary values of the relaxation time, and thereby include dissipation.

By varying τ between infinity and zero our diabatic approach allows us to treat the continuous transition between the two elastic limits, *i.e.* the diabatic limit($\tau \to \infty$), where the dynamical distortions of the local Fermi sphere are not destroyed by two-body collisions, and the adiabatic limit ($\tau = 0$), where the Fermi sphere is assumed to be restored instantaneously. When expressed in terms of the temperature, the relaxation time of a Fermi-liquid is practically independent of the density ϱ, yielding rates $\hbar/\tau \approx T^2/3$MeV. In addition to the adiabatic spinodal we find also diabatic spinodals for the bulk modes of infinite nuclear matter and nuclear droplets, however not for surface modes.

As discussed in [1], the eigenvalue equation for the collective modes in harmonic approximation reads (eq. (1.19))

$$-B_{\lambda\lambda'}\,\omega^2 + C'_{\lambda\lambda'}\frac{\omega}{\omega + i/\tau} + \overline{C}_{\lambda\lambda'} = 0 \qquad (1)$$

with the mass tensor $\mathbb{B} \equiv \{B_{\lambda\lambda'}\}$, the adiabatic stiffness tensor $\overline{\mathbb{C}} \equiv \{\overline{C}_{\lambda\lambda'}\}$ and $\mathbb{C}' = \mathbb{C} - \overline{\mathbb{C}}$ the difference between the diabatic ($\mathbb{C}$) and adiabatic stiffness tensors.

Since the secular equation for the eigenmode energies is of third order, there exist three roots (for each eigenmode) for $0 < \tau < \infty$ instead of two for the adiabatic and diabatic limits. As functions of τ the eigenvalues move around in the complex ω-plane on generic trajectories which depend on the positions in the (ϱ, T)-plane. The main effects of dissipation as compared to the adiabatic limit are summarized as follows.

- The spinodal lines for bulk and surface modes are not changed by dissipation.

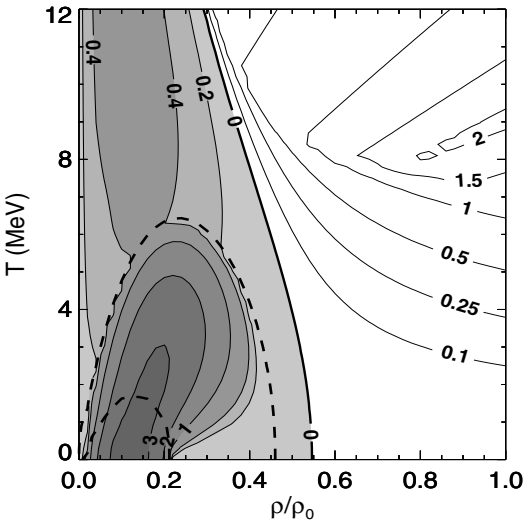


Figure 1: *Combined bulk and surface instabilities (soft EOS) for a gold-like droplet. Shown are the largest growth rates (shaded areas) and the smallest vibrational damping rates in MeV. The dashed lines indicate the adiabatic and diabatic bulk spinodals.*

- However, the growth rates of unstable bulk and surface modes are quite sensitive to dissipation and, due to the sensitivity of the relaxation time τ on temperature T, are reduced from their adiabatic values by factors 1/2 to 1/4 in the region of interest.
- The qualitative differences between soft and stiff equations of state (EOS), with larger spinodal regions and larger growth rates for the stiff EOS, survive, when dissipation is included.
- Dissipation leads to some increase in the splitting of growth rates for modes with different multipolarities l and number n of radial nodes. With decreasing density the quadrupole mode $l, n = 2, 0$ becomes unstable first, followed in sequence by the higher multipoles $l = 3, 4, 5$ and nodal number $n = 1, 2$.

The results show that the qualitative features of multifragmentation by spinodal decomposition survive when dissipation is included. During the clustering process thermalization within the decaying droplet is so fast (relaxation time $\tau \approx 20$ fm/c for $T \approx 5$ MeV) that statistical equilibrium is attained throughout the formation of fragments. This explains why statistical models are so successful in describing various aspects of multifragmentation.

References

[1] W. Nörenberg, G. Papp and P. Rozmej, Eur. Phys. J. A **9**, 327 (2000), GSI Scientific Report 2000.

[2] W. Nörenberg, G. Papp and P. Rozmej, Eur. Phys. J. A (2002, in press), arXiv:nucl-th/0201022.

Permanent address: HAS Research Group for Theoretical Physics, Eötvös University,H-1117 Budapest, Hungary

†*Permanent address:* Institute of Physics, University of Zielona Góra, Pl-65246 Zielona Góra, Poland

Isoscaling and its Statistical Interpretation.

A.S. Botvina and W. Trautmann, *GSI Darmstadt.*

The scaling properties of cross sections for fragment production with respect to the isotopic composition of the emitting systems were studied long ago in light-ion induced reactions [1]. Recently, the isoscaling was also reported for heavy-ion reactions [2]. It is constituted by the exponential dependence of the production ratios R_{21} for fragments with neutron number N and proton number Z in reactions with different isospin asymmetry:

$$R_{21}(N,Z) = \frac{Y_2(N,Z)}{Y_1(N,Z)} = C \cdot exp(N \cdot \alpha + Z \cdot \beta), \quad (1)$$

with three parameters C, α and β. Here Y_2 and Y_1 denote the yields from the more neutron rich and the more neutron poor reaction system, respectively. In some reactions, the parameters α and β have the tendency to be quite similar in absolute magnitude but of opposite sign [2]. This suggests an approximate scaling with the third component of the isospin $t_3 = (N-Z)/2$ of the form

$$R_{12}(N,Z) = Y_1(N,Z)/Y_2(N,Z) = C \cdot exp(-t_3 \cdot \beta_{t3}). \quad (2)$$

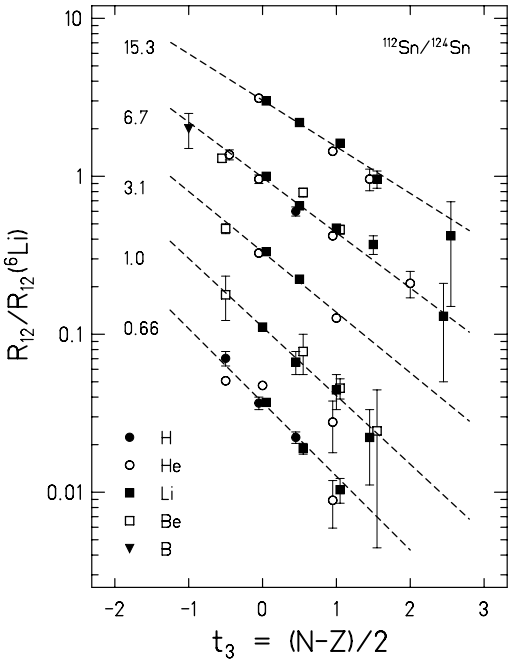


Figure 1: Normalized isotopic effect R_{12} for five reactions, labeled with the projectile energy (in GeV) and shifted by factors of three for clarity. The lines are the results of the exponential fits according to Eq. (2).

The isotope ratios measured in five pairs of reactions induced by light particles from protons of 0.66 GeV to α-particles of 15.3 GeV incident energy on ^{112}Sn and ^{124}Sn targets, and normalized with respect to the ratio for ^{6}Li, are shown in Fig. 1. The parameter β_{t3} decreases from 1.08 to 0.68 with increasing energy [3]. The inverse scaling parameter $1/\beta_{t3}$ is found to increase approximately in proportion to the isotope temperature deduced from the yields of He and Li isotopes.

The isoscaling phenomenon arises naturally in a statistical fragmentation mechanism. In the grand canonical approximation of the Statistical Multifragmentation model (SMM) [4] the mean yield of a fragment with mass number A and charge Z is given by

$$\langle Y_{AZ} \rangle = g_{AZ} \frac{V_f}{\lambda_T^3} A^{3/2} \exp\left[-\frac{1}{T}\left(F_{AZ} - \mu A - \nu Z\right)\right], \quad (3)$$

where, within the brackets, T is the temperature, $F_{AZ}(T)$ is the individual free energy of the fragment, and μ and ν are the chemical potentials responsible for the mass and charge conservation in the system, respectively. As evident from Eq. (3), for two systems 1 and 2 with different total mass numbers (A_1 and A_2) and charges (Z_1 and Z_2) but with the same temperature and density, the ratio of fragment yields produced in these systems is given by Eq. (1) with parameters $\alpha = (\mu_1 - \mu_2)/T$ and $\beta = ((\mu_1 - \mu_2) + (\nu_1 - \nu_2))/T$.

In the SMM the isoscaling coefficients are connected with properties of the produced fragments. In particular, their symmetry energy is $E_{AZ}^{sym} = \gamma(A-2Z)^2/A$, where $\gamma \simeq 25$ MeV is the symmetry energy parameter, reflecting also the symmetry energy of nuclear matter. We have obtained that the potential differences depend essentially only on the coefficient γ of the symmetry term and on the isotopic compositions of the sources:

$$\mu_1 - \mu_2 \approx -4\gamma\left(\frac{Z_1^2}{A_1^2} - \frac{Z_2^2}{A_2^2}\right),$$
$$\nu_1 - \nu_2 \approx 8\gamma\left(\frac{Z_1}{A_1} - \frac{Z_2}{A_2}\right). \quad (4)$$

This formula is relevant for any temperature in the grand-canonics, and it was confirmed for the multifragmentation region ($T \gtrsim 5$ MeV) with the microcanonical Markov chain SMM calculations [3]. We suggest to use the isoscaling phenomenon for experimental determination of the symmetry energy coefficient [3]: 1) First, the isoscaling parameters and the isospin of the thermal sources should be extracted. 2) The temperature should be found in an independent way, e.g. as the isotope temperature. 3) By using Eq. (4) one can find γ. 4) Since the secondary deexcitation of the produced fragments can influence the isoscaling parameters, the corresponding correction has to be applied.

References

[1] O.V. Lozhkin and W. Trautmann, *Phys. Rev. C* **46**, 1996 (1992)

[2] M.B. Tsang et al., *Phys. Rev. Lett.* **86**, 5023 (2001)

[3] A.S. Botvina, O.V. Lozhkin and W. Trautmann, *nucl-th/0112049*, 2001

[4] J.P.Bondorf et al., *Phys. Rep.* **257**, 133 (1995).

Signatures of the liquid-gas phase transition in multifragmentation

Al. H. Raduta (GSI, NIPNE-Bucharest), Ad. R. Raduta (GSI, NIPNE-Bucharest)

The identification of a possible liquid-gas phase transition in nuclear matter is presently a subject of great interest. From the experimental point of view the equilibrated systems formed in heavy ion collisions follow an *unknown* path in the excitation energy (E)-freeze-out volume (V) plane, not necessarily along the order parameter of the system, which prevents any deduction concerning the existence of a liquid gas phase transition from the simple analysis of the nuclear caloric curve [1]. It was recently shown that a constant microcanonical pressure path is a good order parameter even for small systems with long range forces like the nuclear ones [2]. It is believed that the experimentally formed equilibrated nuclear systems have a freeze-out volume fluctuating from one event to another, somewhat similar to a "constant λ" ensemble [with the partition function given by $Z(E,\lambda) = \int \mathrm{d}V W(E,V)\exp(-\lambda V)$, where $W(E,V)$ is the microcanonical density of states and λ is the Lagrange multiplier corresponding to the volume observable] [1]. It was recently argued that, if one has to deal with fluctuating volume systems, their spinodal regions are (likely to be) signaled by negative values of the heat capacity curves irrespective to the path followed by the system in the (E,V) plane [1, 3]. Therefore rigorous microcanonical formulas are required in order to evaluate these quantities. Such formulas can be simply obtained starting from the observation that the microcanonical density of states corresponding to a given excitation energy may be written as:

$$W(E) = \oint\!\!\!\sum \mathrm{d}\mathcal{E}\mathcal{F}(C)\,(E-\mathcal{E})^{\frac{3}{2}(N-n)-1}\,, \qquad (1)$$

where $\oint\!\!\!\sum \mathrm{d}\mathcal{E}() \equiv \sum_{N=1}^{A}\prod_{i=1}^{N}\left(\sum_{A_i,Z_i}\int \mathrm{d}\mathbf{r}_i\int \mathrm{d}\epsilon_i\right)() \equiv \sum_C W(C)$ and $\mathcal{F}(C)$ is a function depending on the specific system's configuration $C : \{A_i, Z_i, \epsilon_i, \mathbf{r}_i,\ i = 1,\ldots,N\}$ and n is an integer number depending on the imposed restrictions (i.e. E const.: $n=0$; E and $\mathbf{P}$ const.: $n=1$; E, $\mathbf{P}$ and $\mathbf{L}$ const.: $n=2$). The microcanonical temperature and heat capacity formula are respectively given by $T^{-1} = \partial S/\partial E$ and $C^{-1} = -T^2\left(\partial^2 S/\partial E^2\right)$, with $S = \ln W(E)$. *If* the limits of the above integral are not depending on E, then the derivative versus E can be performed *inside* the integral. The resulting expressions are:

$$\begin{aligned}
T^{-1} &= \left\langle \frac{\frac{3}{2}(N-n)-1}{K}\right\rangle,\\
C^{-1} &= 1 - T^2\left\langle \frac{\left[\frac{3}{2}(N-n)-1\right]\left[\frac{3}{2}(N-n)-2\right]}{K^2}\right\rangle,\\
\frac{\partial^2 S}{\partial E^2} &= \left\langle \frac{\left[\frac{3}{2}(N-n)-1\right]\left[\frac{3}{2}(N-n)-2\right]}{K^2}\right\rangle\\
&- \left\langle \frac{\frac{3}{2}(N-n)-1}{K}\right\rangle^2, \qquad (2)
\end{aligned}$$

with $\langle X\rangle = \sum_C W(C)X/W(E)$. Similar expressions can be obtained for the case when one has information about only a (small) number of fragments ($N_1 < N$) [3]. The applicability of the above formulas is restricted by the condition that the integration domains over $\mathcal{E}$ not to depend on E. This can be translated by the condition that the kinetic energy probability distribution not to intersect the $K=0$ axis at a non-negligible value [3]. An exemplification of the functioning of the obtained formulas [eqs. (2)] is given in Fig.1. There the results of these formulas for T, C and $\partial^2 S/\partial E^2$ are compared with evaluations of the same quantities by means of a different method dealing with probability distributions of isobaric canonical ensembles [2, 3]. The agreement is very good. The first order phase transition is signaled in the first two situations [the sources (50,23) with Coulomb interaction included and (200,82) without Coulomb interaction in a constant λ ensemble] through backbendings in the caloric curves, negative branches of the heat capacity curves or positive values of $\partial^2 S/\partial E^2$.

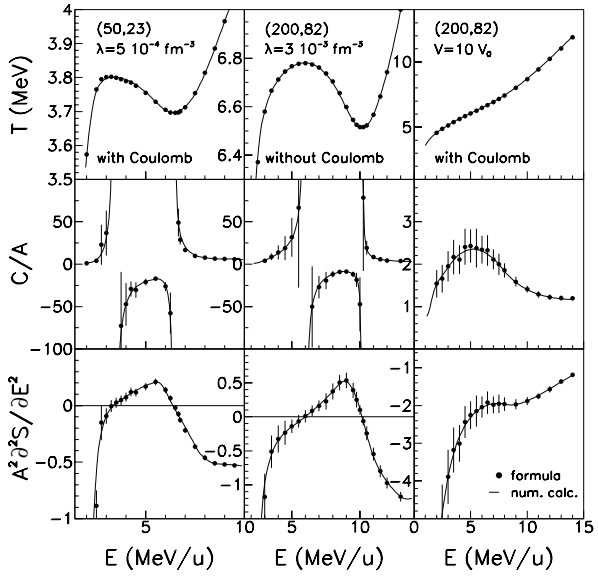


Figure 1: $T(E)$, $C(E)$ and $\partial^2 S/\partial E^2(E)$ curves calculated by means of eqs. (2) (black circles) in comparison with the corresponding results calculated from the probability distributions of a canonical ensembles at given volume constraints (constant λ; constant V).

References

[1] Ph. Chomaz, V. Duflot, F. Gulminelli, Phys. Rev. Lett. **85**, 3587 (2000).

[2] Al. H. Raduta and Ad. R. Raduta, Phys. Rev. Lett. **87**, 202701 (2001).

[3] Al. H. Raduta and Ad. R. Raduta, Nucl. Phys. A, in press.

Chiral dynamics of nuclear matter[1]

S. Fritsch [a], N. Kaiser [a] and W. Weise [a,b]

[a] Physik Department, Technische Universität München, D-85747 Garching, Germany

[b] ECT*, I-38050 Villazzano (Trento), Italy

We calculate the equation of state of isospin-symmetric nuclear matter in the 3-loop approximation of chiral perturbation theory [1]. The contributions to the energy per particle $\bar{E}(k_f)$ from 1π- and 2π-exchange graphs are ordered in powers of the Fermi momentum k_f (modulo functions of k_f/m_π). It is demonstrated that, already at order $\mathcal{O}(k_f^4)$, 2π-exchange produces realistic nuclear binding. The underlying saturation mechanism is surprisingly simple (in the chiral limit), namely the combination of an attractive k_f^3-term and a repulsive k_f^4-term. The empirical saturation point $\bar{E}(k_{f0}) \simeq -15.3\,\mathrm{MeV}$, $\rho_0 \simeq 0.17\,\mathrm{fm}^{-3}$ and the nuclear compressibility $K \simeq 255\,\mathrm{MeV}$ are well reproduced at order $\mathcal{O}(k_f^5)$ with one single momentum cut-off of $\Lambda = 7 f_\pi \simeq 0.65\,\mathrm{GeV}$ which parametrizes all necessary short-range dynamics. In the same framework, we calculate the density-dependent asymmetry energy and find $A(k_{f0}) \simeq 34\,\mathrm{MeV}$, in very good agreement with the empirical value. The pure neutron matter equation of state is also in fair agreement with sophisticated many-body calculations and a resummation result of effective field theory, for low neutron densities $\rho_n < 0.25\,\mathrm{fm}^{-3}$.

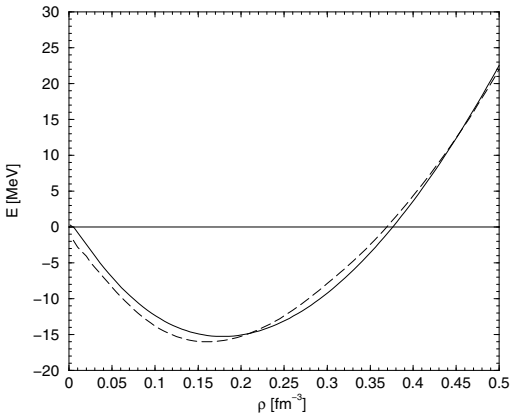


Figure 1: Energy per particle $\bar{E}(k_f)$ of isospin symmetric nuclear matter versus the nucleon density ρ.

In the next step, we evaluate the momentum and density dependent complex single particle potential $U(p,k_f) + i\,W(p,k_f)$ [2] (i.e. the average nuclear mean field). Chiral 1π- and 2π-exchange give rise to a potential depth (for a nucleon at the bottom of the Fermi sea) of $U(0,k_{f0}) = -53.2\,\mathrm{MeV}$, in very good agreement with the depth of the optical model and the nuclear shell model potential. The momentum dependence of the real single particle potential $U(p,k_{f0})$ is non-monotonic in the region $0 < p < k_{f0}$ and can be translated into a mean effective nucleon mass of $\bar{M}^* \simeq 0.82M$. The imaginary single particle potential $W(p,k_f)$ is generated entirely by iterated 1π-exchange. The half width of a nucleon-hole state at the bottom of the Fermi sea comes out as $W(0,k_{f0}) = 29.7\,\mathrm{MeV}$. The basic theorems of Hugenholtz-Van-Hove and Luttinger are satisfied in our perturbative calculation.

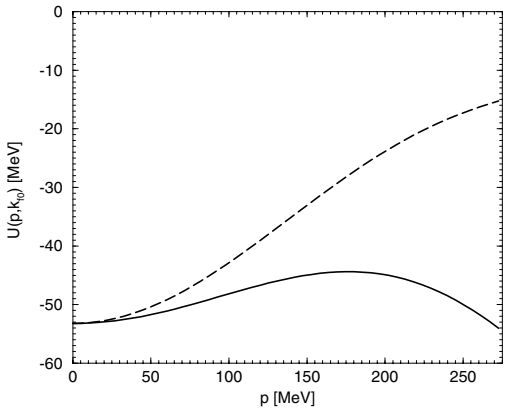


Figure 2: The real part of the single particle potential $U(p,k_{f0})$ versus the nucleon momentum p at saturation density $k_{f0} = 272.7\,\mathrm{MeV}$. The dashed line includes in addition the kinetic energy $T_k(p) = p^2/2M - p^4/8M^3$.

Finally, we extend the three-loop chiral perturbation theory calculation of nuclear matter to finite temperatures T [3]. The free energy per particle $\bar{F}(\rho,T)$ is derived from the energy density functional by inserting a Fermi-Dirac distribution for the density of states in momentum space. The calculated pressure isotherms display the familiar first-order liquid-gas phase transition of isospin symmetric nuclear matter. The predicted critical point, $T_c \simeq 24\,\mathrm{MeV}$ and $\rho_c \simeq 0.08\,\mathrm{fm}^{-3}$, lies slightly higher in temperature than the values of $T_c \simeq 16-19\,\mathrm{MeV}$ commonly discussed. This may point to the necessity of some fine-tuning in the treatment of the short-range NN-interaction, but the overall picture achieved with this (systematic) one-parameter calculation to yield a large number of nuclear matter properties is quite remarkable.

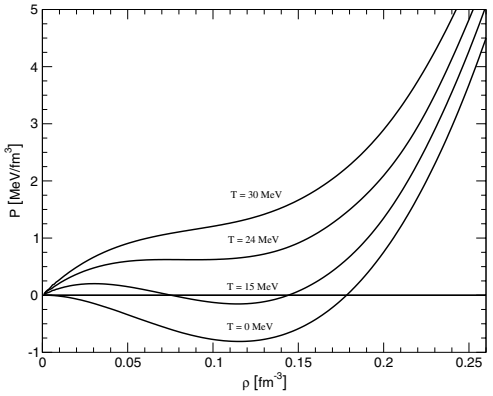


Figure 3: Pressure isotherms $P(\rho,T)$ of isospin symmetric nuclear matter versus the nucleon density ρ.

References

[1] N. Kaiser, S. Fritsch and W. Weise, Nucl. Phys. **A697** (2002) 255; and refs. therein.

[2] N. Kaiser, S. Fritsch and W. Weise, Nucl. Phys. **A700** (2002) 343; and refs. therein.

[3] S. Fritsch, N. Kaiser and W. Weise, submitted to Phys. Lett. **B**. (2002)

[1] Supported in part by BMBF, GSI and DFG.

Determination of the Equation of State of Dense Matter

Pawel Danielewicz (MSU and GSI), Roy Lacey (SUNY, Stony Brook) and William G. Lynch (MSU)

Features of the nuclear equation of state (EOS) at supranormal densities ρ can be inferred from flow in collisions of heavy nuclei at high beam energies E_{lab}. At low impact parameters, large regions of high ρ are formed and matter is best equilibrated. The collective flow can provide access to pressure generated in the collision, as seen in the hydrodynamic Euler equation for the nuclear fluid (in a frame where the collective velocity vanishes, $v = 0$): $(e+p)\,\frac{\partial}{\partial t}\,\vec{v} = -\vec{\nabla} p$. The velocity becomes an observable at the end of a reaction. In comparing to the Newton equation, we see that the pressure $p = \rho^2 \frac{\partial (e/\rho)}{\partial \rho}$ plays role of a potential for the hydrodynamic motion, while the sum of energy density e and p plays the role of mass. At moderate energies, we have $e + p \approx \rho\, m_N$ and we see that the collective flow can tell us about the pressure in comparison to ρ. For that, we need to know the spatial size where the p-gradients develop and this will be determined by the nuclear size. However, we also need the time during which the hydrodynamic motion develops.

Equilibrium, required for hydrodynamics that gave insights, is not quite achieved in reactions and transport theory is called for. In theory based on the Boltzmann equation, the system is described in terms of the distribution functions f for different particles. Net energy is a functional of f and can be parametrized to yield different EOS. The f follow a set of the Boltzmann equations with 1-particle energies $\epsilon = \delta e/\delta f$: $\frac{\partial f}{\partial t} + \frac{\partial \epsilon}{\partial \mathbf{p}} \frac{\partial f}{\partial \mathbf{r}} - \frac{\partial \epsilon}{\partial \mathbf{r}} \frac{\partial f}{\partial \mathbf{p}} = I$, where I is the collision integral.

The first observable to consider for extracting EOS is the net radial collective energy which may reach as much as half of all energy in a reaction. Despite its magnitude, this energy is not useful for EOS because of the lack of information on time Δt during which the expansion develops. Large p acting over a short Δt can produce the same collective energy as low p acting over a long Δt. This makes apparent the need for a timer.

The timer role may be taken on by the spectator matter in the periphery of an energetic reaction, proceeding virtually at original velocity. As the central participant matter expands after compression, the spectators shadow its expansion. If central p are high and the expansion is rapid, the anisotropies generated by the spectators are strong. On the other hand, if p are low and, correspondingly, the expansion of the matter is slow, the shadows left by spectators cannot be very pronounced.

The spectators can produce different anisotropies in participant emission. Early on, the participant matter gets locked in a channel between the spectators, titled at an angle. Hence, the forward and backward emitted particles get an average deflection away from the beam axis. Another anisotropy results for particles with no longitudinal velocity. The central region is open to the vacuum in the direction perpendicular to the reaction plane, but in the direction within the reaction plane the region is shadowed by the spectators. Thus, more particles can be transversally emitted perpendicular to than in the plane direction.

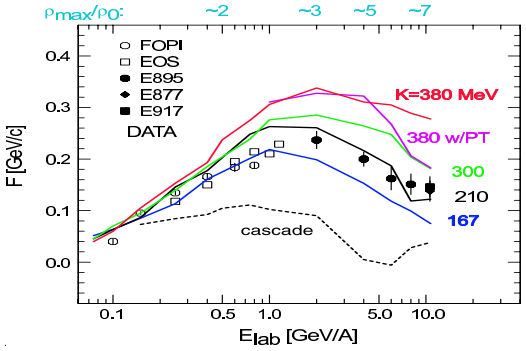


Figure 1: Sideward flow in Au + Au [1].

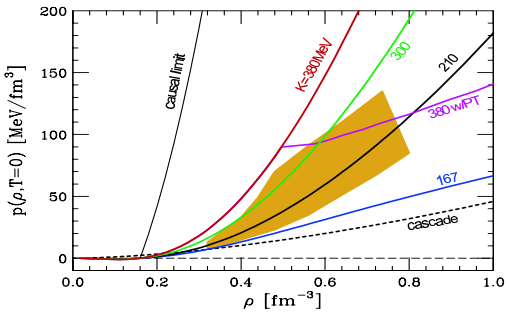


Figure 2: Constraints from flow on the $T = 0$ pressure-density relation, indicated by the shaded region [1].

The different anisotropies have been measured over a wide range of E_{lab}. Fig. 1 shows the measure F of the sideward deflection in Au + Au, vs E_{lab}. Symbols represent data and lines – simulations for different EOS. On top of the figure, maximal ρ reached at each E_{lab} are shown. Without interaction contributions to p, the simulations labelled cascade produce far too weak anisotropies. The simulations with EOS characterized by the incompressibility $K = 167$ MeV yield adequate F at lower E_{lab}, but too low at higher E_{lab}. On the other hand, for the EOS characterized by $K = 380$ MeV, F appears too high at virtually all E_{lab}. Here, K merely label the different utilized EOS, as p in the expansion are generated at much higher ρ than normal ρ_0 and, in fact, changing in the course of the reaction.

No one EOS allows to describe both types of measured anisotropies at all E_{lab}. The $K = 210$ MeV EOS is best for F, and the $K = 300$ MeV EOS is the best for the other elliptic anisotropy. We use the discrepancy as a measure of inaccuaracy of the theory and draw broad boundaries on $p(\rho)$ from what is common in the conclusions. To ensure that the effects of compression dominate in the reaction, we limit ourselves to $\rho > 2\rho_0$. The boundaries on p are shown in Fig. 2 and they eliminate some of the more extreme models for EOS utilized in nuclear physics, such as the NL3 model and models assuming a phase transition at relatively low ρ.

[1] P. Danielewicz *et al.*, submitted to Nature.

Remarks on Delta Radiative and Dalitz Decays

M. I. Krivoruchenko and Amand Faessler
Institut für Theoretische Physik, Universität Tübingen

The $\Delta(1232)$ resonance is expected to give an important contribution to the dilepton yield in nucleon-nucleon and heavy-ion collisions. In refs. [1, 2, 3, 4, 5], expressions are derived for the $\Delta \to Ne^+e^-$ decay rate, which, however, are not equivalent with respect to the kinematical factors. In refs. [2, 5, 6, 7], the radiative decay $\Delta \to N\gamma$ is calculated. The results, surprisingly, are also not equivalent. We thus give an independent calculation of these two decays.

In terms of helicity amplitudes, the decay width of a resonance, R, decaying into a nucleon, N, and a photon, γ^*, can be written as

$$\Gamma(R \to N\gamma^*) = \frac{k}{8\pi m_R^2(2J_R+1)} \sum_{\lambda\lambda'\lambda''} \left| < \lambda|S|\lambda'\lambda'' > \right|^2 \tag{1}$$

where m_R is the resonance mass, J_R its spin, k is the photon momentum in the resonance rest frame, λ, λ', and λ'' are the resonance, nucleon, and photon helicities, and $< \lambda|S|\lambda'\lambda'' >$ the corresponding amplitudes.

For the $\Delta \to N\gamma^*$ transition, there are three independent helicity amplitudes which can be found in paper by Jones and Scadron [8], eqs.(18). Using these amplitudes, we obtain the Δ resonance width for decay into a nucleon and a virtual photon:

$$\begin{aligned}\Gamma(\Delta \to N\gamma^*) = \frac{\alpha}{16}\frac{(m_\Delta+m_N)^2}{m_\Delta^3 m_N^2}((m_\Delta+m_N)^2 - \\ -M^2)^{1/2}((m_\Delta-m_N)^2-M^2)^{3/2} \\ \left(G_M^2 + 3G_E^2 + \frac{M^2}{2m_\Delta^2}G_C^2\right).\end{aligned} \tag{2}$$

Here, m_N and m_Δ are the nucleon and Δ masses, $M^2 = q^2$ where $q_\mu = (\omega, 0, 0, k)$ is the photon four-momentum, G_M, G_E, and G_C are magnetic, electric and Coulomb transition form factors, as defined in ref. [8], eqs.(15).

The factorization prescription (see *e.g.* [9]) allows to find the dilepton decay rate of the Δ resonance:

$$d\Gamma(\Delta \to Ne^+e^-) = \Gamma(\Delta \to N\gamma^*)M\Gamma(\gamma^* \to e^+e^-)\frac{dM^2}{\pi M^4}, \tag{3}$$

with

$$M\Gamma(\gamma^* \to e^+e^-) = \frac{\alpha}{3}(M^2+2m_e^2)\sqrt{1-\frac{4m_e^2}{M^2}} \tag{4}$$

being the decay width of a virtual photon into the dilepton pair with the invariant mass M.

The physical $\Delta(1232) \to N\gamma$ decay rate is given by eq.(2) at $M = 0$. The last three equations being combined give the $\Delta(1232) \to Ne^+e^-$ decay rate.

In ref. [1] the $\Delta \to Ne^+e^-$ transition is calculated. The width $\Delta \to N\gamma$ can be extracted from eqs.(10) - (12) of this work. It does not coincide with our eq.(2). The $M = 0$ limits of eqs.(4.9) - (4.13) of ref. [2] and of eqs.(3) - (13) of ref. [5] do not coincide with our eq.(2) also. In ref.[6], the physical $\Delta \to N\gamma$ decay is calculated in the light cone QCD assuming $F_1 = \sqrt{\frac{3}{2}}g_{\Delta N\gamma} \neq 0$ and $F_2 = F_3 = 0$, with the form factors F_i defined as in ref. [8], eq.(4), and the coupling constant $g_{\Delta N\gamma}$ defined as in ref.[6], eq.(3). Using eqs.(15) of ref. [8] and our eq.(2), we obtain an expression for the $\Delta \to N\gamma$ width, which differs from eq.(13) of ref.[6] (by a factor of 2/3 in the heavy-baryon limit). In ref. [7], an expression is derived for the radiative decay of a spin J_R baryon resonance. We agree with eq.(2.59) of this work. The results [1, 2, 5, 6, 7] for the $\Delta \to N\gamma$ decay are distinct from each other.

Our result for the $\Delta \to Ne^+e^-$ width, eqs.(2) - (4), is distinct from the results of refs. [1, 2, 5], since we disagree already on the $\Delta \to N\gamma$ width. In ref. [3], the $\Delta \to Ne^+e^-$ decay is calculated using the chiral perturbation theory. We reproduce kinematical factors of the $M1$ part of the decay width in eq.(2) of ref. [3]. In the soft dilepton limit, $m_e = 0$ and $M \to 0$, we agree also with the $E2$ part, but disagree with it at finite values of M. Our expression for the Δ decay rate differs from that of ref. [4], eqs.(8) and (9). The results of refs. [1, 2, 3, 4, 5] for the $\Delta \to Ne^+e^-$ decay are distinct from each other.

In the first order of the perturbation, the decay rates of the on-mass-shell spin-3/2 particles are well defined theoretically. The discrepancies between refs.[1-6] and our paper [10] can probably be attributed to errors in calculations of refs.[1-6].

References

[1] L. Xiong, Z. G. Wu, C. M. Ko and J. Q. Wu, Nucl. Phys. A **512**, 772 (1990).

[2] G. Wolf, G. Batko, W. Cassing, U. Mosel, K. Niita and M. Schaefer, Nucl. Phys. A **517**, 615 (1990).

[3] M. N. Butler, M. J. Savage and R. P. Springer, Phys. Rev. C **48**, 917 (1993) [nucl-th/9303015].

[4] A. I. Titov, B. Kampfer and E. L. Bratkovskaya, Phys. Rev. C **51**, 227 (1995).

[5] C. Ernst, S. A. Bass, M. Belkacem, H. Stocker and W. Greiner, Phys. Rev. C **58**, 447 (1998) [nucl-th/9712069].

[6] T. M. Aliev and M. Savci, Phys. Rev. D **60**, 114031 (1999) [hep-ph/9905284].

[7] R. C. Devenish, T. S. Eisenschitz and J. G. Korner, Phys. Rev. D **14**, 3063 (1976).

[8] H.F. Jones and M.D. Scadron, Ann. Phys. (N.Y.) **81**, 1 (1973).

[9] A. Faessler, C. Fuchs and M. I. Krivoruchenko, Phys. Rev. C **61**, 035206 (2000) [nucl-th/9904024].

[10] M. I. Krivoruchenko and A. Faessler, Phys. Rev. D **65**, 017502 (2002) [arXiv:nucl-th/0104045].

Dilepton production in heavy ion collisions at intermediate energies

K. Shekhter, Amand Faessler, C. Fuchs, M. Krivoruchenko, B. Martemyanov
Institut für Theoretische Physik, Universität Tübingen

During the last decade, the problem of the description of hadrons in dense and hot nuclear matter received great attention. The purpose of the current investigations is to determine experimentally mass shifts and the broadening of hadronic resonances at finite density and temperature. The dilepton spectra from heavy-ion collisions are a suitable tool for this purpose. The dilepton spectra measured by the CERES and HELIOS-3 Collaborations at CERN SPS found a significant enhancement of the low-energy dilepton yield below the ρ and ω peaks [1]. In contrast to the spectra taken at the SPS the spectra obtained by the DLS Collaboration at the BEVALAC [2] for the incident energies around 1 A.GeV cannot be reproduced by present transport calculations [3], even if full spectral functions and/or a dropping mass scenario for the vector mesons is taken into account. This fact is known as the DLS *puzzle*.

Therefore a precise and rather complete knowledge of the relative weights for existing decay channels is indispensable in order to draw reliable conclusions from dilepton spectra and to try to solve the DLS puzzle. In [4] we performed a systematic study of meson decay channels including channels which have been neglected up to now such as e.g. $\rho^0 \to \pi^0\pi^0 e^+e^-$. Recently in [5], we derived phenomenological kinematically complete relativistic expressions for decays rates of nucleon resonances with arbitrary spin and parity into the dilepton pairs in terms of the magnetic, electric, and Coulomb transition form factors. For the description of the transition form factors of the nucleon resonances the VMD model was extended to include higher radially excited ρ-mesons $\rho(1450)$ and $\rho(1700)$ in the transition form factors $RN\gamma$ to ensure the correct asymptotic behavior of the amplitudes in line with the quark counting rules. The free parameters of the model are fixed by fitting the experimental data on the photo- and electroproduction amplitudes and by fitting the results of the multichannel πN-scattering partial-wave analysis and the quark model predictions for these amplitudes. Thus one obtains an *unified* description of radiative $R \to N\gamma$ and the mesonic $R \to NV$ decay data. The transition form factors determined this way are used for the calculation of the dilepton branching ratios and dilepton spectra from decays of the nucleon resonances $R \to Ne^+e^-$ with masses below 2 GeV.

With this input we performed QMD transport calculations for $C + C$ reactions at 1 AGeV. In Fig. 1 we compare the results to the DLS data. Although we included significantly more decay channels and apply an improved description of the baryonic resonance decays our results are close to those obtained in [3]. As in [3] we underestimate the DLS data below the ρ peak by the same order of magnitude. To describe the resonance decays we introduced radially excited ρ-mesons in the transition form factors to ensure the correct asymptotic behavior of the amplitudes in line with the quark counting rules. Thereby we required the destructive interference of the ground-state and the excited ρ-mesons. In heavy-ion collisions, the interference between the virtual ρ, ρ', and ρ''-resonances produced in the nucleon resonance decays can be destroyed at least partially by interactions with the hot and dense nuclear medium. In the case of total decoherence, the ρ, ρ', and ρ'' contributions to the subthreshold part of the cross section $pp \to e^+e^-X$ must be summed up decoherently which leads to an enhancement of the resonance contributions due to the presence of the nuclear medium.

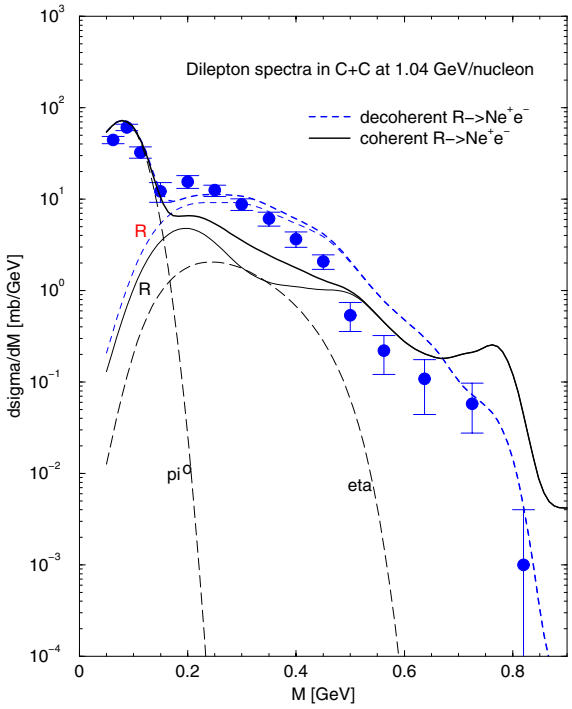


Figure 1: Dilepton spectra in $C + C$ reactions at 1.04 AGeV. Results using vacuum formfactors (solid, coherent) for $R \to Ne^+e^-$ decays of baryonic resonances are compared to the DLS data [2]. The contributions from π, η and resonances (R) are shown seperately. The dotted line (decoherent) shows the result where total decoherence of the virtual vector mesons in the resonance decays to dileptons is assumed.

We estimated this decoherence effect assuming total decoherence between the various intermediate ρ states in the decay of the baryonic resonances. The resulting curve is also shown in Fig. 1. It is seen that this leads to a significant enhancement of the dilepton yield in the kinematical region where the DLS data are underpredicted. We conclude that this fact provides a strong indication for such a destruction of quantum interference due to the presence of the nuclear medium which can explain the DLS puzzle.

References

[1] G. Agakichiev et al., Phys. Rev. Lett. 75, 1272 (1995).

[2] R.J. Porter et al., Phys. Rev. Lett. 79, 1229 (1997).

[3] C. Ernst, S.A. Bass, M. Belkacem, H. Stöcker and W. Greiner, Phys. Rev. C58, 447 (1998); E.L. Bratkovskaya and C.M. Ko, Phys. Lett. B445, 265 (1999).

[4] Amand Faessler, C. Fuchs and M.I. Krivoruchenko, Phys. Rev. C61, 035206 (2000).

[5] M. Krivoruchenko, B. Martemyanov, Amand Faessler, C. Fuchs, nucl-th/0110066, Ann. Phys. (2002) in press.

QUASIPARTICLES IN QCD THERMODYNAMICS AND DILEPTON RADIATION*

R.A. Schneider[a], T. Renk[a] and W. Weise[a,b]

[a]TU München, Garching (Germany); [b]ECT*, Trento (Italy)

A first-principles understanding of the equation of state (EOS) of hot QCD is of great interest in order to reliably identify and calculate experimental signatures of that elusive state in ultra-relativistic heavy-ion collisions. However, perturbative results show bad convergence, and current experiments only probe that non-perturbative temperature regime close to the critical temperature T_c where the underlying physics, the confinement and chiral symmetry breaking mechanism, is not sufficiently understood. Phenomenological models incorporating as much physics as is known are therefore necessary. Here, we propose a new quasiparticle model of the quark-gluon plasma (QGP) that incorporates a parametrization of confinement, supplemented by thermal masses compatible with lattice results. Details can be found in [1].

From asymptotic freedom, we expect that at very high temperatures the plasma consists of quasifree quarks and gluons. As long as the spectral function of the thermal excitations at lower temperatures resembles qualitatively this asymptotic form, a quasiparticle description of the QGP is expected to be applicable. Their dispersion relation reads

$$\omega_k^2 \simeq k^2 + m_*^2(T), \tag{1}$$

where $m_*(T)$ acts as an effective mass generated dynamically by the interaction of the partons with the heat bath background.

However, the picture of a simple massive gas is presumably not appropriate close to T_c because the driving force of the transition, the confinement process, is not taken into account. While the confinement mechanism as such is still not understood, it is not necessary to know it in detail since we consider a *statistical* system. All confinement does on a *large* scale is to cut down the number of thermally active partons as the temperature is lowered: since the confined particles have large masses, their contribution to thermodynamics is negligible. This effect can be included in a quasiparticle picture by modifying the distribution function f of the partons by a temperature-dependent *confinement factor* $C(T)$: $f(\omega_k) \to C(T) f(\omega_k)$. Since there are indications that the confinement mechanism is only weakly flavour-dependent, we assume that the function $C(T)$ acts in a universal way on quarks and gluons. Reassuringly, the pressure of the confinement model for $N_f = 2$ lies then well within a narrow lattice estimate for the continuum EOS in the chiral limit.

Based on the observation that the gluon Debye screening mass m_D evaluated on the lattice in pure gauge theory shows approximate critical behaviour, in accordance with a weakly first order phase transition and in contrast to perturbative results, we parametrize

$$m_*(T) \sim G_0 T \left(1 - \frac{T_c}{T}\right)^{\beta}. \tag{2}$$

The explicit temperature dependence of the confinement factor $C(T)$ can be obtained as the ratio of the lattice entropy - that is a measure for the number of degrees of freedom - and the entropy calculated with a dropping input mass. $C(T)$ again shows near-critical behaviour: $C(T) \sim (1 - T_c/T)^{\gamma}$.

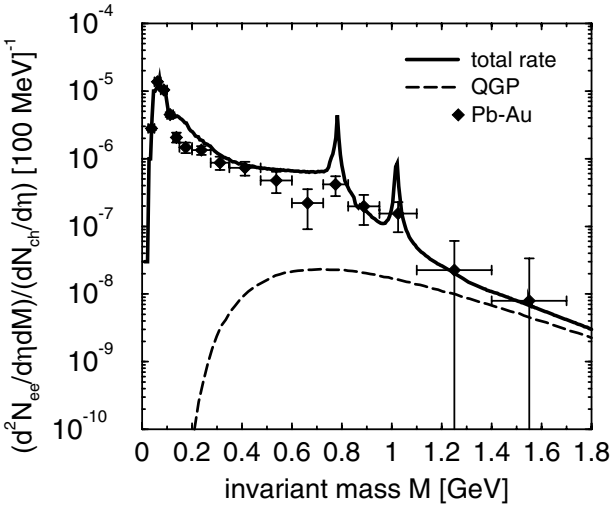
Comparing the EOS with lattice data, as a function of T, a good and economic parametrization is achieved. The so-called interaction measure, related to the trace of the energy-momentum tensor, $T^{\mu}_{\ \mu} = \epsilon - 3p$, is also nicely reproduced.

We apply the proposed model now to dilepton production in URHIC where it enters in two ways: the EOS serves as input for the construction of the fireball that is discussed at length in [2]. Second, the dilepton emissivity of a static hot spot,

$$\frac{d\mathcal{N}_{ee}}{d^4x d\omega d^3k} \sim \frac{\rho_V(\omega, k; T)}{\exp(\omega/T) - 1}, \tag{3}$$

is proportional to the vector spectral function ρ_V that is calculated from the photon self energy. By construction, the quasiparticle $q\bar{q}$-loop is the only contribution above T_c. In addition, the confinement mechanism reduces the probability of thermally exciting a quark by $C(T)$ and thus the total rate by $C(T)^2$. Below T_c, the hadronic photon self-energy is obtained using Vector Meson dominance in combination with chiral dynamics and medium effects.

To compare with experiment, the rate (3) has to be convoluted with the space-time fireball expansion [2]. The figure shows a comparison of our calculation with the dilepton rate from the CERES/NA45 experiment at 160 AGeV Pb-Au collisions, with the explicit QGP contribution plotted.



References

[1] R.A. Schneider, W. Weise, Phys. Rev. **C64** (2001) 055201.

[2] T. Renk, R.A. Schneider and W. Weise, hep-ph/0201048.

* Work supported in part by BMBF and GSI.

$\pi N \to \omega N$ in a Coupled-Channel Approach

G. Penner and U. Mosel
University of Giessen

For pion-induced dilepton production at HADES an understanding of the elementary reactions on the nucleon is mandatory. Here, because of vector meson dominance, the vector meson production plays a special role.

With this aim in mind we developed in [1] a unitary coupled-channel effective Lagrangian model that already incorporated the final states γN, πN, $2\pi N$, ηN, and $K\Lambda$ and was used for a simultaneous analysis of all avaible experimental data on photon- and pion-induced reactions on the nucleon. In an extension of the model to higher c.m. energies, i.e. up to center of mass energies of $\sqrt{s} = 2$ GeV for the investigation of higher and so called hidden nucleon resonances, the consideration of other final states becomes unavoidable and hence the model is extended to also include $K\Sigma$ and especially ωN. However, the ωN channel resisted up to now a theoretical description in line with experiment. Especially the inclusion of nucleon Born contributions overestimated the data at energies above 1.77 GeV and only either the neglect of these diagrams or very soft formfactors led to a rough description of the experimental data. Our analysis differs from previous investigations on $\pi N \to \omega N$ since a larger energy region is considered, which means there are more restrictions from experiment. Furthermore, due to rescattering being of great importance (s. fig. 1), the reaction process is influenced by all other channels and vice versa. This leads to strong constraints in the choice of ωN contributions and it is therefore possible to extract them more reliably. The calculation presented

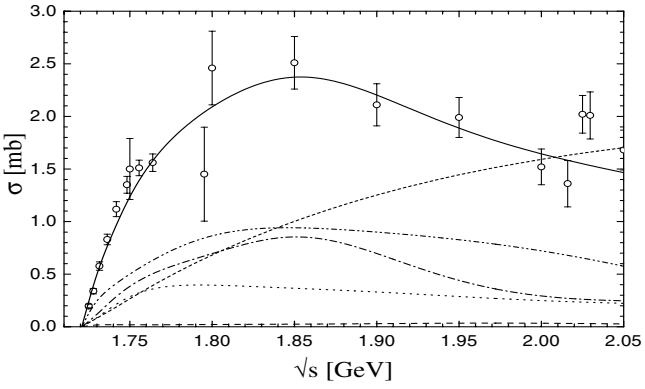


Figure 1: $\pi^- p \to \omega n$ total cross section. The contributions of various partial waves are given by $J^P = \frac{1}{2}^-(S_{11})$: dashed, $\frac{1}{2}^+(P_{11})$: dotted, $\frac{3}{2}^+(P_{13})$: dash-dot, $\frac{3}{2}^-(D_{13})$: dash-dot-dot (in brackets the πN notation is given). The sum of all partial waves is given by the solid line, short dashed is the same coupling set, but ignoring rescattering.

here lead to an overall χ^2 of 3.08 per degree of freedom by comparison to a total of 2360 data points in the channels $\pi N \to \pi N, 2\pi N, \eta N, K\Lambda, K\Sigma, \omega N$, where for the last one alone the χ^2 resulted in 2.53. There were claims in the literature that the threshold data of $\pi N \to \omega N$ [2]

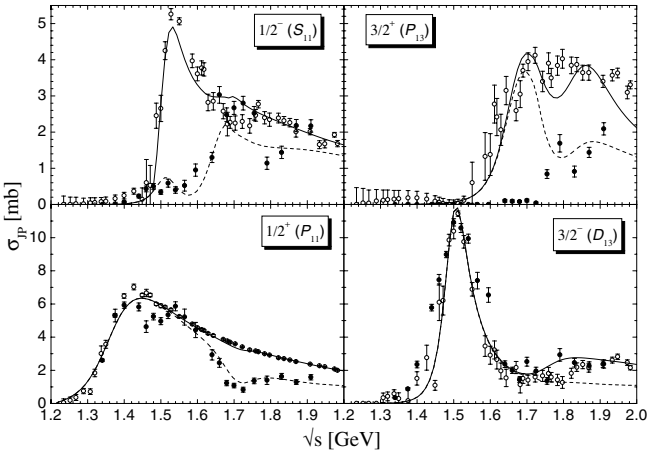


Figure 2: $\pi N \to \pi N$ inelastic ($\circ$ as extracted from SM00 [4], calculation: solid line) and $\pi N \to 2\pi N$ partial-wave cross sections ($\bullet$ as extracted by [5], calculation: dashed line), both for $I = \frac{1}{2}$.

(as presented in fig. 1) – being an important input of our calculations – were incorrectly extracted from the experimental count rates. However, as we show in [3], these data points were indeed correctly deduced.

The total ωN cross section (cf. fig. 1) is dominantly composed of two partial waves contributing with approximately the same magnitude $J^P = \frac{3}{2}^-(D_{13})$ and $\frac{3}{2}^+(P_{13})$, and also a smaller $\frac{1}{2}^+(P_{11})$ contribution, while the $\frac{1}{2}^-(S_{11})$ partial wave is almost negligible (in brackets the πN notation is given). The main contributions in these partial waves stem from the $D_{13}(1950)$, the $P_{13}(1720)$, the nucleon, and the $P_{11}(1710)$. The $D_{13}(1950)$ is especially interesting, since it is only listed in the PDG at 2.08 GeV, but was already found as an important contribution in πN and $K\Lambda$ channels (cf. [1]) at around 1.95 GeV. In our calculation it turns out to be an important production mechanism as well, in particular at threshold. Since the data in all other channels (including πN inelasticities and $2\pi N$ partial wave cross sections in the isospin $\frac{1}{2}$ partial waves, s. fig. 2) are also very well described in the ωN threshold region (1.72 GeV $< \sqrt{s} <$ 1.76 GeV), our partial wave decomposition of $\pi N \to \omega N$ is on safe grounds.

References

[1] T. Feuster and U. Mosel, Phys. Rev. C **59**, 460 (1999).
[2] H. Karami et al., Nucl. Phys. **B154**, 503 (1979).
[3] G. Penner and U. Mosel, submitted to Eur. Phys. J. A, e-Print ArXive: `nucl-th/0111024`.
[4] M.M. Pavan et al., Phys. Scripta **T87** 62 (2000), R.A. Arndt et al., Phys. Rev. C **52**, 2120 (1995).
[5] D.M. Manley et al., Phys. Rev. D **30**, 904 (1984).

Finite Momentum of the $\pi\pi$-Pair in the $A(\pi\ ,2\pi)$ Reaction

C. Isselhorst , Z. Aouissat, J. Wambach
Institut für Kernphysik, Technische Universität Darmstadt

The knockout reaction $\pi A \to \pi\pi A$ has been thoroughly studied in the past [1]. However, only recently the inclusion of final-state interactions has been discussed [2]. This was motivated by the experimental findings of both CHAOS collaboration [3] and Crystal Ball collaboration [4], where a strong enhancement of the $\pi\pi$ mass distribution is observed around 2π threshold.

Indeed, the $\pi\pi$ interaction is known to be strongly attractive and might even lead in nuclear medium to a 2π bound-state, which could provide an explanation of the experimental results. For a thorough investigation of this conjecture, one needs to develop a model for interacting pions. This is being undertaken in the framework of the linear-sigma model which is treated in the large N limit approach [5]. Besides, the usual p-wave coupling of the pion to the nuclear medium, in this context, the σ-meson undergoes as well a strong mean-field renormalization and a direct coupling to particle-hole (p–h) excitations. Indeed for a finite total momentum of the $\pi\pi$-pair or equivalently of the σ mode, the direct coupling to $p-h$ excitations is very important. The magnitude of this coupling is traced back through the experimentally accessible scalar polarization propagator [7]. In a recent work we addressed this question using the standard σ-ω model [6], and fine tuning the σNN and ωNN couplings to ensure the nuclear matter stability (see [6] for details).

The effect of the above on the $\pi\pi$ scattering S-matrix and the σ propagator is shown below. One notice in particular the strong downward shift of both the σ pole and the strength in the $\pi\pi$ scattering matrix. At finite momentum of the $\pi\pi$ pair, the strength is dramatically weakened at threshold in the scattering matrix while an important build up of strength is seen in the imaginary part of the sigma propagator at very low energy due to the $p-h$ coupling.

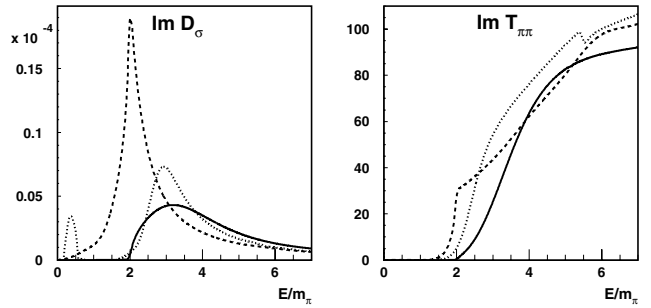


Figure 1: Imaginary part of the σ propagator (left panel), and the $T_{\pi\pi}$ matrix (right panel). The full lines denote the vacuum case. The dashed lines are for normal nuclear matter density and the zero three-momentum case . The dash-dotted lines are for nuclear matter density and a three-momentum of the pair of 200 MeV.

Regarding the knockout reaction, a closer investigation of the phase-space for the produced $\pi\pi$-pair, precisely in the 2π threshold region, reveals that most events contributing to the total cross-section of the process

$$\begin{aligned}\sigma \;=\; & \tfrac{\pi}{q}\int d^2\mathbf{b}\, dz\, A_{in}(\rho(\vec{r}))\, A^{+}_{out}(\rho(\vec{r}_1))\, A^{-}_{out}(\rho(\vec{r}_2)) \\ & \int \tfrac{d\vec{k}}{(2\pi)^3}\tfrac{d\vec{q}_1}{(2\pi)^3}\tfrac{d\vec{q}_2}{(2\pi)^3}\, n(\vec{k})\, \Big[1 - n(\vec{q}+\vec{k}-\vec{q}_1-\vec{q}_2)\Big] \\ & \delta(q^0+\mathcal{E}_{\vec{k}}-\omega_{\vec{q}_1}-\omega_{\vec{q}_2}-\mathcal{E}_{\vec{q}+\vec{k}-\vec{q}_1-\vec{q}_1}) \\ & \tfrac{1}{2\omega(q_1)}\tfrac{1}{2\omega(q_2)}\,\overline{|T|^2}_{(\pi N\to\pi\pi N)}\,|\tfrac{T_{\pi\pi}}{V_{\pi\pi}}|^2 \times \textit{acceptance}\end{aligned} \tag{1}$$

carry an average total momentum of about 260 MeV [6]. In the light of what we have learned earlier concerning the behavior of the in-medium $\pi\pi$ scattering at finite total momentum Fig. 1, one expects weak final state interaction (FSI) reversing the conclusion of an old result [2] which attributed the near-threshold enhancement observed in CHAOS data to the strong 2π FSI.

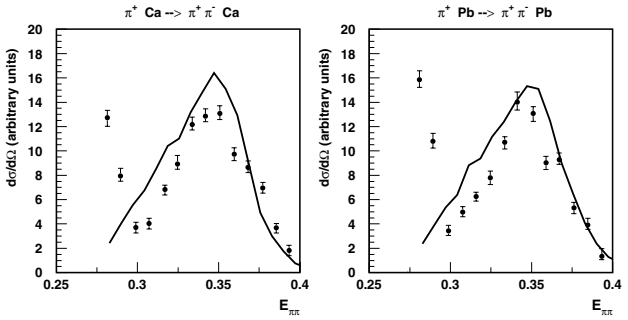


Figure 2: Differential cross-section for the knockout process off Ca and Pb. At threshold the experimental data show a strong enhancement missing in the theoretical (solid) curve due to the finite three momentum of the pair as explained in the text.

As shown in Fig. 2, the theoretical calculations fail to account for CHAOS data in the near-threshold region. It should be mentioned also that the strong nuclear absorption plays an important role in moderating the FSI effects. More work is therefore needed to understand the mechanism behind the experimental findings.

References

[1] E.Oset, M.J.Vicente Vacas, Nucl. Phys. A446 (1985) 584.
[2] P. Schuck, Z. Aouissat, F. Bonutti, G. Chanfray, E. Fragiacomo, N. Grion, J.Wambach, Proceedings of the XXXVI, international Winter Meeting on Nuclear Physics, Ed. I. Iori, Bormio (Italy), January 1998.
[3] F. Bonutti et al., Phys. Rev. Lett. 77 (1996) 603.
[4] A. Starostin et al., Phys. Rev. Lett. 85 (2000) 5539.
[5] Z. Aouissat, P. Schuck, J. Wambach, Nucl. Phys. A618 (1997) 402.
[6] Z. Aouissat, C. Isselhorst, P. Schuck, J. Wambach, to appear in Proceedings of the workshop Chiral fluctuations in hadronic matter, Orsay, France, Sept. 2001, and references herein.
[7] G. Chanfray, M. Ericson, Nucl-Th/0106069.

Scattering of photons and vector mesons off nucleons[G]

M.F.M. Lutz[1,2] , Gy. Wolf[1,3] and B. Friman[1,2]
[1]GSI, [2]TU-Darmstadt, [3]KFKI

To leading order in the baryon density, the properties of vector mesons in nuclear matter are determined by the vector-meson nucleon scattering amplitudes. Since these amplitudes are not directly constrained by data, there are presently large theoretical ambiguities in predictions of the vector-meson spectral densities in nuclear matter. We address this problem by implementing the constraints from data on pion- and photon-nucleon reactions in a systematic way [1]. The framework for this calculation is a coupled-channel approach for meson-baryon and photon-baryon scattering, including the $\gamma N, \pi N$, ρN, ωN, $\pi\Delta$, ηN, $K\Lambda$ and $K\Sigma$ channels where the interaction kernel is approximated by quasi-local 4-point interaction vertices. Nucleon and isobar resonances are generated dynamically. In such a scheme the amplitudes for experimentally non-accessible processes like ρN and ωN scattering are constrained by the data on elastic πN scattering and inelastic reactions like the pion- and photon-induced production of vector mesons. Here we report on the role of the photo-induced reactions in the determination of the vector meson-nucleon scattering amplitudes.

The description of photon-induced reactions is based on an assumption of the vector-meson dominance type which directly relates the electromagnetic quasi-local 4-point interaction vertices to the corresponding vertices involving the ρ and ω fields. Given the model for the hadronic reactions, this allows us to compute a wealth of data on photo-induced reactions with a minimal extension of the model. This is particularly useful, since we find that the available data sets on hadronic reactions does not uniquely determine hadronic model parameters. Furthermore, the generalized vector-meson dominance assumption provides a constraint on the otherwise undetermined relative phases of amplitudes involving ρ_0 and ω mesons. This phase is needed e.g. in calculations of e^+e^- pair production off nucleons [2] and of inelastic electron-nucleon scattering.

We obtain a reasonable description of the $\gamma p \to \pi N$ multipole amplitudes, the πN elastic scattering data as well as the photo- and pion-induced production reactions. In Fig. 1 the d-wave electric $E_{2-}(D_{13})$ and magnetic $M_{2-}(D_{13})$ multipole amplitudes are shown as illustrative examples. We emphasize that an improved description of the latter multipole amplitudes is expected once ρN and ωN states with subleading angular momentum characteristics are considered. For a detailed discussion of our results we refer the reader to [1]. We note that in our model, which accounts only for s-wave vector-meson nucleon interactions, the cross section is expected to fall short in channels where the long-ranged one-pion interaction can contribute and leads to important strength in non-s-wave-like ρN or ωN states. This is the case e.g. in the reaction $\gamma p \to \omega p$ shown in Fig. 2. The main effect of the inclusion of photo-induced reactions is a stabilization of the solution in the $S11$ channel and a fairly strong suppression of the ρ-meson coupling to the $N(1520)$ resonance compared to previous analyses [5].

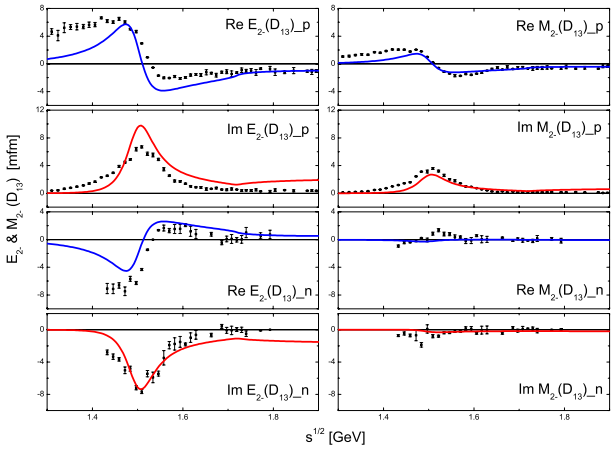


Figure 1: The $E_{2-}(D_{13})_{p,n}$ and $M_{2-}(D_{13})_{p,n}$ multipole amplitudes for photo-induced pion production compared to the SM00 solution of Arndt *et al.* [3].

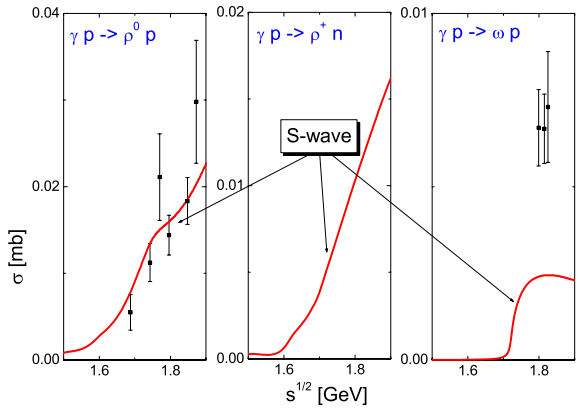


Figure 2: Photo-induced vector-meson production cross section. Data from [4]

References

[1] M.F.M. Lutz, Gy. Wolf and B. Friman, submitted to Nucl. Phys. **A**, nucl-th/0112052.

[2] M.F.M. Lutz, B. Friman and M. Soyeur, nucl-th/0202049

[3] R.A. Arndt *et al.*, Phys. Rev. **C42**(1990) 1853; `http://gwdac.phys.gwu.edu/`.

[4] Aachen-Berlin-Bonn-Hamburg-Heidelberg-München Collaboration, Phys. Rev. **175** (1968) 1669.

[5] D.M. Manley and E.M. Saleski, Phys. Rev. **D 45** (1992) 4002; Phys. Rev. **D 30** (1984) 904.

The χ-BS(3) approach

M.F.M. Lutz[1,2] and E.E. Kolomeitsev[3]
[1]GSI, [2]TU-Darmstadt, [3]ECT*

We report on our recent non-perturbative application of the chiral $SU(3)$ Lagrangian to meson-nucleon scattering [1]. The most striking phenomena arise in the strangeness sector. At leading chiral order the kaon- and antikaon-nucleon interactions are supposedly described by the Weinberg-Tomozawa term,

$$\begin{aligned}\mathcal{L}_{WT} &= \frac{i}{8\,f^2}(\bar N\,\gamma_\mu\,N)\big((\partial^\mu\,K)^\dagger\,K - K^\dagger(\partial^\mu\,K)\big)\\ &+ \frac{3\,i}{8\,f^2}(\bar N\,\gamma_\mu\,\vec\tau\,N)\big((\partial^\mu\,K)^\dagger\,\vec\tau\,K - K^\dagger\vec\tau\,(\partial^\mu\,K)\big)\,,\end{aligned}$$

where the parameter $f \simeq f_\pi \simeq 92.4$ MeV is known from the decay process of charged pions. In contrast to the successful application of the chiral Lagrangian in the flavor $SU(2)$ sector, its application to the strange sector of QCD is flawed by a number of subtleties if the machinery of chiral perturbation theory is applied. The leading interaction term fails miserably in describing the s-wave scattering lengths of both kaons and antikaons off a nucleon. Most stunning is the failure of reproducing the repulsive K^-p scattering length [2]. The chiral Lagrangian predicts an attractive scattering length at leading order instead. This is closely linked to the presence of the $\Lambda(1405)$ resonance in the K^-p scattering amplitude just below the K^-p threshold. Considerable theoretical progress has been made over the last few years by incorporating the dynamics of that $\Lambda(1405)$ resonance into the chiral dynamics [3, 4]. These early works consider s-wave interactions to leading [4] and subleading [3] chiral order only. The key point is to change approximation strategy and expand the interaction kernel rather than the scattering amplitude directly. That amounts to solving some type of coupled-channel scattering equation like the Lippmann-Schwinger or the Bethe-Salpeter equation. As a consequence the $\Lambda(1405)$ resonance is generated dynamically by coupled channel effects. The advantage of the chiral approach over previous phenomenological K-matrix analyses (see e.g. [5]), which also lead to a dynamic generation of the $\Lambda(1405)$ resonance, is the systematic parameter reduction implied by the chiral SU(3) symmetry of QCD.

A realistic description of the antikaon-nucleon scattering process requires the inclusion of all SU(3) channels $\bar KN, \pi\Lambda, \pi\Sigma, \eta\Sigma, \eta\Lambda$ and $K\Xi$ together with correction terms predicted by the chiral $SU(3)$ Lagrangian. In the χ-BS(3) approach [1], which considers s- p- and d-wave interactions to subsubleading order, the number of free parameters controlling the chiral correction terms is significantly reduced by insisting on sum rule relations as they arise from QCD in the large-N_c limit. It is demonstrated for the first time that the chiral $SU(3)$ Lagrangian does describe all low-energy pion-, kaon- and antikaon-nucleon scattering data fairly well, once chiral perturbation theory is applied to the covariant scattering kernel of the Bethe-Salpeter scattering equation.

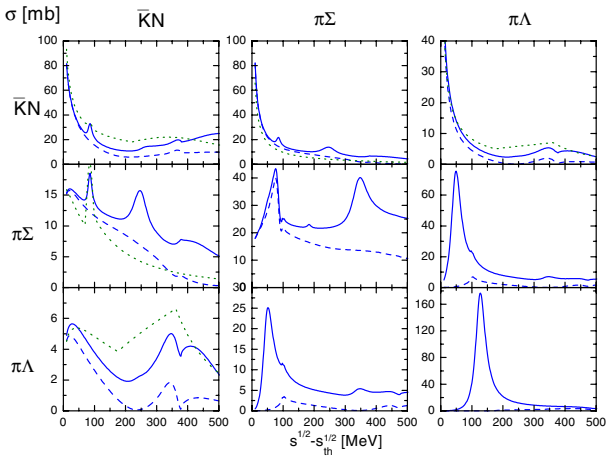


Figure 1: Total isospin averaged cross sections $\bar KN \to \bar KN$, $\bar KN \to \pi\Sigma$, $\bar KN \to \pi\Lambda$ etc compared to the parameterization of [6]. The solid and dashed lines give the results of the χ-BS(3) approach with and without p- and d-wave contributions respectively.

Crossing symmetry relates the $\bar KN$ and KN scattering amplitudes at subthreshold energies. A problem arises because the kaon- and antikaon-nucleon scattering processes are described by two distinct Bethe-Salpeter equations. That would lead to a violation of crossing symmetry unless an appropriate mechanism is devised to protect that symmetry. It is important to face this problem since for instance the in-medium antikaon spectral function tests the subthreshold $\bar KN$ amplitudes. This problem was not addressed in [3, 4] but is solved in the χ-BS(3) approach by supplementing the Bethe-Salpeter equation with an appropriate renormalization program that leads to the matching of the subthreshold KN and $\bar KN$ amplitudes.

In Fig. 1 we confront the isospin averaged cross sections of the channels $\bar KN, \pi\Sigma$ and $\pi\Lambda$ with typical parameterizations used in transport model calculations. We find most interesting the sizeable cross section of about 30 mb for the $\pi\Sigma \to \pi\Sigma$ reaction. We believe that the χ-BS(3) approach is particularly well suited to determine cross sections like those for the $\pi\Sigma \to \pi\Sigma, \pi\Lambda$ reactions not directly accessible in scattering experiments and so far not considered in transport model simulations of heavy ion reactions.

References

[1] M.F.M. Lutz and E.E. Kolomeitsev, nucl-th/0105042.
[2] M. Iwasaki et al., Phys. Rev. Lett. **78** (1997) 3067.
[3] N. Kaiser, P.B. Siegel and W. Weise, Nucl. Phys. **A 594** (1995) 325; N. Kaiser, T. Waas and W. Weise, Nucl. Phys. **A 612** (1997) 297.
[4] E. Oset and A. Ramos, Nucl. Phys. **A 635** (1998) 99.
[5] A.D. Martin, Nucl. Phys. **B 179** (1981) 33.
[6] G.Q. Li, C.H. Lee and G.E. Brown, Nucl. Phys. **A 625** (1997) 372.

Self consistent propagation of hyperons and antikaons in nuclear matter based on relativistic chiral $SU(3)$ dynamics

M.F.M Lutz[1,2] and C.L. Korpa[3]
[1]GSI, [2]TU-Darmstadt, [3]University of Pecs

Results on antikaon production in heavy ion collisions at subthreshold energies may help to study the modification of the K^- properties inside a dense nuclear medium [1, 2, 3, 4, 5].

An antikaon spectral function with support at energies smaller than the free-space kaon mass was already anticipated in the 70's by the many K-matrix analyses of the antikaon-nucleon scattering process (see e.g. [6]) which predicted considerable attraction in the subthreshold scattering amplitudes. This leads in conjunction with the low-density theorem to an attractive antikaon spectral function in nuclear matter. Nevertheless, the quantitative evaluation of the antikaon spectral function is still an interesting problem [7, 8, 9]. The challenge is first to establish a solid understanding of the vacuum antikaon-nucleon scattering process, in particular reliable subthreshold antikaon-nucleon scattering amplitudes are required, and secondly, to evaluate the antikaon spectral function in a systematic many-body approach.

The antikaon-nucleon scattering is complicated due to the open inelastic $\pi\Sigma$ and $\pi\Lambda$ channels and the presence of the s-wave $\Lambda(1405)$ and p-wave $\Sigma(1385)$ resonances just below and the d-wave $\Lambda(1520)$ resonance not too far above the antikaon-nucleon threshold. In this work we apply the newly formulated χ-BS(3) approach, for chiral Bethe-Salpeter approach to the SU(3) flavor group [10]. It constitutes a systematic and non-perturbative application of the chiral SU(3) Lagrangian to the meson-baryon scattering problem consistent with covariance, crossing symmetry, large-N_c sum rules of QCD and the chiral counting concept. The low-energy pion-, kaon- and antikaon-nucleon scattering data were reproduced successfully demonstrating that the chiral SU(3)flavor symmetry is a powerful tool to analyze and predict hadron interactions systematically. The amplitudes obtained in that scheme are particularly well suited for an application to the nuclear kaon dynamics, because it was demonstrated that they are approximately crossing symmetric in the sense that the KN and $\bar{K}N$ amplitudes smoothly match at subthreshold energies.

As was pointed out in [8] the realistic evaluation of the antikaon self energy in nuclear matter requires a self consistent scheme. In particular the feedback effect of an in-medium modified antikaon spectral function on the antikaon-nucleon scattering process was found to be important for the $\Lambda(1405)$ resonance structure in nuclear matter. We present a selection of results obtained in our novel covariant many-body framework [11]. Self consistency was implemented in terms of the free-space meson-nucleon scattering amplitudes, where the amplitudes of the χ-BS(3) approach were used. We computed a realistic antikaon spectral function and studied the in-medium structure of the s-wave $\Lambda(1405)$ and p-wave $\Sigma(1385)$ resonances.

In Fig. 1 we present the antikaon spectral function together with the antikaon-nucleon scattering amplitudes of selected channels at various nuclear matter densities [11]. The antikaon spectral function exhibits a rich structure with a pronounced dependence on the antikaon three-momentum. That reflects the coupling of the $\Lambda(1405)$ and $\Sigma(1385)$ hyperon states to the $\bar{K}N$ channel. Typically the peaks seen are quite broad and not always of quasi-particle type. The most important contributions, the s-wave $\Lambda(1405)$ and p-wave $\Sigma(1385)$ resonances, experience strong medium modifications as demonstrated in Fig. 1. Whereas for pure s-wave dynamics the $\Lambda(1405)$ effective mass is changed very little [8], the consideration of higher partial waves leads to an attractive mass shift of about 60 MeV at nuclear saturation density. The results at $2\,\rho_0$ should be considered cautiously because nuclear binding and correlation effects were not yet included in [11].

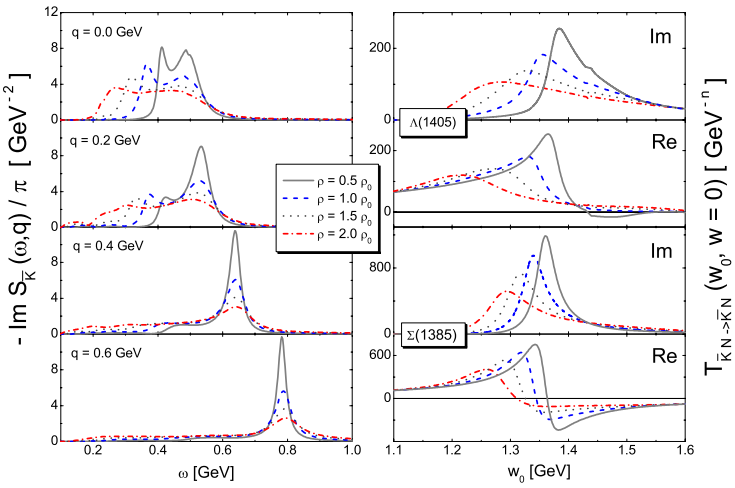


Figure 1: Spectral functions of antikaons and hyperon resonances in cold nuclear matter.

References

[1] F. Laue, Ch. Sturm et al., Phys. Rev. Lett. **82** (1999) 1640.
[2] M. Menzel et al., Phys. Lett. **B** 495 (2000) 26.
[3] C.Q. Li and G.E. Brown Phys. Rev. **C 58** (1998) 1698.
[4] Z.S. Wang et al., Phys. Rev. **C 57** (1998) 3284.
[5] Ch. Hartnack, H. Oeschler and J. Aichelin, nucl-th/0109016.
[6] A.D. Martin, Nucl. Phys. **B 179** (1981) 33.
[7] T. Waas, M. Rho and W. Weise, Nucl. Phys. **A 617** (1997) 449.
[8] M.F.M. Lutz, Phys. Lett. **B 426** (1998) 12.
[9] A. Ramos and E. Oset, Nucl. Phys. **A 671** (2000) 481.
[10] M.F.M. Lutz and E.E. Kolomeitsev, nucl-th/0105042.
[11] M.F.M. Lutz and C.L. Korpa, nucl-th/0105067.

Strange Particle Production in Heavy Ion Collisions[B]

P. Braun-Munzinger, GSI
J. Cleymans, University of Cape Town, South Africa
H. Oeschler, Technische Universität Darmstadt
K. Redlich, University of Wrocław, Poland and GSI, Darmstadt

Strangeness production in heavy ion collisions at relativistic energies provides one of the key information about the reaction mechanism and could indicate the onset of new phenomena.

The attempts to describe the measured particle ratios including strange hadrons at AGS and SPS and recently also at RHIC using a strangeness fugacity are very successful [1]. However, the usual grand-canonical treatment of strangeness conservation is not sufficient, if the number of strange particles is small [2]. This requires local strangeness conservation which is done in the statistical model using the canonical formulation of strangeness conservation [3]. The canonical approach describes the measured particle ratios at SIS energies and is able to explain the different excitation functions of K^+ and K^- around 1 A·GeV [3].

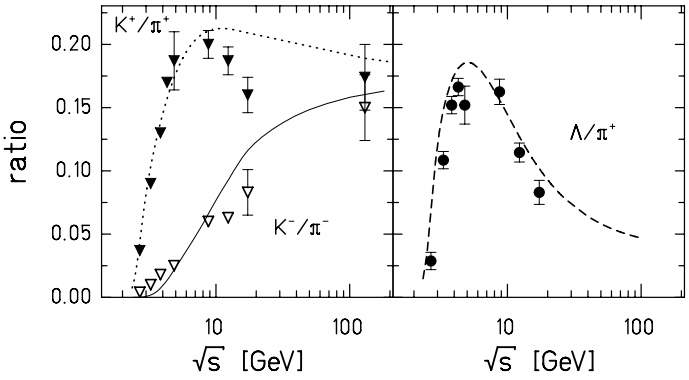


Figure 1: *Trend of particle ratios as a function of $\sqrt{s}$. The lines represent the statistical-model calculations. Left: K^+/π^+ ratio (full points, dotted line) and K^-/π^- ratio (open points, solid line). Right: Λ/π ratio.*

Recently, the evolution of the K^+/π^+ ratio as a function of $\sqrt{s}$ has attracted great interest as a maximum seemed to appear around 40 A·GeV. Figure 1 shows this ratio obtained at midrapidity from SIS energies up to RHIC [4]. Indeed, a maximum around the data point obtained at 40 A·GeV seems to show up.

The behaviour of K^-/π^-, however, is very different. At low incident energies it is much lower than K^+/π^+. Yet it rises continuously up to the highest energies.

These trends predicted by the statistical model are nicely confirmed by the new results from RHIC: With increasing energy K^+/π^+ decreases while K^-/π^- increases.

The origin of these trends can be explained by the evolution of the freeze-out parameters T and μ_B with $\sqrt{s}$ [6]. A study of the K^+/π^+ ratio or even clearer of the more general quantity strange-to-nonstrange partciles (Wroblewski factor $\lambda_s \equiv 2\langle s\bar{s}\rangle/(\langle u\bar{u}\rangle + \langle d\bar{d}\rangle)$, (where the quantities in angular brackets refer to the number of newly formed quark-antiquark pairs) has evidenced a maximum in the strangeness content around 30 A·GeV [5] as shown in fig. 2.

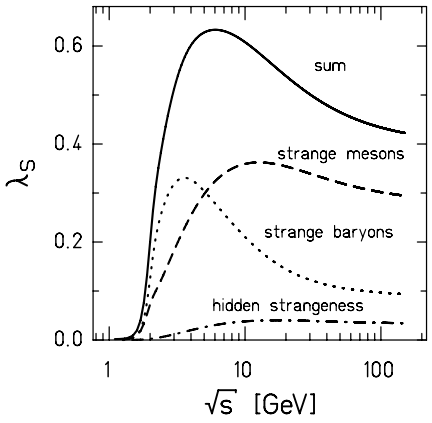


Figure 2: *Contributions to the Wroblewski factor (for definition see text) from strange baryons (dotted line), strange mesons (dashed line) and mesons with hidden strangeness (dash-dotted line). The sum of all contributions is given by the full line.*

This maximum arises from the shape of the freeze-out curve. The decrease towards higher energies occurs as T is no longer increasing but μ_B decreases strongly. The change of μ_B causes that the respective contribution of strange mesons and strange baryons as given in fig. 2. As can be seen, strange baryons exhibit a very pronounced maximum. Recent data allow to test this prediction. The measured Λ/π ratio is given in fig.1 together with the results from the statistical model confirming the strong decrease towards higher incident energies.

References

[1] J. Cleymans and H. Satz, Z. Phys. **C57** (1993) 135; P. Braun-Munzinger, J. Stachel, J.P. Wessels and N. Xu, Phys. Lett. **B344** (1995) 43; J. Sollfrank, J. Phys. G: Nucl. Part. Phys. **23** (1997) 1903; P. Braun-Munzinger, I. Heppe, J. Stachel, Phys. Lett. **B465** (1999) 15.

[2] R. Hagedorn, K. Redlich, Z. Phys. **A27** (1985) 541.

[3] J. Cleymans, H. Oeschler and K. Redlich, Phys. Rev. **C59** (1999) 1663; Phys. Lett. **B485** (2000) 27.

[4] C. Sturm et al., Phys. Rev. Lett. 86 (2001) 39; L. Ahle et al., (E802 Collaboration), Phys. Rev. **C60** (1999) 044904; L. Ahle et al., (E866/E917 Collaboration), Phys. Lett. B476 (2000) 1.; C. Blume, (NA49 Collaboration), "Quark Matter 2001", Stony Brook, Jan. 2001; J. Harris, (STAR Collaboration), idem.

[5] P. Braun-Munzinger, J. Cleymans, H. Oeschler, K. Redlich, Nucl. Phys. A 697 (2002) 902.

[6] J. Cleymans and K. Redlich, Phys. Rev. Lett. **81** (1998) 5284; Phys. Rev. **C60** (1999) 054908.

[7] A. Wroblewski, Acta Physica Polonica **B16** (1985) 379.

What determines the K^- Multiplicities at Energies Around 1–2 A·GeV?[B,G]

Ch. Hartnack, J. Aichelin
SUBATECH, University of Nantes - IN2P3/CNRS - Ecole des Mines de Nantes
H. Oeschler
Institut für Kernphysik, Darmstadt University of Technology, D-64289 Darmstadt, Germany

In heavy ion reactions at energies around 1-2 AGeV the measured K^- yields appear rather high in comparison to pp collisions as shown by the KaoS collaboration [1]. Even more astonishing is that the K^-/K^+ ratio occurs to be nearly independent of the impact parameter [1, 2].

These observations may have a simple explanation, i.e. the contribution of the strangeness exchange channel $\Lambda\pi \rightleftharpoons K^-N$. For our study we use IQMD simulations [3]. A more detailed theoretical study can be found [4].

Figure 1 displays the integrated number of produced K^- and the net number of K^- present in the system as a function of time. Two production channels $\pi\Lambda \to K^-B$ and $BB \to BBK^+K^-$ occur where B is either a nucleon or a Δ. The difference between "sum" and "net" is due to absorption. From Fig. 1 can be concluded that $\pi\Lambda \to$

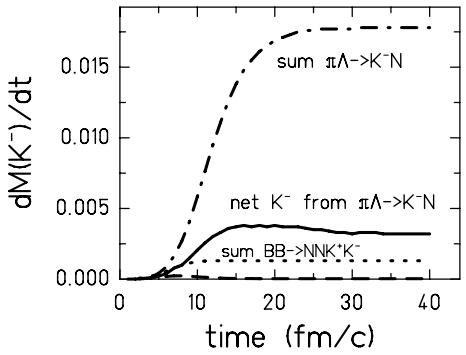


Figure 1: *Integrated number of produced K^- and the net number of K^- present at time t for the different K^- production channels for Au+Au collisions at 1.5 A·GeV.*

K^-B is the dominant K^- production channel. The K^- from the BB channel (dotted line) are produced in the high-density phase. Produced early, the K^- from the BB channel have a high chance to be absorbed and finally almost all of them have disappeared (dashed line).

Up to now we have studied the K^- production assuming that both, the K^- and the K^+, have a mass as given by the relativistic mean field calculation [5]. These calculations are yet far from being confirmed by experimental results. It is therefore important to see how the predicted mass change of the kaons in the medium influences their multiplicity. The K^-N potential is attractive, leading to lower "in-medium" masses, while the K^+N potential is slightly repulsive. Therefore, We compare the standard calculation (K^+ : w, K^- : w, where w stand for "with potential") with those in which either the K^+N potential or the K^-N potential switched off as well as with a calculation in which no KN potential is applied (K^+ : w/o, K^- : w/o).

The results shown in Fig. 2 evidence that the final K^- yield depends strongly on the K^+N potential but is al-

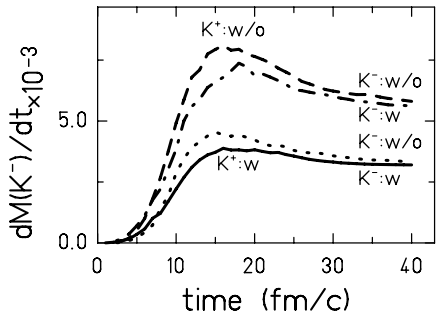


Figure 2: *Influence of the KN potentials on the final K^- yields for central Au+Au collisions at 1.5 AGeV. The net K^- yields for the various combinations of with and without KN potential as a function of time.*

most independent on the K^-N potential. The K^+N potential determines how many Λ are produced in the initial $BB \to \Lambda K^+B$ reaction. This reaction takes place when the baryon density is high. The K^+N potential increases the "mass" of the K^+ and hence lowers the Λ multiplicity. On the contrary, the mass change of the K^- has little influence on the result because the observed K^- are created very late at a density where the mass change due to the K^-N potential is small.

This discussion raises the question whether the strangeness-exchange channel has reached chemical equlibrium. An attempt to answer this question based on experimental results is given in [2].

In conclusion, we have given an interpretation of the experimental observation that a) in heavy ion reactions the yields for K^- compared to K^+ is much higher than in pp collisions and b) that the K^+/K^- ratio is independent of the impact parameter. Almost all K^- are produced by the pionic channel $\Lambda\pi \to K^-B$ which is not available in pp. Because the Λ is produced simultaneously with the K^+, the K^- and the K^+ production are strongly correlated. The final yield of kaons depends on the K^+N potential (which determines how many Λ are produced initially) but depends very little on the K^-N potential because the observed K^- are produced very late at low densities where this potential is small.

References

[1] KaoS Collaboration: R. Barth et al., Phys. Rev. Lett. 78 (1997) 4007; F. Laue, Phys. Rev. Lett. 82 (1999) 1640; M. Menzel et al., Phys. Lett. **B 495** (2000) 26.
[2] A. Förster, (KaoS Collaboration), SQM2001.
[3] C. Hartnack et al., Eur.Phys.J. A1 (1998) 151.
[4] C. Hartnack, H. Oeschler, J. Aichelin, nucl-th/0109016.
[5] J. Schaffner et al., Nucl. Phys. **A625** (1997) 325.

Extracting information on the nuclear equation of state from K^+ production in heavy ion collisions

C. Fuchs, Amand Faessler, E. Zabrodin
Institut für Theoretische Physik, Universität Tübingen

In [1] we studied the question if decisive information on the nuclear EOS can be extracted from subthreshold kaon production in heavy ion collisions. The KaoS Collaboration has performed systematic measurements of the K^+ production far below threshold in heavy ($Au+Au$) and light ($C+C$) systems [2]. Looking at the ratio R built from heavy and light systems possible uncertainties which might still exist in the theoretical calculations should cancel out to a large extent which allows to draw reliable conclusions. Furthermore, far below threshold the kaon production is a highly collective process and a particular sensitivity to the compression of the participant matter is expected. In [1] we calculated this excitation function for a soft/hard EOS including the in-medium kaon potential shown in Fig. 1. The comparision to the KaoS data [2] strongly favours a soft EOS. To base this conclusion on even more model

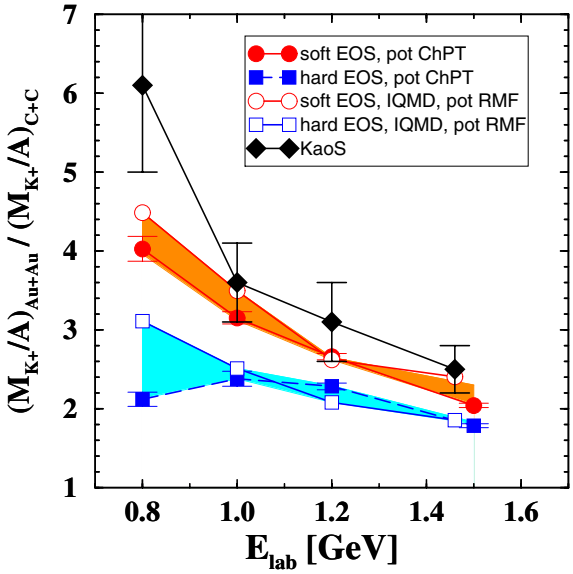


Figure 1: Excitation function of the ratio R of K^+ multiplicities obtained in inclusive $Au+Au$ over $C+C$ reactions. The calculations are performed with in-medium kaon potential and using a hard/soft nuclear EOS and compared to the data from the KaoS Collaboration [2]. results from independent IQMD calculations [3] are shown as well.

independent grounds Fig. 1 compares also to independent calculations from the Nantes group using IQMD [3]. Both calculations show an increase of R with decreasing incident energy down to 1.0 A·GeV. However, this increase is much less pronounced for both, the Tübingen and the Nantes results when the stiff EOS is employed. In our case R even decreases at 0.8 A·GeV whereas the soft EOS leads to an unrelieved increase of R. At 1.5 A·GeV which is already very close to threshold the differences between the two models become small. The strong increase of R can be directly related to higher compressible nuclear matter. The comparison to the experimental data from KaoS [2] where the increase of R is even more pronounced strongly favours a soft equation of state. For the soft EOS the IQMD calculations almost coincide with the present results [1]. For the hard EOS there exists still deviations concerning the slope of R going far below threshold. This can be due to the different in-medium kaon potentials used. Hence, the shaded areas in the figure indicate the present range of uncertainty concerning the theoretical description of this observable. This has still to be reduced by future investigations. The dependence of

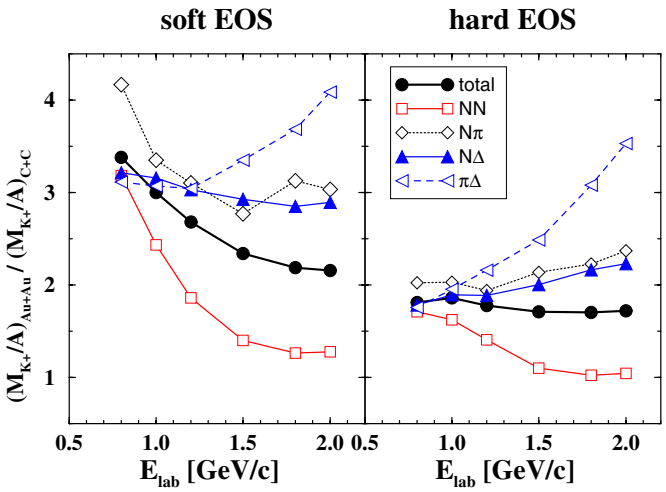


Figure 2: Dependence of the excitation function of R on the various K^+ production channels. Central (b=0 fm) $Au+Au$ and $C+C$ reactions are considered. The calculations are performed with in-medium kaon potential.

R on the various production channels is shown in Fig.2. There the ratios R_i are built separately for the production channels with initial states $i = NN, \pi N, N\Delta, \pi\Delta, \Delta\Delta$. Here one has to keep in mind that the NN and πN cross sections are quite well under control whereas the $N\Delta$, $\pi\Delta$ channels are experimentally unknown. Thus one has to rely on model predictions. However, the shape of R is not strongly influenced by these two channels which are the most insecure ones. The excitation function for the $N\Delta$ contribution varies only little as a function of energy and is similar using the different EOSs. The contribution of the $\pi\Delta$ channel is decreasing for both, a hard and a soft EOS. The shape of R is to most extent determined by the NN and πN contributions. In our calculations the latter channel is responsible for the decrease of R very far below threshold when the hard EOS is applied. Since we consider ratios theoretical uncertainties in the knowledge of elementary cross sections cancel out in first order anyway, which makes the conclusions drawn form this observable more reliable.

References

[1] C. Fuchs, A. Faessler, E. Zabrodin, Y.-M. Zheng, Phys. Rev. Lett. **86**, 1974 (2001).

[2] C. Sturm *et al.*, KaoS Collaboration, Phys. Rev. Lett. **86**, 39 (2001).

[3] C. Hartnack and J. Aichelin, proc. to SQM2001, to appear in J. Phys. **G**.

Phi **meson propagation in a hot hadronic gas**

L. Alvarez-Ruso and V. Koch (GSI-Darmstadt and LBNL-Berkeley)

The Φ is a nice probe for the properties of the matter created in ultra-relativistic heavy ion collisions, since it is not masked behind other resonances in the mass spectra. It decays,among several other possibilities, into kaon pairs (K^+K^-), and more rarely into dileptons (e^+e^-, $\mu^+\mu^-$); both channels have been detected at CERN-SPS [1, 2]. Dileptons have negligible final state interactions with the hadronic environment, so they sense the entire evolution of the system. On the contrary, detectable kaons from Φ decay probably emerge only at freeze out.

It is widely believed that the Φ mean free path in a hot hadronic fireball is large due to the small cross section for scattering with non strange hadrons. This implies that Φ spectra would retain the information about the stage of the collision at which the plasma hadronizes [3]. Available calculations [4, 5, 6] seem to support this idea. However, Φ production in $Pb-Pb$ collisions at SPS shows some intriguing features that are difficult to match with the picture of a Φ weakly interacting with the hadronic medium. Both absolute yields and inverse slope parameters in the transverse mass (m_t) distributions exhibit different values when measured via $\mu^+\mu^-$ or K^+K^- decays [7]. The inverse slope, as obtained from the hadronic measurement, suggests that the Φ's flow together with pions, kaons and protons, while the dilepton measurement is consistent with the assumption of an early freeze out. It has also been observed that the rapidity distribution (extracted from kaon pairs) in $Pb-Pb$ is about 50 % broader than in pp [1]. The modification of visible Φ spectra due to kaon re-scattering inside the fireball is an obvious and important correction but does not fully explain the discrepancies [8].

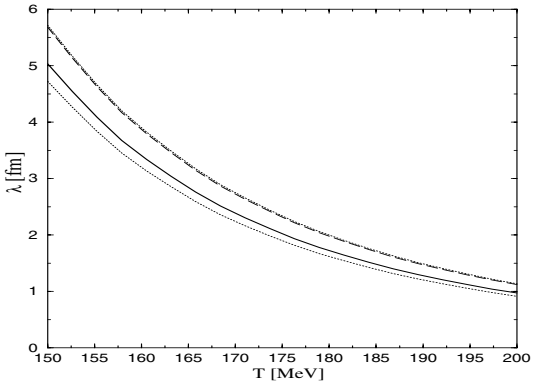


Figure 1: Mean free path of Φ meson as a function of temperature (solid line). The dotted lines constrain the region of possible values when the model parameters are changed as described in the text. The dashed line is the contribution from Φ-number changing processes alone.

Here we calculate Φ collision rates and mean free path in a hot hadronic gas of pseudo-scalar (π, K) and vector mesons (ρ, ω, K^*, Φ). The reaction cross sections are obtained within the Hidden Local Symmetry Lagrangian (HSL) [9], which includes both Goldstone boson and vector mesons in a manner consistent with the symmetries of QCD. The use of such a realistic model allows us to take into account many mechanisms that are not present in calculations that rely only in couplings extracted from observed decays but are allowed by the symmetries. This is, for instance, the case of vertices like ΦK^*K, ρK^*K^* and many others. As a consequence, we shall see that at temperatures between 150 and 200 MeV the Φ mean free path in hadronic matter is considerably smaller than what has been estimated so far (see Fig. 1). Finally, using a simple model for the expansion dynamics we find a moderate (20 %) reduction of the Phi-yield due to this rescattering (Fig. 2). Our findings thus cannot explain the difference between the observed Phi-mesons in the leptonic and hadronic channel at the CERN-SPS.

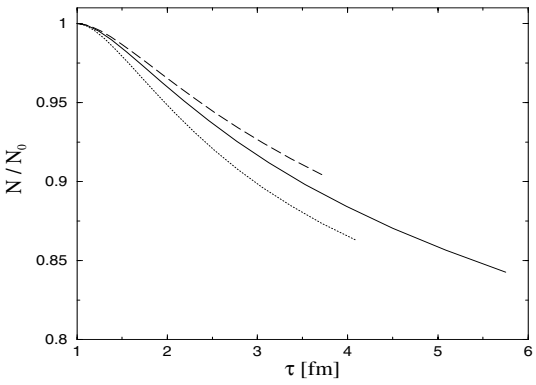


Figure 2: Time dependence of the ratio N/N_0 at zero (solid line) and nonzero (dashed line) chemical potentials, as described in the text. The dotted line stands for the case of $\mu_{K^*} = 0$ while keeping $\mu_{\pi,K,\rho,\omega} \neq 0$.

References

[1] S. V. Afanasiev et al. (NA49), Phys. Lett. **B491**, 59 (2000).

[2] M. C. Abreu et al. (NA50), J. Phys. **G27**, 405 (2001).

[3] A. Shor, Phys. Rev. Lett. **54**, 1122 (1985).

[4] C. M. Ko and D. Seibert, Phys. Rev. **C49**, 2198 (1994), `nucl-th/9312010`.

[5] K. Haglin, Nucl. Phys. **A584**, 719 (1995), `nucl-th/9410028`.

[6] W. Smith and K. L. Haglin, Phys. Rev. **C57**, 1449 (1998), `nucl-th/9710026`.

[7] D. Rohrich, J. Phys. **G27**, 355 (2001).

[8] S. C. Johnson, B. V. Jacak, and A. Drees, Eur. Phys. J. **C18**, 645 (2001), `nucl-th/9909075`.

[9] M. Bando, T. Kugo, and K. Yamawaki, Phys. Rept. **164**, 217 (1988).

Off-shell pions in the BUU transport theory

A.B. Larionov*, S. Leupold, U. Mosel
University of Giessen

Due to the large resonance πN scattering cross section a pion with momentum ~ 0.3 GeV/c acquires a width in nuclear matter. The pion spectral function in nuclear matter is, therefore, different from the vacuum one. The present work is the first attempt to include the pion spectral function into the BUU transport theory.

We have calculated the pion polarization function $\Pi_c(k)$ in isospin symmetric nuclear matter applying the Δ-hole model (c.f. [1, 2]) with the relativistic nucleon and delta propagators [3]. The pion spectral function is defined as follows:

$$A_\pi(k) \equiv -\frac{1}{\pi}\mathrm{Im}\, G(k)\ , \qquad (1)$$

where $G(k) = (k^2 - m_\pi^2 - \Pi_c(k))^{-1}$ is the pion propagator, $m_\pi = 0.138$ GeV is the vacuum pion mass.

The mass squared of the outgoing pion in the decay of a resonance with mass M_R has been sampled in the interval $[0; (M_R - m_N)^2]$ according to the distribution $\propto A_\pi(\mathbf{k}, M_\pi^2)$. In the case of the direct (background) pion production $NN \to NN\pi$ the value of M_π^2 has been sampled in the interval $[0; (\sqrt{s} - 2m_N)^2]$ using the same distribution.

The propagation of the off-shell pion between its production in the resonance decay (or in the direct process $NN \to NN\pi$) and absorption in the collision with a nucleon $\pi N \to R$ (or with two nucleons $\pi NN \to NN$) has been described according to Refs. [4, 5] by introduction of an artificial scalar off-shell potential $s_{\pi,i}$ acting on the i-th pion test particle:

$$s_{\pi,i}(\mathbf{r}_i(t), t) = \frac{M_{\pi,i}(t_{cr}) - m_\pi}{\rho_N(\mathbf{r}_i(t_{cr}), t_{cr})}\rho_N(\mathbf{r}_i(t), t)\ , \qquad (2)$$

where $\rho_N(\mathbf{r}, t)$ is the density of nucleons in the local rest frame of nuclear matter. t_{cr} is the production time of the test particle. Thus pions are propagated by solving the Hamiltonian equations of motion with the single-particle Hamiltonian

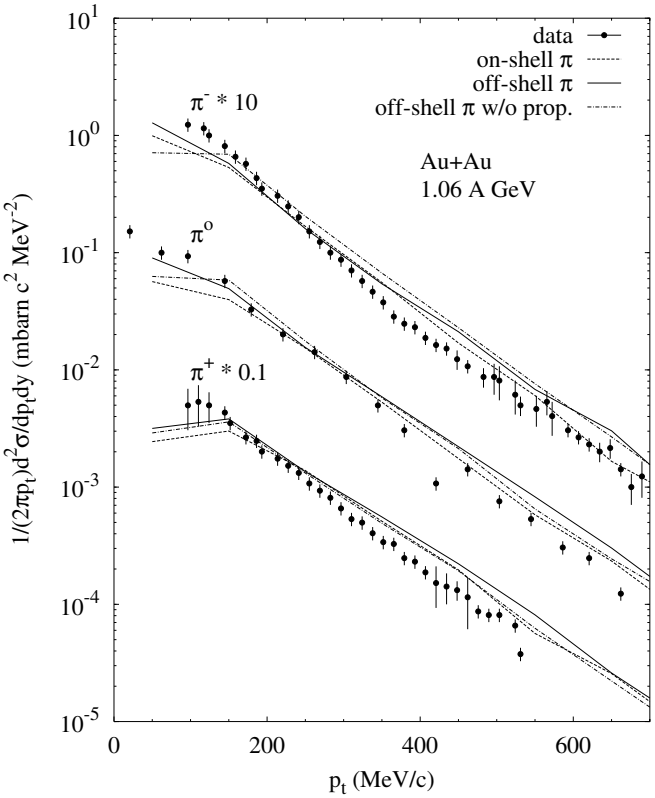
$$H_{off-shell,\,i} = \sqrt{\mathbf{k}_i^2 + M_{\pi,i}^2(t)} \qquad (3)$$

with

$$M_{\pi,i}(t) = m_\pi + s_{\pi,i}(\mathbf{r}_i(t), t)\ . \qquad (4)$$

being the mass of the i-th pion test particle. Eqs. (2),(4) provide the correct boundary condition for large times, i.e. the pions once emitted in vacuum come back to their mass shell.

In Fig. 1 we present the inclusive transverse momentum spectra at midrapidity for the system Au+Au at 1.06 A GeV in comparison with the experimental data from Refs. [6, 7]. The calculation with on-shell pions (dashed lines) describes reasonably well the high-p_t part of the spectra, but underpredicts the data at low p_t. Taking into account the pion off-shellness (solid lines) increases the low-p_t pion yields improving, thus, the agreement with the data. The low-p_t pion enhancement is caused by the off-shell pion propagation. To check this, we performed the BUU calculation without off-shell potential, i.e. keeping the off-shell masses of pions time independent (dash-dotted lines). We see that, indeed in this case the low-p_t enhancement disappears. The effect is caused by the low mass pions ($M_\pi < m_\pi$) produced by the resonance decays at early stage of the collision. These pions experience the attractive off-shell potential (2), and, therefore, they are decelerated propagating out of the dense region of the nuclear system.



References

[1] G.E. Brown and W. Weise, Phys. Rep. **22**, 279 (1975).
[2] P.A. Henning, H. Umezawa, Nucl. Phys. A **571**, 617 (1994).
[3] A.B. Larionov, S. Leupold, U. Mosel, in preparation.
[4] M. Effenberger, E.L. Bratkovskaya, and U. Mosel, Phys. Rev. C **60**, 44614 (1999).
[5] M. Effenberger and U. Mosel, Phys. Rev. C **60**, 051901 (1999).
[6] D. Pelte et al., Z. Phys. A **357**, 215 (1997).
[7] O. Schwalb et al., Phys. Lett. B **321**, 20 (1994).

*On leave of absence from RRC "I.V. Kurchatov Institute", 123182 Moscow, Russia

Equal-time formulation for off-shell transport theory[B]

R.A. Ionescu*, H.H. Wolter
Sektion Physik, Universität München

The conventional approach to the description of heavy ion collisions is based on the Boltzmann equation with a self-consistent mean field and a collision term of the Uehling-Uhlenbeck form. The main improvements were the formulation in terms of a relativistic hadronic field theory [1] and the inclusion of some non-equilibrium effects in a Local (phase space) Configuration Approximation [2]. Only recently there has been an increasing interest in the inclusion of further quantum effects in the description of heavy ion collisions, in particular in the inclusion of the off-shell propagation of the baryons [3]. In these formulations the Kadanoff-Baym equations are solved with test particles in 8-dimensional phase space. This leads to certain problems with the initial conditions and the persistence of the off-shellness.

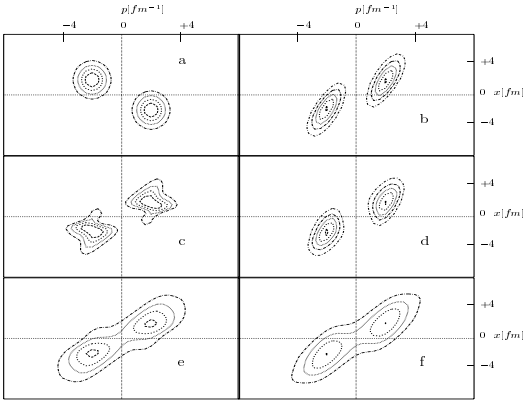


Figure 1: Contour plots of the phase space distribution of slab-on-slab collisions at 80 MeV per nucleon. Panel (a) initial distribution. Other panels distributions (at 10 fm/c) in the following approximations: (b) free motion; (c) Vlasov approximation; (d) Vlasov plus next order gradient terms; (e) Vlasov plus collision term (i.e. BUU approximation); (f) Vlasov plus next order gradient plus collision terms.

We have developed an alternative method by a systematic energy moment expansion of the spectral functions of finite width by formulating an equal-time theory for the one-particle Green functions [4]. These energy moments measure the spreading of the Green function in energy, e.g. the second order energy moment is a measure of the width of the spectral function. From the Kadanoff-Baym equations we obtain two hierarchies of equations for each of the two independent components of the one-particle Green function, spectral and kinetic. We discuss the compatibility of the two hierarchies of equations and the possibility of their systematic truncation. The hierarchies for the spectral Green function truncate by themselves. The lowest order truncation of the hierarchies for the kinetic Green function is a Bolzmann-like equation.

We have tested this scheme using a nonrelativistic self-interacting fermionic field. Our formulation in principle keeps all the terms in the gradients for space coordinates. We investigated the effects of higher order terms in a gradient expansion. These terms represent quantum effects and we investigated them numerically in a simple model of one-dimensional slab-on-slab collisions. The contour plots of the results of various approximations are shown in Fig.1. We find that the gradient corrections to the drift term result in a much smoother behaviour of the phase-space distribution function.

The time evolution of the width of the spectral function is presented in Fig.2. We found that it increases from the initially nonequilibrated momentum configuration, being largest for the maximum overlap of the two slabs. The width goes to zero outside of the range of the system.

We derived, in the gradient approximation, the modification in the Boltzmann equation in the next order truncation of the hierarchies with improved approximations for the collision integral, including memory effects. These are found to be controlled by a parameter related to the width of the spectral function. The equations could be applied to a realistic description of heavy ion collisions using non-relativistic or relativistic formulations.

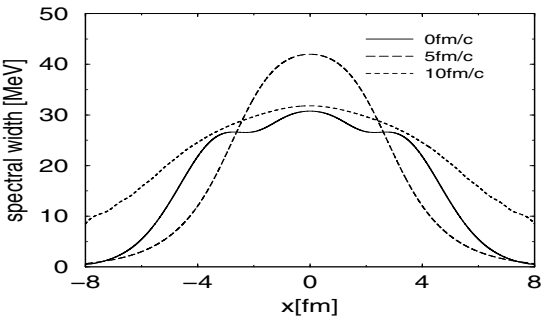


Figure 2: Width (i.e. second order energy moment) of the spectral function at different times as a function of the coordinate of the one-dimensional model.

References

[1] W. Botermans, R. Malfliet, Phys. Rep. **198** (1990) 115

[2] T. Gaitanos, C. Fuchs, H.H. Wolter, Nucl. Phys. **A650** (1999) 97

[3] W. Cassing, S. Juchem, Nucl. Phys. **A665** (2000) 377; S. Leupold, Nucl. Phys. **A672** (2000) 475; J. Knoll, Prog. Part. Nucl. Phys. **42** (1999) 177; M. Effenberger, U. Mosel, Phys. Rev. **C60** (1999) 051901

[4] R.A. Ionescu, R. Fauser, H.H. Wolter, nucl-th/0009022

*permanent adress: National Institute for Physics and Nuclear Engineering "H. Hulubei", P.O.Box MG-6, Bucharest, Romania

Renormalization of self-consistent Schwinger-Dyson equations at finite temperature[G]

H. van Hees (Universität Bielefeld), J. Knoll (GSI)

The description of particles in a hot and dense medium commonly requires approximations in terms of non-perturbative "dressed" propagators. One of the prominent self-consistent schemes is the so called Φ-derivable approximation [1, 2, 3] or effective action formalism [4]. There the self-energy of the dressed propagator G is generated from a functional Φ by means of a variational principle

$$\Sigma_{12} = 2\mathrm{i}\frac{\delta\Phi[G]}{\delta G_{12}}, \qquad (1)$$

where Φ is given by a truncated set of closed 2-particle irreducible (2PI) diagrams which cannot be split by cutting two lines. Hence Φ is the generating functional for *skeleton diagrams* and thus avoids double counting problems. It was shown by Baym [5] that for so defined approximations the expectation values of Noether charges are exactly conserved, especially those which arise from space-time symmetries (i.e. energy, momentum, angular momentum), while Ward Takahashi identities of external symmetries and even crossing symmetry for the self-energy and higher vertex functions [6] are violated.

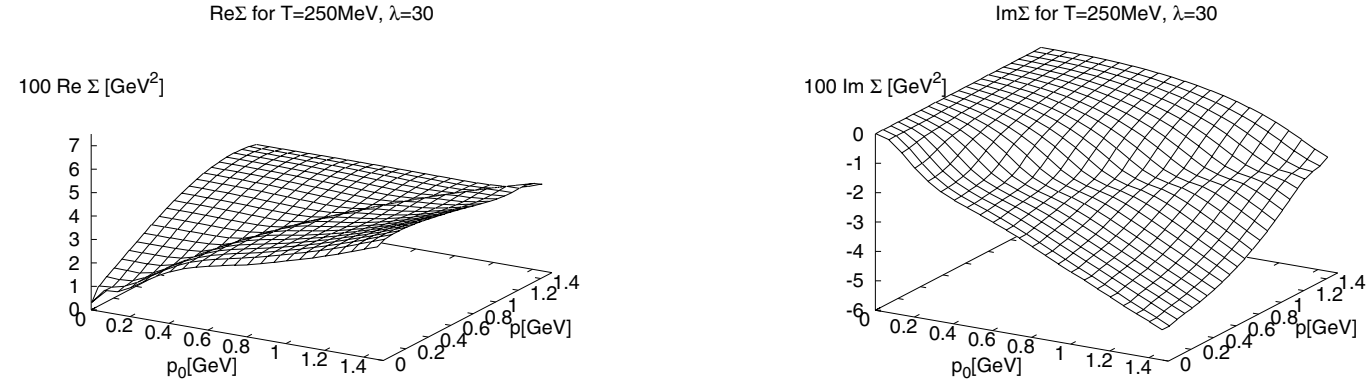
For long time the question could not be settled, to which extend self-consistent approximations of this kind can be renormalized by *temperature independent counter terms*. The problem is to isolate the divergent vacuum structure which are inherent and mostly hidden in the self-consistent self-energy due to the implied partial resummation. A further complication is that these hidden sub-divergences can be overlapping. Within the real-time formalism [7, 8], however, we could show that such a separation is possible [9]. In order to isolate the divergent vacuum sub-diagrams from the temperature dependent remainder the use of the real-time formulation and the BPHZ-prescription of renormalization theory is crucial. Besides the renormalization of the *vacuum* self-energy the procedure arrives at a Bethe-Salpeter (BS) type equation for the *vacuum* four-point function which also needs to be renormalized. For this BS-equation, the structure of which is determined by the chosen Φ-functional, overlapping divergences occur. The latter could be resolved and the problem could be cast into a set of renormalized implicit equations for the vacuum four-point function.

Furthermore we could show that also the generating functional can be renormalized by the same counter-terms and finally the renormalized self-energy is defined by Eq. (1), where Φ is to be read as the *renormalized functional*. An analytic continuation from the real time to imaginary time quantities then provides renormalized expressions for thermal equilibrium such as the thermodynamic potentials (like pressure or entropy) which are thermodynamically and dynamically consistent. It is clear that the violation of crossing symmetry also violates the running of the coupling beyond the orders of the expansion parameter used for defining the approximation of the functional. The general problem concerning symmetries in this context is attacked in a forthcoming publication [10].

First applications in next to leading order approximation to ϕ^4-theory, including both, the self-consistent tadpole and the sunset-diagram for the self-energy, were presented [11]. We could demonstrate that not only the UV-problem but also the resulting singularities at the on-shell pole of the vacuum propagator could be tackled numerically. The scheme provides fully self-consistent and renormalized self-energies at finite temperature in their full dependence on energy and three-momentum (see the figure). Such self-consistent treatments are important for future applications to QCD or hadronic matter problems at finite temperature and finite baryon densities. There further complications arise due to the gauge structure of the gluon or vector mesons [12]. Further applications concern the derivation of renormalized conserving quantum transport equations [13] which permit to consistently treat broad resonances [14].

References

[1] J. Luttinger, J. Ward, Phys. Rev. **118** (1960) 1417
[2] T. D. Lee, C. N. Yang, Phys. Rev. **117** (1961) 22
[3] G. Baym, L. Kadanoff, Phys. Rev. **124** (1961) 287
[4] M. Cornwall, R. Jackiw, E. Tomboulis, Phys. Rev. **D10** (1974) 2428
[5] G. Baym, Phys. Rev. **127** (1962) 1391
[6] G. Baym, G. Grinstein, Phys. Rev. **D15** (1977) 2897
[7] J. Schwinger, J. Math. Phys **2** (1961) 407
[8] L. Keldysh, ZhETF **47** (1964) 1515, [Sov. Phys JETP **20** 1965 1018]
[9] H. van Hees, J. Knoll, Phys. Rev. **D65** (2002) 025010
[10] H. van Hees, J. Knoll, in preparation
[11] H. van Hees, J. Knoll, hep-ph/0111193, Phys. Rev. **D** in press
[12] H. van Hees, J. Knoll, Nucl. Phys. **A683** (2001) 369
[13] J.Knoll, Y.B. Ivanov and D.N.Voskresenski, Ann.Phys. (NY) **293** (2001) 126
[14] Y.B. Ivanov, J.Knoll and D.N.Voskresenski, Nucl.Phys. **A 672** (2000) 313.



The real and imaginary part of the self-consistent self-energy for $\lambda/24\phi^4$ were calculated. A full calculation without further approximations could be achieved. The main effect of self-consistency is that the higher masses due to the tadpole contribution, which is dominant for the real part of the self-energy lowers the phase-space available for decays into three particles while the growing finite width itself induces a further broadening.

Non-equilibrium time evolution of Φ^4-theory in 2+1 dimensions

S. Juchem, W. Cassing
University of Giessen

Quantum transport theory is of strong interest in the study of systems out-of-equilibrium which can be generated in present and upcoming high-energy heavy ion experiments. In this context it is important to describe the time evolution of non-equilibrium systems in a fundamental way rather than relying on widely used approximation schemes since the validity of the underlying assumptions might be questionable. Especially the quasi-particle Ansatz appears to be doubtful when considering the huge collision rates in such reactions.

First studies in this respect have been preformed for non-relativistic nuclear matter [1] and the relativistic Φ^4-theory in 1+1 dimensions [2]. We now investigate the time evolution of the real scalar Φ^4-theory in 2+1 space-time dimensions out of equilibrium. For reasons of numerical expense we restrict ourselves to homogeneous systems in space.

The self-consistent evolution equations are derived by loop expansion of the 2PI action of the underlying quantum field theory. Taking into account contributions up to the three loop order for the action one ends up with the Kadanoff-Baym equation, which governs the time evolution of the two-point Green function $iG^<(x,y) = < \Phi(y)\,\Phi(x) >$. It includes the influence of a mean field on the particle propagation - generated by the tadpole diagram - as well as of scattering processes inherent in the sunset diagram. It, furthermore, incorporates memory effects in contrast to the local time structure of Boltzmann-type evolution equations.

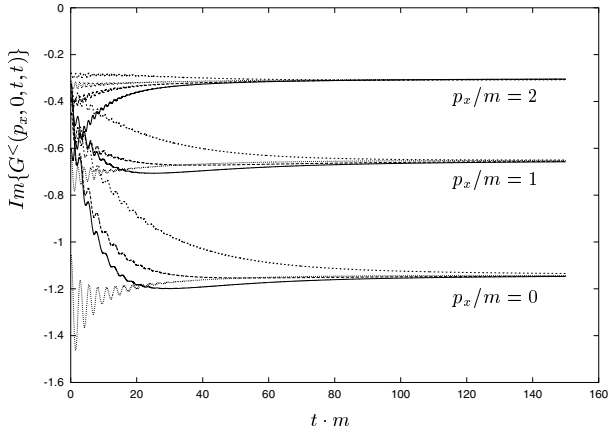


Figure 1: Time evolution of three momentum modes of the equal-time Green function $G^<(p_x, p_y = 0, t, t)$ for four different initial conditions characterized by the same energy density.

As already observed in the 1+1 dimensional case the inclusion of the mean field self energy, only, does not lead to an equilibration of arbitrary initialized momentum distributions since it only modifies the propagation of particles by generation of an effective mass. Thermalization in 2+1 dimensions requires to take into account the collisional self energies stemming from the sunset diagram.

In Figure 1 we show a typical time evolution of various initial value problems for a coupling constant of $\lambda/m = 15$, where m is the mass of the particle. Displayed are three momentum modes of the equal time two-point function $G^<(\vec{p}, t, t)$ for four different Green function initializations (characterized by common line type) with the same energy density. In course of the - energy conserving - propagation in time all respective momentum modes approach their equilibrium value. The evolution of each momentum mode might be characterized by different timescales as already discussed for the 1+1 dimensional case in [2].

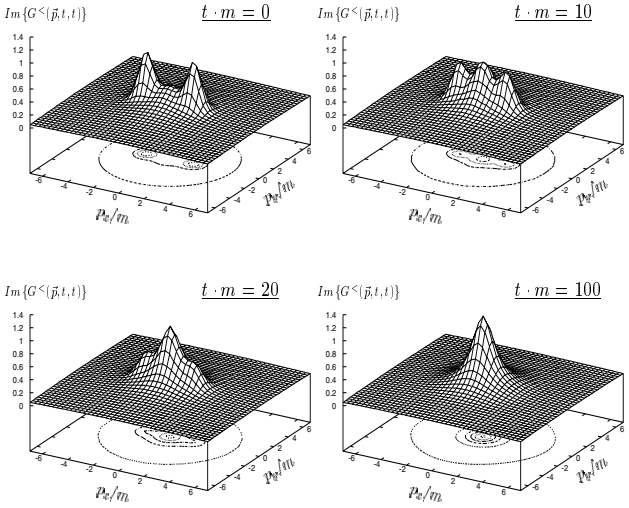


Figure 2: Non-equilibrium time evolution of the equal-time Green function $G^<(\vec{p}, t, t)$ for dimensionless times $t \cdot m = 0$ (initial), 10, 20 and 100.

The equilibration in two-dimensional momentum space is shown in Figure 2 for a coupling of $\lambda/m = 15$. Starting from an non-isotropic initial state the time propagation leads towards an isotropic final distribution.

All calculations so far have been performed within a regularization as appropriate for the momentum grid used. Further studies will need a complete renormalization prescription for the logarithmically divergent sunset self energy as addressed recently also in [3].

References

[1] P. Danielewicz, Annals of Physics 152 (1984) 305-326.
[2] J. Berges, J. Cox, Phys. Lett B 517, 369-374 (2001), J. Berges, hep-ph/0105311.
[3] H. van Hees, J. Knoll, Phys. Rev. D 65: 025010 (2002), hep-ph/0111193.

Boson Expansion For Quantum Field Theory

Z. Aouissat and J. Wambach
Institut für Kernphysik, Technische Universität Darmstadt.

For the last decades Boson expansion theory has played an effective role in the development of approximate solutions to the many-body problem in nuclear physics [1]. These techniques also provide promising tools to address solutions for quantum field theories [2]. In a recent work, we have succeeded in combining an extended form of the Holstein-Primakoff mapping (EHPM) [3] with thermo-field-dynamics [4] to generate a consistent thermal boson expansion for quantum mechanical systems such as the bosonic $O(N)$ anharmonic oscillator as well as the fermionic Lipkin model [7]. The analogue of the first of these two models in four space-time dimensions can be used to address important questions such as the chiral transition for two flavors QCD or the scattering of pions at zero and finite temperature. It is also found that the EHPM removes number of ambiguities when computing anharmonicities in the next-to-leading order of the $1/N$ expansion [7], which are very much relevant to the $\pi\pi$ scattering problem, for instance. Furthermore, the EHPM allows to extend the use of the boson expansion approach to quantum systems with internal $SU(N)$ symmetry where one is confronted with theories having tensor couplings

$$\mathcal{L}_I = f_{ijkl}\phi_i\phi_j\phi_k\phi_l + g_{ijk}\phi_i\phi_j\phi_k + ... \ , \qquad (1)$$

and which calls for a simultaneous bosonization of both pair and single modes. This opens, indeed, the possibility to ultimately address the question of the chiral transition in $SU(3)$ flavor QCD in four space-time dimensions. This point, although crucial for the understanding of the QCD phase diagram, has not been adequately addressed before due to the fact that the $1/N_f$ expansion cannot be correctly sorted out with known techniques [6].
The approach highlighted above and which fundamentally relies on the bosonization of the generators of the $Sp_2 \otimes N_1$ semidirect product group,

$$\begin{aligned}
(aa)_I &= \sqrt{2+4(n+m)}A \ , \qquad (a^+a)_I = 2n+m \ , \\
(a)_I &= \sqrt{2+4(n+m)}\,\Gamma(m)\alpha + 2\alpha^+ A\,\Gamma(m) \ , \\
(a^+a^+)_I &= (aa)_I^+ \ , \qquad (a^+)_I = (a)_I^+ \ , \\
\Gamma(m) &= \left[\frac{m-1}{2(2m+1)(2m-1)}\right]^{\frac{1}{2}} , \\
n &= A^+A \ , \qquad m = \alpha^+\alpha \ , \qquad (2)
\end{aligned}$$

is very appealing from many aspects and particularly from its symmetry conserving character. However, it has a serious drawback. The (asymptotic) particles constructed in that way are 'Hartree' particles, thus semi-classical objects. They are also the building blocks for all higher n-point functions in the theory. To assume the full wave function of the quantum particles, various attempts were made in the context of the Gaussian functional approach (GFA) [8] but failed, so far, to correct for this problem. Indeed, assuming the full wave function of the quantum states induces an uncontrollable order mixing which inevitably destroys the symmetries.
In the case of chiral symmetry, a method that allows to build a non-perturbative pion state was suggested in [2]. This consists in mapping the canonical pion field into the axial current. The idea is supported by the exact (Goldstone) statement: $Q_5^a|vac\rangle \propto |\pi^a\rangle$, which allows to build a pion state by acting with the symmetry generator on the correlated vacuum of the theory. In an effective model, the generator Q_5^a is simply given by Noether's theorem. Therefore one can use the field structure of Q_5^a to model an excitation operator for the asymptotic pion field. This point was successfully developed in several papers and the approach was shown to accommodate finite temperature and chemical potential situations.
In spite of the fact that this technique gives the first approximate but fully quantum solution to the problem, it does not provide, however, a systematic procedure which helps one to tackle the anharmonicities beyond the random phase approximation (RPA). Here again the answer to this question can be found in the boson expansion theory. However, since in most cases (except for gauge symmetry) the symmetry generator is a one-body operator, one has to create a new mapping which can accommodate the bosonization of pairs of two different kinds of bosons at least. Technically this amounts to a new realization of the algebra of the symplectic Sp_4 group which was already derived in [3]. However, in the case of broken symmetries one needs to take into account single boson mapping as well. Thus one needs to make a realization of the algebra of the 15 generators-large semidirect product group $Sp_4 \otimes N_2$. As pointed out above, since this new bosonization is aimed at preserving the quantum statistic of the particles one expects to finally obtain, in the case of the $\pi\pi$ scattering, the first non-perturbative solution with the crossing symmetry built in. This important symmetry is simply lost in the $1/N$ solution.

References

[1] A. Klein, E. R. Marshalek, Rev. Mod. Phys. 63 (1991) 375.
[2] Z. Aouissat, P. Schuck, J. Wambach, Nucl. Phys. A618 (1997) 402
[3] Z. Aouissat, Phys. Rev. C62 (2000) 012201(R).
[4] Y. Takahasi, H. Umezawa, Coll. Pheno., 2 (1975) 55.
[5] Z. Aouissat, A. Storozhenko, A. Vdovin, J. Wambach, Phys. Rev. C64 (2001) 015201
[6] H. Meyer-Ortmanns, B-J. Schaefer, Phys. Rev. D53 (1996) 6586.
[7] Z. Aouissat, A. Storozhenko, A. Vdovin, J. Wambach, work in progress.
[8] G. A. Camelia, Phys. Lett. B407 (1997) 268.
[9] Z. Aouissat, J. Wambach, work in progress.

Finite-Temperature Gluon Condensate with Renormalization Group Flow Equations

B.-J. Schaefer, O. Bohr and J. Wambach
Institut für Kernphysik, Technische Universität Darmstadt.

QCD at low energies can be approximated by effective models which have to satisfy the observed symmetry properties and anomaly structure of the theory. Besides the important approximate and spontaneously broken chiral symmetry at low energy, the classical QCD-Lagrangian exhibits an additional scale invariance in the limit of vanishing current quark masses which is embedded in a larger conformal group. This symmetry is broken at the quantum level by radiative corrections – the so-called trace anomaly. In order to mimic the trace anomaly in an effective framework one introduces a scalar ($J^{PC} = 0^{++}$) dilaton field χ with scaling dimension one and a logarithmic potential with coupling h of the form [1]

$$V = h\left(\frac{\chi}{\chi_0}\right)^4 \ln\left(\frac{\chi}{\chi_0 e^{1/4}}\right) . \qquad (1)$$

This potential breaks scale invariance and leads therefore to a finite vacuum expectation value (VEV) $\chi_0 \equiv \langle 0|\chi|0\rangle$. This effective realization allows for an identification of the gluon condensate $\langle 0|G_{\mu\nu}G^{\mu\nu}|0\rangle$ with the VEV χ_0 of the effective theory with broken scale invariance. Here $G_{\mu\nu}$ denotes the non-Abelian field strength tensor of QCD. Following the suggestion of Campbell et al. [2] χ_0 can be regarded as an effective order parameter for the deconfining phase transition.

In order to investigate the possible gluonic phase transition we perform a finite-temperature analysis of the effective theory within the framework of a proper-time renormalization group (PTRG) approach [3]. Within the PTRG approach we can directly calculate the full non-truncated effective dilaton potential for any value of the field and not just at the minimum, χ_0. This in principle allows to analyze the order of the phase transition.

In this work the glueball mass m_χ and bag constant B are taken as an input. We choose values around $m_\chi = 1.5$ GeV which is motivated by recent lattice results and vary the bag constant in between 0.149^4 and 0.276^4 GeV^4. From previous studies it is observed that the temperature scale, where thermal excitations become important, is determined by the value of the bag constant at $T = 0$. For $B^{1/4} = 0.14$ GeV, the onset of a significant shift of the minimum is seen at $T \sim 0.25$ GeV while for $B^{1/4} = 0.24$ GeV this happens only for temperatures above $T \sim 0.4$ GeV. The value for the "critical" temperature T_c is dominated by the value of the bag constant. A larger bag constant results in a higher critical temperature.

In Fig. 1 the change of the normalized 'order parameter' $\chi_0^4(T)/\chi_0^4(0)$ with temperature is shown for two different chosen bag constants B but equal glueball masses $m_\chi = 1.5$ GeV. For both bag constants the condensate stays almost constant up to temperatures of the order 200 MeV which is beyond the chiral phase transition temperature for two quark flavors.

In Fig. 2 the temperature-dependent glueball mass m_χ

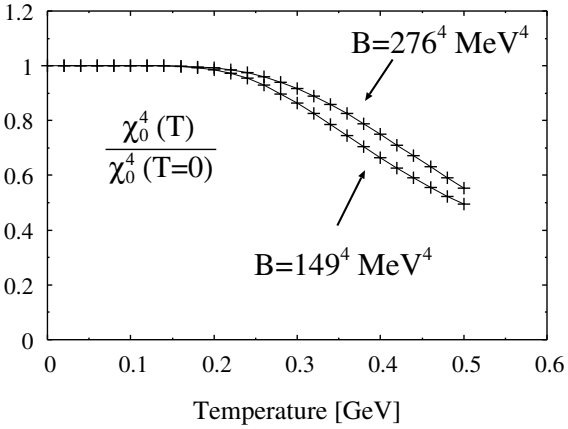


Figure 1: The temperature behavior of the normalized gluon condensate $\chi_0^4(T)/\chi_0^4(0)$ for two different bag constants.

is displayed for two different bag constants. The mass as function of temperature is independent on the bag constant below temperature of 180 MeV. For the larger bag constant $B^{1/4} = 0.276$ GeV it then decreases and increases again for very large temperatures above 800 MeV. For the smaller bag constant $B^{1/4} = 0.149$ GeV the mass grows almost linearly with temperature around $T \sim 350$ MeV. At very high temperatures such a behavior is expected since perturbation theory is applicable.

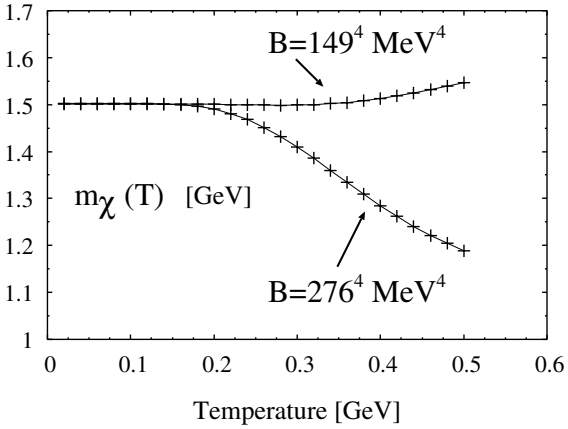


Figure 2: The glueball mass versus temperature for two different bag constants.

References

[1] J. Schechter, Phys. Rev. **D21** (1980) 3393;
[2] B.A. Campbell, J. Ellis and K.A. Olive, Phys. Lett. **235B** (1990) 325; Nucl. Phys. **B345** (1990) 57.
[3] B.-J. Schaefer, O. Bohr and J. Wambach, `hep-th/0112087`, to be published in Phys. Rev. **D**.

Cooling of Neutron Stars with Superconducting Quark Matter Cores

D. Blaschke[1,2], H. Grigorian[2,3], D.N. Voskresensky[4,5]
[1] JINR Dubna, [2] Univ. Rostock, [3] Yerevan State Univ., [4] MEPhI Moscow, [5] GSI Darmstadt

Interiors of compact stars are considered as systems where high-density phases of strongly interacting matter do occur in nature. Consequences of different phase transition scenarios for the cooling of compact stars have been reviewed recently, see e.g. [1], in comparison with X-ray data.

A completely new situation might arise if scenarios suggested color superconductivity (CS), see [2, 3], with large diquark pairing gaps ($\Delta_q \sim 50 \div 100$ MeV) in quark matter are applicable to neutron star interiors. Various phases are possible. The two-flavor (2SC) or the three-flavor (3SC) superconducting phases allow for unpaired quarks of one color, whereas in the color-flavor locking (CFL) phase all the quarks are paired. CS may, in principle, also manifest itself in heavy ion reactions in strangelets and for $T > T_c$ via correlation effects.

Estimates of the cooling evolution have been performed [4] for a self-bound isothermal quark core neutron star (QCNS) which has a crust but no hadron shell, and for a quark star (QS) which has neither crust nor hadron shell. It has been shown there that in the case of the 2SC (3SC) phase of QCNS the cooling is governed by the quark direct Urca process (QDU) and the consequences for the cooling curves are similar to the scenario of enhanced cooling of the hadronic neutron stars. For the CFL case it has been shown that the cooling might still be much faster, inspite of opposite naive expectations, since the drop in the specific heat of CS quark matter dominates over the reduction of the neutrino emissivity. As has been pointed out in [4], it should be however an additional delay of the cooling at an early stage due to the heat transport disregarded there. Ref. [5] estimated the cooling of hybrid neutron stars (HNS), which have a crust, a wide hadronic shell and CS core, disregarding heat transport effects.

We have developed a more detailed scenario for the thermal evolution of HNS and QCNS which includes the heat transport in both the quark and the hadronic matter [6]. A detailed comparison of the cooling evolution (lg T_s vs. lg t) of HNS for different values of quark and hadron gaps is given in Fig. 1. We have found that the curves for $\Delta_q > 1$ MeV are very close to each other demonstrating typical large gap behaviour. As representative example we take $\Delta_q = 50$ MeV. The behaviour of the cooling curve for $t \leq 50 \div 100$ yr is determined by the heat transport within the CS core. The subsequent time evolution is governed by the processes in the hadronic shell and by a delayed transport within the quark core with a dramatically suppressed neutrino emissivity from the CS region. In order to demonstrate this feature we have also performed a calculation with the nucleon gaps ($\Delta_i(n)$, $i = n, p$) being artificially suppressed by a factor 0.2. The curves labelled "MMU" are calculated with the rates of modified Urca processes, with inclusion of appropriate medium modifications in the NN interaction [7].

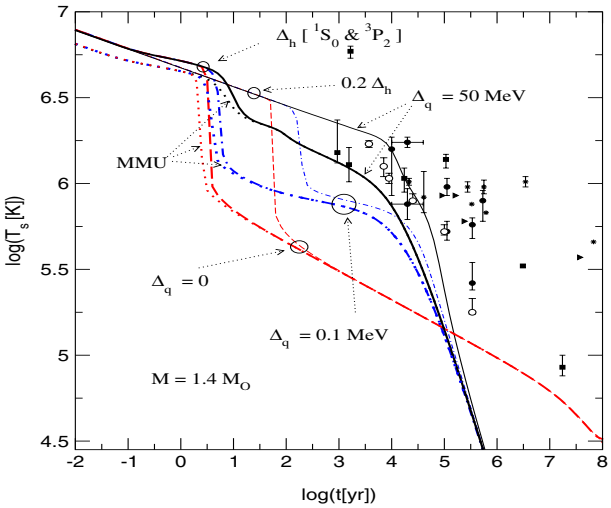


Figure 1: Evolution of the surface temperature T_s of HNS with $M = 1.4 M_\odot$ for $T_s \propto T_m^{2/3}$, where T_m is the mantle temperature, see [6] for details.

Summarizing, we have found for the CFL phase with large quark gap, which was expected to exhibit the most prominent manifestations of CS in HNS and QCNS, an essential delay of the cooling during the first $50 \div 300$ yr due to a dramatic suppression of the heat conductivity in the CS region. It seems, however, rather difficult to explain the majority of the presently known data both in the cases of the HNS and QCNS, whereas in the case of pure hadronic stars the available data are much better fitted within the same model for the hadronic matter we used here. For 2SC (3SC) phases we expect analogous behaviour to that demonstrated by $\Delta_q = 0$ since QDU processes on unpaired quarks are then allowed. We do not exclude that new observations may lead to lower surface temperatures for some supernova remnants and will be better consistent with the model which also needs further improvements. On the other hand, if future observations will show very large temperatures for young compact stars they could be interpreted as a manifestation of large gap CS in their interiors.

References

[1] Ch. Schaab et al., A & A 346, 465 (1999)
[2] M. Alford et al., Phys. Lett. B 422, 247 (1998)
[3] R. Rapp et al., Phys. Rev. Lett. 81, 53 (1998)
[4] D. Blaschke et al., ApJ 533, 406 (2000)
[5] D. Page et al., Phys. Rev. Lett. 85, 2048 (2000)
[6] D. Blaschke et al., A & A 368, 561 (2001)
[7] D.N. Voskresensky, in: *Physics of Neutron Star Interiors*, LNP 578, Springer (2001), p. 467

Understanding Nuclear Effects with QCD

J. Hüfner[1,3], B.Z. Kopeliovich[2,3], A. Schäfer[2], A.V. Tarasov[1−3]
[1]University of Heidelberg, [2]University of Regensburg, [3]MPI-Kernphysik Heidelberg

Jet quenching and partonic energy loss

High-p_T hadron production is expected to provide a sensitive probe for dense QCD matter created in heavy ion collisions. This probe, usually called jet quenching, exploits the theoretical expectation of an enhanced energy loss of a parton propagating through hot matter. The effect is predicted to be proportional to the density of the medium. In spite of much theoretical work done over the last decade, no experimental evidence for energy loss even in a cold nuclear medium has been found so far. Moreover, the existing analysis of nuclear effects in Drell-Yan reactions which is sensitive to energy loss detected no effect at all. This confusing conclusion contradicting theoretical expectations has raised doubts about the correctness of our understanding of the QCD dynamics of induced gluon radiation.

The main difficulty one faces trying to single out the effect of energy loss from Drell-Yan reactions is a strong overlap with the phenomenon of nuclear shadowing. This problem needs a more profound analysis employing the best of our knowledge of the dynamics of shadowing. A new analysis based on reliable and well tested predictions for the net shadowing effect was undertaken in [1, 2]. The combined analysis of data from the E772 and E866 experiments at Fermilab resulted in a rather large energy loss rate,

$$-\frac{dE}{dz} = 2.73 \pm 0.37 \pm 0.5\,\mathrm{GeV/fm}\ , \qquad (1)$$

which is, however, consistent with theoretical expectations [2]. This it the first time that a energy loss was extracted from data.

Cronin effect

Unfortunately, there is no direct access to final state interactions of high-p_T partons with the medium. It always comes in combination with the nuclear effects originating from multiple interactions with bound nucleons in the colliding nuclei. Those effects cannot be measured, but only computed theoretically. They have been known over many years as Cronin effect which is an observed nuclear enhancement of high-p_T hadron production in pA collisions.

Recent data from RHIC for high-p_T hadrons in gold-gold collisions raised again the long standing problem of a quantitative understanding of the Cronin effect for which no parameter-free explanation has been achieved so far.

A phenomenological description based on the light-cone QCD-dipole approach which allows to explain available data and to provide predictions for pA collisions at RHIC and LHC was suggested recently in [3] . The crucial observation is that the underlying mechanism changes with energy being controlled by the coherence length of the process,

$$l_c = \frac{\sqrt{s}}{m_N k_T}\ , \qquad (2)$$

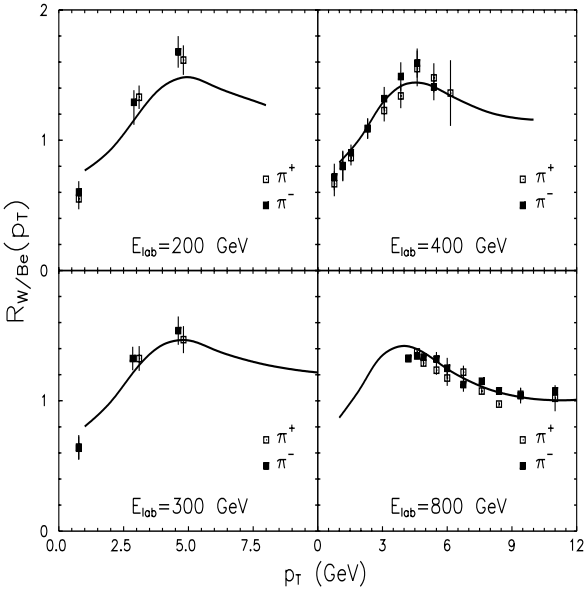


Figure 1: Ratio of the charged pion production cross sections for tungsten and beryllium as function of the transverse momentum of the produced pions. The curves correspond to the parameter free calculation [3], the depicted data are from fixed target experiments.

where k_T is the transverse momentum of the parton produced at mid-rapidity. It turns out that at the SPS energy l_c is short compared to the nuclear radius, and the high-p_T partons are produced incoherently on different nucleons. The effect of multiple soft initial state interactions was calculated using the color-dipole approach suggested earlier in [4]. The key entry in this formalism is the universal phenomenological color dipole cross section fitted to HERA data for the proton structure function. We calculated the nuclear effects for high-p_T pions produced in pA collisions in fixed target experiments ($200 - 800\,\mathrm{GeV}$ lab. energy), in good agreement with data as is demonstrated in Fig. 1.

At very high energies l_c substantially exceeds the nuclear size and production amplitudes interfere. Correspondingly, the mechanism causing Cronin effect drastically changes between the energies of fixed target experiments and RHIC-LHC. In particular, nuclear enhancement of high-p_T hadrons at these energies is predicted to be much smaller than at SPS. This is demonstrated in Fig. 2 where the prediction for $\sqrt{s} = 200\,\mathrm{GeV}$ is depicted by a solid curve. This predictions will be checked in deuteron-gold collisions at RHIC, probably within a year.

Probing the QGP with charmonium production

It is expected that the modification of the charmonium production rate due to final state interactions (FSI) with the matter created in relativistic heavy ion collisions may serve as a probe for its properties. However, it is still a challenge to disentangle the effects of initial state in-

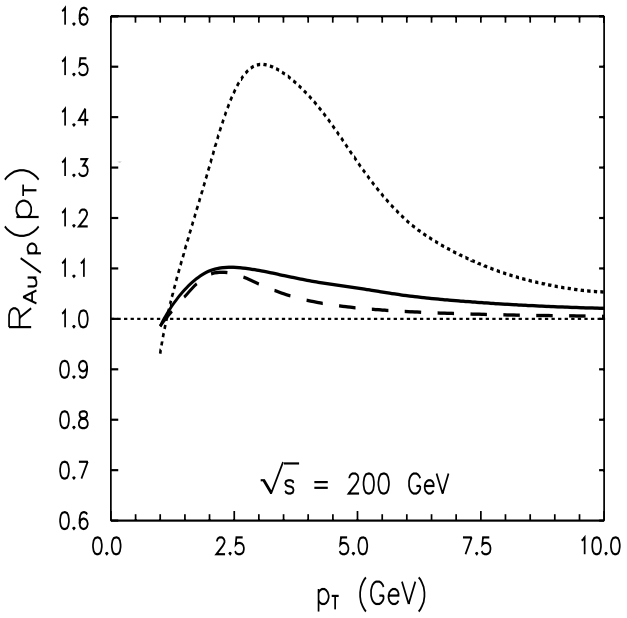


Figure 2: Predictions for RHIC. The dotted and dashed curves are calculated at $\sqrt{s} = 200\,\mathrm{GeV}$ using QCD factorization and asymptotic high energy ($l_c \gg R_A$) prescriptions respectively. The final prediction taking into account the coherence length is shown by the solid curve.

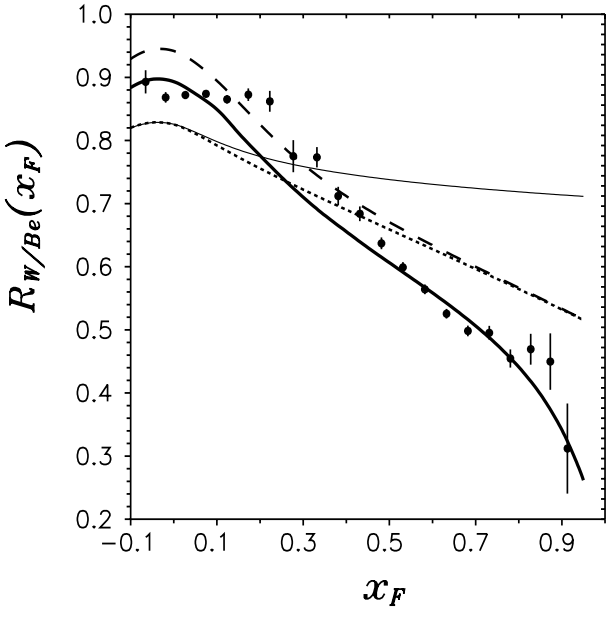


Figure 3: Tungsten to beryllium cross section ratio as function of Feynman x_F for J/Ψ production at proton energy $800\,GeV$. The thin solid curve represents contribution of initial state quark shadowing and finals state $\bar{c}c$ attenuation for χ production. The dotted curve includes also gluon shadowing. The dashed curve is corrected for gluon enhancement at large x_2 (small x_F). Experimental points are from the E866 experiment.

teraction (ISI) at the early stage of a collision, when the nuclei propagate through each other, from the late stage FSI, when charmonium with a low speed travels through the comoving debris of the nuclei. Since ISI seems to be the main source of suppression, uncertainties in our understanding of the early stage nuclear effects are transferred to the interpretation of FSI.

Remarkably, nuclear effects for charmonium production were not properly analyzed quantitatively so far for pA collisions. Apparently, lacking a good understanding of nuclear effects in pA collisions one should not jump to any certain conclusions about the mechanisms of nuclear suppression (or enhancement) in HI collisions.

The mechanism of ISI which is usually called "standard" is simply fitted to data for J/Ψ production at $x_F = 0.15$ in pA collisions. It is oversimplified, since it predicts no x_F dependence, while data demonstrates a dramatic enhancement of nuclear suppression of J/Ψ at large x_F.

First of all, it was realized in [5] that the mechanisms of nuclear effects for J/Ψ production change drastically as function of energy from SPS via Fermilab to RHIC and LHC. This is controlled by the coherence length of charmonium production. The first successful attempt to understand quantitatively the nuclear effects for J/Ψ production and to describe available data at different energies and as function of x_F in a parameter-free way was undertaken in [6]. The dominant source of x_F dependence is energy loss at SPS energies, at Fermilab nuclear effects get a substantial contribution from gluon shadowing, which then becomes the main mechanism of nuclear suppression at RHIC and LHC. Fig. 3 compares the contributions of these different mechanisms for pA collisions with data from the E866 experiment at 800 GeV at Fermilab (see the figure caption).

A nontrivial observation made in [6] is that nuclear gluon shadowing at the charm mass scale substantially deviates from universality prescribed by QCD factorization. In the case of charmonium production it is much stronger than in deep-inelastic scattering or the Drell-Yan process (see below). This fact becomes especially important at the higher energies of RHIC and LHC where gluon shadowing is expected to be the main source of nuclear suppression. One can see from the prediction for RHIC depicted by the dotted curve in Fig. 4 that J/Ψ is indeed enormously suppressed by ISI, namely by about an order of magnitude.

On the other hand, the x_F dependence of FSI suppression may serve as a novel probe [5] for the properties of the matter produced in HI collisions. Indeed, the density of the created matter is not homogeneous, but peaks at the mid-rapidity. Therefore, one should expect a strong variation of suppression (or enhancement is some scenarios) with x_F caused by FSI which may serve as its signature. The calculations [7] performed with two popular models for FSI, one with QGP production and another one with comoving hadrons, are depicted in Fig. 4 by solid and dashed curves respectively. Comparison with the dotted curve shows that the deep and minimum in x_F dependence due to FSI nearly compensate the peak at $x_F = 0$ which is expected be formed by ISI.

Nuclear suppression for Drell-Yan lepton pairs

The Drell-Yan cross section has been used at SPS in the NA38/50 experiments as a baseline for nuclear effects in charmonium production. Indeed, at this energy shadowing is absent and only energy loss affects the cross section,

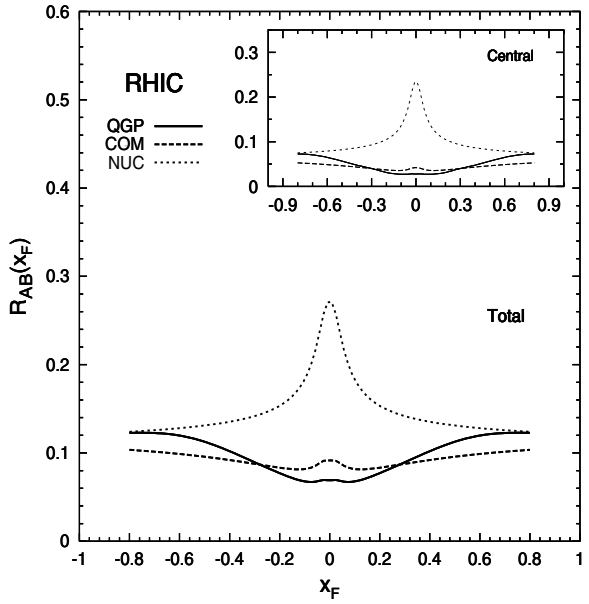


Figure 4: Ratios of cross sections of charmonium production as function of x_F for gold-gold collisions at RHIC at $\sqrt{s} = 200\,\mathrm{GeV}$, with respect to the pp case. The dotted curve presents the effect of nuclear suppression alone. Dashed and full lines refer to the full suppression resulting from nuclear effects and also from the interaction with plasma or comovers, respectively. The large and small panel represent the results for total cross section and central collisions, respectively.

mostly at large x_F. Already at Fermilab energies one faces the onset of nuclear shadowing which is sizeable at large x_F. At the energies of RHIC and LHC shadowing of quarks and gluons in nuclei becomes very strong and spans the whole x_F range. The parton model is unable to predict these effects, especially for heavy ion collisions, starting from currently available experimental information. The effects of shadowing were calculated within the light-cone dipole formalism in [8]. It was found that gluon shadowing for the Drell-Yan process is much weaker that for charmonium production. This deviation from QCD factorization is caused by presence of a semihard scale which emerges due to the strong nonperturbative interaction of light-cone gluons. The parameters of this interaction are well fixed by high statistics data for diffractive dissociation of protons into states of large invariant mass [9].

Nuclear effects and color transparency

One of the main manifestations of QCD in terms of nuclear effects is the phenomenon of color transparency (CT). As is easy to understand intuitively, a point-like colorless object cannot interact with external color fields, therefore the strength of interaction correlates with the size of the hadronic system. Consequently, if a colorless partonic configuration (pre-hadron) is produced in a hard exclusive reaction, it is expected to have a small size and propagate through nuclear matter without attenuation. A confirmation for this simple prediction has been desperately searched for in many experiments, however, only very few were successful.

High-statistics measurement for electroproduction of ρ-mesons, a process sensitive to CT, has been performed recently in the HERMES experiment at HERA. Although CT has a strong impact on the cross section of this reaction, it may be easily mixed up with the coherence length effect which varies with Q^2. A novel technique to take both effects into account based on the light-cone Green function formalism was suggested in [10]. These calculations made it possible to discriminate between the CT and coherence length effects, and the preliminary results of a new analysis of the HERMES data demonstrate a rather strong signal for CT. In addition, possible effects of higher order $\alpha_{em}Z$ corrections which might be essential for heavy nuclear targets, were investigated in [11]. Indeed, it was found that these corrections may be large and the problem needs further investigation. In particular, it can be important for coherent Coulomb production in peripheral heavy ion collisions.

References

[1] M.B. Johnson, B.Z. Kopeliovich, I.K. Potashnikova, + the E772 Collaboration, *Energy loss of fast quarks in nuclei*, Phys. Rev. Lett. **86** (2001) 4483.

[2] M.B. Johnson, B.Z. Kopeliovich, I.K. Potashnikova, P.L. McGaughey, J.M. Moss, J.-C. Peng, G.T. Garvey, M. Leitch, C.N. Brown, D.M. Kaplan, *Energy Loss versus Shadowing in the Drell-Yan Reaction on Nuclei*, hep-ph/0105195, to appear in Phys. Rev. C.

[3] B.Z. Kopeliovich, J. Nemchik, A. Schäfer, A.V. Tarasov, *Cronin Effect in Hadron Production off Nuclei*, hep-ph/0201010, submitted to Phys. Rev. Lett.

[4] M.B. Johnson, B.Z. Kopeliovich, and A.V. Tarasov, Phys. Rev. **C63** (2001) 035203.

[5] B.Z. Kopeliovich, *Charmonium Production off Nuclei: from SPS to RHIC*, Nucl. Phys. **A698** (2002) 547c

[6] B.Z. Kopeliovich, A.V. Tarasov, J. Hüfner, *Coherence Phenomena in Charmonium Production off Nuclei at the Energies of RHIC and LHC*, Nucl. Phys. **A696** (2001) 669.

[7] B.Z. Kopeliovich, A. Polleri, J. Hüfner, *Scanning the Quark-Gluon Plasma with Charmonium*, Phys. Rev. Lett. **87** (2001) 112302.

[8] B.Z. Kopeliovich, J. Raufeisen, A.V. Tarasov, M.B. Johnson, *Nuclear effects in the Drell-Yan process at RHIC and LHC*, hep-ph/0110221, to appear in Phys. Rev. C.

[9] B.Z. Kopeliovich, *From Hard to Soft Diffraction and Return*, Nucl. Phys. Proc. Suppl. **99A** (2001) 29.

[10] B.Z. Kopeliovich, J. Nemchik, A. Schäfer, A.V. Tarasov, *Color Transparency versus Quantum Coherence in Electroproduction of Vector Mesons off Nuclei*, hep-ph/0107227, to appear in Phys. Rev. C.

[11] B.Z. Kopeliovich, A.V. Tarasov, O.O. Voskresenskaya, *Long-Range Coulomb Forces in DIS: Missed Radiative Corrections?*, Eur. Phys. J. **A11** (2001) 345.

Contribution of ρ–Mesons to Charge Fluctuations

Michael Döring, Volker Koch
(GSI Darmstadt, LBNL, Berkeley

One major goal in heavy ion collisions is to produce evidence of the quark gluon plasma (QGP). A possible signature are reduced charge fluctuations due to the fractional charge of the quarks in the QGP. In the hadronic phase fluctuations may be screened or enhanced by hadronic interaction. Using an effective Lagrangian based on vector dominance, we calculate the charge fluctuations up to second order in a hot pion gas applying finite temperature field theory.

The observable sensitive to fractional charge is the ratio of charge fluctuations and the charge multiplicity [1]

$$\frac{\langle \delta Q^2 \rangle}{\langle N_{ch} \rangle}. \tag{1}$$

Since $\langle \delta Q^2 \rangle \sim q^2 \langle N_{ch} \rangle$, this quantity is sensitive to the squared charge q^2 and enhances the 1/3–charge effect of a QGP in contrast to a purely hadronic initial state with $|q| = 1$. We can compute the mean number of particles by assuming entropy conservation and exploiting $S \sim \langle N_{ch} \rangle$. Charge fluctuations can be linked to finite temperature field theory by

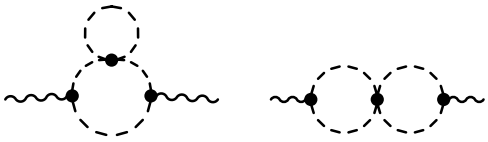
$$\langle \delta Q^2 \rangle = -VT\Pi^{00}(k_0 = 0, \mathbf{k} \to 0), \tag{2}$$

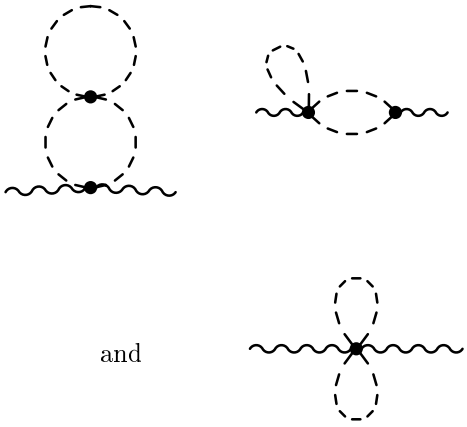
the photon self energy in the static limit.[2]

Assuming small momentum transfers in comparison with the ρ–mass of 770 MeV at the current temperature scale of 150 MeV, we use the effective Lagrangian

$$\mathcal{L} = -\frac{1}{4}F_{\mu\nu}^2 - m_\pi^2|\phi|^2 + |D_\mu \phi|^2 - \frac{ig^2}{m_\rho^2}\left(\phi^\star \overset{\leftrightarrow}{D_\mu}\, \phi\right)^2 \tag{3}$$

with the ρ–resonance removed from the heatbath. This Lagrangian originates from the $\rho\pi\pi$ interaction in second order. Two 3–vertices are combined to a direct 4–vertex with derivative couplings containing the universal strong coupling constant $g \sim 6$. The Lagrangian is then gauged in the canonical way, leading to a set of couplings to the electromagnetic current by the covariant derivative $D_\mu = \partial_\mu + ieA_\mu$. Based on this Lagrangian, we investigate the first order corrections to the self energy in the order e^2g^2. In the imaginary time formalism this leads to the set of diagrams





(4)

involving pions and photons. We have verified that this class of diagrams satisfies the Ward–Takahashi identity. Carrying out the Matsubara summation by contour integration we get the correction as depicted in Fig. 1 ($\sigma = S/V$)

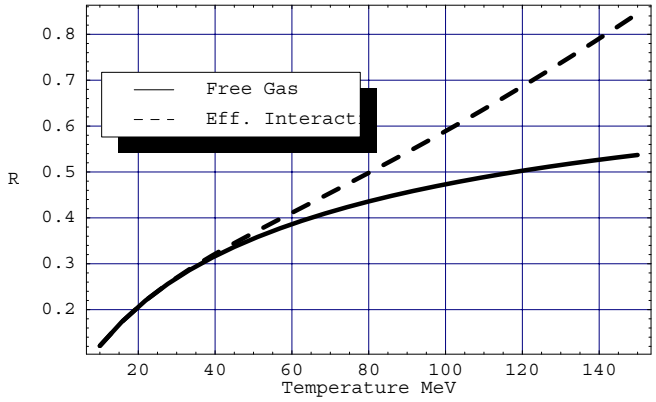


Figure 1: Correction to Charge Fluctuations per Entropy Density, $R = -VT\Pi^{00}_{0+1}(k_0 = 0, \mathbf{k} \to 0)(T)/\sigma_{0+1}(T)$, assuming effective ρ–interaction at the 2 loop level

We find that the effective interaction increases the charge fluctuations of the free pion gas. Both curves show the expected low temperature behaviour.

References

[1] S. Jeon, V. Koch, Phys.Rev.Lett.**85**:2076-2079,2000
[2] J.I. Kapusta, *Finite Temperature Field Theory*, Cambridge 1989

Spectral Function of Quarks in Quark Matter

F. Frömel, S. Leupold, and U. Mosel
University of Giessen

We have investigated the spectral function of light quarks in infinite quark matter using a simple, albeit self-consistent model [1]. Relations between the spectral function and the collisional self-energies in the Born approximation were used to calculate the spectral function in an iterative process beyond the quasiparticle approximation. The quark interactions were described by the SU(2) Nambu–Jona-Lasinio (NJL) model [2]. It has the same symmetries as QCD and describes an effective quark-quark interaction with a constant coupling strength. Mean field effects have been neglected in the calculations.

This study has been motivated by similar calculations for nucleons in nuclear matter [3]. It was found there that the results are in good agreement with calculations from many-body theory. In particular the model was very successful in describing the influence of short-range correlations on the properties on nuclear matter using a simple pointlike nucleon interaction with constant scattering amplitude.

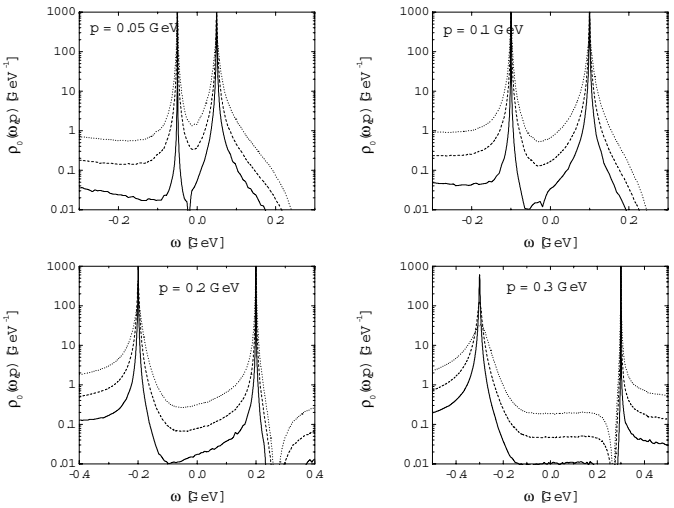


Figure 1: The spectral function of quarks at different momenta. The solid line corresponds to the usual NJL coupling strength, the dashed line is the result at a coupling twice as large and the dotted line has been obtained with a coupling four times larger than the usual value.

Our calculations were performed at zero temperature and in the chirally restored phase. We chose the quark matter such that it is comparable to regular nuclear matter, $\rho_{\mathrm{qm}} = 3 \cdot \rho_{\mathrm{nm}} = 3 \cdot 0.17\,\mathrm{fm}^{-3}$. This yields a Fermi energy of $\omega_F = 0.268\,\mathrm{GeV}$. The (three-momentum) cutoff Λ and the coupling constant G of the NJL model were chosen so that the model gives the known values [2] for the quark condensate and the pion coupling constant f_π in vacuum. In addition we did calculations with two times and four times larger coupling strengths to investigate the influence on the spectral function.

Fig. 1 shows our results for the spectral function at several momenta and coupling strengths. Physically the most interesting area lies in the energy range $0 < p_0 < \omega_F$ since that is the location of the populated quark states. All states above the Fermi energy as well as the anti-quark states at negative p_0 are unoccupied (no holes in the Dirac sea). The structure of the spectral function is dominated by the on-shell peaks of the quarks and anti-quarks at $p_0 = |\vec{p}|$ and $p_0 = -|\vec{p}|$. As one would expect the peaks get broader when the coupling is increased. Strength is distributed away from the peaks to the off-shell regions, the width of the peaks increases from $0.1-1\,\mathrm{MeV}$ at the lowest to $10\,\mathrm{MeV}$ at the largest value for the coupling constant.

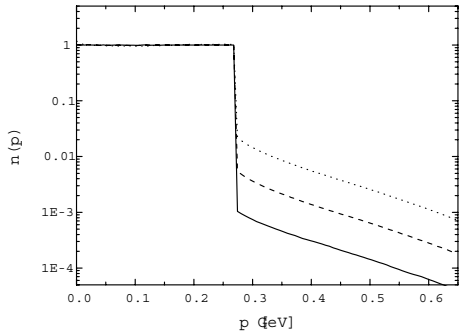


Figure 2: Quark momentum distribution in quark matter at different coupling strengths (see Fig. 1 for details).

The momentum distribution of nucleons in nuclear matter shows a depletion of occupation probabilites by about 10% [3]. The resulting high energy tail is taken as a universal sign of short-range correlations. In Fig. 2 we show the momentum distribution of the quarks that we have found for the different coupling strengths. As expected for an infinite system a sharp step at the Fermi momentum appears. At the lowest coupling a depletion of only 0.1% is found. For the coupling twice as large the short-range correlations increase but still the depletion effect is below 1%. Only for the largest couplings we find a high momentum tail of a few percent, comparable to the case of nucleons.

The results indicate that the influence of short-range correlations is small compared to nuclear matter. This finding, however, might be an artefact of the present model, the NJL model with vacuum parameters in the Born approximation. Since we know now that the model is technically feasible we plan to go beyond the simple model presented here. It is our plan to use more sophisticated interaction models for future calculations.

References

[1] F. Frömel, S. Leupold, U. Mosel, nucl-th/0111004.
[2] S.P. Klevansky, Rev. Mod. Phys. 64 (1992) 649.
[3] J. Lehr, M. Effenberger, H. Lenske, S. Leupold, U. Mosel, Phys. Lett. B 483 (2000) 324; J. Lehr, H. Lenske, S. Leupold, U. Mosel, nucl-th/0108008.

Nonequilibrium quark dynamics in ultrarelativistic heavy ion collisions[B,G]

S. Scherer[1], M. Hofmann[1], M. Bleicher[2], L. Neise[1], H. Stöcker[1], W. Greiner[1]
[1] Institut für Theoretische Physik, J. W. Goethe-Universität Frankfurt am Main, Germany,
[2] Nuclear Science Division, Lawrence Berkeley Laboratory, Berkeley, U.S.A.

Heavy ion collisions at the CERN-SPS (and possibly at the upper end of the planned SIS/200 at GSI) are supposed to reach the transition form hadronic matter to the quark-gluon plasma. The analysis of collective observables such as flow allows to speculate that this transition may show up even down to AGS energies. The description of such a collision by microscopic models thus must treat properly the degrees of freedom emerging from soft QCD.

Such a model can be realized by treating quarks as classical particles interacting according to a two-body color potential [1]. The Hamiltonian of this quark molecular dynamics (qMD) reads

$$\mathcal{H} = \sum_{i=1}^{N} \sqrt{\mathbf{p}_i^2 + m_i^2} - \frac{1}{2} \sum_{i,j} C_{ij}^{\mathrm{c}} \left(\frac{3}{4} \frac{\alpha_s}{|\mathbf{r}_i - \mathbf{r}_j|} + \kappa \, |\mathbf{r}_i - \mathbf{r}_j| \right)$$

where the well known Cornell-potential is used to describe the quark interaction. Sign and relative strength of the interaction are described by the color factor C_{ij}^{c}, depending on the color combination of each pair. Confining properties are ensured by the linear increase of $V(r)$ at large distances. The time evolution of such a system yields colorless quark clusters which are mapped to hadrons.

When coupled to a hadronic transport model such as UrQMD[2] to create the initial quark distribution, the qMD can provide us with detailed information about the dynamics of the quark system and the parton-hadron conversion. Correlations between the quarks clustering to build new hadrons can be studied [3].

Hadrons of the colliding nuclei are propagated in UrQMD, producing new hadrons in inelastic collisions and preformed hadrons in string excitations. Once complete overlap of the impinging nuclei is reached, all hadrons with at least one collision or within their formation time are broken up in their (valence) quark content. These quarks are then propagated in qMD, finally hadronizing again.

Hadrons of the colliding nuclei are propagated in UrQMD, producing new hadrons in inelastic collisions and preformed hadrons in string excitations. Once complete overlap of the impinging nuclei is reached, all hadrons with at least one collision or within their formation time are broken up in their (valence) quark content. These quarks are then propagated in qMD, finally hadronizing again.

A measure of the relative mixing within the quark system and thus for thermalization is the relative number of hadrons formed by quarks from the same initial hadron versus hadrons formed by quarks from different initial hadrons. This ratio is surprisingly flat ($r \simeq 0.3$ for the Pb+Pb collision – spectators are not included!) over the whole energy range from SIS/200 to SPS from 20 to 160 GeV/N. It also shows only a moderate dependence on the impact paramter (figure 1).

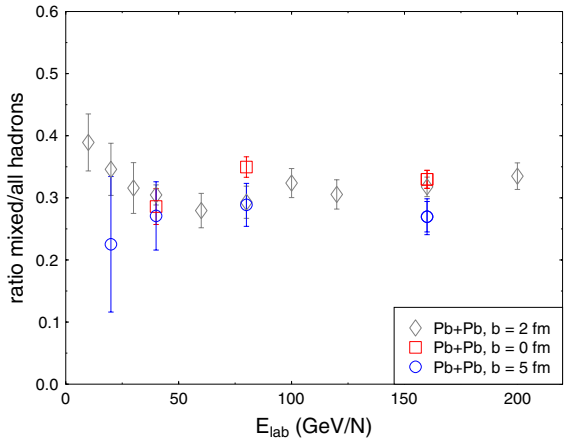


Figure 1: Excitation function of ratio of mixed to total hadrons for Pb+Pb collisions with differnt impact parameters (b= 0, 2, 5 fm).

Since a value of $r = 1$ indicates complete rearrangement of quarks and thus complete loss of correlations in the quark system, one would expect a much larger value of r, considering the presumed transition to the quark-gluon plasma in Pb+Pb collisions at 160 GeV/N,

One finds, however, in increase in the ratio of mixed to direct hadrons if one takes into account in the qMD phase only those hadrons (and preformed hadrons) from UrQMD which have undergone at least two collisions (figure 2 – circles and squares).

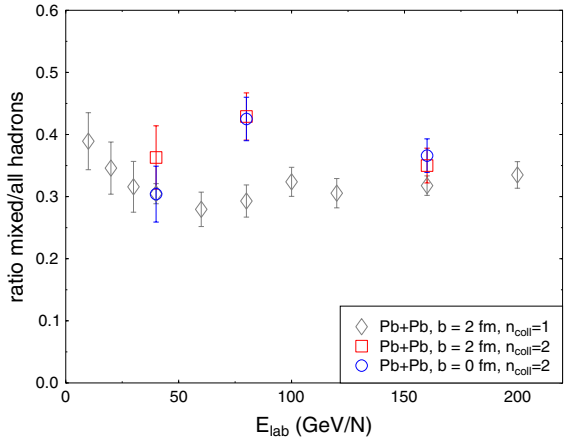


Figure 2: Excitation function of ratio of mixed to total hadrons for Pb+Pb collisions.

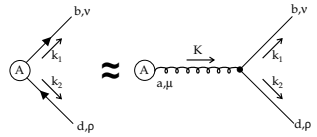
References

[1] M. Hofmann et al., Phys. Lett. **B478** (2000) 161
[2] S. A. Bass et al., Phys. Rev. C **60** (1999) 021902
[3] S. Scherer et al., New J. Phys. **3** (May 2001) 8-8

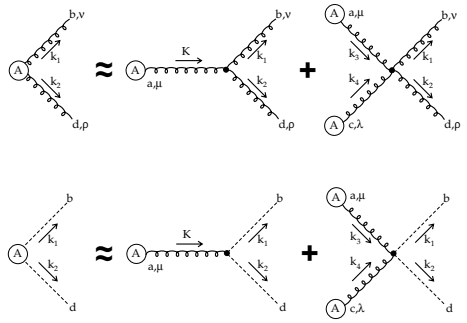
Parton Production Scenarios^{B+G}

Dennis D. Dietrich, Gouranga C. Nayak,and Walter Greiner, Johann Wolfgang Goethe Universität

Initially an ultrarelativistic heavy-ion collision is gluon dominated to a degree that these bosons can be described as a classical vector potential A. The question is now, whether the production of quark-antiquark pairs or the production of quantum gluons from the field dominates. In the background field method of quantum chromodynamics a classical gauge field and quantum fluctuations are treated at the same time [1]. We choose a perturbative approach (see succeeding Figs) as analytical non-perturbative results exist only for very few special choices of the form of the field.



Dominant contribution to the production of quarks

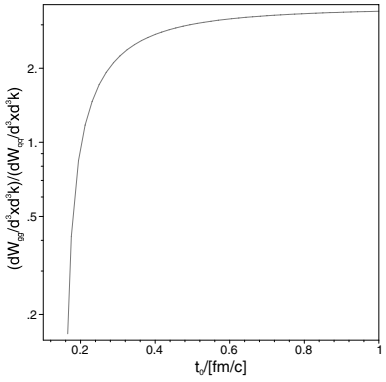


Dominant contribution to the production of gluons

Our perturbative approach is satisfied for particles with an energy greater than the product of the field strength A and the coupling constant g. Additionally, gA has got be large compared to Λ_{QCD}. So, the approach is limited to times less than t_f after which this requirement is no longer fulfilled. For $gA_{in} >> \Lambda_{QCD}$ the contribution to the quantum sector after the final time of applicability t_f is negligible [2]. The classical description of the low-energy bosonic sector is more likely to be sufficient for faster decaying fields. Here, there is no description of the low energy region of the fermions. We have got to elaborate on this point. A treatment in the framework of the constant field Schwinger szenario [3] is not consistent with the big slopes of the decaying field. Nevertheless, a quantitative comparison would be interesting.

The formulae for fields with a general space-time dependence are rather lengthy [4]. So we take an exclusively time-dependent field in order to learn about the features of the source terms for quarks and gluons: $A^{a\,3}(t) = A_{in}e^{-|t|/t_0}$, $t_0 > 0$, $a = 1,...,8$ and all other components are equal to zero. This is no unique choice but was inspired by the result of a different numerical study [5]. For LHC the parameters $A_{in} = 1500MeV$ for the initial value of the field, $\alpha_S = 0.15$ for the coupling constant, and $t_0 \in \{0.1fm, 1.0fm\}$for the decay-time are consistent with the envisioned energy density of $1TeV/fm^3$.

The measure for the dominance of one of the channels is the ratio of the respective number of produced pairs, say gluons devided by quarks. For values considerably less than one quark anti-quark production dominates, for values substantially greater than one quantum gluon production does so. In the given range of the decay-time t_0 both scenarios are feasible. Smaller values of the decay-time promote the fermionic channel. Larger values advantage the bosonic sector. A priori, none of the possibilities can be discarded and a selfconsistent calculation remains essential.



If the production of gluons dominated clearly, additional quarks and antiquarks must be produced in subsequent inelastic collisions; also after multiple elastic scattering processes [6]. The fermions can be important for the production of hadrons in ultrarelativistic heavy-ion collisions. Here, further calculations also including gluon fragmentation are needed.

References

[1] B. S. Dewitt, Phys. Rev. **162** (1967) 1195; and Phys. Rev. **162** (1967) 1239; G. 't Hooft, Nucl. Phys. B **62** (1973) 444; L. F. Abbott, Nucl. Phys. B **185** (1981) 189.

[2] D. D. Dietrich, G. C. Nayak and W. Greiner, arXiv:hep-ph/0009178.

[3] J. S. Schwinger, Phys. Rev. **82** (1951) 664.

[4] D. D. Dietrich, G. C. Nayak and W. Greiner, Phys. Rev. D **64** (2001) 074006 [arXiv:hep-th/0007139]; G. C. Nayak, D. D. Dietrich and W. Greiner, arXiv:hep-ph/0104030.

[5] R. S. Bhalerao and G. C. Nayak, Phys. Rev. C **61** (2000) 054907 [arXiv:hep-ph/9907322].

[6] J. Ruppert, G. C. Nayak, D. D. Dietrich, H. Stocker and W. Greiner, Phys. Lett. B **520** (2001) 233 [arXiv:hep-ph/0109043].

Partonic Scattering in the Pre-equilibrium Stage of the Gluonic Minijet Plasma

Jörg Ruppert, Dennis D. Dietrich, Gouranga C. Nayak, Horst Stöcker, and Walter Greiner,
Johann-Wolfgang-Goethe-Universität, Frankfurt am Main

If the QGP is formed at sufficientely high energy densities during an ultrarelativistic heavy-ion collision, it is an important question whether the partonic medium will equilibrate and form a thermalized plasma before hadronization sets in. This kind of investigation is also essential for the determination of experimental signatures which crucially depend on the space-time evolution of the parton distributions. The study of the evolution of the minijet plasma requires detailed knowledge about the elementary partonic collisions in the medium. The problem of infrared divergences appearing in the collision integral when using an in-vacuum description of these scattering processes is inevitable. Therefore, a treatment of in-medium effects which removes the poles becomes necessary. As most of the initially produced partons are gluons, hence we consider the gluonic scattering process here only.

We use a medium-modified gluon propagator [1] to evaluate the relevant transport scattering cross section in the QCD medium [2]. The medium modified gluon propagator can be split into longitudinal and transverse parts:

$$\Delta^{\mu\nu}(K) = \frac{P_T^{\mu\nu}}{-K^2+\Pi_T} + \frac{P_L^{\mu\nu}}{-K^2+\Pi_L} + (\alpha-1)\frac{K^\mu K^\nu}{K^4} \quad (1)$$

where α is the gauge fixing parameter. $P_T^{\mu\nu}$ and $P_L^{\mu\nu}$ are longitudinal and transverse tensors. The expressions for Π_L and Π_T in the high temperature expansion are derived by perturbative methods in [1]. The relevant matrix element for the process $gg \to gg$ in the medium is given by:

$$\begin{aligned} M &= g^2 f_{aed} f_{ebc} \epsilon_1^\lambda \epsilon_4^\sigma V^{\lambda\tau\sigma}(-q_1, q_1-q_4, q_4) \\ &\quad \times \Delta_{\tau'\tau}(q_1-q_4) V^{\tau'\mu\nu}(q_2-q_3, -q_2, q_3) \epsilon_2^\mu \epsilon_3^\nu, \quad (2) \end{aligned}$$

where $V^{\mu\lambda\nu}(p_1,p_2,p_3)$ is the three gluon vertex, $\epsilon^\mu(p)$ are the polarization vectors of the gluons, and $\Delta^{\mu\nu}(k)$ is the medium modified gluon propagator as given by Eq. (1). After summing over the final and averaging over the initial spin (we used explicit polarization sums for the gluons [2]) and color degrees of freedom, the general result of the squared matrix element can be obtained. It is explicitly given in [2], especially in Eqs.(14-19). Considering the former leading divergent terms, an effective transport cross section is obtained in the rest frame of the plasma which can directly be incorporated into the transport calculations. The explicit expression is given by:

$$\begin{aligned} \sigma_{\text{tr medium}} = \frac{9\pi\alpha^2}{4}\{ & 2\frac{\ln(\frac{s}{2\Pi_L}+1)+\ln(\frac{s}{2\Pi_T}+1)}{s} \\ & - \frac{4}{s} - \frac{1}{s+2\Pi_L} - \frac{1}{s+2\Pi_T} + \frac{8\ln(\frac{s}{2\Pi_L}+1)\Pi_L^2}{s^2(\Pi_L-\Pi_T)} \\ & - \frac{2s(1-2\ln(\frac{s}{2\Pi_L}+1))\Pi_L}{s^2(\Pi_L-\Pi_T)} \\ & - \frac{4(\ln(\frac{s}{2\Pi_L}+1)-\ln(\frac{s}{2\Pi_T}+1))\Pi_T\Pi_L}{s^2(\Pi_L-\Pi_T)} \\ & + \frac{2\Pi_T(s(1-2\ln(\frac{s}{2\Pi_T}+1))-4\ln(\frac{s}{2\Pi_T}+1)\Pi_T)}{s^2(\Pi_L-\Pi_T)}\}. \end{aligned}$$

In the kinematic situation considered, the self energies are $\Pi_L = m_D^2 = g^2T^2$ and $\Pi_T = m_{mag}^2 = \frac{3}{2}(0.255g^2T)^2$, where the nonperturbative magnetic screening is taken from [3]. These considerations are important for the actual determination of the evolution of the quark-gluon plasma. It can be seen that the above transport cross section gives results different from the transport cross section obtained by using an in-vacuum gluon propagator with the Debye screening mass acting as an infrared cut-off [2]. Hence, it can be expected that all the global quantities and the equilibration times change in comparison to other studies when the vacuum propagator is replaced by the medium modified propagator. All dynamical quantities have to be calculated by the self-consistent evolution of the parton distribution in an analogous manner as in [4]. This requires considerable numerical effort and will be presented elsewhere.

Dynamical effects, which have been taken into account in the derivation of the medium modification, may change the resulting time-dependent transport cross sections. That could lead to a change in the relaxation time and hence to the time evolution of the gluonic plasma. However, these questions will be checked thoroughly by including all features self-consistently in a transport study.

We have restricted the present study to the regularization of the cross section of the purely gluonic part of the plasma. The basic techniques of incorporating in-medium modifications presented here will also play an important role in future studies which will take into account additional degrees of freedom of the quark-gluon plasma. Especially the phase space population of the light and in particular the strange quarks is expected to depend strongly on such in-medium effects. On the one hand the gluon evolution will influence the quark production and distribution; on the other hand the quark evolution itself experiences similiar modification by the medium.

Changes of the cross sections due to effects of the medium will play a crucial role in predicting the energy densities, number densities, effective temperatures, and in fact nearly all signatures of the QGP constituents.

References

[1] H. A. Weldon, Phys. Rev. D **26**, 1394 (1982).

[2] J. Ruppert, G. C. Nayak, D. D. Dietrich, H. Stocker and W. Greiner, Phys. Lett. B **520**, 233 (2001) [hep-ph/0109043].

[3] T. S. Biro and B. Muller, Nucl. Phys. A **561**, 477 (1993) [nucl-th/9211011].

[4] G. C. Nayak, A. Dumitru, L. McLerran and W. Greiner, Nucl. Phys. A **687**, 457 (2001) [hep-ph/0001202].

ATOMIC HEAVY ION PHYSICS

Experiments 85

Developments 105

Theory 116

Experiments

New Determination of the Electron's Mass 85
T. Beier, H. Häffner, N. Hermanspahn, S. G. Karshenboim,H.-J. Kluge, W. Quint,
S. Stahl, J. Verdu, G. Werth

A Study of the Accuracy of ISOLTRAP by Use of Carbon Cluster Ions and New Mass Measurements of ^{32}Ar and ^{72}Sr 86
F. Ames, G. Audi, D. Beck, K. Blaum, G. Bollen, J. Dilling, F. Herfurth, A. Kellerbauer,
H.-J. Kluge, V. Kolhinen, M. Kuckein, D. Lunney, R.B. Moore, D. Rodríguez, E. Sauvan,
C. Scheidenberger, S. Schwarz, L. Schweikhard, G. Sikler, C. Weber

Measurement of the 1s-Lambshift of H-like Gold at the ESR Gasjet-Target by Absorption-Edge Technique 87
M. Czanta, C. Strietzel, S. Toleikis, H.J. Besch, H.F. Beyer, F. Bosch, M. Steck,
A. Gumberidze, O. Klepper, C. Kozhuharov, J. Lawall, D. Liesen, X. Ma, B. Manil,
Th. Stöhlker, A.H. Walenta

The Crucial Consequences of Beam Displacements for High-Resolution Spectroscopy at the ESR Gasjet-Target 88
M. Czanta, C. Strietzel, S. Toleikis, H.J. Besch, H.F. Beyer, F. Bosch, A. Gumberidze,
O. Klepper, C. Kozhuharov, J. Lawall, D. Liesen, X. Ma, B. Manil, M. Steck, Th. Stöhlker,
A.H. Walenta

Study of the Two-Electron Lamb Shift in High-Z Helium-Like Ions 89
A. Gumberidze, Th. Stöhlker, G. Bednarz, H.F. Beyer,F. Bosch, X. Cai, S. Hagmann,
S. Toleikis, C.Kozhuharov, D. Liesen, X. Ma, P.H. Mokler, O.Klepper,
D. Sierpowski,Z.Stachura, M. Steck, A.Warczak, Y. Zou

Lifetime Measurement of the Metastable 2^3P_0 State in Helium-Like ^{238}U 91
S. Toleikis, B. Manil, G. Bednarz, E. Berdermann, H.F. Beyer, F. Bosch,
A. Bräuning-Demian, A. Gumberidze, S. Hagmann, P. Indelicato, C. Kozhuharov,
D. Liesen, X. Ma, R. Marrus, P.H. Mokler, Z. Stachura, Th. Stöhlker, A. Warczak

Precise Lifetime Measurement for the $1s^22p\ ^2P_{3/2}$ Level of Li-like Ni 93
Y. Zou, D. Feili, R. Hutton, C. Neacsu, K.-H. Schartner, X. Ma, P.H. Mokler

QED Sensitivity of the $2s^2\ ^1S_0$- $2s2p\ ^3P_1$ Intercombination Transition in Be-like Ag^{43+} and Xe^{50+} Ions 94
D. Feili, Ph. Bosselmann, C. Neacsu, K.-H. Schartner, A.E. Livingston,
F. Folkmann, P.H. Mokler

Photorecombination Studies of Lithium-Like Uranium Ions 95
C. Brandau, T. Bartsch, K. Beckert, S. Böhm, C. Böhme, F. Bosch, B. Franzke, N. Grün,
A. Hoffknecht, H. Knopp, S. Kieslich, C. Kozhuharov, P.H. Mokler, A. Müller, F. Nolden,
W. Scheid, S. Schippers, W. Shi, Z. Stachura, M. Steck, T. Steih, Th. Stöhlker

The Lyman-α_1 Decay in Hydrogen-Like Ions: Interference between the E1 and M2 Transition Amplitudes 97
Th. Stöhlker, A. Surzhykov, S. Fritzsche, A. Gumberidze

Search for Correlated Electron Capture in Relativistic U^{92+} Collisions 98
G. Bednarz, D. Sierpowski, Th. Stöhlker, A. Warczak, H. Beyer, F. Bosch,
A. Bräuning-Demian, H. Bräuning, X. Cai, A. Gumberidze, S. Hagmann, O. Klepper,
C. Kozhuharov, D. Liesen, X. Ma, P.H. Mokler, A. Muthig, Z. Stachura, S. Toleikis

New Results from the GSI REACTION MICROSCOPE 99
R. Moshammer, H. Kollmus, S. Hagmann, M. Schulz, R. Mann, B. Feuerstein, A. Dorn,
D. Fischer, C. Höhr, C.D. Schroeter, J.R. Crespo Lopez-Urrutia, R.E. Olson, J. Ullrich

Orientation Dependence of Multiple Ionization of Diatomic Molecules in Collisions with Fast Highly Charged Ions 101
B. Siegmann, U. Werner, N.M. Kabachnik, H.O. Lutz, R. Mann

Channeling Experiment with 20 MeV/u U^{91+} Ions Extracted from the ESR Storage Ring 102
D. Dauvergne, A. Bräuning-Demian, F. Bosch, H. Bräuning, M. Chevallier, C. Cohen,
A. Gumberitze, A. L'Hoir, R. Kirsch, C. Kozhuharov, D. Liesen, P.H. Mokler,J.-C. Poizat,
C. Ray, Th. Stöhlker, M. Tarisien, S. Toleikis, M. Toulemonde

Multiple Electron Capture from C-foils into Slow Highly-Charged Ions 103
H. Bräuning, A. Bräuning-Demian, G. Bednarz, F. Bosch, X. Cai, C. Cohen, D. Dauvergne,
A. Gumberidze, H. Harutyunyan, R. Kirsch, C. Kozhuharov, D. Liesen, P.H. Mokler,
J.-P. Rozet, Z. Stachura, Th. Stöhlker, M. Terasawa, S. Toleikis, A. Warczak

Impact of Extended Charge Distribution on Energy-Loss Straggling of Heavy Ions 104
H. Weick, A.H. Sørensen, H. Geissel, C. Scheidenberger

Developments

PHELIX, a Petawatt High Energy Laser for Heavy-Ion Experiments 105
Th. Kühl, J. Alvarez, B. Becker-de Mos, R. Bock, S. Borneis, E. Brambrink, H. Brand,
D. Browning, C. Bruske, K. Brück, J. Caird, E. Dewald, H. Duddek, E. W. Gaul, C. Häfner,
T. Hahn, D.H.H. Hoffmann, H.-J. Kluge, D. Marx, P. Neumayer, M. Perry, K. Poppensieker,
D. Reemts, I. Reinhard, M. Roth, S. Samek, W. Seelig, A. Tauschwitz, R. Wilcox

X-Ray Laser Spectroscopy on Lithium-like Ions 107
P. Neumayer, J. Alvarez, A. Bardonner, B. Becker-de Mos, S. Borneis, K. Brück,
C. Bruske,E.W. Gaul, C. Häfner, K. Janulewicz, H.-J. Kluge, T. Kühl, D. Marx,
I. Reinhard, M. Tomaselli,P.V. Nickles, W. Sandner, W. Seelig

Preparation for High-Resolution Isotope Shift Measurements of ^{8,9,11}Li 108
H. Wang, A. Dax, W. Nörtershäuser, I. Katayama, R. Kirchner, H.-J. Kluge,
T. Kühl, R. Sanchez, I. Tanihata, M. Tomaselli, C. Zimmermann

SHIPTRAP : A Capture and Storage Facility for Radionuclides from SHIP 109
D. Ackermann, H. Backe, F. Bosch, J. Dilling, A. Dretzke, H. Geissel, D. Habs, F.P. Heßberger,
S. Hofmann, H.-J. Kluge, C. Kozhuharov, W. Lauth, R. Mann, G. Marx, G. Münzenberg,
M. Mukherjee, J. Neumayr, W. R. Plaß, W. Quint, S. Rahaman, D. Rodríguez, C. Scheidenberger,
M. Sewtz, G. Sikler, T. Stöhlker, P.G. Thirolf, M. Tarisien, C. Weber, Z. Zhou, L. Beck,
O. Engels, D. Habs, S. Heinz, V. Varentsov, F. Voit, A. Wilfart, H. Backe, A. Dretzke, T. Kolb,
G. Kube, A. F. Dodonov, S. A. Elisseev, Yu.N. Novikov, Z.Wang, M. Weidenmüller

HITRAP: A Facility for Experiments with Trapped Highly Charged Ions 113
S. Djekic, H.-J. Kluge, G. Marx, W. Quint, U. Ratzinger, D. Rodríguez, T. Stöhlker, M. Tarisien, T. Valenzuela, J. Verdú, G. Werth

Micro Structure Electrodes: A New Multipurpose Plasma Source 114
A. Bräuning-Demian, O. Hohn, T. Jahnke, C. Penache, S. Schößler, L. Spielberger, H. Schmidt-Böcking

Theory

Structure of Degenerate Boson-Fermion Mixtures 116
R. Roth, H. Feldmeier

Nuclear Anapole Moments from Beams of Highly-Charged Ions 117
I. Bednyakov, F. Erler, C. Lucke, I. Nandori, G. Schaller, R. Schützhold, A. Nefiodov, G. Plunien, G. Soff, L.N. Labzowsky, R. Kuhn, D. Liesen

Nuclear and Electron Polarization Contributions to the HFS of Hydrogen- and Lithium-Like Ions 118
M. Tomaselli, T. Kühl, W. Nörtershäuser, D. Marx, A. Dax, H. Wang, R. Sanchez, S. Fritzsche

Recoil Correction to the g Factor of H-like Ions to all Orders in αZ 119
V.M.Shabaev, V.A.Yerokhin

QED Calculations of the Interelectron Interactions in Li-like Ions 120
I. Bednyakov, F. Erler, C. Lucke, R. Kuhn, I. Nandori, G. Schaller,R. Schuetzhold, G. Plunien, G. Soff, O.Yu. Andreev, L.N. Labzowsky, V.M. Shabaev, V.A. Yerokhin

Two-Photon Processes in Dielectronic Recombination 121
S. Zakowicz, Z. Harman, N. Grün, W. Scheid

Photon Polarization in Radiative Recombination of Bare High-Z Ions 122
A. Surzhykov, S. Fritzsche, Th. Stöhlker

Scaling Law for the Recombination Enhancement in Electron Coolers 123
C. Heerlein, C. Toepffer

Ion Stopping in a Magnetized Anisotropic Electron Plasma 124
M. Walter, G. Zwicknagel, C. Toepffer, B. Möllers

Interaction of Fast Ion Beams with Low- and High-Density Targets 125
O. Rosmej, Th. Stöhlker, V.P. Shevelko, I.Yu. Tolstikhina

Fast Electron Emission in Atomic Collisions under Strong-Field, Nonperturbative Conditions and the Fermi-Shuttle Mechanism 126
D.-C.Ionescu



New Determination of the Electron's Mass

T. Beier[a], H. Häffner[a,b], N. Hermanspahn[b], S. G. Karshenboim[c,d], H.-J. Kluge[a], W. Quint[a], S. Stahl[b], J. Verdú[a,b], and G. Werth[b]

[a] *Gesellschaft für Schwerionenforschung, 64291 Darmstadt, Germany*

[b] *Institut für Physik, Universität Mainz, 55099 Mainz, Germany*

[c] *D. I. Mendeleev Institute for Metrology (VNIIM), 198005 St. Petersburg, Russia*

[d] *Max-Planck-Institut für Quantenoptik, 85748 Garching, Germany*

The mass of the electron is a fundamental physical constant, up to now known to a relative precision of 2.1×10^{-9} from an experiment by Farnham *et al.* [1] who carried out measurements subsequently observing a single $^{12}C^{6+}$ ion and alternately clouds of $5 - 13$ electrons in a Penning trap. They obtained $m_e = 0.000\,548\,579\,911\,1\,(12)$ u. The recent compilation of the Recommended Values of Fundamental Physical Constants [2] is mainly based on this value.

We have successfully developed and tested a setup for investigating g factors of highly charged ions [3, 4]. Microwave irradiation induces spin-flip transitions within the system. For zero nuclear spin, the transition frequency is equal to the electronic Larmor precession frequency ω_L, given by $\omega_L = g\,(e)/(2\,m_e)\,B$ where e is the positive elementary charge unit. Calibrating the magnetic field by the cyclotron frequency $\omega_c = B(q/m_{ion})$ of an ion, the mass of the electron is obtained as

$$m_e = \frac{g}{2}\frac{e}{q}\frac{\omega_c}{\omega_L} m_{\rm ion} \qquad (1)$$

where $m_{\rm ion}$ denotes the mass of the ion. Thus only the g factor and the frequency ratio ω_L/ω_c have to be known to determine the electron's mass in units of the ion mass from our experiment. For hydrogenlike systems, the g factor can be accurately calculated ([5], for low-Z systems also [6]; and references therein). The frequency ratio ω_L/ω_c for $^{12}C^{5+}$ was recently measured by us [3].

Employing the published value for the electron's mass [2], we obtain $g(^{12}C^{5+}) = 2.001\,041\,596\,3\,(10)\,(44)$ where the first error results from the uncertainties of the measured frequency ratio and the second one is due to the uncertainty in the known value of the electron's mass.

The theoretical value of $g(^{12}C^{5+})$ is given by the Dirac value for the g factor in the ground state of a hydrogenlike ion with nuclear charge Z, $g_{1s} = (2/3)(1+2\sqrt{1-(Z\alpha)^2})$, plus additional corrections for finite nuclear size and mass, and for QED effects. The QED effects are calculated up to order $(\alpha/\pi)^4$ for the free electron (cf. [7] and references therein). Additional bound-state QED corrections are known non-perturbatively in $Z\alpha$ up to order (α/π) ([5] and references therein). For the current theoretical value we adopt

$$g(^{12}C^{5+}) = 2.001\,041\,589\,9\,(10) \quad . \qquad (2)$$

The individual contributions to the theoretical value are presented in Table 1. A detailed discussion of this table and all theoretical contributions is provided by [8].

One essential improvement is the evaluation of the recoil effect to the g factor to all orders in $Z\alpha$ for the order (m_e/M_N) where M_N is the mass of the nucleus [9, 10], cf. also the corresponding article of Shabaev and Yerokhin in this annual report. It did not change the numerical value but diminished the theoretical uncertainty considerably.

Table 1: Theoretical contributions to $g(^{12}C^{5+})$.

Dirac theory (incl. binding)	1.998 721 354 4(0)
Finite-size correction	+0.000 000 000 4(0)
Recoil	+0.000 000 087 6(0)
QED, order (α/π)	+0.002 323 663 7(9)
QED, orders $(\alpha/\pi)^2$ to $(\alpha/\pi)^4$	−0.000 003 516 2(4)
Total theoretical value:	2.001 041 589 9(10)

Experiment and theory for the g factor of $^{12}C^{5+}$ agree within 1.5 standard deviations. The largest uncertainty results from the knowledge of the electron's mass. Therefore it is reasonable to turn around our arguments and instead derive a new value for the atomic mass of the electron. Hereby we rely on the validity of quantum electrodynamics to our level of precision.

We obtain for the atomic mass of the electron

$$m_e = 0.000\,548\,579\,909\,24\,(29)(27)\ \text{u} \quad . \qquad (3)$$

The first error margin results from the experimental uncertainty of the ratio ω_L/ω_c and the second one from the error margin of the theoretical prediction. In total, our uncertainty amounts to 4×10^{-13} u which corresponds to a relative precision of 7.3×10^{-10}.

Comparing our result (3) with the one from [1], we find but a small difference of about 1.5 standard deviations. Our error margins are three times smaller and also three times smaller than those of [2]. We consider our value as an important consistency check. For the proton-electron mass ratio, we obtain $m_p\,/\,m_e = 1836.152\,673\,3\,(14)$ where the CODATA value for the atomic mass of the proton was employed, $m_p = 1.007\,276\,466\,88\,(13)$ u. Further details of the presented investigation are provided by [8].

We are grateful to R. N. Faustov, P. J. Mohr, V. M. Shabaev, G. Soff, B. N. Taylor, A. S. Yelkhovsky, and V. A. Yerokhin for many enlightening and stimulating discussions. Financial support was obtained from the European Union under the contract number ERB FMRX CT 97-0144 (EUROTRAPS network).

References

[1] D. L. Farnham, R. S. Van Dyck, Jr., and P. B. Schwinberg, Phys. Rev. Lett. **75**, 3598 (1995).
[2] P. J. Mohr and B. N. Taylor, Rev. Mod. Phys. **72**, 351 (2000).
[3] H. Häffner *et al.* Phys. Rev. Lett. **85**, 5308 (2000).
[4] N. Hermanspahn *et al.* Phys. Rev. Lett. **84**, 427 (2000).
[5] T. Beier, Physics Reports **339**, 79 (2000).
[6] S. G. Karshenboim, V. G. Ivanov, and V. M. Shabaev, Zh. Eksp. Teor. Fiz., **120**, 546 (2001) [JETP **93**, 477 (2001)]
[7] V. W. Hughes and T. Kinoshita, Rev. Mod. Phys. **71**, 133 (1999).
[8] T. Beier *et al.*, Phys. Rev. Lett. **88**, 011603 (2002).
[9] V. M. Shabaev, Phys. Rev. A **64**, 052104 (2001).
[10] V. M. Shabaev and V. A. Yerokhin, Phys. Rev. Lett. **88**, 091801 (2002)

A Study of the Accuracy of ISOLTRAP by Use of Carbon Cluster Ions and New Mass Measurements of ^{32}Ar and ^{72}Sr

F. Ames[1], G. Audi[7], D. Beck[3], K. Blaum[3], G. Bollen[5], J. Dilling[3], F. Herfurth[1], A. Kellerbauer[1], H.-J. Kluge[3], V. Kolhinen[4], M. Kuckein[1], D. Lunney[7], R.B. Moore[6], D. Rodríguez[3], E. Sauvan[1], C. Scheidenberger[3], S. Schwarz[5], L. Schweikhard[2], G. Sikler[3] and C. Weber[3]

CERN[1], Greifswald[2], GSI[3], Jyväskylä[4], Michigan[5], Montreal[6], Orsay[7]

The ISOLTRAP system is a tandem Penning trap mass spectrometer installed at the on-line mass separator ISOLDE/CERN. The mass determination of short-lived nuclides is carried out via determination of the cyclotron frequency of stored ions. The magnetic field is calibrated by measuring the well-known mass of a stable isotope. So far ISOLTRAP has been used for mass measurements of more than 200 radioactive nuclides [1]. The high accuracy achieved ($\delta m/m \sim 10^{-7}$) improved our knowledge of binding energies far from stability considerably and served for e.g. testing nuclear models and astrophysical calculations.

Figure 1 shows the present layout of the ISOLTRAP spectrometer. The linear gas-filled radiofrequency quadrupole (RFQ) trap has the task to stop the 60 keV ISOLDE beam and to prepare it for efficient transfer into the first Penning trap. The gas-filled cylindrical Penning trap is used for further cooling and isobaric separation of the ions. The precision hyperbolic Penning trap is the actual mass spectrometer where the mass measurement is performed via the determination of the cyclotron frequency $\omega_c = q \cdot B/m$ of the ion with mass m and charge q revolving in the magnetic field of strength B.

Recently, we have introduced a new method to determine the accuracy of these measurements by use of singly charged carbon clusters C_n ($n \geq 2$) for magnetic field calibration. The carbon cluster ions are produced externally by use of nanosecond laser desorption, fragmentation and photoionization of C_{60} at 532 nm [2]. They are then injected and stored in the Penning trap system.

Based on the definition of the atomic mass unit as 1/12 of the mass of ^{12}C, carbon clusters are ideal mass references for absolute mass measurements, since they eliminate by definition the uncertainty of the mass of the reference ion. In addition, the observation of cyclotron frequencies of different cluster sizes up to n = 20 allowed for the study of systematic effects. The mass-dependent systematic error was determined to be $2.0(7) \cdot 10^{-10} \Delta m/u$ (the previously estimated value was $\sim 2 \cdot 10^{-9} \Delta m/u$), with Δm the mass difference between the measured isotope and the reference ion, and the present limit of mass accuracy $\delta m/m$ is $8 \cdot 10^{-9}$ (previously $\sim 1 \cdot 10^{-7}$) [3] .

In addition, due to technical developments like improving different parts of the ion transfer, we were able to increase our overall efficiency by a factor of ~100. This allowed us to successfully measure the mass of ^{72}Kr and ^{32}Ar, both with a relative accuracy of better than $1 \cdot 10^{-7}$, during the two beam times carried out in 2001.

In the first beam time, using a thin Nb foil target, the mass of the rp-process waiting point nucleus ^{72}Kr was measured. Furthermore we verified last year's measurements of $^{73-78}$Kr and confirmed the deviation of the mass of ^{78}Kr from the Audi/Wapstra mass table [4].

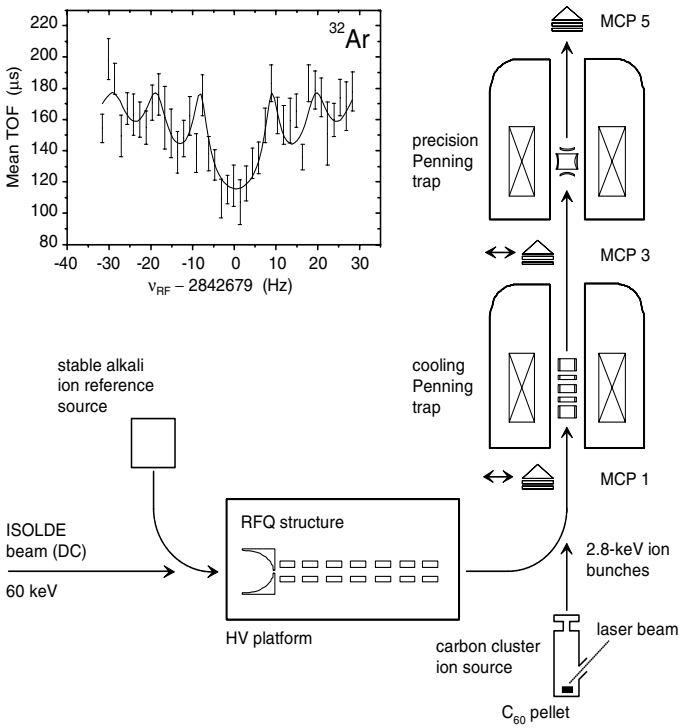


Figure 1: Schematic drawing of ISOLTRAP with the new carbon cluster laser ion source. Multi-channel plate (MCP) detectors are used to monitor the ion transfer as well as to record the time-of-flight resonance (MCP5) for the determination of the cyclotron frequency. The spectrum shows the cyclotron resonance curve of $^{32}Ar^+$ with a fit of the theoretically expected line shape to the data points.

The second beam time was dedicated to the measurement of the mass of ^{32}Ar produced in a CaO target. A very accurate mass value of this isotope is of importance for the search of scalar currents in weak interaction in the experiment performed by Adelberger et al. [5] and for a stringent test of the Isobaric-Multiplet-Mass-Equation. Although the ISOLDE yield for ^{32}Ar was only ~100 atoms/proton pulse, ISOLTRAP succeeded in measuring the mass with the desired accuracy of better than 3 keV within two days.

Supported by the European Union (EUROTRAPS Network) and by BMBF.

References :

[1] G.Bollen, Nucl. Phys. A 693 (2001) 3-18.

[2] K. Blaum *et al.*, in: Proc. ENAM 2001 Conf., EPJA (submitted).

[3] A. Kellerbauer *et al.*, in: Proc. APAC 2001 Conf., Hyp. Int. (submitted).

[4] F. Herfurth *et al.*, in: Proc. ENAM 2001 Conf., EPJA (submitted).

[5] E.G. Adelberger et al., in: Phys.Rev.Lett. 83 (1999) 1299

Measurement of the 1s-Lambshift of H-like Gold at the ESR Gasjet-Target by Absorption-Edge Technique

M. Czanta[1], C. Strietzel[2], S. Toleikis[1], H.J. Besch[2], H.F. Beyer[1], F. Bosch[1], A. Gumberidze[1], O. Klepper[1], C. Kozhuharov[1], J. Lawall[4], D. Liesen[1], X. Ma[1], B. Manil[3*], M. Steck[1], Th. Stöhlker[1], A.H. Walenta[2]
[1] GSI Darmstadt, Germany; [2] Universität Siegen, Germany;
[3] Université de Paris, France; [4] NIST Gaithersburg, USA.

While QED is very well tested in the case of light atoms, a crucial test in the strong-field domain is still missing. Such a test can be realized by the spectroscopy of Ly-α lines of H-like heavy ions. However, new experimental concepts with a substantially higher spectral resolution than existing methods have become indispensible.

Absorption-edge techniques have the capacity to overcome the remaining gap in accuracy between experiment and theory. Therefore, an experiment was performed taking advantage of the $(20-50)$ eV wide absorption edges of heavy absorbers [1]. These edges serve as a precise energetic reference to determine the photonic energies of the characteristic x-rays emitted by highly-charged heavy ions. In the experiment, the Ly-$\alpha 2$ photons of Au^{78+} were detected in coincidence with down-charged ions at three observation angles simultaneously, as depicted in Fig. 1. Moreover, the measurement was carried out at the two different ion velocities $\beta = 0.2530$ and $\beta = 0.4196$.

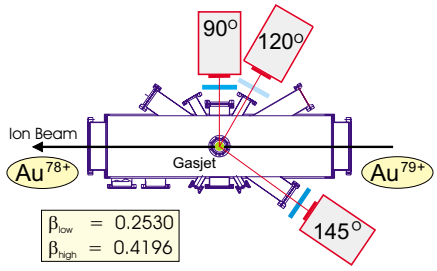


Figure 1: Experimental setup of the experiment. Three position-sensitive drift chambers measure the intensity variations resulting from the shift of the Ly-$\alpha 2$ lines of Au^{78+} over the absorption edges of heavy absorbers due to the angle-dependent Doppler-effect.

In order to determine the energy of the Ly-$\alpha 2$ line, three position-sensitive drift chambers [1, 2] measured the intensity variation of the corresponding photons across the K-edges of the absorbers arising from the angle-dependent Doppler shift. Fig. 2 shows the result for 90° at $\beta = 0.2530$. Plotted is the observed intensity along the horizontal coordinate in the central plane of the detector, integrated over height and depth. The peaks to the left and right arise from geometrical effects of the detector.

The analysis was carried out by a Monte-Carlo simulation of the spatial intensity variation of the detected photons. In this program, the size of the emitting volume, the observation angle and the photonic energy in the rest frame are free parameters. The latter two are varied independently and χ^2 serves as a measure for the agreement between the measured and the simulated intensity variation. The uncertainty in the energy of the photons or in the corresponding angle respectively was defined by a 10% deviation from the χ^2-minimum.

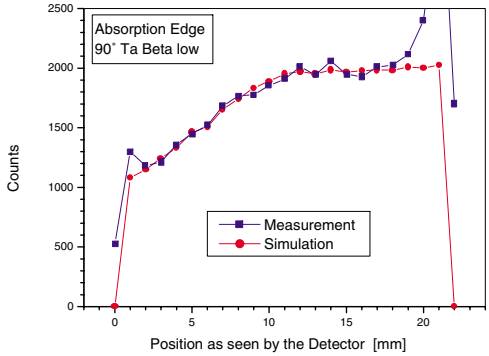


Figure 2: Measured and simulated intensity variation of the Ly-$\alpha 2$ line of Au^{78+} along the K-edge of an Ta-absorber at 90° and $\beta = 0.2530$. The sharp peaks arise from a geometrical effect inside the drift chamber.

The result in the determination of the 1s-Lambshift of H-like Gold is summerized in Tab. 1 together with results of theoretical calculations [3] and of a former experiment at the ESR electron-cooler [4]. The uncertainty is dominated by the geometrical situation as found at the gasjet-target of the ESR [5].

1s-Lambshift of Au^{78+}	
Theory	(205.7 ± 1.0) eV
Electron-Cooler	(212.0 ± 7.9) eV
Absorption-Edge Technique, 90°	(210.5 ± 8.8) eV

Table 1: The 1s-Lambshift of Au^{78+} according to theory [3], the former experiment at the ESR electron-cooler [4] and the experiment with the absorption-edge technique [1].

A value of (210.5 ± 8.8) eV for the 1s-Lambshift of Au^{78+} has been found. Moreover, a more stringent beam control and a reduction of the visible size of the emitting volume are indispensible.

* supported by EC-HPRI-CT-1999-00001.

References

[1] M. Czanta, Thesis, Universität Siegen, 2001
[2] C. Strietzel, Thesis, Universität Siegen, 2000
[3] T. Beier et al., Phys. Lett. A **236**, 329 (1997)
[4] H.F. Beyer et al., Z. Phys. D **35**, 169 (1995)
[5] M. Czanta et al., GSI Scient. Rep. 2001, *The Crucial Consequences of Beam Displacements*

The Crucial Consequences of Beam Displacements for High-Resolution Spectroscopy at the ESR Gasjet-Target

M. Czanta[1], C. Strietzel[2], S. Toleikis[1], H.J. Besch[2], H.F. Beyer[1], F. Bosch[1], A. Gumberidze[1], O. Klepper[1], C. Kozhuharov[1], J. Lawall[4], D. Liesen[1], X. Ma[1], B. Manil[3*], M. Steck[1], Th. Stöhlker[1], A.H. Walenta[2]
[1] GSI Darmstadt, Germany; [2] Universität Siegen, Germany;
[3] Université de Paris, France; [4] NIST Gaithersburg, USA.

Taking advantage of the great progress in storage-ring technology in the last decade of the past millennium, it became possible to access very heavy atomic systems in the highest ionized states.

At the storage ring ESR at the GSI Darmstadt, cooled brilliant ion beams of the heaviest, fully stripped atoms up to bare uranium with corresponding small momentum spreads and low emittance are available. At the gasjet-target, fundamental questions with regard to recombination processes, the internal structure and the dynamics of highly-charged heavy ions can be adressed by the spectroscopy of the radiation emitted by these systems.

Resulting from the relativistic velocities of the ions in the ESR, the characteristics of the observed radiation are influenced by the Lorentz-transformation. The photonic energies in the laboratory frame E_{lab} result from the ones in the emitter frame E_{em} according to $E_{lab} = \frac{E_{em}}{\gamma \cdot [1-\beta\cos(\Theta)]}$ with $\gamma = \frac{1}{\sqrt{1-\beta^2}}$. They are strongly depending on both transformation parameters, namely the observation angle Θ and the ion velocity β.

Former experiments aiming for a high-precision spectroscopy of the characteristic radiation from heaviest, highly-charged ions were focused on an increased spectral resolution. As a result, the 1s-Lambshift of H-like uranium has been measured to (-468 ± 13) eV [1].

To overcome the inherent limitations in the spectral resolution of the existing methods, a new experimental approach was designed which is based on an absorption-edge technique. Based on the greatly enhanced spectral resolution of this technique, an experiment at the gasjet-target of the ESR was performed to measure the 1s-Lambshift of H-like gold [2, 3]. The radiated photons were observed at three different angles simultaneously: $90°$ and $120°$ inside and $145°$ outside of the ESR. Moreover, the measurement was carried out at two ion velocities: $\beta = 0.2530$ and $\beta = 0.4196$.

As a result of these geometrical conditions, displacements of the ion beam were identified. While the observation was independent of vertical tilts and shifts of the beam, tilts and parallel displacements in the horizontal plane were found. Fig. 1 shows the geometry.

The data of the observation angle $90°$ reveals a tilt of the beam at high energies with respect to the case of low beam energy of $-1,4$ mrad. This implies a shift in the photonic energy in the emitter frame of (52 ± 18) eV.

The measurements at $120°$ inside and $145°$ outside the ESR depend in addition on horizontal parallel beam displacements. The data imply that the low-energy beam was shifted approximately 5 mm to the inside of the storage ring. In the case of high ion velocity the beam was shifted to the outside of the ring by 5 mm. The results are shown in Fig. 2, indicating a relative beam displacement of approximately 10 mm which corresponds to a change in the photonic energies in the emitter frame of nearly 200 eV for the chosen setup.

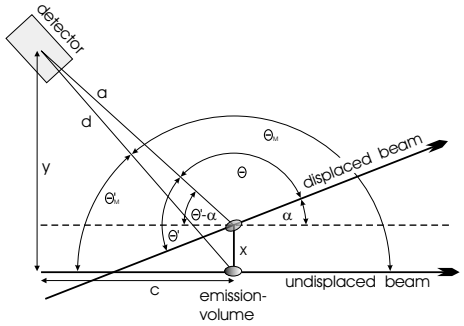


Figure 1: Geometrical position of the ion beam at the ESR gasjet-target in the horizontal plane. The beam displacement includes a tilt α and a parallel shift x.

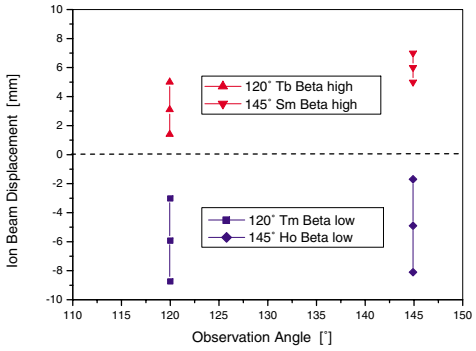


Figure 2: Parallel displacements of the ion beam in the horizontal plane as found by the observation at $120°$ at the inside and $145°$ at the outside of the ESR for two ion velocities.

Therefore, a stringent geometrical control of the ion beam at the gasjet-target at the ESR has become indispensible for present-day high-resolution spectroscopy. This holds for all experiments which are based on the accurate knowledge of the geometry of the emission volume.

* supported by EC-HPRI-CT-1999-00001.

References

[1] Th. Stöhlker et al., Phys. Rev. Lett. **85**, 3109 (2000)
[2] M. Czanta, Thesis, Universität Siegen, 2001
[3] M. Czanta et al., GSI Scient. Rep. 2001, *Measurement of the 1s-Lambshift of H-like Gold at the ESR Gasjet-Target by Absorption-Edge Technique*

Study of the Two-Electron Lamb Shift in High-Z Helium-Like Ions

A. Gumberidze[1,2,8], Th. Stöhlker[1,2], G. Bednarz[3], H.F. Beyer[1], F. Bosch[1], X. Cai[6], S. Hagmann[5], O. Klepper[1], C. Kozhuharov[1], D. Liesen[1], X. Ma[6], P.H. Mokler[1], D. Sierpowski[3], Z. Stachura[4], M. Steck[1], S. Toleikis[1], A. Warczak[3], Y. Zou[7]

[1]GSI-Darmstadt, Germany, [2]IKF, Univ. of Frankfurt, Germany, [3]Institute of Physics, Cracow University, [4]INP, Cracow, Poland, [5]Kansas State University, Kansas, USA, [6]IMP, Lanzhou , China, [7]Fudan University, Shanghai, China, [8]Tbilisi State University, Georgia

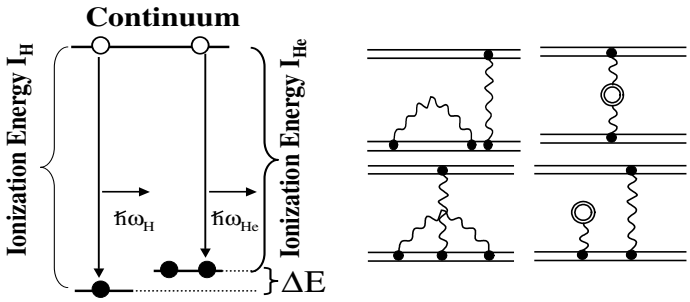


Figure 1: Left side: Schematic presentation of the RR process of free electrons into the initially bare and H-like ions. The energy difference $\Delta E = \hbar\omega_H - \hbar\omega_{He}$ gives exactly the two-electron contribution to the ionization potential in He-like ions. Right side: Feynman diagrams for the two-electron self energy and vacuum polarization.

Helium-like ions are the simplest atomic multi-body systems. Very recently the theoretical as well as the experimental investigations of these fundamental systems gained a considerable improved precision [1, 2]. The experimental progress manifests itself in a novel approach and exploits Radiative Recombination (RR) transitions into the vacant 1s shell of bare and H-like ions [2]. In this process an electron may undergo a direct transition into a bound state of the stationary ion via the emission of a photon carrying away the energy difference between the initial and final electron state, i.e. $\hbar\omega = E_{kin} + E_B$ (compare Fig. 1). The difference in the centroid energies for such radiative recombination transitions into the vacant K-shell of bare and H-like high-Z ions is equal to the difference in the ionization potential between the hydrogen-like and the heliumlike ions formed by the recombination process. It gives exactly the two-electron contribution to the ground-state energy of the heliumlike ions. Most important, all one-electron contributions to the binding energy such as the finite-nuclear size corrections and the one-electron self-energy cancel out completely in this type of experiment [1]. These first experiments on the ground-state of He-like ions conducted at Super-EBIT were very successful and provided to the very first time results which are at the threshold to become sensitive to higher order QED effects [2, 3]. However, at high nuclear charges such as Z = 83 or even Z = 92 it turned out that the production efficiency for bare ions is not sufficient and the results suffered by counting statistics. Very recently we applied this technique at the electron cooler device at the ESR storage ring for the case of He-like uranium. The aim of this experiment is to measure precisely the two-electron contribution to the ionization potential in He-like uranium of 2.2 keV with an accuracy better than 5 eV. Since two-electron QED effects are calculated to contribute 7 eV [1], such an experimental study would therefore provide the very first test of higher-order QED corrections (higher order in α) in the domain of high-Z ions (some of the relevant Feynman diagrams are displayed in Fig. 1).

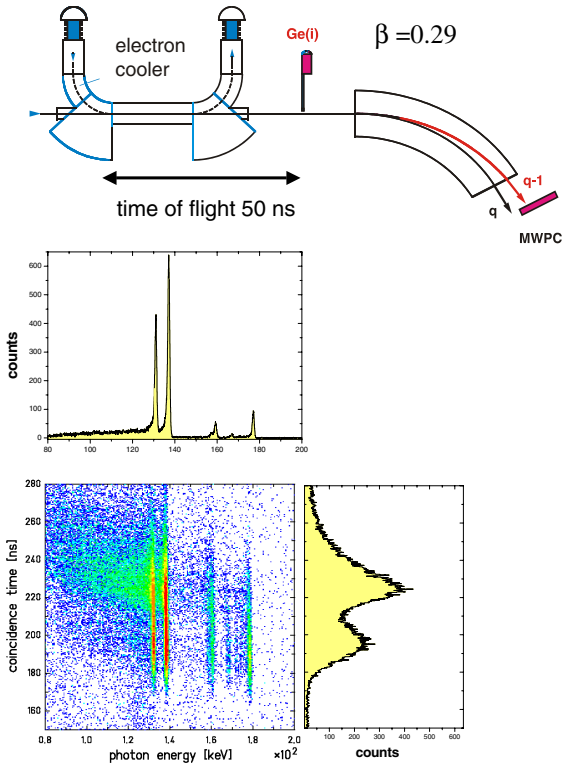


Figure 2: Sketch of the experimental setup (top) and two dimensional scatter plot of the observed x-ray emission versus the coincidence time. The latter refers to the time difference between photon and particle detection. The pronounced structure observed in the time spectrum (right side) allows us to disentangle between photon emission which has occurred inside the electron cooler section and such events where the emission takes place just in front of the x-ray detector.

For the experiment, the setup available at the electron cooler section was used (cf. top of Fig. 2). There, the x-rays emitted via RR of the cooler electrons into the ground

state of the bare- or H-like ions can be detected by a solid state detector which views the interaction region at an observation angle close to 0° [4]. Because the key feature of the experiment is a relative measurement of RR into the K-shell of initially bare and H-like uranium, we changed during the experiment three times between the two charge states. Compared to a simultaneous storage of both charge states, also possible at the ESR, this applied method has the advantage to allow us to measure the x-ray emission in coincidence with the down-charged ions by using a particle detector located behind the next dipole magnet (compare scheme of the experimental set-up displayed in Fig. 2).

In particular the experiment benefits from the recent established deceleration technique [5]. At low energies, all uncertainties associated with Doppler corrections are strongly reduced compared to high-energy beams. Also, for decelerated ions the bremsstrahlung intensity caused by the cooler electrons is strongly reduced (due to the comparably small cooler voltage of 27 kV and current of 100 mA). Consequently, very clean conditions for x-ray spectroscopy are present at the cooler section. This is depicted in Fig. 3 where a preliminary calibrated, coincident x-ray spectrum is plotted as observed for initially bare uranium ions at an energy of 43 MeV/u. Note, the strongly reduced bremsstrahlung intensity allowed us for the very first time to observe even RR transitions into the L-shell, located at the low-energy part of the spectrum. In the spectrum, the x-ray transitions for RR into the ground state show up in the high energy part of the spectrum which are of particular interest for the current study. Most important, the tails of the Lyman-α transition lines, caused by cascade feeding of the L-shell levels [4], are consequently not present in the case of the RR photon emission. A further important aspect of our study is that due the low β-value of 0.29 and the experimental time resolution of about 20 ns, photon events which occurred inside the cooler section can be distinguished from events where the emission took place just in front of the x-ray detector. For the latter x-ray events, the set-up possesses a comparably large solid angle and the photon energy appears markedly shifted leading to the low-energy tails of the Lyman radiation.

In Fig. 4 we depict the photon spectra which were accumulated by using a time condition (see Fig. 2) which excludes most of the cascade contributions leading to the low-energy tails. Indeed, as observed in Fig. 4, the time condition used eliminates almost completely the low energy tails and reduces also the intensity of the Lyman transitions but leads the K-RR lines practically unaffected. However, even the centroids of the K-RR lines might be affected by this time condition applied, because Lyman transition arising from high-n levels may contribute to the x-ray background located at the low-energy region of the K-RR lines. In the inset of Fig. 3 the energy regime relevant for K-RR transitions is displayed. There the line intensities as measured for initially bare- and H-like uranium are compared. From a first preliminary analysis, a statistical accuracy for the splitting close to 9 eV can already be stated. Keeping in mind that for collection of the data a total beam time of 4 days has been used, a second more extended run should

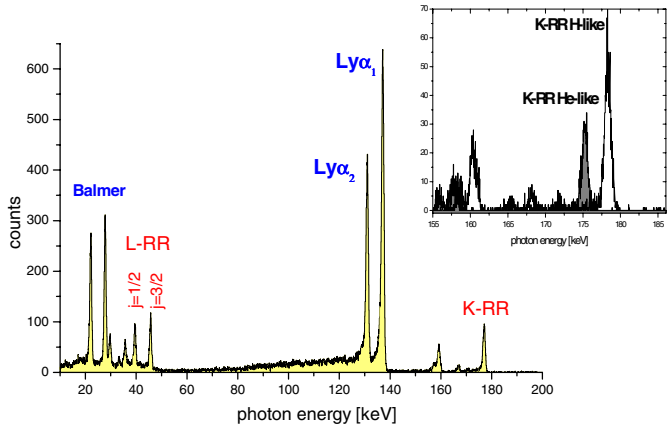


Figure 3: X-ray spectrum for H-like uranium as observed for decelerated ions at the electron cooler of the ESR storage ring. For details compare text. The inset compares H- and He-like spectra at the RR region.

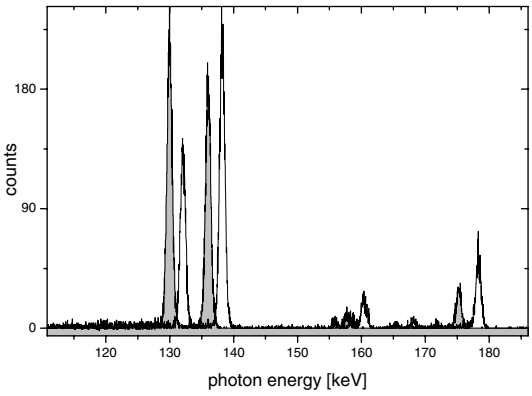


Figure 4: X-ray spectra of H- and He-like (filled) uranium as measured at the ESR cooler. For accumulation, a time condition (compare text) has been used.

provide us with the desired experimental accuracy of 4 eV or even below.

Acknowledgements

We gratefully acknowledge the support by the EU grant EC-HPRI-CT-1999-00001.

References

[1] H. Persson, S. Salomonson, P. Sunnergren, and I. Lindgren, Phys. Rev. Lett. **76** (1996) 204 .

[2] R.E. Marrs, S.R. Elliott, and Th. Stöhlker, Phys. Rev. **A52** (1995) 3577.

[3] Th. Stöhlker, S.R. Elliott, and R.E. Marrs, Hyperfine Interactions **99** (1996) 217.

[4] H.F. Beyer et al., Z. Phys. **D35** (1995) 169.

[5] Th. Stöhlker et al., Phys. Rev. **A58** (1998) 2043.

Lifetime Measurement of the Metastable 2^3P_0 State in Helium-like ^{238}U

S. Toleikis[1], B. Manil[2*], G. Bednarz[3**], E. Berdermann[1], H.F. Beyer[1], F. Bosch[1], A. Bräuning-Demian[1], A. Gumberidze[1], S. Hagmann[1], P. Indelicato[2*], C. Kozhuharov[1], D. Liesen[1], X. Ma[6], R. Marrus[4], P.H. Mokler[1], Z. Stachura[5], Th. Stöhlker[1], A. Warczak[3]

[1] *GSI, Darmstadt, Germany,* [2] *Université P. et M. Curie, Lab. Kastler Brossel, Paris, France,*

[3] *IFUJ, Cracow, Poland,* [4] *University of California, Berkeley, U.S.A.,*

[5] *INP, Cracow, Poland,* [6] *IMP, Lanzhou, China*

The measurement we report here is the second of a series of lifetime measurements on helium-like heavy ions for investigations of fundamental atomic properties. In the first experiment on helium-like ^{197}Au we were able to determine the lifetime of the hyperfine quenched 2^3P_0 state with an accuracy of ~3% [1]. Due to the hyperfine interaction, the ^{197}Au nucleus has spin $I = 3/2$, the metastable 2^3P_0 state couples to the prompt 2^3P_1 state hereby reducing its lifetime. As the coupling strength depends on the 2^3P_0-2^3P_1 fine-structure splitting, one can determine this fine-structure splitting by measuring the lifetime of the 2^3P_0 state.

The situation in helium-like ^{238}U is fundamentally different because the ^{238}U nucleus has no nuclear spin. The consequence is that no hyperfine interaction occurs. The lifetime of the 2^3P_0 state is therefore determined by the decay rate of the 2^3P_0 state to the 2^3S_1 state which itself decays to the ground state by a fast M1 transition (see Figure 1). As the decay rate, respectively the

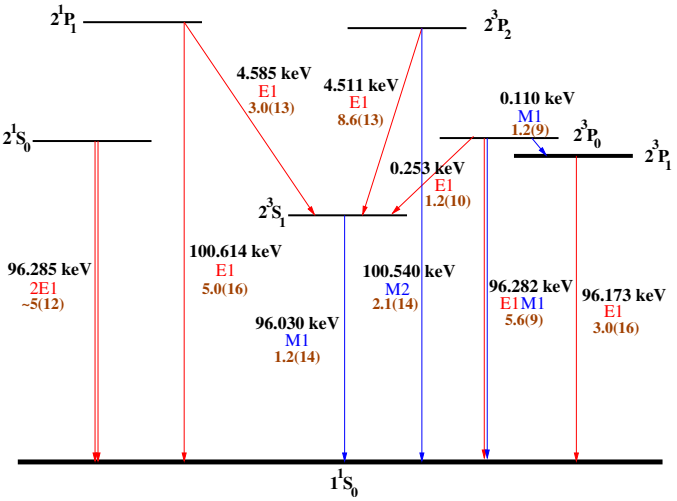


Figure 1: Level scheme of helium-like uranium with transition energies, decay modes and transition probabilities indicated. Numbers are taken from [2] and [5]. The transition probabilities are in 1/s with numbers in brackets indicating powers of 10.

lifetime, mainly depends on the energy difference between the 2^3P_0 and the 2^3S_1 state which is in fact the n=2 Lamb shift, one can in principle deduce the Lamb shift from a lifetime measurement of the 2^3P_0 state. A previous experiment at the Lawrence Berkeley Laboratory's Bevalac resulted in a value of 54.4±3.4 ps for the lifetime of the 2^3P_0 state [3].

The basic method for the measurement of the lifetime of metastable atomic states in heavy ions is beam foil spectroscopy. Figure 2 shows the apparatus used in our experiment.

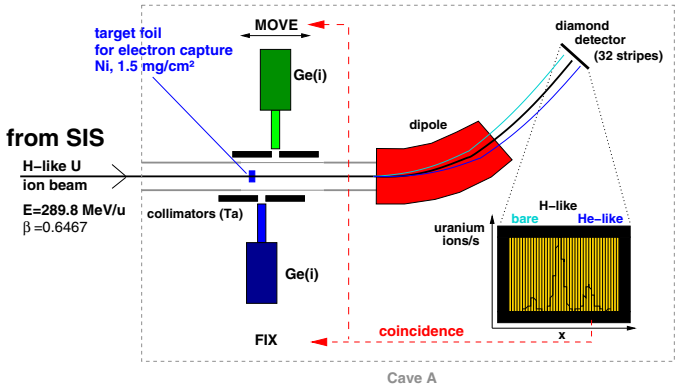


Figure 2: Experimental setup of the lifetime measurement in Cave A performed in May 2001. The different charge states of the uranium ions produced in the target foil are separated by a magnet spectrometer and are detected by a position sensitive diamond detector.

A hydrogen-like uranium beam with an energy of 289.8 MeV/u ($\beta = 0.6467$) passes through a target foil (1.5 mg/cm^2 Ni) and hereby produces excited helium-like ions by single electron capture. The radiation of the subsequent decay of the excited states is detected downstream of the foil by two Ge(i) detectors, located on opposite sides of the beam. The position of one detector is fixed while the other detector is moveable. By varying the distance between the target foil and the moveable detector and by measuring the ratio of counts of the 2^3S_1-1^1S_0-transition in the moveable detector relative to the fixed detector, a decay curve can be traced out. Measuring the ratio allows normalisation to the ion population in the excited state of interest and has the additional advantage that most systematic errors are eliminated. The fact that one detects the 2^3S_1-1^1S_0-transition and not directly the 2^3P_0-2^3S_1-transition has several reasons. First of all, the accurate detection of the direct 253 eV transition (see Figure 1) is not possible, because no detector with a sufficient energy resolution and efficiency is available in this energy region. Secondly, all other feeding mechanisms of the 2^3S_1 state have died out long before the metastable 2^3P_0 state starts to decay. A possible contamination of the line of interest (2^3S_1-1^1S_0-transition) due to the exotic two-photon (E1M1) branch from the 2^3P_0 state directly to the ground state can be neglected as these photons are almost uniformly distributed over the entire range from 0 to 96.3 keV. Therefore by detecting the 2^3S_1-1^1S_0-transition and tracing the decay curve the lifetime of the 2^3P_0 state can be determined.

A raw sample x-ray spectrum of the moveable detector is shown in Figure 3. The problem of background radiation is ob-

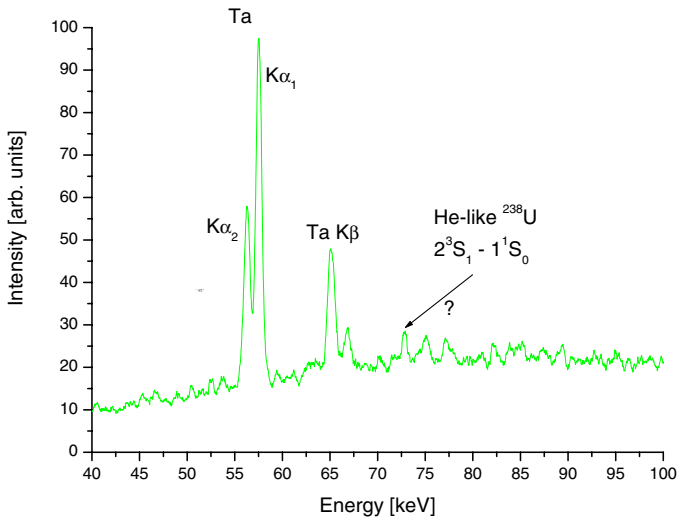


Figure 3: A raw sample x-ray spectrum obtained with the moveable Ge(i) detector. The continuous part of the background is bremsstrahlung while the lines below 70 keV are fluorescence radiation from the tantalum shielding. Whether the line indicated at the expected energy position in the laboratory frame is the 2^3S_1-1^1S_0-line of He-like uranium is not clear.

vious. Now, the possibility to measure the x-rays in coincidence with the down-charged helium-like ions, introduced in the previous experiment [1], allows us to improve the signal-to-noise ratio drastically. Figure 4 shows the coincidence spectrum with the line of interest now clearly visible. This is an improvement

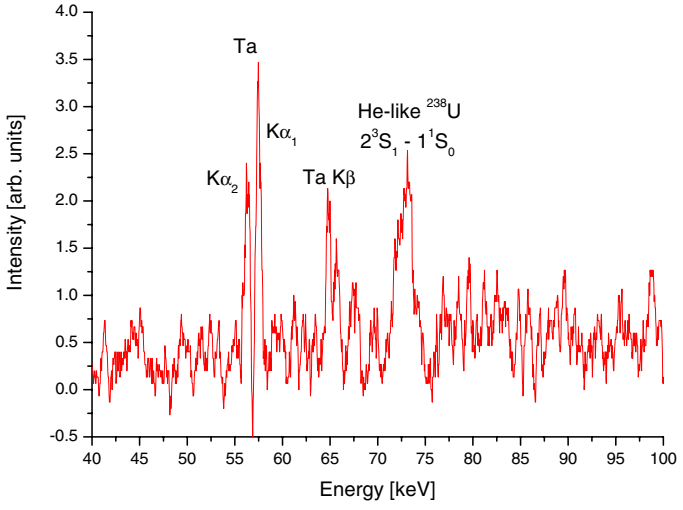


Figure 4: Coincident x-ray spectrum of the moveable Ge(i) detector. The width of the 2^3S_1-1^1S_0-line is coming from the Doppler broadening due to the slit width (3 mm) of the collimator.

compared to the old Bevalac experiment [3], where the x-ray spectra were recorded without coincidences.

The result of a preliminary analysis of the obtained data is shown in Figure 5. The uncertainty bars of the measured ratios are due to the statistical uncertainty at a 1σ confidence level. In order to extract the decay length l out of the decay curve, a single exponential has been fitted to the data points. With the extracted decay length l, the value for the speed of light c, the velocity of the ions β and the Lorentz factor γ the lifetime is

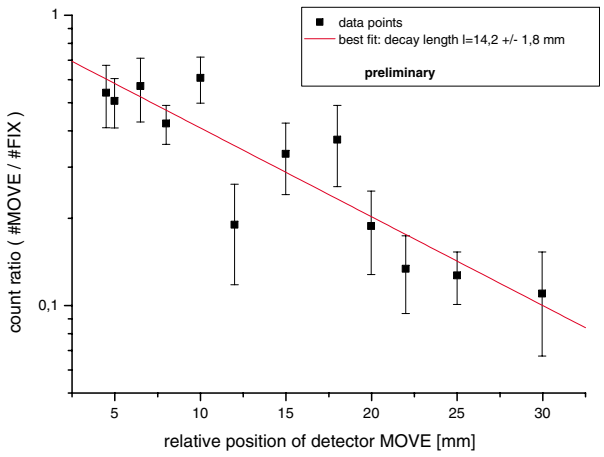


Figure 5: Measured decay curve of the 2^3P_0 state.

determined by $\tau = \frac{l}{c\beta\gamma}$ resulting in $\tau = 55.9 \pm 7.3$ ps for the 2^3P_0 state. The given uncertainty for the lifetime is associated with the fitting procedure and is assumed to be the sole major contribution to the total experimental uncertainty. Our experimental result, the previous result of the Bevalac experiment and the theoretical prediction are summarised in Table 1.

2^3P_0	Theory	Experiment	
	[2]	this work	[3]
τ [ps]	56	55.9±7.3	54.4±3.4

Table 1: Comparison of the lifetime τ of the 2^3P_0 state between experiments and theory.

Our final value agrees well with the theory. However an improvement in accuracy has not been achieved because of poor statistics. As the beam intensities in this run were comparable to those in the gold run, the main conclusion one can draw is the fact that the 2^3P_0 state in helium-like uranium was not populated with the same efficiency as in helium-like gold. This unexpected reduction in population efficiency needs more investigations, as it would heavily influence the feasibility of the third experiment, where the lifetime of the 2^3P_0 state in nuclear-excited helium-like uranium is planned to be measured [4].

* supported by EC-HPRI-CT-1999-0001.

** supported by a Marie Curie Fellowship of the European Community Programme IHP under contract number HPMT-CT-2000-00197.

References

[1] S. Toleikis et al., GSI-2001-1, 87 (2001)

[2] W.R. Johnson, D.R. Plante, J. Sapirstein, Adv. At. Mol. Phys. 35, 255 (1995)

[3] C.T. Munger and H. Gould, Phys. Rev. Lett. 57, 2927 (1986)

[4] L.N. Labzowsky, A.V. Nefiodov, G. Plunien, G. Soff and D. Liesen, Phys. Rev. Lett. 84, 851 (2000)

[5] G.W. Drake, Can. J. Phys. 66, 586 (1988)

Precise Lifetime Measurement for the $1s^2 2p\ ^2P_{3/2}$ Level of Li-like Ni

Y. Zou[1,5], D. Feili[2], R. Hutton[3], C. Neacsu[2], K.-H. Schartner[2], X. Ma[4,5] and P.H. Mokler[5]

[1] Applied Ion Beam Lab., Fudan University, Shanghai, China,
[2] I. Physik. Inst., University of Giessen, Giessen, Germany,
[3] Dept. of Physics, Lunds University, Lund, Sweden,
[4] Institute of Modern Physics, Lanzhou, China,
[5] GSI, Darmstadt, Germany.

Beyond measurements of accurate transition energies giving access to the atomic structure, a precise determination of lifetimes of excited states yields detailed information on the electronic wave functions involved. For heavy few-electron ions relativistic and quantum-electrodynamic effects determine these atomic quantities. Using the GSI 5m grazing incidence spectrometer intra L-shell VUV-transitions mainly in Li-like heavy ions in the mid-Z range ($28 \le Z \le 54$) have been measured on a $5 \cdot 10^{-5}$ level of accuracy [1]. (For results of Be-like ions see Feili *et al.* in this report.) In this high field domain of atomic species, both higher order QED terms and relativistic effects could sensitively be tested. For this Z region deviations in the oscillator strengths are also expected due to the relativistic character of the wave functions. This is especially true for the $1s^2 2p\ ^2P_{3/2}$ level in Li-like ions, and the lifetime of this level can precisely be determined in this Z region with the available VUV spectrometer using the beam foil technique.
Moreover, in two recent papers, systematic problems with beam foil lifetime measurements were reported [2], [3]. One of these problems, blending of the line of interest by satellite lines [2], leads to a systematic shortening of the measured lifetimes. The other problem, caused by foil aging [3], also leads to systematic changes in measured decay rates. Remedies for both of these problems were mentioned in these papers. In the work described here the previous results are extended to a higher member of the Li I iso-electronic sequence, to Li-like Ni where high-resolution spectroscopy measurements have already been performed at GSI (the $2p\ ^2P_{3/2} - 2s\ ^2P_{1/2}$ transition wave length is in the region of 16.5 nm) [4].

A high-intensity and very stable beam of 5.9 Mev/u Ni^{9+} ions penetrated a typically 90 $\mu g/cm^2$ thick C exciter foil in the spectrometer. The foil distance to the viewing slit of the spectrometer was remotely varied; and the beam was normalized to the integrated current in a down-stream Faraday cup. The ion energy was chosen on the low side of that required to produce most abundantly Li-like charge states, i.e. it was optimized to produce also a high fraction of satellite lines. The spectrometer was calibrated using an on-line penning light source and checking in-beam Be-like reference lines. After intensive pre-bombardement of the foil in order to avoid aging effects, a high statistic decay curve was obtained for the decay of the $1s^2 2p\ ^2P_{3/2}$ state over a period of 36 hours. Between each foil position a separate recording at a fixed foil position was obtained in order to correct for beam fluctuations. The measuring procedure is described in [3]. The experimental points and the fitted final decay curve are shown in Fig 1. The only known deviation in the lifetime extracted from the measured decay curve should come from the satellite problem.

At the beam energy used here, there was a possible line-blending problem for a Be-like $2s2p\ ^3P - 2p^2\ ^3P$ transition. The influence of this line on the decay curve was taken into account

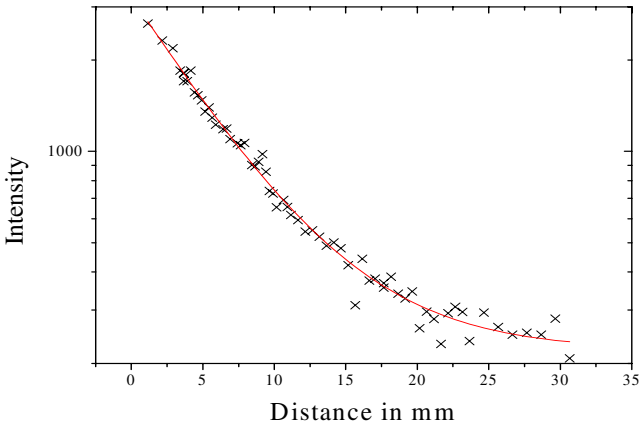


Figure 1. The decay of the $1s^2 2p\ ^2P_{3/2}$ level for Li-like Ni.

using other branches from the same multiplet and measuring the decay of the upper level in another channel and doing a blend reduction using the ANDC computer code [5]. The final result assuming a constant background is shown in Fig. 1 by the full curve. The present data evaluation yields a final decay time of 0.168 ±0.006 ns which is in full agreement with theory (0.174 ns) [6] within the error bar. An influence of satellite lines cannot be stated for this case: Already in [2] it was suggested that satellite problems may only appear for a small range of Z values within each iso-electronic sequence due to the different scalings with Z for the decays involved.

The present measurement is the first precise lifetime measurement utilizing the GSI 5m grazing incidence spectrometer. It demonstrates its unique capability to determine accurately lifetimes for excited states with transitions in the extreme VUV range, here with an accuracy of 4%. The case study chosen is sensitive on the relativistic influence to the wave functions. Actually it is at the minimum of the scaled oscillator strengths for this transition where relativistic effects start to dominate. Here, the result is in full agreement with the relativistic calculation and fits to the sequence of neighboring measured values. A satellite contribution was not observed for the case studied.

Acknowledgement: The help of Ruediger Schill and Sven Kammer during the beam time is highly appreciated. Work partially supported by EU grant EC-HPRI-CT-1999-00001.

References

[1] Feili D. *et al.,* Phys. Rev. A62, 022501 (2000).
[2] Zou Y, Hutton R. *et al.,* Phys. Rev. A60, 982 (1999).
[3] Zou Y., Hutton R. *et al.,* Phys. Script. T92, 253 (2001).
[4] Staude U. *et al.*, Phys. Rev. A58, 3516 (1998).
[5] Curtis L. *et al.*, Phys. Lett. 34A, 169 (1971).
[6] C. E. Theodosiou, *et al.*, Phys. Rev. A44, 7144 (1991).

QED Sensitivity of the $2s^2\ ^1S_0$ - $2s2p\ ^3P_1$ Intercombination Transition in Be-like Ag^{43+} and Xe^{50+} Ions

D. Feili, Ph. Bosselmann, C. Neacsu, K.–H. Schartner, Universität Gießen
A.E. Livingston, University of Notre Dame
F.Folkmann, University of Aarhus, Denmark
P.H. Mokler, GSI Darmstadt

In the strong central fields of heavy ions, $Z\alpha \Rightarrow 1$, the detailed atomic structure is – beyond relativistic effects – sensitively determined by quantum electrodynamic effects (QED). A rigorous theoretical treatment of these effects is compulsory. Using Lyman transitions in H-like Uranium, the ground state Lamb-shift is experimentally determined with a precision of 2.8% (468 ± 13 eV) [1]. Still this high precision has to be improved by another factor of 10 in order to really be able to test QED calculations. In contrast to ground state transitions in H- or He-like ions, the relative QED contributions for intra-L shell transitions is considerably larger. Hence those transitions in Be and Li-like ions can reveal even higher order QED contributions.

In systematic spectroscopic investigations of Li-like ions up to Xe^{51+} the precise determination of $2s\ ^2S_{1/2} - 2p\ ^2P_{1/2}$ transition energies using the GSI 5m VUV grazing incidence spectrometer yielded an accuracy level of $5 \cdot 10^{-5}$ [2-4]. This allows already to test sensitively two loop QED terms. Encouraged by this success we started to concentrate on $2s^2\ ^1S_0$ - $2s2p\ ^3P_1$ intercombination transitions in Be-like heavy ions. We determined the wavelengths of this transition in berylliumlike Xe and Ag with an accuracy of bellow 100 ppm. For Ag this is the first precise measurement at all, while for the transition in Xe the experimental wavelength accuracy is improved by more than one order of magnitude.

For these transitions the relative QED contributions to the total transition energy (see Fig.1) are in the order of 10% for the one-electron and up to almost 1% for the two-electron QED terms. Berylliumlike ions are the simplest atomic systems where both intrashell and intershell interactions are simultaneously important. Heliumlike ions and lithiumlike ions provide examples where intrashell (heliumlike) and intershell (lithiumlike) interactions are separately important. The latter isoelectronic sequences are studied in more detail than the beryllium sequence. From the many relativistic structure calculations for Be-like ions given in literature we use the relativistic many-body perturbation theory (RMBPT) [5] and the multiconfiguration Dirac-Fock (MCDF) [6] method for the comparison between our present wavelength evaluation and the calculations.

The comparison between the experimental transition energy of $2s^2\ ^1S_0$ - $2s2p\ ^3P_1$ transition in Be-like Ag and theoretical value from Safronova shows a very good agreement between RMBPT calculations and the experimental values. For Ag there exists no CI-Calculation at present. The same transition in Xe shows a deviation of 7 meV between the experimental value and RMBPT based calculations of Safronova [5]. In this case the experimental error amounts to 20 meV, so the real deviation can be larger. The RCI calculations of Chen and Cheng [6] indicate even larger deviations in both cases.

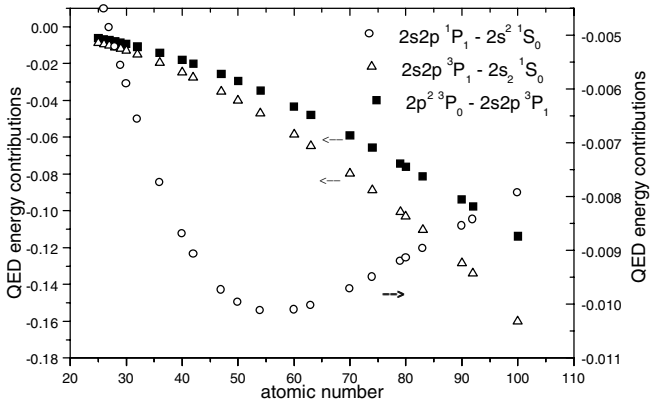


Fig. 1 : QED energy contributions of the noted transitions in Be-like ions along the isoelectronic series.

The study along the iselectronic series is continued by the evaluation of our corresponding data for Be-like Sn.

Table.1 : Experimental and theoretical values of $2s^2\ ^1S_0$ - $2s2p\ ^3P_1$ intercombination transition wavelength (Å) in Be-like Ag^{43+} und Xe^{50+} Ions.

Xe^{50+}		
Experiment:	This Work	97.426(20)
	Möller *et al.*[7]	98.1(5)
Theory:	Safronova *et al.*[5]	97.421
	Chen and Cheng[6]	97.395
Ag^{43+}		
Experiment:	This Work	118.164(9)
Theory:	Safronova *et al.*[5]	118.169

References:
[1] Th. Stöhlker *et al.* GSI 98-1, 99 (1998).
[2] U. Staude *et al.*, Phys. Rev. A **58**, 3516 (1998).
[3] Ph. Bosselmann *et al.*, Phys. Rev. A **59**, 1874(1999).
[4] D. Feili *et al.*, Phys. Rev. A **62**, 022501 (2000).
[5] M. S. Safronova,*et al.*, Phys. Rev. A **53**, 4036 (1996).
[6] M. H. Chen and K. T. Cheng, A **55**, 166 (1997).
[7] G. Möller, Z.Phys. D **11**, 333 (1989).

Photorecombination Studies of Lithium-Like Uranium Ions

C. Brandau[a], T. Bartsch[a], K. Beckert[b], S. Böhm[a], C. Böhme[a], F. Bosch[b], B. Franzke[b], N. Grün[c], A. Hoffknecht[a], H. Knopp[a], S. Kieslich[a], C. Kozhuharov[b], P.H. Mokler[b], A. Müller[a], F. Nolden[b], W. Scheid[c], S. Schippers[a], W. Shi[a], Z. Stachura[d], M. Steck[b], T. Steih[c], T. Stöhlker[b]

[a]Institut für Kernphysik, Justus-Liebig-Universität, 35392 Gießen
[b] Gesellschaft für Schwerionenforschung (GSI), 64291 Darmstadt
[c]Institut für Theoretische Physik, Justus-Liebig-Universität, 35392 Gießen
[d]Instytut Fizyki Jądrowej, 31-342 Kraków, Poland

During the last year detailed data analysis of previous photorecombination measurements with Li-like uranium U^{89+} was performed. Photorecombination (PR) is the capture of a free electron under emission of one or more photons. In the independent processes approximation (IPA) PR usually is described to proceed either via a non-resonant direct pathway, radiative recombination (RR), or as a resonant two step mechanism, dielectronic recombination (DR).
The main focus of this report is on the DR of U^{89+}. Here RR is considered as a background process. In the first step of DR the free electron is captured radiationless by the ion (inverse to autoionisation), and a doubly-excited compound system is formed. If the intermediate state decays by emission of a photon, DR is completed. Due to the possibility to excite a bound electron within one shell ($\Delta n = 0$), the according DR resonance energies of Li-like ions are comparatively low. Hence, DR associated with $2s_{1/2} \rightarrow 2p_j (j = 1/2, 3/2)$ core excitations is an ideal candidate to be studied experimentally at the merged electron and ion beams arrangement of electron coolers at ion storage rings.

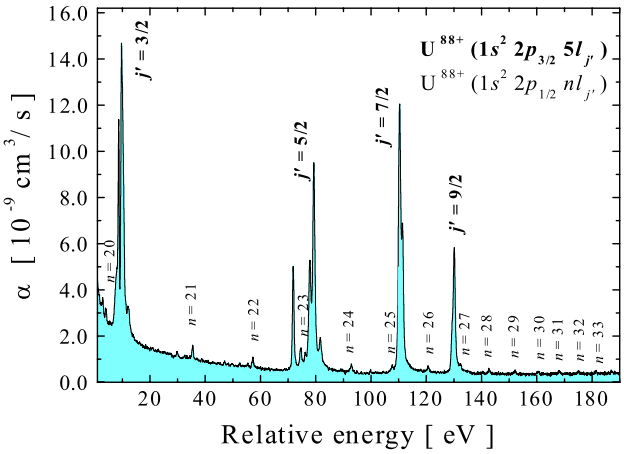


Figure 1: Photorecombination of U^{89+} in the energy range 1–190 eV. The smooth background is the contribution due to radiative recombination. Some of the smaller DR resonances $1s^2\,2p_{1/2}\,nl_{j'}$ are partially covered by the much stronger $1s^2\,2p_{3/2}\,5l_{j'}$ resonances.

Overview

The experiments were carried out at the electron cooler of the ESR. Li-like U^{89+} ions were stored and cooled in the ESR at an ion energy of 92.3 MeV/u. Non-zero relative energies between electrons and ions were introduced by applying a sequence of well-controlled potentials on drift tubes located around the overlap region of the ion and electron beams.
Within the c.m.-energy-range of 0–400 eV, which can be covered with our present experimental set-up at the ESR, for U^{89+} two types of DR resonances can be found in the spectra (Fig. 1). First, a series of high-n Rydberg resonances $1s^2\,2p_{1/2}\,nl_{j'} (n \geq 20)$ can be observed all the way to the series limit $n \rightarrow \infty$ ($E(2s_{1/2} \rightarrow 2p_{1/2}) = 280.44$ eV, [1]), and, second, individual $1s^2\,2p_{3/2}\,5l_{j'}$ DR resonances associated with $2s_{1/2} \rightarrow 2p_{3/2}$ excitations.
By extrapolation of the $2p_{1/2}\,nl_{j'}$ resonance energies to the series limit the $2s_{1/2} \rightarrow 2p_{1/2}$ excitation energy can be determined experimentally with high precision. With this method a splitting of 280.56(20) eV has been obtained. Furthermore, a comparison of the experimental data with our fully relativistic calculations shows the relevance of high angular momentum components up to $j = 31/2$ for the total rate coefficient. Further details can be found in [2, 3, 4].
The excitation energy to $2p_{3/2}$ is more than 15 times larger ($E(2s_{1/2} \rightarrow 2p_{3/2}) = 4459.37$ eV, [5]), and the free electron can already be captured into $n = 5$. The resulting $1s^2\,2p_{3/2}\,5l_{j'}$ resonance manifold is split by about 200 eV, which allows a deep insight into the individual couplings of the $j = 3/2$ core electron and the $n = 5$ Rydberg electron. The $n = 5$ resonances are arranged into groups with the same angular momentum j' of the Rydberg electron. The additional substructure within each j' manifold results from the different couplings of j and j' to the total angular momentum J. Doubly excited $1s^2\,2p_{3/2}\,5l_{j'}$ states with $j' = 1/2$ are below the autoionization threshold and therefore DR via these resonances is energetically not possible.

Lifetime of the compound ion: Radiative and autoionization rates

The lifetimes of the $1s^2\,2p_{3/2}\,5l_{j'}$ doubly excited intermediate states are mainly determined by the fast radiative decay modes of the $n = 5$ Rydberg electron. Natural widths in the range of 0.2 - 1 eV are expected. At low relative energies, the experimental energy resolution is sufficient to be sensitive to these natural widths, which for instance can directly be seen by comparing the two resonance structures displayed in Fig. 2. The $1s^2\,2p_{1/2}\,20l_{1/2}$ peaks are considerably smaller than the $(1s^2\,2p_{3/2}\,5p_{3/2})_2$ resonance.
DR experiments utilizing the electron cooler of storage

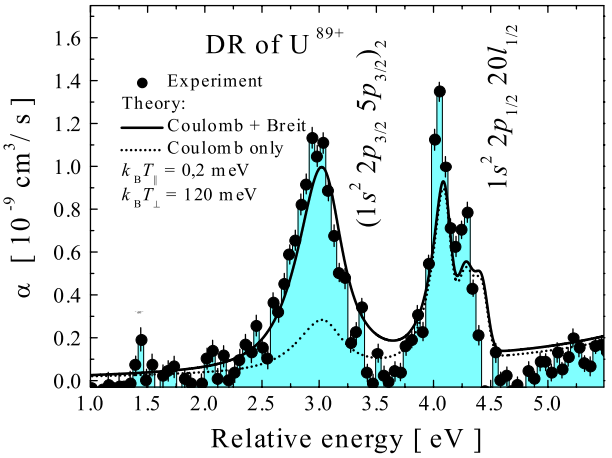


Figure 2: DR of U^{89+} in the energy range 1–5.9 eV. The full circles are the experimental data, the lines are fully relativistic DR calculations including Breit interaction (full line) and without Breit interaction (dashed line). For a better comparison with the experiment the theory has been convoluted with the experimental response function, described by an anisotropic Maxwell-Boltzmann distribution with parameters $k_BT_{||} = 0.2$ meV and $k_BT_{\perp} = 120$ meV. Background and contributions from RR have been treated independently and subtracted from the data.

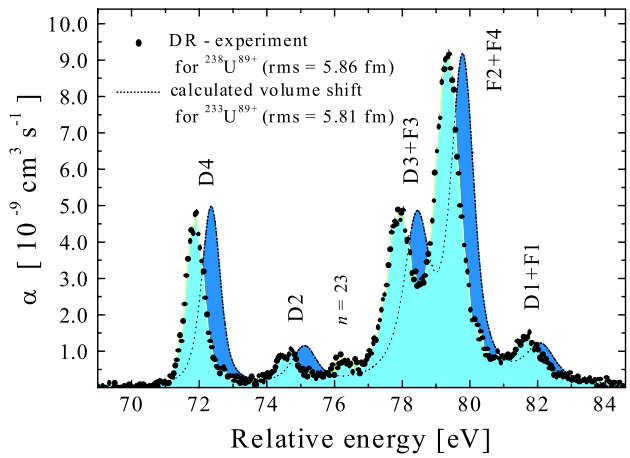


Figure 3: DR of U^{89+} in the energy range of the $1s^2\,2p_{3/2}\,5l_{5/2}$ resonance manifold. The full circles denote the measurement carried out with the uranium isotope ^{238}U (rms-radius of 5.86 fm). The dotted line/dark shaded area is the expected (calculated) isotopic volume shift for ^{233}U (rms-radius of 5.81 fm). The labels characterize the configuration of the peaks. The letter represents the angular momentum l of the Rydberg electron, whereas the number denotes the total angular momentum J of the compound system.

rings as a target for free electrons yield the recombination rate coefficients α on an absolute scale. Therefore, DR experiments not only allow for the precise measurement of energy levels but also provide a versatile tool for the investigation of radiative transition rates and autoionization rates. For few-electron heavy ions the influence of relativistic effects and quantum electrodynamic (QED) corrections to the electron-electron interaction is of particular interest as they scale with the nuclear charge proportional to Z^2 and Z^4, respectively. DR cross sections are mainly determined by the *slowest* decay mode of the doubly excited intermediate state, and hence DR of heavy highly-charged ions is highly sensitive to autoionization probabilities. The $(1s^2\,2p_{3/2}\,5p_{3/2})_2$ resonance of U^{88+} provides a nice example for this sensitivity (Fig. 2). The experimental data are compared to our fully relativistic calculations which are based on the multi configuration Dirac Fock (MCDF) computercode GRASP. The autoionization rates have been calculated with Coulomb interaction only and secondly with Coulomb interaction and general Breit interaction

$$\hat{V}_{i,j}^{Br} = -\vec{\alpha}_i\vec{\alpha}_j\frac{\cos(\omega R)}{R} + (\vec{\alpha}_i\vec{\nabla}_i)(\vec{\alpha}_j\vec{\nabla}_j)\frac{\cos(\omega R)-1}{\omega^2 R}. \quad (1)$$

Here $R = |\vec{r}_i - \vec{r}_j|$ is the distance between the two electrons, $\vec{\alpha}_{i,j}$ are Dirac matrices and ω is the frequency of the exchanged transversal photon. Details of the theoretical approach can be found in [6, 7]. Typically the Breit interaction contributes to the DR rate coefficient α_{DR} of heavy Li-like ions on a level of up to 10 - 15 %. For individual configurations like the $(1s^2\,2p_{3/2}\,5p_{3/2})_2$ resonance the Breit interaction enhances α_{DR} by more than a factor of 4.

Influence of the atomic nucleus

Another important issue that comes into play for very heavy ions like uranium is the extended size of the atomic nucleus. The finite size contribution to the $2s_{1/2}-2p_{1/2}$ energy splitting of U^{89+} amounts to -33.35 eV which is nearly 12% of the total energy shift [8]. In connection with the high experimental resolution this opens up the possibility to utilize DR for probing nuclear parameters. Our DR/MCDF calculations predict energy shifts of about 0.30–0.45 eV depending on the underlying excitation channel $2s_{1/2} \rightarrow 2p_{1/2}$ or $2s_{1/2} \rightarrow 2p_{3/2}$ for switching from the uranium isotope ^{238}U to ^{233}U (Fig. 3). In the calculations the charge distribution of the nucleus has been modeled by a Fermi distribution with rms radii 5.86 fm (^{238}U) and 5.81 fm (^{233}U) [9]. A high accuracy in measuring the isotopic shift can be expected as the complete DR resonance pattern which belongs to a distinct excitation channel is shifted by the same value. Furthermore, due to the different overlap of $2p_{1/2}$ and $2p_{3/2}$ wave functions with the nucleus the according two resonance patterns are shifted by ≈ 0.1 eV with respect to each other.

References

[1] V. A. Yerokhin et al., PRL **85**, 4699 (2000).
[2] C. Brandau, Dissertation, Universität Giessen, 2001 http://bibd.uni-giessen.de/ghtm/2001/uni/d01008.htm
[3] C. Brandau et al., GSI Sci. Rep. 2000, p. 97f.
[4] C. Brandau et al., submitted to PRL
[5] P. Beiersdorfer et al., PRL **71**, 3939 (1993).
[6] P. Zimmerer et al., J. Phys. B **24**, 2633 (1991).
[7] M. Zimmerermann et al., J. Phys. B **30**, 5259 (1997).
[8] V. A. Yerokhin et al., PRA **60**, 3522 (1999).
[9] J. D. Zumbro et al., PRL **53** 1888 (1984).

The Lyman–α_1 Decay in Hydrogen-like Ions: Interference between the E1 and M2 Transition Amplitudes

Th. Stöhlker[1,2], A. Surzhykov[3], S. Fritzsche[3], and A. Gumberidze[1,2,4],
[1]IKF, Univ. of Frankfurt, Germany; [2]GSI-Darmstadt, Germany; [3]Univ. of Kassel, Germany; [4]Tbilisi State University, Georgia

We report on an interference between the **E1** and **M2** transition amplitudes in the decay of the $2p_{3/2}$ level in hydrogen–like heavy ions which significantly alters the photon angular distribution of the *Lyman–*α_1 transition ($2p_{3/2} \rightarrow 1s_{1/2}$). In the past, the angular distribution of this decay was subject of intense experimental and theoretical studies in order to elucidate the magnetic substate population of Radiative Electron Capture (REC) in relativistic collisions of bare uranium with low-Z target atoms [1, 2]. If the magnetic sublevels with different absolute magnetic quantum numbers μ are populated non-statistically, alignment occurs leading to an anisotrope emission pattern. For the particular case of the $2p_{3/2}$ state this angular distribution is given by [1]

$$W(\theta) \propto 1 + \beta_{20}(1 - \frac{3}{2}\sin^2\theta) \qquad (1)$$

where θ is the angle between the direction of the excitation photon and the beam direction (emitter frame) while β_{20} denotes the anisotropy coefficient. In the case of the $2p_{3/2}$ level, the anisotropy coefficient can be expressed as:

$$\beta_{20} = \tfrac{1}{2}\cdot \frac{\sigma(\frac{3}{2},\pm\frac{3}{2}) - \sigma(\frac{3}{2},\pm\frac{1}{2})}{\sigma(\frac{3}{2},\pm\frac{3}{2}) + \sigma(\frac{3}{2},\pm\frac{1}{2})}, \qquad (2)$$

Here $\sigma(3/2,\mu_n)$ describes the population of substate μ_n of the $2p_{3/2}$ level. The well known expression (2) takes into account only the dominant electric dipole (**E1**) term whereas the weaker magnetic quadrupole component (**M2**) is neglected. Based on expression (2), the theoretical and observed angular distributions were compared in detail and a remarkable variance was found [1, 2]. This deviation was surprising also in the sense that the REC is otherwise one of the best studied processes for high-Z, hydrogen-like ions for which an excellent agreement between theory and experiment is typically found. By using the density matrix theory one can consider the magnetic (**M2**) decay branch in a coherent way. As a result, the alignment coefficient parameter β_{20} must now be replaced by the product $\beta_{20} \cdot f(E1,M2)$ where $f(E1,M2)$ is a *structure* function which takes into account the interference effect. Note, for H-like uranium the structure parameter $f(E1,M2)$ reaches a value of as large as 1.28 [3]. In Fig. 1 we compare the experimental results for H-like uranium (solid points) with the corresponding theoretical findings (full line) and the results obtained assuming $f(E1,M2) = 1$ (dashed line), i.e. neglecting the interference term. From the figure it is evident that the former departure of the theoretical results from the experimental values is removed then taking the interference term into account. This proves the importance of the interference between the **E1** and **M2** decay branches for the decay of $2p_{3/2}$ state. Also, we have to add that one may expect similar sizeable corrections for any other atomic transitions in the high-Z regime where beside the leading **E1** term, higher multipole contributions are small but allowed. Here, e.g. doubly excited states in He-like ions such as produced by KLL-dielectronic recombination must be mentioned [4, 5]. More general, the study of decay rates and transition matrix elements of atomic transitions are of great importance to test and advance our basic knowledge about the physics of strong Coulomb fields as they are present at high-Z. However, at high-Z, most of these transitions exhibit such fast decay rates that lifetime measurements are excluded. Because of the sensitivity of the effective alignment parameter on the reduced matrix elements of the multipole transitions involved, the latter can be addressed by measuring precisely the associated photon angular distributions. It represents therefore an experimental tool to study the decay properties of atomic states in the realm of high-Z ions.

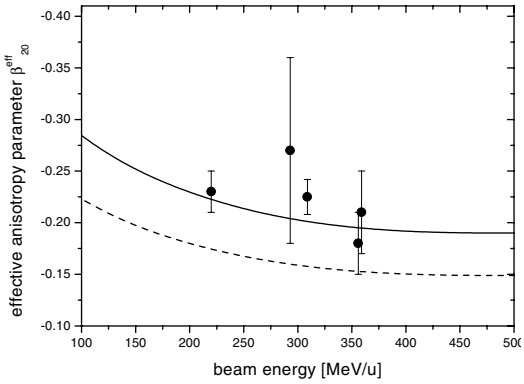


Figure 1: The experimentally determined effective anisotropy parameters $\beta_{20}^{\rm eff}$ (solid points) for the *Lyman–*α_1 radiation of U^{91+} produced in $U^{92+} \rightarrow N_2$ collisions as a function of collision energy [2]. The dashed line represents the theoretical predictions for $f(E1,M2) \equiv 1$, i.e. when the interference term is neglected. The solid line shows the corresponding theoretical result which considers the interference term $f(E1,M2)$, i.e. $\beta_{20} \cdot f(E1,M2)$.

References

[1] J. Eichler, Nucl. Phys. **A 572**, 147 (1994).
[2] Th. Stöhlker et al., Phys. Rev. Lett. **79**, 3270 (1997).
[3] A. Surzhykov et. al., submitted to PRL (2002).
[4] M. H. Chen and J. H. Scofield, Phys. Rev. **A 52**, 2057 (1995).
[5] M. Gail, N. Grün, and W. Scheid, J. Phys. **B 31**, 4645 (1998).

Search for Correlated Electron Capture in Relativistic U^{92+} Collisions

G. Bednarz[1], D. Sierpowski[1], Th. Stöhlker[2], A. Warczak[1], H. Beyer[2], F. Bosch[2], A. Bräuning-Demian[2], H. Bräuning[2], X. Cai[2], A. Gumberidze[2], S. Hagmann[2], O. Klepper[2], C. Kozhuharov[2], D. Liesen[2], X. Ma [2], P.H. Mokler[2], A. Muthig[2], Z. Stachura[3], S. Toleikis[2]

[1] *IFUJ-Cracow (Poland),* [2] *GSI-Darmstadt (Germany),* [3] *INP Cracow (Poland)*

Double photoionization of two-electron systems is a key process for the study of correlation effects in atomic multi-body systems [1]. Collision experiments with bare ions provide us with the unique possibility to study this effect under time reversal conditions, i.e. correlated capture of two electrons via simultaneous emission of one single photon (RDEC - Radiative Double Electron Capture) [2].

At the jet target of the ESR storage ring several experiments have been performed to identify this process in collisions of bare uranium ions with gaseous matter. So far, however, this process has not been confirmed experimentally.

During a recent uranium beam time at the ESR, a new attempt has been undertaken by using a considerably improved experimental setup. The main intention of this experiment was to detect RDEC photons in coincidence with double charge exchange, the signature of this particular process. For this purpose, projectile photon emission was observed simultaneously at various observation angles. Compared to the former experiments the overall photon efficiency could be enhanced by almost two orders of magnitude.

In the experiment bare uranium ions at an energy of 297 MeV/u bombarded a thin Ar-target. The target area has been viewed by an array of x-ray detectors [3] gated with signals from the particle detector mounted behind the bending magnet, next to the gas-jet target. The trajectory of the circulating ion beam was especially tuned in order to enable the registration of ions, which captured two electrons.

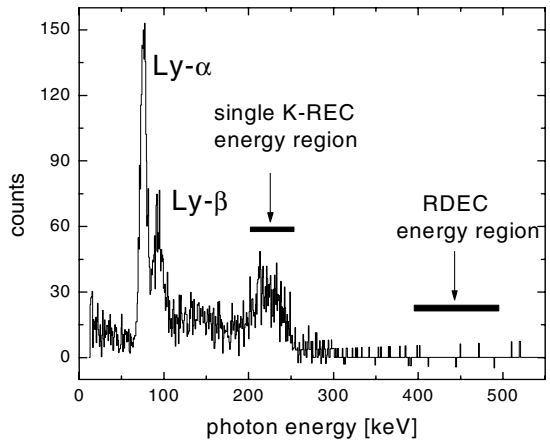


Fig. 1: *X-ray spectrum (corrected for random events and detector efficiency) measured at 90° in coincidence with double charge exchange. A REC line for photons with a single K-REC energy associated with double electron capture is clearly observed.*

A sample x-ray spectrum measured at 90° in coincidence with double charge exchange is depicted in Fig.1. A REC line for photons with the single K-REC energy, associated with double electron capture, is clearly observed. However, within the energy region relevant for RDEC, only a few events have been detected and no x-ray line shows up. From the present state of the data analysis we can already conclude that the cross section of this extremely rare process is below 10 mb. This is in contradiction to the presently available theoretical predictions, concerning relativistic effects [4].

Tab. 1: *Capture cross-sections*

capture	experimental value [barn]	theoretical predictions [barn]	
		nonrelativistic	relativistic
RDEC	$<10^{-2}$	$5 \cdot 10^{-6}$	5

Simultaneously, the total cross-section for double electron capture was measured and amounts to 400±70 mb. In addition, the angular distribution of single K-REC photons, associated with double charge exchange, was registered. We realise that the corresponding emission pattern (Fig.2) is similar to that for K-REC photons measured in coincidence with single electron capture [3].

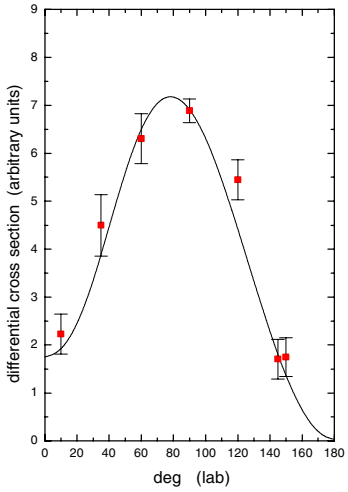


Fig. 2: *Angular distribution of photons with single K-REC energy associated with double electron capture. Solid line – full relativistic description for K-REC associated with single electron capture normalised to the experimental data.*

This work was supported by EU, grant: EC-HPRI-CT-1999-00001 and by a Marie Curie Fellowship of the European Community Programme IHP under contract number HPMT-CT-2000-00197.

[1] *Electron Correlation Dynamics in Atomic Collisions*, J.H. McGuire, Cambridge University Press (1997).
[2] A. Warczak et al., Nucl. Instr. Meth, **B98**, 303 (1995).
[3] Th. Stöhlker et al., Phys. Rev. Lett. **82**, 3232 (1999).
[4] V.L. Yakhontov, M.Ya Amusia, Phys. Rev. **A 55**, 1952 (1997).

New results from the GSI REACTION-MICROSCOPE

R. Moshammer[1], H. Kollmus[1,2], S. Hagmann[2,4], M. Schulz[3], R. Mann[2], B. Feuerstein[1], A. Dorn[1], D. Fischer[1], C. Höhr[1], C.D. Schroeter[1], J.R. Crespo Lopez-Urrutia[1], R.E. Olson[3], J. Ullrich[1]

[1]MPI-Heidelberg, [2]GSI Darmstadt, [3]UMR Missouri, [4]Uni-Frankfurt

After many years of intense research the dynamical response of quantum-mechanical many-particle systems perturbed by an external time dependent force still remains as one the most fundamental and challenging problems in physics. Among them the three-body Coulomb problem represents the most prominent example. It can be studied in great detail in atomic collisions and ionization of simple atoms by charged particle impact can be viewed as a prototype of a three-particle problem.

In the case of electron-impact ionization the first exact theoretical treatment was published just recently [1] for the simplest system, namely ionization of atomic hydrogen, more than thirty years after the pioneering experiments of Ehrhardt [2]. The possibility to obtain fully differential ionization cross section data with these kinematically complete so called (e,2e) experiments is indispensable for the progress achieved in theory.

In the case of ion-impact ionization a large data set was collected in numerous experimental investigations since the first measurements by Rudd and coworkers in the sixties [3]. But, and in contrast to (e,2e) measurements, only total cross sections or those differential in the ejected electron energies and angles have been measured. The measurement of projectile scattering angles, and thus of the transferred momentum during the collision, were possible only for the very specific situation of unlikely large projectile deflections. Based on this limited experimental information the continuum distorted wave (CDW) theories have proven to be remarkably successful representing the theoretical basis for charge transfer and for ionization in fast ion-atom collisions [4].

In this report we summarize recent experimental results obtained for single ionization of helium and for simultaneous ionization of both, projectile and target in fast ion-atom collisions. Both experiments have been performed at the UNILAC using the GSI REACTION-MICROSCOPE [5] to collect for the first time kinematically complete data sets for ion impact ionization with sufficient statistics to allow an unsurpassed test of ionization theories.

Three-body dynamics:
Triply differential single ionization cross sections

For fast but still non-relativistic projectiles with low charge the interaction with the target atom can be considered as weak and the 1st Born approximation is expected to provide an adequate description of the ionization process. Based on this model the total as well as any differential cross section scales with the square of the perturbation strength $Q_p/v_p << 1$ (projectile charge divided by projectile velocity in atomic units) and the ionization dynamics is independent of the projectile mass (i.e there is no difference between e.g. electron and ion impact) as long as the perturbation is the same. The projectile transfers only some momentum during the collision and its influence on the final state continuum electron is negligibly small; in fact, ionization can be reduced to an effective two-particle problem. A deviation from this situation occurs when the perturbation approaches or even exceeds unity. Then the outgoing projectile strongly interacts with both, the ionized electron and the recoiling target-ion long after the electron is set free and any attempt of a description on a two-particle basis fails. With fast highly charged ions this strongly non-perturbative regime is easily reached allowing to test theoretical models [6] in a domain of collision time scales and perturbation strengths not accessible by electron impact.

Most kinematically complete (e,2e) studies focused on triply differential cross sections (TDCS), i.e. on the energy and angular distribution of electrons ejected into the scattering plane (so called coplanar geometry), which is defined by the momentum vector of the incoming and that of the scattered projectile. Typically, and in particular at low perturbation, the angular distribution of ionized electrons exhibits two maxima, one occurring near the direction of the momentum transfer **q** (binary peak) and a second one opposite to **q** (recoil-peak). Exactly the same features are observed for ionization of He with 100 MeV/u C^{6+} ions as shown in fig. 1a. The angular distribution of 6.5 eV electrons emitted into the scattering plane is plotted for collisions where the direction (see fig. 1a) and the magnitude of the momentum transfer vector is kept fixed (q = 0.9 a.u.). A comparison with results obtained by a 1st Born calculation exhibits a good agreement, as expected [7].

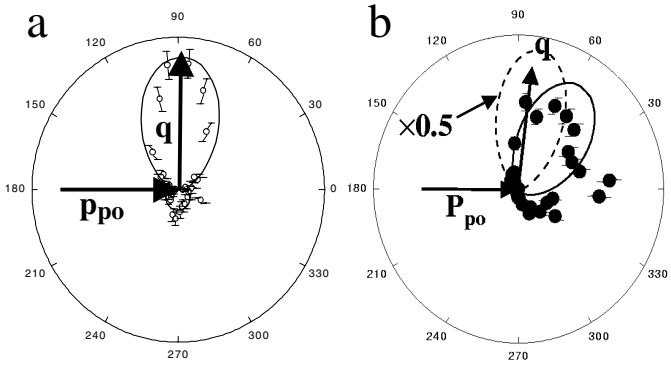


Figure 1: *Angular distribution of electrons emitted into the scattering plane for fixed electron energy E_e and fixed momentum transfer q. The projectile is comming from the left. a) For 100 MeV/u C^{6+} + He with E_e = 6.5 eV and q = 0.88 a.u. solid line: 1st Born result. b) For 3.6 MeV/u Au^{53+} + He with E_e = 17.5 eV and q = 1.0 a.u. dashed line: 1st Born. solid line: CDW calculation.*

When the perturbation is increased from Q_p/v_p = 0.1 (C^{6+} ions) up to 4.4 by using 3.6 MeV/u Au^{53+} projectiles instead the shape of the TDCS undergoes a dramatic change (fig. 2b). In contrast to the C^{6+} case a considerable fraction of electrons is emitted into the forward direction which can be understood as a result of the final state interaction between the electron and the receding highly charged projectile. It is no surprise, that the 1st Born approximation no longer provides an adequate

description of the data (dashed line in fig. 1b), but, it is surprising that even the CDW calculation, which predicts with high accuracy total cross sections as well as electron energy distributions, is in very poor agreement (solid line in fig. 1b). A more detailed comparison shows, that the momentum exchange between projectile and target nucleus is not properly taken into account in standard CDW calculations [8]. Thus, though this interaction does not contribute directly in the release of the electron, it plays an important role in the three-particle momentum balance and the proper consideration of all interactions represents a still unsurmountable problem for theory.

Four-body dynamics:
Simultaneous ionization of projectile and target

Electron impact ionization of ions belongs to the most important and fundamental reactions in atomic physics with enormous importance for our understanding and modelling of plasmas. But, due to the experimental difficulties fully differential cross sections like those routinely measured in atomic (e,2e) experiments are not at hand. Within a kinematically complete experiment for projectile ionization in ion-atom collisions we were able to extract for the first time fully differential electron impact ionization cross sections of ions by applying inverse kinematics and by separation of a specific reaction mechanisms as described below.

When energetic partially stripped projectile-ions collide with an atomic target the projectile can be ionized via an interaction with one of the target electrons (electron-electron (e-e) interaction) making this process equivalent to electron impact ionization of the projectile. This requires, that the target electron is weakly bound and therefore can be treated as a quasi-free electron. As a result, projectile ionization due to an (e-e) interaction is always accompanied by a simultaneous ionization of the target. But there is a second mechanism contributing to projectile ionization: It might be ionized by an interaction with the target nucleus (nucleus-electron interaction). Thus, electron impact ionization of ions may be studied in very detail, if a distinction and separation of both competing mechanisms becomes possible experimentally.
Such a separation has successfully been demonstrated for 3.6 MeV/u C^{2+} projectiles in collisions with He atoms [9]. In the experiment the momentum vectors of all four emerging charged fragments has been measured giving full access to the collision dynamics, which is a prerequisite to enable an event by event separation of the mentioned mechanisms according to their distinctively different fragmentation kinematics. The subset of data where the (e-e) interaction was found to be the dominant contribution is considered as electron-impact ionization of the projectile-ion, i.e. the target electron is interpreted as a quasi-free electron hitting the C^{2+} ion with a kinetic energy of 2 keV in the projectile frame. The validity of this assumption can be checked by comparison with differential cross sections obtained with standard (e,2e) measurements. This is shown in fig. 2 for coplanar geometry in a two-dimensional representation plotting the momentum transfer versus the polar emission angle of the ionized electron with respect to the momentum transfer direction for electron-impact ionization of C^{2+} (fig 2a) and for 2 keV electron on He [10] collisions (fig. 2b). The striking similarities clearly support our interpretation and, even more important, indicate that this

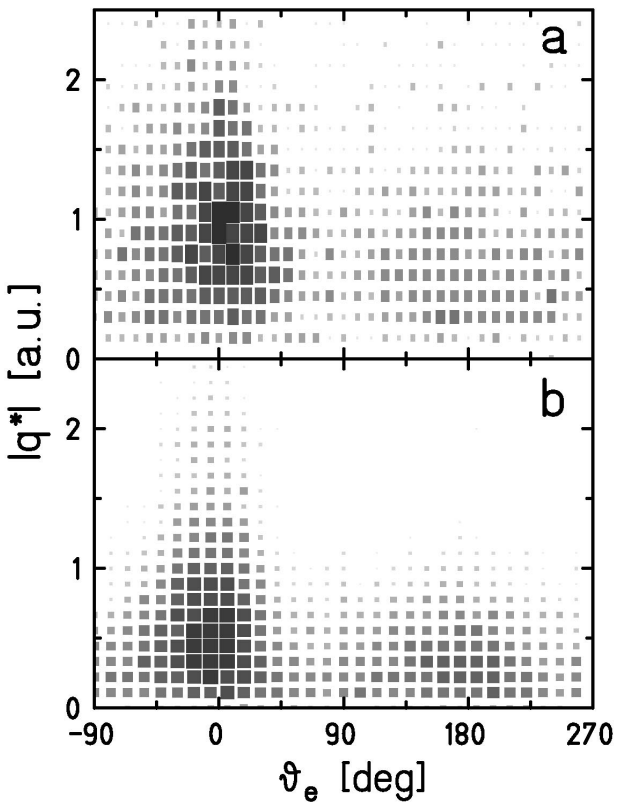


Figure 2: *Momentum transfer q^* versus electron emission angle in coplanar geometry for (a) ionization of C^{2+} projectiles selecting the (e-e) mechanism (see text) and (b) for ionization of He by 2 keV electron impact.*

technique may provide the key to systematic (e,2e) investigations on ions.

Purely classical CTMC calculations indicate that collision partners with more asymmetric electronic binding energies are desirable to really fulfill the equivalence to electron impact ionization. The ESR is the ideal device to study such systems. Presently work is in progress to implement a REACTION-MICROSCOPE into the ESR which will, in combination with the already installed zero-degree high-energy electron spectrometer, allow for the first time to explore the collision dynamics involving one or few-electron heavy-ions in a kinematically complete way.

This work was supported by the Gesellschaft für Schwerionenforschung, the Leibniz-program of the Deutsche Forschungsgemeinschaft DFG, and BMBF.

References

[1] T.N. Rescigno et al., Science 286, 2474 (1999)
[2] H. Erhardt et al., Phys. Rev. Lett. 22, 89 (1969)
[3] M.E. Rudd and T. Jorgensen, Phys. Rev. 133, 666 (1963)
[4] D.S.F. Crothers, J. Phys. B 15, 2061 (1982)
[5] J. Ullrich et al., J. Phys. B 30, 2917 (1997)
[6] P. Fainstein, Phys. Rev. A 53, 3243 (1996)
[7] M. Schulz et al., J. Phys. B 43, L305 (2001)
[8] R. Moshammer et al., Phys. RevLett. 87, 223201 (2001)
[9] H. Kollmus et al., Phys. Rev. Lett. accepted
[10] A. Dorn et al., Phys. Rev. Lett. 82, 2496 (1999)

Orientation dependence of multiple ionization of diatomic molecules in collisions with fast highly charged ions

B. Siegmann, U. Werner, N.M. Kabachnik, H.O. Lutz, University of Bielefeld
R. Mann, GSI Darmstadt

The multiple ionization and fragmentation of simple molecules has been the subject of many recent experimental and theoretical investigations (see e.g. [1, 2]). One of the important characteristics of these processes is the angular distribution of ionized fragments. In case of diatomic molecules, it is simply related to the dependence of the probability for multiple ionization on the alignment of the molecular axis with respect to the ion beam.

The collimated beams of 5.9MeV/u Xe^{18+} and Xe^{43+} ions provided by UNILAC interact with an effusive N_2-gas target. The slow ions and electrons generated in the collision process are separated by a weak homogenous electric field of 333V/cm perpendicular to the beam and the detector plane. Electrons are detected by a channeltron at one side of the interaction region; positive ions are accelerated towards the time- and position-sensitive multiparticle detector at the other side. The detector is based on microchannel plates in combination with a crossed-wire anode structure consisting of independent x- and y-wires [3]. For each positive fragment ion the position on the detector and the time of flight relative to the electron signal are recorded. Thereby, the experimental set up is sensitive to all reaction channels resulting in at least one electron and one or more positive fragment ions. From the measured positions and flight times of the correlated fragments their initial velocity vectors can be determined using classical mechanics. If both fragments from a particular fragmentation are detected, these data yield a kinematically complete image of the molecular break up process, and the dissociation energy and the orientation of the molecular axis can be derived for each individual event.

As an example, Fig.1 shows the measured intensities for six- and tenfold ionization of N_2 as a function of the orientation of the molecular axis relative to the projectile beam. The results for $(N_2)^{6+}$ contain contributions from the $N^{3+} + N^{3+}$ and the $N^{2+} + N^{4+}$ channels; the $(N_2)^{10+}$ channel contains contributions from the $N^{5+} + N^{5+}$ and the $N^{4+} + N^{6+}$ coincidences. In both cases the symmetric fragmentation reaction is clearly more abundant than the asymmetric one. In case of an isotropic fragmentation the distribution of the angle θ is described by a $\sin\theta$-function (dotted line); a deviation from the sin-function indicates an anisotropy. Fig.1 clearly shows a strong orientation effect for Xe^{18+} impact: the probability of tenfold ionization is suppressed when the molecule is oriented perpendicular to the beam. The effect is much smaller for the more highly charged Xe^{43+} projectiles. The orientation effect is practically absent for the $(N_2)^{6+}$ ionization.

In order to interpret these experimental observations we have applied a modified statistical energy deposition model as originally developed by Russek-Meli[4] and Cocke[5]. The model considers the process of multiple ionization as proceeding in two steps. At first, part of the kinetic energy of the fast projectile is transferred to the target electrons. The deposited energy may be calculated using the well-developed approach of the stopping-power theory. In the second step, when the projectile is already far away from the target, electrons are emitted, their number being proportional to the volume of the available phase space. Higher-order corrections to the stopping power, applied by the so-called unitary convolution approximation (UCA) [6], make the modified SED-UCA model applicable to more highly charged ions [7, 8].

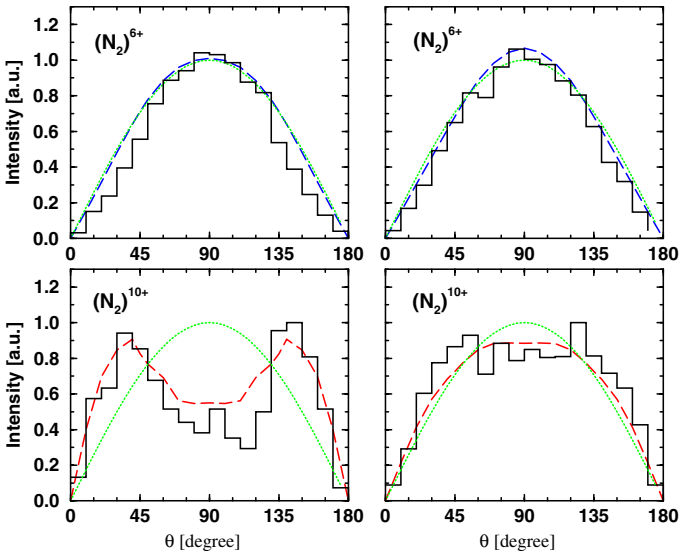


Figure 1: Orientation dependence of the cross section for $(N_2)^{6+}$ and $(N_2)^{10+}$ ionization channels in collisions with 5.9 MeV/u Xe^{18+} (left) and Xe^{43+} (right) projectiles. (- -) SED-UCA model, $(\cdots)$ sin-function

The results of our calculations reproduce the experimental observations. For a diatomic molecule oriented along the beam the probability of a large energy deposition is greater than for an orientation perpendicular to the beam. In collision with fast highly charged ions this effect occurs at much higher degrees of ionization than in previous experiments with singly charged projectiles [9].

References

[1] L. Adoui et al., J. Phys. **B 32**, 631 (1999)
[2] B. Siegmann et al., Phys. Rev. **62**, 022718 (2000)
[3] U. Werner et al., Nucl. Instrum. Methods **B124**, 298 (1997)
[4] A. Russek and J. Meli, Physica **46**, 222 (1970)
[5] C.L. Cocke, Phys. Rev. **A 20**, 749 (1979)
[6] G. Schiwitz et al., Nucl. Instrum. Methods **B153**, 1 (1999)
[7] B. Siegmann et al., Phys. Rev. **65**, 010704 (2001)
[8] Z. Kaliman et al., Phys. Rev. **65**, 012708 (2001)
[9] U. Werner et. al. Phys. Rev. Lett. **79**, 1662 (1997)

Channeling experiment with 20 MeV/u U^{91+} ions extracted from the ESR storage ring

D. Dauvergne[1], A. Bräuning-Demian[2], F. Bosch[2], H. Bräuning[3], M. Chevallier[1], C. Cohen[4], A. Gumberidze[2], A. L'Hoir[4], R. Kirsch[1], C. Kozhuharov[2], D. Liesen[2], P. Mokler[2], J.-C. Poizat[1], C. Ray[1], Th. Stöhlker[2], M. Tarisien[2], S. Toleikis[2] and M. Toulemonde[5]

[1] IPNL, Villeurbanne, France, [2]GSI, Darmstadt, Germany, [3]JLU, Giessen, Germany, [4]GPS, Paris, France, [5]CIRIL, Caen, France

A new domain in physics is opened, with the possibility to study the recombination of highly-charged decelerated ions, far from their equilibrium charge state in matter. In particular, in solids, a strong polarization of the electron gas will be induced in the vicinity of the ion, thus influencing both the charge exchange probabilities, and the energy deposition along the ion track.

Crystal channeling presents the unique feature to provide a dense quasi-free electron gas target for ions travelling far from the target atomic rows or planes. It also allows, by selecting impact parameters, to study in details the competition between Radiative Electron Capture (REC) and Mechanical Electron Capture (MEC). Indeed, REC probabilities depend mainly on the electron density sampled by the projectile, and thus REC (dominated by the capture into K- and L-shells) can occur in regions where only valence or conduction electrons are present. On the other hand MEC probabilities are much more peaked at small impact parameters, because, first, the target atom recoil is needed for energy and momentum conservation during the charge exchange process, and, second, the overlap between initial and final wave functions of the transferred electron is required both in spatial and momentum spaces.

After the first success of the deceleration–extraction technique for Au^{78+} ions at 53 MeV/u in 1995 [1], experiments at lower energies had been performed only inside the ESR storage ring, using the internal gas target. The present experiment, performed in December 2001, succeeded in decelerating, cooling, extracting and transporting a U^{91+} ion beam at 20 MeV/u into cave A.

Fig.1 presents a spectrum of transmitted ions at the focal point after a magnetic analysis by the cave A spectrometer. This spectrum was obtained in axial channeling conditions along the <110> direction of a 11.7 µm thick silicon crystal. A broad charge state distribution is observed, that is governed by the large REC probabilities for channeled ions. For a random crystal orientation none of these high charge states are transmitted. The significant fraction of the ions frozen in their initial 91+ state is an encouraging indication that thicker crystals could be used to decelerate highly-charged ions down to very low velocities.

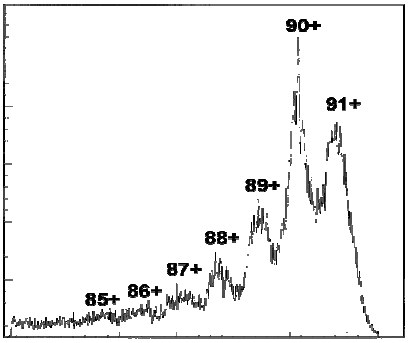


Figure 1 : transmitted ion charge state distribution for axial crystal orientation

More information will be extracted from the X-ray spectra, as shown in figs. 2-a and b for random and axial crystal orientations, respectively. These spectra were recorded at 90° from the beam direction by a collimated Ge detector. For the random orientation, the MEC probabilities are more than two orders of magnitude higher than the REC ones, and incident U^{91+} ions captured, in average, more than 15 electrons in the target; Thus the only visible lines are projectile K- and L-lines, resulting from the decay after capture into high n,l states. When transmitting the ions along the <110> crystal axis, K- and L-REC peaks appear nicely, because most of the ions, travelling far from the atomic strings in the crystal, can no longer undergo MEC. The comparison of the two spectra shows that, for the random orientation, the projectile K and L shells are filled already within the very first thousands Angströms by MEC, thus inhibiting K-and L-REC during the whole path inside the target. On the other hand, the K-and L-REC line shape reflect the electron momentum distribution in the initial state (Compton profile). Indeed, these lines, observable in channeling conditions, are very narrow. This clearly shows that only valence electrons can be captured by REC, because MEC is already dominant at impact parameters of the order of the spatial extension of the silicon core electrons (i.e. about 0.5 Å). A detailed analysis of the experiment is currently carried out.

Support by IN2P3-GSI collaboration agreement is highly acknowledged.

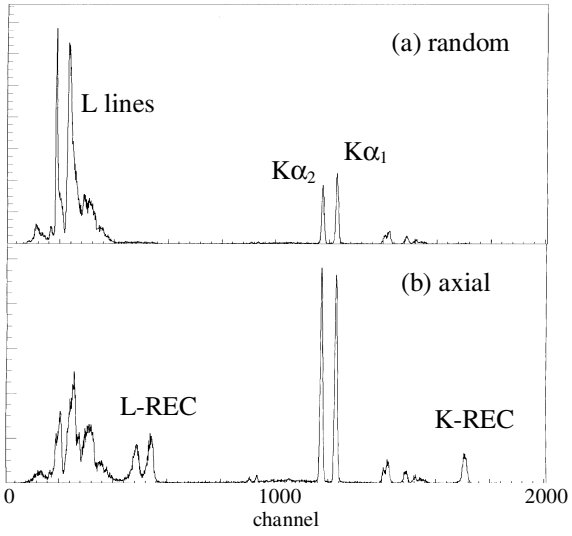


Figure 2 : X-ray spectra obtained at 90° for 20 MeV/ u U^{91+} ions incident on a 11.7µm thick Si crystal (a) random crystal orientation (b) <110> axial orientation

References

[1] H. T. Prinz et al., Hyperfine Interactions 108(1997)325, S. Andriamonje et al., J. Phys. B30(1997)5099.

Multiple Electron Capture from C-foils into Slow Highly-Charged Ions

H. Bräuning[1], A. Bräuning-Demian[2], G. Bednarz[3], F. Bosch[2], X. Cai[4], C. Cohen[5], D. Dauvergne[6], A. Gumberidze[2], H. Harutyunyan[7], R. Kirsch[6], C. Kozhuharov[2], D. Liesen[2], P.H. Mokler[2], J.-P. Rozet[5], Z. Stachura[8], Th. Stöhlker[2], M. Terasawa[9], S. Toleikis[2], A. Warczak[3], ESR-Team[2]
[1]JLU Giessen (Germany), [2]GSI (Germany), [3]University of Cracow (Poland)
[4]IMP Lanzhou (China), [5]GPS Paris (France), [6]IPNL Villeurbanne (France),
[7]Yerevan SU (Armenia) [8]INP Carcow (Poland), [9]Himeji Inst. of Technology (Japan),

The differences in ion-atom collisions with gas targets on one side and solid targets on the other side constitute a well known problem in collision physics which is still not well understood [1]. The SIS-ESR facility at GSI with the newly installed charge state spectrometer in Cave A provides an ideal tool to study the interaction of ultimately charged very heavy ions ($Z\alpha \rightarrow 1$) with solids at moderate velocities down to about 15 MeV/u.

In the first experiment in 1999 [2, 3] we have observed an unexpected increase in the multiple electron capture yield with decreasing target thickness for 46 MeV/u Pb^{81+} ions traversing thin C foils (see fig. 1). In contrast, the yields for

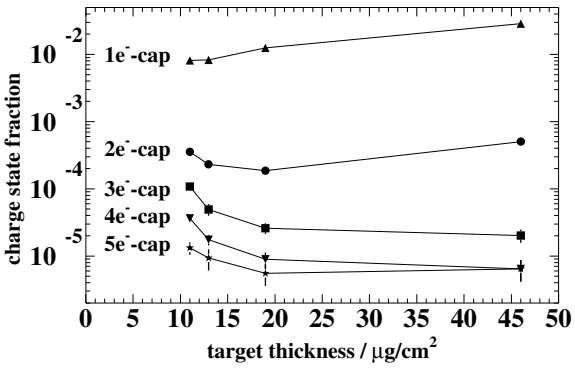


Figure 1: *Electron capture yields for collisions of 46 MeV/u Pb^{81+} with thin carbon foils.*

single capture and projectile ionization (not shown here) show the expected linear dependence on the target thickness. The targets were evaporated graphite-like C foils prepared in the GSI target laboratory following standard procedures.

Using targets from the same production lot we have repeated the experiment using a beam of 46 MeV/u U^{91+} ions (see fig. 2 top). Again single capture and projectile ionization show the expected linear dependence on the target thickness. Although the data now show an increase in the multiple electron capture yield for the thickest target, we consistently observe also an increase for the thinnest targets as in the previous experiment.

Very thin targets can be realized with diamond like carbon (DLC) foils [4]. Fig. 2 (bottom) shows the results for 4 and 8 $\mu g/cm^2$ thick DLC targets (circles) and for a stack of 2×4 $\mu g/cm^2$ thick targets (triangle). For capture as well as projectile ionization, the yield for the thicker DLC target is higher than for the thinner one. For single electron capture and ionization no difference in yield between the stack and the single 8 $\mu g/cm^2$ thick target could

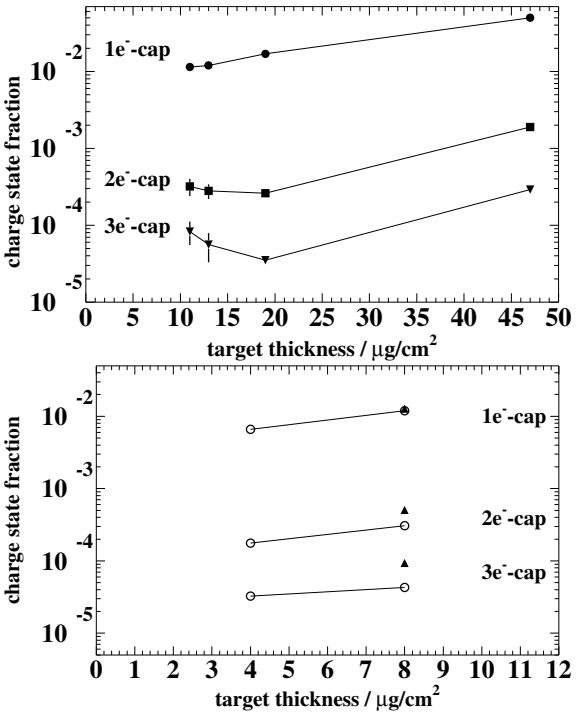


Figure 2: *Electron capture yields for collisions of 46 MeV/u U^{91+} with thin carbon foils (top) and DLC foils (bottom).*

be observed within the error bars. However, the multiple electron capture yield in the stack is significantly higher as compared to the single target.

To invesitgate the influence of target preparation and surface structure we have measured multiple electron capture yields also for targets prepared by a commercial manufacturer (Arizona Company, USA) and for targets specially prepared by the GSI target lab to achieve a smooth surface. The analysis of these measurements as well as the invesitgation of the surface structure with an electron microscope is currently in progress.

We gratefully acknowledge support by EC-HPRI-CT-1999-00001 and IN2P3-GSI collaboration contract.

References

[1] M. Jäger. PhD thesis, Univ. Frankfurt, Germany, 1996.
[2] H. Bräuning et al. *Phys. Rev. Lett.*, 86:991, 2001.
[3] H. Bräuning et al. *Physica Scripta*, T92:43, 2001.
[4] P. Maier-Komor. TU München.

Impact of Extended Charge Distribution on Energy-Loss Straggling of Heavy Ions

H. Weick[1], A.H. Sørensen[2], H. Geissel[1,3], C. Scheidenberger[1]

[1] GSI, [2] Aarhus Universitet, [3] Universität Gießen

The energy-loss straggling of partially ionized heavy ions is determined by the stochastic fluctuations of the energy loss in atomic collisions remaining in a fixed charge state, (collisional straggling) and by the influence of charge-state fluctuations (charge-exchange straggling) [1, 2]. Besides the charge-changing cross sections the charge-exchange straggling depends critically on the differences between the partial stopping powers of ions in different charge states, and small modifications can influence the variance of the energy loss (Ω^2) considerably. Therefore, new measurements of energy-loss straggling for few-electron uranium ions penetrating different solids at (200-1000) MeV/u were performed with the fragment separator FRS using the same method as already described in ref.[1] and the theory of partial stopping powers was improved.

To determine the difference in stopping number (ΔL_{Z-n}) between an ion of nuclear charge (Ze) carrying (n) electrons with a realistic charge distribution and a point-like system of charge $(Z-n)e$, the method described in ref.[3] for a homogenously charged nucleus was extended to a realistic charge distribution as given by the relativistic quantum-mechanical probability density of 1s-state electrons [4, 5]. As the de Broglie wavelength of a scattered target electron in the rest frame of the projectile is comparable to the radius of the K-shell of an uranium ion in the considered energy range, the electron will probe the true charge distribution of the projectile and scattering will be different from that pertaining to a point charge. In Fig.1 one can clearly see that perturbation theory underestimates the difference ΔL_{Z-1} by far for high energies. Towards lower velocities close collisions contribute less to the total stopping power and the difference decreases.

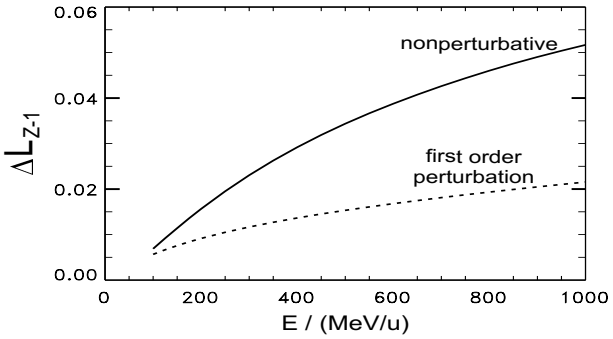


Figure 1: Difference in stopping number ΔL_{Z-1} for a uranium nucleus screened by a 1s-electron compared to a point-charge model as a function of projectile energy. Shown are the nonperturbative solution and the result of the calculation in first-order quantum perturbation theory.

The small differences shown in Fig. 1 are not detectable in direct stopping power measurements. However, the positive values of ΔL imply that the stopping power for few electron ions is closer to the one for bare ions at high velocities than for the corresponding point-like ion. This reduces the energy-loss straggling compared to our former Monte-Carlo simulations [2] which used partial stopping powers for point-like projectiles and thereby tended to overestimate Ω^2 at higher energies. At lower energies, on the other hand, the agreement between simulation and experiment was excellent. Taking into account the realistic charge distribution of the projectile the discrepancy vanishes in the new measurements on U and is reduced by more than half for the older (see [2]) Bi data, cf. Fig. 2. Again one notices the strong contribution from charge-exchange straggling in beryllium and aluminum targets, whereas in lead or gold there is no significant deviation from pure collisional straggling. The figure also indicates the importance of exact compared to perturbation theory.

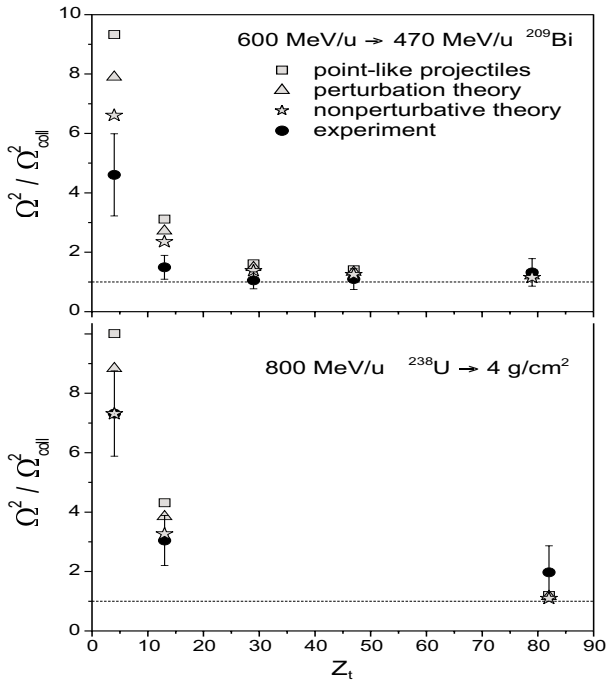


Figure 2: Measured energy-loss straggling of 600 MeV/u Bi ions after losing on average 130 MeV/u in each target material (Z_t) and of 800 MeV/u U ions after penetrating targets of approximately 4 g/cm^2 thickness. The experimental results are plotted normalized to the predictions for pure collisional straggling [3] and compared with a Monte-Carlo simulation including charge exchange assuming point-like projectiles or a realistic charge distribution in perturbative and nonperturbative theory.

References

[1] H. Weick *et al.*, Nucl. Instr. & Meth. **B164/165** (2000) 168.

[2] H. Weick *et al.*, Phys. Rev. Lett. **85** (2000) 2725.

[3] J. Lindhard, A.H. Sørensen, Phys. Rev. **A53** (1996) 2443.

[4] H. Weick, A.H. Sørensen, et al., Nucl. Instr. & Meth. B (2002) in print.

[5] A.H. Sørensen, submitted to Nucl. Instr. & Meth. B.

PHELIX, a Petawatt High Energy Laser for Heavy-Ion Experiments

Th. Kühl[1,3], J. Alvarez[1], B. Becker-de Mos[1], R. Bock[1], S. Borneis[1,5], E. Brambrink[1,2], H. Brand[1], D. Browning[4], C. Bruske[1], K. Brück[3], J. Caird[4], E. Dewald[2], H. Duddek[1], E. W. Gaul[1], C. Häfner[1], T. Hahn[1], D.H.H. Hoffmann[2], H.-J. Kluge[1], D. Marx[1], P. Neumayer[1], M. Perry[5], K. Poppensieker[1], D. Reemts[1], I. Reinhard[1], M. Roth[1], S. Samek[6], W. Seelig[2], A. Tauschwitz[2], R. Wilcox[4]

[1]Gesellschaft für Schwerionenforschung mbH, Planckstr.1, 64291 Darmstadt, Germany
[2]TU Darmstadt, Schlossgartenstr. 7, 64283 Darmstadt, Germany
[3]Universität Mainz, Staudingerweg 7, 55099 Mainz, Germany
[4]Lawrence Livermore National Laboratory, 7000 East Ave., Livermore, CA 94550, USA
[5]General Atomics, P.O. Box 85608, San Diego, CA 92186, USA
[6]Jagiellonian University, Reymonta 4, Krakow 30-059, Poland
http://www.gsi.de/phelix

Construction at the PHELIX laser project [1] continued during the year 2001. A major milestone was reached in May, when the projected performance values were demonstrated at the femtosecond front-end (see Fig.1.). This front-end comprises of a commercial femtosecond oscillator (Coherent Mira), pumped by a 10 W diode-pumped Nd:YVO_3 laser, a compact chirped-pulse stretcher unit, and a specially designed combination of each a linear and a ring-configuration regenerative amplifier. Each of these regenerative amplifiers is pumped by a Nd:YAG laser operating at 10 Hz repetition rate. The laser system provides frequency chirped, stretched pulses with nearly 10 nm bandwidth (FWHM) and an energy of 40 mJoule for the injection into the pre-amplifier section.

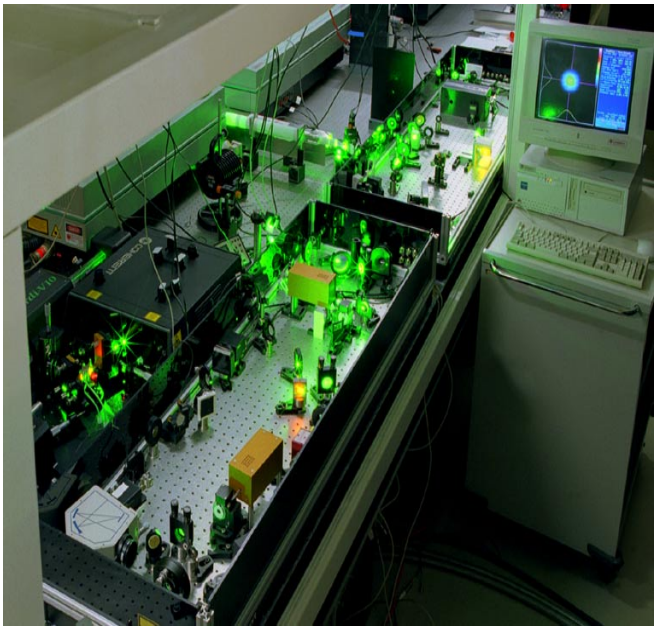


Figure 1.: In May the required performance data were demonstrated of the femtosecond-frontend. In the foreground linear regenerative amplifier is shown, behind it the ring amplifier. In the background the two Nd:YAG pump lasers are visible. Lids normally covering the light pass have been removed for better visibility.

These laser pulses are synchronized to sub-ns precision to an external RF-clock and it is feasible to link the clock to the timing of the UNILAC or the SIS. The synchronization between laser pulses and ion pulses has been worked out to ns precision and is straightforward to implement.



Fig. 2 : The 45 mm amplifier of the pre-amplifier section. The Nd:Glass amplifier rod is surrounded by 12 flash lamps.

Components of the pre-amplifier were tested and delivered later in the year, including the 45 mm amplifier shown in Fig. 2. The implementation into the front-end section was prepared and will soon start. Implementation of adaptive optics is now foreseen using an 80 mm deformable mirror immediately after the pre-amplifier section. This will compensate for distortion in the glass rods and partly also pre-compensate the effects of the high-energy amplifier. Components of this system will be evaluated in a test set-up at the Vulcan-Laser facility at the CLF [2] in spring 2002.

For the diagnosis of the laser pulse profile at various positions along the beamline, which requires simultaneously triggered acquisition of several pictures, a FireWire based camera

solution has been successfully implemented and tested using LabVIEW.

The prototype of the charging and firing circuits of the capacitor bank that powers the flash-lamps of the main amplifiers has been developed and tested. For the control of these components a fiber optic based Profibus system with LabVIEW has been implemented and taken into operation.

The optical pass through the amplifier chain was simulated using a raytracing code and a beam propagation code. While the raytracing code is more suitable to minimize wavefront aberrations and to design missing lenses for beam transport telescopes, the beam propagation code includes the laser gain, B-integral, and spatial filter effects. Wavefront distortions, laser gain, and beam shape were simultaneously optimized. Critical parameters like the amplification of stray reflections from the optical surfaces and the fluence on delicate components have been studied in detail.

In parallel, the mechanical preparation of the main amplifier section was continued. The GSI design [3], using components of the Phebus- and Nova-lasers in a folded double-pass, instead of the original single-pass linear chain, requires a number of modifications. In particular the center section of the large spatial-filter telescope on the left side in Fig. 3 has to be changed. Here the pulse from the pre-amplifier is injected through a slightly off-axis pinhole in the focal plane. It will then be directed through the amplifiers on the right hand side via two mirrors, and send back for a second amplification pass.

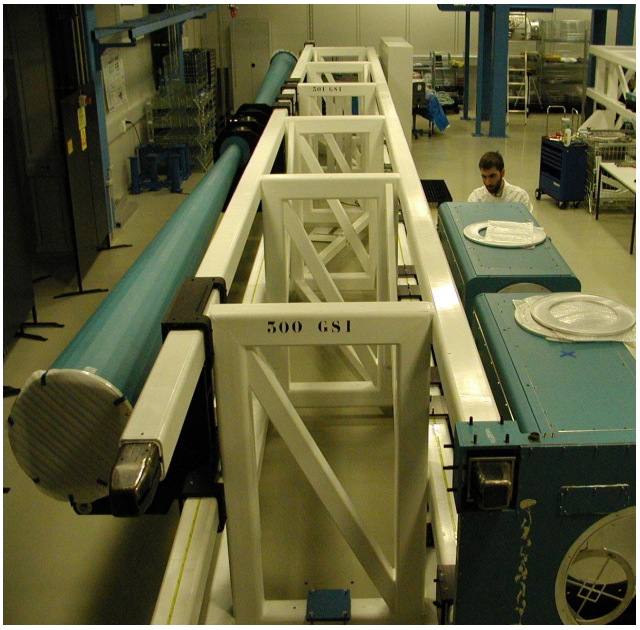


Fig. 3: Mechanical adaptation of the laser components for the main amplifier chain has proceeded. On the right hand side, amplifier modules are mounted. On the left hand side, the spatial filter telescope is modified for the 2-pass design.

An important step towards the installation of laser optics was the completion of the class-100 clean room area. This facility is needed for the final cleaning and assembly of the main amplifier components. It is located in the upper floor of the laser building. As the last missing equipment the large high pressure water spray booth for the cleaning of the amplifier housings, shown in Fig. 4, was installed in November. This unit also serves as an entrance gateway for mechanical components being introduced into the clean-room.



Fig. 4: The high pressure water spray booth for the cleaning of the amplifier housings operates with de-ionized water to avoid residues on the optics, at temperatures up to 60C. It also serves as lock-gate for components being introduced into the class-100 clean room facility located at the other side of the wall.

References

[1] PHELIX Project, GSI-98-10 Report, December 1998

[2] Adaptive Optics trials on Vulcan, S. Hawkes, J. Collier, C.Hooker, C.Reason, C. Edwards, C.Hernadez-Gomez, C.Danson, I.Ross, C. Haefner, Central Laser Facilility Annual Report 2000/2001, RAL-TR-2001-030, ISBN 0902376160, P153-155

[3] PHELIX - A Petawatt High-Energy Laser For Heavy-Ion Experiments, R. Bock, S. Borneis, Ch. Bruske, J. Caird, D. Habs, D. Hoffmann, H. Kluge, Th. Kühl, D. Marx, P. Nickles, M. Perry, M. Roth, W. Sandner, W. Seelig, A. Tauschwitz, Inertial Fusion Sciences and Applications 99, C. Labaune, W.J. Hogan, K.A. Tanaka Eds., Elsevier Publishing, Paris, Amsterdam, Lausanne, New York, Oxford, Shannon, Tokyo (2000), 703

X-Ray Laser Spectroscopy on Lithium-like Ions

P. Neumayer[a], J. Alvarez[b], A. Bardonner[b], B. Becker-de Mos[b], S. Borneis[b], K. Brück[b], C. Bruske[b], E.W. Gaul[b], C. Häfner[b], K. Janulewicz[c], H.-J. Kluge[b], T. Kühl[b], D. Marx[b], I. Reinhard[b], M. Tomaselli[a], P.V. Nickles[c], W. Sandner[c], W. Seelig[a]

[a]TU Darmstadt, Germany; [b]GSI-Darmstadt, Germany; [c]Max-Born-Institut, Berlin, Germany

Atomic spectroscopy on highly charged ions with one or only few electrons offers the advantage that the electron wave function and thus the atomic hyperfine fields at the site of the nucleus can be precisely calculated. In this way, nearly model free absolute charge radii can be determined. For laser spectroscopy, lithium-like ions represent a good compromise between the request for reliable calculations of the electronic factor and low atomic excitation energy. The photon energies required to excite the ground state transition $2s_{½}$-$2p_{½}$ go up to 280 eV for lithium-like uranium.

The short pulse front-end and the preamplifier of PHELIX represent a laser system well suited for pumping plasma based X-ray lasers with wavelengths down to 10 nm. Such an X-ray laser system is presently under construction. The large Doppler shift in the ESR can be exploited to reach the necessary excitation energy and, by varying the beam velocity, the transition resonance can be scanned using the fixed frequency X-ray laser. The experimental procedure will be similar to the established scheme used for laser spectroscopy of the ground state hyperfine splitting in hydrogen-like ions [1]. With the low repetition rate of the X-ray laser of 1 shot per 10 minutes there is no direct benefit from performing the experiment inside the storage ring. An alternative scheme would be to kick the cooled bunch out into the re-injection channel for this experiment.

Table top X-ray lasers have been realized with wavelengths down to 11.9 nm or photon energies of 99 eV [2]. The most reliable and efficient X-ray lasers up to date are those based on the transient collisional excitation (TCE) scheme [3]. A nanosecond pulse focused to a line focus onto a metal target creates a plasma column. This plasma is then rapidly heated by a high intensity ps-pulse which leads to a non-stationary population inversion and this way to a high transient gain.

In order to provide the necessary pulses from the PHELIX front-end, a single grating pulse compressor has been calculated and designed, which can compress laser pulses with energies up to 15 J. Special mounts had to be built to hold the large size optics. To eliminate spatial and temporal distortions due to nonlinear effects the entire pulse compressor has to be placed in vacuum (Fig. 1). The optical tables inside the vacuum chamber are mechanically isolated from the walls of the chamber by means of bellows and separately fixed to the floor. For the target chamber a vacuum vessel from a former experiment was put into operation again, only slight modifications were necessary.

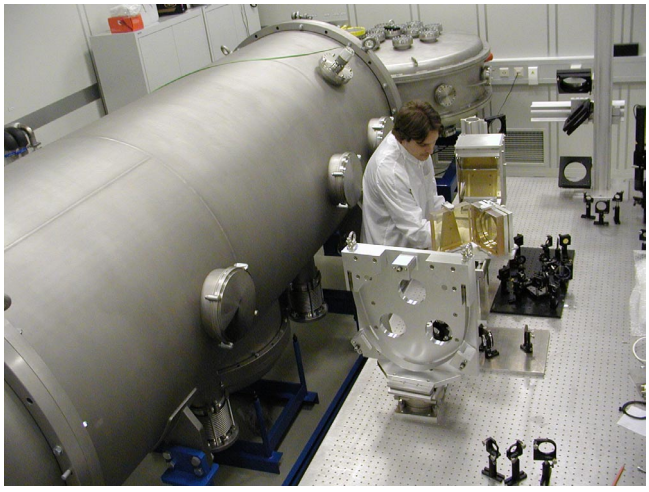


Fig. 1: Vacuum chamber and optics mounts for the pulse compressor (front) and target chamber (background).

An on-axis parabola tilted at an incidence angle of 22 degrees is used to generate a line focus less than 0.1 mm wide and over 10 mm long. The lifetime of the high gain in the TCE scheme is typically in the order of a few picoseconds. Therefore the focus of the short pulse creating the population inversion in the plasma has to run along the plasma column with approximately the speed of light *c* ("traveling wave excitation", TWE) to maximize the overlap of the x-ray pulse and the gain peak.

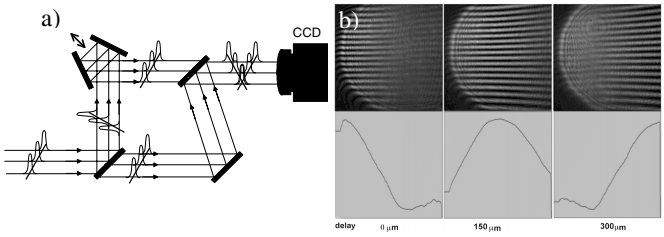


Fig. 2: a) Scheme of the "Inverted Field Autocorrelator", b) interference patterns and corresponding contrast functions along the horizontal axis. The shift in the maximum of the contrast function for different delays results from a pulse front tilt of 18 mrad.

Due to the intrinsic tilt of the wavefront, the proposed focusing geometry by itself produces a travelling wave of approximately 1.4 *c*. This is quite appropriate compared to other off-axis arrangements. The additional pulse front tilt necessary to slow down the traveling wave to *c* is only 55 mrad, which can be achieved by changing the angle of incidence in the compressor by 4 mrad. As a sensitive tool to check the small changes in the TW velocity induced by the compressor misalignment we built a so called *inverted field autocorrelator* [4]. This is a Mach-Zehnder–type interferometer in which in one arm the beam is spatially inverted by a fold mirror (Fig. 2a). A test to verify the resolution of the device is shown in Fig. 2b.

The major parts for the realization of an X-ray laser have arrived at GSI and are being assembled. The focusing optics and part of the optical diagnostic has been tested. After the compressor optics has been installed we expect to be ready to receive pulses from the PHELIX front-end system for first shots on target by mid of 2002.

References

[1] I. Klaft *et al.*, Phys. Rev. Lett. **73**, 2192, 1994
[2] J. Dunn *et al.*, Phys.Rev.Lett. **84**, 4834-37, 2000
[3] P.V. Nickles *et al.*, Phys. Rev. Lett. **78**, 2748-2751, 1997
[4] G. Pretzler *et al.*, Appl. Phys. B **70**, 1-9, 2000

Preparation for High-Resolution Isotope Shift Measurements of ^{8,9,11}Li

H. Wang[a,c], A. Dax[a], W. Nörtershäuser[a,b], I. Katayama[c,d], R. Kirchner[a], H.-J. Kluge[a], T. Kühl[a], R. Sanchez[a], I. Tanihata[e], M. Tomaselli[a,f], C. Zimmermann[b]

[a]GSI Darmstadt; [b]Univ. Tübingen; [c]Univ. Tokyo; [d]IPNS, KEK, Japan; [e]RIKEN, Japan; [f]TU Darmstadt

The investigation of halo nuclei has attracted much attention within the last decade and many approaches for a description of this exotic structure have been developed [1]. However, the fundamental question of how much the core nucleons are affected by the presence of the halo-forming nucleons has not yet been resolved. Hence, an experimental determination of the rms charge radius of the neutron halo-nucleus ^{11}Li, particularly its change from that of ^{9}Li, is of great interest and would constitute a sensitive test for various nuclear models.

A high-precision isotope shift (IS) measurement in the 2S→3S transition of atomic lithium combined with a theoretical evaluation of the mass shift contribution [2] will provide a model-independent value for this quantity [3, 4, 5]. This approach is actually the only method currently available to determine the charge radii of unstable Li isotopes, especially of ^{11}Li, since standard methods like electron scattering and x-ray spectroscopy in muonic atoms are excluded due to the short half life of 8.6 ms and the limited production rate for this isotope. The contribution of the nuclear volume effect to the overall isotope shift is only a small fraction of the natural transition linewidth and requires a measurement with a relative accuracy of better than 10^{-5} in order to obtain the charge radius of ^{11}Li with an uncertainty of less than 2 %. Hence, high efficiency and high accuracy must be achieved at the same time which represents a challenge.

Two-photon laser excitation from the ground state $2S$ to the $3S$ state has been chosen to probe the IS. The excited atoms undergo spontaneous decay into the $2P$ state and are then efficiently ionized via the $3D$ intermediate level. Subsequent low-background single-ion detection provides a sufficiently high signal-to-noise ratio. This excitation scheme has been tested for the stable isotopes ^{6,7}Li [3]. From the results of these measurements an ionization efficiency of $\approx 10^{-3}$ has been estimated.

The experimental setup consists of three major parts: A hot source for converting the energetic nuclei into thermal atoms, the laser system for resonant excitation and ionization of the neutral atoms and a mass spectrometer for detection of the produced ions. The 735 nm radiation for the resonant two-photon transition from $2S$ to $3S$ is provided by a titanium-sapphire (Ti:Sa) laser while a dye laser produces the 610 nm radiation for the resonance-enhanced two-photon ionization. Both laser beams are coupled into an optical cavity, which is constructed around the excitation region to provide the high laser intensities needed for the excitation and ionization processes. To assure the necessary frequency precision of the order of 100 kHz the Ti:Sa laser will be stabilized by RF-offset locking relative to a 735 nm diode laser, which in turn is stabilized to a molecular iodine transition as a fixed frequency reference point. An appropriate transition in iodine has been located at 13603.22 cm^{-1}and its hyperfine structure was recorded using FM-saturation spectroscopy. The iodine cell was heated to ∼600°C to provide sufficient population of the lower level of the hot-band transition. A saturation signal recorded with laser powers of 20 mW in the pump and 1 mW in the probe beam (1 mm diameter) is shown in Fig. 1(a). Three groups of unresolved and three single hyperfine lines were observed. The strongest isolated line (a_1) is well separated from all others and will be used for locking the diode laser. A signal-to-noise ratio of about 300 was achieved for this line and it shows a peak-to-peak width of ∼10 MHz. Thus an accuracy of about 30 kHz for locking to the reference point can be expected.

The ions obtained by the resonance ionization process are mass separated and detected with a commercial quadrupole mass spectrometer (QMS). Its axial electron beam ion source was replaced by ion optics constructed to meet the requirements of our experiment. The mass peak shape of the QMS has been optimized using lithium ions produced by surface ionization to yield an abundance sensitivity of better than 10^{-7}. A recorded mass spectrum is shown in Fig. 1(b).

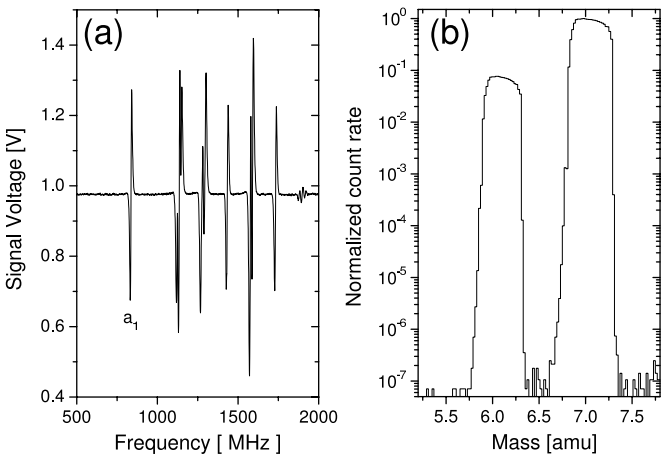


Figure 1: (a) Hyperfine spectrum of the iodine transition $X^1\Sigma_g^+ \rightarrow B0_u^+$ R(114) 2-11 at 600°C; (b) shapes of the mass peaks of the stable lithium isotopes ^{6,7}Li

References

[1] I. Tanihata, J. Phys. G **22**, 157 (1996)
[2] Z.-C. Yan, G.W.F. Drake, Phys. Rev. A **61**, 022504 (2000)
[3] A. Dax *et al.*, Jahresbericht GSI, 83 (1999)
[4] A. Dax *et al.*, CERN/INTC 2000-006 INTC/P118 (http://isolde.web.com.ch/ISOLDE/)
[5] F. Schmitt *et al.*, Hyperfine Interact. **127**, 111 (2000)

SHIPTRAP: A Capture and Storage Facility for Radionuclides from SHIP

G. Marx and W. Quint for the SHIPTRAP Collaboration
Gießen[1], GSI[2], Mainz[3], München[4], Vancouver[5]

Status of SHIPTRAP at GSI

D. Ackermann[2], H. Backe[3], F. Bosch[2], J. Dilling[5], A. Dretzke[3], H. Geissel[2], D. Habs[4], F.P. Heßberger[2], S. Hofmann[2], H.-J. Kluge[2], C. Kozhuharov[2], W. Lauth[3], R. Mann[2], G. Marx[2], G. Münzenberg[2], M. Mukherjee[2], J. Neumayr[4], W. R. Plaß[1], W. Quint[2], S. Rahaman[2], D. Rodríguez[2], C. Scheidenberger[2], M. Sewtz[3], G. Sikler[2], T.Stöhlker[2], P.G. Thirolf[4], M. Tarisien[2], C. Weber[2], Z. Zhou[1]

First successful on-line tests at the ion trap facility SHIPTRAP were performed at the end of 2001. The facility was set up to deliver very clean and cooled beams of singly-charged recoil ions produced at the SHIP velocity filter at GSI. SHIPTRAP consists of a gas cell for stopping high-energy recoil ions from SHIP, a radiofrequency (RF) ion guide for extraction of the ions from the gas cell, a linear RF trap for accumulation and bunching of the ions, and a Penning trap for isobaric purification.

SHIPTRAP will start operation in autumn 2002. The experimental programme which is envisaged by the SHIPTRAP user community promises to give new insights into the nuclear, atomic and chemical properties of elements beyond radium, which is the heaviest element available at usual ISOL facilities.

On-line test with the stopping chamber and RFQ buncher at SHIP

In the SHIPTRAP set-up the beam of exotic nuclei produced and pre-separated at SHIP enter a helium-filled stopping chamber through a thin window. This gas cell had been tested at the tandem accelerator in Garching and was coupled to SHIPTRAP for the first time. Due to the gas flow and applied electric fields, the ions (predominantly singly charged) are guided through the exit nozzle. The extracted beam is guided by a radiofrequency quadrupole (RFQ) and injected into another RFQ which is used as an ion accumulator and buncher. In a first on-line test, ^{40}Ca ions from the UNILAC filtered by SHIP (pulse duration: 6ms, repetition rate: 50Hz) were stopped in the gas cell at 50 mbar He pressure. The $^{40}Ca^{+}$ ions extracted from the cell were guided and accumulated into the RFQ buncher with a repetition rate of 10 Hz. The $^{40}Ca^{+}$ ions were finally extracted as a short ion bunch (FWHM: 580 ns) and identified by time of flight with a microchannel plate (MCP) detector (fig.1).

The Penning traps

A double trap system was installed in a 7 Tesla super-conducting magnet. Both Penning traps have cylindrical electrodes with an inner diameter of 32 mm. In the first trap the ion bunches from the RFQ buncher are captured and isobarically purified by mass-selective RF excitation of the ion motion. The second trap is optimized for high-accuracy mass measurements. The traps are separated by a diaphragm for differential pumping (distance between the centers of the traps: 20 cm).

Penning trap mass spectrometers at ISOLDE/CERN [1], Stockholm [2], and Argonne [3] use a time-of-flight method developed by Gräff et al. [4] to measure the cyclotron frequency of trapped ions. The ions are ejected out of the trap and their time of flight to a detector is recorded. Typically this requires the detection of 100 – 1000 ions. Assuming a production rate in the order of 10^{-3} ions/s, e.g. for Sg (Z = 106), this would lead to a beam time of about 1 - 10 days.

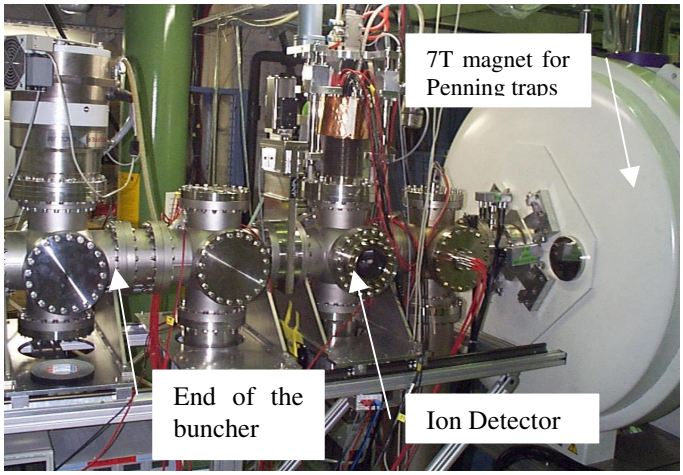


Figure 1: SHIPTRAP set-up : During the on-line test, the ions stopped in the gas cell are accumulated in the buncher before being detected by the ion detector (MCP) .

A non-destructive way to obtain eigenfrequencies of trapped ions is the FT-ICR (Fourier transform ion cyclotron resonance) detection method where the image currents induced in the trap electrodes by the oscillating ions are monitored (Fig. 2). This method is employed, e.g., at the University of Washington [5] and at the University of Mainz [6]. It allows for the non-destructive identification of single trapped ions, and the required beam time for the mass measurement of a heavy element is less than one day. In order to reach single-particle sensitivity, the image currents are detected via a cryogenic LC resonance circuit with high quality factor [7]. The set-up at SHIPTRAP will consist of a cryogenic system with the trap environment at 77 K and the detection electronics at 4 K.

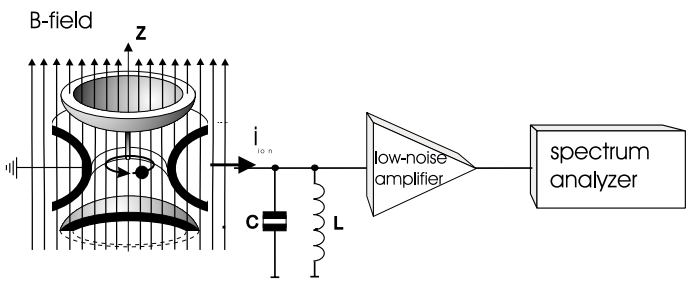


Figure 2: Principle of FT-ICR technique: The image current of stored ions is picked up by a trap electrode, amplified and frequency analyzed.

We acknowledge financial support by the European Union (Network EXOTRAPS and NIPNET), BMBF and GSI F&E programme.

The gas stopping cell and extraction RFQ for SHIPTRAP*

J. Neumayr[4], L. Beck[4], O. Engels[4], D. Habs[4], S. Heinz[4], P. Thirolf[4], V. Varentsov[4], F. Voit[4] and A. Wilfart[4]

Improved set-up of buffer gas cell and extraction RFQ

Based on tests with a first prototype set-up [8], the design of the buffer gas stopping cell and the extraction RFQ has been optimized. Special attention has been paid for the acceptance of the full SHIP beam dimensions of about 50 x 30 mm^2, resulting in a significant enlargement of the set-up.

The cell (fig. 3) is designed for stopping heavy ions from energies between 10 keV/u and 500 keV/u in helium at pressures between 10 and 100 mbar. The lower energy limit is given by the availability of large area (60 mm diameter), thin (< 2.5 µm), pinhole-free metallic (Al, Ti, Ni) entrance windows. Since any impurities inside the cell drastically reduce the extraction efficiency via molecule formation and recombination, purity inside the cell is a prime prerequisite. UHV conditions (< 10^{-9} mbar) have to be achieved by effective pumping, heating and usage of only metallic and ceramic components. During operation it is necessary to use very clean gas (He 7.0) combined with an effective purification system (< 1 ppb).

For the transport of the stopped ions inside the SHIPTRAP gas cell (length: 330 mm, diameter: 250 mm) RF and DC fields are employed to guide the ions towards the nozzle where they are extracted via the gas flow. In addition to the cylindrical DC electrodes, a funnel-shaped system of 40 ring electrodes is installed in front of the nozzle. The voltage applied to the funnel consists of both an RF (phase shift of 180^0 between adjacent ring electrodes) and a DC component to combine the effects of focussing and acceleration in an optimum way.

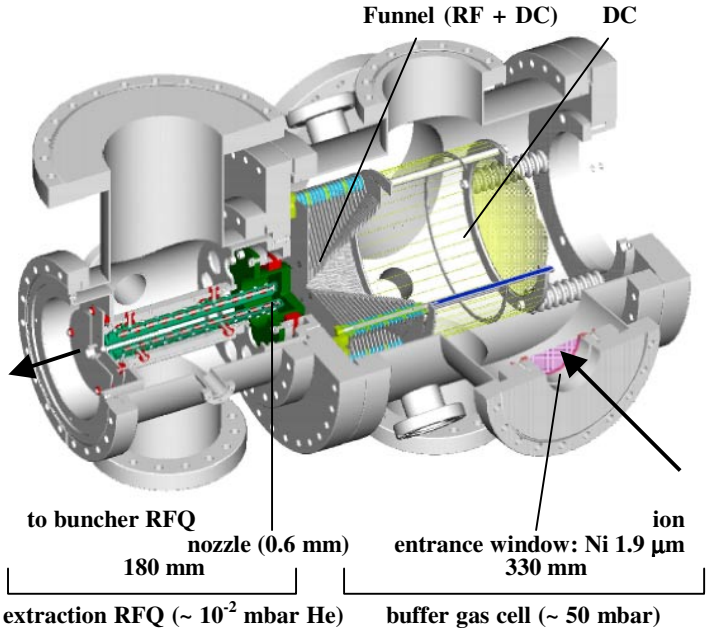


Figure 3: The Munich part of SHIPTRAP with the buffer gas cell and the extraction RFQ connected by the nozzle. Inside the cell the RF/DC-funnel electrode and the DC back electrode are visible. The entrance window into the cell has a diameter of 60 mm (20 mm for the actual tests).

The nozzle has an inner diameter of 0.6 mm, where both sides of the nozzle throat have a conical shape that has been optimized with gas dynamical simulations [9]. The convergent subsonic nozzle entrance was optimized to achieve gas velocities high enough to drag the ions through the nozzle, while the divergent nozzle exit was optimized for the transfer into the extraction RFQ as well as for the transversal cooling within the first RFQ segments. In the segmented extraction RFQ the ions are separated from the neutral gas and transversally cooled for the following transfer into the buncher RFQ. Each rod of the extraction RFQ consists of 12 segments with a total length of 180 mm. The diameter of the rods is 11 mm with an aperture (diameter) of 10 mm.

The set-up has been tested off-line in Munich with ions produced by a pulsed (50 Hz) Nd-YAG laser inside the cell and on-line using Au and iodine ions from the tandem accelerator in Garching. In both cases the extracted ions have been mass selectively detected with a quadrupole mass spectrometer and a subsequent MSP (microsphere plate) [10].

Measurements with laser-produced erbium ions

In first tests with laser-produced erbium ions measurements of extraction times at a He gas pressure of 32 mbar were performed. For these tests DC fields between 5 and 10 V/cm and an RF field at 1 MHz frequency with an amplitude of 200 Vpp was applied inside the gas cell. The extraction RFQ was operated with an RF-voltage of 200 Vpp at 800 kHz in addition to a 6 V dragging ramp between the first and the last segment.

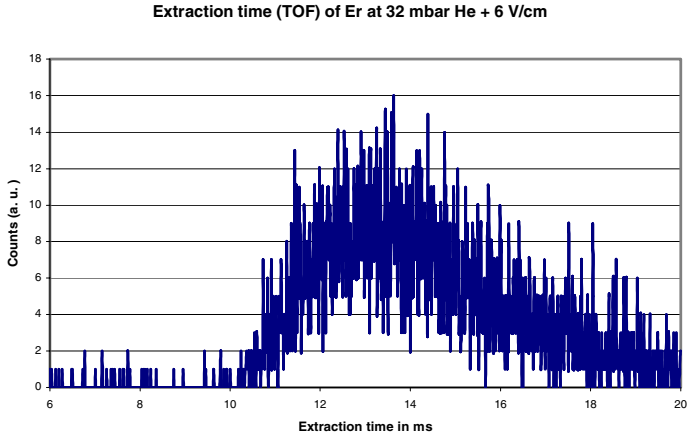


Figure 4: Extraction times of laser-produced Er ions at 32 mbar He and 6 V/cm inside the gas cell set-up. With these parameters a mean extraction time of 13 ms was achieved.

Extraction times were determined via a time-of-flight measurement between the laser pulse and the ion detection with ions created at the expected centre of the stopped ion cloud inside the cell. With the settings above mean extraction times between 12 and 15 ms could be achieved (fig.4)

The gas cell/extraction RFQ combination was successfully operated in the first commissioning beam-time of the complete SHIPTRAP set-up with fusion products at A ~ 150. Further on- and off-line tests will focus on the optimization of the extraction efficiency and extraction time as well as on the characterization of the ion beam emittance after the extraction RFQ.

* Funded by BMBF – Nr. 06LM973, and GSI F&E programme – Nr. LM-HA2

Investigation of ion chemical reactions of erbium with an FT-ICR spectrometer

H. Backe[3], A. Dretzke[3], T. Kolb[3], G. Kube[3], W. Lauth[3], M. Sewtz[3]

The aim of this project is the investigation of ion-chemical reactions of trans-einsteinium elements (Z>99) in the SHIPTRAP buffer-gas cell. Stopped singly charged ions of heavy elements as e.g. ^{254}No or ^{256}Lr will react with admixtures to the inert buffer gas as, e.g., O_2, H_2O, or CH_4. The reaction products are extracted from the cell with the aid of electrical fields and mass analyzed in a quadrupole mass spectrometer. The changes of reaction constants in a group of chemical homologues may provide detailed information on the electronic structure of valence electrons of the heavy elements. The method is being developed for the element erbium (Z=68) which is the chemical homologue of fermium (Z=100). In a first step it will be shown that reaction constants can be measured in an inert buffer-gas atmosphere with sufficient precision. As a prerequisite, precise reaction constants must be known under well-defined experimental conditions [11]. This has been achieved by examining various ion-chemical reactions of erbium ions in a Fourier Transform Ion Cyclotron Resonance Spectrometer (FT-ICR).

The ions are created by laser ablation from a solid target using a pulsed CO_2-laser, quenched to their electronic ground state by a pulsed source of argon gas [12], and stored in the FT-ICR cell in the presence of the reaction gas at a constant pressure. After a well-defined reaction time T, mass spectra are recorded with the FT-ICR. Typical examples are shown in Fig. 5.

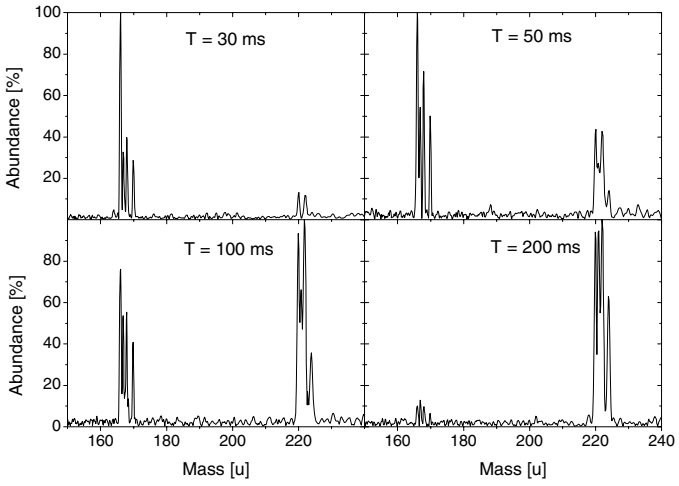


Figure 5: Er^+ and $ErC_4H_6^+$ mass spectra at reaction times T as indicated for the reaction $Er^+ + C_4H_8 \rightarrow ErC_4H_6^+ + H_2$. The groups around mass number 167 and 221 belong to Er^+ and $ErC_4H_6^+$.

The ratio $Er^+/(Er^+ + ErR_1^+)$, taken from such mass spectra, as function of the reaction time T contains information on the reaction constant k of the corresponding reaction $Er^+ + R \rightarrow ErR_1^+ + R_2$. So far, reactions with R = O_2, CH_4, and C_4H_8 (butene) were investigated.

Two series of experiments have been carried out for the reaction $Er^+ + O_2 \rightarrow ErO^+ + O$. In the first reaction electronic excitations after laser ablation of Er^+ were quenched with a pulse of argon gas, the second without. No difference was found for the reaction constant which amounts to k_{O2} = (3.8 ± 0.2) $\cdot 10^{-10}$ cm^3 / (molecule·s), see Fig. 6.

For the reaction $Er^+ + CH_4 \rightarrow ErCH_2^+ + H_2$ only the very low upper limit of the reaction constant of $k_{CH2} < 7\times10^{-15}$ cm^3 / (molecule×s) could be determined. This result means that the reaction is virtually energetically forbidden, in agreement with ref. [13]. Distinct differences were found for the reaction $Er^+ + C_4H_8 \rightarrow ErC_4H_6^+ + H_2$ with and without argon quenching. The reaction constant with quenching amounts to $k(C_4H_8)$= (1.6 ± 0.3)×10^{-10} cm^3 / (molecule×s).

In the next steps of the experiment the same reaction constants will be measured in a buffer-gas cell. The Er^+ ions will be created by evaporation of Er atoms from a filament and subsequent laser resonance ionization. In the last step of the preparatory experiments the reaction constants will be measured after implantation of 50 MeV Er^{7+} ions from the tandem accelerator facility at the MPI-K Heidelberg. This experiment is of crucial importance since it is expected that the energy loss of the ions produces a hot spot at the end of their range. As a consequence, reaction constants may be subject to changes since measured at higher effective temperatures.

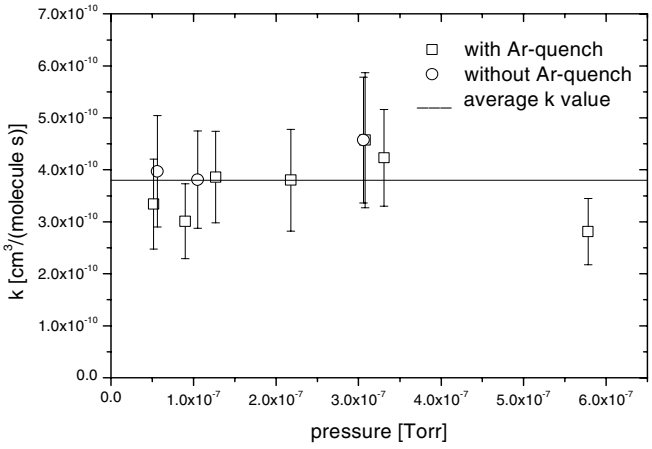


Figure 6: Measured reaction constants k_{O2} of the reaction $Er^+ + O_2 \rightarrow ErO^+ + O$ obtained with Ar-quenching and without (O) Ar-quenching.

The time-of-flight mass spectrometer at the SHIPTRAP facility

W. R. Plaß[1], A. F. Dodonov[1], S. A. Elisseev[1], H. Geissel[1,2], G. Marx[2], Yu.N. Novikov[2], D. Rodriguez[2], C. Scheidenberger[2], M. Tarisien[2], Z.Wang[2], M. Weidenmüller[1], Z. Zhou[1]

A time-of-flight mass spectrometer (TOF-MS) [14] is being developed and coupled to the SHIPTRAP facility for mass measurements of very shortlived nuclei ($T_{1/2}$ << 1 s). The TOF-MS will receive ions from the SHIPTRAP linear RF trap. The TOF-MS system consists of a 90-degree-bender, an RF quadrupole (RFQ) that can also be used as a linear RF trap [15], and a TOF-MS with orthogonal extraction. Recent activities include the construction, building and test of the 90-degree-bender, measurements of the accumulation and storage properties of the TOF-MS linear RF trap, the operation of the TOF-MS with pulsed injection (bunch mode) to increase mass resolution and sensitivity, and transmission tests using the SHIPTRAP and TOF-MS RF quadrupoles.

The 90-degree-bender

In order to transfer the ions coming from the SHIPTRAP linear RF trap into the TOF-MS system, an electrostatic 90-degree-

bender has been designed. It has been built and tested off-line with a cesium ion source and a Faraday cup detector. A transmission of 70% has been achieved. The energy acceptance of the bender is 2.5 eV (FWHM) at a beam energy of 20 eV. This matches well with the measured energy spread of the ions injected from the SHIPTRAP linear RF trap.

Linear RF trap

The linear RF trap is an RF quadrupole with 4 additional rectangular electrodes, which create a longitudinal electric field to drag the ions through the system [16]. At the exit of the system, additional trapping and skimmer electrodes are located to generate a trapping potential in the longitudinal direction. The system can be operated in continuous mode and in bunch mode. In continuous mode, the ions are dragged through the system continuously, while in bunch mode they can be accumulated, stored in the trap and then extracted in a bunch. In both modes, the ions are cooled by collisions with the buffer gas. This cooling is essential to increase the mass resolution and sensitivity of the TOF-MS. Simulations show that ion temperatures corresponding to a few hundred meV and a spatial spread of a few hundred µm can be achieved. Off-line experiments were done using an atmospheric pressure electrospray ion source [17]. In the continuous mode, the longitudinal energy spread after extraction from the ion guide is measured as 250 - 300 meV. In bunch mode, by comparison of the slope of the injection curve (Fig. 7a) (405 counts/s) and the ion counts in continuous mode (350 counts/s), the injection efficiency was determined to be of the order of unity. The storage time for alkali ions is several hundred milliseconds (Fig. 7b).

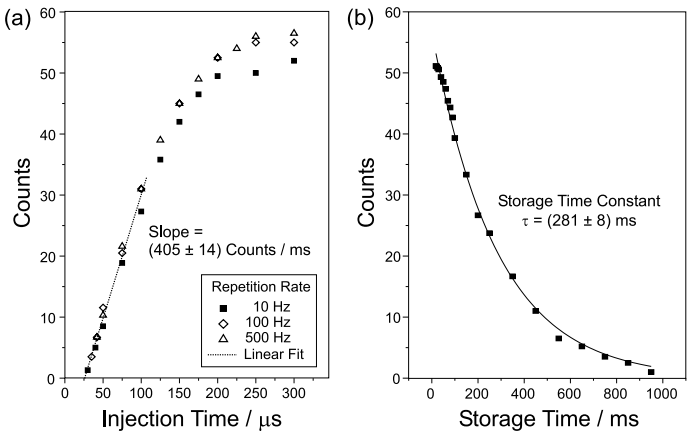


Figure 7: Accumulation and storage properties of the linear RF trap studied for cesium ions cooled with dried air as buffer gas at 10^{-2} mbar pressure. Number of detected ions as a function of (a) the injection time for different cycle repitition rates and (b) the storage time in the trap.

Time-of-flight mass spectrometer

By operating the linear RF trap in bunch mode, the sensitivity and mass resolution of the mass spectrometer can be enhanced significantly compared to the conventional continuous mode. The sensitivity is increased by accumulating the ions in a packet and thus increasing the duty cycle. Measurements with cesium ions yielded an increase in the number of detected ions by a factor of roughly 100. Also, in bunch mode the ions are spatially focused in the extraction region of the TOF-MS and suffer less from the unavoidable mechanical misalignment and field imperfections. Thus the mass resolution could be increased by roughly a factor of two from typically 13000 in continuous mode to 24000 (FWHM) (Fig. 8).

Transmission tests

In order to investigate the coupling of the TOF-MS to the SHIPTRAP beam, transmission tests were performed using the SHIPTRAP linear RF trap and the TOF-MS linear RF trap. Relative transmission efficiencies were measured for different operation modes of the linear RF traps. Relative to continuous operation of both quadrupoles, the transmission efficiency through both quadrupoles is 7% for operation of the SHIPTRAP RFQ in bunch mode and the TOF-MS in continuous mode. The efficiency is 60% for operation of the SHIPTRAP RFQ in continuous mode and the TOF-MS RFQ in bunch mode. This indicates that operation of the TOF-MS in bunch mode is possible with sufficient transmission efficiency.

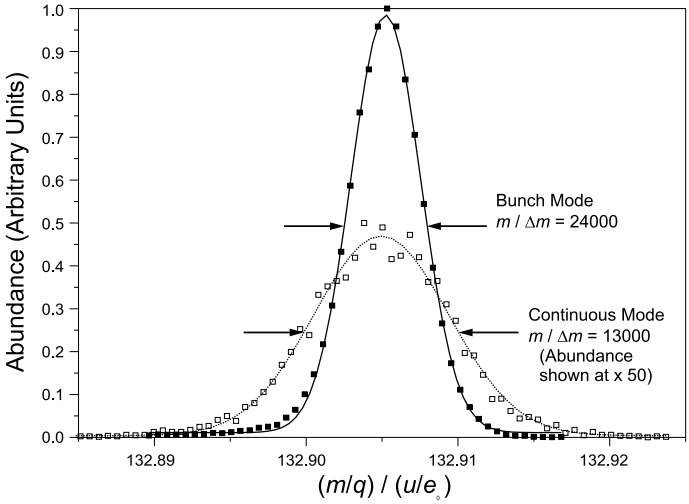


Figure 8: Mass peak of $^{133}Cs^{+}$ measured in the TOF-MS, showing the improvement in mass resolution in the bunch mode compared to the continuous mode. The difference in abundance is shown only schematically. The sensitivity in the bunch mode is larger roughly by a factor of 100 compared to the continuous mode.

References :

[1] G. Bollen et al., Nucl. Instr. Meth. A 368 (1996) 675.

[2] C. Carlberg et al., Phys. Rev. Lett. 83 (1999) 4506.

[3] G. Savard et al., Nucl. Phys. A 654 (1999) 961c.

[4] G. Gräff et al., Z. Phys. A 297 (1980) 35.

[5] D.L. Farnham et al., Phys. Rev. Lett. 75 (1995) 3598.

[6] H. Häffner et al., Phys. Rev. Lett. 85, 5308 (2000).

[7] S. Stahl, PhD-thesis, Mainz (1998).

[8] O. Engels et al., Hyperfine Interactions **132** (2001) 505.

[9] V.L. Varentsov et al., Nucl. Instr. Meth. **A 413** (1998) 447.

[10] R. Naaman et al., Rev. Sci. Instrum. **67** (1996) 3332.

[11] A. Dretzke et al., Hyperfine Interactions **132** (2001) 501.

[12] J. Marçalo et al., Int. J. Mass Spectrom. Ion Proc. **157/158** (1996) 265.

[13] H.H. Cornehl et al., Organometallics **14** (1995) 992.

[14] A.F. Dodonov et al., Eur. J. Mass Spectrom. **6** (2000) 481.

[15] J.M. Campbell, B.A. Collins, D. J. Douglas, Rapid Commun. Mass Spectrom. **12** (1998) 1463.

[16] A. Loboda et al., Eur. J. Mass Spectrom. **6** (2000) 531.

[17] S.J. Gaskell, J. Mass Spectrom. **32** (1997) 677.

HITRAP: A Facility for Experiments with Trapped Highly Charged Ions

S. Djekic[3], H.-J. Kluge[2], G. Marx[2], W. Quint[2], U. Ratzinger[1], D. Rodríguez[2], T. Stöhlker[2]
M. Tarisien[2], T. Valenzuela[3], J. Verdú[3], G. Werth[3]
Frankfurt[1], GSI[2], Mainz[3]

The GSI midterm project HITRAP is an ion trap facility planned for capturing and cooling of highly charged ions (HCI) produced at GSI in the heavy-ion complex of the UNILAC-SIS accelerators and the ESR storage ring. In this facility heavy highly-charged ions up to uranium will be available as bare nuclei, hydrogen-like ions or few-electron systems. The physics programme of the HITRAP project comprises a broad spectrum of physics experiments with heavy HCI up to bare uranium (U^{92+}) at low energies (<1 eV/u) which can presently not be performed at any other institution using light or medium-heavy HCI or heavy HCI at MeV energies [1].

In 2001, the European Commission approved the RTD Network "HITRAP Facility". Nine European research teams participate in the HITRAP Network aiming at the development of novel instrumentation and prototypes for experiments on highly charged ions including:

- Linear decelerator for deceleration of HCI from high energies (few MeV/u) down to rest.
- Cooler Penning trap for capturing, cooling and accumulation of HCI at low energies (< eV/u).
- Experimental set-ups and detectors for investigation of the interaction of low-energy HCI with photons, atoms, molecules, clusters, surfaces, microstructures and solids.

Highly charged ions are accelerated in the heavy-ion synchrotron SIS, stripped in a foil to the desired charge state and injected into the Experimental Storage Ring (ESR). For stripping of heavy species to bare or hydrogen-like ions, energies of a few hundred MeV/u are required. In the ESR the ions will be decelerated to an energy of 3 MeV/u. It is planned to demonstrate this low-energy operation mode of the ESR during 2002. They will then be extracted in a fast-extraction mode as short ion bunches. The extracted ion bunches will be post-decelerated to a final energy of the order of 30 keV/q in a combination of a linear interdigital H-mode (IH) drift tube structure and a radiofrequency quadrupole structure (RFQ). This post-decelerator is being developed in collaboration with the University of Frankfurt.

In 2001, we started designing a cooler Penning trap for capturing and cooling the highly charged ions from the post-decelerator. The trap for receiving these ions is designed for operation at extremely high vacuum by cooling to cryogenic temperatures (T = 4 K). In the cooler Penning trap the HCI are cooled to T = 4 K with a combination of electron or positron cooling and resistive cooling. The stored highly charged ions can be investigated in the trap itself or can be extracted from the trap at energies up to about 30 keV/q. The HITRAP facility will provide about 10^6 charges per second, i.e. about 10^4 ions/s in the case of U^{92+}.

The HITRAP physics programme includes collision studies with highly charged ions at well-defined low energies (eV/u), laser spectroscopy of hyperfine structure transitions in HCI, X-ray spectroscopy on HCI, and high-accuracy measurements to determine the magnetic moment anomaly (or g-factor) of the electron bound in hydrogen-like heavy ions and the atomic binding energies of few-electron systems.

For the determination of the g-factor of the bound electron in highly charged ions as a stringent test of Quantum Electrodynamics (QED) a precision Penning trap has been developed in a joint effort of the University of Mainz and GSI. The g-factor of the bound electron is determined from the Larmor precession frequency of its magnetic moment in the magnetic field B and the cyclotron frequency of the hydrogen-like ion. Our measurement of the g-factor of the electron in hydrogen-like carbon ($^{12}C^{5+}$) yielded a value of $g_{exp}(^{12}C^{5+})$ = 2.001 041 596 (5) [2], in excellent agreement with the theoretical value of $g_{th}(^{12}C^{5+})$ = 2.001 041 589 9 (10). Further improvement of the theoretical as well as the experimental accuracy made it possible to determine the atomic mass of the electron with an unprecedented precision of a few parts in 10^{-10} [3,4].

In 2001 we performed a g-factor measurement on hydrogen-like oxygen ($^{16}O^{7+}$). The experimental value of $g_{exp}(^{16}O^{7+})$ = 2.000 047 028 (8) is in excellent agreement with the theoretical prediction of $g_{th}(^{16}O^{7+})$ = 2.000 047 022 (5). This is our second high-accuracy test of bound-state QED. At the HITRAP facility, the g-factor measurements will be performed up to the heaviest hydrogen-like ions, where the product of proton number and fine-structure constant (Zα) approaches unity. This will provide a crucial test of QED calculations in extreme electromagnetic fields.

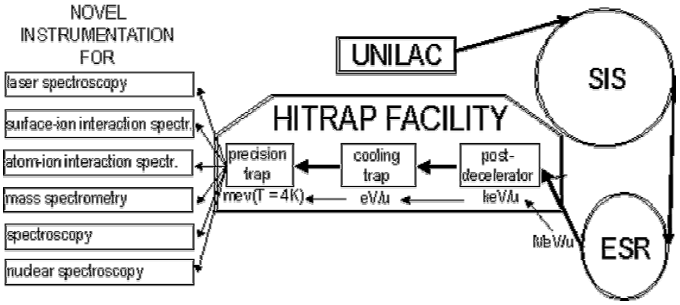


Fig. 1: Schematic of the GSI accelerator complex and the planned HITRAP facility. Highly charged ions are extracted from the ESR storage ring at 3 MeV/u, decelerated in a post-decelerator to some keV/u, and then transferred into a Penning trap system.

We acknowledge financial support by the European Union (Networks EUROTRAPS and HITRAP), BMBF and GSI F&E programme.

References :

[1] W. Quint *et al.*, Hyp. Int. 132, 457 (2001).
[2] H. Häffner *et al.*, Phys. Rev. Lett. 85, 5308 (2000).
[3] T. Beier et al., this report.
[4] T. Beier *et al.*, Phys. Rev. Lett. 88, 011603 (2002).

Micro Structure Electrodes: A New Multipurpose Plasma Source

A.Bräuning-Demian[1], O. Hohn[2], T. Jahnke[2], C. Penache[2],
S. Schößler[2], L. Spielberger[2] and H. Schmidt-Böcking[2]

[1]GSI, Darmstadt, Germany, [2]J.W.Goethe-Universität, Frankfurt am Main, Germany

The production of exotic atomic, molecular and ionic beams is of fundamental interest in atomic and plasma physics as well as in technical applications in surface science and plasma surface processing [1]. All these applications require intense sources in order to obtain sufficient reaction rates. Commonly used sources are limited in their operating pressure.

The present work is concerned with the development of a compact and simple multipurpose plasma source for the production of beams of excited, metastable atoms as well as singly charged ions, based on a high-pressure micro-discharge. Scaling down the dimensions of classical low-pressure discharge geometries, we found a micro-electrode system suitable for generating non-thermal, homogeneous discharges at pressures up to several 100 kPa [2].

In contrast to classical planar electrode arrangements we use a multi-layer system of two metallic electrodes separated by an insulating layer. The system has an overall thickness of 250-650 µm, depending on the insulator used. This basic system is provided with micro holes with a typical diameter of 60–400 µm. Structures with single holes and arrays of multiple holes have been tested. If biased with a DC-voltage, a gas discharge is ignited in the micro hole and the structures serve as plasma micro reactors. In the following we call these multi-layer system with holes Micro Structure Electrodes (MSE).

Glass, polyimide (Kapton®) and ceramic have been tested as insulating layers [3,4]. Best results were reached with ceramic, which has suitable thermal and electric properties and a low sputtering coefficient that enables a longer lifetime.

Apart from the 'static' operation of the MSE [2,3,4,5] with equal pressures on both sides, up to 1 atmosphere, it is also possible to operate the MSE in 'flow mode'. Pure gas or a mixture of different gases flows through the micro holes when a pressure difference between the frond and the back side of the MSE is created, e.g. > 500 hPa at the high-pressure side and <1 Pa at the low-pressure side.

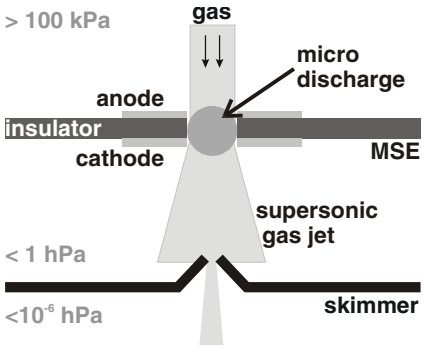


Figure 1: Principle of the plasma jet

Even under this condition, applying a dc voltage of only several hundred volts to the electrodes, a stable discharge can be ignited in the micro hole. The species produced in the micro-discharge (ions, excited atoms, radicals, etc.) are extracted with the gas stream. The extraction of ions can be enhanced by applying an external field.

The pressure difference between the two sides of the MSE drastically effects the characteristics of the obtained beam. A pressure of at least 0.1 MPa at the high-pressure stage combined with <1 hPa at the low-pressure stage produces an adiabatic expansion of the gas and thus a supersonic gas jet is created. If simultaneously a discharge is ignited in the micro-hole, a supersonic 'plasma jet', consisting of excited/metastable atoms and ions, is generated.

The key issue of this versatile source is the composition of the plasma: cold ambient gas, excited atoms and molecules together with high energetic electrons. The composition and characteristics of the plasma jet can be influenced by gas mixture, gas flow, discharge current, etc. Starting from this basic set-up two interesting applications have been realized: a spin polarized He*-target and a source of singly charged ions.

The spin polarized He*gas-target

Gas targets of atoms with polarized electron spins are of a major interest for atomic physics experiments as they provide a very well defined initial state. So called 'quantum-mechanically complete' experiments are possible with a target of that kind [6]. A suitable spin polarized target is helium in the $[1s_{1/2},2s_{1/2}]_{j=1}$ $^3S_1$-state, with its both electron spins being aligned parallel. The lifetime of this particular state is 7900 s as it is a metastable state due to atomic selection rules. The $^3S_1$-He* is produced in the micro-discharge via electron impact. An excitation by photons out of the ground state is not possible since one electron has to perform a spin flip. The high quality of the target is ensured by the free-jet-like properties.

To obtain a spin polarized He*-beam it is necessary to separate the different (L+S) He*-states created in the micro-discharge. This is performed by using a permanent hexapole magnet with a total length of 100 mm placed right after a skimmer (fig. 2).

The inhomogeneous magnetic field B of the hexapole separates different (L+S)-states according to the relation:

$$F = (2S + L)\mu_B \cdot grad(B) \qquad (1)$$

where μ_B is the Bohr Magneton and S and L are the sums over the electron spins and electron angular momenta.

As the gradient of a hexapole field is proportional to the distance r to its longitudinal axis, a magnet of this type behaves like a lens for atoms with J=L+S different from zero. Therefore one of the two $^3S_1$-states is focused onto a certain point while passing the magnet, while the other one is defocused. In the focus point the yield of the spin polarized helium and the dimension of the beam are measured. A detailed description of the experimental set-up is given in [7]. The He*-source is operated at a temperature of 80 K. This reduces the mean velocity of the beam to 900 m/s and consequently enables a

good separation of the spin-polarized state from the primary beam.

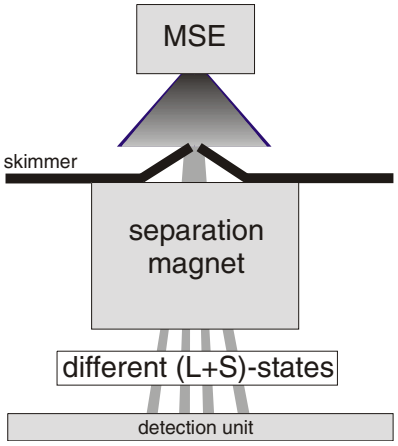


Figure 2: Schematic view of the spin polarized He*-target with hexapole magnet for (L+S)-separation.

First results in a prototype set-up show indeed free-jet-like properties of the beam and a metastable $^3S_1$ flux of $8x10^{13}s^{-1}sr^{-1}$. This yield is a factor of 10 lower than that of state-of-the-art sources which use, for example, low-pressure glow discharges at about 10 mbar. However, the beam quality is supposed to be higher due to the fact that the quality of a supersonic jet increases dramatically at higher pressures. Thanks to further optimization possibilities, it is most likely that the amount of metastable He can still be increased.

The Micro Ion-Source

The second application is a simple and compact ion source based on a MSE with a single 100 µm micro hole. Due to the fact that at high-pressure the ions are generated mostly inside the hole, they are extracted from a well-defined volume with an emissive area of 100 µm in diameter. The high operating pressure of several 100 kPa is an advantage also for the production of molecular ions like HeH^+.

The basic set-up of the micro ion-source is similar to that of the He* gas-target: between the two electrodes a dc voltage of several hundred volts is applied, where the high-pressure side (>100 kPa) serves as anode, the low-pressure side (<1 Pa) as cathode. The body of the ion source, on which the MSE is fixed, is mounted in an insulating housing, which is, at the same time, a high-pressure gas supply (fig.3).

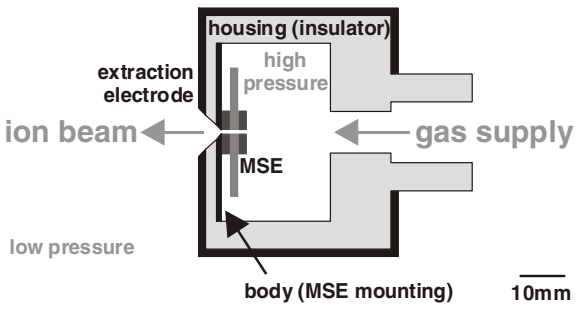


Figure 3: The micro ion-source.

The housing is enclosed by an extraction electrode which usually is grounded, while the MSE is on 1–3 kV positive potential. In this way positive ions are extracted from the plasma. At the same time the extraction electrode shields the space outside the ion source from the high potential inside. Therefore, the ignition of unwanted discharges inside the low-pressure vacuum chamber is suppressed. A second advantage of this set-up is that no high-voltage terminal is needed for the operation of the micro ion-source.

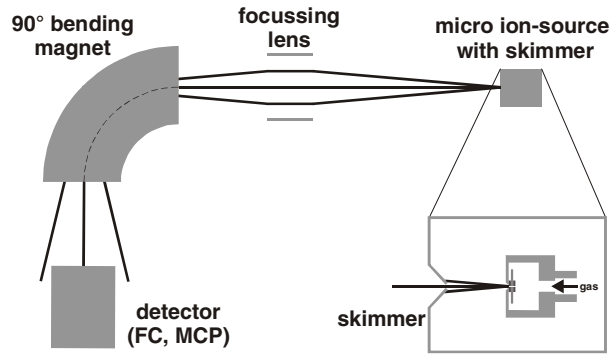


Figure 4: Schematic view of the charge state analysis set-up.

An orifice of 1 mm in diameter, placed in short distance to the micro plasma, skims the ion beam and separates the plasma chamber from the beam line (see fig. 4).

Figure 5 shows a typical mass spectrum behind the 90° bending magnet for a mixture of helium and hydrogen at 2 kV extraction voltage. In order to determine the beam quality, emittance measurements are currently carried on.

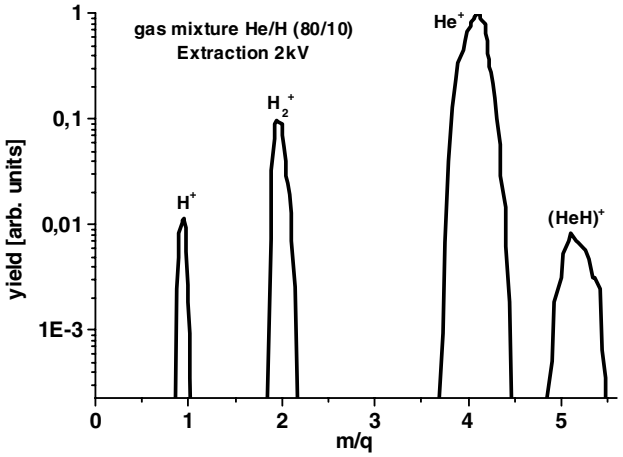


Figure 5: Mass spectrum for a mixture of helium and hydrogen at 2 kV extraction voltage.

References

[1] L.G. Christophorou (ed), Electron Molecule Interaction Vol. 1 and 2, Academic, Orlando (1984).

[2] A. Bräuning-Demian et al., Proceedings of the Int. Conf. on Gas Discharges and their Applications, Glasgow, 2000.

[3] A. Bräuning-Demian et al., Jahresbericht 1999, IKF-60 p. 26 (2000).

[4] O. Hohn et al., Jahresbericht 2000, IKF-61 p. 59 (2001)

[5] O. Hohn et al., Jahresbericht 2000, IKF-61 p. 64 (2001).

[6] H. Klar and H. Kleinpoppen, J. Phys. B: At. Mol. Opt. Phys. **15,** p. 933 (1982).

[7] T. Jahnke, O. Hohn, S. Schößler, S. Schwientek, A. Bräuning-Demian, C. Penache, L. Spielberger, R. Dörner and H. Schmidt-Böcking, A $^3S_1$-Helium gas target with polarized electron spin, to be published.

Structure of Degenerate Boson-Fermion Mixtures

R. Roth and H. Feldmeier (GSI)

Recent experimental successes in the trapping and cooling of mixtures of bosonic and fermionic atoms [1,2] constitute a new branch in the field of trapped ultracold gases. Similar to the purely bosonic gases boson-fermion mixtures offer unique possibilities to study fundamental quantum phenomena. One of the ultimate experimental goals is the observation of a BCS transition of the fermionic component to a superfluid state, which may be achievable by sympathetic cooling of the fermionic component in a boson-fermion mixture.

Within the mean-field approximation using an effective contact interaction [3] the density distribution $n_{\rm F}(\vec{x})$ of the fermionic component is given by

$$n_{\rm F}(\vec{x}) = \frac{\sqrt{2m^3}}{3\pi^2}\left[\mu_{\rm F} - U_{\rm F}(\vec{x}) - \frac{4\pi a_{\rm BF}}{m} n_{\rm B}(\vec{x})\right]^{3/2}, \quad (1)$$

where $U_{\rm F}(\vec{x})$ is the external trapping potential and $\mu_{\rm F}$ is the chemical potential of the fermionic component. We have assumed equal mass m for both species. The interaction between the bosonic and fermionic atoms – characterized by the boson-fermion s-wave scattering length $a_{\rm BF}$ – couples the bosonic and fermionic density. The boson density $n_{\rm B}(\vec{x}) = \Phi_{\rm B}^2(\vec{x})$ is obtained from a modified Gross-Pitaevskii equation

$$\left[-\frac{1}{2m}\vec{\nabla}^2 + U_{\rm B}(\vec{x}) + \frac{4\pi a_{\rm BF}}{m} n_{\rm F}(\vec{x}) + \frac{4\pi a_{\rm B}}{m}\Phi_{\rm B}^2(\vec{x})\right]\Phi_{\rm B}(\vec{x}) = \mu_{\rm B}\Phi_{\rm B}(\vec{x}). \quad (2)$$

Here $\mu_{\rm B}$ is the chemical potential of the bosons and $a_{\rm B}$ the s-wave boson-boson scattering length. We solve these coupled nonlinear differential equations through an efficient imaginary time evolution algorithm. In order to keep the discussion simple we restrict ourselves to spherical symmetric systems with identical parabolic trapping potentials $U_{\rm B}(x) = U_{\rm F}(x) = x^2/(2m\ell^4)$. The oscillator length $\ell = (m\omega)^{-1/2}$ serves as fundamental length unit for the numerical treatment.

First we consider the case of repulsive boson-boson and attractive boson-fermion interactions ($a_{\rm B} \geq 0, a_{\rm BF} < 0$). The upper row of Fig. 1 shows the density profiles of (meta)stable configurations with $N_{\rm B} = N_{\rm F} = 10^4$ particles for three different values of the boson-fermion scattering length $a_{\rm BF}$ and fixed $a_{\rm B}/\ell = 0.001$ (corresponds to $a_{\rm B} \approx 20\, a_{\rm Bohr}$ for a typical trap with $\ell = 1\,\mu$m). Due to the Pauli principle the fermionic density distribution is much more spread out and has a significantly lower central density than the bosonic distribution with the same particle number [notice the different scales for $n_{\rm B}(\vec{x})$ and $n_{\rm F}(\vec{x})$ in Fig. 1]. Attractive boson-fermion interactions generate an attractive mean-field for bosons proportional to the density of the fermions and vice versa. This causes an increase of both densities in the overlap region as can be seen in panel (b) of Fig. 1. With increasing strength of the boson-fermion attraction the fermion density grows substantially. As shown in Fig. 1(c) the fermion density can easily be increased by a factor 3 compared to the noninteracting case.

Second we consider mixtures with attractive boson-boson and repulsive boson-fermion interactions ($a_{\rm B} < 0$, $a_{\rm BF} \geq 0$). The ^{6}Li/^{7}Li mixture used in the experiment of Truscott *et al.* [1] belongs to this class of interactions. The lower row of Fig. 1 shows the density profiles for three different values of $a_{\rm BF} \geq 0$. Already for a very weak boson-fermion repulsion the two species separate spatially [see Fig. 1(e)], the bosons occupy the central region of the trap (boson core) and the fermions constitute a shell around it. The fermionic shell compresses the boson core, i.e. increases the maximum boson density as it is clearly seen in Fig. 1(f).

Any attractive interaction component — either boson-boson or boson-fermion interaction — can induce a mean-field instability of the degenerate mixture. In this case the attractive mean-field is not stabilized by the positive kinetic energy contribution any more, i.e. the gas can lower its energy by contracting and increasing the density in the central region. This collapse sets severe limitations on the numbers of bosons and fermions in order to retain the stability of the mixture. Thus it restricts that parameter ranges in which sympathetic cooling schemes can be applied experimentally. We investigate these phenomena in detail in Refs. [4,5].

[1] A.G. Truscott *et al.*; Science 291 (2001) 2570.
[2] F. Schreck *et al.*; Phys. Rev. Lett. 87 (2001) 080403.
[3] R. Roth, H. Feldmeier; Phys. Rev. A 64 (2001) 043603.
[4] R. Roth, H. Feldmeier; Phys. Rev. A 65 (2002) 021603(R).
[5] R. Roth; *in preparation*.

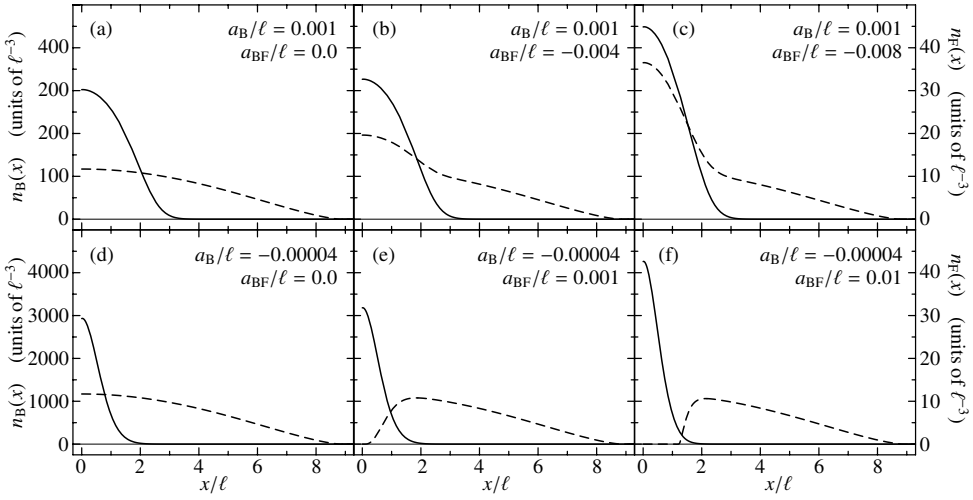


Fig. 1: Radial density profiles of a boson-fermion mixture with $N_{\rm F} = N_{\rm B} = 10\,000$ for different interaction strengths. The boson density $n_{\rm B}(\vec{x})$ is given by the solid line (left scale) and the fermion density $n_{\rm F}(\vec{x})$ by the dashed line (right scale). The upper row shows examples with increasing boson-fermion attraction and fixed $a_{\rm B}/\ell = 0.001$. The lower row depicts examples with increasing boson-fermion repulsion and $a_{\rm B}/\ell = -0.00004$.

Nuclear Anapole Moments from Beams of Highly-Charged Ions

I. Bednyakov, F. Erler, C. Lucke, R. Kuhn, I. Nandori, G. Schaller, R. Schützhold, A.V. Nefiodov, G. Plunien, G. Soff, *Technische Universität Dresden*,
L.N. Labzowsky, *St. Petersburg State University*,
D. Liesen, *GSI Darmstadt*

Investigations of QED effects and parity non-conservation (PNC) in neutral atoms and highly-charged ions represent an active and many-facet field of research [1]. The most accurate theoretical and experimental analysis of PNC has been performed for neutral Cs atoms. Main uncertainties result from theoretical evaluation of the PNC matrix elements that require the inclusion of electron-electron correlation effects and of QED radiative corrections. The latter has been demonstrated recently for the vacuum-polarization correction [2].

Highly-charged ions can provide an alternative source of information on the Standard Model since PNC effects can become relatively large. Most of the discussions addressed in recent literature (see e.g. [3] and references therein) have been restricted to the nuclear spin-independent part of the effective electroweak interaction Hamiltonian $\hat{H}_{\rm W}$. P-odd effects in highly-charged ions arising from the nuclear spin-dependent part of $\hat{H}_{\rm W}$ can be dominated by the (contact) electromagnetic interaction of electrons with the nuclear anapole moment. Usually, an anapole moment occurs as a multipole of an electromagnetic current distribution in a system without centre of inversion. In nuclei it is induced by parity-violating nuclear forces. First hints for an anapole moment have been reported in the Cs system only. To explore the anapole moment in much more detail one could exploit the near degeneracy of the $2^1{\rm S}_0$ and $2^3{\rm P}_1$ levels in He-like ions with odd-A nuclear isotopes and with charge numbers close to $Z \simeq 32$. We propose a method for the direct measurement of the nuclear anapole moment by detecting the angular asymmetry of the photon emission due to the hyperfine-quenched (hfq) decay of the $2^1{\rm S}_0$ level in a polarized beam of helium-like ions [4]. Utilizing beam-foil time-of-fight techniques seems to be most effective for this purpose. The one-photon hfq $M1$ transition $2^1{\rm S}_0 \to 1^1{\rm S}_0$ results from the hyperfine mixing of the $2^1{\rm S}_0$ and the $2^3{\rm S}_1$ levels due to the hyperfine magnetic-dipole operator $\hat{H}_{\rm hfs}$. The mixing coefficient ξ_s is given by

$$\xi_s = \frac{1}{\Delta_s} \sum_{k=1}^{2} \left\langle 2^3{\rm S}_1 \left| \hat{H}_{\rm hfs}(\boldsymbol{r}_k) \right| 2^1{\rm S}_0 \right\rangle , \qquad (1)$$

where $\Delta_s = E(2^1{\rm S}_0) - E(2^3{\rm S}_1)$ denotes the energy difference between the level configurations. The P-odd part of the electroweak interaction $\hat{H}_{\rm W}$ opens uniquely yet another one-photon $E1$-decay channel $2^1{\rm S}_0 \to 1^1{\rm S}_0$ since it mixes $2^1{\rm S}_0$ and $2^3{\rm P}_1$ levels. The corresponding weak mixing coefficient η is defined via

$$i\eta = \frac{1}{\Delta_0} \sum_{k=1}^{2} \left\langle 2^3{\rm P}_1 \left| \hat{H}_{\rm W}(\boldsymbol{r}_k) \right| 2^1{\rm S}_0 \right\rangle , \qquad (2)$$

where $\Delta_0 = E(2^1{\rm S}_0) - E(2^3{\rm P}_1)$. It contains direct informations on the nuclear anapole moment. The total amplitude of the quenched one-photon transition $2^1{\rm S}_0 \to 1^1{\rm S}_0$ appears as a mixture of the basic $M1$ amplitude $\mathcal{A}_s$ and of the additional $E1$ amplitude $\mathcal{A}_p$. In the proposed experiment PNC shows up as a violation of the reflection symmetry with respect to the preferred axis $\boldsymbol{\zeta}$ defined by the direction of the spin polarization of the He-like ions prepared in the $2^1{\rm S}_0$ state. The polarization of the latter may be described by the density matrix

$$\rho = \frac{1}{2I+1} \left[1 + \frac{3\lambda_0}{I+1} \left(\boldsymbol{\zeta} \cdot \boldsymbol{I} \right) \right] . \qquad (3)$$

For these levels the ion polarization coincides with the polarization of the nucleus, which is determined by the nuclear spin $\boldsymbol{I}$. A challenging problem and crucial for the experiment is the degree of polarization $\lambda_0 = |\langle \boldsymbol{I} \rangle|/I$ of the prepared ion beam. The resulting asymmetry coefficient of the photon counting rates of the hfq one-photon transition $2^1{\rm S}_0 \to 1^1{\rm S}_0$ to be observed is given by

$$\varepsilon = \frac{3\lambda_0 \eta}{(I+1)\xi_s} \left| \frac{\mathcal{A}_p}{\mathcal{A}_s} \right| . \qquad (4)$$

This difference in the counting rates should result after changing the direction $\boldsymbol{\zeta}$ of the ion polarization or , equivalently, after rotating the detector around the beam direction by an angle π. The total angular asymmetry effect turns out to be relatively large. Numbers for ε have been calculated for various isotopes in the range $29 \le Z \le 36$ [4]. E.g. assuming complete beam polarization ($\lambda_0 = 1$) the magnitude of the asymmetry coefficient can reach a value of about $\varepsilon \simeq 0.63 \times 10^{-4}$ for He-like arsenic. Assuming realistic parameters characterizing the experimental conditions a required number of events is achieved at beam intensities of about $J \simeq 4 \times 10^{12}$ ions/s over an observation time of about two weeks. At ion storage rings hyperfine-quenching type experiments become feasible due to modern developments of high-intensity beam facilities, the preparation of polarized gas targets and the beam-foil time-of-flight technique. The determination of nuclear anapole moments would provide a new testing ground for PNC effects in atomic systems.

References

[1] G. Soff *et al.*, Hyperfine Interactions **132**, 75 (2001)
[2] W.R. Johnson, I. Bednyakov, G. Soff, Phys. Rev. Lett. **87**, 233001 (2001)
[3] L.N. Labzowsky, A.V. Nefiodov, G. Plunien, G. Soff, R. Marrus, D. Liesen, Phys. Rev. A**63**, 054105 (2001)
[4] A.V. Nefiodov, L.N. Labzowsky, D. Liesen, G. Plunien, G. Soff, *Nuclear anapole moment from beams of highly-charged ions*, preprint (2001)

Nuclear and Electron Polarization Contributions to the HFS of Hydrogen- and Lithium-like Ions

M. Tomaselli [a,b], T. Kühl [b], W. Nörtershäuser [b], D. Marx [b], A. Dax [b], H. Wang [b], R. Sanchez [b], and S. Fritzsche [c]

[a] University of Darmstadt, [b] GSI Darmstadt, [c] University of Kassel

Hydrogenlike high-Z atoms offer fascinating possibilities for testing the interplay of nuclear and atomic structure. They have recently become available for experiments at GSI in Darmstadt [1] and at the LLNL in Livermore [2, 3] and have been used to test the theory of quantum electrodynamics (QED) in extremely strong electric and magnetic fields. Measuring the ground-state hyperfine structure (HFS) of these hydrogenlike systems is a sensitive method to explore QED and nuclear contributions to the electron energy. Experiments at GSI included laser spectroscopic investigations of $^{209}Bi^{82+}$ and $^{207}Pb^{81+}$ at the heavy-ion storage ring [1]. These measurements, with a relative accuracy $< 10^{-3}$, allowed the first test of QED in the strong electromagnetic field of highly-charged heavy ions. At Livermore, hydrogenlike $^{165}Ho^{66+}$ [2], $^{185}Re^{74+}$, and $^{187}Re^{74+}$ [2], $^{203}Tl^{81+}$, and $^{205}Tl^{81+}$ [3] have been produced and stored in a high-energy electron-beam ion trap (SuperEBIT) by an energy variable electron beam, axially compressed by a strong magnetic field. In this contribution we present results of calculations performed for the hyperfine splitting by using the Dynamic Correlation Model (DCM) [4]. The DCM describes the structure of open-shell nuclei with an odd number of valence particles in terms of clusters: the valence and the core cluster. In contrast to Hartree-Fock approaches the DCM includes a coupling mechanism acting between the core and the valence particles, which modifies the Hartree-Fock (HF) description and polarizes the core via particle-hole excitations ($2\hbar\omega$) of protons and neutrons. Thus, the valence particle becomes "dressed " in the sense that it coexists with complex excitations of the core. From a Hartree-Fock point-of-view, these dressed particles correspond at most to a particular solution of an extended, nonlinear HF Hamiltonian. DCM corrections applied to hyperfine splitting calculations [5] show good agreement with experimental data [1, 2, 3] if the QED corrections [6,7] are neglected, however, by adding these corrections a systematic deviation between theory and experiment has been observed. In order to clarify this open point an analysis of the nonlinear terms contributing to the HFS was provided in [5] by performing a term-to-term comparison with the results of other theoretical models [6, 8]. Since the calculated Bohr-Weisskopf term (ϵ) is larger than that obtained in perturbation theories [8, 6], the reason for this systematic disagreement could be associated with the modification of the single-hole magnetization distribution as shown in Fig. 1 for the Pb and Tl isotopes. By comparing the HFS of the lithiumlike ions with those calculated for hydrogenlike ions, we obtain further information about the hyperfine interaction of the nucleus with the electronic cloud of high-Z ions. The simplest systems which have a closed $K-$shell are lithiumlike ions. For the ground state hyperfine transition for lithiumlike bismuth a similar situation was found as for hydrogen-like bismuth. In the zeroth-order, the hyperfine interaction of the nuclear moment with the motion of the electrons is represented by a dipole field with a $1/r^3$ behaviour. This behaviour leads to the typically strong dependence of the hyperfine splitting on nuclear parameters.

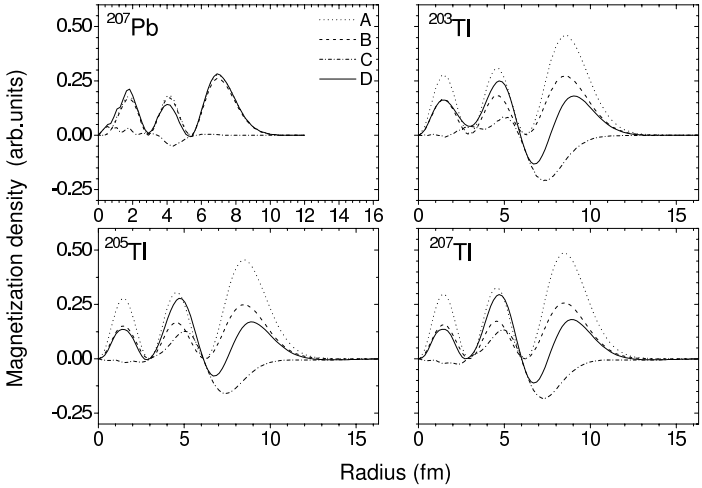


Figure 1: Calculated magnetization distribution for ^{207}Pb and $^{203,205,207}Tl$. Line A shows the single-hole result, line B has been normalized with the spectroscopic factor of the single-hole, line C shows the contributions of the DCM terms and line D is the total magnetization.

In the traditional approach to the theoretical hyperfine splitting studies, the contributions from the electron-electron interaction, QED effects, and the extended nucleus are obtained *additively*. An alternative point of view is taken by DCM which includes both the coupling of the internal nuclear motion as well as the electronic interaction and the creation and annihilation of virtual electron-positron pairs within the same framework.

References

[1] I. Klaft *et al.*, Phys. Rev. Lett. **73**, 2425 (1993); P. Seelig *et al.*, Phys. Rev. Lett. **81**, 4824 (1998).

[2] J. R. Crespo Lopez-Urrutia *et al.*, Phys. Rev. Lett. **77**, 826 (1996); Phys. Rev. A **57**, 879 (1998).

[3] P. Beiersdorfer, Phys. Rev. A **64**, 032506 (2001).

[4] M. Tomaselli, Ann. Phys. **205**, 362 (1991).

[5] M. Tomaselli *et al.*, Phys. Rev. C **51** 2989 (1995); Phys. Rev. C **58**, 1524 (1998); Phys. Rev. A **65**, 22502 (2002).

[6] V.M. Shabaev et al., Phys. Rev. A **56**, 252 (1997); J. Phys. B **27**, 5825 (1994).

[7] P. Sunergren *et al.* Phys. Rev. A **58**, 1055 (1998).

[8] M.G.H. Gustavsson *et al.*, Hyperfine Interact. **127**, 437 (2000).

Recoil Correction to the g Factor of H-Like Ions to all Orders in αZ

V.M. Shabaev [a,b] and V.A. Yerokhin [a,b]
[a] St.Petersburg State University, St.Petersburg, Russia
[b] Gesellschaft für Schwerionenforschung (GSI), Darmstadt, Germany

Recent progress in high-precision measurements of the bound-electron g factor for H-like carbon [1, 2] and the related theoretical investigations ([3] and references therein) provide a new independent determination of the electron mass. The accuracy of this determination presented in [3] is three times better than that of the accepted value for the electron mass [4]. The theoretical predictions for electronic g factors in H-like systems with zero nuclear spin are affected by four main sources of error: the numerical error in the evaluation of the bound-state quantum electrodynamical (QED) correction to first order in α, the error caused by employing the αZ expansion for the QED correction of second order in α, the error resulting from the αZ expansion of the nuclear recoil correction accounting for non-infinite nuclear mass, and, for heavy ions, the error due to the insufficiently known finite nuclear size.

We have recently evaluated the nuclear recoil correction for spin-zero nuclei non-perturbatively to *all* orders in αZ [5, 6] which considerably reduced the error of the theoretical prediction of $g(^{12}\mathrm{C}^{5+})$. Only this allowed the gain in precision for m_e.

We consider a H-like atom with a spinless nucleus that is put into a classical homogeneous magnetic field, $\mathbf{A}_{\rm cl}(\mathbf{r}) = [\mathcal{H} \times \mathbf{r}]/2$. For simplicity, we assume that $\mathcal{H}$ is directed along the z axis. The energy shift of a state to first order in $\mathcal{H}$ and to first order in m/M is conveniently written as the sum of the lower-order and the higher-order term [5], $\Delta E = \Delta E_{\rm L} + \Delta E_{\rm H}$. The recoil correction to the bound-electron g factor is defined as $\Delta g = \Delta E/(\mu_0 \mathcal{H} m_j)$, where $\mu_0 = |e|/(2m)$ is the Bohr magneton and m_j is the angular momentum projection of the state under consideration.

For the $1s_{1/2}$ state, the analytical evaluation of the lower-order term yields [5, 7]

$$\Delta g_{\rm L} = \frac{m}{M}(\alpha Z)^2 - \frac{m}{M}\frac{(\alpha Z)^4}{3(1+\sqrt{1-(\alpha Z)^2})^2}\,. \qquad (1)$$

The higher-order term is represented by the sum of the Coulomb, the one-transverse-photon, and the two-transverse-photon contribution, $\Delta E_{\rm H} = \Delta E_{\rm H}^{\rm Coul} + \Delta E_{\rm H}^{\rm tr1} + \Delta E_{\rm H}^{\rm tr2}$. For the $1s_{1/2}$ state, we transform them to a form appropriate for numerical evaluation [6].

In Table 1 we present the individual contributions to the g factor of the $1s_{1/2}$ state for H-like oxygen and uranium. The error ascribed to the Dirac point-nucleus value results from the current uncertainty of the fine structure constant, $1/\alpha = 137.03599976(50)$ [4]. The uncertainty of the finite-nuclear-size correction was estimated as the difference between the result obtained with the Fermi model of the nuclear charge distribution and with the homogeneously-charged-sphere model of the same rms radius. The one-loop QED correction was taken from [8], where it was evaluated numerically to all orders in αZ . The α^2 QED correction includes the existing αZ expansion terms for the QED correction of second order in α [9, 10] and the known free-QED terms of higher orders in α (see, e.g., [8]). Its relative uncertainty was estimated as the ratio of the part of the one-loop QED correction, that is beyond the $(\alpha Z)^2$ approximation, to the part, that is within the $(\alpha Z)^2$ approximation. The recoil correction incorporates the total recoil correction of first order in m/M, calculated in this work, and the known corrections of orders $(m/M)^2$ and $\alpha(m/M)$ [11]. For low Z, the theoretical uncertainty is mainly determined by the numerical error of the one-loop QED correction [8], while for high Z it results from the αZ expansion of the α^2 QED correction and from the finite nuclear size correction. Calculations of the QED corrections up to the desirable accuracy seem to be feasible in the near future if we consider recent progress in calculations of the corresponding corrections to the Lamb shift in H-like ions [12, 13]. As to the uncertainty due to the finite nuclear size effect, one may expect that, like in the case of the hyperfine splitting [14], it can be significantly reduced in a specific difference of the bound-electron g factor in H- and Li-like ions.

Table 1: Contributions to the $1s_{1/2}$ bound-electron g factor in some H-like ions.

	$^{16}\mathrm{O}^{7+}$	$^{238}\mathrm{U}^{91+}$
Dirac value (point)	1.997 726 003 1	1.654 846 173(3)
Fin. nucl. size	0.000 000 001 5	0.001 275 0(25)
QED, order (α/π)	0.002 324 416(1)	0.003 088 93(3)
QED, order $(\alpha/\pi)^2$	−0.000 003 517 1(4)	−0.000 003 8(9)
Recoil	0.000 000 117 0	0.000 002 491
Total	2.000 047 021(1)	1.659 208 9(27)

We thank T. Beier, S. Karshenboim, J. Kluge, W. Quint, and A. Yelkhovsky for valuable discussions.

References

[1] N. Hermanspahn *et al.*, Phys. Rev. Lett. **84**, 427 (2000).
[2] H. Häffner *et al.*, Phys. Rev. Lett. **85**, 5308 (2000).
[3] T. Beier *et al.*, Phys. Rev. Lett. **88**, 011603 (2002).
[4] P.J. Mohr and B.N. Taylor, Rev. Mod. Phys. **72**, 351 (2000).
[5] V.M. Shabaev, Phys. Rev. A **64**, 052104 (2001).
[6] V. M. Shabaev and V. A. Yerokhin, Phys. Rev. Lett. **88**, 091801 (2002).
[7] A. Yelkhovsky, E-print, hep-ph/0108091 (2001).
[8] T. Beier, Phys. Rep. **339**, 79 (2000).
[9] A. Czarnecki, K. Melnikov, and A. Yelkhovsky, Phys. Rev. A **63**, 012509 (2001).
[10] S.G. Karshenboim, in *The Hydrogen Atom*, eds. S.G. Karshenboim et al., p.651, Springer, Berlin (2001).
[11] A.P. Martynenko and R.N. Faustov, JETP **93**, 471 (2001).
[12] U.D. Jentschura, P.J. Mohr, and G. Soff, Phys. Rev. Lett. **82**, 53 (1999); Phys. Rev. A **63**, 042512 (2001).
[13] V.A. Yerokhin and V.M. Shabaev, Phys. Rev. A **64**, 062507 (2001).
[14] V.M. Shabaev *et al.* Phys. Rev. Lett. **86**, 3959 (2001).

QED Calculations of the Interelectron Interaction in Li-like Ions

I. Bednyakov, F. Erler, C. Lucke, R. Kuhn, I. Nandori, G. Schaller, R. Schützhold, G. Plunien, G. Soff, *Technische Universität Dresden*,
O.Yu. Andreev, L.N. Labzowsky, V.M. Shabaev,V.A. Yerokhin, *St. Petersburg State University*

Investigations of heavy few-electron atoms provide an excellent opportunity for testing QED in strong Coulomb fields. A remarkable high experimental precision has been reached in Lamb-shift measurements of Li-like ions. The uncertainty obtained e.g. for the $2p_{1/2}$ - $2s$ transition energy in Li-like Ni and Zn [1], Ag and Xe [2, 3] and U [4] is by an order of magnitude smaller than the QED contribution of second order in the fine structure constant α. To achieve that level of accuracy in theoretical predictions rigorous calculations of all Feynman diagrams of order α^2 had to be carried out [5, 6, 7].

Traditional approaches for calculating energy levels in high-Z Li-like ions such as relativistic many-body perturbation theory, multiconfigurational Dirac-Fock, and the relativistic configuration-interaction method account for the correlation and the relativistic corrections but do not provide a rigorous treatment of the QED effects, which is required in high-Z systems. Since correlation effects cannot be separated from the QED radiative corrections *ab initio* calculations valid up to order α^2 must be carried out starting from the complete set of QED-Feynman diagrams. Two-electron QED corrections of order α^2 for a Li-like ion consist of three sets of Feynman diagrams, each of which is separately gauge invariant: the self-energy screening diagrams, the vacuum-polarization screening diagrams and the two-photon exchange diagrams. The two-photon exchange diagrams do not require any renormalization. Explicit expressions for the energy shifts can be derived either by means of the two-time Greens-function method [5, 6] or within the lineprofile approach [7].

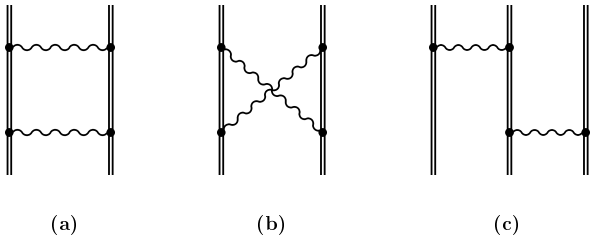


Figure 1: The two-photon exchange diagrams.

Numerical calculations have been performed in Feynman and in Coulomb gauge, respectively. The numerical values obtained exhibit an excellent agreement. The direct and the exchange parts are found to be separately gauge invariant on the level of the numerical accuracy. The results of the numerical calculation of the two-photon exchange corrections are presented in Table 1 for the $2p_{1/2}$-$2s$ transition energy in Li-like ions within the range of nuclear charge numbers $50 < Z < 100$ [5]. The estimated numerical accuracy is about 0.005 eV. Some results obtained from complete QED calculations including all available two-electron QED corrections of order α^2 are presented in Table 2. A detailed description of the formalism and of the QED effects included can be found in Refs. [6, 7]. The values from Ref. [7] also account partially for three-photon interactions. A comparison is made between theoretical calculations and experimental results for the $2p_{1/2}$-$2s$ transition in high-Z Li-like ions. The overall agreement with the experimental data reveals a significant improvement of the accuracy in the theoretical predictions.

Z	$2p_{1/2}$	$2s$	$2p_{1/2}$-$2s$
50	-13.398	-8.234	-5.164
60	-15.155	-8.953	-6.202
70	-17.547	-9.899	-7.649
80	-20.827	-11.146	-9.681
83	-22.046	-11.598	-10.448
90	-25.449	-12.823	-12.626
92	-26.596	-13.226	-13.370
100	-32.244	-15.146	-17.098

Table 1: Two-photon exchange correction to the $2p_{1/2}$-$2s$ transition energy in heavy Li-like ions (in eV).

Z	Ref. [6]	Ref. [7]	experiment	
30	57.384(4)(4)	57.34(1)	57.384(3)	[1]
47	99.43(1)(1)		99.438(7)	[2]
50	107.90(1)(2)		107.911(8)	[3]
70	176.44(6)(7)	176.52(10)		
80	220.93(15)(11)	220.92(20)		
92	280.48(11)(20)	280.36(21)	280.59(9)	[4]

Table 2: Theoretical predictions and experimental results for the $2p_{1/2}$-$2s$ transition energy in heavy Li-like ions (in eV).

References

[1] U. Staude *et al.*, Phys. Rev. A**58**, 3516 (1998)
[2] Ph. Bosselmann *et al.*, Phys. Rev. A**59**, 1874 (1999)
[3] D. Feili *et al.*, Phys. Rev. A**62**, 22501 (2000)
[4] J. Schweppe *et al.*, Phys. Rev. Lett. **66**, 1434 (1991)
[5] V.A. Yerokhin, A.N. Artemyev, V.M. Shabaev, M.M. Sysak, O.M. Zherebtsov, G. Soff , Phys. Rev. Lett. **85**, 4699 (2000)
[6] V.A. Yerokhin, A.N. Artemyev, V.M. Shabaev, M.M. Sysak, O.M. Zherebtsov, G. Soff, Phys. Rev. A**64**, 32109 (2001)
[7] O.Yu. Andreev, L.N. Labzowsky, G. Plunien, G. Soff, Phys. Rev. A**64**, 42513 (2001)

Two-photon processes in dielectronic recombination

Stephan Zakowicz, Zoltán Harman, Norbert Grün, Werner Scheid
Institut für Theoretische Physik, Justus-Liebig-Universität Gießen

In the two-step process of dielectronic recombination (DR), a free electron is captured into an ion with simultaneous excitation of a bound electron. The so-formed doubly excited state decays radiatively.

Perturbative calculations applying the method of projection operators lead to the following expression of the total DR cross section [1]:

$$\sigma_{i\to d\to f} = \frac{2\pi^2}{p^2}\frac{A_r(d,f)}{\Gamma_d}\frac{\Gamma_d/(2\pi)}{(E-E_d)^2+\Gamma_d^2/4}\,V_a^{C+B}(d).$$

Here, $A_r(d,f)$ stands for the rate of the radiative decay from the intermediate state d to the final state f, E_d and Γ_d are the energy and width of the intermediate state, respectively, and $V_a^{C+B}(d)$ denotes the capture rate depending on the electron-electron interaction. This interaction consists of the Coulomb (C) and Breit (B) interactions in transversal gauge of the photon field. The Breit interaction, which originates from the exchange of a transversal photon between two electrons, has shown to be of great importance for DR at highly charged very heavy ions [2].

Here we consider the effects of two photons in the dielectronic recombination: the influence of an additional exchange of a second virtual photon and the subsequent decay of the de-excited state by the emission of a second real photon.

The next order of the perturbative expansion of the capture operator yields perturbative terms of the intermediate states due to the Breit interaction and leads to a mixture of the intermediate states:

$$|d\rangle \to |d\rangle + \sum_{d'(\neq d)} \frac{\langle d'|V_B|d\rangle}{E_d - E_{d'}}|d'\rangle,$$

where the quantities $\langle d'|V_B|d\rangle$ are the non-diagonal matrix elements of the Breit interaction. Preliminary calculations result in small correction terms. Further contributions from an exchange of two and more virtual photons arise in an expansion of the transition operator and correct the Breit interaction.

We now focus on the KLL-DR into hydrogen-like very heavy ions, where the system is not stable until both electrons are de-excited into the K-shell. As a consequence, two photons are emitted. The former intermediate and final states d and f now become the first and second intermediate states d_1 and d_2, respectively. The partial cross section is given by

$$\sigma_{i\to d_1\to d_2\to f} = g_{d_1,d_2}(E)\cdot\sigma_{i\to d_1\to d_2}.$$

The factor

$$g_{d_1,d_2}(E) = \frac{A_r(d_2,f)}{\Gamma_{d_2}}\frac{V_a(d_1,p)}{V_a(d_1)}\int_0^{E-E_f} d\omega\,\frac{A_r(d_1,d_2;\omega)}{A_r(d_1,d_2)} \times \frac{\Gamma_{d_2}/(2\pi)}{(E_{d_2}+\omega-E)^2+\Gamma_{d_2}^2/4}\,\frac{A_r(d_2,f;E-E_f-\omega)}{A_r(d_2,f)}$$

contains the off-shell rates $A_r(d_1,d_2;\omega)$ and $A_r(d_2,f;E-E_f-\omega)$ for both radiative emissions, where E is the total energy of the inital state. The factor $V_a(d_1,p)/V_a(d_1)$ respects the energy dependence of the capture rate. The integration is performed over the energy of the first photon. For small widths Γ_{d_2} of the second intermediate state and radiative rates $A_r(d_2,f)$, g approaches 1, and the result of the one-photon calculation is reproduced.

Figure 1 shows the relative correction which is due to the emission of the second photon in the case of KLL-DR into U^{91+}. The bound state wavefunctions and energies were generated with the GRASP package of Dyall et al. [3]. The effect is seen to be rather small.

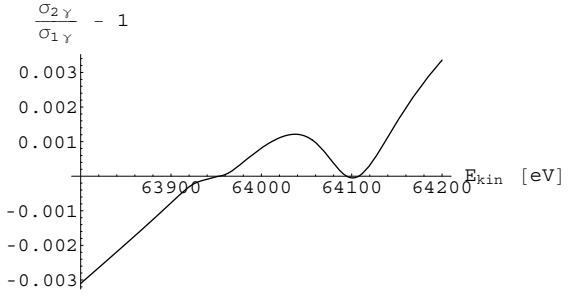


Figure 1: Relative change of the total cross section plotted against the electron energy for KLL-DR into U^{91+}

Another point of interest is the angular distribution and correlation of the two emitted photons. In the most general form, this distribution for a single cascade can be written as an expansion in spherical harmonics:

$$\frac{d^3\sigma_{i\to d_1\to d_2\to f}}{d\omega_1\,d\Omega_1\,d\Omega_2} = \frac{d\sigma_{i\to d_1\to d_2\to f}}{d\omega_1}\times \frac{1}{4\pi}\sum_{\nu}\sum_{\nu_1,\nu_2}\sum_{\substack{i,j=1\\ i\neq j}}^{2}\beta_{(\nu_1,\nu_2)\nu}^{d_1,d_2,i,j}\,[Y_{\nu_1}(\theta_1,\phi_1)\otimes Y_{\nu_2}(\theta_2,\phi_2)]_{\nu,0}\,.$$

Here the sum over i,j counts the two possible time orders of photon emission. The parameters $\beta_{(\nu_1,\nu_2)\nu}^{d_1,d_2,i,j}$ describe the anisotropy and correlation of the photons; they contain 3j-, 6j- and 9j-symbols of the involved angular momenta.

An integration over the angles of the second photon yields the angular distribution of the first photon, which was found to be identical to the one calculated in the one-photon theory [2]. Moreover, both photons show the same angular distribution when only dipole radiation is considered. Angular correlations between the two photons exist.

References

[1] P. Zimmerer, N. Grün, W. Scheid, *Phys. Lett.* A **148**, 457 (1990)

[2] M. Gail, N. Grün, W. Scheid, *J. Phys.* B **31**, 4645 (1998)

[3] K. G. Dyall et al., *Comput. Phys. Commun.* **55**, 425 (1989)

Photon Polarization in Radiative Recombination of Bare High–Z Ions

Andrey Surzhykov[1], Stephan Fritzsche[1], and Thomas Stöhlker[2]
[1] Fachbereich Physik, Universität Kassel, D–34132 Kassel, Germany
[2] Gesellschaft für Schwerionenforschung, D–62491 Darmstadt, Germany

The radiative recombination (RR) and radiative electron capture are two well–established processes from the study of electron–ion and atom–ion collisions. In these processes, a free or quasi–free electron is captured into a bound state of the ion, accompanied by the simultaneous emission of a photon. For bare high–Z ions, for example, the radiative recombination has been explored in detail by Stöhlker and co–workers [1] at the GSI storage ring during recent years. So far, however, most experiments were focused on measuring the total and angle–differential recombination cross sections which are typically found in good agreement with theoretical predictions, based on Dirac's theory [2]. Much less attention, in contrast, has been paid previously to the polarization of the emitted radiation, mainly because of the lack of efficient polarization detectors for hard x–rays. Only in the light of recent improvements in detector techniques, the observation of the photon polarization has become more likely within the next few years.

To predict the polarization of the photons which are emitted in the recombination of free electrons into a bound state of the bare ions, theoretical studies have been carried out in the framework of the *density matrix approach* [3]. In the past, this approach has been utilized successfully in a large number of case studies on the *polarization* as well as *correlation* phenomena in many areas of the nuclear and atomic physics. In fact, this formalism provides us with a tool of great elegance in the theoretical analysis of collision and decay processes.

In the framework of the density matrix theory, the photon polarization is directly related to three *Stokes parameters* (P_i, i=1..3). While the first two parameters are usually used for the characterization of the linear polarization $P_L = \sqrt{P_1^2 + P_2^2}$, the third Stokes parameter describes the circular polarization of the photons $P_C = P_3$ [4]. As for the computation of cross sections, these parameters are closely connected to the matrix element

$$M^{RR}_{b,\mathbf{p}}(m_s, \lambda, \mu_b) = \int d^3r \psi^\dagger_{j_b\mu_b}(\mathbf{r})\, \alpha\, \hat{\mathbf{u}}^*_\lambda\, e^{-i\mathbf{kr}}\, \psi_{\mathbf{p},m_s}(\mathbf{r}) \quad (1)$$

which refers to the radiative transition of a free electron with asymptotic momentum $\mathbf{p}$ and spin projection m_s in the bound–state of the bare ion. In recent years, this *relativistic* form of the transition matrix has been widely used for studying the radiative recombination of high–Z ions at intermediate and high collision energies [2]. For a capture into bare ions, $\psi_{j_b\mu_b}(\mathbf{r})$ and $\psi_{\mathbf{p},m_s}(\mathbf{r})$ are the known solutions of Dirac's Hamiltonian for a bound or continuum electron, respectively. Moreover, the unit vector $\hat{u}_\lambda$ denotes the polarization of the photons. For the numerical calculations of the matrix element (1) and, hence for, the photon polarization, we used the computer code DIRAC [5].

Calculations for different polarization parameters of the emitted photons have been carried out as function of the projectile ion energy [4]. For instance, Figure 1 shows the degree of linear polarization P_L of the photons which are emitted due the capture of a free electron into the K shell of Bi^{83+} projectiles. Since, in experiment, the radiative recombination of ions is usually studied by collisions of bare, high–Z projectiles with (low–Z) target atoms, here we present the Stokes parameter for angles measured in the *laboratory system* (the rest frame of the target atoms) with respect to the *beam direction*. As seen from Figure 1, a very high degree of polarization arises for a wide range of angles.The density matrix theory provides a consistent framework to investigate not only the *polarization* properties of the photons and residual ions but also the total as well as differential cross sections of the electron capture processes [4]. Moreover, this theory can be easily extended to study the two– (or multi–) step radiative recombination. In such processes, an electron is captured into any of the excited ion states which will further decay by emission of one or several subsequent photons. This subsequent photon decay in the high–Z hydrogen–like ions can provide new information about the electron structure of atoms and ions in strong Coulomb fields [5].

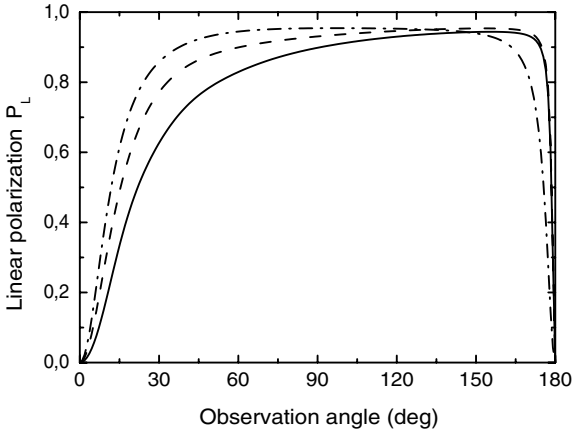


Figure 1: Degree of linear polarization of the emitted photon as a function of the *laboratory* photon angle for the K–RR of Bi^{83+} projectiles. The linear polarization is shown for three projectile energies: T_p = 10 MeV/u (– - –), T_p = 100 MeV/u (– –), and T_p = 220 MeV/u (—).

References

[1] Th. Stöhlker *et al.*, Phys. Rev. A **51** (1995) 2098.
[2] J. Eichler and W. Meyerhof, *Relativistic Atomic Collisions*, Academic Press, San Diego, 1995.
[3] K. Blum, *Density Matrix Theory and Applications*, Plenum, New York, 1981.
[4] A. Surzhykov *et al.*, Phys. Lett. A **289** (2001) 213.
[5] A. Surzhykov *et al.*, submitted to Phys. Rev. Lett. .

Scaling Law for the Recombination Enhancement in Electron Coolers

C. Heerlein and C. Toepffer, Universität Erlangen-Nürnberg

Experiments on ion-electron recombination in electron coolers show an enhancement of the recombination rate with respect to the standard theory of radiative recombination. So far no satisfactory theoretical explanation of the observed effects had been reached.

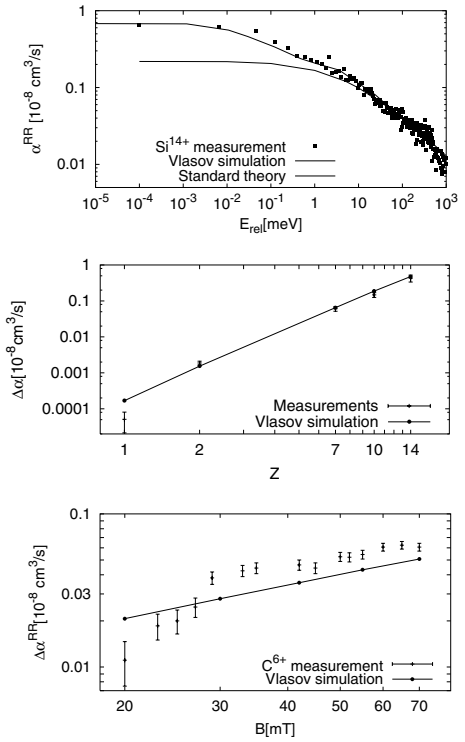


Figure 1: Scaling of the excess recombination $\Delta\alpha^{\mathrm{RR}}$ as a function of the relative energy E_{rel} between the beams, the ionic charge Z, and the magnetic guiding field B. Measurements from [3, 4] are compared to simulation results [2].

The cross section σ for radiative recombination [1] is unaffected in average by the magnetic guiding field in the electron cooler. The standary theory integrates σ over free electrons in an anisotropic Maxwell distribution with the longitudinal and transversal temperatures $T_\parallel$ and $T_\perp$, respectively, to determine the rate coefficient $\alpha_{\mathrm{st}}^{\mathrm{RR}}$. However, electrons may acquire negative energy when the ion enters the electron beam. The measured rate coefficients are independent of the bulk density, therefore the electronic mean field can be neglected. Thus the Vlasov equation for the time-dependent phase space density f of both free and bound electrons reads

$$\frac{\partial f}{\partial t} + \boldsymbol{v}\cdot\frac{\partial f}{\partial \boldsymbol{r}} - \left(\boldsymbol{v}\times\boldsymbol{e}_z + \frac{Y}{r^2}\,\boldsymbol{e}_r\right)\cdot\frac{\partial f}{\partial \boldsymbol{v}} = 0\,. \qquad (1)$$

It is formulated in units of the magnetic guiding field with the only parameter

$$Y = \frac{ZBe^3}{4\pi\epsilon_0\,\sqrt{m}\,(k_{\mathrm{B}}T_\perp)^{3/2}}\,, \qquad (2)$$

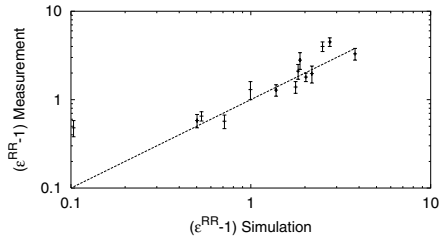


Figure 2: Correlation between the simulated enhancement factors and the experimental results available in the literature.

which can be understood as the ratio of the Coulomb parameter and the cyclotron radius. This governing differential equation (1) is provided with an initial condition depending merely on the anisotropy parameter $\zeta = \sqrt{T_\parallel/T_\perp}$.

We have performed numerical simulations [2] at the parameters of the experiments available in the literature. In the model merging of the beams was modeled in zeroth order as an instantaneous process. The scaling with external parameters is shown in Figure 1. The Vlasov simulation identifies initially bound electrons as drivers of the excess recombination $\Delta\alpha^{\mathrm{RR}} = \alpha^{\mathrm{RR}} - \alpha_{\mathrm{st}}^{\mathrm{RR}}$.

In physical units the recombination coefficient for vanishing relative energy between the beams depends on the ion charge Z, the guiding field B, and both temperatures $T_\parallel$ and $T_\perp$. Contrary, in units of the magnetic field, only the parameters Y and ζ occur. Thus if locally the enhancement factor $\epsilon^{\mathrm{RR}}-1 = \Delta\alpha^{\mathrm{RR}}/\alpha_{\mathrm{st}}^{\mathrm{RR}}$ scales as $\epsilon^{\mathrm{RR}}-1 \propto Y^\mu\zeta^\nu$ we have in physical parameters

$$\Delta\alpha^{\mathrm{RR}} \propto Z^{2+\mu}B^\mu\; T_\perp^{-\frac{3\mu+\nu+1}{2}}\; T_\parallel^{\frac{\nu}{2}}\,. \qquad (3)$$

Figure 2 presents a correlation plot of the enhancement factors $\epsilon^{\mathrm{RR}}-1$ of these experiments against measurements; it shows good agreement. Averaged over the available experiments the scaling $\Delta\alpha^{\mathrm{RR}} \propto Z^{2.4}\; B^{0.4}T_\perp^{-0.8}T_\parallel^{-0.4}$ was found. Numerical simulations, however, show that the scaling coefficients are not precisely constant over the studied parameter space. The above scaling law form is supported by the numerical results. The quantitative agreement with experimental findings is significantly improved while the assumption of some effective temperature [5] could be waived. – This work has been supported by GSI collaboration contract.

References

[1] M. Stobbe, Ann.Phys.(Leipzig) 7 (1930) 661.

[2] C. Heerlein, *Radiative Rekombination im Elektronenkühler: Numerische Analyse im Phasenraum* (Diss.), Erlangen, 2002.

[3] H. Gao, R. Schuch, et al., J.Phys. B: At.Mol.Opt. Phys. 30 (1997) L499.

[4] G. Gwinner, A. Hoffknecht, et al., Phys.Rev.Lett. 84 (2000) 4822.

[5] Q. Spreiter, C. Toepffer, J.Phys. B: At.Mol.Opt. Phys. 33 (2000) 2347.

Ion Stopping in a Magnetized Anisotropic Electron Plasma

M. Walter, G. Zwicknagel, C. Toepffer, B. Möllers
Institut für Theoretische Physik II, Universität Erlangen

Trapped charged particles, like highly charged ions or antiprotons, can be cooled by colder charged particles, e.g. electrons or positrons. Electron cooling is also used to obtain ion beams of high phase space density. In these applications the presence of strong external magnetic fields constitutes a theoretical challenge, as its influence on the energy loss of the ions dE_i/ds is not so obvious as early kinematical models might suggest. There are basically two approaches. The dielectric theory is a continuum treatment, in which the polarization of the electrons by the ion is calculated. In this framework we calculated dE_i/ds in a PIC simulation, in which the underlying nonlinear Vlasov equation for the electrons is solved for test-particles [1], as well as through a linear response evaluation of the dielectric function [2]. In the complementary binary collision approximation one accumulates the energy transfer from individual collisions between ions and magnetized electrons. This has been calculated by treating the Coulomb interaction as a perturbation to the helical motion of the electrons up to second order including a correction for hard collisions [3], as well as by classical trajectory Monte Carlo (CTMC) calculations [4]. The figures show $-dE_i/ds$ in units of $Z^2e^4n_e/(4\pi\epsilon_0^2 m v_{th\|}^2)$ as function of the ion velocity in units of the longitudinal thermal velocity $v_{th\|}$ of the electrons, and α is the angle between the magnetic field and the motion of the ion. The binary collision results obtained to second order (Fig. 1) agree well with those from CTMC calculations (Fig. 2). There is a small energy gain for very small velocities, but the major effect of the magnetic field is an enhancement of the energy loss, other calculations show that it increases with α. On the other hand the binary collision model yields much smaller energy losses than the linearized dielectric theory, as shown in Fig. 3. However, if the dielectric theory is evaluated without linearization and the full dynamics of the magnetized electron plasma, it gives energy losses which are even smaller than in the binary collision model (Fig. 4). We surmise that the linear response theory has problems for strong magnetic fields. – This work has been supported by GSI collaboration contract.

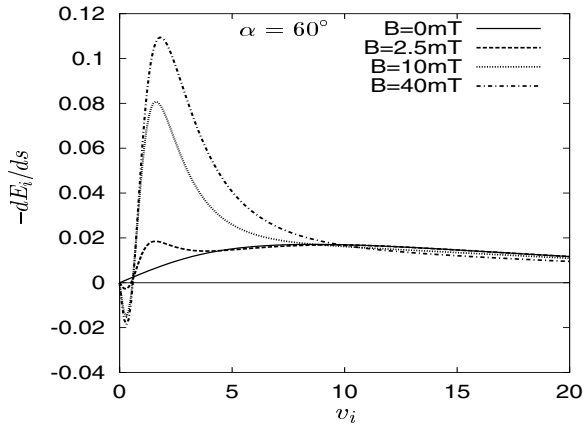


Figure 1

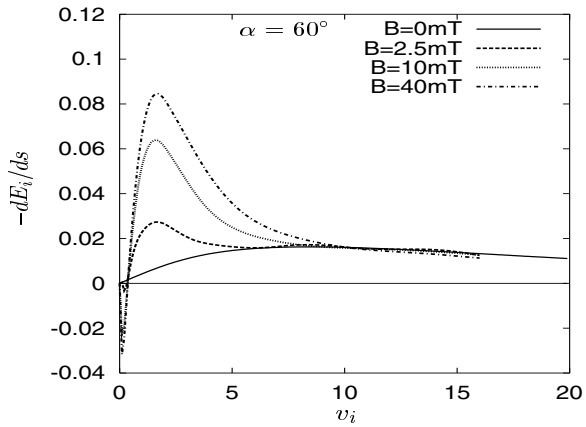


Figure 2

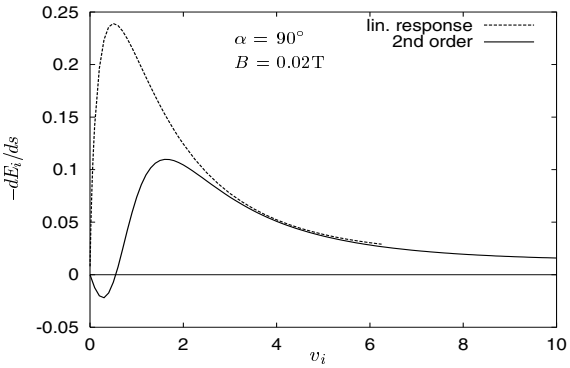


Figure 3

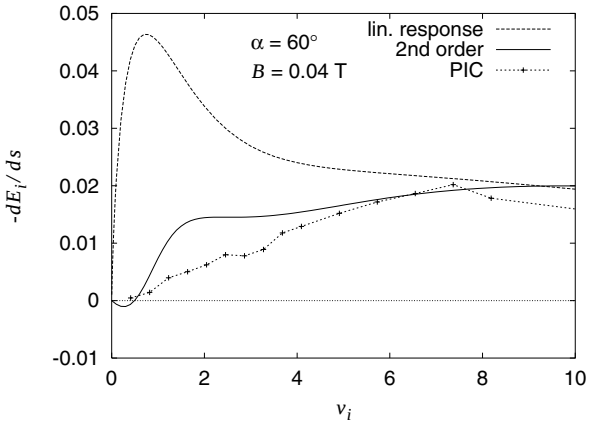


Figure 4

References

[1] M. Walter, C. Toepffer, G. Zwicknagel, Nucl. Inst. & Meth. B **168** (2000) 347.

[2] H. B. Nersisyan, M. Walter and G. Zwicknagel, Phys.Rev. E **61** (2000) 7022.

[3] C. Toepffer, Scattering of magnetized electrons by ions, preprint (2002), submitted to Phys.Rev. A.

[4] G. Zwicknagel, C. Toepffer, AIP Conference Proceedings **606** (2002) 499.

Interaction of Fast Ion Beams with Low- and High-Density Targets

O. Rosmej[1], Th. Stöhlker[1], V.P. Shevelko[2,3], I.Yu. Tolstikhina[3]

[1]Gesellschaft für Schwerionenforschung, Darmstadt, Germany; [2] MPI-K Heidelberg, Germany;

[3] P.N. Lebedev Institute, Moscow, Russia

Electron capture processes into excited states

$$X^{q+} + A \rightarrow X^{(q-1)+}(n) + A^{+} \qquad (1)$$

are considered in collisions of fast positive ions X^{q+} with low- and high-density targets A. In the case of a low density, the electron-capture cross section $\sigma_{ec}(n)$ has a certain distribution over the principal quantum number n with a maximum at $n = n_{max}$ and asymptotic behavior $\sigma_{ec}(n) \approx n^{-3}$ at $n \gg n_{max}$. For Rydberg states $n \gg 1$, ions with the orbital quantum numbers $\ell = 0$ and 1 are created with the highest probability (see, e.g. [1]).

The distribution of σ_{ec} over n states depends not only on the relative velocity v and the atomic structure of colliding systems but also on the target density. In a dense target, the largest possible principal quantum number n_{cut} which the $X^{(q-1)+}(n)$ ion can be created with, is limited because the population of highly excited n states is destroyed by ionization collisions with the target:

$$X^{(q-1)+}(n) + A \rightarrow X^{q+} + A + e^{-}. \qquad (2)$$

The ionization rate from the n state is quite large and proportional to $N \cdot n^4 \cdot Z_T^2$ where Z_T and N are the nuclear charge and density of the target particles, respectively.

The value of n_{cut} can be estimated from equality condition of the radiative decay rate $A(n, n_0)$ into all low-lying states of the $X^{(q-1)+}$ ion and the ionization rate:

$$A(n_{cut}, n_0) = N \cdot \sigma_{ion}(n) \cdot v, \qquad (3)$$

where n_0 is the ground state and $\sigma_{ion}(n)$ is the ionization cross section from the n state induced by the target. Employing the Kramers formula for $A(n, n_0)$ and the Thomson formula for $\sigma_{ion}(n)$, one has from (3):

$$n_{cut} = n_0 + \Delta n, \qquad (4)$$

$$\Delta n \approx Z_P \left(\frac{10^{18}}{Z_T^2 N[\mathrm{cm}^{-3}]} \right)^{1/7} \left(\frac{E[\mathrm{keV/u}]}{260\, Z_P^2} \right)^{1/14}, \qquad (5)$$

where E and Z_P are the projectile energy and ion charge. As is seen from (5), the higher is the target density and the target charge, the lower is the largest possible quantum number n_{cut} and, therefore, the lower is the total capture cross section $\sigma_{tot} = \sum_{n=n_0}^{n_{cut}} \sigma_{ec}(n)$.

In Fig. 1, the electron-capture cross sections for collisions of bare Ni^{28+} ions with low- and high-density SiO_2 molecules are shown. The cross sections were calculated by the CAPTURE code based on the normalized electron-capture probabilities in the impact parameter representation and described in [2]. At energies E = 100 keV/u – 10 MeV/u, the capture of L and M subshells of the low-density SiO_2 molecules (curve 1) is suppressed by the density effect (curve 2) leading mainly to the capture of K electrons. At energies E > 10 MeV/u, both cross sections are approximately equal because only K electrons of SiO_2 molecules are mostly captured with $n_{cut} \approx 4$.

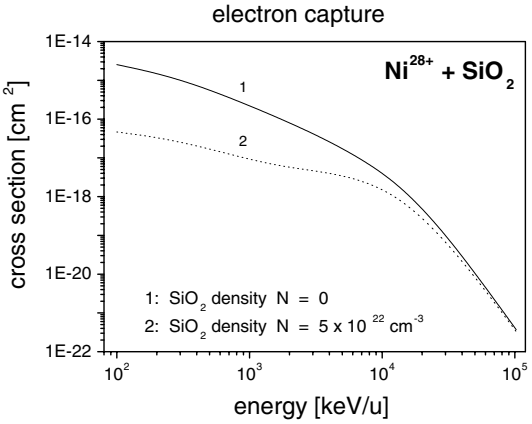


Figure 1: Influence of the target-density effect on the total electron-capture cross sections in Ni^{28+} + SiO_2 collisions:
1 – low-density target, $N = 0$;
2 – high-density target, $N = 5 \times 10^{22}$ cm^{-3}.

Due to the density effect considered, the average (mean) charge of the ion beam after the solid target is larger than that after a low-dense target. This problem was studied in [3] for collisions of fast U^{q+} ions with the hydrogen-carbon plasma in the MeV/u energy regime.

In general, consideration of the charge-changing processes arising in collisions of fast beams with atomic and plasma targets [2]–[4] shows the following peculiarities:

1) the distribution of the projectiles over excited states after interaction with a target depend on the target density: interaction with high-density targets cuts off the maximum possible principal quantum numbers of the projectile after collision and *reduces* the total electron-capture cross sections,

2) the distribution over the quantum numbers nl of the projectile due to charge-changing collisions with a target defines the *spectroscopic* properties (radiative spectra) of the projectile,

3) account for the density effect together with the Coulomb distortion of the projectile wave functions and multi-electron processes allows one to describe the *mean charge* of the fast-ion beams penetrating through atomic and plasma targets.

References

[1] P. Richard (ed.): *Methods of Experimental Physics*, Vol. 17, (Academic, N.Y. 1980) p. 108

[2] V.P. Shevelko: JTP, **71**, 20 (2001)

[3] H. Wahl et al.: Short Commun. Phys. **8**, 28 (2001) (Lebedev Institute, Moscow)

[4] V.P. Shevelko et al.: NIMB **184**, 295 (2001)

Fast electron emission in atomic collisions under strong-field, nonperturbative conditions and the Fermi-shuttle mechanism

Dorin-Cesar Ionescu

Atomic Physics Division, GSI-Darmstadt and Institut für Theoretische Physik, Technische Universität Dresden

Using a nonperturbative approach based on the exact numerical solution of the two-center time-dependent Dirac equation we investigate the electron dynamics in relativistic heavy-ion collisions. By directly visualizing the collision dynamics in encounters between 100 MeV/u Au^{79+} projectile ions ($v/c \simeq 0.43$) impinging on a hydrogen-like uranium target we identify a new ionization mechanism in which electrons are emitted from the internuclear region preferentially in the *transverse* direction with respect to the projectile trajectory [1]. A striking characteristic of this new ionization mechanism is that the velocity of the emitted electron is *higher* than the projectile velocity.

The acceleration of electrons to high energies is similar to the "Fermi-shuttle" acceleration discussed in recently reported measurements [2] of electron emission to the continuum in ion-atom collisions at intermediate energies. In [2] a multiple scattering mechanism, also referred to as "Fermi-shuttle" mechanism, where the electron scatters several times between projectile and target, was proposed to explain the observed fast electron emission.

In our theoretical description the nuclear motion is treated using classical dynamics, and we fix the origin of the coordinate system at the center of the target nucleus. Within this semiclassical approach the projectile ion moves with constant velocity $\mathbf{v} = (0, 0, v)$ at an impact parameter b parallel to the z-axis such that the xz-plane is the scattering plane. In the numerical analysis we enclose the collision system in a finite volume in momentum space. In contrast to grid methods in configuration space where the boundary conditions are not fullfilled for realistic grid sizes due to continuum components of the wave function associated with ionization and charge exchange that spread over the entire space, in momentum space the wave function is confined to a finite volume and stays localized around the origin at all times.

In Fig. 1 we display snapshots of the electron probability density $\Psi^\dagger(\mathbf{r}, t)\Psi(\mathbf{r}, t)$ in coordinate space at two different times for a head-on, 100 MeV/u collision between a bare Au^{79+} projectile ion and a hydrogen-like uranium target. The electron is initially bound in the U^{91+} 1s-state, the projectile is approaching the target from negative z-values, and the target is located at the origin $x = z = 0$ of the scattering plane. Thus, target-centered electron emission appears centered around the origin while electrons captured to bound or continuum states of the projectile are located around $x = 0$ and $z = vt$.

In addition to the local maxima at the origin $x = z = 0$ and $x = 0, z = vt$ associated with target and projectile, respectively, it is seen that at $t = 22$ the density displays a third maximum which is located around $x = 0$ and $z \simeq 4$. However, as it is evident from the lower plot, this maximum separates into two distinctly different maxima moving symmetrically and roughly perpendicular with respect to the beam direction. Thus, at $t = 27$ we find two symmetric distributions peaking around $x = \pm 2.5$ and $z = 5$ from which the velocity components of the associated electrons are estimated as $v_x \simeq 0.5c$ and $v_z \simeq 0.2c$. We interpret this as a new ionization mechanism in which electrons are emitted with relatively *high transverse* and *low longitudinal velocities*. As the projectile passes the target a very strong combined field is produced leading to a high acceleration of the electron which initially follows the projectile ion, scatters several times in the strong field associated with the collision partners, and at later positive times, as the system relaxes, is ejected from the internuclear region preferentially in the transverse direction. In conclusions, our present investigation extends the results on the Fermi-shuttle acceleration into the nonperturbative regime associated with highly-charged ions as heavy as uranium and provides new insights into the dynamics of ionization in relativistic heavy-ion collisions.

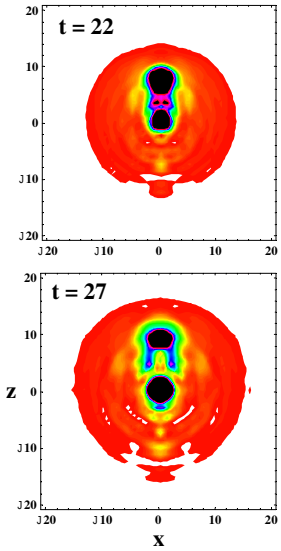


Figure 1: Snapshots of the probability density at $t = 22$ and $t = 27$. The units of length and time are $\lambda_C \simeq 386.16$ fm and $\tau_C \simeq 1.29 \times 10^{-21}$ s, respectively.

References

[1] D.C. Ionescu and A. Belkacem, The European Physical Journal D (2002). In print.

[2] G. Lanzano et al., Phys. Rev. A **63**, 032702 (2001); see also E. Fermi, Phys. Rev. **75**, 1169 (1949).

HEAVY ION RESEARCH IN OTHER FIELDS

Plasma Physics 127

Heavy Ion Induced Effects in Solids 137

Biophysics and Therapy with Highly Ionized Beams 151

Chemistry 179

Plasma Physics

Beam Initiated Discharge Channels for Neutralized Ion-Beam Transport 127
C. Niemann, A. Tauschwitz, D. Penache, S. Neff, R. Birkner, J. Jacoby,
C. Constantin, F.B. Rosmej, R. Knobloch, R. Presura, D.H.H. Hoffmann

Determination of Target Line Density 128
U. Geissler, N. Borisenko, E. Dewald, D.H.H. Hoffmann, K. Tsigutkin, O. Rosmej,
J. Wieser

Multiple Shockwaves Driven by Heavy Ion Beams in Solid Matter 129
E. Dewald, C. Constantin, C. Niemann, D.H.H. Hoffmann, J. Jacoby, T. Schlegel,
S. Udrea, D. Varentsov, A. Tauschwitz

Radiography with Protons Generated by Ultrashort High Intensity Lasers 130
A. Blazevic, M. Roth, T.E. Cowan, J.C. Gauthier, P. Audebert, J. Fuchs, M. Hegelich,
S. Karsch, M. Geißel, E. Brambrink, T. Schlegel

Simulations of Hydrodynamic and Thermodynamic Response of Solid Targets Heated By Future SIS-100 Beam 131
N.A. Tahir, D. Varentsov, A. Shutov, P. Spiller, D.H.H. Hoffmann, J. Jacoby, J. Wieser

Simulations of Two-Beam Irradiation of Cylindrical Targets at the Upgraded SIS-18 132
N.A. Tahir, D. Varentsov, A. Shutov, P. Spiller, D.H.H. Hoffmann, J. Jacoby, J. Wieser

Target Design for Equation-of-State Measurements of Shock Compressed Matter with the Current SIS-18 Beam 133
A. Kozyreva, M. Basko, R. Bock, E. Dewald, D.H.H. Hoffmann, J. Jacoby,
J. Meyer-ter-Vehn, T. Schlegel, A. Shutov, P. Spiller, A. Tauschwitz, J. Wieser

Unique Capabilities of Intense Heavy Ion Beam as a Tool for EOS Studies 134
D.H.H. Hoffmann, V.E. Fortov, I.V. Lomonosov, N.A. Tahir, D. Varentsov

Heavy Ion Induced Effects in Solids

Thermal Behaviour of Nanostructured ZrO^2 after Heavy Ion Irradiation 137
W. Berky, A.G. Balogh

Defect Creation by Energetic Heavy Ions in Different Fluoride Crystals 138
A.S. El-Said, C. Müller, R. Neumann, K. Schwartz, C. Trautmann

Critical Analysis of Ion Track Micrographs Recorded by Scanning Force Microscopy 139
C. Müller, M. Lang, K.O.Voss, R. Neumann

Electronic Excitation Effect in Ion-Irradiated $EuBa_2Cu_3O_y$ 140
N. Ishikawa, A. Iwase, Y. Chimi, O. Michikami, T. Hashimoto, T. Kambara,
C. Müller, R. Neumann

Scanning Force Microscopy of Natural and Heavy Ion Induced Damage in Phlogopite 141
M. Lang, U.A. Glasmacher, R. Neumann, G.A. Wagner

Voltage-Gated Nanopores Analogous to Biochannels 142
Z. Siwy, Y. Gu, H.A. Spohr, D. Baur, A. Wolf-Reber, R. Spohr, P. Apel, Y.E. Korchev

Relevance of Surface Gels for Ion Track Etching in Polymers 143
D. Baur, P. Apel, Y.E. Korchev, C. Müller, Z. Siwy, H.A. Spohr, R. Spohr

Flexible Microchannels with Integrated Nanoporous Membranes 144
S. Metz, C. Trautmann, A. Bertsch, M. Schlund, P. Renaud

Micron-Sized Ion-Track Pores in Glass for Bilayer Recording 145
N. Fertig, C. Meyer, R.H. Blick, C. Trautmann, J.C. Behrends

Preparatory Experiments for a Second-Generation Radiation-Biological Single Hit Facility 146
M. Cholewa, B.E. Fischer, M. Heiß

Preparation of a Single Metal Wire by Electrochemical Filling of an Etched Ion Track 147
M.E. Toimil Molares, Z. Siwy, R. Neumann, I.U. Schuchert, R. Spohr, C. Trautmann

Electrodeposition of Cu/Co Multilayered Nanowires 148
I. Enculescu, R. Spohr

Formation of Metal Membranes by Direct Duplication of Ion-Track Templates 149
D. Dobrev, R. Neumann, J. Vetter

Biophysics With Highly Ionizing Beams

Direct Evidence for the Spatial Correlation Between Individual Particle Traversals and Localized CDKN1A Response Induced by High-LET Radiation 151
M. Scholz, B. Jakob, G. Taucher-Scholz

Fast CDKN1A Foci Formation at Sites of Heavy Ion-Induced Damage does not Depend on Activation Mediated by TP53 152
G. Taucher-Scholz, B. Jakob, M. Scholz, G. Becker, G. Kraft

Ion-induced Electron Emission Patterns in Condensed Matter 153
S. Dreuil, S. Hagmann, H. Rothard, G. Kraft

Microdosimetric Characterization of the Therapeutic Heavy Ion Beam 154
R. Gerlach, H. Roos, A.M. Kellerer

A new Irradiation Facility for Biological Samples at the UNILAC 155
W. Becher, M. Konradt, G. Lenz, R. Lotz, I. Ragaller, H. Schaub, M. Scholz, B. Voss, G. Kraft

Induction of Checkpoint Proteins TP53 and CDKN1A after Heavy Ion Irradiation 156
C. Fournier, C. Wiese, S. Brons, G. Taucher-Scholz, G. Kraft

Investigation of Radiation-Induced Damage in Plasmid DNA by Scanning Probe Microscopy 157
Y. Zhao, F. Hubenthal, F. Träger

Non-Random Distribution of Double-Stranded DNA Fragments Generated by Highly Ionizing Beams 158
A. Fricke, M. Kühne, M. Löbrich

Influence of Radiation Quality and Additives on the Release of Bases after Ionising Irradiation of DNA 159
H.M. Luxenburger, C. Pal, A.-K. Hoffmann, J. Hüttermann

Complex Chromosome Aberrations Induced by Carbon Ions of Different Energies in Tumor Cells 160
H. Hofman-Hüther, M. Rave-Fränk, P. Virsik-Köpp

Use of Human Lymphocytes for Radiation Risk Assessment 161
T. Größer, P. Hessel, S. Ritter, E. Nasonova, E. Gudowska-Novak

Heavy Ion Irradiation of Human Colon Adenocarcinoma Cells in Multilayer Culture 162
J. Topsch, W. Müller-Klieser, M. Scholz, G. Kraft

RBE Measurements in the Epithelial Megacolony, a Simplified in Vitro Tumour Model 163
J. Kummermehr, R. Sanchez-Brandelik, M. Scholz

Treatment Planning for the GSI Radiotherapy 164
M. Krämer, B. Hasch, E. Rietzel, U. Weber, O. Jäkel

Compensation of Target Motion in Magnetic Raster Scanning at GSI 165
S.O. Grözinger, W. Becher, Th. Haberer, E. Rietzel, G. Kraft, Q. Li

The Patient Fixation Unit for the Treatment Chair in Cave M 166
P. Heeg, D. Schardt, J. Störmer

X-ray Image Intensifiers for Patient Positioning 167
E. Rietzel, D. Schardt, I. Ragaller, P. Heeg

Viewing Screen Systems for Diagnostic and Quality Assurance Purposes 168
A. Weiss, B. Spielberger, H. Eickhoff, Th. Haberer, A. Peters

A Versatile Heavy-Ion Irradiation Facility 169
D. Schardt, W. Becher, Th. Haberer, G. Lenz, M. Krämer, E. Rietzel, E. Schubert, U. Weber, E. Badura, H. Brand, H. Essel, J. Hoffmann, N. Kurz, W. Ott, K. Poppensieker, M. Richter, H. Eickhoff, B. Franczak, R. Steiner, B. Voss

Evaluation of Avalanche Photodiode Arrays for the Readout of High Granularity Scintillator Matrices 170
P. Crespo, M. Kapusta, M. Moszysnki, W. Enghardt, J. Pawelke, M. Szawlowski

An Interactive Approach for Local Dose Quantification from In-Beam PET Data 171
K. Parodi, W. Enghardt

In-Beam PET Measurements of Proton-Induced β^+-Activity 172
K. Parodi, W. Enghardt, Th. Haberer

A New Fully 3D Maximum Likelihood PET Reconstruction Applicable to Different Detector Arrangements 173
P. Crespo, W. Enghardt, K. Lauckner

A Scatter Correction for Iterative Tomographic Reconstruction 175
F. Pönisch, W. Enghardt

The Evaluation of Carbon Ion Therapy PET Data within the Time Domain 176
C. Kausch, W. Enghardt

Progress Report of the Carbon Ion Therapy Project at GSI 177
Th. Haberer, J. Debus, H. Eickhoff, W. Enghardt, G. Kraft, D. Schardt

Patient Irradiations at GSI 178
D. Schulz-Ertner, C. Thilmann, M. Wannenmacher, J. Debus

Chemistry

Chemical Investigation of Hassium (Hs, Z=108) 179
Ch.E. Düllmann, H.W. Gäggeler, S. Soverna, A. Türler, R. Dressler, B. Eichler, F. Glaus, D.T. Jost, D. Piguet, T.N. Ginter, K.E. Gregorich, U. Kirbach, D.M. Lee, R. Sudowe, D.C. Hoffman, H. Nitsche, J.B. Patin, P. Zielinski, W. Brüchle, R. Eichler, E. Jäger, V. Pershina, M. Schädel, B. Schausten, E. Schimpf, H.-J. Schött, G. Wirth, S.N. Timokhin, A.B. Yakushev, K. Eberhardt, P. Thörle, N. Trautmann, Z. Qin, A. Vahle

Confidence Intervals for Experiments with Background and Small Numbers of Events 180
W. Brüchle

Deposition of Osmium Tetroxide on Reactive Surfaces 181
A. von Zweidorf, R. Angert, W. Brüchle, E. Jäger, J.V. Kratz, G. Langrock, M. Mendel, A. Nähler, M. Schädel, B. Schausten, E. Schimpf, E. Stiel, N. Trautmann, G. Wirth

Preparation of Targets for the New GSI Rotating Wheel Target Assembly 182
K. Eberhardt, P. Thörle, N. Trautmann, M. Schädel, E. Schimpf

Vacuum Thermochromatography of Radon on Transition Metals Cu, Ag, Au, Pd, and Ni 183
R. Eichler, E. Jäger, E. Schimpf, M. Schädel

A Monte-Carlo Model of Vacuum Thermochromatography 184
R. Eichler, M. Schädel

Prediction of Adsorption Enthalpies of the SHE 112 and 114 on Transition Metals 185
R. Eichler, M. Schädel

Intermetallic Compounds of Element 112: the Electronic Structure and Bonding of HgX and 112X (X = Pd, Ag and Au) 186
V. Pershina, T. Bastug, T. Jacob, B. Fricke

Towards a Calculation of Adsorption Enthalpies for Molecules of Superheavy Elements 187
C. Sarpe-Tudoran, T. Jacob, B. Fricke, S. Fritzsche,W.-D. Sepp, V. Pershina

Theoretical Predictions of Hydrolysis and Complex Formation of Element 104, Rf, in HF and HCl Solutions 188
V. Pershina, J. V. Kratz



Beam initiated discharge channels for neutralized ion-beam transport

C. Niemann[1], A. Tauschwitz[1], D. Penache[1], S. Neff[1], R. Birkner[1], J. Jacoby[2], C. Constantin[1], F.B. Rosmej[1], R. Knobloch[1], R. Presura[1], D.H.H. Hoffmann[1,2]

[1] *Technische Universität Darmstadt*
[2] *Gesellschaft für Schwerionenforschung mbH*

High current discharge channels are an interesting alternative for the transport of intense ion beams. A sufficiently dense plasma can neutralize both beam-space charge and current and provides a strong focusing magnetic field all the way along the channel. Laser initiated discharge channels were subject to detailed investigations in the past few years at GSI [1, 2]. Recently, stable discharges were alternativley initiated by an ion-beam pulse from the UNILAC, which creates a trace of seed electrons in a gas fill of a few mbar along the desired path of breakdown. The discharge chamber is integrated into the beamline by a multi-stage differential pumping system. A beam mask with a single 2 mm diameter circular hole, aligned exactly to the channel axis prepares a narrow ion-beamlet of 11.4 AMeV Ni^{12+} ions, which defines the size of the ionization channel. First experiments produced stable, free-standing 50 cm long discharge channels in ammonia and argon with currents of up to 55 kA. The discharge is triggered 20 μs after the beginning of a 50 μs long macro pulse with an electric current of less than 5 μA inside the metallic 60 cm diameter discharge chamber. A low energy electric prepulse can optionally be applied before the high current discharge, to stabilize the channels. An upper limit for the electron density induced by the beam, can be estimated from the total energy loss of the beam in the gas. At this current and a gas pressure of 10 mbar the total energy loss of the beam in ammonia during 20 μs is around 10^{14} eV/cm^3. Neglecting recombination of free electrons and assuming that the whole energy is used to ionize only electrons with the lowest ionization potential, the maximum electron density becomes roughly 10^{13} cm^{-3}. Although the real density can be one or two orders of magnitude lower, the value is comparable or even higher than the electron densities produced by UV-laser induced ionization of organic molecules, which was used so far for the initiation of discharge channels [3] The discharges were found to be stable and reproducible even at times after the current maximum, with and without the electric prepulse in ammonia and argon at currents in excess of 55 kA. Channels in NH_3 could only be produced at pressures below 5 mbar. The maximum pressure for Ar discharges was only limited by the differential pumping system. Figure 1 shows some fast-shutter pictures of a high currnet discharge in ammonia, 1 μs and 9 μs after the breakdown. The current maximum is reached at 4 μs. Even after the current reversal the channels are very straight and stable. The discharge current as well as the channel-diameter evolution for discharges in ammonia and argon with and without the optional low-energy prepulse are compared in figure 2. For both gases, the prepulse leads to an increased channel diameter due to the lower initial gas pressure and faster expansion. The initial diameter is in all cases comparable to the size of the ion beamlet. The discharge diameter in argon is considerably smaller than in ammonia, which is important for beam transport applications where the channel has to be as small as possible.

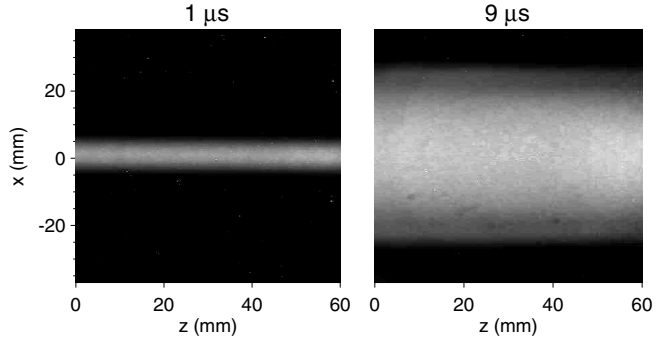


Figure 1: Fast shutter images of beam initiated discharge channels at 1 μs and at 9 μs after breakdown.

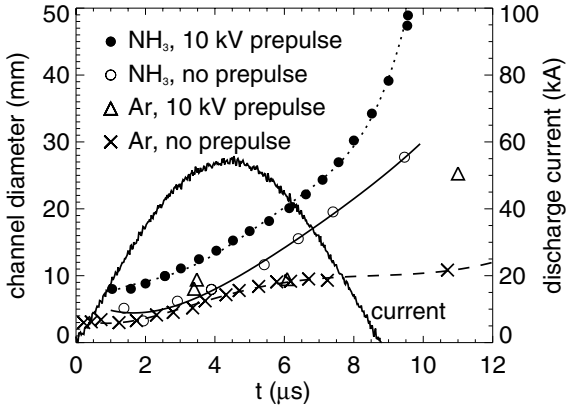


Figure 2: Channel-diameter as a function of time for discharges in ammonia and argon with and without prepulse.

The improved stability, the simple initiation mechanism and the possibility to create channels in any gas makes this scheme especially interesting for beam transport in heavy-ion fusion [4]. Discharges in gases like air, N_2, He, Kr and Xe have successfully been initiated in a later beam time.

This work is supported by the BMBF.

References

[1] C. Niemann et al., J. Appl. Phys. **91**(2), 617 (2002)
[2] A. Tauschwitz et al., GSI AR 2001-1 (2001)
[3] C.A. Frost et al., Appl. Phys. Lett. **41**(9), 813 (1982)
[4] A. Tauschwitz et al., Fus. Eng. Des. **32-33**, 493 (1996)

Determination of target line density

U. Geissler[2], N. Borisenko[3] E. Dewald[2], D.H.H. Hoffmann[1,2], K. Tsigutkin[4] O. Rosmej[1] J. Wieser[1]
[1]*GSI-Darmstadt,* [2]*TU-Darmstadt,* [3]*Lebedev Physical Institute, Moscow,* [4]*Weizmann Institute of Science, Rehovot*

For many experiments investigating the interaction between heavy ion beams and matter, such as determination of charge state distribution or inducing hydrodynamic reactions and shock waves, the precise knowledge of the target's line density distribution is of importance. As for bulk materials, such as plain metal solids, this value is well known, however for self prepared targets, such as rare gas crystals or silica aerogel foams, these parameters have to be defined for each individual sample and should be controlled during the fabrication process. Furthermore, such sensible targets often change their properties during the experiment, leading to misinterpretation of the results, obtained. Thus, a versatile setup has been installed to measure the target line density ρx of rare gas crystals and other target materials in an image-giving way, as shown in Fig 1. Integrated target line density is being determined by x-ray absorption, using Lambert-Beer's law $I = I_0 e^{-\kappa x}$, where κ represents the density (and wavelength) dependent absorption coefficient. A commercial 50kV x-ray source is used to illuminate the target with x-ray radiation. The transmitted radiation is converted into visible light by a phosphor screen, which in turn is being observed by an intensified camera, giving a two dimensional picture of the relative line density distribution of the target. Since the absorption, as well as the response function of the phosphor screen is wavelength dependent, an absolute measure of the line density cannot be obtained by a pure light intensity measurement. A pinhole aperture may thus additionally be installed, defining a single sight line at the target, on which the transmitted x-ray spectrum can be measured, e.g. by a SiLi x-ray detector. A phosphor brightness normalization along that sight line then can be performed.

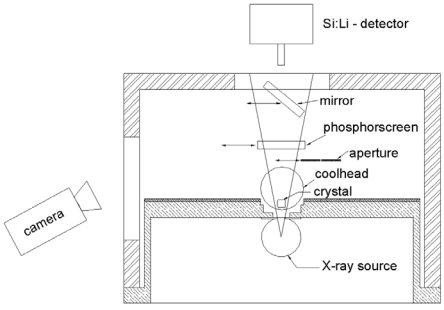


Figure 1: Schematic x-ray transmission setup. The target material (rare gas crystals, aerogel foam, etc.) is irradiated by x-rays. The transmitted x-ray intensity is being converted into visible light by a phosphor, which is being observed by a intensified camera.

As a first sample, a 0.1g/cm^3 silica aerogel target, used during an UNILAC beamtime in order to measure charge state distribution inside matter, was investigated. Before ion beam irradiation, this target was a 2.6mm thick, homogeneous block. During the ion beam experiment, caverns developed on both sides at the beam-target interaction area, reaching a depth of 0.4mm each, after about 10h of beam irradiation and a total fluence of 10^{14} ions/cm^2. Space resolved data, gained in that particular experiment, were severely deteriorated, since the important absolute position of the beam-target interaction surface has changed during data acquisition due to cavern formation. To avoid this effect in following experiments, the formation mechanism of the caverns had to be known. Essentially two possibilities were considered: Sputtering and/or sublimation of Si and O atoms from the target surface, which would result in a decreased line density by leaving the bulk material unchanged and just decreasing the thickness, or collapsing of the aerogel structure due to partially melting, which would keep the line density unchanged.

The result of the transmission measurement is shown in Fig 2. As can be seen, the x-ray absorption in the beam-target interaction region is *higher* than in the undisturbed target material, indicating a *higher* line density in spite of *reduced* thickness. A thin rim of reduced line density can be found at the edge of the interaction volume. Integrating over the entire region of enhanced and reduced absorption, the average mass covering was found to be constant. No sputtering thus has occurred and a partially melting and collapsing process took place, acquiring material from the surrounding into the beam heated volume. A reduced UNILAC beam pulse intensity during the following experiments could avoid this melting, improving significantly the accuracy of the data, obtained.

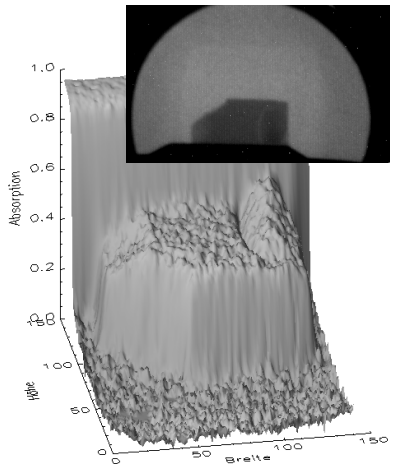


Figure 2: The x-ray intensity, transmitted through an aerogel target after ion beam irradiation is shown (insert). Higher absorption (increased line density) is seen at the interaction region.

work funded by BMBF and DIP

Multiple shockwaves driven by heavy ion beams in solid matter

E. Dewald[1], C. Constantin[2], C. Niemann[2], D.H.H. Hoffmann[1,2], J. Jacoby[1], T. Schlegel[2], S. Udrea[2], D. Varentsov[2] and A. Tauschwitz[2]
[1]GSI Darmstadt, [2]TU Darmstadt

At the high energy density experimental area (HHT), strongly coupled plasmas are created by the interaction of the SIS heavy ion beams with solid targets. Presently, the generated plasmas have densities close to the solid state, large volumes of several mm^3 and temperatures up to 1 eV. Besides experiments of direct matter heating by heavy ion beams, a complete study of the low entropy shock compression of solid matter driven by the ion beams was performed, with relevance for the equation of state of matter at low temperatures, astrophysics and others [1]. In these experiments layered metal-plexiglass targets were used [2], whereby the fine focused ion beam (FWHM < 0.5 mm) is fully stopped in different metal absorbents and the induced shocks are investigated in a plexiglass layer. The shock dynamics was studied time and space resolved by two-dimensional schlieren measurements performed simultaneously with a framing and a streak camera (Fig. 1).

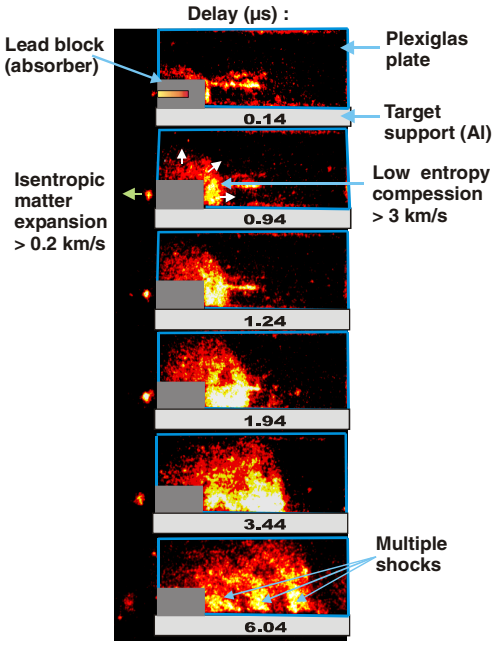


Fig.1 Two-dimensional schlieren multi-framing pictures of the weak shockwaves induced by an $^{197}Au^{65+}$ beam (300 MeV/u, 700 ns pulse).

The obtained pictures are mapped in density gradients induced in the transparent regions and besides the shockwave dynamics they show the isentropic expansion of the Pb target heated directly by the ion beam. Furthermore, the improved resolution and target design as compared to [2] allowed the measurement of the shock velocity variation along the plexiglass window (Fig.2). The highest shock velocity in plexiglass, was obtained for the Fe absorbent (4 km/s) and was considerably higher than the sound speed at room temperature (2.6 km/s). As expected, much lower shock velocities were obtained for the Pb absorbent for an unfocused ion beam (Fig. 2). The corresponding pressures in the shock are proportional to the measured velocities and were estimated for PMMA from empirical data [2] to values considerably higher than 14 kbar which corresponds to 3.4 km/s.

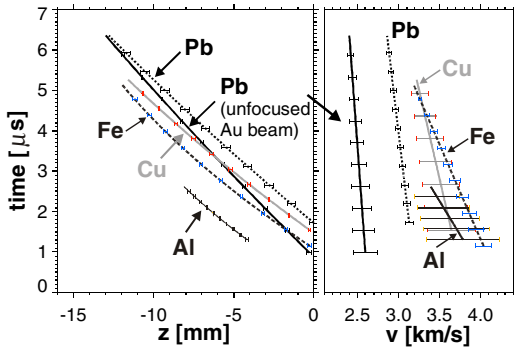


Fig.2 Axial shock expansion and the corresponding shock velocity in plexiglas for different absorbent materials.

Another interesting point is that the velocity decrease is the highest for Al and the lowest for Pb, showing that the radii of the spherical shock front (Fig.1) is larger e.g. for Pb than for Al. This can be explained by the fact that the shape of the shock front is determined by the hydrodynamics of the heated matter in the Bragg peak region, which is very pronounced for Pb and reduced for Al and Fe due to their high melting points or binding energy. The shock time history and density gradients were measured locally in plexiglass, along the ion beam axis, by laser deflection measurements, method which measures directly the deflection of a laser beam due to transversal refractive index (density) gradients (Fig. 3).

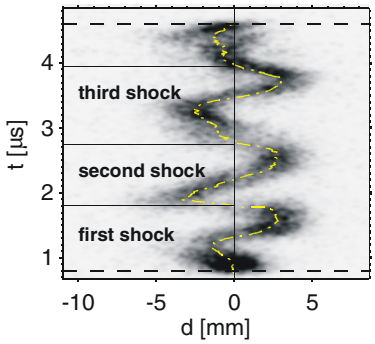


Fig.3 Typical streak picture obtained with laser deflection measurements for an Fe-Plexiglas-Al target [1].

As schlieren, this method showed that the shock frequency and strength depends on the absorber material. Along with schlieren and laser deflection, interferometric and pressure gauge measurements were employed to measure directly the induced densities and pressures. Metal–cryogenic crystal layered targets will be employed in the near future in similar experiments.
(*Supported by BMBF*)

References

[1] N.A. Tahir *et al.*: Phys. Rev. E, vol 16, no. 2, 1975-1980 (2000).
[2] C. Constantin *et al*, GSI-2001-4, 4 (2000).
[3] Bao-Ping Zhang, F. Mueller, High Temperatures-High Pressures, vol. 16, 475-480 (1984).

Radiography with protons generated by ultrashort high intensity lasers

A. Blažević[1], M. Roth[2], T.E. Cowan[3], J.C. Gauthier[4], P. Audebert[4], J. Fuchs[4], M. Hegelich[5], S. Karsch[5], M. Geißel[1], E. Brambrink[1], T. Schlegel[1]

[1] Technische Universität Darmstadt, Germany
[2] Gesellschaft für Schwerionenforschung mbH, Darmstadt, Germany
[3] General Atomics, San Diego, USA
[4] LULI, École Polytechnique, Palaiseau, France
[5] Max-Planck-Institut für Quantenoptik, Garching, Germany

The recent development of ultra-intense short-pulse lasers has opened a new field of investigation. Experiments, using laser pulses with intensities exceeding 10^{19} W/cm^2 have shown, that proton beams with very low emittance, high intensity (up to 10^{13} particles) and high energy (up to 50 MeV) can be produced by irradiating thin conductive foils with a smooth rear surface. The dominant acceleration process can be described within the TNSA (Target Normal Sheath Acceleration) model. Thereby the interaction of the laser pulse with the target front surface produces relativistic electrons with temperatures of several MeV, which are ponderomotivly pushed through the foil. Those electrons envelope the target foil and form an electron plasma sheath on the non-irradiated rear surface. The electric field, which reaches out a few μm can reach up to 10^{12} V/m and hence field ionize the atoms on the surface and accelerate them laminarly and normal to the surface. Due to their largest charge-to-mass ratio preferentially protons from contaminants on the surface are accelerated. The protons form a collimated beam with an emittance better then any conventional accelerator and a pulse duration of only a few picoseconds. These exceptional, high quality properties of the proton beams make them interesting for some applications, which are now performed with radio-frequency accelerator beams or x-rays, and open new fields of applications, where conventional techniques reach their limits. One such application is to radiograph objects by energy-loss imaging of transmitted protons. Because protons interact differently with matter than either x-rays or neutrons, such proton imaging can provide complementary information about a particular sample, with high temporal resolution.
To demonstrate the feasibility of the laser accelerated proton radiography applications first experiments were performed at the 100 TW laser at LULI, with pulses up to 30 J at 350 fs and a wavelength of 1.05 μm. Intensities of 5×10^{19} W/cm^2 were reached by focusing the beam to a spot size of 8 μm. To image objects we placed them about 3 cm behind the target, which was usually a 10 - 20 μm thick gold foil. Directly behind the objects we used a stack of radiochromic films. Due to the pronounced energy loss of the protons at the end of their range (Bragg-peak) different layers of the RCF allow the imaging of the object with different mass distributions. Fig. 1 shows the imaging of a 1 mm thick epoxy ring with engraved names of the collaborating institutes, 250 μm thick copper wires, a hollow cylinder with 300 μm walls of steel, four sheets of 100 μm thick Ti and a glass hemisphere of 900 μm diameter and 20 μm wall thickness. All details are clearly visible. The spatial resolution of the images was $\approx$ 20 μm, which is determined by the resolution of the RCF.

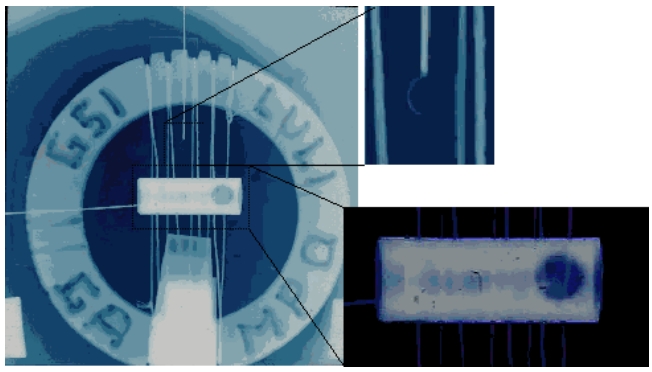


Figure 1: *Proton radiography of an epoxy ring with wires, hollow cylinder and glass hemispere*

A great advantage to x-ray imaging is the fact, that with proton radiography low-Z material can be analyzed even behind high-Z walls. To demonstrate this we imaged four stripes of 50 μm thick kapton foil behind a layer of 100 μm thick Tantalum. The image and a line scan is shown in Fig. 2. All four kapton stripes are clearly separated. The three peaks on the right in the line scan belong to copper wires.

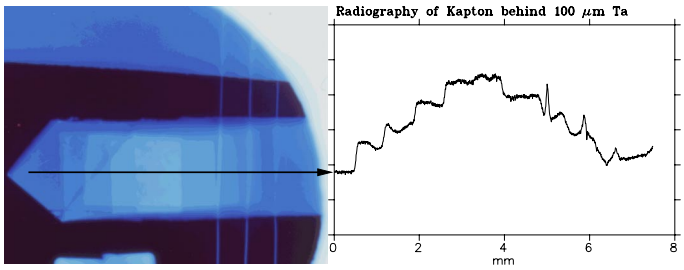


Figure 2: *Proton radiography of four 50 μm thick kapton foils behind 100 μm Ta.*

Hence this technique may become a new and promising tool for target diagnostic in the GSI future project, where a heavy ion beam heats a cylindrical target to compress a low-Z material in the center.

This work was supported by the EU Program No.: HPRI CT 1999-0052

Simulations of Hydrodynamic and Thermodynamic Response of Solid Targets Heated By Future SIS-100 Beam

N. A. Tahir[1], D. Varentsov[2], A. Shutov[3], P. Spiller[4], D. H. H. Hoffmann[2,4], J.Jacoby[4], J.Wieser[4]

[1]Uni. Frankfurt, [2]TU Darmstadt, [3]ICPR Chernogolovka, [4]GSI Darmstadt

The new 100 Tm magnetic rigidity synchrotron SIS-100 will be a powerful tool to induce very high-energy-density states in matter and then study the equation-of-state (EOS) properties of matter under such extreme conditions. According to the present design studies [1], the SIS-100 will generate a U^{28+} beam with a total number of 2×10^{12} particles with a particle energy range of 400 MeV/u to 2.7 GeV/u and this entire energy range will be useful to the plasma physics experiments. The particles will be delivered in a single bunch whose duration will depend on the particle energy. It has been estimated that beams consisting of 400 MeV/u and 2.7 GeV/u will have pulse durations of 90 ns and 20 ns respectively.

In this contribution we present numerical simulation results of thermodynamic and hydrodynamic response of solid as well as hollow lead cylinders that are irradiated with the future SIS-100 beam. These simulations have been carried out using a two-dimensional model, BIG-2 [2]. Different beam target geometries used in these calculations are shown in Fig.1 and we present these results in the following.

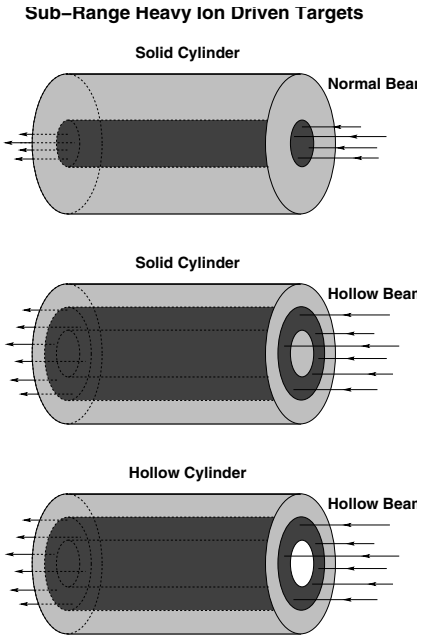


Figure 1: Different beam-target geometries considered

I: Solid lead cylinder and normal beam with circular focal spot

We consider a more conservative value for the beam intensity and assume a total number of 1.5×10^{12} particles of 2.7 GeV/u uranium that are delivered in a 20 ns long bunch. The range of 2.7 GeV/u uranium ions in lead is 5.95 cm. We assume a target which is 2.0 cm long and the energy deposition is still very uniform along the particle trajectory. The beam radius, r_b is another very important parameter as the specific energy deposition is inversely proportional to the square of r_b. We assume two values for r_b (FWHM of the Gaussian distribution), namely 0.5 mm and 1.0 mm. In Fig.2 we plot the specific energy deposition, E_s along the target radius at L = 1.0 cm and at t = 20 ns. It is seen that for r_b = 1.0 mm, E_s = 200 kJ/g while for r_b = 0.5 mm, E_s = 660 kJ/g instead of 800 kJ/g. This reduction in E_s is due to hydrodynamic expansion[3]. Using an r_b = 1.0 mm we achieve a maximum temperature, T_{max} of about 18 eV and a maximum pressure, P_{max} of 9.2 Mbar. For an r_b = 0.5 mm, on the other hand, we get a T_{max} of 30 eV and a P_{max} of 18 Mbar.

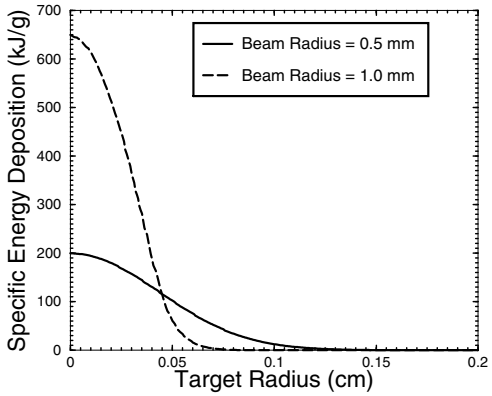


Figure 2: Specific energy deposition vs cylinder radius

II: Solid lead cylinder and hollow beam

This case corresponds to the second picture in Fig.1. The target is irradiated with a hollow beam which has an annular focal spot. A ring of hot material with very high pressure is created in the center of the target. The high pressure launches shock waves outwards and inwards along the cylinder radius. When the shock converges at the cylinder axis, a density of about 60 g/cm^3, a pressure of 35 Mbar and a temperature of about 11 eV is created in this region.

III: Hollow lead cylinder and hollow beam

This case is shown in the third picture of Fig.3. The inner cylinder radius is taken to be the same as the inner radius of the focal spot and is 0.5 mm. When the target material collapses at the cylinder axis, a density of 74 g/cm^3, a pressure of 124 Mbar and a temperature of 23 eV is created.

References

[1] P.Spiller, Private Communication.

[2] V.E.Fortov et al., Nucl. Sci. Eng. 123 (1996) 169.

[3] N.A.Tahir et al., Phys. Plasmas 8 (2001) 611.

Supported by the German ministry for education and science (BMBF)

Simulations of Two-Beam Irradiation of Cylindrical Targets at the Upgraded SIS-18

N. A. Tahir[1], D. Varentsov[2], A. Shutov[3], P. Spiller[4], D. H. H. Hoffmann[2,4], J.Jacoby[4], J.Wieser[4]
[1]Uni. Frankfurt, [2]TU Darmstadt, [3]ICPR Chernogolovka, [4]GSI Darmstadt

Previous numerical simulations have shown[1,2] that the future upgraded SIS-18 beam[3] will be capable of inducing extreme high-energy-density states in solid matter. Such samples of matter will be used to study the equation-of-state (EOS) properties of matter. However diagnosing these highly dense targets is a very difficult problem.

A new diagnostic method has been developed at GSI which uses the information on the energy loss of the projectile ions to determine the target density as a function of time [4]. However this method requires that the pulse is long, which will not be the case when the SIS-18 is fully upgraded because the pulse length will then be about 50 ns. To overcome this difficulty, it has been proposed [5] to accelerate two beams simultaneously, a main intense bunched beam of a heavy element that is responsible for target heating and a low intensity unbunched imaging beam of a lighter element. A typical combination for the upgraded SIS-18 is given in [5] and is presented below.

The main beam consists of 2.0×10^{11} particles of 200 MeV/u U^{28+} with a pulse length of 50 ns and a beam radius (FWHM of Gaussian) of 1.0 mm. The imaging beam consists of 10^6 particles of 216 MeV/u Ar^{5+} with a pulse length of 1.0 μs. In the following we present numerical simulation results using this combination of beams.

I: Solid Pb cylinder, U and Ar beams with circular focal spot

The cylinder length is 4.0 mm, the range of 200 MeV/u U ions in lead is 1.67 mm and that of 216 MeV/u Ar ions is 6.55 mm. The uranium ions are stopped in the target while the Ar ions emerge from the opposite face of the target with a reduced energy. In Fig.1 we plot energy of the Ar ions escaping along the cylinder axis as a function of time. It is seen that the energy of the escaping ions increases with time due to the decrease in the linear density along the axis.

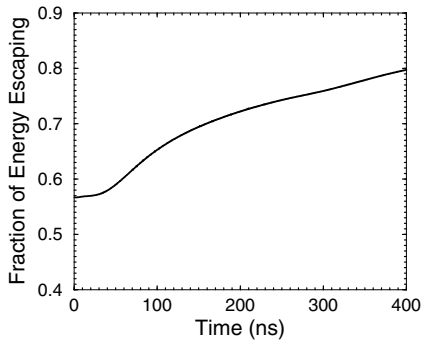


Figure 1: Energy of escaping Ar ions vs time (Case I)

II: Solid Pb cylinder, hollow U beam and circular Ar beam spot

The cylinder length in this case is 2.0 mm and the results are plotted in Fig.2. It is seen that initially about 80 % energy is carried out by the Ar ions, but as the shock converges at the axis and the linear density increases, energy loss also increases that leads to a decrease in the ion energy that escapes the target.

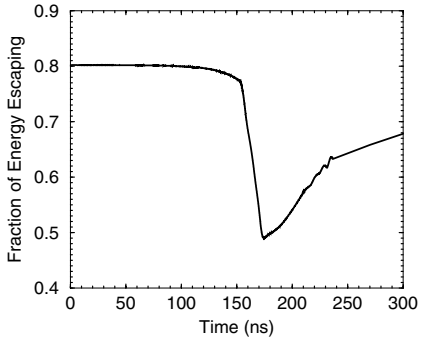


Figure 2: Same as in Fig.1, but Case II

III: Hollow Pb cylinder, hollow U beam and circular Ar beam

The target length in this case is 3.0 mm and the results are presented in Fig.3. It is seen that since the cylinder is hollow, initially there is no energy loss of Ar ions along the axis and 100 % of the energy escapes the target. However at t = 160 ns, the target collapses at the axis and due to the high density, a significant fraction of the ion energy is lost in the target.

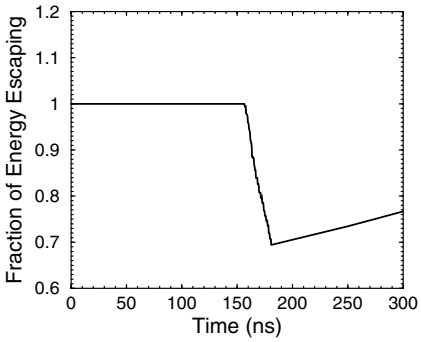


Figure 3: Same as in Fig.1, but case III

References

[1] N. A. Tahir, D. H. H. Hoffmann et al., Phys. Rev. E 61(2000) 1975.
[2] N. A. Tahir, D. H. H. Hoffmann et al., Phys. Rev. E 62(2000) 1224.
[3] R.W.Müller and P.Spiller, GSI Rep., GSI-96-07 (1998).
[4] D.Varentsov et al., Nucl. Inst. Meth. B174 (2001) 215.
[5] I.Hofmann et al., GSI Rep., GSI-2001-4 (2001) 29.

Supported by the German ministry for education and science (BMBF)

Target Design for Equation–of–State Measurements of Shock Compressed Matter with the Current SIS-18 Beam

A. Kozyreva[1], M. Basko[2], R. Bock[3], E. Dewald[3], D.H.H. Hoffmann[1,3], J. Jacoby,[3]
J. Meyer-ter-Vehn[2], Th. Schlegel[1], A. Shutov[4], P. Spiller[3], A. Tauschwitz[1], J. Wieser[3]

[1] *Technische Universität Darmstadt, Germany*

[2] *Max-Planck-Institut für Quantenoptik, Garching bei München, Germany*

[3] *Gesellschaft für Schwerionenforschung Darmstadt, Germany*

[4] *Institute of Problem of Chemical Physics, Chernogolovka, Russia*

Heavy ion beams deposit their energy in the target volume. The distribution of energy that is deposited by a single ion in a target is well known and defined by the Bragg function. The energy deposition of an ion beam in matter however depends strongly on the duration of the beam pulse due to hydrodynamic motion of the target material. The SIS-18 synchrotron at GSI Darmstadt is currently able to provide 5×10^9 U ions of 200 MeV/u delivered in a single pulse of 500 ns. A plasma lens at the HHT experimental area is used to focus the beam down to 0.5 mm (FWHM). Fig. 1a (top) shows the density distribution in solid Xe irradiated with such a beam. Numerical simulations were carried out with the 2D hydrodynamic code BIG–2 [1] using SESAME equation-of-state data. The dashed line shows the initial position of the Bragg peak. Due to the propagation of a radial shock during the deposition time the range of the ions in the target continually increases. This effect can be avoided with *a low energy beam*. The density distribution in Xe irradiated with a 40 MeV/u beam is shown in Fig. 1a (bottom). The Bragg peak location does not change and the shock wave has almost spherical shape. The shock wave induced by the ion beam becomes stronger, if a target material with *a low sound velocity* is used. In Fig. 1b we compare the pressure distribution in solid Xe which has a sound velocity of 1 km/s and in Al, with a sound velocity of 5.3 km/s. Significantly less hydrodynamic motion is induced in the case of Xe.

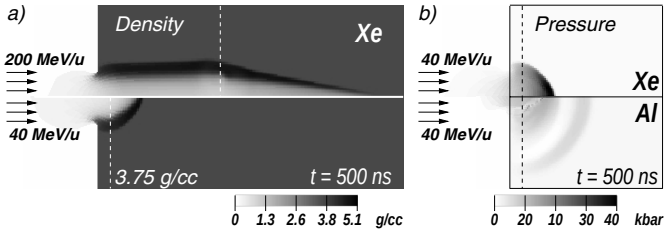


Figure 1: a) Density in solid Xe irradiated with 200 MeV/u U ions (top) and 40 MeV/u U ions (bottom), b) pressure in Xe (top) and Al (bottom).

Direct determination of the equation-of-state of shock compressed matter requires planar shock wave geometry. Evaluation of measurements in other geometries need hydrodynamic simulations, which depend on EOS data. A low diameter tube surrounded by a stiff shell can be used as a simple target to create a planar shock wave. Fig. 2 shows the pressure distribution for such a target that consists of a W shell which contains frozen Xe. Numerical simulations predict a pressure of 80 kbar, a density of 5.8 g/cm^3, and a temperature of about 700 K behind the planar shock

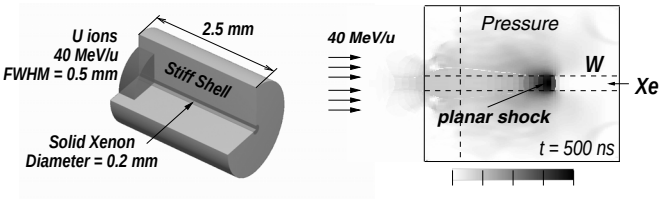


Figure 2: Pressure in a low diameter Xe tube surrounded by a W shell after irradiation with a low energy beam.

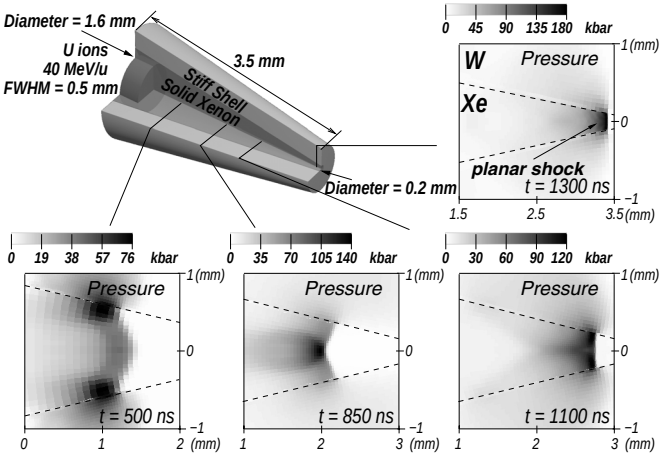


Figure 3: Pressure in a tapered tube, irradiated with 40 MeV/u U ions, at different times.

front. This target can be used for equation-of-state measurements with the present beam parameters.

An advanced target to generate a planar shock is shown in Fig. 3. It consists of a tapered tube made of W filled with solid Xe. The tube is irradiated from the wide side with a low energy beam. The entire diameter of the tube is such that the beam does not heat the W shell. A shock wave induced by the ion beam in Xe propagates to the narrow end of the tube and becomes planar due to multiple reflections at the interface to the W shell [2]. According to the simulations a pressure of 180 kbar, a density of 6.5 g/cm^3, and a temperature of 2800 K can be achieved in planar geometry using such target design. This target is a new promising design for equation-of-state measurements with present beam parameters.

References

[1] V.E. Fortov at al., Nucl. Sci. Eng. **123** (1996) 169.

[2] R. Courant, K.O. Friedrichs, Supersonic Flow and Shock Waves, N. Y., Springer-Verlag, 1976.

Supported by Bundesministerium für Bildung und Forschung and by Hessische Ministerin für Wissenschaft und Kunst (HWP–Programm)

Unique Capabilities of Intense Heavy Ion Beam As a Tool for EOS Studies

D.H.H. Hoffmann[1,2], V.E. Fortov[3], I.V. Lomonosov[3], N.A. Tahir[4], D. Varentsov[1]
[1]TU Darmstadt, [2]GSI Darmstadt, [3]IPCP Chernogolovka, [4]Uni. Frankfurt

Abstract. Intense heavy ion beams open new horizons in high-energy-density matter research. Due to the unique feature of energy deposition process of heavy ions in dense matter (volume character of heating) it is possible to generate high entropy states in matter without necessity of shock compression. Previously, such high entropy states could only be achieved by using most powerful shock wave generators like nuclear explosions or powerful lasers. We propose to use this novel technique of heavy ion heating and expansion (HI-HEX) to explore new fascinating regions of the phase diagram including liquid phase, evaporation region with the critical point and strongly coupled plasmas.

Equation of state (EOS) describes fundamental thermophysical properties of matter. This information can only be obtained by using sophisticated theoretical models or from experiments [1]. The EOS is of considerable interest for basic research and has numerous important applications [2]. States of matter characterized by high-energy-density occupy a broad region of the phase diagram, for example, hot compressed matter, strongly coupled plasmas, hot expanded liquid and quasi-ideal plasmas. Our knowledge about these states is very limited, because theoretical modeling is extremely complicated and experiments are very difficult to perform.

The main difficulty in developing a theoretical EOS model in this region is the necessity to take into account correctly the strong collective inter-particle interactions in disordered media, which meet a special difficulty in a region occupied by dense disordered non-ideal plasmas. It is therefore very important to have more experimental data in this region. The possibilities of various experimental techniques are shown in Fig. 1.

The most significant information so far has been obtained using shock wave methods [3]. Due to the shock, material is compressed and irreversibly heated, leading to high values of pressure and entropy. Using the shock wave compression method, only a narrow region of the principle and porous Hugoniots have been investigated (see Fig. 1). Pressure range of up to 10 Mbar [3] has been investigated using high explosive generators of shock waves. Much higher pressures in Gbar range have been achieved in underground nuclear explosion experiments [4]. Progress in powerful lasers allows one to access the Gbar region as well [5].

Following the ideas of Zeldovich [3], investigation of shock adiabats of porous samples extends investigated region of the phase diagram to lower density and higher entropy in comparison to the principle Hugoniot. High entropy states along release isentropes, originating from shocked material, have also been measured in few experiments. It is also shown in Fig. 1 that the states of liquid metal near the critical point can be accessed by isobaric

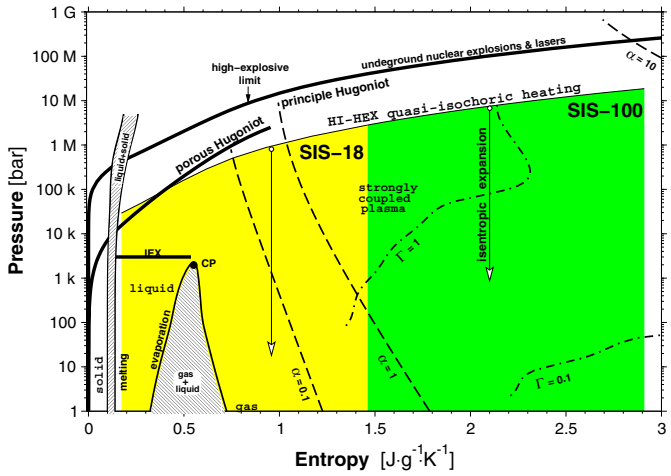


Figure 1: Pressure-entropy phase diagram for lead. The principle and porous Hugoniots (shock wave compression) and isobaric expansion (IEX) are shown along with the parameter space which will be accessible with HI-HEX technique. The physical characteristics such as melting and evaporation curves, the critical point, isolines of ionization degree (α) and non-ideality parameter (Γ) are also shown.

expansion technique (exploding wires) [6]. It is to be noted that for most of the metals the region of the phase diagram below the principle Hugoniot has never been experimentally investigated.

We propose to generate high entropy states in matter using quasi-isochoric heating by intense heavy ion beam. These states could be studied during the heating and expansion phases. Due to this intrinsic feature of volume heating by heavy ions, in the proposed HI-HEX technique, these exotic high entropy states can be generated *without any shocks.*

In such an experiment the heated material would expand, passing through different states. For example if we start from solid density a metal would be heated forming a hot liquid characterized by a disordered arrangement of ions and degenerate electrons. It will then expand to a quasi-nonideal Boltzmann plasma and a rarefied vapor. Upon expansion of the system the degree of degeneracy of the electronic subsystem is decreased and a marked rearrangement of the energy spectrum of atoms and ions occurs, and a partial recombination of the dense plasma takes place. In the disordered electron system a metal-to-insulator transition takes place and a non-ideal (with respect to different forms of inter-particle interactions) plasma is formed in the vicinity of the liquid-vapor equilibrium curve and the critical point. When the isentropes enter the two-phase liquid-vapor region evaporation occurs; on the gas side condensation occurs. If on the other hand, we induce a higher entropy in the sample, more ex-

otic states of strongly coupled plasma will be generated from the very beginning. The states on the expansion adiabat of this system will be characterized by very interesting plasma effects, such as, a significant variation of degree of ionization (α) and plasma non-ideality parameter (Γ) shown in Fig. 1. The range of thermodynamic parameters that can be covered in a single HI-HEX experiment is extremely wide: six orders of magnitude in pressure and four orders of magnitude in density.

The GSI-Darmstadt is a unique laboratory worldwide which has a heavy ion synchrotron SIS-18 that delivers intense beams of heavy ions. At present this facility can provide about $\mathbf{10^{10}}$ uranium particles with energy of a few hundred MeV/u. The pulse duration is few hundred nanosecond. It is expected that in the near future the beam intensity will increase to $\mathbf{2 \times 10^{11}}$ particles while the pulse duration will be reduced to less than $\mathbf{100}\,\boldsymbol{ns}$.

Numerical simulations have shown [7] that a beam with these parameters will deposit a specific energy of 50–100 kJ/g in solid lead. GSI has also plans to build a new synchrotron ring SIS-100 that will deliver an intense uranium beam having $\mathbf{10^{12}}$ particles with energy range of 400–2700 MeV/u. This beam will deposit a specific energy of at least 350 kJ/g in lead [8].

It is seen from Fig. 1 that use of these two heavy ion machines will enable us to investigate regions of hot liquid metal, strongly coupled plasmas, evaporation region with the critical point and quasi-ideal plasmas. One should note that these exotic high entropy states could only be accessed by underground nuclear explosions. However these regions have not been investigated before. The proposed HI-HEX method therefore opens a gate to "Terra Incognita" of the phase diagram.

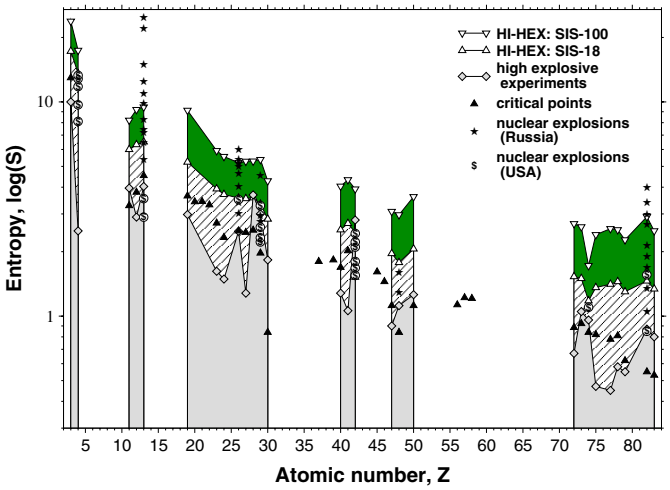


Figure 2: High entropy states obtained by different experimental methods for various metals. The states that can be investigated by HI-HEX technique with SIS-18 and SIS-100 facilities are also shown.

In our method the thermophysical parameters like temperature, density, expansion velocity and electrical conductivity will be measured during the heating phase and the following adiabatic expansion with time resolution. Together with numerical modeling this information will be sufficient to determine EOS properties of a material under investigation.

In Fig. 2 we show the high entropy states for various metals that can be achieved using the HI-HEX method compared to other existing techniques. We used the available data obtained in shock compression experiments performed with high explosives and underground nuclear explosions to calculate these entropy states. Evaluated critical points [2, 9] indicating the typical entropy region of strongly coupled plasmas are also shown in Fig. 2. Estimated regions of isochoric heating in future HI-HEX experiments using SIS-18 and SIS-100 are plotted as well.

Our calculations show that using the HI-HEX technique with the existing SIS-18 machine one can access the region of the phase diagram that previously was accessible only by powerful nuclear explosions. Therefore the HI-HEX method is a unique and very promising tool for generation and investigation of exotic states of high energy density matter.

Acknowledgments We wish to thank V. Gryaznov for providing calculations for lead plasma. We also would like to thank V. Mintsev, M. Kulish and members of the GSI plasma physics group for many fruitful discussions.

References

[1] A.V. Bushman and V.E. Fortov. Sov. Phys. Usp., **26** (1983) 465.

[2] V.E. Fortov, I.T. Yakubov, *Physics of Nonideal Plasmas,* London, World. Sci. Publ. Co. (1999).

[3] Ya.B. Zeldovich and Yu.P. Raizer, *Physics of Shock Waves and High-Temperature Hydrodynamic Phenomena,* Academic Press, New York (1966, 1967).

[4] A.S. Vladimirov, N.P. Voloshin, V.N. Nogin, A.V. Petrovtsev, V.A. Simonenko, Sov. Phys. - JETP Lett. **39(2)**(1984) 85.

[5] R. Cauble, D.W. Phillion, T.J. Hoover, N.C. Holmes, J.D. Kilkenny, R.W. Lee, Phys. Rev. Lett. 1993. **70** (1993) 2102.

[6] G.R. Gathers, Rep. Progr. Phys., **49** (1986) 341.

[7] N.A. Tahir, D.H.H. Hoffmann et al., Phys. Rev. **E61** (2000) 1975.

[8] N.A. Tahir, et al., Phys. of Plasmas **8** (2001) 611.

[9] V.E. Fortov, K.V. Khishchenko, P.R. Levashov, I.V. Lomonosov, Nucl. Instr. Meth. **A415** (1998) 604.

Thermal Behaviour of Nanostructured ZrO_2 after Heavy Ion Irradiation

W. Berky and A.G. Balogh, Darmstadt University of Technology, Institute of Materials Research, Thin Films Division, Petersenstraße 23, D-64287 Darmstadt, Germany

As was shown in the past by XRD, TEM and RBS measurements, heavy ion irradiation of nanocrystalline ZrO_2 samples using 4 MeV Kr^+ ions causes the formation of a tetragonal zirconia phase that is stable at room temperature [1]. This phase is employed in solid oxide fuel cells and oxygen sensors, but usually has to be stabilized by addition of a second phase, e.g. Y_2O_3, which is not necessary when using the process mentioned above. To investigate the thermal stability of tetragonal zirconia, a new series of zirconia samples has been prepared by means of the inert gas condensation technique (IGC) and sintered afterwards at temperatures of 900 or 1000 °C using forces of 12 up to 40 kN. This procedure resulted in a density higher than 5 g/cm^2 corresponding to about 90% of the theoretical value.

The samples were then irradiated by 4 MeV Kr^+ ions with fluences from $2x10^{15}$/cm^2 to $2x10^{16}$/cm^2 and investigated by means of x-ray diffraction (XRD). The formation of the tetragonal ZrO_2 phase, which was observed as well as the (common) monoclinic phase could be reproduced. The samples were heated at temperature steps of 100 or 200 °C up to 1300 °C and studied by means of XRD after each step.

Apart from the thermal stability of the tetragonal phase we were also interested in the development of the grain sizes of both phases depending on the ionic fluence [2]. Samples that had been irradiated with a fluence of $1x10^{16}$/cm^2 or above showed a thermal stability of the tetragonal phase up to the sintering temperature (see Fig. 1), whereas samples irradiated with lower fluences showed only a residual amount of this phase of about 5 vol. % at temperatures of 400-500 °C. The same holds for samples irradiated with higher fluences above the sintering temperature.

No significant change in the grain size of both phases could be observed. The grain size of the monoclinic ZrO_2 phase was approximately 60 nm, and that of the tetragonal phase about 20 nm (see Fig. 2). The value of the sintering temperature and the compaction forces during the sintering process did not influence the thermal behaviour of both zirconia phases significantly. Apart from the fact that depending on the ionic fluence of the samples a thermal stability of the tetragonal phase could be achieved, an ageing stability of the tetragonal ZrO_2 phase was also observed within a time period of several years.

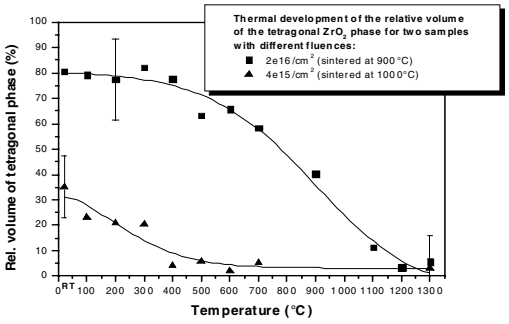


Fig. 1: Thermal development of the tetragonal phase for two different samples

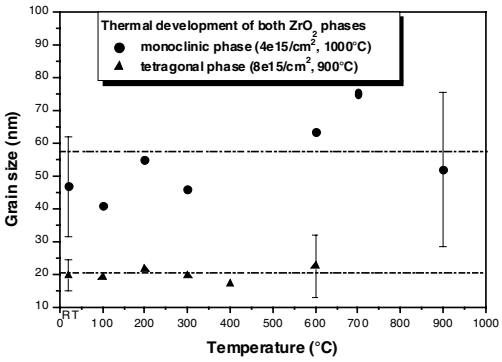


Fig. 2: Thermal development of the grain size of both ZrO_2 phases

References

[1] M. Rose, G. Gorzowski, G. Miehe, A.G. Balogh, H. Hahn, *Phase stability of nanostructured materials under heavy ion irradiation,* Nanostructured Materials 6 (1995) 731-734.

[2] W. Berky, G. Bejarano, S.S. Bhattacharya, M. Müller, A.G. Balogh, *Thermal behaviour of nanostructured ZrO_2 after heavy ion irradiation*, Nucl. Instr. and Meth. B, submitted for publication.

Defect creation by energetic heavy ions in different fluoride crystals

A.S. El-Said, C. Müller, R. Neumann, K.Schwartz, C. Trautmann

GSI Darmstadt

To better understand the peculiarities of damage creation in ionic crystals under heavy ion irradiation, various experimental techniques (scanning force microscopy (SFM), optical spectroscopy, and profilometry) were applied. As samples we used single crystals of different fluorides LiF (100), MgF_2 (001), CaF_2 (111), BaF_2 (111), and LaF_3 (random). The irradiations were performed with Ne (1.4 MeV/u) and with Ni (9.3 MeV/u), Zn (1.9 MeV/u), Xe (4.1) MeV/u), and U (2.0, 5.8 MeV/u) ions at the HLI and UNILAC, respectively. The energy, stopping power, and range of the ions were determined with the TRIM 92 code.

The surface of the irradiated crystals was investigated with a homebuilt scanning force microscope operated in contact mode and at loading forces around 10 nN. Topographical and lateral-force images were recorded simultaneously. As examples, some SFM images are shown in Fig.1. For all crystals, we find clear evidence that (1) the ions produce circular hillocks protruding from the surface and (2) the hillocks exhibit a different friction than the undamaged area. Depending on the ion species, the diameter and the height of the hillocks are around 15-30 nm and 1-2.5 nm, respectively.

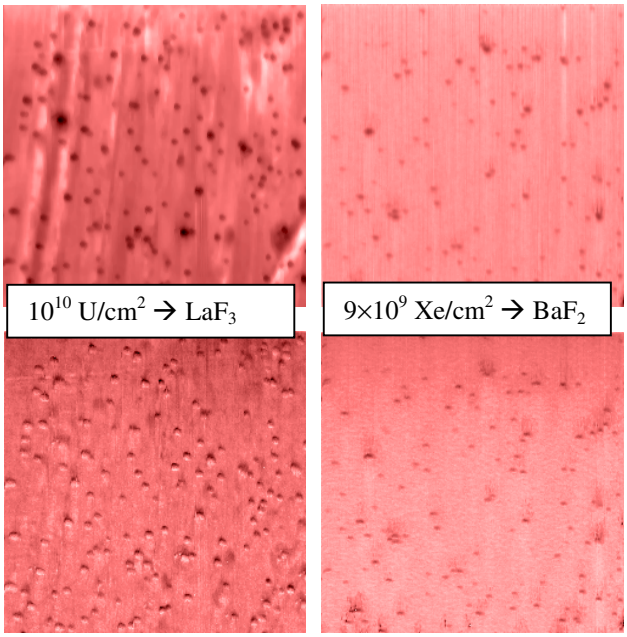


Fig. 1. Topographic (top) and lateral-force (bottom) SFM images (1μm × 1μm). Left: LaF_3 irradiated with U (2.0 MeV/u). Right: BaF_2 irradiated with Xe (4.1 MeV/u)

The creation of electronic defects such as F-centers (electron on anion vacancy), F_2-centers, or their aggregates (e.g., F_n-centers, colloids) was studied by UV-absorption spectroscopy in the spectral range from 200-900 nm. As shown in Fig. 2, the spectrum of LiF and MgF_2 is dominated by the bands of single defects, namely F- and F_2-centers (in the tetragonal lattice of MgF_2 there exist two different F_2-centers (a) and (b) corresponding to the symmetry groups D_{2h} and C_{2h}, respectively). Note that the number of F-centers is significantly larger in LiF than in MgF_2 although the applied ion fluence is much smaller. In the case of CaF_2 and BaF_2, the spectrum shows a broad absorption region ascribed to more complex aggregate centers such as metallic colloids. Finally, there is LaF_3, which does not show any specific absorption indicating that no color centers are created even at largest energy losses as for U ions.

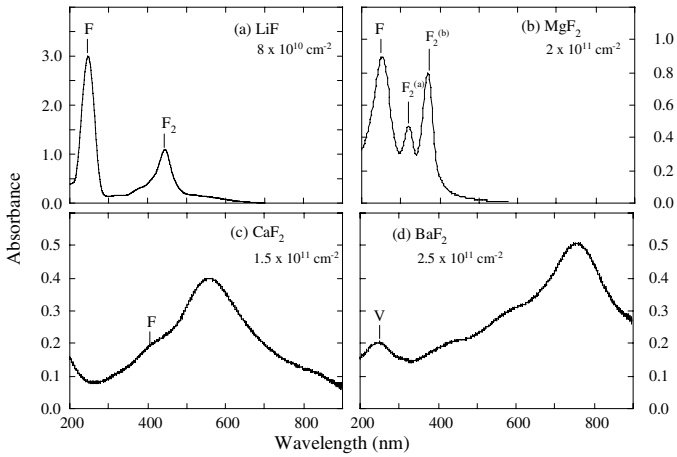


Fig. 2. UV-absorption spectra of various fluoride crystals.

Under ion irradiation, all crystals exhibited some more or less pronounced volume increase. The out-of-plane swelling was quantitatively analyzed with a profilometer (Dektak 8000) where a diamond-tipped stylus scans over the border line between an irradiated and a virgin sample area. As shown earlier [1], swelling increases linearly in the initial stage and then saturates at high fluences. The effect increases for projectiles with larger ranges and energy losses. The initial slope and the saturation level strongly depend on the crystal type (Fig. 3). The largest effects are observed for LiF. Surprisingly enough, also LaF_3 exhibits rather strong swelling although there are no point defects or defect aggregates created.

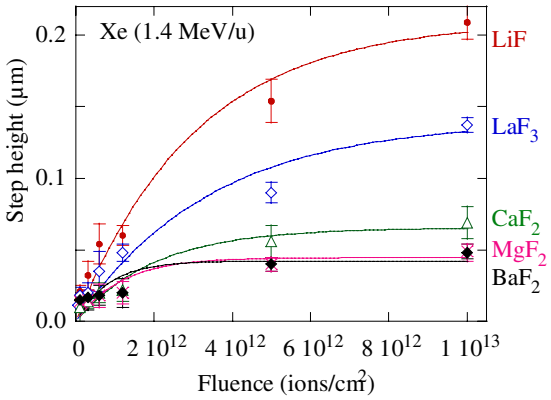


Fig. 3 Step height as a function of ion fluence for various crystals.

[1] C. Trautmann, M. Toulemonde, K. Schwartz, J.M. Costantini, A. Müller, Nucl Instr. Meth. B 164–165 (2000) 365.

CRITICAL ANALYSIS OF ION TRACK MICROGRAPHS RECORDED BY SCANNING FORCE MICROSCOPY

C. Müller, M. Lang, K.O.Voss, R. Neumann, GSI

Scanning force microscopy (SFM) has been used to characterize heavy-ion induced damage in many kinds of solids (for numerous references see e.g. [1]). The importance of quantitative information on shapes and dimensions of damage structures such as craters and hillocks gave rise to critically analyze the interaction between SFM probe tip and sample in order to recognize and take into account systematic imaging errors, originating especially from the finite size of the tip [2].

Our study is based on the observation that a SFM micrograph is not an objective image of the sample but always contains also features of the tip. We generalized this experience by assuming that scanning the sample with the tip is equivalent to scanning the tip with the sample. This idea was converted into a computer code whose basic operation principle is displayed in Fig. 1.

The first ingredient is the *model* of an object, called a *calibration standard*, whose geometrical structure and quantitative measures are assumed to be known precisely from some independent imaging process (e.g. from high-resolution scanning electron microscopy). Secondly, the code uses a *SFM image* of this standard, recorded with an individual tip. From a comparison of the model and the image of the standard, form and size of the tip are extracted (*model of probe tip*). With this information, a *SFM sample image* recorded with this tip can now be corrected (*corrected sample image*). A simulated reimaging of the corrected sample image allows an efficiency check of the code by comparing this *"reimaged" sample micrograph* with the initial sample image, which results in the residual *difference image*. During this simulation, the contacts between tip and sample and their positions are registered. At those positions where multiple contacts ocurred during the initial imaging, one obtains also multiple contacts in the simulated reimaging (*visualization of multiple contacts*).

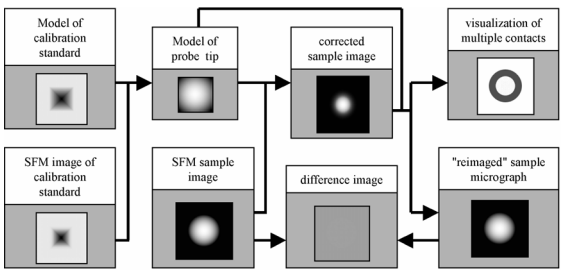


Fig. 1. Overview of the processes (flow chart) performed by our code.

The processes outlined in Fig. 1 were tested with artificially generated images of various samples and tips, as illustrated in Fig. 2. The pyramid (base 25x25 nm², height 20 nm) in Fig. 2a, representing a sample, and an inverse pyramid (base 100x100 nm^2, depth 70 nm) indicated in Fig. 1, serving as a standard, were imaged with a hemispherical tip (curvature radius 20 nm). Imaging Fig. 2a provided Fig. 2b. Feeding the exact model of the inverse pyramid, which now functioned as tip, and its image into the code reconstructed the tip quantitatively. Subsequent correction of Fig. 2b by means of the reconstructed tip resulted in Fig. 2c. The sharp peak of the pyramid is reproduced perfectly, only the edges along the base lines, where multiple contacts occurred, remain rounded. Imaging Fig. 2c once again with the reconstructed tip leads to Fig. 2d.

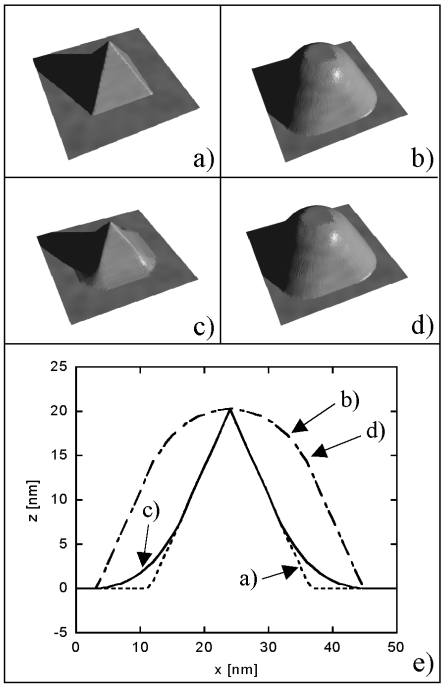


Fig. 2. Simulation of SFM imaging. (a) Sample: pyramid; (b) image of a; (c) corrected image of b; (d) reimaging of c; (e) vertical cuts of a-d.

References

[1] R. Neumann, Nucl. Instr. and Meth. B 151 (1999) 42.

[2] C. Müller, *Untersuchung schwerioneninduzierter Defekte an der Oberfläche von Lithiumfluorid mittels Rasterkraftmikroskopie*, Diploma Thesis, University of Heidelberg, 1999.

Electronic Excitation Effect in Ion-Irradiated $EuBa_2Cu_3O_y$

N. Ishikawa[a], A. Iwase[a], Y. Chimi[a], O. Michikami[b], T. Hashimoto[b], T. Kambara[c], C. Müller[d], R. Neumann[d]
[a]Japan Atomic Energy Research Institute(JAERI), Tokai -mura, Ibaraki 319-1195, Japan
[b]Iwate University, Morioka, Iwate 020-0066, Japan
[c]The Institute of Physical and Chemical Research(RIKEN), Wako, Saitama 351-0198, Japan
[d] Gesellschaft für Schwerionenforschung (GSI), Planckstrasse 1, D-64291 Darmstadt, Germany

In a lot of oxide materials, when irradiated with high-energy heavy ions, continuous linear defects are produced along the ion paths. The defect production is attributed to the high-density electronic excitation. The electronic stopping power, S_e, has been considered as a parameter that determines the electronic excitation effects [1][2][3]. However, in some ion-irradiated oxide materials such as $Y_3Fe_5O_{12}$, although the electronic stopping power is the same, larger electronic excitation effects have been found for irradiation with slower ions ($v \leq 2.6x10^9$ cm/s) than with faster ions [4]. This velocity dependence has been often called "velocity effect". The electronic stopping power can be divided into two parts: the energy that is carried as the kinetic energy of secondary electrons and the energy that is stored as the electrostatic energy of target atoms ionized by passing ions. It is expected that a careful investigation of the velocity effect gives us a clue to clarify which part of the energy transfer is responsible for the atomic displacements. In this study, the velocity effect is systematically investigated.

Thin films of oxide superconductors $EuBa_2Cu_3O_y$ with 300 nm thickness were irradiated at room temperature. Irradiation was performed with the following ions: 90-200 MeV ^{35}Cl - ^{197}Au ions from the tandem accelerator at JAERI, 3.5 GeV ^{136}Xe and 3.8 GeV ^{181}Ta ions from the ring cyclotron at RIKEN, and 1.51 GeV ^{132}Xe and 2.71 GeV ^{238}U from the UNILAC accelerator at GSI. An X-ray (Cu Kα) diffraction pattern was measured to estimate the change in c-axis lattice parameter as a function of ion fluence.

A linear increase is observed for all the irradiations. The slope of the increase represents the irradiation effect per unit ion fluence. It is already known that electronic excitation rather than elastic displacements dominates the irradiation effect in this ion mass and energy regime [5]. In Fig.1, we find that for the irradiation with faster ions ($v \geq 2.6x10^9$ cm/s) the data points scale with the 4th power of S_e, whereas for $v \leq 1.7x10^9$ cm/s they deviate from this scaling line. Since S_e is merely a line density of energy transferred from incident ions to the electron system, there have been trials to explain the velocity effect by taking account of the radial distribution of energy carried by secondary electrons [6][7]. But they cannot explain the present result, which shows the absence of the velocity effect in the high ion-velocity region. Therefore, the thermal spike model that is based on the radial energy distribution is ruled out for explaining the electronic excitation effect in ion-irradiated oxide superconductors.

A practical scaling parameter to explain the present result is the primary ionization rate [8][9], dJ/dx, where J is the number of atoms primarily ionized by an incident ion, and x is the path length of this ion. The electronic excitation effect is scaled with dJ/dx over all ion-velocity regions. Since the primary ionization rate is a number density of ionized atoms, we conclude that the energy stored as electrostatic energy is the origin of electronic excitation effects in the ion-irradiated superconductors.

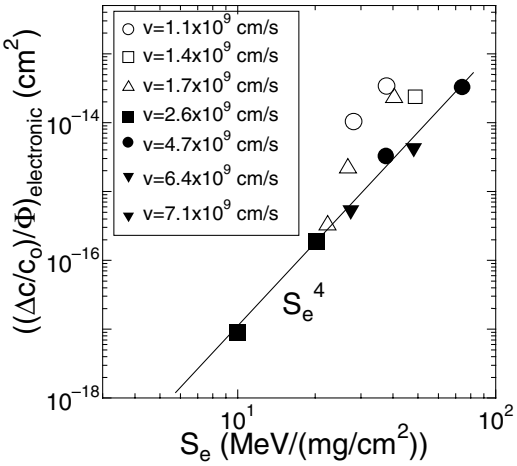


Figure 1. Contribution of the electronic excitation to elongation of c-axis lattice parameter per unit fluence plotted against S_e. Ion-velocities are listed in the figure. $\Delta c/c_o$ is the elongation of the c-axis lattice parameter normalized by the c-axis lattice parameter for the unirradiated sample, and Φ the ion-fluence.

References

[1] B. Hensel, B. Roas, S. Henke, R. Hopfengärtner, M. Lippert, J. P. Ströbel, M. Vildić and G. Saemann-Ischenko, Phys. Rev. B 42 (1990) 4135.

[2] V. Hardy, D. Groult, M. Hervieu, J. Provost, B. Raveau and S Bouffard, Nucl. Instrum. Methods B 54 (1991) 472.

[3] Y. Zhu, Z.X. Cai, R.C. Budhani, M. Suenaga and D.O. Welch, Phys. Rev. B 48 (1993) 6436.

[4] A. Meftah, F. Brisard, J.M. Costantini, M. Hage-Ali, J.P. Stoquert, F. Studer and M. Toulemonde, Phys. Rev. B 48 (1993) 920.

[5] N. Ishikawa, Y. Chimi, A. Iwase, H. Maeta, K. Tsuru, O. Michikami, T. Kambara, T. Mitamura, Y. Awaya and M.Terasawa, Nucl. Instrum. Methods B 135 (1998) 184.

[6]]M. Toulemonde, C. Dufour and E. Paumier, Phys. Rev. B 46 (1992) 14362.

[7] Z.G. Wang, Ch.Dufour, B. Cabeau, J. Dural, G. Fuchs, E. Paumier, F. Pawlak and M. Toulemonde, Nucl. Instrum. Methods B 107 (1996) 175.

[8] H.A. Bethe, Ann. Phys. 5 (1930) 325.

[9] R.L. Fleischer, P.B. Price, R.M. Walker and E.L. Hubbard, Phys. Rev. 156 (1967) 353.

Scanning force microscopy of natural and heavy ion induced damage in phlogopite

[1]Lang, M., [2]Glasmacher, U.A., [1]Neumann, R., [2]Wagner, G.A.
[1]Gesellschaft für Schwerionenforschung (GSI), Planckstr. 1, D-64291 Darmstadt, Germany,
[2]Forschungsstelle Archäometrie der Heidelberger Akademie der Wissenschaften am Max-Planck-Institut für Kernphysik, Postfach 103980, D-69029 Heidelberg, Germany,

A new geological dating technique uses alpha-recoil tracks (ART), created by natural α-decay of U, Th, and their daughter products, to determine the formation age of Quaternary volcanic rocks (< 10^6 a). Visualization of etched ART by scanning force microscopy (SFM) enables the access to track densities beyond 10^8 cm^{-2} and thus the extension of the ART technique to an age range > 10^6 a. To simulate natural radiation damage, samples of phlogopite, originating from Quaternary and Tertiary volcanic rocks of the Eifel (Germany) and the Kerguelen Islands (Indian Ocean) were irradiated with U, Ni (11.4 MeV/u), Xe, Cr, and Ne (1.4 MeV/u) ions at GSI, and with Bi (200 keV) ions at JAERI (Takasaki, Japan) [1].

When cleaving natural phlogopite, latent ART near to the cleavage plane form small hillocks imageable by SFM [2]. There occurs also a second kind of hillocks, subsequently called H_N (N denoting 'natural'). Not observable with SFM 8 h after cleaving, the H_N were found when imaging again after 21 h (see Fig. 1). The areal density increase after cleaving can be described by a growth curve not saturating even after 147 h. Also the mean hillock diameter grew with time. The H_N whose origin could not be clarified yet, always appear, and therefore latent ART cannot be used for dating.

To better understand these findings, samples were first annealed at 500 °C for 3.5 h, secondly irradiated and then studied with SFM. A further type of hillocks (denoted by H_T) was found [3], which can be attributed to ion tracks. These hillocks were observed without time delay after irradiation with U and Xe, with areal density about equal to the fluence for U ions, and about 30 % for Xe ions. In the case of Ne, Ni, and Cr ions, no H_T were observed. Within the time period indicated above, the H_N always appeared also on the annealed and irradiated samples. Remarkably, H_N do not transform into etch pits, and thus ART and ion tracks can be separated from them by etching. It is interesting to note that muscovite (white mica) exhibits no H_N.

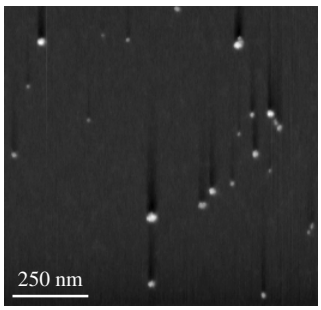


Fig. 1. SFM image of non-irradiated phlogopite 21 h after cleaving. Hillocks appear on an initially flat area.

Hexagonal etch pits are typical of U, Xe, and Cr ion tracks, while the pits of Ni, Ne, and Bi ion tracks are triangular (see Fig. 2). After etching for 900 s with 0.4 % HF, the pits show similar depths for U and Xe, whereas the depths scatter and shrink with decreasing electronic energy loss, *dE/dx*, for Cr, Ni, and Ne. This can be explained by a transition from a continuous to a discontinuous track with decreasing *dE/dx*. The etching rate v_H (parallel to the cleavage plane) depends on the chemical composition of the phlogopite. The etching rate v_T (along the track) becomes greater with increasing *dE/dx* (see Fig. 3) [4].

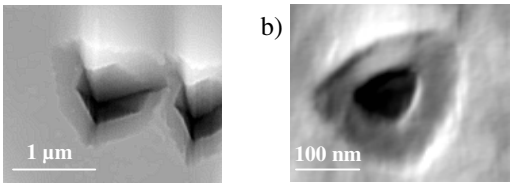


Fig. 2. SFM image of irradiated phlogopite samples after etching with HF. The pits are hexagonal for U (a) and triangular for Bi (b).

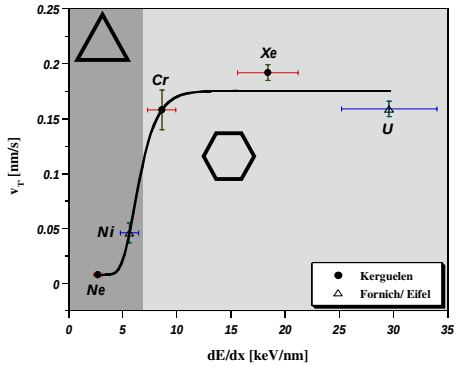


Fig. 3. Etch rate v_T as a function of the energy loss in phlogopite after etching with HF.

[1] Lang, M., *Rasterkraftmikroskopie an natürlichen und Ionen-induzierten Strahlenschäden in Phlogopit*. Diploma thesis, University of Heidelberg, 2001.

[2] von Grabczewski, N., *Untersuchung von Alpha-Rückstoß-Spuren in Biotit mittels Rasterkraft-mikroskopie*. Diploma thesis, University of Heidelberg, 2000.

[3] Lang, M., Glasmacher, U.A., Moine, B., Müller, C., Neumann, R., Wagner, G.A., *Heavy-ion induced defects in phlogopite imaged by scanning force microscopy*. Surface and Coatings Technology, spec. vol., Elsevier, Amsterdam, accepted for publication.

[4] Lang, M., Glasmacher, U.A., Moine, B., Müller, C., Neumann, R., Wagner, G.A., *Artificial ion tracks in volcanic dark mica simulating natural radiation damage: A scanning force microscopy study*. Nucl. Instr. and Meth. B, in press.

Acknowledgment. The authors thank Dr. T. Kume (JAERI, Takasaki, Japan) for irradiation with Bi ions.

Voltage-gated nanopores analogous to biochannels

Zuzanna Siwy [1,2], Yuchun Gu[3], Hilmar A. Spohr[3], Dagmar Baur[2], Alexander Wolf-Reber[2], Reimar Spohr[2], Pavel Apel[4], and Yuri E. Korchev[3]
[1] Silesian University of Technology, Strzody 9, 44-100 Gliwice, Poland
[2] Gesellschaft für Schwerionenforschung (GSI), Planckstr.1, D-64291 Darmstadt, Germany
[3] Imperial College of Science, Technology and Medicine, London, U.K.
[4]Flerov Laboratory of Nuclear Reactions, JINR, 141980 Dubna, Russia

Voltage gating is a well-known phenomenon in biological channels. It controls ion exchange across the otherwise impermeable cell membrane [1] [2]. We have designed a synthetic asymmetric nanopore [3] behaving analogous to a biochannel. It has a nonlinear current-voltage characteristic, rectifying the ion current. Ion currents through the pore show voltage-dependent fluctuations and even bistability, whose kinetics are similar as in voltage-gated biological ion channels.

A single conical pore was produced in a PET membrane by asymmetric etching in NaOH, performed in a conductivity cell [3]. The diameter of the pore's openings were ~500 and ~2 nm, respectively. To examine ion transport through this nanopore, we measured its current-voltage characteristic (I-V) as well as its ion current at constant voltage. Two independent experimental methods were used. In a first experiment, single pore recordings were performed in a conductivity cell using a single-pore PET foil. Figure 1 shows the I-V characteristics of a single conical pore at different pH values of the KCl solution.

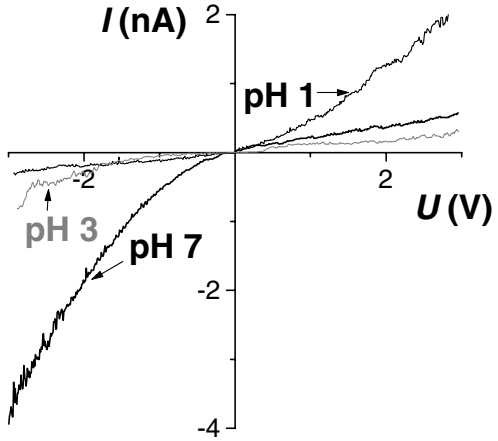


Fig. 1 Current-voltage characteristics of a single asymmetric pore for 0.1 M KCl and various pH values as indicated in the Figure.

In order to observe fast current transients a scanning ion conductance microscope (SICM) with low-capacitance circuit was used. It had a micropipette of 100 nm tip diameter and enabled to precisely position the pipette over the etched pore on the PET film [4]. The examined sample had a pore density of $10^6/cm^2$. A topographic image of the polymer surface (Fig. 2a) was obtained. After completion of a full scan, the pipette was positioned over one hole and lowered into the large opening of the conical pore, as indicated in Fig. 2b. During docking the resistance increased steeply. Finally, a small suction was applied to form a tight seal between the pipette and the inner pore surface. Fig. 2c shows an example of recorded ion current fluctuations.

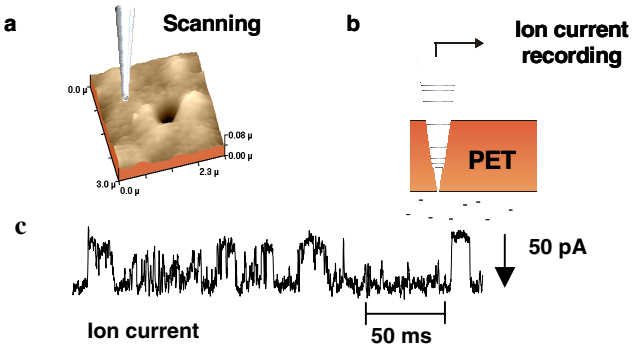


Fig. 2 Principle of ion current measurements through a selected conical pore by scanning ion conductance microscopy:

- **(a)** The surface of the polymer film is scanned and a pore localised.
- **(b)** The pipette, having a diameter smaller than the larger opening of the conical pore, is docked into the pore.
- **(c)** A typical recording of ion current (-120 mV, 1 M KCl, pH 7).

Our results show that an asymmetric conical nanopore is a current rectifier. Its current-voltage characteristics is governed by the electrolyte pH. Additionally, the ion current through a single conical pore shows a voltage-dependent bistability, similar to that produced in voltage-gated biological channels.

[1] Hille, B. *Ionic Channels of Excitable Membranes* (Sinauer, Sunderland, MA, ed. 2, 1992).
[2] Zhou, Y., Morais-Cabral, J.H., Kaufmann, A. & MacKinnon, R. *Nature* **414**, 43 (2001).
[3] Apel, P., Korchev, Y.E., Siwy, Z., Spohr, R. & Yoshida, M. *Nucl. Instrum Meth. B* **184**, 337 (2001).
[4] Korchev, Y.E., Negulyaev, Y.A., Edwards, C.R.W., Vodyanoy, I. & Lab, M.J. *Nature Cell Biology* **2**, 616 (2000).

Relevance of surface gels for ion track etching in polymers

D. Baur*, P. Apel[+], Y.E. Korchev[#], C. Müller*, Z. Siwy*, H. Spohr[#], R. Spohr*

* Gesellschaft für Schwerionenforschung, Planckstr.1, D-64291 Darmstadt, Germany
[+] Flerov Laboratory of Nuclear Reactions, JINR, 141980 Dubna, Russia
[#] Imperial College, Hammersmith Campus, Du Cane Road, London W12 0NN, U.K.

Nanoscopic cones of etched ion tracks in polymer foils, immersed in an electrolyte, show an asymmetric current-voltage characteristic (Fig. 1) as well as electric current fluctuations [1,2]. These phenomena depend on size and structure of the pore close to the cone tip. The consistence of the cone material can be best studied on etched polymer surfaces. Scanning Electron Microscopy (SEM) allows imaging of the polymer surfaces only in the dry state and shows smooth surfaces and tracks. Scanning Force Microscopy (SFM) and Scanning Ion Conductance Microscopy (SICM) offer the possibility of studies in a wet state. SFM measurements suggest that the pore diameter is smaller in water than in the dry state (Fig. 2). To check whether this effect is due to swelling of the polymer surface, SICM studies have been performed, confirming the existence of a highly conductive surface gel. Approaching the surface with the pipette at a selected position reveals water-filled conductive structures (Fig. 3). The pipette current decreases while approaching the surface, the entering into the gel structure is identified by a slope change.

Our results prove that etching modifies the polymer surface leading to fixed surface charges and an increased surface roughness. Surface charges are responsible for water uptake (swelling) and play a functional role for ion transport through narrow pores.

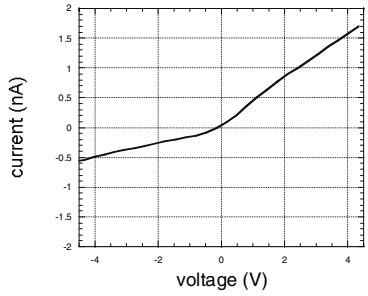


Fig.1. Current-voltage characteristic of a conical pore in polycarbonate (1M KCl, pH 8).

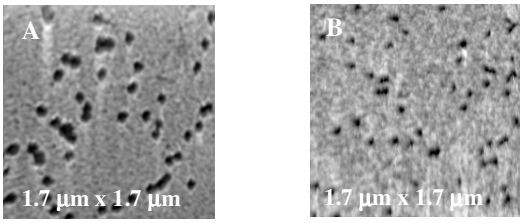


Fig. 2. SFM images of a polyethylenterephthalate membrane **A** in air and **B** in water

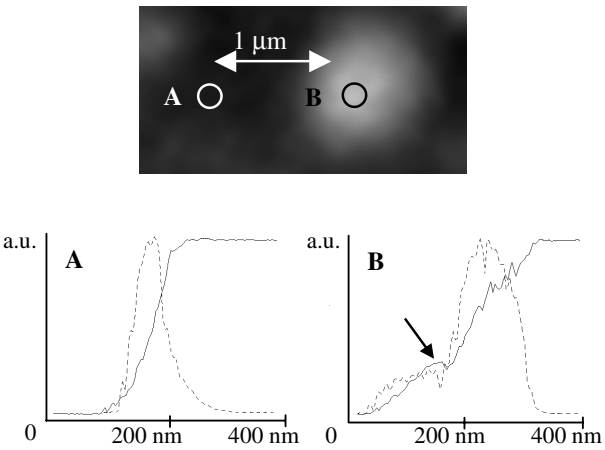


Fig.3, Top: SICM image of a gel structure on etched polycarbonate. The position of the pipette approach is indicated as a circle of the size of the pipette aperture
Fig.3, Bottom: The solid line represents the current through the pipette, the dotted line its derivative. In **B,** starting from the position indicated by an arrow, the pipette was moved 150 nm into the gel.

References

[1] Apel, P., Korchev, Y.E., Siwy, Z., Spohr, R. & Yoshida, M. *Nucl. Instrum Meth. B* **184**, 337 (2001).

[2] Siwy, Z., Gu, Y., Spohr, H., Baur, D., Wolf-Reber, A., Spohr, R., Apel, P. and Korchev, Y.E. Rectification and Voltage Gating of Ion Currents in a Nanofabricated Pore, submitted to Proceedings of the National Academy of Sciences USA.

Flexible microchannels with integrated nanoporous membranes

Stefan Metz[1], Christina Trautmann [2], Arnaud Bertsch[1], Mario Schlund[1], Philippe Renaud[1]

[1] Institute of Microsystems EPFL Lausanne, [2] GSI Darmstadt

Polymer-based microfluidic systems with integrated ion-track membranes were produced by combining lithographic and curing techniques [1] with the ion-track technology. Such devices can be used for cross-flow filtration of particles in fluids or as microstructures for drug delivery.

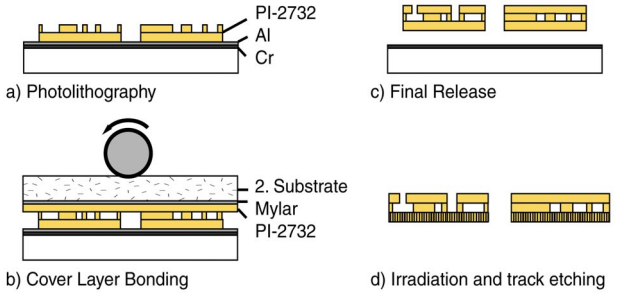


Fig. 1. Fabrication process for polyimide-based microchannels with integrated nanoporous membranes.

In the first fabrication step, photosensitive polyimide (PI-2732) from DuPont is spin coated on a metallized silicon carrier-substrate. The PI film is then structured by means of photolithography and partially imidized via thermal curing (Fig. 1a). A second layer of incompletely imidized PI is bonded to the pre-structured film covering the open channel structures (Fig. 1b). Due to high diffusion within the two partially cured PI-interfaces, the applied technique yields a high bond strength without visible interface between the two laminated layers.

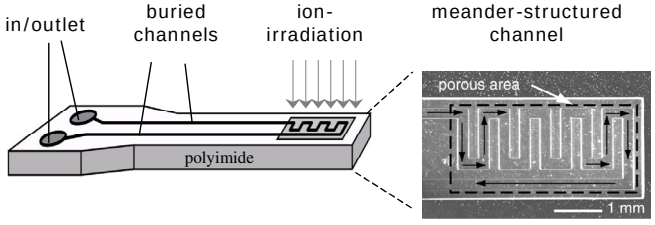


Fig. 2. Microfluidic system with buried channels in polyimide. In selected areas, nanopores can be created by irradiation with energetic heavy ions followed by track etching. The meander geometry helps to increase the filter area.

Before final curing, the upper PI layer is photostructured to obtain in- and outlets of the channel systems (Fig. 1c and 2). If flexible microchannels are required, the entire polyimide device can be detached from the silicon substrate by dissolving the sacrificial Al layer (Fig. 1c).

The microchannels in the polyimide have typically a width between 30 - 500 µm, a height from 5 to 20 µm and a length up to 6 cm. It should be mentioned that the buried channels show no leakage failure and can be operated at pressures up to 19 bar. The technique also allows embedding of microelectrodes giving access to many biomedical applications.

In a second step, the prefabricated polyimide device is irradiated with heavy ions of typically a few MeV per nucleon. Depending on the final application, the initial energy of the beam is adjusted in such a way that either one or both, i.e., the top and bottom layer of the channel system are perforated. Masking allows the irradiation of selected regions of the microdevice as e.g. the meandering channels of increased filter area in Fig. 2. After irradiation, the created ion tracks are enlarged to cylindrical or conical pores by chemical etching in a sodium hypochlorite solution [2].

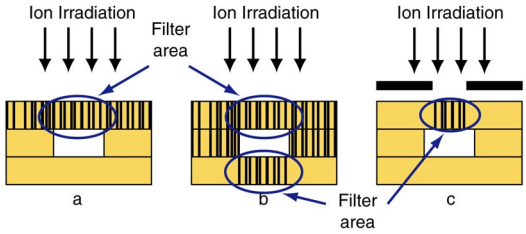


Fig. 3. Illustration of different irradiation methods.

The pore density of the filter region is given by the ion fluence and varied between 10^6 and 10^8 ions/cm^2. The pore diameter was controlled by the etching process (e.g. temperature, pH, and concentration of etchant) and ranged from 50 nm up to several µm. Fig. 4 gives an example of a microchannel containing pores in the irradiated bottom layer.

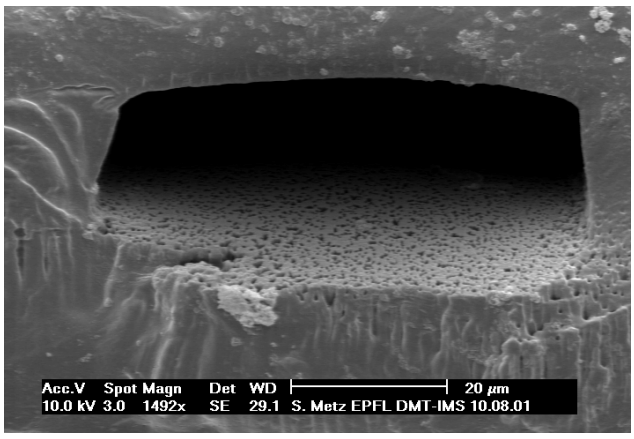


Fig. 4. Cross-section of microchannel (20 µm height, 50 µm width) with etched ion tracks (pore diameter 200 nm) in the bottom layer.

[1] S. Metz, R. Holzer, P. Renaud, Lab on a Chip 1 (2001) 29.

[2] C. Trautmann, W. Bruechle, R. Spohr, J. Vetter, N. Angert, Nucl. Instr. Meth. B 111 (1996) 70.

Micron-sized ion-track pores in glass for bilayer recording

N. Fertig[1,2], C. Meyer[1,2], R.H. Blick[1], C. Trautmann[3], J.C. Behrends[1,2]

[1] Center for NanoScience & Sekt. Physik LMU Munich, [2] Physiologisches Institute LMU Munich, [3] GSI Darmstadt

Apertures with diameters in the low micrometer to submicrometer range are achieved by irradiation of a glass chip with a single heavy ion and subsequent wet track etching. By this technique it is possible to produce a planar sensor for ion channel electrophysiology from a glass substrate. The function of the device is demonstrated by recordings of single-channel currents mediated by the model ion channel Gramicidin A in artificial lipid bilayers spanning the micromachined aperture.

Ion channels play key roles in most functions and dysfunctions of all cells. The most direct and accurate methods for studying ion channel behaviour record the transmembrane current that results when the channels open to allow ions to flow, whilst keeping the transmembrane voltage constant. The most precise of these voltage-clamp techniques is patch clamping [1], where a tight, high resistance seal is formed between the tip of an electrolyte-filled glass pipette and the cell membrane. This high resistance increases the resolution of recording so that currents mediated by few or even single open channels can be directly observed.

The minimal requirement for an electrophysiological ion channel sensor is a small (micron-sized) aperture in an insulating material that separates two electrolyte-containing compartments. Pulling out a glass pipette to provide a micro-sized orifice is an elegant way of producing an aperture of small dimensions at the tip of a device that can be handled. However, this also produces a relatively long pathway through which current must flow to the opening, leading to a considerable access resistance and capacitance of the device. The fabrication of submicron apertures using the ion-track etching technique allows on-chip single channel recording with low access resistance and low capacitance. Such an 'on-chip pore' in glass, fulfils in particular the desired low-noise requirement [2].

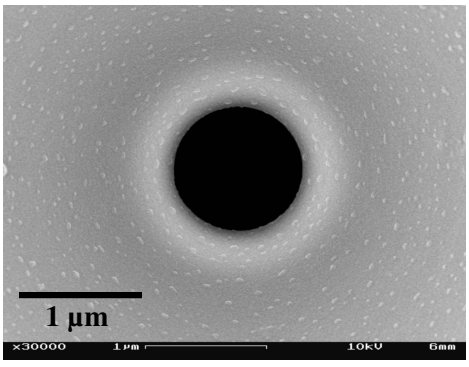


Fig. 1. Scanning electron micrograph of an aperture in the glass chip microstructured with the ion track technique.

The glass substrates have a thickness of 200 micron and are partitioned into 5x5 mm^2 chips. Circular areas with a diameter of 200 microns are thinned down to 80 microns by isotropic etching in hydrofluoric acid. An etch mask is defined by photolithography and evaporation of a 200 nm thick layer of gold. In a second step, the pre-thinned glass film is exposed to a gold ion beam of 2260 MeV available at the linear accelerator UNILAC. This experimental facility allowed us to penetrate each chip with precisely one ion. The resulting ion track exhibits a much higher etching rate than the surrounding bulk material. Upon etching with HF from one side of the chip, a conical-shaped groove forms along the track. The etching process is stopped as soon as the etching cone reaches the opposite side of the chip. Circular, smooth apertures on a submicron scale can be fabricated. Fig. 1 shows a scanning electron micrograph of such an aperture in a glass chip.

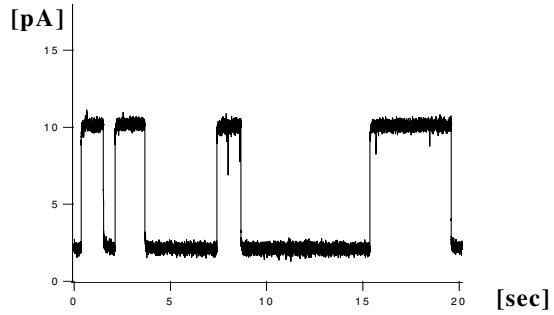


Fig. 2. Current vs time recording from gramicidin A channels in a lipid bilayer suspended in the aperture of a glass chip.

To test our device, ionic currents through gramicidin A channels were recorded as shown in Fig. 2. Here, a lipid bilayer is spread over a glass chip with an aperture of 2-µm diameter. Gramicidin is added to both sides of the membrane in an appropriate amount for single-channel events. Gramicidin is a low molecular weight peptide, well characterized and widely applied as model pore [3]. As a driving force for ion flux, a voltage typically around 200 mV is applied across the bilayer. Gramicidin is selective for monovalent cations and as CsCl-solution is used, Cs^+ currents are recorded. The single-channel conductance steps corresponding to the formation/dissociation of a gramicidin dimer are clearly resolved, even at 3 kHz bandwidth.

In conclusion, we have developed a technique for producing micron or submicron-sized single pores in pre-thinned glass chips. Based on the low background noise, ionic currents through single ion channels in lipid bilayers can be recorded at high bandwidth.

[1] O.P. Hamill, A. Marty, E. Neher, B. Sakmann and F.J. Sigworth, Improved patch-clamp techniques for high-resolution current recording from cells and cell-free membrane patches. Pflügers Archive 391, (1981) 85.

[2] N. Fertig, C. Meyer, R.H. Blick, C. Trautmann, J.C. Behrends, Microstructured glass chip for ion-channel electrophysiology, Phys. Rev. E **64**, 040901 (2001).

[3] G.A Woolley, B.A. Wallace, Model ion channels: gramicidin and alamethicin. J. Membr. Biol. 129(2) (1992) 109.

Preparatory Experiments for a Second-Generation Radiation-Biological Single Hit Facility

M. Cholewa, B.E. Fischer, and M. Heiß, GSI, Darmstadt

Introduction

More than a decade ago, radiobiological investigations of low radiation dose effects connected to the radon problem inspired a new irradiation technique: Instead of exposing cells in a petri dish to an extremely low dose, where no cell might be hit at all, every single cell was exposed to exactly one or a fixed number of ionising particles using ion microprobes.

These ion microprobes used capillaries which let only a micron-size beam pass onto the biological samples. Two fairly advanced facilities of this type are now in operation at the Gray-Laboratory in London, GB and at RARAF, Columbia University, USA. One facility is under construction at JAERI, Takasaki, Japan.

Although much effort went into better beam forming capillaries over the years, the aiming accuracy of these instruments is no better than 3 to 5 µm. Moreover, their micro-beam is always contaminated by ions scattered within the capillary and having therefore an unknown LET.

Both limitations can be overcome by the GSI *focusing* ion microprobe. All its ions will have the same LET and the micro-beam can be focused to less than 0.5 µm diameter. Moreover, the research, presently done mainly with protons and alpha particles, can be extended to ions of higher mass.

The GSI Single-Ion-Hit-Facility

Traditional facilities use vertical beams, because biological cells can more easily be kept in a nutrient solution in a horizontal petri dish, and irradiated through a thin membrane at the bottom of the dish. To bend the Unilac-beam into the vertical direction would have required a prohibitive building effort. Therefore, the single hit facility at GSI will use the horizontal beam of the existing microprobe with some few modifications.

The principle of the single particle irradiation is shown in fig.1. One cell is moved into the position of the micro-beam-focus using an optical microscope and a computerised cell recognition program. When the cell nucleus is in the focus position, a beam switch opens until the hit detector records a secondary electron cloud from the vacuum window after ion impact. Then another cell is moved into the focus position....

Some rare biological effects require that hits are detected with at least 99.7% reliability. Therefore, we have optimised the secondary electron yield of the window material to allow the reliable detection of low mass ions like carbon. Presently, the best window candidates are B-doped diamond or 500 nm Si_3N_4 covered with 20 nm Au + 20 nm CsI.

To check the reliability of hit detection and aiming we took a CR-39 track detector covered with 20nm Au + 20nm CsI instead of the window and produced microscopic 10 x 10 hit patterns of single ion impacts (fig.2) using the long established ability of the GSI microprobe to write single ion patterns.

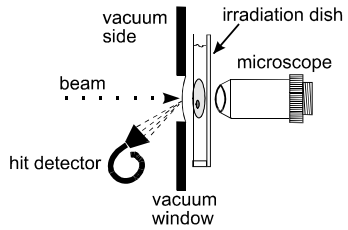


Fig.1 Principle of the single-cell single-hit facility

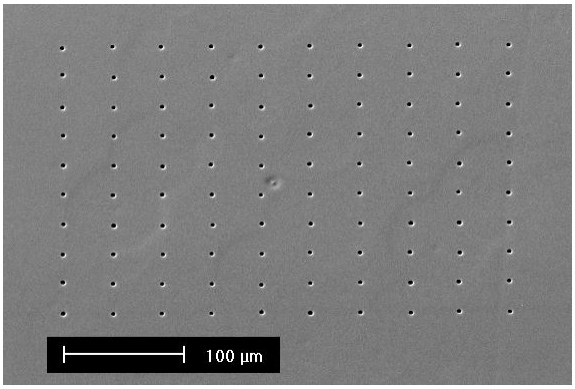


Fig.2 Micro-pattern of 10 x 10 single ion hits recorded in CR-39 and developed 20h in 6nNaOH at 40°C. Ions: 4.8MeV/u carbon. One out of 8 perfect patterns from a sample of 25.

Taking all 25 10x10 hit patterns together, 0.5% hits have been misidentified, 0.4% hits have been misplaced due to a defect aiming electronic, and 0.4% due to ions with wrong energies and charge states because of scattering along the beamline.

To check the amount of scattering by the window we placed the CR-39 track detector 2 mm behind the window, and repeated the 10x10 pattern this time with 15 hits per position (see Fig.3).

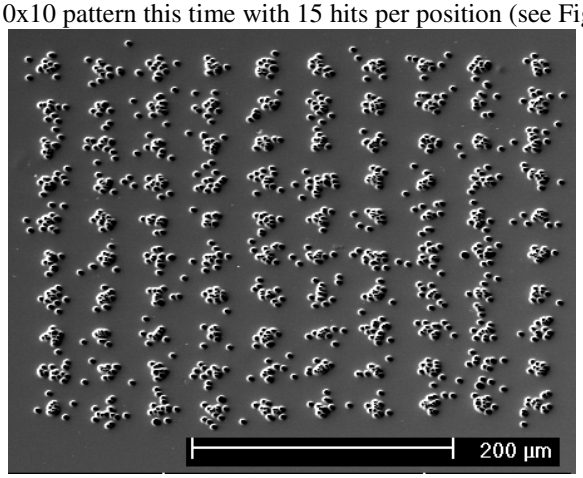


Fig.3 Pattern of scattered particles. In the final single-hit-facility the cell dish is at 100µm distance from the window and the effects of scattering are 20 times less.

Preparation of a single metal wire by electrochemical filling of an etched ion track

Maria Eugenia Toimil Molares, Zuzanna Siwy, Reinhard Neumann, Ingrid U. Schuchert, Reimar Spohr, Christina Trautmann
GSI Darmstadt

Metallic nanowires are acquiring increasing importance due to the efforts of microtechnology to reduce structures to sizes as small as 100 nm and less. One of the techniques mostly employed to produce nanowires is the electrochemical or electroless deposition in templates [1,2]. Using this method, several groups have prepared large arrays (10^6-10^{10} cm^{-2}) of different kinds of structures such as for instance metallic wires or multilayered needles. Due to the limited size, nanowires exhibit novel optical, electrical or magnetic properties. In some cases, they have been investigated as an ensemble still embedded in the template matrix [2]. However, in particular for electric and magnetic studies, it is desirable to select individual wires and produce reliable electrical contacts, which is a demanding and difficult challenge.

In this paper, we report a new possibility of preparing single nanowires that can be easily connected to an external electrical circuit for further studies. The technique, schematically shown in Fig. 1, is based on ion-track etching in combination with electrochemical deposition.

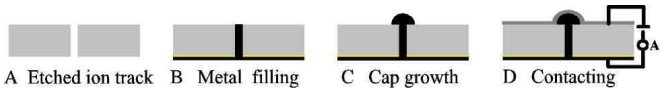


Fig.1. Scheme of the template method where a single pore is filled with metal by electrochemical deposition.

To produce single-pore membranes, 30 µm thick polycarbonate foils were irradiated with individual heavy ions (e.g. Xe, Au, U) of several hundred MeV kinetic energy at the UNILAC. The irradiations were performed through a mask with a circular aperture of diameter 0.1 mm. A detector behind the polymer sample together with a fast beam-switching system allowed the controlled production of a single track per membrane [3]. The irradiated foil was then exposed to a suitable etchant (e.g. NaOH) where the latent track was enlarged to a cylindrical pore with a diameters between 200 nm and 1 µm (Fig. 1A).

After etching, a thin gold film was sputtered onto one side of the membrane and subsequently electrochemically reinforced with copper. The polymer foil was then mounted in a two-electrode electrochemical cell, where the conductive membrane surface acts as cathode and a copper piece serves as anode. The copper deposition in the pore was performed potentiostatically at room temperature.

Chronoamperometric curves recorded during the growth process of individual 1-µm diameter wires for various applied voltages (-100 – -120 mV) are presented in Fig. 2. Qualitatively, the current-vs-time data show the same evolution as large ensembles of nanowires when the current is averaged over the filling of millions of pores [4].

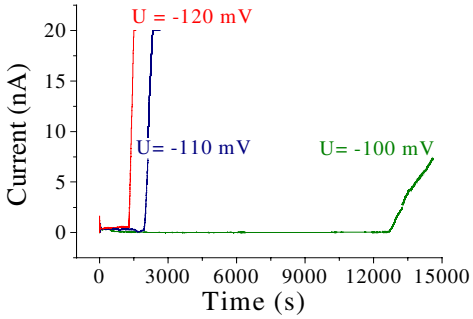


Fig. 2. Current-vs-time curves for filling of 1-µm diameter pore at different overvoltages.

When the growing nanowire reached the upper membrane surface (Fig. 1B), the deposition process was continued for some extra time, in order to produce a copper cap typically of about 10 µm in diameter (Fig 1C). Caps of single nanowires grown at -120 and -100 mV are shown in Fig. 3A and 3B, respectively. The morphology of the caps gives us an indication for the kind of crystallinity (single or polycrystalline) of the wire [5]. In agreement with earlier results, larger grain sizes are formed for lower overvoltages. The preparation of single monocrystalline copper nanowires requires deposition experiments at higher temperatures and lower overvoltages [4].

For electrical measurements, the cap and therefore the wire can easily be contacted by evaporating another metal layer (e.g. gold) on the membrane surface (Fig. 1D) avoiding large contact resistances. Up to now, single wires with diameter 200 nm have been successfully produced and contacted. Further investigations will focus on electrical properties not only of polycrystalline but also of single-crystal nanowires.

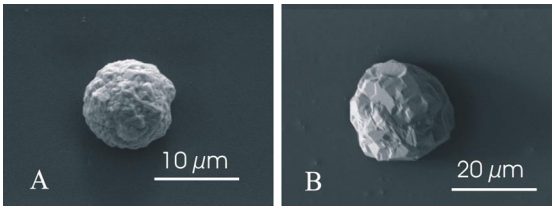


Fig. 3. Micrographs of caps of 1 µm single wires grown at (A) –120 mV and (B) –100 mV.

[1] J. Vetter, R. Spohr, Nucl. Instr. and. Meth. B 79 (1993) 691.
[2] J.C. Hulteen and C.R. Martin, J. Mater. Chem. 7 (1997) 1075.
[3] R. Spohr, German Patent DE 2951376 C2 (1983), United States Patent 4369370 (1983).
[4] M.E. Toimil Molares, V. Buschmann, D. Dobrev, R. Neumann, R. Scholz, I.U. Schuchert, J. Vetter, Adv. Mater. 13 (2001) 62.
[5] M.E. Toimil Molares, J. Brötz, V. Buschmann, D. Dobrev, R. Neumann, R. Scholz, I.U. Schuchert, C. Trautmann, J. Vetter, Nucl. Instr. Meth. B 185 (2001) 192.

Electrodeposition of Cu/Co multilayered nanowires

Ionut Enculescu[1,2] , Reimar Spohr[1]
[1] Gesellschaft für Schwerionenforschung (GSI), Planckstr.1, D-64291 Darmstadt, Germany
[2]National Institute for Materials Physics, 76900 Bucharest Magurele, Romania

The study of low dimensional layered magnetic structures is one of the hottest topics in solid-state physics today, due largely to growing technological applications. These studies were triggered by the discovery of giant magnetoresistance (GMR) effects in Fe/Cr multilayers [1, 2]. In the first experiments made on such structures the current flows in the plane of the layers, this is the CIP (current in plane) geometry. Soon, the magnetoresistance measurements were extended to the case where the current is perpendicular to the plane, the so-called CPP geometry, which presents an effect several times larger than the CIP geometry. This difference is explained by the fact that the main parameter in the CIP geometry is the electron mean free path, which is much shorter than the main parameter that must be taken into account in the CPP geometry, the spin diffusion length. Thus the number of magnetic layers experienced by the electron is larger for the CPP geometry.

Electrodeposited multilayered nanowires using a pulsed technique having the diameter below 100 nm are ideally suited for studying CPP GMRs, this preparative technique producing multilayered samples with a measurable change in magnetoresistance. The nanowires were deposited into the pores of ion-track-etched polycarbonate membranes and for the studies reported here the diameters were of about 1µm in order to allow direct observation by scanning electron microscopy.

We focused our research on the Co/Cu structures, which present the advantage that the reduction potentials of the components are sufficiently far apart to allow separate electrodeposition of both metals. However the main problem arising is the possibility that the magnetization of cobalt layers is expected along the axis of the nanowire the result being a very weak magnetoresistance effect.

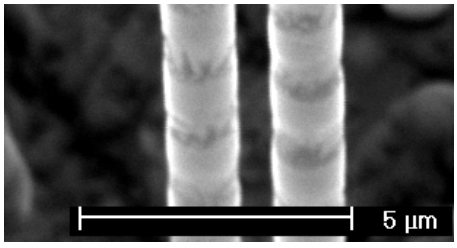
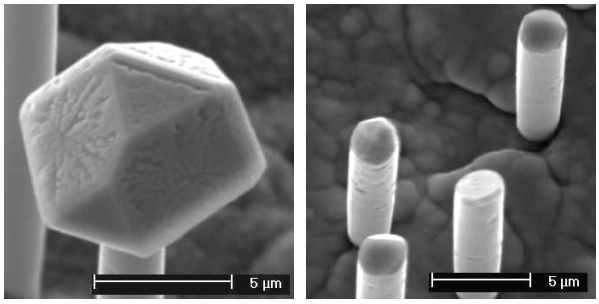


Figure 1. Columnar structure of a cobalt layer in a multylayered wire electrodeposited from a solution containing 320g $CoSO_4.7H_2O$/l, 3.2g $CuSO_4.5H_2O$/l and 32g H_3BO_3/l, at room temperature

The reason of this is that the structure of cobalt deposits is usually columnar or fibrous along the growth direction (figure 1). Moreover, cobalt structure is usually hexagonal with a strong magnetic anisotropy oriented perpendicular to the hexagonal planes and parallel to the growth direction increasing the tendency of the magnetization to be along the wire axis. In order to avoid this nuisance we have decided that more attention should be paid to the structure of the substrate on which cobalt is deposited, in our case the copper layer. The effect of the structure of the base metal on that of the deposits depends on several factors. If the interatomic distances in a particular lattice plane of the base metal closely match those in a lattice plane of the deposit, which is the case for Cu and Co, it is possible for the structure of the former to be continued into the latter. This fact should decrease the crystalline anisotropy and also should produce a structure without columns allowing an easier orientation of the magnetization vector perpendicular to the wire axis and thus stronger MR effects. Even better results in the epitaxial growth could be achieved if the substrate is single crystalline. Mono - crystalline copper wires were previously grown by the template method from single baths [3, 4].



(a) (b)

Figure 2. Single crystalline copper wires grown from the same solution as in figure 1, applied voltage (a) –70mV; (b) –60mV at 55 °C

By carefully choosing the growth conditions it was possible to grow single crystalline wires of copper from a double bath containing both Co and Cu ions. This was proven by SEM observations of the growth facets and of the caps grown after the pores were filled with metal (figure 2).

The template growth method of nanowires could be even more effective using single ion track substrates. The growth of a single wire will make electrical measurements less complicated especially by simplifying the problem of contacting.

This work was supported by European CONTRACT N° HPRN-CT-2000-00047.

[1]. M. N. Baibich, J. M. Broto, A. Fert, F. Nguyen Van Dau, F. Petroff, P. Etienne, G. Creuzet, A. Friederich and J. Chazelas, Phys. Rev. Lett. 61 (1988) 2472
[2]. G. Binasch, P. Grünberg, F. Saurenbach and W. Zinn, Phys. Rev. B 39 (1988) 4828
[3]. D. Dobrev, J. Vetter, N. Angert, R. Neumann, Appl. Phys. A 69 (1999) 233
[4]. M.E. Toimil Molares, V. Buschmann, D. Dobrev, R. Neumann, R. Scholz, I. Schuchert, J. Vetter, Adv Mater. 13 (2001) 62

Formation of metal membranes by direct duplication of ion-track templates

D. Dobrev, R. Neumann and J. Vetter
GSI, Darmstadt

A novel method for direct electrochemical duplication of pores in ion track polymer membranes is described. It allows fabrication of metal membranes using metals, which are readily deposited by electroplating from aqueous solutions. For this purpose, one side of the irradiated and etched polymer foil is made conductive by sputtering or evaporation of a thin metal film. The lateral growth of the deposit, facing the anode, leads to the tapping of the pores when a certain thickness is reached. This is avoided by a distinct increase of the electrochemical polarization in the proximity of the pore orifices applying a counter-solution with some overpressure from the opposite non-metallized side of the plastic membrane. The simplest way is to contact the electrolyte through the pores with pure water or indifferent electrolyte, which decreases the ion concentration in the neighborhood of pore orifices and increases the concentration polarization. An alternative is to use solutions containing ligands that form complexes with the metal ions and thus increase the deposition potentials. A third way is the application of a very low concentration of specifically adsorbed species, which block the actively growing sites in the deposit, for example pyridine or CN^- in the case of platinum plating. Thus, deposition of metal over the pores is prevented, and the lateral growth of the deposit is significantly reduced.

The experimental procedure for fabrication of metal membranes by the direct electrochemical duplication is shown in Fig. 1. We employed bisphenol-A *poly-carbonate* foils (Makrofol, Bayer Leverkusen) 30-100 µm thick, irradiated with U^{238} ions with kinetic energy 11.4 MeV/u and fluence 10^5-10^6 ions/cm^2 at the UNILAC linear accelerator of GSI. Conventional 6M NaOH solution containing 10 % CH_3OH was used for etching of the tracks at a temperature of 313 K, to pore diameters typically between 2 and 3 µm.

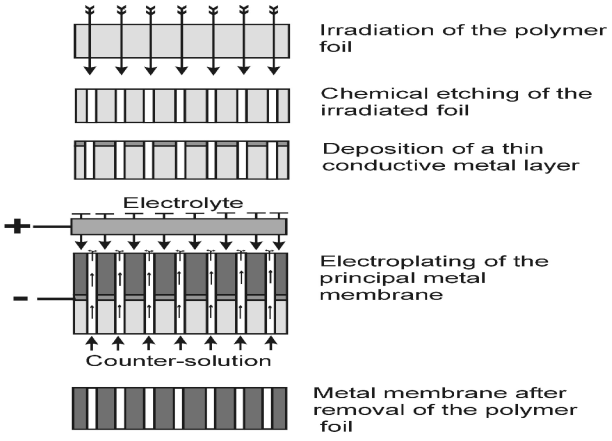


Fig. 1. Fabrication procedure

The conductive layer was formed by depositing gold with a magnetron sputter source. For the preparation of copper, gold, nickel and platinum membranes, we used commercial electrolytes. As counter-solutions 25 % sulfuric acid, pure water, and 1 % EDTA (ethylenediaminetetraacetic acid, disodium salt) were used. The hydrostatic pressure was maintained within 0-100 mm of a column of the counter-solution. Variation of this pressure leads to generation of metal membranes with different shapes and sizes of the pores.

The substrate polycarbonate foils were removed by dissolution in CH_2Cl_2. We visualized the bare metal duplicas with a Philips XL30 scanning electron microscope (SEM). A Vickers Instruments light microscope was used for optical observations in a transmission mode.

Copper membranes deposited from an acid electrolyte in contact through the pores of the template polymer filter with 25% H_2SO_4 or 1 % ADTA solution are displayed in Figs. 2 and 3, respectively. A gold membrane deposited from a sulfite electrolyte balanced through the template pores by water is shown in Fig.4.

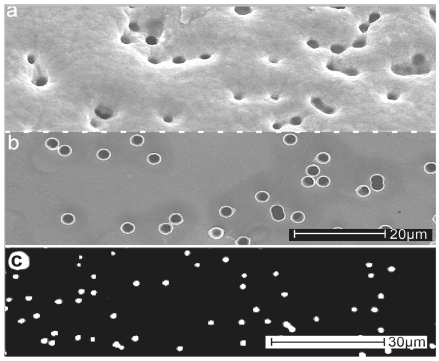


Fig. 2. Copper membrane (counter-solution of H_2SO_4): SEM images of top side (a) and bottom side facing the polymer (b); transmission light image (c)

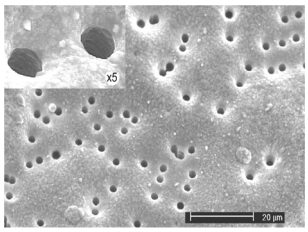


Fig. 3. Copper membrane (EDTA as counter-solution)

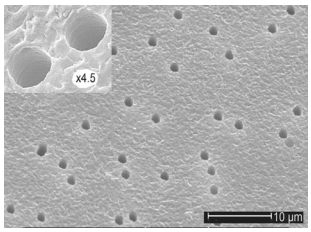


Fig. 4. Gold membrane (water as counter-solution)

The pores in the metal membranes have the same appearance as those in the polymer filter, which served as a template. By this method, such membranes can be fabricated with pore diameters in the nano- and micrometer range, and with areal densities from single pores up to 10^6 – 10^7 pores/cm^2. These membranes are of interest in cases when an application of plastic membranes is not desirable or not feasible. They could be advantageous particularly in catalysis as well as in biological science and technology. Further, they may be useful as apertures and collimators for different kinds of radiation.

Direct evidence for the spatial correlation between individual particle traversals and localized CDKN1A response induced by high-LET radiation

M. Scholz[1,2], B. Jakob[1], G. Taucher-Scholz[1]
[1]GSI Darmstadt [2]Radiologische Klinik Heidelberg

In a recent study, we showed that heavy ion irradiation of human fibroblasts leads to an extremely localized nuclear response of the CDKN1A (p21) protein (*1*). The number of CDKN1A foci per cell nucleus after heavy-ion irradiation suggested a direct correlation with the number of particle traversals and therefore also a spatial correlation between foci and particle traversals. However, this conclusion was essentially based on statistical arguments, comparing the number of foci with the average number of particle hits which are expected at a given fluence and geometrical size of the nucleus.

But using a method based on retrospective detection of traversals in nuclear track detection material, we were now also able to directly assign the individual foci to the sites of individual particle traversals (2,3). The procedure of fluorescence imaging and track image matching includes the following steps:

1. Cells are grown on CR39 plastic material which is used as a nuclear track detector. Individual particle tracks can be made visible in this material by etching in NaOH.
2. Cells are irradiated and immunostained using a CDKN1A antibody as described previously.
3. Images of the nuclei showing CDKN1A foci are taken and the positions of the cells are stored using a computerized microscope stage control (image type I). At the same time, phase contrast images are taken at the same position (image type II).
4. After taking the images of CDKN1A foci, cells are removed from the CR39 plates, and the plates are etched for track detection.
5. The plate positions for which images of CDKN1A foci were taken are relocated and images are taken at the same position, showing now the pattern of particle traversals (image type III). They can be distinguished from the reference tracks by their smaller size.
6. By comparing the different images, the spatial correlation of tracks and foci is determined. Possible displacements due to repositioning inaccuracies can be detected by means of reference tracks, which are produced by pre-irradiation of the CR39 with charged particles.

Images were then further processed to facilitate the analysis. First, images of type I were optimized by manually adjusting the contrast. Secondly, images of type II were transformed using a threshold procedure to specifically select only the reference track structures. The resulting images are then combined using a false color coding, so that the reference tracks appear in green, whereas the fluorescence intensity of the CDKN1A signal remains as a gray scale pattern (Fig. 1a). Images of type III were segmented also according to a manually adjusted threshold, and the corresponding objects are subsequently classified according to their size into two groups. Again, color coding was chosen as green for the reference tracks, whereas the tracks corresponding to the cell irradiation are coded in red.

In Fig. 1, light blue lines indicate the important structures. An ellipse represents the approximate shape and size of the cell nucleus. Straight lines interconnect individual CDKN1A foci in order to enhance the particular pattern. The same pattern is shown in the lower panel (Fig. 1b) as overlay to the track image, and the patterns of CDKN1A foci and particle traversals coincide precisely.

A similar coincidence was found for all but one of about 35 cells analyzed in this experiment. Furthermore, the same type of correlation has been found for other proteins like e.g. hMre11 (4).

These results thus represent further confirmation that the response of CDKN1A and hMre11 on the microscopic level reflects the typical spatial energy deposition pattern of charged particles and thus the distribution of primary induced damage.

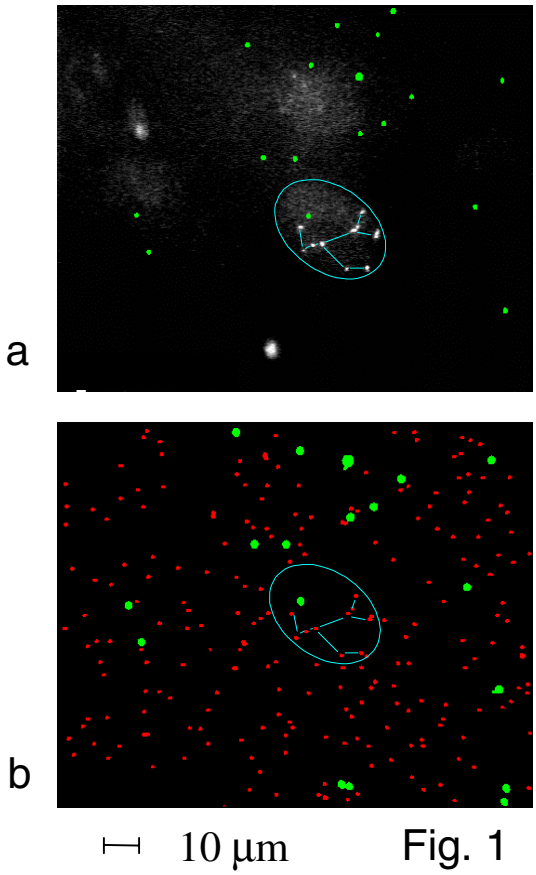


Fig. 1

References:
(1) B. Jakob et al., Rad. Res. 154, 398-405 (2000)
(2) C. Soyland and S.P.Hassfjell, Rad. Env. Biophys. 39, 125-130 (2000)
(3) M. Scholz et al., Rad. Res. 156, 558-563 (2001)
(4) B. Jakob et al., Int. J. Radiat. Biol. 78, 75-88 (2002)

Fast CDKN1A foci formation at sites of heavy ion-induced damage does not depend on activation mediated by TP53

G. Taucher-Scholz, B. Jakob, M. Scholz, G. Becker and G. Kraft (GSI, Biophysik)

We have recently described the rapid accumulation of CDKN1A (p21) protein to foci at sites of heavy ion traversals in nuclei of human fibroblasts (1,2). Immunofluorescence staining and confocal laser microscopy were used to detect the protein signals. With the aim of understanding the role of this CDKN1A response, we now extended these studies to investigate the dependency of protein aggregation on transcriptional activation mediated by TP53, a key signal transducer known to induce CDKN1A after ionizing irradiation.

The promptness of CDKN1A localization to foci after particle irradiation provided a first indication for this response being independent of induction mediated by TP53. The kinetics of the formation of protein foci at sites of DNA damage produced by particle irradiation was now examined in detail in normal human fibroblasts (AG1522) after exposure to low energy ions focusing on short time intervals between irradiation and fixation of the cells. In these experiments CDKN1A foci could be observed in some cells already between 2 and 5 min after particle traversals. During approximately the first 30 min after irradiation, the CDKN1A foci seem to develop and gain brightness, being detectable in an increasing fraction of cells at later timepoints. This is exemplarily shown in Fig. 1 after exposure to uranium ions at 5 and 15 min postirradiation. The extremely fast concentration of the protein to foci suggests that CDKN1A is at least in part relocalized to the sites of damage from the pool of existing protein. In addition, the development of foci argues against a non-specific binding of the CDKN1A antibody to artificially created epitopes.

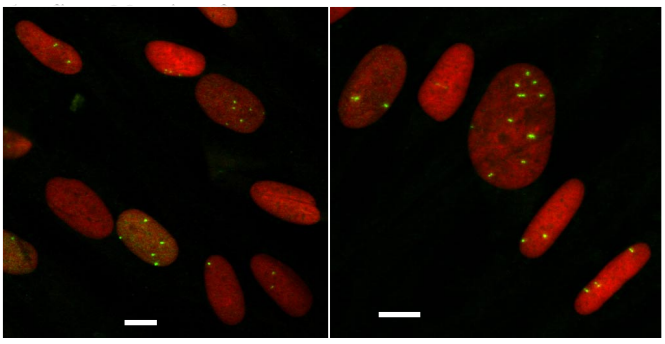


Fig.1: Rapid CDKN1A response (bright spots) in nuclei of normal human fibroblasts 5 min **(left)** and 15 min **(right)** after irradiation with uranium ions (8.9 MeV/u) at a fluence of $2.2*10^6$ P cm^{-2}. Size of bars: 10µm.

Further evidence that the accumulation of CDKN1A is not related to the TP53-dependent function of CDKN1A in cellcycle arrest is obtained from studies of cell lines with abrogated TP53 transactivation capability (3). First, ion traversal-dependent CDKN1A foci were detected in HPV-E6 transfected fibroblasts lacking functional TP53 (Fig. 2, left). Although very low basal levels of both TP53 and CDKN1A in these cells made signal recognition more difficult, clearly detectable foci were observed in about 40 % of the G0/G1 cells. Secondly, AT-cells that are deficient in the ATM gene product and do not perform normal cell cycle arrest in response to ionizing radiation (4) show normal CDKN1A foci induction after particle irradiation (Fig. 2, right).

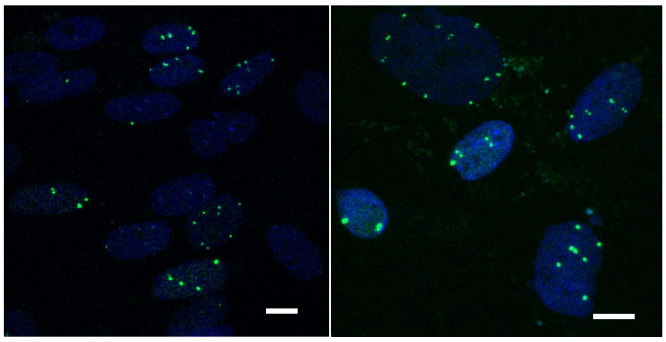


Fig.2: CDKN1A response (bright spots) in nuclei of HPV16-E6 transfected human fibroblasts **(left)** and AT-cells **(right)** after irradiation with xenon ions (5.3 MeV/u) at a fluence of $2.0*10^6$ P cm^{-2}. Size of bars: 10µm.

The hypothesis of an early function of CDKN1A independent of transcriptional induction is further strengthened by observations showing a lack of inhibition of foci formation in the presence of cycloheximide, a potent inhibitor of protein synthesis. Interestingly, cycloheximide affected the persistance of CDKN1A foci suggesting a dynamic turnover of the protein in the aggregates.

Although the functional significance of the CDKN1A concentration at sites of damaged DNA after heavy ion traversal remains largely unclear and needs further studies, an interpretation based on the known induction pathway downstream of TP53 seems rather unlikely. Our data support a new, but yet unknown role of CDKN1A in sensing or early processing of radiation induced DNA lesions.

[1] B. Jakob et al., *Radiat.Res.*, 154, 398-405, (2000).
[2] M. Scholz et al., *Radiat.Res.*, 156, 558-63, (2001).
[3] B. Jakob et al., , *Int.J.Radiat.Biol.*, 78, 75-88, (2002).
[4] M.F.Lavin, *Int.J.Biochem.Cell Biol.*, 31, 735-40 (1999).

Ion-induced electron emission patterns in condensed matter

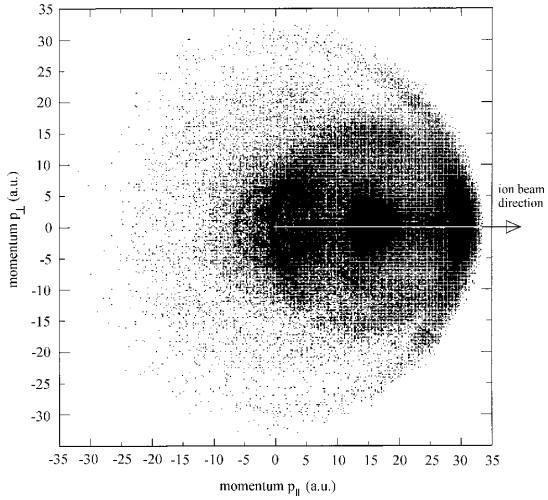
Serge Dreuil[1], Siegbert Hagmann[1,2], Hermann Rothard[3], Gerhard Kraft[1]
[1] GSI, Darmstadt; [2] Institut für Kernphysik, Universität Frankfurt;
[3] Centre Interdisciplinaire de Recherche Ions Lasers, Caen, France.

We will briefly present here a collaboration work that has recently started in the frame of the GSI Heavy Ion Radiotherapy project. The motivation of this work is to obtain valuable and systematic data of the ion-induced electron emission in condensed matter, especially emission patterns for slow electrons in terms of direction and energy and their dependencies on target density, projectile mass and projectile energy.

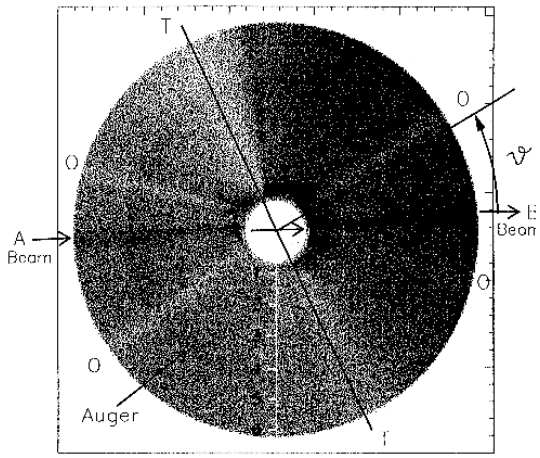
The main force of the GSI Heavy Ion Radiotherapy project is its ability to deliver a highly conformal radiation dose to deep-seated tumors, thus minimizing the risks for the healthy tissues in the beam path and/or surrounding critical organs. This is achieved by means of the inverse dose profile of carbon ions and their enhanced biological efficiency. To take the best advantage of these intrinsic properties, two major scientific and technical achievements were merged together: the active beam delivery system Rasterscan and the inverse treatment planning code TRiP. The latter does not only optimize the physical dose but also takes into account the Relative Biological Efficiency (RBE) of carbon ions. This optimization of the biologically effective dose [1] is based on the Local Effect Model of Scholz and co-workers [2]. The dominant input parameters of this model are the transverse dose distribution along the particle track, its overlap with cell nuclei and the specific radiosensitivity of the irradiated tissue. A track structure model is therefore necessary in order to compute the microscopic transverse dose. The total electron yield information is not sufficient for this purpose, more precise knowledge of the emission pattern is needed: doubly differential cross sections (DDCS) for electron emission $\partial^2\sigma(\theta)/\partial E\partial\Omega$.

Due to lack of data in condensed matter for the most relevant electron energy range with respect to damage of biological structures, electron emission spectra currently used by TRiP are scaled from experiments using gaseous targets. Figure 1(a) represents a typical electron emission pattern in the momentum space, showing characteristic structures such as binary encounter ridge and target Auger electron emission circle. First measurements on solid targets showed some deviations from the gas measurements, cf. fig. 1(b). This plot is a zoom into the small momentum values: 6 a.u. radius, to compare with 30 a.u. in fig. 1(a). The characteristic circle of Auger electron emission can still be seen as indicated. The major difference with the gas-target plot is the presence of two narrow jets in the forward and backward directions with respect to the beam. Such structures were never observed in the dilute phase experiments and might be a consequence of a nuclear track channelling effect [4]. If confirmed, such condensed phase specific effects would lead to small corrections of the TRiP track structure model and therefore to an increased accuracy of the RBE calculation.

A previously developed electrostatic toroidal spectrometer is currently under minor modification and will be used to perform systematic measurements of the electron emission DDCS in solid foils of various Z number and density. A variety of light to heavy projectiles with beam energies from 0.1 to few 100 MeV/u will be studied, with a particular emphasize on carbon ions. Experiments will take place at UNILAC and SIS in GSI, as well as at MP-Tandem in MPI-Heidelberg for the low projectile energy range.



(a) 5.88 MeV/u U^{29+} on C_3F_8 [3]



(b) 2 MeV/u F^{6+} on a 10 μg.cm^{-2} C foil [4]

Figure 1: Electron momentum distributions (laboratory frame)

References

[1] M. Krämer and M. Scholz. *Phys. Med. Biol.* **45**:3319, 2000.
[2] M. Scholz et al. *Rad. Environ. Biophys.* **36**(1):59, 1997.
[3] U. Bechthold et al. *Phys. Rev. Lett.* **79**(11):2034, 1997.
[4] T. Zäpfel et al. *Nucl. Instr. and Meth. B*, in press, 2002.

Microdosimetric Characterization of the Therapeutic Heavy Ion Beam

R. Gerlach, H. Roos, A.M. Kellerer, Strahlenbiologisches Institut, Universität München

Relative Biological Efficiency in a complex and spatially variable radiation field of charged particles depends on several variables, such as the projectile type, the particle energy, the irradiated tissue, and the absorbed dose. Correct determination of the relative biological efficiency is therefore an integral part of the treatment planning system in heavy ion therapy. We compare the novel local effect model (LEM) for RBE determination [1] with the experience in the tumor therapy aquired with neutrons and protons in the past twenty years [2]. In the microdosimetric approach developed for neutron therapy [3, 4] the radiation field is characterized by measurements of the microdosimetric single event distributions of energy deposition. From a set of measured microdosimetric spectra and a corresponding set of biological experiments a so called biological weighting function *r(y)* is derived. The function *r(y)* characterizes RBE in its dependence on *y*, the microdosimetric analogue to LET. For the complex radiation fields applied in radiation therapy the overall RBE is calculated by weighting the measured microdosimetric spectrum with the biological weighting function:

$$RBE = \int r(y)d(y)dy \qquad (1)$$

The application of the algorithms developed for neutron therapy to heavy ion therapy leads to tentative values for radiation quality. From microdosimetric spectra measured in heavy ion fields, heavy ion RBE can be determined using the algorithm developed for neutron therapy. To implement this has been chosen as a first approach.

For the therapeutic carbon ion fields a special microdosimetric detector (TEPC) has been developed to determine the energy deposition in tissue volumes with diameter 1µm. The small tissue volume of density 1 g/cm^3 is simulated in terms of larger sensitive volume of a proportional counter. Due to the low density of the filling gas, one micrometer in tissue can be simulated by a detector diameter of 3 mm. Detector can be positioned in various depths of a Perspex phantom.

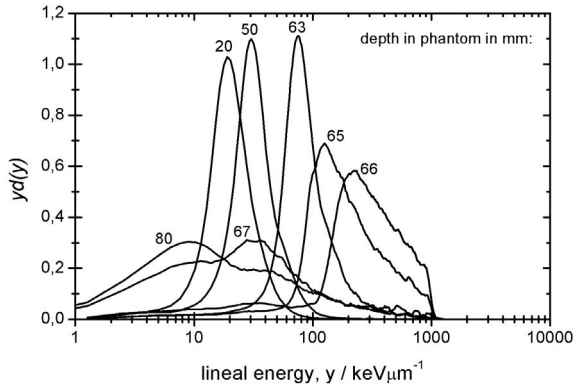


Figure 1: Dose distribution of lineal energy of ^{12}C ions at 194 MeV/u at different phantom depths.

Measurements were performed in the ^{12}C therapy beam at various energies and depths in the phantom. For a beam energy of 194 MeV/u, the microdosimetric distributions are given in Figure 1. In the plateau region, the distributions of lineal energies are shifted to higher values with decreasing ion energy. Close to the Bragg peak position the spectra are appreciably broadened due to the simultaneous presence of Bragg peak ions and fragments with their relatively low LET. Behind the Bragg peak the distributions are due to fragments - primarily protons and neutrons - with their smaller lineal energy.

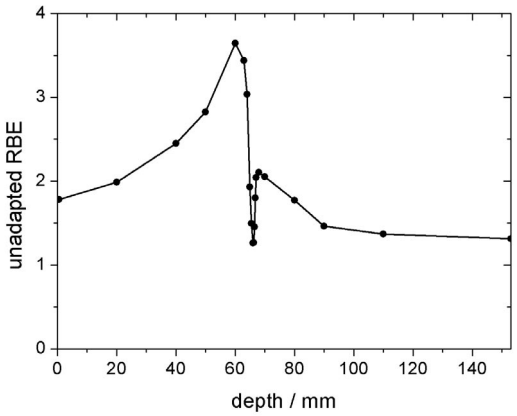


Figure 2: The tentative RBE versus depth. RBE values are calculated with the neutron therapy algorithm using the weighting function for neutrons.

The preliminary application of the algorithm from neutron therapy is a first step towards the comparison of models (Figure 2). The approximations that are acceptable for the neutron therapy model, need not be realistic with regard to heavy ions. RBE values for plateau in figure 2 agree with expected values of 1.7 of LEM but are overestimated in the Bragg peak at 69 mm. Figure 2 shows the increase of RBE towards the Bragg peak, but the maximum RBE values occur at lower depth than those derived in terms of the LEM of the GSI approach. The determination of a suitable biological weighting function for heavy ions will be the next step in these investigations. Tracks of recoil protons released by neutrons are less narrow then for Carbon ions and the saturation effect will therefore become important at higher values of LET, i.e. the weighting function for Carbon ions should be shifted toward larger values of linear energy. Another crucial aspect is the fragmentation of the primary beam projectile and target atoms. One needs to study the potential distortion of the microdosimetric distributions due to simultaneous traversal of the detector by pairs of fragments.

References

[1] A.M. Kellerer AM, GSI Report 97-09, September 1997
[2] P. Pihet *et al*, Radiat Prot Dosim Vol **31** No. 1/4, 437-442 (1990)
[3] A. Wambersie, Radiat Prot Dosim Vol **52**, nos 1-4,pp 453-460 (1994)
[4] T. Loncol *et al,* Radiation Protection Dosimetry, Vol. **52**, Nos 1-4, pp 347-352 (1994)

A new irradiation facility for biological samples at the UNILAC

W. Becher, M. Konradt, G. Lenz, R. Lotz, I. Ragaller, H. Schaub, M. Scholz, B. Voss, G. Kraft
GSI Darmstadt

The irradiation facility BIBA at the UNILAC has been used for more than 20 years for radiobiological experiments [1]. The facility had to be replaced now by a new, more flexible facility based on more advanced technology. At the same time, the newly constructed facility satisfies the legal regulations for handling of potentially hazardous biological material like e.g. tumor cells.

The new facility consists of a commercially available housing (glove box), in which an automatic sample changer is fitted. Samples are kept in up to 3 magazines filled with cell culture medium, containing up to 20 petri dishes each. 2 magazines are operated at room temperature and the third magazine is prepared for temperature control at 37°C or 4°C.

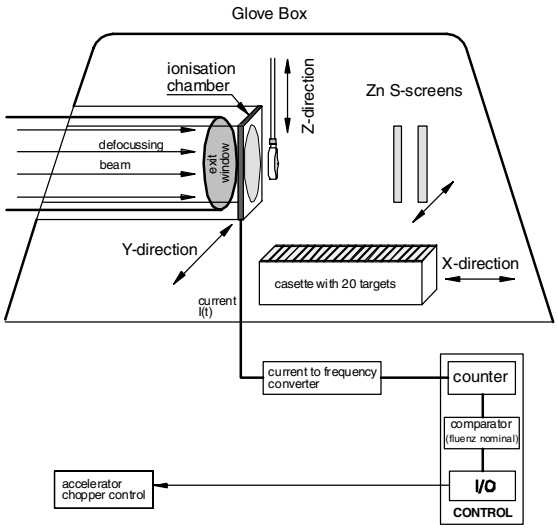
The titanium exit window of the beam pipe has been replaced by a kapton foil. The advantage is, that due to the higher mechanical stability no support grid has to be used. Consequently, sample wobbling is not necessary to achieve the required homogeneity of irradiation, and thus the sample holder and positioning mechanics could be kept simple.

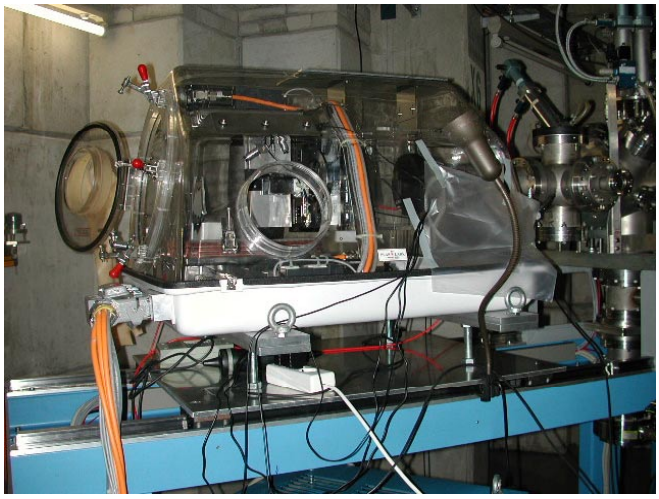
The sample changer consists of a stepper motor driven XY-stage for positioning of the desired magazine and sample below the exit window of the beam pipe. The samples are then picked by a vacuum grab and moved to the irradiation position using a stepper motor in z-direction. The vacuum grab allows to directly taking the petri dishes, whereas in the former system the individual samples had to be put in gold-coated steel rings that were taken by an electromagnetic grab.

Control of the irradiation facility is based on a PC-system, which replaces the formerly used dedicated hardware control. For the local motion control, a position controller (SIG Positec Automation) is used. The system is prepared for fully automatic irradiation of the samples. Irradiation control is now performed using an ionization chamber directly behind the exit window of the beam pipe. The monitor signal is obtained by means of a current amplifier (SR570, Stanford Research) and a voltage-to-frequency converter. If the desired dose or fluence is reached, the beam is switched off using the accelerator chopper control

The disadvantage of the additional energy degradation due to the thickness of the ionization chamber (30mm) is more than compensated by their better signal to noise ratio as compared to the formerly used secondary electron emission counter. This leads to a more reliable dosimetry and a higher dynamic range of beam intensities which can be handled now. Comparison with dosimetry based on nuclear track detectors (CR39) revealed a good linearity of the ionization chamber system in the fluence range from 10^3-10^7 particles/cm^2.

The system was installed at the beginning of 2001, and during the first beam times essentially the overall performance and the





dosimetric system were tested. Since June 2001, the new facility is used routinely for biological experiments.

The experience gained in these experiments lead to design of minor modifications, which will be realized in near future and will contribute to further optimization of the system.

The system is made for irradiations with carbon ions up to uranium ions; experiments using lighter particles down to protons are planned for the near future. For the lighter ions, energies in the range from 2 to 15 MeV/u can be used; for the heavier ions, the maximal energy is restricted at the moment to approx. 8 MeV/u. Irradiation of a sample typically lasts less than 1 min, so that any side effects due to irradiation on air can be kept at a minimum.

Reference:
[1] Kraft G, Daues H., Fischer B. et al., **NIM** 168 (1980), 175-179

Induction of checkpoint proteins TP53 and CDKN1A after heavy ion irradiation

C. Fournier, C. Wiese, S. Brons, G. Taucher-Scholz and G. Kraft (GSI, Biophysik)

CDKN1A (p21) was identified as a mediator of TP53-induced growth arrest [1] and a direct regulator of cyclin dependent kinase (CDK) activity [2]. Cyclin-CDK complexes promote cell cycle progression under normal conditions. In the presence of DNA damage, the TP53 tumor suppressor protein becomes stabilized and transcriptionally activates the cell cycle inhibitor CDKN1A. CDKN1A interacts with cyclin-CDK complexes to arrest cells in G1 phase of the cell cycle. Elevated levels of CDKN1A protein can lead to transient or permanent arrest in human fibroblasts. Permanent cell cycle arrest may progress into accelerated terminal differentiation and senescence, both of which have previously been described as fibrosis-related parameters after X-rays [3] and heavy ion irradiation [4].

Human fibroblasts (AG1522B) were exposed to X-rays (250 kV) or 11 MeV u^{-1} Carbon ions and TP53 and CDKN1A protein levels were examined using the western blot technique at several intervals following irradiation. Enhanced levels of TP53 were detected in AG1522B as early as 1.5 h after X irradiation, reaching a maximum at 3 h and declining to control levels within 24 h post exposure. The detected relative increase in TP53 protein correlated to the radiation dose applied. As shown in figure 1, the induction of CDKN1A protein was somewhat delayed with a detectable increase in protein levels only at 3 h and highest levels at 3 to 6 h after irradiation. For lower doses (≤ 4 Gy, in the graph shown for 0.5 Gy), CDKN1A decreased to nearly control levels within 24 h after irradiation. However, CDKN1A remained elevated (≥ 2-fold) to 8 or 16 Gy even 24 h after exposure. Preliminary data suggest that for these higher doses CDKN1A is still at elevated levels when AG1522B cells were analyzed 9 days post irradiation.

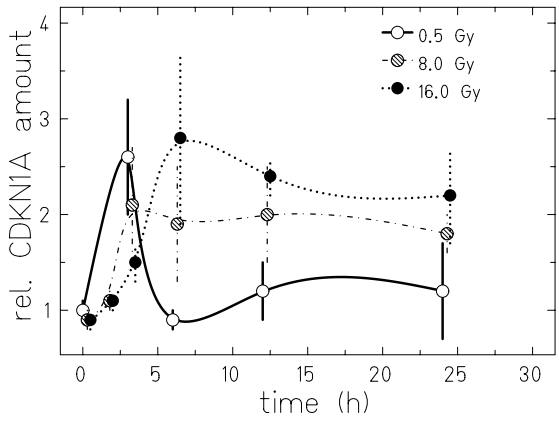


Figure 1: Relative increase of CDKN1A protein based on densitometric analysis of western blot signals of CDKN1A protein. AG1522B fibroblasts were exposed to X-rays (0.5 Gy, 8 Gy and 16 Gy) and incubated for various times before cell lysates were prepared. The signal intensities for CDKN1A were quantified by measuring the photons emitted by chemoluminescence and normalized to the corresponding tubulin signals. Data points represent the mean of two or three experiments ± 1 SEM.

Figure 2 shows a representative western blot obtained after irradiation of AG1522B fibroblasts with 11 MeV u^{-1} carbon ions. Compared to control levels, TP53 was elevated as early as 1.5 h following irradiation (fluences: 2×10^6 to 1.6×10^7 P cm^{-2}, corresponding to 0.5 to 4 Gy). At early times (up to 3 h post irradiation), higher levels of TP53 were detected compared to X irradiation. The induction of TP53 and the subsequent increase of CDKN1A were dose and time dependent. The highest levels of CDKN1A (approx. 4-fold over control) were reached 3 h after irradiation. For higher fluences (1.6×10^7 P cm^{-2}), the level of induced CDKN1A did not rise further but persisted at higher levels up to 24 h after irradiation. Interestingly, in preliminary experiments with low-energy Bi- and U-ions the maximum level of CDKN1A levels detected did not exceed a 4- to 5-fold induction.

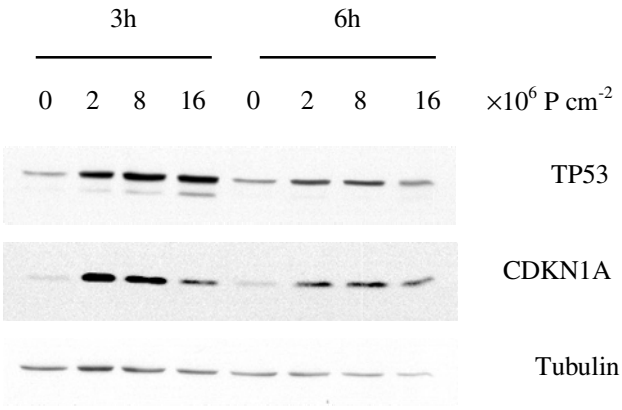


Figure 2: Western blot analysis of TP53 (upper panel), CDKN1A (middle panel) and tubulin as a loading control (lower panel) from cell lysates of human skin fibroblasts prepared 3 h and 6 h after irradiation with C ions.

The presented data are in line with results obtained for the radiation-induced cell cycle arrest [5] and the accelerated terminal differentiation of human fibroblasts [4]. The levels of the inducer protein TP53 and the effector protein CDKN1A are increased in a dose- and radiation-dependent manner. In addition, when DNA damage is more severe (8 Gy or 16 Gy X-rays, 4 Gy high-LET C-ions), CDKN1A persists at elevated levels for at least 24 h following the irradiation. We speculate that the persisting higher amounts of CDKN1A might be related to a permanent arrest as well as to accelerated terminal differentiation of human fibroblasts. These responses have both been observed after high-LET irradiation [4,5].

References

1 W.S. el-Deiry *et al.*, Cell 75, 817-825 (1993)

2 J.W. Harper *et al.*, Cell 75, 805-816 (1993)

3 H.P. Rodemann *et al.*, Kidney Int. 54, 32-36 (1996)

4 C. Fournier *et al.*, Int. J. Radiat. Biol. 77, 713-722 (2001)

5 S. Berger, Thesis Univ. Mainz, Germany (2001)

Investigation of radiation-induced damage in plasmid DNA by scanning probe microscopy

Y. Zhao, F. Hubenthal and F. Träger
Universität Kassel, Fachbereich Physik
Heinrich-Plett-Straße 40, D-34132 Kassel, Germany

DNA is undoubtedly an exceptionally important biological macromolecule; it is the medium encoding the information that directly or indirectly determines the structural and functional properties of all living organisms. Small structural differences in DNA induced, for example, by particle bombardment or electromagnetic radiation, often have far-reaching consequences and may lead to deleterious stages such as mutation, transformation or even cell death. The purpose of this work is to image the intact as well as damaged DNA using high resolution scanning probe microscopies with the objective to investigate the structural changes of DNA induced by ion radiation.

Since their invention, scanning probe microscopies have been used to image a variety of biomolecules [1-3]. In particular, imaging of DNA holds great promise for contributing to a detailed knowledge of the substructure of individual DNA molecules and the understanding of processes involving DNA. However, complications in sample preparation have until now hindered scanning probe microscopy from contributing vigorously to this field. One of the major difficulties is to deposit DNA onto a well-defined surface without aggregation. The concentration of DNA is an essential parameter that affects sample preparation and imaging. High concentrations tend to induce aggregation when depositing DNA onto the substrate, low concentrations make imaging difficult. We have imaged plasmid of different sizes deposited at different concentrations with scanning force microscopy (SFM). The DNA solution in 10 mM Hepes and 10 mM $MgCl_2$ buffer was deposited onto freshly cleaved mica, rinsed with distilled water and dried with compressed air. The results show that the longer the strand, the stronger the tendency to form entanglements; therefore, the optimal concentration depends on the size of plasmids.

The investigation of radiation-induced damage in DNA is of great importance for many applications, like for example clinical radiotherapy and the study of damaged DNA repair methods. So far, we have investigated UV-induced DNA damages by SFM, further experiments being planned to study the effects of heavy ion radiation on DNA. The effects of UV radiation on DNA have been widely studied [4]. Several methods have been applied to analyze DNA damage. SFM permits direct measurement of individual DNA molecules with an accuracy of a few nanometers independent of theoretical models, which was not previously achievable by other techniques. Using SFM, we have investigated UV-induced DNA strand breaks in plasmids. The supercoiled plasmid pGem7z(+) were irradiated with a pulsed UV-laser that emits 6 ns pulses at 266 nm. The plasmid may exist in supercoiled, relaxed-circular or linear conformation. Only one single strand break (SSB) is sufficient to relax DNA in supercoiled form to relaxed-circular form. One double strand break (DSB) will produce linear molecules. The SFM images showed that the extent of strand breakage was dose dependent. As a function of dose, the number of supercoiled DNA decreased and the number of relaxed-circular and linear molecules increased. With increasing dose we observed the appearance of heterogeneous linear pieces of DNA that were less than unit length. The shortest fragment was observed with about 300 bp. These results provide clear experimental evidence of the existence of DNA double strand breaks and demonstrate that short DNA fragments may be produced by high intensity UV radiation.

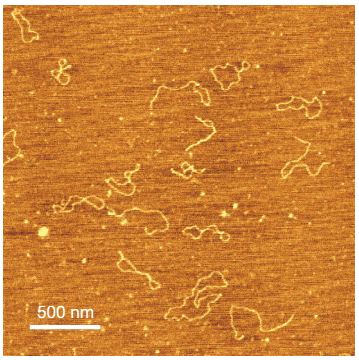


Fig. 1 Plasmids after UV-irradiation with the dose of 10 kJ/m^2.

We thank Prof. Dr. W. Nellen, Department of Genetics, University of Kassel, for providing DNA samples.

References

[1] O. Marti and M. Amrein, STM and SFM in Biology, Academic Press, New York, 1993.

[2] H. G. Hansma, Annual Review of Physical Chemistry 52:71, 2001.

[3] W. Schonert, PhD thesis, University of Kassel, 1997.

[4] for a review see, for example, E. Rabbow, PhD thesis, RWTH Aachen, 1999.

Non-random distribution of double-stranded DNA fragments generated by highly ionizing beams

A. Fricke, M. Kühne, M. Löbrich
Fachrichtung Biophysik, Universität des Saarlandes, Homburg

The high biological effectiveness of heavy ions for endpoints like mutation induction, neoplastic cell transformation or cell inactivation cannot be explained by the mere number of induced DNA double-strand breaks (DSBs), which does not vary substantially for varying radiation qualities. This has been taken as an indication that more complex DSBs are induced by high LET particles. Additionally, the size distribution of DNA fragments is different for different radiation qualities, because damaged sites are produced in close spatial proximity to each other along the track of the particle for densely ionizing radiations. The distribution of DSBs is also influenced by the organization of the DNA inside the nucleus. Sites which are considerable distances apart on the linear DNA molecule but were brought into close proximity by the structural organization of the chromatin are more likely to become simultaneously damaged by a single particle than sites which are kept distant by the chromatin organization [1]. This concept is utilised for our study to investigate higher order structure of chromatin in living mammalian cells.

Primary human lung fibroblasts (MRC 5) were grown to confluent monolayers, at which time the cells were in the G_0 stage of the cell cycle. After irradiation the cells were trypsinized, embedded in agarose plugs and lysed. DNA fragments of sizes between 20 kbp and 10 Mbp were separated by pulsed-field gel electrophoresis (PFGE) using different conditions. As an example, figure 1 shows the separation of fragments between 20 kbp and 400 kbp. X-ray experiments were performed in comparison to experiments with carbon (10 MeV/u) and uranium (6 MeV/u) particles, generated at the UNILAC accelerator.

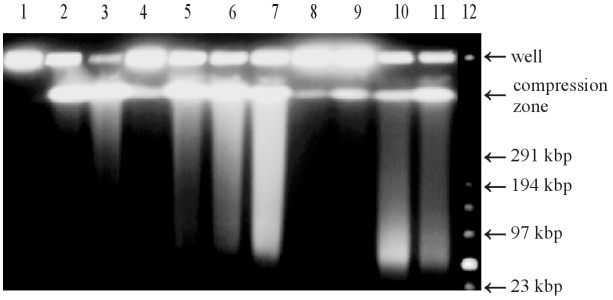


Figure 1: Example of a PFGE gel. *Lanes 1-3*: DNA irradiated with X-rays (control, 100 and 200 Gy). *Lanes 4-7*: DNA of carbon ion-exposed cells (control, 100, 200 and 400 Gy). *Lanes 8-11*: DNA of uranium ion-exposed cells (control, 800, 8000 and 4000 Gy). *Lane 12*: DNA size marker.

The fragment distributions were determined by quantifying the ethidium bromide fluorescence. Figure 2 shows DNA mass distributions as a function of migration distance. It can be seen that the shape of the intensity distributions is vastly different for the used radiation qualities. The distribution produced by uranium particles shows an excess of fragments particularly in the size range between 50 kbp and 100 kbp. This excess is much higher than that produced by an equal particle fluence of carbon ions. This clustering of double-stranded fragments might be influenced by the higher order chromatin structure of genomic DNA. If so, DNA loop structures [2] could correspond to the size range for which we observed DSB clustering.

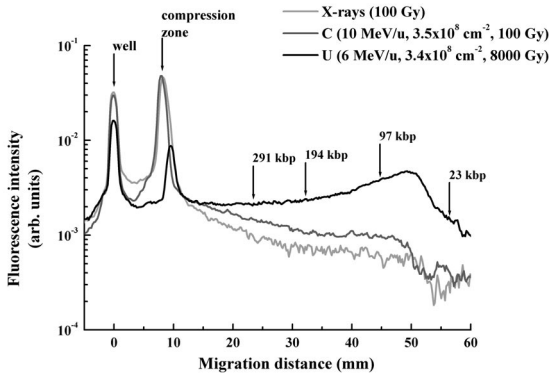


Figure 2: Fluorescence intensity distributions obtained from figure 1 (Lanes 2, 5 and 10). Data were normalized to equal DNA mass and the gel background was substracted.

Further studies aim at elucidating the heterogeneity of DSB induction within the genome and investigate the influence of chromatin structure on the non-random fragment distribution. Domains which are in a transcriptionally active form might be more susceptible to DNA lesions than genomic regions which are inactive such as centromeric or telomeric heterochromatin. To investigate the different genomic regions, PFGE gels were blotted onto nylon membranes, followed by Southern hybridization with region-specific DNA probes [3]. This approach is in progress (figure 3).

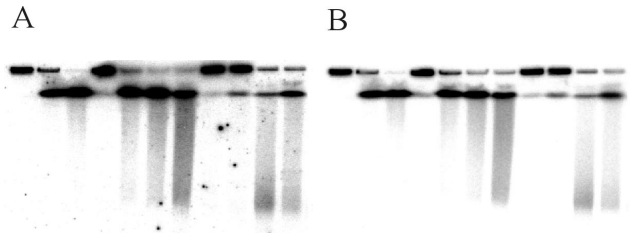


Figure 3: Southern blot of the gel in figure 1 analyzed with probe D21S1 (A) for measuring DSBs in transcriptionally active regions and probe D21Z1 (B) for measuring DSBs in centromeric heterochromatin.

References

[1] B. Rydberg et al., J. Mol. Biol. **284**, 71-84 (1998)
[2] J. W. Bodnar, J Theor. Biol. **132**, 479-507 (1988)
[3] K. Rothkamm, M. Löbrich, Mutat. Res. **433**, 193-205 (1999)

Influence of radiation quality and additives on the release of bases after ionising irradiation of DNA

Heike Maria Luxenburger, Chandrima Pal, Anne-Kathrin Hoffmann and Jürgen Hüttermann,
Fachrichtung Biophysik, Universität des Saarlandes, Klinikum Bau 76, D-66421 Homburg, Germany

DNA and its components irradiated at 300 K as solid samples (X-irradiation under nitrogen atmosphere; heavy ion bom - bardment in the beam vacuum) were used to study specificall the direct radiation effect [1]. Heavy ion bombardment with Bi, C, Ti, Xe (all 11.4 MeV/u) and Ni (6.0 and 11.4 MeV/u) gives a modified picture of radiation quality and therefore can be used as a comparative tool with X ray irradiation. The products generated after heavy ion bombardment and X-irradiation were investigated using HPLC and NMR. First, the diamagnetic products were identified by the chemical shift in 1D - ^{1}H-NMR and quantified relative to TSP as internal standard. Second, the bases were qualitatively characterised by their retention time in HPLC. For quantitative measurements the peak areas were evaluated and compared with the areas from external standards. Previous heavy ion experiments with nucleotides as model fo nucleic acids resulted in the formation of free bases as main diamagnetic products [2]. Ionising irradiation of dry DNA itself leads to release of the unaltered bases cytosine, guanine, thymine and adenine as well as the modified bases, e.g., 4,6 - Diamino-5-(formylamino)-pyrimidine (FAPY from adenine), 8-hydroxyadenine (8OHA) and 8-hydroxyguanine (8OHG). Furthermore we found an aldehyde-derivative (formate) as a final product of the sugar oxidation. The combination of two different methods i.e. HPLC and NMR allows to compare and mutually amend the results, because e.g. NMR can not be used for the analysis of guanine, 8OHG and FAPY, whereas the formate could be verified only with the help of NMR. Our first results show a good agreement of the product yield obtained from both methods (Fig. 1). The G-values of the products after X-irradiation and bombardment with accelerated ions are in the same order of magnitude. X -irradiation and heavy ion bombardment with Ti and Ni (11.4 MeV/u) lead to simila release of bases, whereas bombardment with Ni (6.0 MeV/u), Xe and Bi (both 11.4 MeV/u) ga ve a decreasing release. In comparison to low-LET irradiation bombardment with heav charged particles effected an increased formation of formate. The release of unaltered bases cytosine and guanine show opposite responses when irradiated with X-ray and heavy ions respectively. Among the two cytosine is found to strongly increase and guanine seems to decrease slightly in amount on heavy ion bombardment (data not shown).

We also compared the results from the pure DNA with that of DNA containing different el ectron scavengers for heavy ion bombardment with carbon. The modulating effect on the product formation of the electron scavengers potassium hexacyanoferrate(III), 2-nitroimidazole and riboflavin were used to elucidate the reactions leading to the reductiv e products. The use of the electron scavengers causes a reduction of the yield of the released bases. In this case the electron scavenging capacity decreases from potassium hexacyanoferrate(III) to riboflavin (Fig. 2). Our results lead to the assumption, t hat the radical anions are involved in the release of bases, which in turn is connected with strand breaks in DNA.

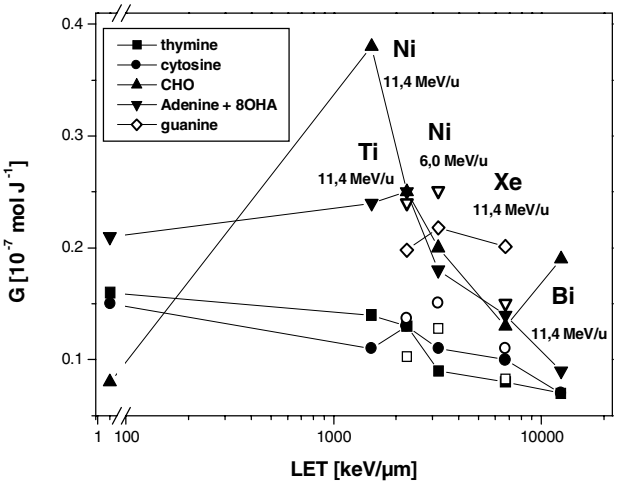


Fig.1 LET-dependence of product formation from DNA b NMR (closed symbols) and HPLC (open symbols)

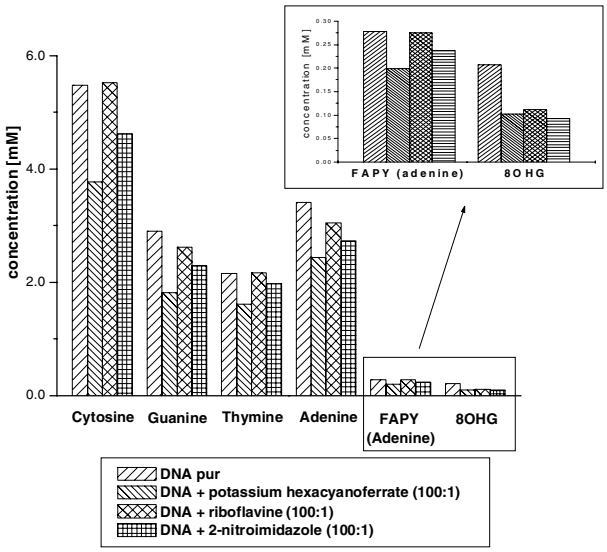


Fig.2 Base release from DNA after bombardment with carbon ions in the presence of electron scavengers (molar ratio 100 nucleotides / 1 additive) in comparison with pure DNA

References

[1] A.-K. Hoffmann and J. Hüttermann, Int. J. Radiat. Biol. 1997, 72, 735-744

[2] A.-K. Hoffmann and J. Hüttermann, Int. J. Radiat. Biol. 2000, 76, 1167-1178

Complex chromosome aberrations induced by carbon ions of different energies in tumor cells.

Hana Hofman-Hüther, Margret Rave-Fränk, Patricia Virsik-Köpp

Centre of Radiology, Medical Faculty, University of Goettingen, Germany

High-LET radiation tracks induce clustered damage, i.e. multiple closely spaced complex DNA lesions in irradiated cells. DNA damage induced by high-LET radiation is more difficult to repair. Complex exchange-type rearrangements are likely to result from interactions among these multiple lesions. Complex chromosome aberrations result from three or more DNA lesions in two or more chromosomes. Their formation also depends upon the chromosome distribution within the cell nuclei.

We investigated the induction of complexes by carbon ions in a radiosensitive human breast adenocarcinoma cell line MCF-7 and in a radioresistant colon carcinoma cell line WiDr. Both cell lines contain the same number of chromosomes, but differ in their nuclear size, MCF-7 cells have much larger cell nuclei than WiDr cells. Chromosomes No. 2, 4, and 5, which show a low rate of clonal and non-clonal structural aberrations, were chosen for a detailed FISH analysis.

The total visible complexes (complexes including insertions) TVC per cell observed in WiDr and MCF-7 cells after irradiation with D = 4 Gy of 200 kV X-rays or carbon ions are shown in Fig. 1.

The biological effectiveness of carbon ions was strongly increased for all three chromosomes in both cell lines, whereby MCF-7 cells were more sensitive than WiDr cells. At a low dose of 1 Gy, X-rays as well as carbon ions induced none or negligibly few complex exchanges in either of the evaluated chromosomes (data not shown).

Extended Bragg peak ions damaged MCF-7 cells heavily, most cells displayed decondensed chromosomes, and thus aberrations were not scorable. This effect was not observed in WiDr cells.

In general, carbon ions induced aberrations of a greater complexity than X-rays did. Insertion frequencies in relation to translocations were characterized by the index I.

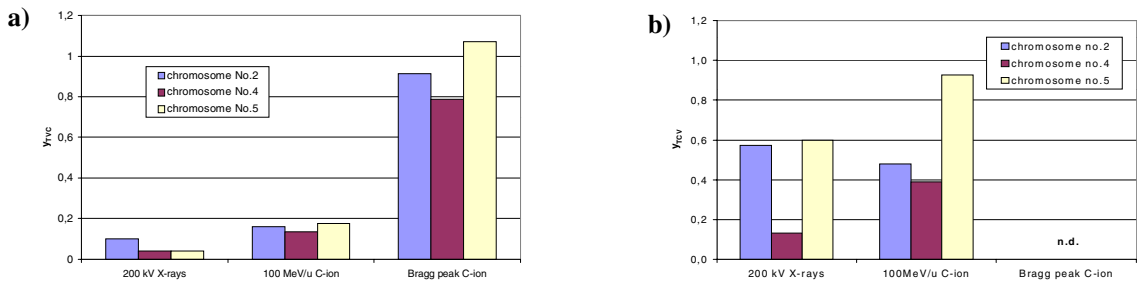


Figure 1: Frequencies of total visible complexes per cell, y_{TVC}, observed after irradiation with D = 4 Gy of 200 kV X-rays or carbon ions are plotted for WiDr cells (a) and for MCF-7 cells (b). Carbon ions with energy of 100 MeV/u and ions of the extended Bragg peak were used for irradiation performed at SIS (GSI Darmstadt).

Complex aberrations involving the painted chromosomes were scored; when two or more painted chromosomes were damaged, each complex exchange was scored separately. Insertions and various multiple translocations combined with dicentrics were frequently induced, together with a variety of other even more complex exchanges.

Additionally, insertions were evaluated as a separate class and compared with simple translocations. The index I (defined as sum of all translocations / sum of all insertions) implied as a fingerprint of high-LET radiation in normal cells was then determined.

Index I values calculated for cells irradiated with D = 4 Gy of 200 kV X-rays or (100 MeV/u and extended Bragg peak) carbon ions, are shown in Table 1. In comparison with X-rays, insertions were induced more frequently by carbon ions in both tumor cell lines, with MCF-7 cells being far more sensitive than WiDr cells. The index I decreased strongly for carbon ions, suggesting the suitability of this index as a fingerprint of high-LET radiation in the investigated tumor cells as well. The role of chromosomal topology remains unclear and needs further investigations.

Table 1: The mean values of index I for both cell lines irradiated with D = 4 Gy. The partial chromosome data were summed up for the three evaluated chromosomes and the corresponding mean values were calculate d.

Cell-line	200 kV X-rays	100 MeV/u C-ions	Extended Bragg peak C-Ions
MCF-7	7.0	2.5	n.d.
WiDr	12.5	9.2	2.5

Use of Human Lymphocytes for Radiation Risk Assessment

T. Größer, P. Hessel and S. Ritter (GSI, Darmstadt), E. Nasonova (JINR, Dubna, Russia),
E. Gudowska-Novak (Institute of Physics, Krakow, Poland)

Chromosome aberrations are regarded as the most sensitive indicator of radiation-induced genetic alterations. In particular the frequency of aberrations in peripheral blood lymphocytes (PBLs) is used to estimate the dose to which an individual has been exposed. Moreover, aberrations in PBLs are considered as a promosing tool in predictive assay research aiming to develop a test for individual normal tissue tolerance.

According to the standard protocol cytogenetic damage is analysed in first generation metaphases collected at one sampling interval. In the case of PBLs, metaphases are routinely harvested 48h after initiation of the culture. Yet, there is increasing evidence that radiation-induced cell cycle delays affect the aberration yield. In particular after high LET exposure a drastic increase in chromosomal damage with sampling time has been observed, i.e. heavily damaged cells have been found to enter mitosis later than slightly damaged cells. Consequently, depending on the subpopulation of cells which reachs mitosis at that particular sampling time chosen for the analysis, the delivered dose can be substantially under- or overestimated (e.g. [1,2]). To contribute to this issue in first experiments the cell cycle progression of PBLs obtained from 5 healthy donors has been measured. Exemplarily in figure 1 the fraction of mitotic cells found 48h after initiation of the culture is plotted indicating a pronounced intra- and inter-donor variability. Interestingly, the data obtained for donor C do not show a significant intra-donor variation.

Further, more detailed investigations of the proliferation of PBLs revealed a marked difference in the cell cycle transition time of untreated control cells, i.e. PBLs needed up to 96h to reach the first mitosis after initiation of the culture (see fig. 2). Following irradiation a dose-dependent delay in the entrance time to mitosis, reflected in the shift of the maximum of the mitotic indices, was found. Also, a general depression of the mitotic activity occurred as exemplarily shown in figure 2. Again, all cell cycle studies perforemed up to now demonstrate a pronounced intra- and interdonor variability.

As expected (3) similar variations are found on chromosomal level. For example, following X-irradiation cells of donor A were more sensitive to aberration induction than those of donor B (fig. 3). The same trend was observed after exposure to 400 MeV u C ions. Interestingly, neither after X-irradiation nor high energy C ion exposure a significant fluctuation in the aberration yield with sampling time has been detected. In contrast, in first experiments where PBLs of donor A were exposed to high LET particles, i.e. 200 MeV/u Fe ions with a LET of 500 keV/µm, a dramatic increase in the frequency of lesions with time has been observed. Thus, after high LET exposure the restriction of cytogenetic studies to only one sampling time will unavoidable lead to misleading results. Morever, intra- and interdonor variability, which effect significantly the yield of radiation-induced aberrations has to be considered.

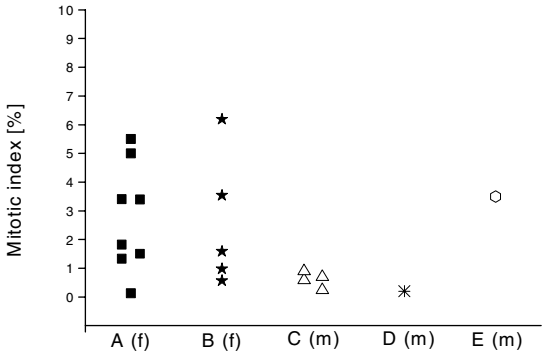


Fig. 1: Inter- and intradonor variability in the fraction of PBLs reaching mitosis by 48h. Cells have been obtained from healthy non-smoking volunteers (age: 38 to 50, f=female, m=male). Measurements were performed within a period of 3 years.

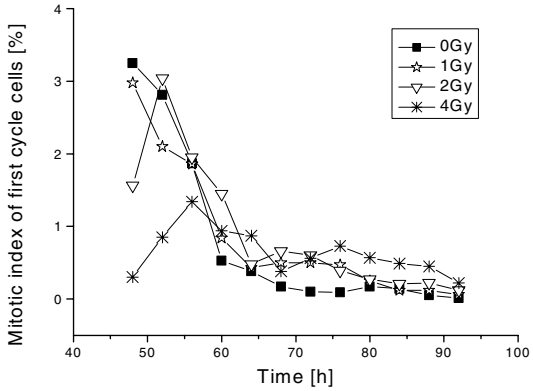


Fig. 2: Proportion of cells reaching the first post-irradiation mitosis as a function of sampling time. In this experiment PBLs of donor B have been exposed to 100 MeV/u C ions.

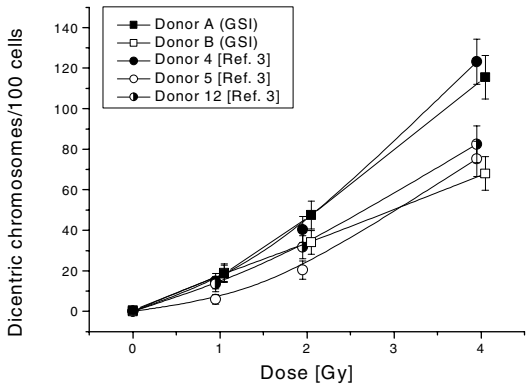


Fig. 3: Yields of X-ray induced dicentric chromosomes. PBLs of donor A (2 experiments) and B (1 experiment) were exposed in vitro and dicentrics were scored in first generation metaphases 48h post-irradiation. For comparison data from reference [3] are plotted.

References

[1] Nasonova, E. et. al., Phys. Med. XVII, 198-201 (2001)

[2] Ritter, S. et al., GSI Scientific Report 2000, 154 (2001)

[3] Virsik-Peukert, P. et al., Radiat. Res. 148, 209-215 (1997)

Heavy Ion Irradiation of Human Colon Adenocarcinoma Cells in Multilayer Culture

J. Topsch, W. Müller-Klieser, University of Mainz
M. Scholz, G. Kraft, GSI Darmstadt

Introduction

In this project we study the effect of heavy ion irradiation on radioresistant human tumor cells which are grown in a three-dimensional tissue-like culture model.

Materials and Methods

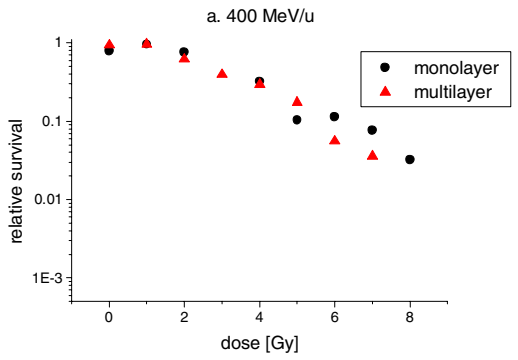
WiDr colon adenocarcinoma cells were cultured in either conventional monolayers or cellular multilayers in a specific culture chamber [1]. Cell cultures were irradiated with 250 kV x-rays or with a ^{12}C-beam. Heavy ion irradiation was performed at 400 MeV/u in the plateau region, simulating the situation of normal tissue, and in the extended Bragg-peak for mimicking the targeting of tumor tissue. After radiation the cells were trypsinized and diluted for standardized clonogenic assays. The relative cell survival was determined as a function of radiation dose.

Results

The relative cell survival at 400 MeV/u shows only little differences between monolayers and multilayers (Fig. 1a). In contrast, in the extended Bragg-peak we notice a reduced sensitivity in multilayers compared to monolayers (Fig. 1b). Unlike in monolayers, there is a little or no difference in cell survival of multilayers between irradiation at 400 MeV/u (Fig. 2a) and the extended Bragg-peak (Fig. 2b). Such a radioresistance emerged only in a three-dimensional tissue-like culture of the cells. Our observations are in accordance with results obtained previously in a preliminary study [2].

Discussion

The extremly high radioresistance of human WiDr colon adenocarcinoma cells in monolayers can be further enhanced by three-dimensional cell-cell interaction. There is evidence from the literature that such a multicellular resistance may be induced by the overexpression of the rad51 gene the product of which is involved in the repair of double strand breaks [3]. Since heavy ions generate this type of DNA damage, it may be worth assaying WiDr mono- and multilayers for the expression of this gene.



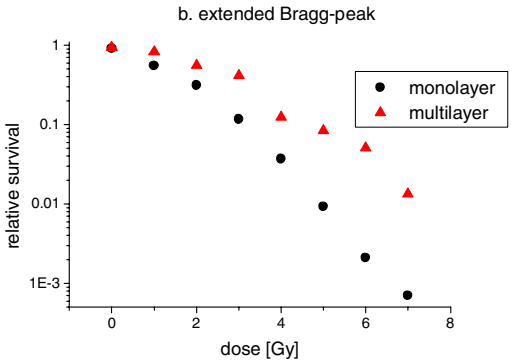
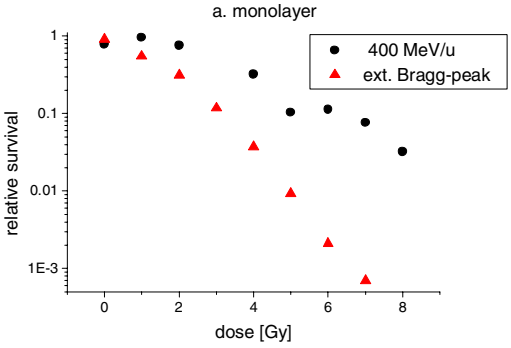


Fig. 1: Relative cell survival of WiDr human colon adenocarcinoma cells as a function of heavy ion energy and dose: a. 400 MeV/u, b. extended Bragg-peak



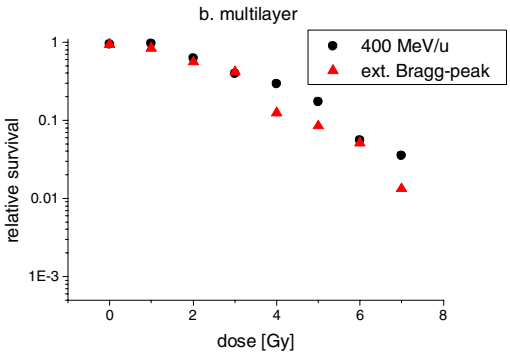


Fig. 2: Relative cell survival of WiDr human colon adenocarcinoma cells as a function of heavy ion energy and dose: a. monolayer, b. multilayer

References

[1] Minchinton A.I., Wendt K. R., Clow K. A. and Fryer K. H., Acta Oncologica 36, 13-16 (1997)

[2] Winhart S., Müller-Klieser W., GSI Scientific Report 2000

[3] Maacke H, Jost K, Opitz S, Miska S, Yuan Y, Hasselbach L, Luttges J, Kalthoff H, Sturzbecher HW, Oncogene 2000 May 25;19(23):2791-5

RBE measurements in the epithelial megacolony, a simplified *in vitro* tumour model

J. Kummermehr[1], R. Sanchez-Brandelik[1], M. Scholz[2]
[1]GSF Neuherberg, [2]GSI Darmstadt

Megacolonies generated from squamous carcinoma cells are tightly packed quasi-epithelial aggregates, organized into a highly proliferative marginal rim and a multilayered contact-inhibited core region [1]. Using a murine cell line (AT478) this model has been employed to quantify RBE values of the accelerated carbon ion beam versus a Cs-137 reference source, as it is well suited to quantitative measurements by in situ endpoints such as surviving clonogen expansion, megacolony growth delay and permanent megacolony cure.

In a qualitative way, i.e. regarding morphological expression of cell damage, dead cell clearance or regrowth rate of surviving cells, megacolony behaviour appeared independent of the LET. By contrast, the RBE values measured for the quantitative endpoints demonstrated a higher than expected effectiveness of carbon ions, in particular if one considers the high single doses that were used in most of the experiments. Thus, in megacolonies exposed to 75MeV/u monoenergetic ions (endpoint growth delay, dose level 12-14Gy) the observed RBE amounted to 1.4-1.5, while exposure to a 1 cm SOBP (endpoint colony cure, dose level 12-18 Gy) rendered an RBE of 1.9-2.0 (figure 1).

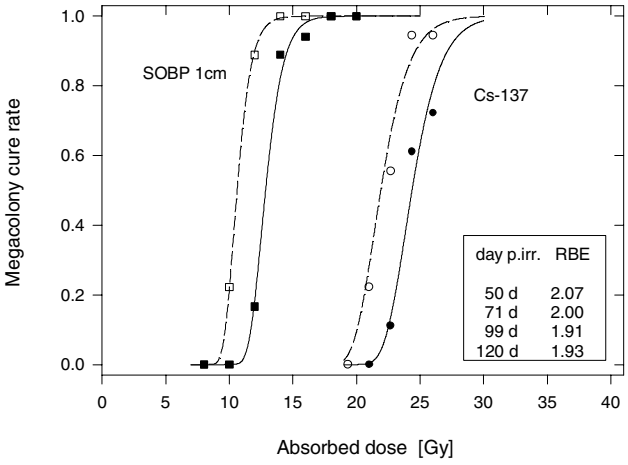


Figure 1: Dose dependence of megacolony cure after single dose irradiation with 1 cm SOBP carbon ions or with Cs-137, assessed between 50 days (dashed curves, open symbols) and 120 days (solid curves, full symbols).

These RBE values were consistently higher than those predicted by the biophysical 'local effect model' [2]. Using a protocol that involved 1, 3 or 6 fractions of carbon ions (145 and 75 MeV/u) terminated by a photon top-up dose, it was also possible to measure the response to small dose fractions down to 1.4 Gy; the results showed dose-dependent RBE values up to 2.0 (figure 2).

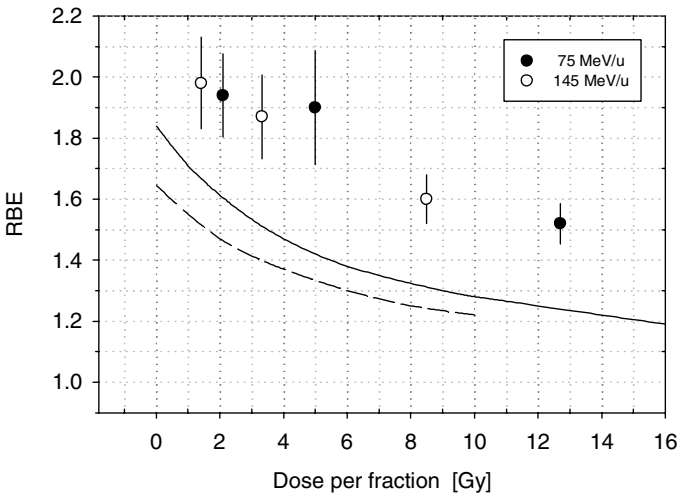


Figure 2: RBE values as a function of dose, as measured in a fractionation experiment for two monoenergetic carbon ion beams (endpoint megacolony cure). Curves indicate predicted RBE's for the two energies

One possible explanation for this unusually enhanced effectiveness could be insufficient oxygenation, imposed by the need to keep the culture bottles filled up and unventilated over prolonged experimental periods. Hypoxia would affect the results differently for photons, plateau and peak ions, due to their different LET, and would render spuriously high RBE values. However, neither direct analysis of pO_2 profiles in sentinel bottles kept unventilated over more than 4 days nor the radiobiological responses measured in photon experiments with increasing occlusion periods supported this possibility. As another source of error the influence of megacolony transport will yet have to be checked, since so far all reference experiments were conducted at GSF (Neuherberg), albeit with the identical megacolony passages and culture conditions as used in the ion beam experiments.

In summary, the results obtained to date indicate a greater than expected biological effectiveness of the energy modulated raster scan beam of ^{12}C ions in squamous cell carcinoma megacolonies in vitro.

References:

[1] J. Kummermehr, E. Malinen, S. Freykowski, M. Sund, K.-R. Trott: The influence of autologous tumor fibroblasts on the radiosensitivity of squamous cell carcinoma megacolonies. Int. J. Radiat. Oncol. Biol. Phys. 50: 229-237 (2001)

[2] M. Scholz M, A.M. Kellerer, W. Kraft-Weyrather, G. Kraft: Computation of cell survival in heavy ion beams for therapy. The model and its approximation. Radiat. Environ. Biophys. 36: 59-66 (1997)

Treatment planning for the GSI radiotherapy

M. Krämer, B. Hasch, E. Rietzel, U. Weber, GSI; O. Jäkel, DKFZ

As in the previous years our standard treatment planning software TRiP98 [1, 2, 4] was used in combination with the Voxelplan environment throughout the year 2001 for the planning of all 39 patients [3]. Specific modifications were the addition of support for the irradiation facility in CAVE A and a new contour format. Work is in progress to include an improved beam model as well as simultaneous optimization of multiple beam ports into the production version.

CAVE A support

In 2001 an additional irradiation facility became operational in CAVE A [5]. Although as many technical features as possible have been replicated from CAVE M, some important ones are not available. From the viewpoint of treatment planning the main restriction is the lack of full "MEFI" operation, that is, only a limited number of accelerator energies with fixed foci are available. Active energy variation thus is not possible so that depth variation can only be achieved with a binary range shifter. It consists of 10 plates of PE material with water-equivalent thicknesses covering the range from 0.06 to 28.8 mm, approximately. For treatment planning this implies that, in order to achieve Bragg peak positions with a given spacing, beam energies are selected "freely" and have to be combined with the given set of range shifter plates. Hence several beam energy slices are generated with the same energy but different shifter settings. Since the limiting resource is the number of available accelerator energies the setup algorithm tries to minimize the use of different energies and exhausts the full shifter range before choosing a new energy. This strategy possibly deteriorates beam quality by introducing additional material in the beam path, generating increased nuclear fragmentation and multiple scattering.

Dose calculation and optimixation is similar to CAVE M with the exception that each energy slice now may include the accumulated plate thickness as an extra water-equivalent offset. Figure 1 shows a planning result under the same conditions for CAVE M and A, respectively. The effective dose distribution appears to be worse than in CAVE M by about 5 to 15%.

Work in progress

With the Heidelberg clinic facility appearing at the horizon our beam model is currently being reworked.

One direction is an improved description of nuclear fragmentation, which led from the currently considered six nuclide species to 18, including deuterons and tritons. Since this leads to significant increases of storage and CPU time requirements appropriate compression methods must be found in order to end up with acceptable turn-around times for treatment planning.

Although carbon ions undergo only very little lateral deflection, their fragments, in particular light ions, might cause a significant broadening of the dose distributions beyond the Bragg peak. Thus additional lateral components must be added to the depth dose distribution. Since they vary with increasing depth they require careful implementation in order not to be too time consuming in regular treatment planning.

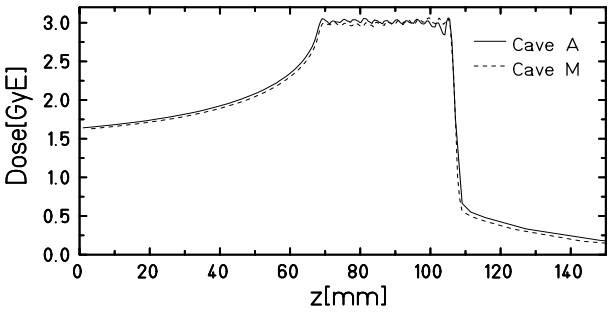


Figure 1: Biologically equivalent depth dose distributions with active (CAVE M, dashed) and passive (CAVE A, solid) energy variation.

Significant improvements are expected from simultaneous multiport optimization similar to techniques for photon IMRT [6]. First TRiP98 calculations with two opposing fields yielded promising results. However, due to the limited number of fields for carbon ions and the physical properties of heavy ion beams like the special shape of the depth dose profile, the parameters of the photon optimization algorithm have to be modified substantially.

Miscellaneous improvements

Further modifications in TRiP98 concerned additional means of 3D dose prescription by allowing dose ramps to level off in their proximal and distal part.

New contour file formats (VDX 2.0, HED 1.4) (implemented in parallel to the old one) support non-equidistant CT slices and allow interoperability with IMRT planning at the DKFZ.

References

[1] M. Krämer et al, Phys. Med. Biol., 45/11 (2000) 3299
[2] M. Krämer et al, Phys. Med. Biol., 45/11 (2000) 3319
[3] O. Jäkel et al., Phys. Med. Biol., 46/4 (2001) 1101
[4] M. Krämer, J. Radiat. Res. 42, 39-46 (2001)
[5] D. Schardt et al, this report
[6] Th. Bortfeld et al, Phys. Med. Biol. 35 (1990) 1423

Compensation of target motion in magnetic raster scanning at GSI

S.O. Grözinger, W. Becher, T. Haberer, E. Rietzel, G. Kraft (GSI)
Q. Li (IMP-CAS Lanzhou, China)

Using the magnetic raster scanning method developed at GSI very precise dose distributions can be applied to immobilized tumors as for example in the head. For moving tumors interferences between target motion and scanning cause intolerable dose inhomogeneities [1] making online correction necessary.

In general any target motion can be regarded as a superposition of three components:

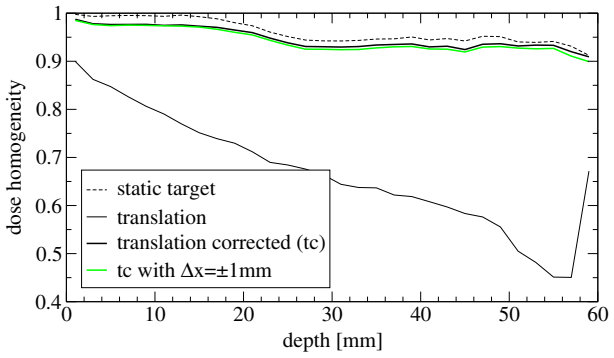
translation the displacement of the volume element's (voxel) center coordinates in all three dimensions

density changes due to conservation of mass any motion inside of matter causes local changes in density

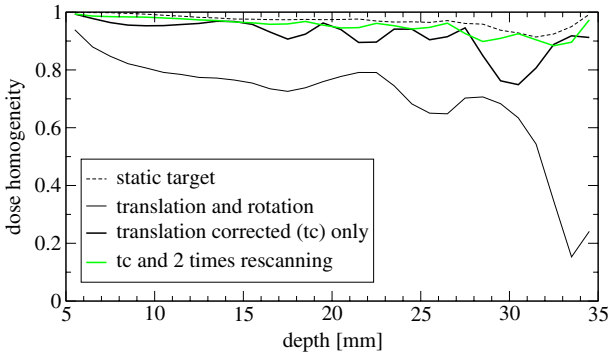
rotation a superposition of three translations but with changed orientation of the voxels relative to each other

If the motion is slower than the maximum scanning velocity the lateral target displacement (in the plane orthogonal to the beam) can be corrected by adapting the beam's position when moving to the next point. In Fig. 1(a) the effect of cyclic breathing related organ translation [2] on the dose distribution inside a spherical target is calculated. As a reference the dose homogeneity defined as the standard deviation of the single-voxel-dose distribution for each iso-energy slice (IES) is plotted agains the depth of the slice. Compared to the static case the presence of a target translation significantly reduces the homogeneity. The peculiar dependence of the homogeneity on the depth of the slice reflects on the one hand the influence of the IES's size[1] (dominating for deeper slices) and on the other hand the positive effect of averaging due to pre-irradiation[2] of the more proximal slices when the distal ones are treated. By actively correcting the beam's position the effect of the target translation can nearly be compensated even with an assumed gaussian-distributed uncertainty in the position measurement of ±1 mm. In the case of rotation the displacement is connected with a change in orientation of the voxels. If the rotation is large the voxels usually in front of the just irradiated one are shifted out of the beam and others in. Consequently the pre-irradiation pattern is dynamically changed and the homogeneity reduced. Since voxels having already received their final dose are included it cannot be actively compensated. The simulations in Fig. 1(b) show that scanning the volume several times with a lower dose (rescanning) improves the homogeneity in these cases.

To verify the calculations a prototype setup for the active target motion compensation is currently being implemented and tested in Cave M. The fast position correction function of the scanning control system can be exploited to compensate the lateral target motion. If in addition to the beam position signal from the MWPC the current target displacement data is provided the function will correct for both deviations. Since the penetration depth of the particles is determined by the particle's energy the compensation for z-displacement as well as density changes require adapting the energy loss along the beam's path. In the prototype setup this will be done using a set of plexiglas wedges driven by linear motors [3].



(a) translation



(b) translation and rotation

Fig. 1: Simulated dependency of dose homogeneity on depth of IES for a spherical dose distribution in water-equivalent material based on the following parameters: (a) translation (12,5,0) mm, ν=0.25 Hz, diameter of sphere 60 mm (b) translation (15,5,0) mm and rotation (0,5,0) °, ν=0.25 Hz, diameter of sphere 30 mm

References

[1] Q. Li et al, GSI-report 2001-1
[2] L. Ekberg et al., Radiother Oncol 48 (1998) 71
[3] U. Weber et al., Phys. Med. Biol. 45 (2000) 3627

[1] The larger the slice the longer the irradiation time and thus the stronger the influence of the motion.

[2] Each IES except of the very last one gets part of it's final dose from pre-irradiation due to the bragg curve's plateau distribution of the deeper slices. The smaller the depth of an IES the more slices contribute to the dose of this slice.

The patient fixation unit for the treatment chair in Cave M

P. Heeg (DKFZ), D. Schardt, J. Störmer (GSI)

Introduction: The GSI treatment chair[1] has been designed as a patient positioning assembly complementary to the patient couch. This chair will be used for treatments within the head and neck region. After adjusting a target point to the isocenter by means of three orthogonal translations, the irradiation angle is adjusted by a rotation around a vertical axis and an isocentric tilt of that axis. The setup consists of the positioning unit with its five motor driven degrees of freedom, a transport unit for carrying the chair conveniently between parking position and irradiation position, and the patient fixation unit which includes seat, mask holder and foot rest. Positioning and transport unit have been installed in Cave M in the second half of 2000 and extensive investigations concerning the mechanical characteristics of the positioning unit, namely the stability of the two rotational axis in the room, have been performed since then. The task of the patient fixation unit is a secure, stable and comfortable fixation of the patient and a steady holding of the target point to the isocenter for all rotation and tilt angles.

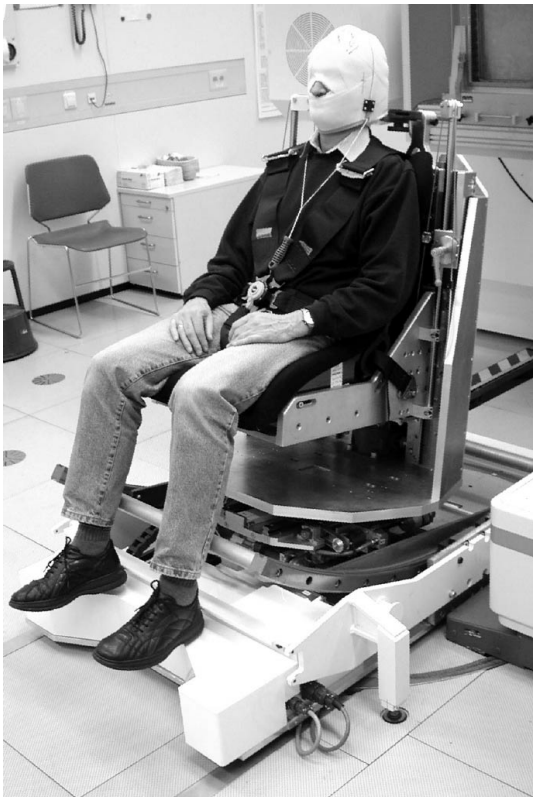


Fig.1: Patient chair in irradiation position with the fixation unit mounted on the positioning unit.

Construction: The fixation unit consists of a main frame fixed to the vertical translation. On this frame are mounted the seat, the mask holder and the foot rest. The seat is a modified seat of a racing car made of fibreglass reinforced plastic with a comfortable yet not too soft surface giving good lateral support to the patients pelvis and trunk. The patient can be buckled up by a 5-point belt system, also manufactured originally for motor sports purposes. The upper part of the seat had to be shortened to give access to the mask holder also for small patients.

The mask holder is adjustable manually relative to the main frame of the fixation unit. The vertical range is large enough to take into account the different patient heights and allows to put the opened mask on the patients head from above. For a safe procedure, the weight of the mask holder is compensated by balancers as used for hand held machines at assembly lines.

Once the patient is fixed in the mask, the position of the mask holder relative to the patient in the seat is locked, and vertical translations can be performed with seat and mask holder securely fixed to each other. For a maximum rigidity the cranial/caudal movement of the mask holder is additionally guided on the linear motion rails of the vertical translation guide of the positioning unit.

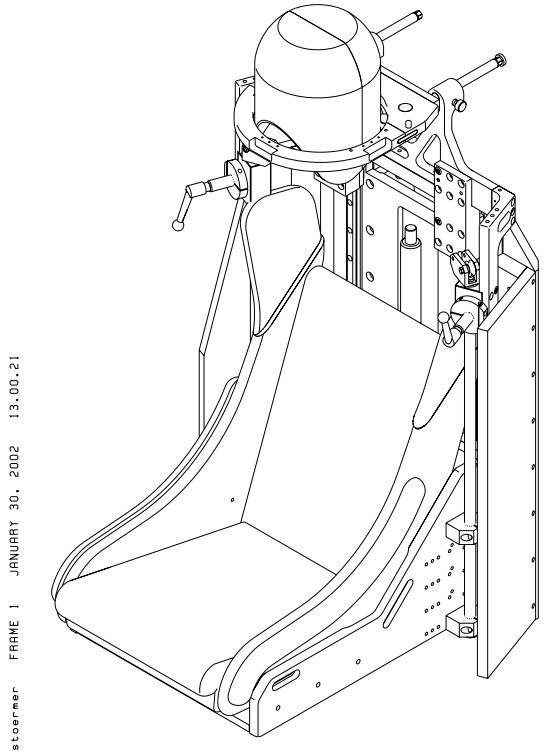


Fig.2: Drawing of the fixation unit and the vertical translation drive.

Conclusion: The realisation of a secure and precise fixation unit required some rather unconventional details in the construction. Despite a very limited space amount behind the seat shell and large lever lengths a position stability of the mask in the room of $< \pm 0.5$ mm is possible.

[1] P. Heeg, S. Kuhn, D. Schardt, D. Schulz-Ertner: A treatment chair for the therapy facility, GSI 2000-1 167

X-ray image intensifiers for patient positioning

E. Rietzel, D. Schardt, I. Ragaller; GSI Darmstadt
P. Heeg; DKFZ Heidelberg

Tumor conform radiotherapy with carbon ions is performed since December 1997 at the GSI treatment unit in Cave M. Using a fully active rasterscan system a high degree of conformity in the range of 1-2 mm has been achieved. In order to assure such a precision for the irradiations, the correct position of the patient relative to the isocenter has to be checked thoroughly before each patient treatment.

For the 3D position verifications a system consisting of three orthogonal X-ray tubes is used. So far the images were recorded on X-ray films. In 2001 two image intensifiers coupled to CCD-cameras were installed.

Image intensifiers in combination with CCD-cameras have several advantages compared to films: lower dose to the patient, no time required for film development, and the possibility of computerized matching of images.

Each of the digital image acquisition systems consists of an X-ray intensifier (Siemens Sirecon 30-2) with a nominal entrance field size of 300 mm coupled directly to a CCD-camera with 756 x 582 pixels. A special control unit connected to the intensifiers, the cameras, and the X-ray generator manages the power supplies as well as the triggering, gain, zoom, and image hold. The recorded images are read out with a dedicated PCI-card (Kappa, Matrix Vision) in a WindowsNT computer.

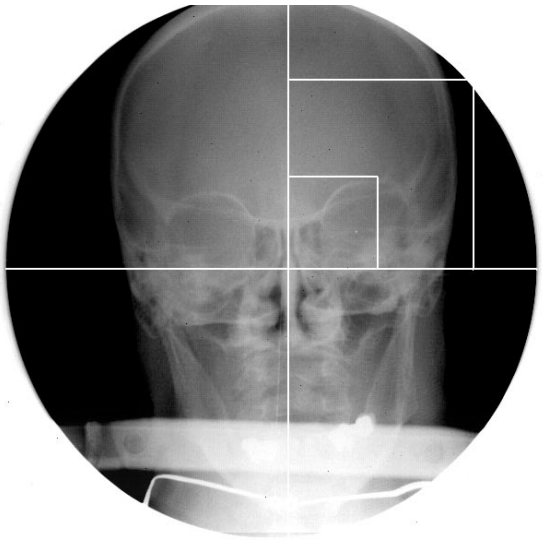
The correct patient position is recorded on a reference image before the first irradiation. To verify the patient's position in the reference image it is matched with a digitally reconstructed radiograph calculated with the planning CT-data.

The top figure shows one image as recorded by the image intensifier in vertical direction. The white lines are shadows of a wire crosshair mounted in front of the image intensifier in order to mark the position of the isocenter.

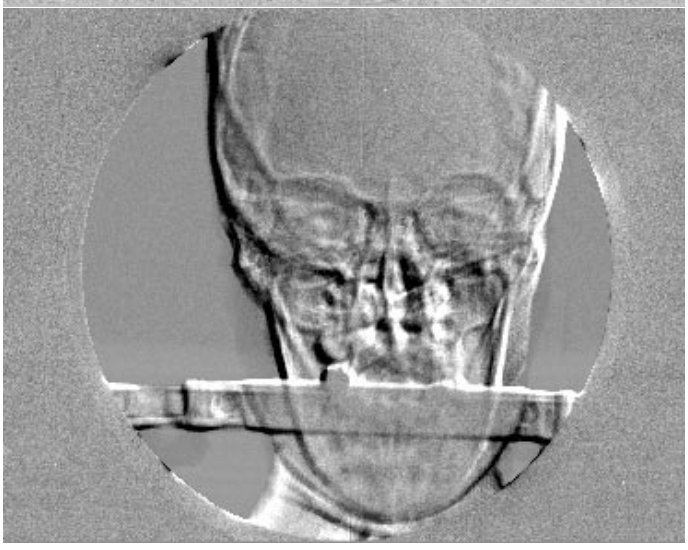
The other images show difference images between the correct and the actual patient position. Shifts of the patient's anatomy lead to high contrast areas especially at bony structures like the skull. The width of the high contrast areas is a measure for the shift.

The difference shown in the middle figure is within the required 1 mm positioning precision. The figure on the bottom shows a larger displacement of the patient, where a repositioning was required.

The resolution of the digitally acquired images, though by far less than that of X-ray films, has shown to be fully sufficient for the verification of the patient's position. The use of the image intensifiers will shorten the overall positioning time and facilitate the work of the medical staff. Operations like image substraction or image matching will help the physician in the fast evaluation of the positioning quality.







Viewing Screen Systems for Diagnostic and Quality Assurance Purposes

A. Weiss, B. Spielberger, H. Eickhoff, Th. Haberer, A. Peters
GSI Darmstadt

Up to now viewing screen systems at GSI are used for beam diagnostics at the accelerator only. The setup consists of Chromox targets and simple TV cameras, so that a qualitative transverse beam profile observation of slowly extracted ion beams from SIS and ESR is possible. With new target materials and modern image acquisition technologies an improved detector system was built up that will be used for the gantry segment test in Cave C during 2002 for the first time. A similar arrangement will be installed at the isocenter with additional features like *online* dose verification.

A usual target material for viewing screens is Chromox, which has a high light output on one hand, but on the other hand shows a long-lasting afterglow behavior (seetable). Two other scintillation materials, selected out of great number of phosphors, were investigated in comparison to Chromox and their behavior concerning efficiency, saturation and timing performance was evaluated [1].

Material	Composition	Maxim. Emission	Decay Time (10%)	Rel. Yield of light
Chromox	Al_2O_3:Ce	700 nm	~ 1 s	1.0
P43	Gd_2O_2S:Tb	545 nm	1 ms	1.5
P46	$Y_3Al_5O_{12}$:Ce	530 nm	300 ns	0.2

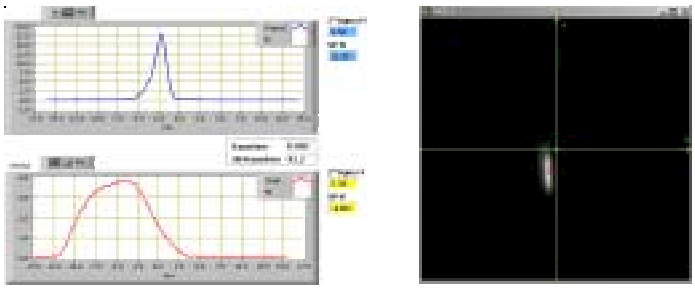
The maximum light output lies in the range of 540nm, which fits ideally to the sensitivity of monochrome CCD sensors. The decay time of the two phosphors is clearly shorter than that of Chromox and allows measurements of beam movements and profile variations in the millisecond region.

Both phosphors were tested with protons and carbon ions, the main beam species foreseen for the cancer therapy facility. The above given table shows the values of the summarized surface luminosity relative to Chromox. All measurements were taken with the same camera settings at 356 MeV/u $^{12}C^{6+}$-beam, a proton beam of 200 MeV shows similar results.

The next important point of the measurement system, which had to be improved, is the image acquisition. Until today the installed CCD cameras transmit the captured images as an analog TV-signal, which is optionally digitized afterwards with a framegrabber. Due to long and noisy cables with additional reflexions the images lose a lot of quality. Direct digital readout of industrial CCD cameras came up in the last years, which avoids all these drawbacks, especially cameras based on the IEEE 1394 high-speed serial bus (also called Firewire). This system has several advantages for beam diagnostic measurement system:

- Standardized and inexpensive interfaces
- A single bus with up to 63 nodes, multiple cameras with different properties on the same network
- Isochronous and asynchronous data transfer, with a throughput up to 400 Mb/s
- Long distance data transfer up to 500m by optic fibers

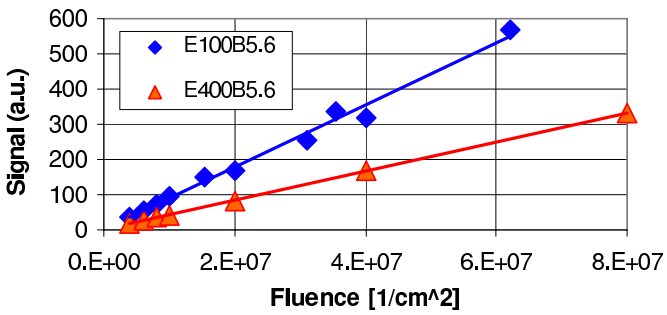
For the investigations we used monochrome cameras from Basler (A301/302f) with medium resolutions. With this new image acquisition systems and the chosen phosphor screens (especially P43) it is possible to grab up to 75 transversal profiles per second for standard therapy parameters. The following image and the horizontal and vertical projections of the beam show a typical result.



The results presented here have triggered new investigations whether fluorescent screens can be used for dose verification in the conformal carbon ion radiotherapy at GSI. In contrast to other radiation detectors (e.g. films, TLD's) fluorescent screens will allow an *online* verification of the applied dose distribution with high spatial resolution.

But dosimetry with solid state detectors is a complex task, because the response varies for particles of different energies and atomic number Z [2], [3].

First experiments using a cooled CCD camera from Hamamatsu (Orca 1394, 1280x1024 pixels) have been performed to study the energy dependence of the fluorescent signal for high-energy carbon ions. The following figure shows the measured data for two different energies (100 and 400 MeV/u). The results up to now illustrate a linear response, no saturation has been found.



Further experiments are necessary to investigate the detector´s response in a wider range of energies, atomic numbers Z and fluences. An optimization of the viewing screen system according to the therapy relevant beam parameters and timing requirements will be done in 2002.

References

[1] A. Peters, P. Forck, A. Bank, A. Weiss, „Transverse beam profile measurements using optical methods", Proceedings of DIPAC 2001

[2] B. Spielberger, M. Scholz,, M. Krämer, G. Kraft, "Experimental investigations of the response of films to heavy-ion irradiation", Phys. Med. Biol., 46/11, 2001, 2889-2897

[3] O. Geiß, M. Krämer, G. Kraft, „ Efficiency of thermoluminescent detectors to heavy-charged particles", Nucl. Instr. and Meth. In Phys. Res. 1998, B142, 592-598

A Versatile Heavy-Ion Irradiation Facility

D. Schardt, W. Becher, T. Haberer, G. Lenz, M. Krämer, E. Rietzel, E. Schubert, U. Weber
(GSI Biophysics)
E. Badura, H. Brand, H. Essel, J. Hoffmann, N. Kurz, W. Ott, K. Poppensieker, M. Richter (GSI DVEE)
H. Eickhoff, B. Franczak, R. Steiner (GSI Accel. Div.), B. Voss (GSI Det. Lab)

Since 1990, when Cave A was put into operation, it was used by the GSI Biophysics group as well as many external groups for a large number of irradiation experiments. Cave A is still equipped with the prototype of a rasterscan system which was thoroughly tested and optimized, resulting in a highly reliable irradiation system [1]. These developments and experiences had a strong impact on the construction of the beam delivery system for the therapy unit which came into operation in 1997. The possibility of irradiating large fields with excellent uniformity over a wide range of energies and fluences has attracted many other groups too. Numerous irradiation experiments with ion beams ranging from ^{12}C to ^{238}U have been performed for the cosmic physics community, material research, dosimetry, or studies of radiation induced effects in electronic systems.
Taking advantage of the technical developments for the therapy project, the irradiation system in Cave A was upgraded and equipped with a new beam monitor system and a new control system. Furthermore, the performance of the new bipolar power supplies of the scanning magnets was successfully tested. This technical achievement is of particlular interest for the Heavy-Ion Gantry study for the planned clinical heavy-ion therapy unit at Heidelberg.

Specifications of the upgraded irradiation facility:

- max. field size 20 x 20 cm^2
- all ion beams up to ^{238}U
- Energies 50 AMeV to 2 AGeV (max. 18 Tm)
- Fluence range 10^2 - 10^{12} ions/cm^2
- Computer-controlled beam delivery
- On-line beam monitoring and visualization
- Range shifter (10-plate system)
- Target positioning systems
- Robot system for remote sample exchange
- Laser alignment system

The implementation of a new control system in 2001 represents a major upgrade of the irradiation system in Cave A. Based on the developments of the SIS control system and the local therapy control system in Cave M which resulted in a most reliable operation of the therapy unit, a similar control system was implemented at Cave A. This system offers unique conditions for irradiation experiments, especially those related to therapy such as cell survival studies or animal studies, which can be performed under the same conditions as in actual treatment (^{12}C beam). The concept of the technical solution developed by the accelerator and DVEE groups does not affect the operation of the therapy unit (Cave M) and required only minor modifications on the accelerator side. For safety reasons, the therapy-like operation mode for Cave A with ^{12}C beam has to be restricted to the night shifts – after the daily patient treatment programme has completed.
The beam delivery system is fully computer controlled based on a VME(E7) frontend system and fast control boards (**S**teuer- und **A**uslese-**M**odul SAM) equipped with DSP processor units. The user interface (FactoryLink ECS software) was adapted from the therapy control system [2] and runs on a IBM RISC-workstation under AIX 4.2. The user-defined precalculated irradiation patterns are loaded and then executed automatically.
The actual beam intensity and beam position are monitored continuously by a parallel plate ionization chamber and a multi-wire chamber [3] in front of the sample, using fast digitizing readout moduls developped at GSI/DVEE.
The irradiation system includes a fast feedback regulation of the beam position which compensates small position shifts due to instabilities of the beam extraction or beam line elements. This ensures that the beam spots in the areal raster-scan patterns are precisely positioned, resulting in an excellent uniformity of the particle fluence (Fig.1). As in the therapy system the current status of the irradiation can be monitored in real time and the actual beam position measured in 150 µs time intervals is visualized (**T**herapy **O**n-line **M**onitor TOM [2]).

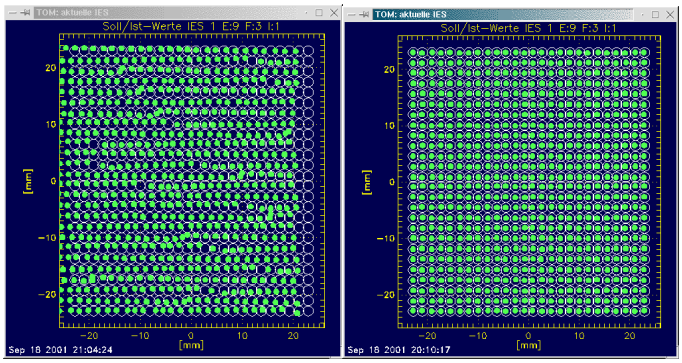


Fig.1 On-line visualization of a typical irradiation field (50x50 mm^2). The two patterns demonstrate the effect of the feedback regulation of the beam position (left: regulation off, right: on). The spacing between two raster points is 2mm.

The new irradiation facility was succesfully operated for radiation hardness tests of electronic components of the data aquistion system by the AMS-collaboration, simulating cosmic ray conditions for an experiment at the International Space Station ISS.

References

[1] T. Haberer et al., *Magnetic scanning system for heavy-ion therapy*, Nucl. Instrum. and Meth. A330, 296 (1993)
[2] H. Brand et al., *Therapy slow control system, data analysis and online monitoring*, GSI Scientific Report 1997,146(1998)
[3] B. Voss et al., *The monitor system of the Therapy Project*, GSI Scientific Report 1997,187(1998)

Evaluation of Avalanche Photodiode Arrays for the Readout of High Granularity Scintillator Matrices

P. Crespo[1], M. Kapusta[2], M. Moszyński[2], W. Enghardt[3], J. Pawelke[3], M. Szawlowski[4]
[1]GSI Darmstadt, [2]Soltan Institute for Nuclear Studies, Świerk-Otwock, Poland
[3]FZ Rossendorf, [4]Advanced Photonix, Inc. Camarillo, USA

In order to provide sufficient flexibility for patient positioning at the Heidelberg charged hadron tumour treatment facility, γ-ray detectors with large sensitive area and small volume are highly desirable for the positron camera to combine with a rotating beam delivery (gantry). Photon detector technology yields increasingly more compact PET-detectors consisting of inorganic scintillators, e.g. bismuth germanate (BGO) or lutetium oxyorthosilicate (LSO), coupled to either a position sensitive photomultiplier (PSPMT) [1] or to avalanche photodiode arrays (APDAs) [2, 3]. We have shown [4] that LSO is a suitable scintillation material for in-beam PET due to its higher light yield and shorter decay time when compared to BGO. APDs are preferable to PMTs due to their higher compactness. Furthermore, the presence of weak stray fields originating from the bending magnets of the gantry may permanently deteriorate the performance of a PSPMT. Therefore, PET-detectors assembled from LSO-crystals and APDAs are the first choice for an in-beam positron camera.

With this goal set, we have evaluated the performance of a recently released large area avalanche photodiode (LAAPD) array from Advanced Photonics, Inc. (API). The device is a monolithic 2 x 2 squared pixels structure with 21 mm^2 total active area and 2.3 mm pitch. Although it presents a high linear fill factor of 90 %, measured in dc-mode with a laser fine scan by the manufacturer, we measured light pulse crosstalk values inferior to 1.7 % between all pixels by sequentially illuminating the center of one pixel with a 1.7 mm diameter light spot and registering the amplitude spectra of all pixels. These good results are due to the fabrication technique used: one single substrate consisting of a p-type epitaxial layer and an n-type neutron transmutation doped layer is etched using deep reactive ion etching, yielding four adjacent diodes with high gain uniformity. We measured an inter-pixel gain variation with X-rays smaller than 1.3 %. Although the APDA allows stable operation with high gains up to 200, we obtained its noise minimum at an excellent low equivalent noise charge of 16 electrons rms with an internal gain of 50 and with 1 μs signal shaping time.

A 2 x 2 LSO crystal matrix (2 x 2 x 10 mm^3 each crystal) optically isolated with teflon tape and coupled with silicon oil to the APDA allowed individual crystal identification to be performed, as summarized in Fig. [1]. An energy resolution of 12.3 % was obtained for the FWHM of the 511 keV photopeak, a promising result when compared to the ~20 % offered by the BGO/PMT solution. The LSO crystals light yield was calibrated with a XP2020Q PMT which allowed the number of electron-hole pairs (e-h) of the APD to be found at 9200 e-h/MeV. Coincidence timing between one LSO/APD channel and a fast scintillator (BaF_2) coupled to a fast PMT resulted in a time resolution of 1.9 ns FWHM, as detailed in Fig. 2. This result is one of the best published for APDAs and corresponds to 2.7 ns FWHM if two LSO/APD detectors are used. Energy and time resolution are essential variables for PET in order to effectively suppress Compton scattered photons and random events, respectively.

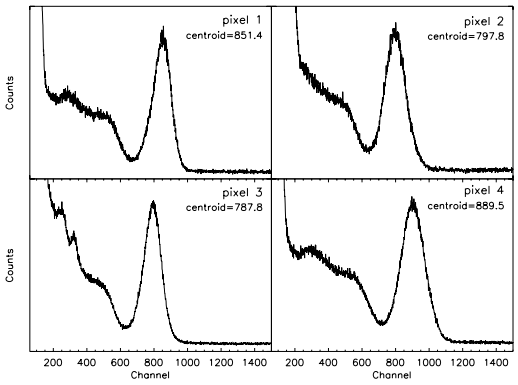


Figure 1: Energy spectra from a ^{22}Na γ-source irradiating a 2 x 2 LSO crystal matrix coupled individually to the 2 x 2 pixels of the API device.

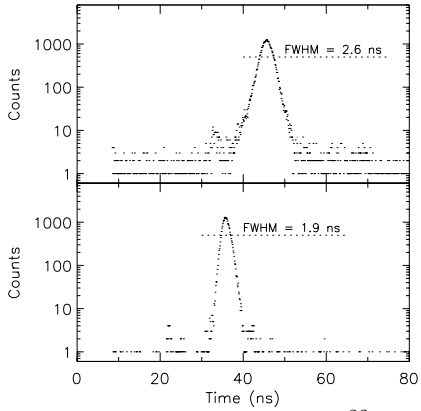


Figure 2: Time spectra measured with a ^{22}Na source. *Upper image:* Threshold set at 350 keV. *Lower image:* Energy window set at the 511 keV photopeak with a fast-slow setup.

References

[1] H. Kyushima et al., IEEE Nucl. Sci. Symp. and Med. Ima. Conf., Lyon (2000), Conference Records.
[2] M. Kapusta et al., IEEE Nucl. Sci. Symp. and Med. Ima. Conf., San Diego (2001), Conference Records.
[3] S.I. Ziegler et al., Eur. J. Nuc. Med. 28 (2001) 136.
[4] K. Lauckner et al., IEEE Nucl. Sci. Symp. and Med. Ima. Conf., Lyon (2000), Conference Records.

An interactive approach for local dose quantification from in-beam PET data

K. Parodi and W. Enghardt; FZ Rossendorf

The in-beam PET monitoring of carbon ion therapy supported the reliability of the treatment planning and patient positioning procedures at the GSI Darmstadt facility [1]. However, in some cases it detected deviations of the measured and the predicted β^+-activity distributions, due to minor inaccuracies in patient positioning or local changes of patient anatomy [1]. These discrepancies may correspond to small deviations of the applied and planned dose. Hence, a local dose quantification from PET images shortly after each therapeutic irradiation is highly desirable. Due to the lack of a feasible solution for the inverse problem relating the β^+-activity to the dose, an interactive approach has been considered. The implementation has been based on the dedicated tool used for the visualization of the PET measured and predicted distributions as contour plots superimposed onto X-ray CT images [2]. In case of deviations, an interactive modification of the patient CT consisting either in geometrical transformation (translation and rotation) or in local Hounsfield unit (HU) modifications in user-selected regions of interest (ROI) can be performed. The reliability of the modification is tested by a recalculation of the β^+-activity distribution with and without the CT changes. Actually, only the spatial distribution of β^+-decays is computed, in order to avoid blurring due to the imaging procedure. The calculation is local and analytical, in order to reach a "fast" (within few minutes) response. Only the pencil-like beams crossing the chosen ROI are taken into account. The depth-distribution of the main β^+-isotopes (^{11}C, ^{15}O and ^{10}C) is extrapolated from the PET database (DB) [3] containing the spatial distributions of positron emitters produced in PMMA ($C_5H_8O_2$) by ^{12}C beams of all the energy values used for therapy. The DB information is combined with the irradiation strategy (ion energy, fluence and position) and with the patient anatomy by means of the HU-ion range correlation [3], [4] and the stoichiometric calibration of the CT numbers suggested in [5]. The lateral-distribution is assumed to be Gaussian with a FWHM dependent on the beam focus and the average positron range in tissue. The lateral spread of the beam in depth is neglected. The distribution of β^+-decays is deduced from the isotope production and the time interval between the beam delivery and the end of the PET acquistion. If the recalculation supports the modification, a new dose distribution based on the elaborated CT is obtained by means of the treatment planning software [4]. Figure 1 and 2 show an example. For this patient an extreme but plausible tissue reduction was assumed on the basis of range and anatomical symmetry considerations. A new CT scan confirmed the conjecture. In such cases a new treatment plan may be defined, according to the physician's decision. Hence, the interactive approach can give an important feedback. The optional introduction of imaging effects on the recalculated distributions for a more direct comparison with the reconstructed PET images is under development. In particular, the effects of minor CT modifications on the PET attenuation corrections are currently studied. Moreover, the sensitivity and accuracy of the method as well as the potential of real quantitative PET data for local dose quantification are under investigation.

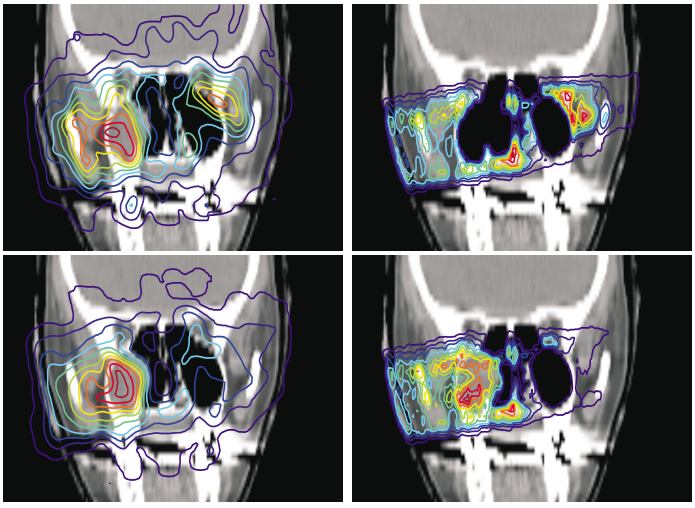


Figure 1: Left: Higher activation at the distal edge of the portal (entering the patient from the left of the picture) in the PET measurement (up) in comparison with the prediction (down). Right: The recalculation with (up) and without (down) CT modification well resembles the PET images (left), thus supporting the hypothesis.

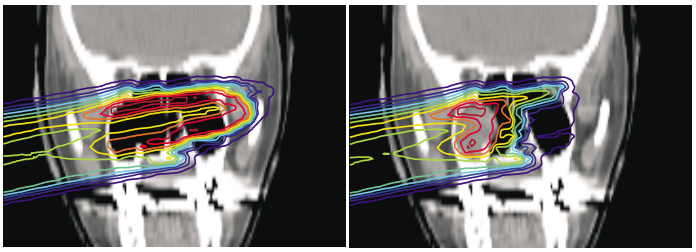


Figure 2: The effect on the recalculated dose distribution (left) in comparison with the planned one (right) is evident and in agreement with the PET observation (cf. Fig. 1).

References

[1] W. Enghardt et al., FZ Rossendorf, Wiss.-Tech. Ber. FZR-271 (1999) 89

[2] F. Pönisch et al., FZ Rossendorf, Wiss.-Tech. Ber. FZR-271 (1999) 91

[3] B. G. Hasch, PhD Thesis, Dresden University of Technology, 1996

[4] M. Krämer et al., Phys. Med. Biol. 45 (2000) 3299

[5] W. Schneider et al., Phys. Med. Biol. 45 (2000) 459

In-beam PET measurements of proton-induced β^+-activity

K. Parodi and W. Enghardt, FZ Rossendorf; T. Haberer, GSI Darmstadt

The important impact of in-beam PET on the quality assurance of carbon ion therapy has been proven by the clinical experience at GSI Darmstadt [1]. The main achievements are *(i)* the monitoring of the maximum carbon ion range, *(ii)* the verification of the field position and *(iii)* the detection of unpredictable deviations of the real treatment from the planned one due to minor errors of the patient positioning or local changes of the patient anatomy (e.g. filling of cavities by mucus) [2]. Based on these results and motivated by the proposed dedicated proton and heavy ion (up to oxygen nuclei) therapy facility at Heidelberg [3], the potential extension of the PET technique to the monitoring of proton therapy is under investigation. In our first experiment [4] three mono-energetic proton beams (energy: 110, 140, 175 MeV; mean intensity: $7 \times 10^7 - 5 \times 10^8$ ions/s) were stopped in targets of PMMA ($C_5H_8O_2$) placed in the centre of the field of view of the in-beam positron camera installed at the GSI heavy ion therapy facility. Each PET measurement was taken over 10 min of irradiation and 20 min of decay. The amount of β^+-activity was found to be three times (3.2 ± 0.4) larger than that induced by carbon ions at the same range and applied physical dose. The lateral profile of the reconstructed activity distributions (Fig. 1) was found in good agreement with calculations [3] of proton beam broadening in depth. These two observations support the sensitivity of the PET method to detect field mispositioning or anatomical changes of the patient in the proton case, too. The control of the maximum proton range is a more challenging issue, since protons cannot suffer the projectile fragmentation process which leads to a peaked activity distribution in close proximity to the dose maximum in the carbon ion case. The reconstructed β^+-activity depth-profiles were well reproduced in shape by the production of the main positron emitters (^{11}C and ^{15}O) calculated on the basis of experimental cross-sections and the proton flux given by the FLUKA Monte Carlo code (Fig. 2). The shown reconstructed datasets contain events measured during the irradiation and later than 10 min after finishing the irradiation, in order to include and rule out the contribution of the short-lived ^{15}O, respectively. There is a unique relation between the position of the distal slope of the depth-activity curve (e.g. the 50% level), mainly determined by the energy thresholds of the fragmentation reactions, and the primary proton range. In our case the 50% level of the distal part of the measured and simulated profiles was found at about 6 mm lower penetration depth than the range. A very weak (< 0.5 mm) dependence on the initial energy and on the ^{15}O contribution was observed. The spatial activity-range correlation supports the possible extraction of range information by means of a comparison between measured and realistically calculated activity distributions, as done in the carbon ion case. The achievable accuracy is the crucial parameter, since millimetre precision is required. First simulation investigations of proton irradiation with a spread out Bragg peak [4] suggest that a millimetre control of the maximum proton range may be feasible. Future experiments at GSI Darmstadt are planned in order to measure the minimum proton range difference that can be resolved by the in-beam limited angle PET scanner. This will allow a final conclusion on the feasibility and achievable precision of proton range monitoring to be drawn. As a general remark we note that the in-beam technique is recommended in order to exploit the higher activity signal without losing the main contribution coming from ^{15}O in the case of patient irradiation and to acquire data directly in the treatment position.

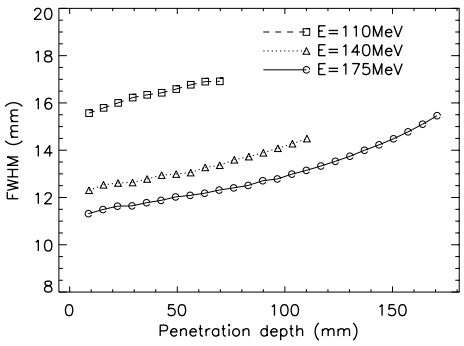


Figure 1: Lateral width of the β^+-activity profile versus depth in the central plane of the positron camera field of view for the three proton irradiations.

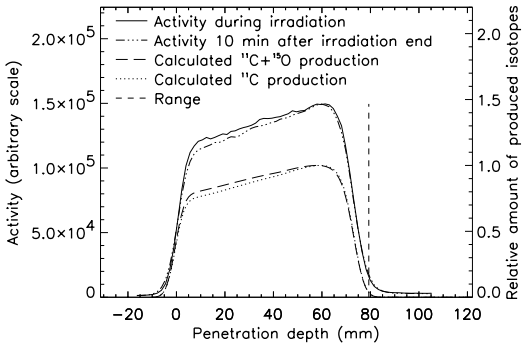


Figure 2: Reconstructed β^+-activity depth profiles in comparison with calculated isotope production for the 110 MeV proton irradiation (see text for explanation).

References

[1] W. Enghardt et al., Nucl. Phys. A 654 (1999) 1047c
[2] W. Enghardt et al., Wiss.-Tech. Ber. FZR-271 (1999) 89
[3] K. D. Gross and M. Pavlovic (eds), Proposal for a dedicated ion beam facility for cancer therapy, Darmstadt, 1998
[4] K. Parodi et al., Phys. Med. Biol. 47 (2002) 21

A New Fully 3D Maximum Likelihood PET Reconstruction Applicable to Different Detector Arrangements

P. Crespo[1], W. Enghardt[2], K. Lauckner[3]
[1]GSI Darmstadt, [2]FZ Rossendorf, [3]The Scientific Consulting Group, Freiburg

We developed a fully-3D, maximum likelihood based, PET reconstruction routine applicable to different coincidence detector arrangements for PET. It allows to study the influence of several γ-ray detector geometries onto the corresponding reconstructed images. The scope of this study is to optimize a tomograph to be fully dedicated to the monitoring of heavy ion tumor therapy with a rotating beam delivery (gantry).

A special purpose routine was needed in order to surpass situations not approached before: *(i)* the low counting statistics acquired during therapy with carbon ions makes the application of already developed 3D iterative algorithms with 2D sampling modes impossible, *(ii)* a fixed dual head PET scanner provides a coincidence detector with spatial variant response, which forbids the application of the algebraic reconstruction methods used in nuclear medicine and *(iii)* for the unprecedent huge size of coincident channels both for a closed ring camera, or a dual head camera with a small gap, the direct application of the routine previously developed for the positron tomograph at the GSI treatment site [1] is not feasible (the number of possible coincidence channels increases from 4 to 170 million).

The new routine first samples the list mode data into coincidence channels according to a self-developed channel factorizing scheme. This scheme, combined with direct memory allocation during runtime, feeds the rest of the reconstruction routine with a packed matrix $\boldsymbol{Y}$ containing only the measured data (no empty coincidence channels). The routine than processes $\boldsymbol{Y}$ to find the most probable image $\boldsymbol{X}$ with the maximum likelihood estimation maximization algorithm [2]:

$$x_i^{(n)} = x_i^{(n-1)} \sum_j a_{ij} \frac{y_j}{\sum_k a_{kj} x_k^{(n-1)}} \qquad (1)$$

where $x_i^{(n)}$ is the calculated activity of the ith voxel, at the nth iteration. Each image voxel i contributes with weight a_{ij} to the jth coincidence channel. y_j is the measured activity at the jth channel of the tomograph.

In order to assess the reliability of the new routine we developed a package being capable of simulating PET list mode data sets for a full ring or dual head positron camera. The detector dimensions and positioning are those of the commercial scanner CTI ECAT EXACT HR+ (∼82 cm diameter, ∼16 cm axial length). Fig. 1 illustrates a dual head camera with the reference system implemented. Whether implemented on an horizontal beam line or under a rotating gantry, the beam will lie on the plane XZ_{PET} in all situations, as detailed in [3].

Fig. 2 shows a reconstructed image obtained from the simulation of 100 million annihilation points homogeneously distributed through a hollow sphere with 3 cm outer radius and 1.5 cm inner radius and detected in a closed ring camera. This volume shape was choosen due to its similarity to β^+ distributions that, in radiotherapeutic situations, often occur surrounding the nasal and paranasal cavities of the treated patients with skull base tumours. For this volume shape the geometrical efficiency was 16.2%. The image shows symmetric, steep edges, corresponding to the simulation.

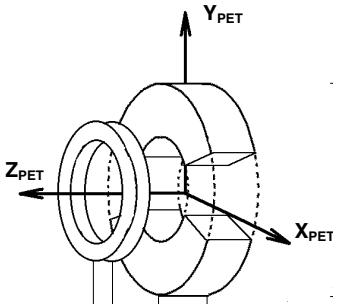


Figure 1: Dual head positron camera and metal support ring. The camera rotates around the Z_{PET} axis.

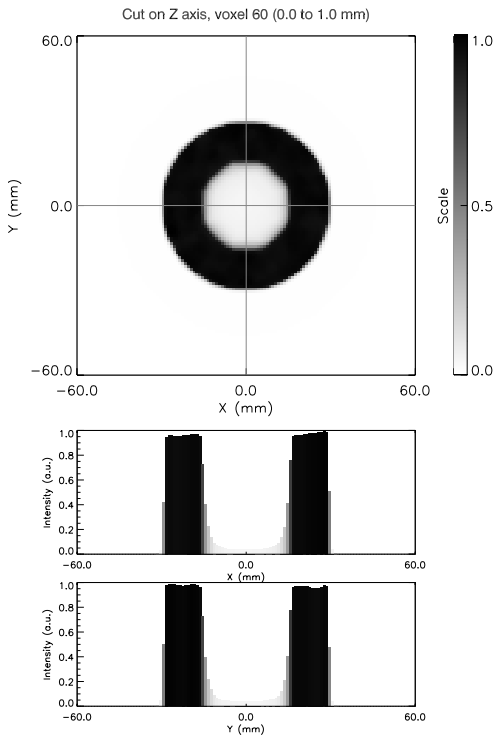


Figure 2: *Upper image:* Reconstructed image (50 iterations) of a simulated hollow sphere. A closed ring PET camera (CTI ECAT EXACT HR+) was simulated, with 16 million events detected. Axes according to Fig. 1. *Lower images:* Linear profiles through the axes of the 2D image above.

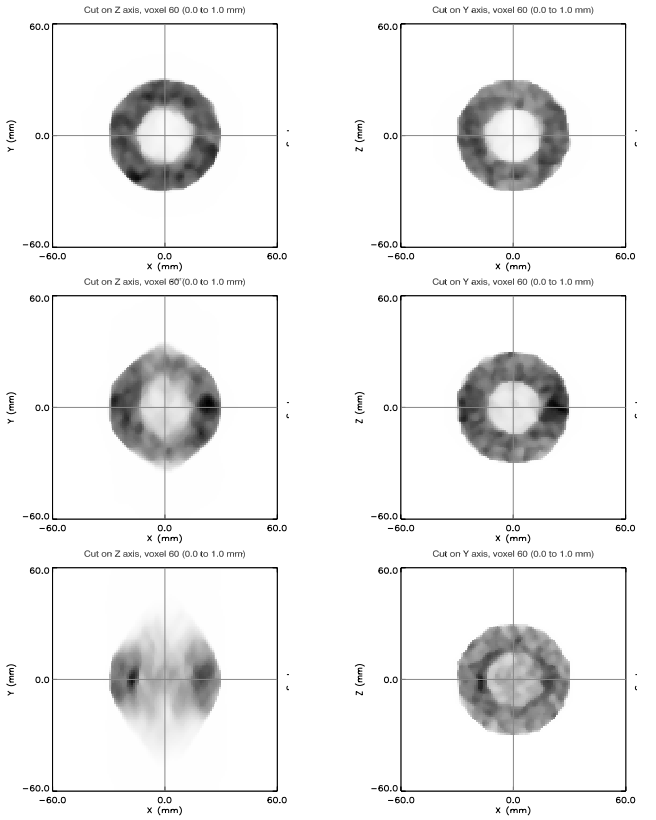


Figure 3: Set of images corresponding to the reconstruction (50 iterations) of simulated events detected with a full ring PET camera (top row, 162000 events), a dual head camera with a gap of 34 cm (middle row, 114000 events) and with a gap of 63 cm (bottom row, 69000 events). All simulations followed 1 million annihilations.

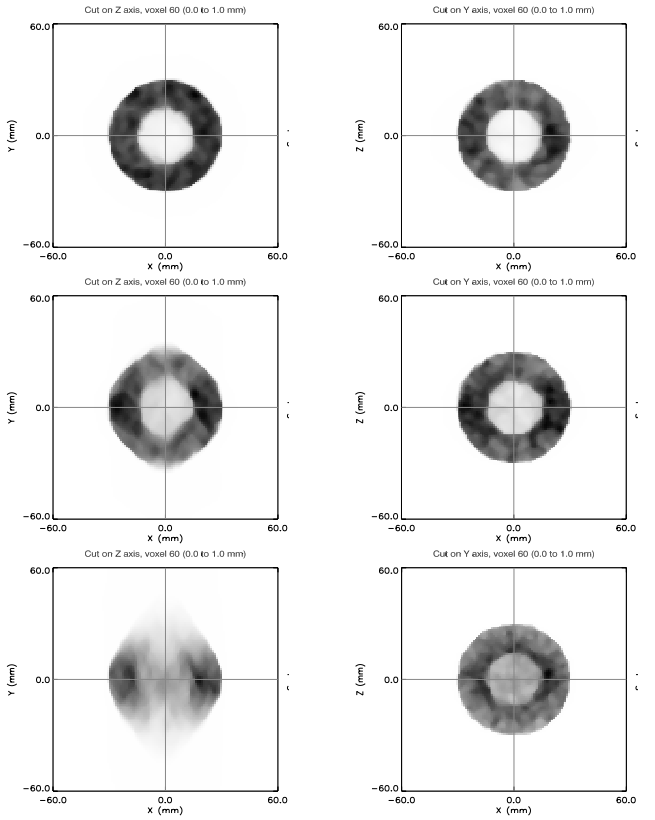


Figure 4: Reconstruction details as in Fig. 4, but with 2 times the number of simulated events (2 million annihilations followed inside the hollow sphere).

Fig. 3 illustrates the image degradation induced by the separation of the detectors in a dual head PET camera. The strongest effect seen is the elongation and decrease of intensity of the image along the Y axis. This expected effect arises from the lack of detectors covering that axis in the case of the dual head cameras. Yet, as pointed out, the beam line lies in all situations within the XZ_{PET} plane, where the images do not show the slightest distortion (due to the fact that this plane is perpendicular and symmetric to the gap). This means that the PET quality control of heavy ion radiotherapy is, and can continue to be in the presence of a rotating gantry, extremelly precise in the monitoring of the beam range and detection of over-ranges (spikes), mostly in regions located near the iso-center. Lateral straggling evaluation is equally precise in the same terms. The verification of organs at risk lying in planes along the gap (Y_{PET}) would strongly benefit from a PET camera with the smallest possible distance between the heads, if a closed ring is not viable.

The influence of the poor statistics data sets collected in in-beam PET can be seen by comparing the top left image in Fig. 3 and the top image in Fig. 2 (100 times more events). The contours are still clear in the low statistics case, but the images become noisier.

Fig. 4 displays the same situations of Fig. 3 but with twice the number of annihilations simulated, with the result that the image contrast sharpens in all cases.

In summary, a dual head positron tomograph brings the advantage of better flexibility in patient positioning at the expense of loss of intensity and irrecoverable image deformation. These losses can now be quantifyed with the present routine in order to find an optimum compromise. Still, in order to be able to evaluate the quality of the images from the several camera configurations in real therapeutic situations, β^+ distributions simulated from real treatments [4] should now be interfaced to the reconstruction routine.

References

[1] K. Lauckner, FZ Rossendorf, Wiss.-Tech. Ber. FZR-264 (1999)

[2] L.A. Shepp and Y. Vardi, IEEE Trans. Med. Ima. MI-1 (1982) 689

[3] P. Crespo, K. Lauckner, W. Enghardt, FZ Rossendorf, Wiss.-Tech. Ber. FZR-319 (2001) 100

[4] B.G. Hasch, Ph.D. Thesis, Dresden University of Technology, 1996.

A Scatter Correction for Iterative Tomographic Reconstruction

F. Pönisch, W. Enghardt FZ Rossendorf

A fully 3D reconstruction algorithm based on the Maximum Likelihood Expectation Maximization (MLE) algorithm has been developed for reconstruction of images from data taken by the limited angle double head camera BASTEI [1]. The process of photon scattering considerably influences the image quality in PET. For head and neck tumors about 30 % of the registered true coincidences are influenced by Compton or Rayleigh scattering, which may deteriorate the correspondence between the source and the reconstructed radioactivity distribution especially in such highly inhomogeneous regions of the human body like the head and neck. Therefore, a scatter correction is required.

The scatter correction algorithm needs the information on the tissue composition and density only within and nearby the camera field of view. This is derived from the X-ray computed tomograms (CT) of the patient (taken for treatment planning purpose) which are automatically combined with a CT of the head rest using characteristic landmarks [2]. This data set is the basis for calculation of the attenuation correction factors. The measured line of response (LOR) are corrected for the individual detector efficiency and the length of the emission line within the image space. The expectation step of the MLE-algorithm [3] is intended for modelling the imaging process in emission tomography. The classical algorithm of Shepp and Vardi [3] estimates the forward projection by computing the ray sums in each projection. We modified this procedure by applying the attenuation correction factors y_i^{att} to the forward projection and adding furthermore, the scattered components y_i^{scatt}:

$$x_j^{(n+1)} = x_j^{(n)} \cdot \sum_{i=1}^{I} \frac{a_{ij} \cdot y_i^*}{y_i^{att} \cdot \sum_{j'=1}^{J} a_{ij'} \cdot x_{j'}^{(n)} + y_i^{scatt}}. \qquad (1)$$

$x_j^{(n)}$ denotes the activity distribution after the n-th iteration step, y_i^* is the modified measured projection for the i-th channel and a_{ij} is the element of the transition matrix.

To calculate the quantity y_i^{scatt} we follow the approximation of Watson [4], the Single Scatter Simulation (SSS). This algorithm simulates the scatter coincidences y_i' in a given LOR i by single Compton scattered events only. Therefore, the total number of scattered events N_{scatt} obtained from the SSS calculation has to be normalized to the number of acquired coincidences N_{meas}. We calculate the global scatter fraction (SF) by means of an additional Monte Carlo (MC) simulation from the n-th solution:

$$SF = \frac{N_{scatt}}{N_{total}}. \qquad (2)$$

The simulation uses the activity distribution of the previous iteration step and the information of the attenuation map. The MC code has been optimized for accuracy and executing time. The number of histories has been chosen that the statistical error in the calculated SF is less than 0.3 %. Watson [4] has shown that a single scaling factor is sufficient for the total scatter distribution. By means of the SF one can estimate the number of scattered events from the measured one. From this follows the normalized scatter contribution of the coincidence channel:

$$y_i^{scatt} = y_i' \cdot \frac{SF \cdot N_{meas}}{\sum_i y_i'}. \qquad (3)$$

Introducing (3) into (1) yields the modified forward projection for each iteration step.

The new reconstruction algorithm has been validated for experimental data. The scatter corrected β^+-activity distributions from phantom experiments as well as patient data show a good agreement with our expectation. The Figure 1 shows the profile of the reconstructed PET image with a size of $256 \times 128 \times 100$ voxels from a ^{22}Na point-like source, which was placed in a water filled cylindrical phantom (diameter 15 cm, height 15 cm). The removal of the scatter components after applying the scatter correction algorithm is obvious.

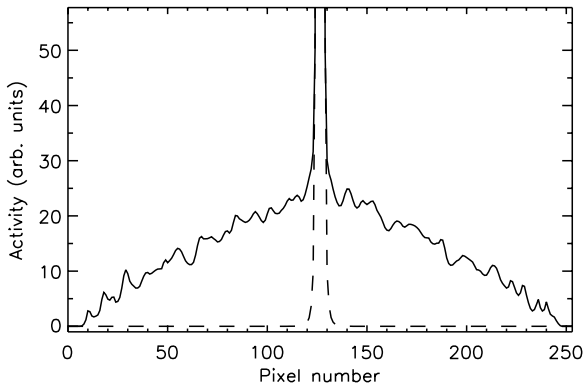


Figure 1: Profile of the reconstructed PET image of a point-like source in a water filled phantom. The solid curve is the reconstructed data set without scatter correction; the dashed curve is the data set using the scatter correction algorithm.

References

[1] K. Lauckner, FZ Rossendorf, Wiss.-Tech. Ber. FZR-264 (1999) 70

[2] F. Pönisch et al., FZ Rossendorf, Wiss.-Tech. Ber. FZR-319 (2001) 95

[3] L.A. Shepp, Y. Vardi, IEEE Trans. Med. Imag. MI-1 (1982) 113

[4] C.C. Watson et al., in Three-Dimensional Image Reconstruction in Radiation and Nuclear Medicine (1996) 255-268

The Evaluation of Carbon Ion Therapy PET Data within the Time Domain

C. Kausch (GSI), W. Enghardt (FZ-Rossendorf)

A large fraction of the positron emitters produced during the heavy ion therapy treatment are ^{11}C fragments with a half-life of 20.4 min. The activity accumulates during the irradiation in bony structures, whereas it is washed out in well perfused tissue (e.g. the brain). This leads to discrepancies between the measured and the simulated PET images [1] and, therefore, a definitive statement on the accuracy of the dose deposition may be complicated or even impossible. Since the PET data is recorded in list mode, it is possible to evaluate the β^+-activity both in space and time domain [2]. To obtain tissue dependent washout data from the large amount of PET scans acquired for more than 100 patients treated at the GSI therapy facility, a software tool has been developed. In a first step volumes of interest – VOI – (i. e. tissue regions where the washout is to be determined) are interactively selected in images showing the β^+-activity distribution superimposed onto X-ray computed tomograms (CT) as shown in Fig.1.

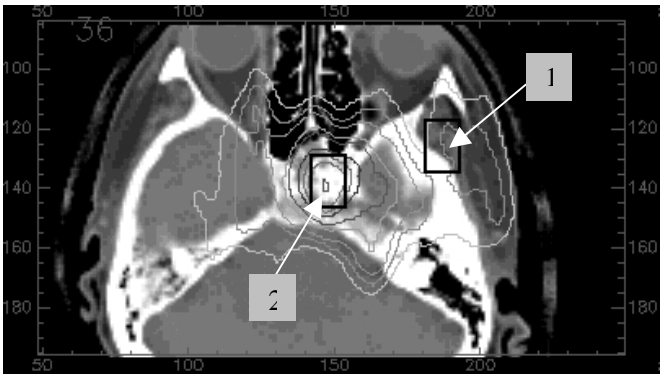


Fig. 1 Transversal CT-image with the β^+-activity distribution through the head of a patient. The black boxes mark the examined VOIs with large (1) and low (2) washout.

In the second step the time histograms of those lines of response, which intersect the VOI, are constructed and an effective lifetime is calulated by means of a fitting procedure (Figs. 2 and 3). For precise fitting results the signal-to-noise ratio of the time histograms should be large. As the count rate is notoriously poor in PET studies performed simultaneously with the therapeutic irradiations and the available time intervals are short compared to the half-life of ^{11}C, it is planned for the future to sum up the PET-measurements for all therapy fractions of a certain patient and portal. Although this has not been implemented yet, the feasibility of the concept can be demonstrated, for an treatment during which the beam delivery was interrupted by more than 15 min. Fig. 1 shows a transversal slice of the CT-images of the head, with the β^+-activity distribution superimposed. VOI(1) is located in a region with large blood flow whereas VOI(2) is placed in the skull base (bone). The corresponding time distributions are shown in Figs. 2 and 3, respectively. The relaxation of activity is an exponential process as well as the washout of emitter concentration. Thus, the measured time dependent count rate *c(t)* is fitted to an exponential function

$$c(t) = p_1 \, e^{-\frac{t}{\tau_p}} + p_1 \, e^{-\frac{t}{\tau_c}} \qquad (1)$$

where p_1 is the is the normalization factor, τ_p and τ_c = 1766s are the mean-lives for the activity washout and the ^{11}C decay, respectively. For comparison the decline of activity due to ^{11}C decay only is shown by the grey curve. the strong washout is represented by the area in-between the two curves.

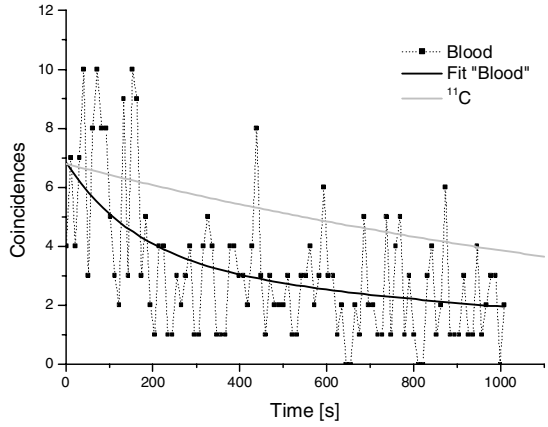


Fig. 2 PET count rate versus time for the well perfused VOI (1). The black line shows the exponential fit of the data, the grey line shows decline due to ^{11}C decay only. The list mode data are rebinned into 10s time intervals.

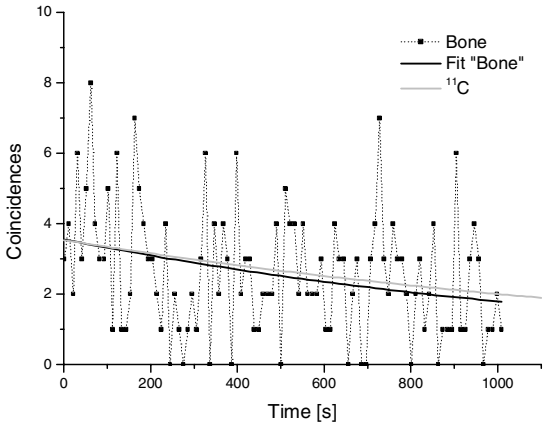


Fig. 3 PET count rate versus time for the lowly perfused VOI (2).

Whereas for the soft tissue in Fig. 2 an effective mean-life of τ_p = 165 s has been found, the emitter concentration in the bone, shown in Fig. 3, drops much slower (τ_p = 1220s).

References

[1] W. Enghardt et al. Nucl. Phys., A 654 (1999) 1047c

[2] R. Hinz, FZ Rossendorf, Wiss.-Tech. Ber. FZR-286 (2000)

Progress Report of the Carbon Ion Therapy Project at GSI

Th. Haberer, J. Debus, H. Eickhoff, W. Enghardt, G. Kraft, D. Schardt
GSI Darmstadt, Radiologische Klinik Heidelberg, FZ Rossendorf, DKFZ Heidelberg

Clinical Trials

In 2001 39 patients were treated within our carbon ion phase I/II and phase II trials. Three beam blocks of 30 days each were used to deliver intensity modulated carbon ion fields via intensity controlled rasterscanning to tumors at the base of the skull and the brain. In addition extracranial stereotactic radiotherapy was included into the spectrum of our running clinical trials as well as a dose escalation from 60 GyE to 70 GyE for chordomas and chondrosarcomas. In total 112 patients could be successfully treated at GSI since 1997. Table 1 presents some general numbers.

patients treated	112
protocol	70% ^{12}C full dose
	30% ^{12}C boost
fields / fractions	3700 / 1600
clinical operation	250 days
fields per fraction	2 ... 4
dose per fraction	3.0 ... 3.5 GyE
beampositions per field	1000 ... 45000
volumes	50 ... 3200 cm^3

Table 1: Patient statistics and typical treatment parameters.

Based on the very promising control rates and the low level of treatment related toxicity we have now applied for an approval following the regulations of standard medical irradiations for the phase II chordoma/chondrosarcoma trial whereas since 1997 our clinical program was classified experimental. This represents another major milestone on our way to establish hadron therapy in the clinical environment.

Physical-technical Aspects

In the fourth year of routine operation $\approx$ 20% of the SIS-beamtime were used to operate the medical cave for 13 weeks in a time-sharing mode with physics experiments. The performance of the GSI accelerators reached an excellent level of $\approx$ 95% beam availability. The effort was focussed on optimizing several subsystems of the GSI treatment facility and the therapy mode at SIS. The performance of the patient monitors, i.e. a stack of 3 parallel-plate ionization chambers plus 2 multi-wire proportional chambers, could be improved by enlarging the gas-filled gaps yielding increased signal/noise-ratios and developing new modules for the combined charge integration and signal digitization of the wire chamber read-out. Functionality could be added to the treatment planning suite (TRiP/Voxelplan) in order to offer an enhanced flexibility in superimposing various fields from different entrance channels within one fraction.

The intensity-controlled rasterscan technique requires an outstanding flexibility and reliability of the accelerator producing the therapy beams. The SIS at GSI offers a library of 25000 different settings for the production of dose distributions with utmost precision. In order to further optimize the quality of the intensity modulated fields the energy-dependent focus settings for the 255 energy steps were reworked using our elaborate accelerator modelling software. Based on these theory settings the homogeneity of monoenergetic scan patterns which are a central part of the dedicated quality assurance programme can be improved and the time consuming tuning and QA procedures can be compressed. Systematic tests were performed to investigate the feasibility of the very promising RF-knock-out extraction method which already is in clinical use at the HIMAC, Chiba. The enhanced spill structure in combination with a high degree of flexibility in switching the beam on and off optimally supports the beam scanning method and will allow for a dramatic reduction of the treatment time.

Patient irradiations at GSI

D. Schulz-Ertner, C. Thilmann, M. Wannenmacher, J. Debus

Dept. of Radiation Oncology, University of Heidelberg and German Cancer Research Center (DKFZ) Heidelberg, Germany

Before patient irradiations started in 1997, a radiation unit was built at the heavy ion synchrotron of the GSI and major future directed technical and radiobiological innovations have been implemented. For the first time, tumor conform application of carbon beams was realized by intensity-controlled rasterscanning with pulse-to-pulse energy variation [1]. All patients had 3D treatment planning including a biological plan optimization using the treatment planning program TRIP developed at GSI [2]. A PET camera is used for online beam verification [3].

Up to now, 111 patients have been treated with carbon ions. The study mainly contained patients with chordomas (51) and low grade chondrosarcomas (24) of the skull base and adenoid cystic carcinomas (16. These tumors are known to be relatively radioresistant against conventional photon irradiation. Proton radiotherapy has been shown to improve outcome in chordomas and low grade chondrosarcomas [4] but its availability is limited. In adenoid cystic carcinomas radiation therapy with heavy particles as neutrons results in improved local control rates compared to photon irradiation but causes severe side effects [5]. Carbon ion therapy presents a promising therapy option in the management of these tumors.

Feasibility of this new therapy approach has been shown. Within a feasibility study, median tumor dose was 60 GyE in chordomas and chondro-sarcomas of the skull base. First results are very promising with local control rates of 83% for chordomomas and 100% for chondrosarcomas at 2 years [6]. Active beam delivery using raster scanning allows for highly conformal dose distributions and therefore results in an optimal sparing of neighbouring normal tissue. The study for chordomas and chondrosarcomas of the skull base has been closed in December 2001 as carbon ion therapy can be considered to be effective and safe in these patients. Patients with adenoid cystic carcinomas and sacral / spinal chordomas and chondrosarcomas are treated within the ongoing phase I/II study with fractionated stereotactic photon irradiation and a carbon ion boost with 18 GyE (6 x 3.0 GyE) to the gross tumor. A rigid immobilization device guarantees the safe irradiation of these extracranial tumors. Up to now, 16 patients with adenoid cystic carcinomas and 6 patients with sacral / spinal chordomas and low grade chondrosarcomas have been treated within this study. Preliminary results show a good effectiveness and no severe toxicity.

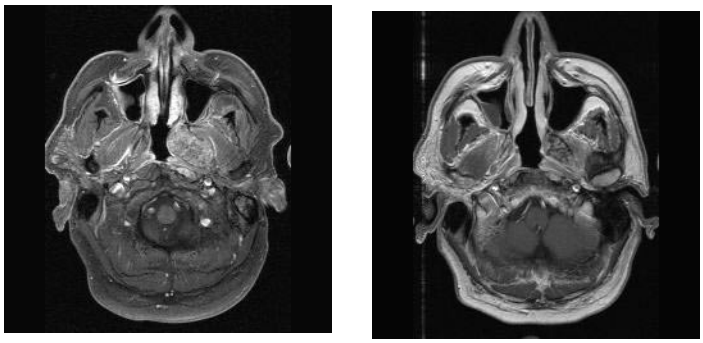


Figure 1+2. Chordoma of the skull base a) prior to RT, b) 3 months after RT with carbon ions.

References

[1] Haberer T et al. Magnetic scanning system for heavy ion thrapy. Nucl Inst Phys Res 1993; 330:296-305.

[2] Scholz M et al. Cell cycle delays induced by heavy ion irradiation of synchronous mammilian cells. Int J Radiat Oncol Biol Phys 1994; 66:59-75.

[3] Enghardt W et al. The application of PET to quality assurance of heavy ion tumor therapy. Strahlenther Onkol 1999; 175:Suppl II:33-36.

[4] Munzenrider JE et al. Proton therapy for tumors of the skull base. Strahlenther Onkol 1999; 175:Suppl II:57-63.

[5] Krull A et al. Neutron therapy in malignant salivary gland tumors: results at European centers. Recent Res Cancer Res 1998; 150:88-99.

[6] Schulz-Ertner et al. Radiation therapy for chordomas and low grade chondrosarcomas of the skull base with carbon ions. Int J Radiat Oncol Biol Phys 2002, in press

Chemical investigation of hassium (Hs, Z=108)

Ch.E. Düllmann, H.W. Gäggeler, S. Soverna, A. Türler (Univ. Bern & PSI), R. Dressler, B. Eichler, F. Glaus, D.T. Jost, D. Piguet (PSI), T.N. Ginter, K.E. Gregorich, U. Kirbach, D.M. Lee, R. Sudowe, (LBNL), D.C. Hoffman, H. Nitsche, J.B. Patin, P. Zielinski (UC Berkeley & LBNL), W. Brüchle, R. Eichler, E. Jäger, V. Pershina, M. Schädel, B. Schausten, E. Schimpf, H.-J. Schött, G. Wirth (GSI), S.N. Timokhin, A.B. Yakushev (FLNR), K. Eberhardt, P. Thörle, N. Trautmann (Univ. Mainz), Z. Qin (IMP Lanzhou), A. Vahle (FZ Rossendorf)

The heaviest element, whose chemical behavior has been studied so far is bohrium (Bh) with Z=107 [1] behaving like a typical member of group 7 of the periodic table. The longest-lived α-decaying isotope of the next heavier element hassium (Hs, Z=108) is ^{269}Hs ($T_{½}$=11.3 s) which has been identified in the decay chain of ^{277}112 [2,3]. Hs is supposed to be a member of group 8 of the periodic table and should thus form a very volatile tetroxide. Relativistic density functional calculations predicted the electronic structure of HsO_4 to be similar to the one of OsO_4 [4]. Application of different semiempirical models of the interaction of a MeO_4 molecule with quartz surface predicted the adsorption behavior of OsO_4 and HsO_4 to be very similar [4]. Extrapolations of trends within group 8 of the periodic table also predicted HsO_4 and OsO_4 to behave similar in a gas adsorption chromatography experiment [5].

Hs isotopes were produced directly in the reaction ^{248}Cm(^{26}Mg;5,4n)^{269,270}Hs at the UNILAC at GSI Darmstadt [6]. Hs isotopes recoiling from the target were thermalized and oxidized in a He/O_2 mixture in the recoil chamber of the In-situ Volatilization and On-line detection apparatus IVO [7]. Volatile HsO_4 was transported with the carrier gas to the Cryo-On-Line-Detector (COLD), a thermochromatography device. Along a narrow channel formed of PIN-diodes registering α-decaying and spontaneously fissioning (SF) nuclides, a temperature gradient form -20 to -170 °C was established. The deposition temperature of volatile species could therefore be determined, allowing for the determination of their adsorption enthalpy. COLD is an improved version of the Cryo-Thermochromatography Separator CTS developed at Berkeley [8].

Five decay chains were detected in the course of the experiment which were attributed to ^{269}Hs or the so far unknown isotope ^{270}Hs [6]. In addition, two α-SF correlations were observed in detectors 3 and 4 that still have a rather low random probability, but could not be assigned with certainty to either ^{269}Hs or ^{270}Hs [6]. The deposition temperature of the Hs containing molecules was determined to (-44±5) °C giving strong evidence of the formation of HsO_4. In an irradiation of a ^{152}Gd target, ^{172}Os ($T_{½}$=19.2 s) was produced in the reaction ^{152}Gd(^{26}Mg;6n) and a deposition temperature of (-82±5) °C was measured for $^{172}OsO_4$. The deposition distribution in the COLD array along the detector pairs is shown in Fig. 1. From these deposition peaks the adsorption enthalpies were deduced applying a Monte-Carlo simulation based on a microscopic description of the transport process in the chromatography column [9], i.e. in the COLD system. Since the half-life of the nuclide is a crucial parameter in this simulation and this value has not yet been measured for ^{270}Hs, only the three events

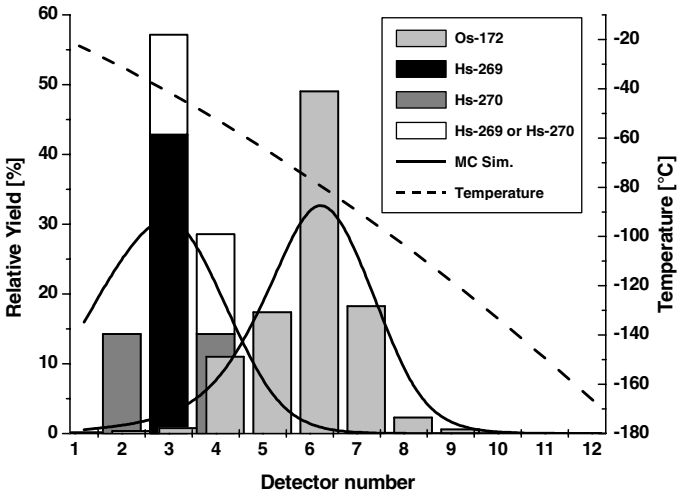


Fig. 1 Merged thermochromatograms of OsO_4 and HsO_4. The solid lines represent results of a Monte-Carlo Simulation with ΔH_{ads} values of -39.5 kJ·mol^{-1} (OsO_4) and -47 kJ·mol^{-1} (HsO_4), respectively. The dashed line indicates the temperature gradient.

assigned to ^{269}Hs were used for the simulation. $\Delta H_{ads}(HsO_4)$=(-47±2) kJ·mol^{-1} (68 % c.i.) was evaluated, compared to $\Delta H_{ads}(OsO_4)$=(-39.5±1.0) kJ·mol^{-1}. The latter value is in good agreement with $\Delta H_{ads}(OsO_4)$= (-38.0±1.5) kJ·mol^{-1} evaluated in earlier experiments.

With the formation of a very volatile oxide, presumably HsO_4, Hs behaves similar to Os, its next lighter homologue in group 8 of the periodic table.

References

[1] R. Eichler et al., Nature **407,** 63 (2000).

[2] S. Hofmann et al., Z. Phys. **A354,** 229 (1996).

[3] S. Hofmann et al., Rev. Mod. Phys. **72,** 733 (2000).

[4] V. Pershina et al., J. Chem. Phys. **115,** 792 (2001).

[5] Ch.E. Düllmann et al., J. Phys. Chem. A (submitted)

[6] A. Türler et al., this Annual Report and submitted to Phys. Rev. Lett.

[7] Ch.E. Düllmann et al., Nucl. Instrum. Meth. **A479,** 631 (2002).

[8] U. Kirbach et al., Nucl. Instrum. Meth. A (in press)

[9] I. Zvara et al., Radiochim. Acta **38,** 95 (1985).

Confidence Intervals for Experiments with Background and Small Numbers of Events

W. Brüchle, GSI

Some nuclear reactions with low cross sections yield only small numbers of atoms or specific events. It is not trivial to give statistically satisfying error bars for this cross sections and derived constants like e.g. fission branches or chemically interesting K_d- values. The right description for low count rates is given by the Poisson distribution (see Fig. 1 and Formula 1).

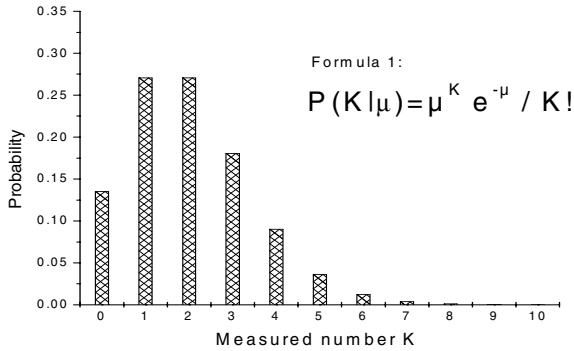


Fig.1 Poisson distribution for mean expectation number μ=2

But often one does not know μ, but measures K events and wants to know the mean μ and its error. Classically the lower and upper limits μ_l and μ_u are given by the following equations (for a 'central' interval with equal errors on both sides)[1,2] :

$$1-\sum_{K=0}^{K_m-1}\frac{\mu_l^K}{K!}e^{-\mu_l}=\varepsilon/2 \qquad \sum_{K=0}^{K_m}\frac{\mu_u^K}{K!}e^{-\mu_u}=\varepsilon/2 \qquad (2)$$

with ε=0.32, corresponding to the conventional 1σ error of a Gaussian, and K_m the observed number. μ_l and μ_u are determined by iteration. Another method is the so called Bayesian. If one covers all possible values of μ, weighing with the probability of μ to give an observation of K, one shall get a probability density distribution of likely μ's. If one integrates the resulting curve to get a central interval, the upper limit is identical with the classical value, but the lower value differs. The reason is the limit K_m-1 in formula 2. To show that this limit yields wrong results one can perform the gedanken experiment to set ε=1 (confidence level zero). Then μ_l and μ_u are expected to have identical values with 50% of all probabilities below and above this value. This is only the case when K_m-1 in formula 2a is replaced by K_m. Now the results are the same as with the Bayes method. From Fig. 2 one can see there is some flaw with the central interval. For skewed curves the central method with equal error probability on both sides cuts at different probability densities (horiz. pattern). For the extreme case k=0, when no event was observed, the central method would even cut off the part with the highest probability. To overcome these difficulties it is recommended to switch to the 'shortest interval' with the highest probability density (vertical pattern). Here the 'middle' interval contains the same area in both cases.

Let us now consider the case of non-negligible background, e.g. from contaminating nuclides, electronic noise, or cosmic showers. Normally these background rates are Poisson distributed, too. It would be wrong to subtract just the mean background rate (BG) from the measured value and go on with the above-mentioned method. One reason for this is, that normally the average BG is no integer number, but our basis is, that only integer numbers (counts) are measured. It is wrong, too, to shift the Poisson curve for the measured K by the value of BG, since this would result in negative count-rates for parts of the distribution. The actual background is restricted to values of less than or equal to the measured value K. First, one has to determine the distribution of background values with formula 1 and μ=BG, and has to normalize to 100% for background values between zero and the measured K; cutting off all possible background contributions higher than the measured value that naturally is the sum of the unknown real events and the unknown actual background. Then one can sum up all Poisson curves for the possible real value, weighing with the probability of (K-background). Fig. 3 shows an example for measured K=3 and BG=1.2. The method can be expanded to ratios of small numbers.

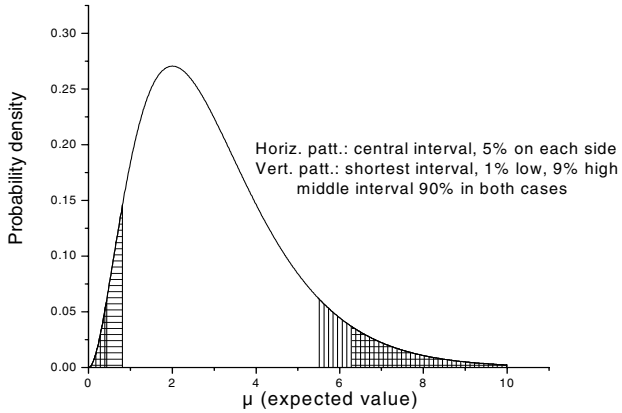


Fig. 2 Poisson distribution for measured K=2

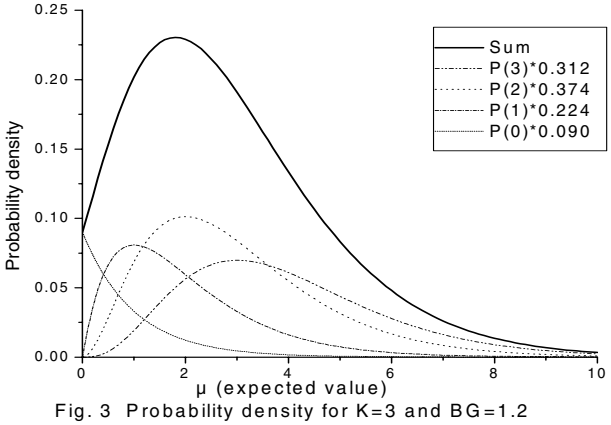


Fig. 3 Probability density for K=3 and BG=1.2

[1] K. H. Schmidt et al., Z. Phys. A 316 (1984) 19-26
[2] Biometrika Tables for Statisticians Vol. 1, 3.ed. 1966

Deposition of osmium tetroxide on reactive surfaces

A. von Zweidorf[1,2], R. Angert[1], W. Brüchle[1], E. Jäger[1], J.V. Kratz[2], G. Langrock[2], M. Mendel[2], A. Nähler[2], M. Schädel[1], B. Schausten[1], E. Schimpf[1], E. Stiel[1], N. Trautmann[2], G. Wirth[1]

[1]Gesellschaft für Schwerionenforschung, Darmstadt, [2]Institut für Kernchemie, Johannes Gutenberg-Universität Mainz

The recent study of the chemistry of element 108, hassium [1], leads to the conclusion, that it forms a volatile oxide, as expected for a member of group 8 of the periodic table [2]. So far, no chemical reaction of this oxide is known. To learn more about the chemical behaviour of hassium, one would like to investigate the chemistry of hassium oxide, the only known compound of hassium. Presumably, it is chemically similar to OsO_4 and RuO_4, which have an acidic character and are able to form salts with alkaline materials.

For that reason, a **C**ontinuously Working **A**rrangement For C**l**uster**l**ess Transport Of **I**n-**si**tu Produced Volatile **O**xides, *CALLISTO*, was developed and successfully used to deposit the volatile OsO_4 on metallic sodium surfaces [3]. Although these surfaces are very efficient for the deposition process, the quality of the α-spectra deteriorates with time. This could be explained by the obvious fact, that the sodium surface is covered with an increasing oxide layer, which doesn't interfere significantly with the deposition process, but disturbs considerably the detection process. Consequently, other deposition materials are required.

It is well known, that OsO_4 reacts with olefins. Mostly this reaction is done in solution. For purposes of α-detection, a solid olefin with the ability to form a smooth layer would be required.

Fortunately, cis-1,4-polybutadiene is such an substance. It contains double bonds and because of its polymeric character one can easily produce reproducible layers of it. (Fig. 1)

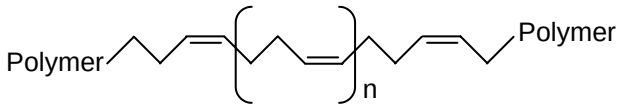


Fig. 1: cis-1,4-polybutadiene

The yield of the reaction of the solid polymer with the gaseous OsO_4 is shown in Fig. 2.

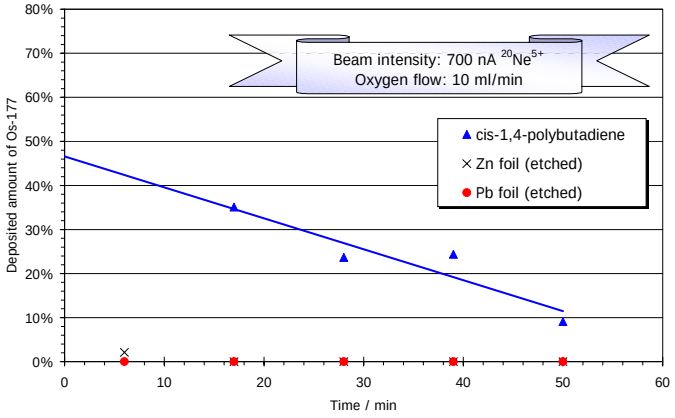


Fig. 2: Deposition of osmium tetroxide on cis-1,4-polybutadiene

Unfortunately, this relatively low yield shows, that this method is not adequate for experiments with hassium oxide. As shown, cis-1,4-polybutadiene is more reactive than etched surfaces of zinc and lead, on which almost nothing is deposited.

This leads to the implication, that alternative materials for the deposition of OsO_4 are needed.

If alkaline materials are suitable for our purposes, an alkaline surface would be most efficient. Unfortunately, it is hardly possible to reproducibly prepare thin layers of an alkali hydroxide without a substrate. Nevertheless, is it possible to coat an inert material with a smooth layer of alkali hydroxide. We choosed at first graphite as inert substrate and coated it with a thin layer of KOH, using the solubility of KOH in C_2H_5OH and preparing the layer from an ethanolic solution. The results for 2 different amounts of helium as transport gas are shown in Fig. 3.

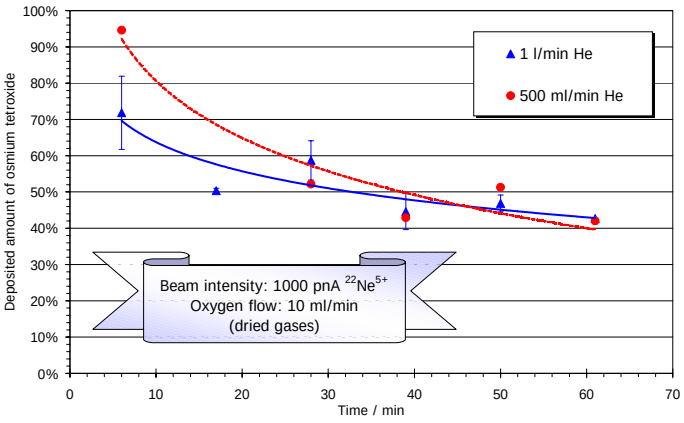


Fig. 3: Deposition of OsO_4 on graphite, coated with KOH

We used our recently developed gas drying-unit to dry the transport gases, remaining less than 0.5 ppm humidity in the gas flow. Surprisingly, the yield of the deposited OsO_4 decreases significantly with time. This behaviour is relatively unexpected, because the macroscopic amount of hydroxide cannot be fully neutralised with the microscopic amount of osmium tetroxide.

In a recent experiment, we found evidence for the important role of catalytic amounts of water. If we add some additional water vapour to the transport gas, the deposition process benefits greatly. This could explain, why an alkaline surface would be less reactive after a certain time of contact with the dried gas. This has to be studied in a forthcoming experiment.

We want to thank Dr. M. Watson, MPI Mainz, for the preparation of cis-1,4-polybutadiene.

[1] http://www.gsi.de/presse/Hassium.html

[2] V. Pershina *et al.*, J. Chem. Phys. **115** (2001), p.792

[3] A. v. Zweidorf, GSI Scientific Report 2000-1, p.171

Preparation of Targets for the New GSI Rotating Wheel Target Assembly

K. Eberhardt[1], P. Thörle[1], N. Trautmann[1], M. Schädel[2], E. Schimpf[2]
[1]Institut für Kernchemie, Universität Mainz; [2]GSI, Darmstadt

Electrodeposition is widely used for the preparation of lanthanide and actinide targets on metallic and non-metallic backing materials.[1] For heavy ion studies often Be is required as backing material. The deposition of lanthanide and actinide elements can be performed from an organic solution (usually isopropanol) with current densities of only a few mA/cm^2 and voltages up to 1200 V. The lanthanide or the actinide compound, normally the nitrate, is dissolved in a small volume (5-20 µl) of 0.1 N nitric acid and then mixed with 7 ml of the organic solvent. With this „Molecular Plating (MP)“ technique target densities in the order of 1 mg/cm^2 are possible.
In order to prevent excessive heating of a stationary target at high beam currents as delivered from heavy-ion accelerators, a rotating wheel system with a multi-target device has been developed at GSI. Here, the rotation speed of the wheel is adapted to the pulse structure of the ion beam. The wheel rotates with a frequency of 2000 rpm in order to distribute each beam pulse evenly over one target segment.
A multi-target device consists of three banana-shaped segments. One segment is shown schematically in Fig. 1. The target area is 1.9 cm^2 per segment and the banana-shaped backing is mounted on a Al-frame prior to deposition.

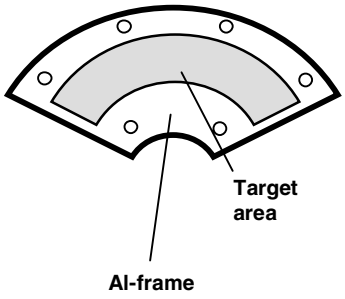


FIGURE 1. Schematic view of one of three segments for a rotating wheel target arrangement. The banana-shaped target covers an area of 1.9 cm^2 (per segment).

Table 1 summarizes the lanthanide and actinide targets produced in the last two years at the Institut für Kernchemie in Mainz for the new GSI rotating wheel target assembly. The ^{248}Cm targets have been used in a recent experiment at GSI to investigate the chemical properties of hassium (Z=108) [2]. Here, a 2.82 mg/cm^2 Be foil was used as backing material. The ^{248}Cm targets were irradiated with an intense $^{26}Mg^{5+}$-beam with an energy of 192.7 MeV applying beam currents up to 6.6 eµA. The ^{248}Cm target material was obtained by chemical separation from a ^{252}Cf-source [3]

Very often, prior to deposition, chemical separation procedures are required to ensure highest possible purity of the target material. This is of special importance in many HI-experiments, since HI-reactions with impurities like Pb have much higher cross sections compared to the HI-reaction of the target material itself. Furthermore, traces of Be present in recycled target material, prevent an effective deposition by molecular plating, and thus must be removed.
For this, the irradiated target material is dissolved in 2 N nitric acid from the Be backing foil and the solution is evaporated to dryness. The residue is dissolved in 2 ml of a nitric-acid/methanol mixture (1 N HNO_3/90 Vol% methanol). This solution is transferred to an anion-exchanger column (AIX; BIORAD AG 1X8) and the column is eluted with 4 x 2 ml of the methanolic solution at room temperature. Under these conditions, Be is completely removed from the column. In the next step the trivalent lanthanides or actinides are eluted with 1 N nitric acid. This procedure is repeated at least twice to get rid of all Be.

Table 1. Targets used in HI reaction experiments with the new GSI rotating wheel assembly.

Isotope	Backing	Thickness [µg/cm^2]	Method
Ba (nat)	Ti / 5 µm	400	MP
Ce (nat)	Ti / 5 µm	800	MP
Nd (nat)	Ti / 5 µm	800	MP
Gd (nat)	Be / 10 µm	1100	MP
Dy (nat)	Ti / 5 µm	800	MP
Er (nat)	Ti / 5 µm	800	MP
Yb (nat)	Ti / 6 µm	300	MP
U(nat)/Nd(nat)	Be / 10 µm	800	MP
Gd-152	Be / 10 µm	800	MP
#Cm-248	Be / 15 µm	240	MP
	Be / 15 µm	730	MP
	Be / 15 µm	690	MP

3 segments form a complete target device

Pb and other impurities are separated from lanthanide or actinide elements by means of a cation-exchanger column (CIX; Dowex 50WX8). 3 ml of a 0.5 N HCl solution are transferred to a CIX-column (150 x 4 mm) operated at 55^{0}C. The column is first washed with 8 x 2 ml 0.5 N HCl. Then Pb is eluted with 10 ml 1,5 N HCl and 5 ml 1.5 N HNO_3, whereas the trivalent lanthanides and actinides remain on the column. In a subsequent step, the lanthanides or the actinides are eluted with 15 ml 8 N HNO_3. This procedure is repeated with a smaller column (50 x 3 mm).

References:

[1] K. Eberhardt et al., AIP Conference Proceedings **576**, 1144 (2001)
[2] Ch. E. Düllmann et al.; to be submitted to Nature
[3] R. Malmbeck et al., Radiochim.Acta **89**, 543 (2001)

Vacuum thermochromatography of radon on transition metals Cu, Ag, Au, Pd, and Ni

R. Eichler, E. Jäger, E. Schimpf & M. Schädel (GSI Darmstadt)

Already in 1975, Pitzer [1] suggested that superheavy elements 112 and 114 may behave chemically like noble gases. Contrary to this assumption, 112 and 114 may behave similar to their homologues in groups 12 and 14, Hg and Pb, respectively, but with a much more noble character [2,3].

Assuming a noble gas like behavior of the elements 112 and 114, the chemically most similar element is Rn, a so-called pseudo-homologue to 112 and 114. A differentiation between a noble gas and a noble metal can be done using gas adsorption chromatographic techniques with metal surfaces as stationary phases. As a model study, we investigated adsorption properties of Rn on transition metal surfaces of Cu, Ag, Au, Ni, and Pd. We choose the method of vacuum thermochromatography. It provides several crucial advantages: (i) no carrier gases = no surface contamination, no co-adsorption effects, (ii) excellent heat isolation = stable temperature gradients to 20 K, (iii) fast separation, (iv) comfortable coupling to physical separators, working at vacuum conditions or at low gas pressures.

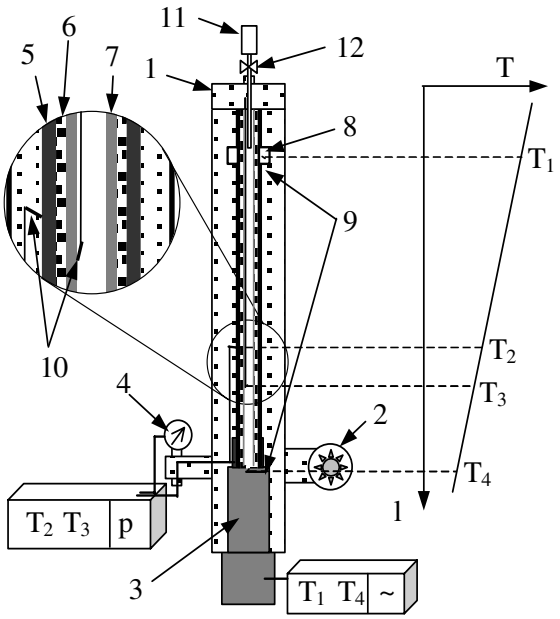


Figure 1. Schematic view of the vacuum thermochromatography setup and the temperature gradient with: **1** vacuum chamber, **2** turbo molecular pump, **3** cryogenic pump, **4** ionization gauge, **5** copper tube (∅i = 5 mm) mounted onto the cryogenic pump head, **6** quartz tube (∅i=3.75 mm), **7** metal foil inlay, **8** oven, **9** thermocouples controlling the temperature gradient (T1 temperature of the cryogenic pump, T4 oven temperature), **10** monitoring thermocouples (T2 stationary, on the outside of the copper tube, T3 inside, moveable along the column), **11** emanation source of ^{220}Rn or ^{219}Rn ($^{232}ThO_2$, $^{227}Ac_2O_3$), **12** valve.

Vacuum thermochromatography has been used already in the 1970's at the mass separator OSIRIS [4,5] and for adsorption investigations of heavy actinides [6] and Po [7]. However, for the first time we have installed and operated a *low temperature vacuum thermochromatography*. Fig. 1 shows a schematic of the device built at GSI.

Off-line vacuum chromatography experiments are performed in the following way. After evacuating the entire set-up to $3x10^{-5}$ Pa, the valve (12) to the Rn-source (11) is opened. Rn isotopes emanate into the chromatography column. They undergo thousands of adsorption-desorption steps along the chromatography column until they decay to their long-lived decay products ^{212}Pb and ^{211}Pb. The Pb atoms keep adsorbed at low temperatures, and thus, they are not moving along the chromatographic surface. Hence, the original distribution of the short-lived radon isotopes is preserved and can be determined after the removal of the chromatographic column by γ-spectroscopy, applying a HPGe-detector with a 1cm lead collimator. The result of such experiment is shown in Fig. 2.

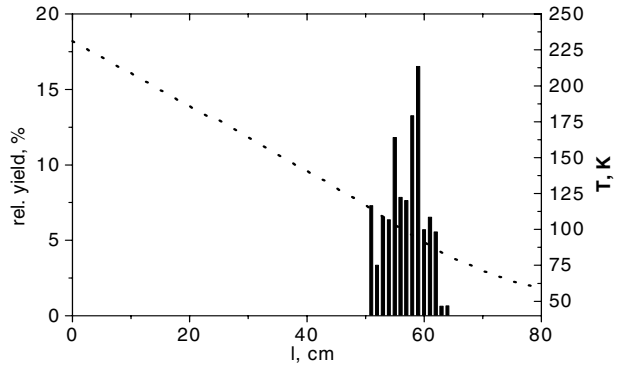


Figure 2. Vacuum thermochromatogram of ^{219}Rn on a poly-crystalline Ag surface treated by heating the metal in a reducing gas mixture of H_2/N_2 at 1000 K. The temperature gradient is shown as a dotted line. Experiment lasted for 3 h.

A thermodynamic model [7,8] connects the isotope half-life, the dimensions of the column, the temperature gradient, the deposition temperature and the standard adsorption enthalpy (ΔH^o_{ads}) of the adsorbate (Rn) on the metal surface. ΔH^o_{ads}-values for Rn on the investigated metal surfaces were deduced from the experimental results and are presented in Table 1.

Table 1. The standard adsorption enthalpies of Rn on transition metal surfaces determined by vacuum thermochromatography

Metal	$-\Delta H^o_{ads}$ / kJ/mol
Cu	37±2
Ag	20±2
Au	29±2
Pd	37±2
Ni	39±2

References

[1] K. Pitzer, *J. Chem. Phys.* **63 (2),** 1032 (1975).
[2] B. Eichler, *Kernenergie* **19 (10),** 307 (1976).
[3] B. Eichler, *PSI Report 00-09*, (Villigen, 2000).
[4] B. Grapengriesser et al., *Radiochim. Acta* **20**, 85 (1973).
[5] G. Rudstam et al., *Radiochim. Acta* **20**, 97 (1973).
[6] B. Eichler et al., *Kernenergie* **30,** 11 (1987).
[7] H. Gäggeler et al., *Radiochim. Acta* **40,** 137 (1986)
[8] B. Eichler, *Report ZfK-346*, (Rossendorf, 1977).

A Monte-Carlo model of vacuum thermochromatography

Robert Eichler & Matthias Schädel (GSI Darmstadt)

Monte-Carlo simulation methods for the evaluation of standard adsorption enthalpies (ΔH^o_{ads}) of chemical species from their deposition temperatures in gas thermochromatography have been suggested by Zvara [1]. Here, we present a new microscopic, kinetic Monte-Carlo model of the gas adsorption process occurring in vacuum thermochromatography to determine ΔH^o_{ads} from the measured deposition temperature of radon [2]. The model powerfully yields deposition temperatures and deposition widths of species with known or predicted ΔH^o_{ads} in a cylindrical stationary phase with a temperature gradient applied in vacuum. It can be easily adapted to different simple macroscopic geometries of the stationary phases (e.g. rectangular channels). It can be applied to select the best design of vacuum thermochromatography set-ups. As an input the model needs: (i) the geometrical dimensions of the stationary phase (tube length and diameter), (ii) the half-life of the nuclide, (iii) the maximum phonon frequency of the stationary phase [3], (iv) the temperature gradient along the stationary phase, and (v) the assumed standard adsorption enthalpy of the adsorbate on the stationary phase. The mean time the atom remaining in the adsorbed state at a defined temperature is determined by a Frenkel-like Ansatz:

$$t_{ads}=1/\nu_B \cdot \exp(-\Delta H^o_{ads}/R \cdot T) \quad (1)$$

The randomly selected lifetimes (τ) (according to the radioactive decay law with the half-life $t_{½}$) and adsorption times (τ_a) are distributed exponentially:

$$P(\tau)=1/\tau \cdot \exp(\tau/t_{½}) \quad (2)$$

$$P(\tau_a)=1/\tau_a \cdot \exp(\tau_a/t_{ads}) \quad (3)$$

The solid angles (φ, θ) of desorption of an adsorbed atom from a surface into the vacuum are selected randomly with a probability distribution using a cosine law according to Knudsen [4], i.e., the probability of adsorption under the angle ϕ or θ is $\cos(\phi)$ or $\cos(\theta)$, respectively. One of these solid angles (ϕ) determines the movement of the atom along the column; see Figure 1.

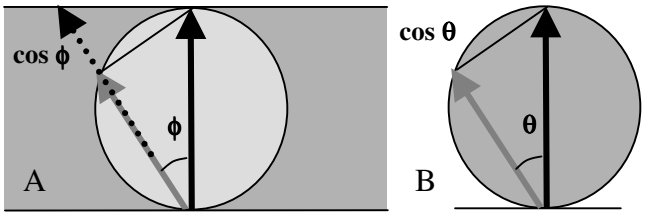


Figure 1. Schematic view of the trajectory of a desorbing atom in a cylindrical tube. Views perpendicular (A) and along (B) to the chromatographic column.

The sticking coefficient, which quantifies the adsorption probability of the adsorbate hitting the surface was set to be unity, as it was determined experimentally for the adsorption of Xe on metals [5]. The fates of about 10000 atoms each were calculated in this microscopic model, producing simulated internal thermochromatograms as shown in Figure 2 A and B (stepped lines). Simulations are repeated with different values for ΔH^o_{ads} until the simulated distribution matches best the experimentally determined activity distribution.

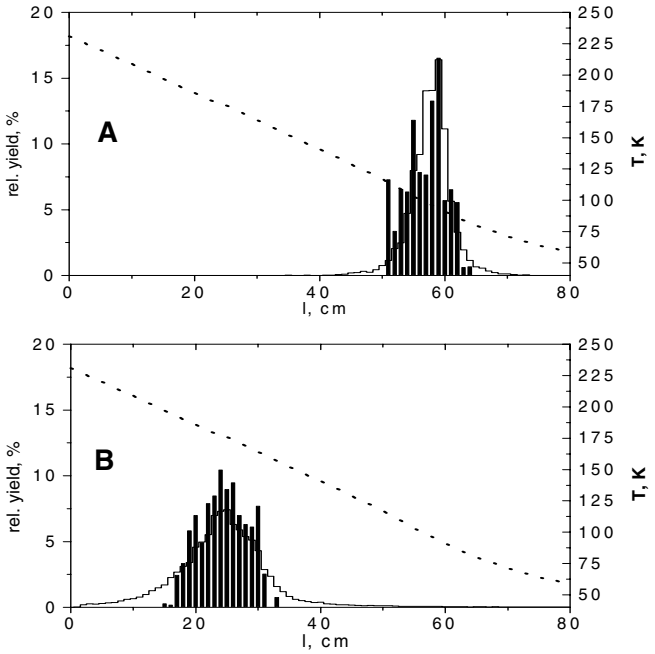


Figure 2. Experimentally observed vacuum thermochromatograms (bars) together with the obtained simulated thermochromatograms using the described model (stepped line). A: ^{219}Rn on a polycrystalline Ag surface treated by heating the metal in a reducing gas mixture of H_2/N_2 at 1000 K. B: ^{220}Rn on a polycrystalline Ni surface treated by heating the metal in a reducing gas mixture of H_2/N_2 at 1000 K. The temperature gradients are shown as dotted lines.

The resulting $\Delta H^o_{ads(kin)}$ for the adsorption of Rn on different transition metals are listed in Table 1 together with the $\Delta H^o_{ads\ (therm)}$ determined using a collective thermodynamic equilibrium model of adsorption [2]. Both values are in good agreement.

Table 1 The standard adsorption enthalpies of Rn on transition metal surfaces determined using a well known thermodynamic collective model of vacuum thermochromatography and the microscopic model developed in this work

Metal	$-\Delta H^o_{ads\ (therm)}$ / kJ/mol	$-\Delta H^o_{ads\ (kin)}$ / kJ/mol
Cu	37±2	40±2
Ag	20±2	23±2
Au	29±2	33±2
Pd	37±2	41±2
Ni	39±2	43±2

References

[1] I. Zvara, *Radiochim. Acta* **38,** 95 (1985).
[2] R. Eichler et al., this report and *J.Phys.Chem B* (submitted).
[3] P.H. Dederichs .et al., Landoldt Börnstein: Metalle, Bd. 13, Springer-Verlag: Berlin, Heidelberg, New York (1981).
[4] M. Knudsen *Ann. Phys. 4* ***28,*** 75 (1909).
[5] P.W. Palmberg, *Surf. Sci.* **25,** 598, (1971).

Prediction of adsorption enthalpies of the SHE 112 and 114 on transition metals

Robert Eichler & Matthias Schädel (GSI Darmstadt)

An empirical adsorption model for the adsorption interaction of light noble gases on metal surfaces is given by Miedema et al. [1]. It assumes a proportionality between the adsorption enthalpy (ΔH^o_{ads}) and the energy of adhesion ($\Delta\gamma_{ad}(A,B)$). The energy of adhesion can be calculated using the surface energies (γ^o) of the elements A (adsorbate) and B (surface) at 0 K[1] (see eqns.1 and 2).

$$\Delta\gamma^{ad}(A,B) = -2\,\Phi\,(\gamma^0(A)\,\gamma^0(B))^{1/2} \quad (1)$$

$$\Delta H^o_{ads} = -0.71*10^9\,F\,\Phi\,V_A^{2/3}\,(\gamma^0(A)\,\gamma^0(B))^{1/2} \quad (2)$$

Φ ... dissimilarity parameter (calculated) [1]
F ... geometrical factor (empirically 0.31) [1]
V_A ... Volume of the spherical, adsorbed atom

A comparison of a large number of experimentally determined adsorption enthalpies for the light noble gases with such a calculation suggests [1], to calculate the adsorption enthalpies of the light noble gas elements Ne, Ar, and Kr by multiplying known adsorption enthalpies of Xe with empirical constant factors ($C_x(Z,Xe)$); see eqn. 3. Recommended factors are compiled in the upper part of Table 1 for Ne, Ar, Kr and Xe.

$$\Delta H^o_{ads}(Z) = C_x(Z,Xe)\cdot\Delta H^o_{ads}(Xe) \quad (3)$$

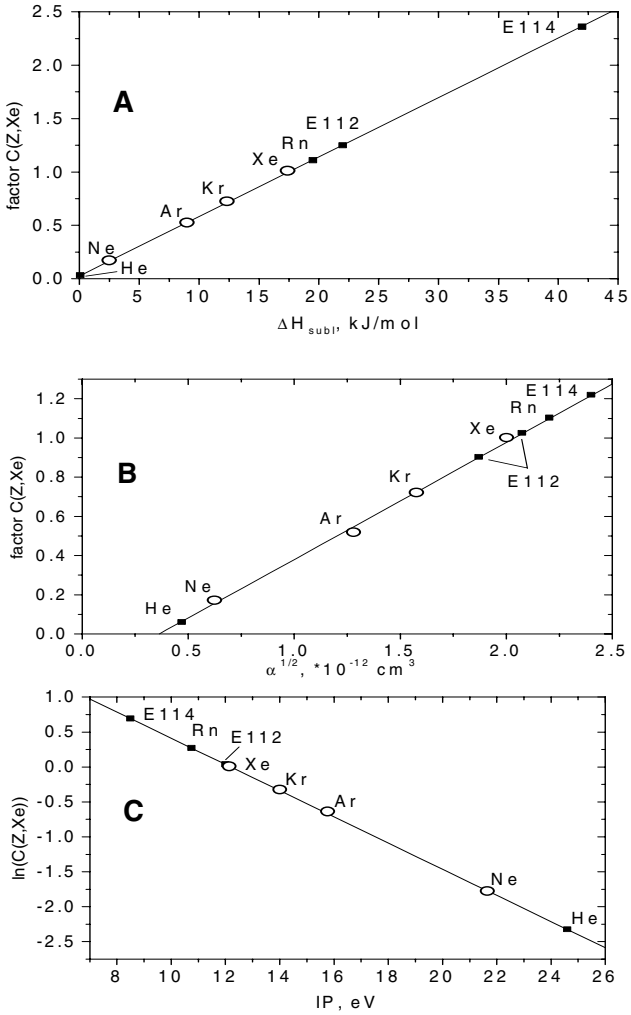


Figure 1. Empirical extrapolations of $C_x(Z,Xe)$.

Three different empirical correlations of $C_x(Z,Xe)$ have been obtained from known properties of adsorbate atoms (circles in Figure 1, A-C): the enthalpy of sublimation (ΔH_{subl}), the polarizability (α), and the ionization potential (IP). The factors extrapolated for the noble gases He and Rn and for the hypothetical noble gas elements 112 and 114 (squares in Figure 1 A-C) are listed in the lower part of Table 1.

Table 1. Empirical factors $C_x(Z,Xe)$ that connect the heat of adsorption of a closed shell atom**, Z,** with the known heat of adsorption of Xe on the same metallic substrate.

Element	$C_A(Z,Xe)$	$C_B(Z,Xe)$	$C_C(Z,Xe)$
Ne	0.17	0.17	0.17
Ar	0.52	0.52	0.52
Kr	0.72	0.72	0.72
Xe	1	1	1
He	0.032	0.12	0.098
Rn	1.11	1.11	1.31
E112	1.25	0.91 1.04	1.04
E114	2.36	1.2	2.00

As a test, adsorption enthalpies of Rn on different transition metals have been calculated with eqn. 3. They agree well with the experimental results from [2]; see Table 2. Even the trend in the adsorption interactions of Rn on the metals Ag<Au<Pd≤Ni is well reproduced. The deviation of Cu is object of further investigations.

Table 2. Comparison of experimental [2] and calculated data for the adsorption of Rn on transition metal surfaces [2]

Metal	$-\Delta H^o_{ads\,(Exp)}$ / kJ/mol	$-\Delta H^o_{ads\,(calc)}$ / kJ/mol
Ag	21±3	26±2
Au	31±3	33±2
Pd	39±3	35±2
Ni	41±3	37±2
Cu	38±3	25±2

Assuming a fictitious noble gas behavior of the elements 112 and 114, we predict adsorption enthalpies on the transition metals Cu, Ag, Au, Pd, and Ni; see Figure 2.

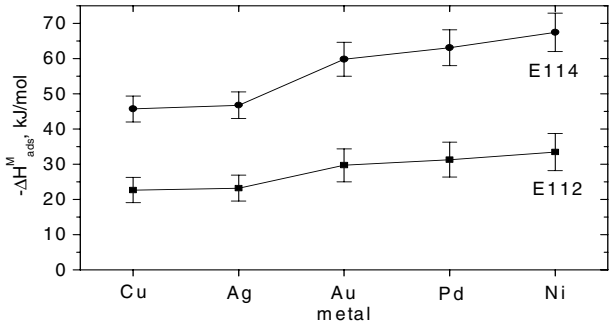


Figure 2. Predicted standard adsorption enthalpies of the hypothetical noble gas elements 112 and 114.

References

[1] A.R. Miedema et al., *Surf. Sci. 104*, 491 (1981).
[2] R. Eichler et al., this GSI report, and *J.Phys.Chem B,* submitted 2001.

Intermetallic Compounds of Element 112: the Electronic Structure and Bonding of HgX and 112X (X = Pd, Ag and Au)

V. Pershina[1], T. Bastug[2], T. Jacob[2], B. Fricke[2]
[1] GSI, Darmstadt
[2]Fachbereich Physik, Universität Kassel, 34109 Kassel

The next heaviest element which is to be studied chemically at the JINR, Dubna, [1] and GSI [2] is element 112. Its properties are expected to be unique: high volatility and inertness due to the very strong relativistic stabilization of the 7s electrons and the closed-shell configuration, $7s^26d^{10}$ [3]. The surface of the chromatography column in the gas-phase chromatography experiments is to be made out of gold and palladium, since the interaction of Hg, the nearest homolog of element 112, with those metals was found to be rather strong [4].

To detect element 112 on those surfaces, the knowledge of its adsorption enthalpy is highly desirable. As a first step in the study of the metal-surface interaction, we have calculated here the electronic structure and bonding of the dimers, HgX and 112X (X = Pd, Ag and Au). The calculations were performed using the fully relativistic density-functional method (DFT) with the relativistic general gradient approximation (RGGA) for the exchange-correlation potential [5]. The Mulliken population analysis was applied additionally to study bonding in these systems. The calculated RGGA binding energies, D_e, optimized bond lengths, R_e, and harmonic frequencies, w, are shown in Table 1. The obtained D_e are probably too large by about 0.2 eV, which is an average error of the DFT method [5].

Table 1. Calculated RGGA binding energies, D_e, bond lengths, R_e, and harmonic frequencies, w, for HgX and 112X (X = Pd, Ag and Au)

Molecule	R_e, Å	D_e, kJ/mol	w, cm^{-1}
HgPd	2.56	61.2	125.62
HgAg	2.72	29.4	90.20
HgAu	2.66	52.7	101.95
112Pd	2.62	45.3	115.00
112Ag	2.76	19.0	75.41
112Au	2.73	31.7	79.17

Table 2. Overlap populations of the valence AO in HgAu and 112Au

Orbitals	HgAu	112Au
ns-ns	0.01	-0.02
ns-$np_{1/2}$	0.04	0.05
ns-$np_{3/2}$	0.06	0.03
np(tot)-ns	0.06	0.04
(n-1)d-np	0.01	0.00
(n-1)d-(n-1)d	-0.01	-0.01
OP(tot)	0.34	0.24

The calculations revealed an increase in R_e and a decrease in D_e of about 15 – 20 kJ/mol from HgX to 112X. The decrease in D_e is explained by a drastic relativistic stabilization and therefore inertness of the $7s^2$ shell. This results in a large decrease in the 7s(112)-Au overlap compared to the 6s(Hg)-Au one, as the data of Table 2 show. The contribution of the other orbitals is almost unchanged.

In Fig. 1, the calculated D_e are shown together with experimental adsorption enthalpies, ΔH_{ads}, of Hg on the corresponding metal surfaces [4]. One can see nice agreement for the trends between the two types of data, with the interaction of Hg and element 112 with Pd being the strongest.

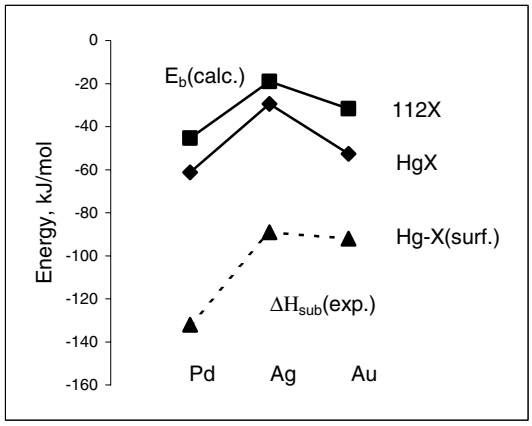


Fig. 2. Calculated binding energies for HgX and 112X (X = Pd, Ag and Au) and measured ΔH_{ads} on the corresponding metal surfaces [4,6]

Thus, the calculations describe the bonding in the right way, so that the difference in D_e between HgX and 112X could be related to the difference in ΔH_{ads} of Hg and element 112 on the metal surfaces. Thus, element 112 is expected to be weaker adsorbed than Hg, though not as weak as was expected earlier.

In the future calculations of adsorption on a cluster, one can foresee even a smaller difference between Hg and element 112, since the 6d orbitals of the latter will be more involved in the coordinated bonding due to their relativistic destabilization and expansion [3].

References

[1] A. Yakushev, presentation at the ASR2001, Tokai, Japan, 2001, to be published.
[2] H. W. Gäggeler, et at. UNILAC Proposal, GSI, 2000.
[3] B. Fricke, *Struct. Bond.* **21**, 89 (1975).
[4] B. Eichler, H. Rossbach, *Radiochim. Acta* ***33***, 121 (1983).
[5] S. Varga *et al. Phys. Rev.* A **59**, 4288 (1999).
[6] S. Soverna, *et al.* Presentation at the GDCh meeting, Würzburg, 2001.

Towards a calculation of adsorption enthalpies for molecules of superheavy elements

C. Sarpe-Tudoran[1], T. Jacob[1], B. Fricke[1], S. Fritzsche[1], W.-D. Sepp[1], V. Pershina[2]
[1]Fachbereich Physik, Universität Kassel, 34109 Kassel
[2]GSI, Darmstadt

In order to be able to calculate adsorption enthalpies for molecules of superheavy elements which can be measured in gas-phase thermochromatography experiments we are presently developing a code which should be able to calculate this quantity. Our starting-point was a full relativistic *ab initio* density functional molecular code [1]. In order to be able to simulate larger clusters which eventually represent the surface of a solid, our first approach was to generate a parallelized version so that clusters of up to 100 atoms can be calculated in reasonable times. This has now been achieved [2].

The cluster-size which is needed to reach convergence for the quantity of adsorption enthalpie is strongly dependent on the elements that are involved. As an example, to describe the adsorption of CO on Pt(111) about 20 Pt atoms are sufficient [3], whereas Al on Al(100) requires much more atoms [4,5]. Especially those surfaces that are good conductors require a huge amount of atoms.

In addition to be able to calculate adsorption of molecules of superheavy elements a fully relativistic code is indispensable. To study the size convergence we present here cluster-size-dependent full relativistic calculations for the adsorption of Cu on Cu(100). We have chosen this system as a test because this allows a comparison with other (non-relativistic) calculations as well as copper is a well conducting element.

The method that is used for the calculations presented here is a relativistic four-component self-consistent field density functional approach. The total energy can be written as

$$E[\varrho] = T^{\mathrm{S}} + E^{\mathrm{N}}[\varrho] + E^{\mathrm{C}}[\varrho] + E^{\mathrm{xc}}[\varrho] \qquad (1)$$

with the electronic density

$$\varrho(\vec{r}) = \sum_{-mc^2<\varepsilon_i\leq\varepsilon_F} \psi_i^+(\vec{r})\psi_i(\vec{r}). \qquad (2)$$

Here the density is obtained from a sum of M auxiliary one-particle Dirac spinors. Then the corresponding relativistic form of the Kohn–Sham equations (rKS) [6] is

$$\left(\hat{t} + V^{\mathrm{N}}(\vec{r}) + V^{\mathrm{C}}(\vec{r}) + V^{\mathrm{xc}}(\vec{r})\right)\psi_i(\vec{r}) = \varepsilon_i\psi_i(\vec{r}), \qquad (3)$$

where $\hat{t} = -ic\vec{\alpha}\cdot\vec{\nabla} + (\beta-1)mc^2$ is the Dirac kinetic energy operator and V^{N} and V^{C} are the Coulomb potentials of the nuclei and the electrons. V^{xc} is the exchange-correlation potential and ε_i are the energy eigenvalues of the Dirac spinors.

During the self-consistent cycles the relativistic local-density approximation (rLDA) for the exchange-correlation functional is applied within the parametrization for the correlation suggested by Vosko, Wilk, and Nusair [7]. Finally the total energy is calculated perturbatively with the relativistic forms of the generalized gradient approximation (rGGA) [8]. For the exchange we use Becke's [9] formulation and for the correlation the functional proposed by Perdew [10] (B88/P86).

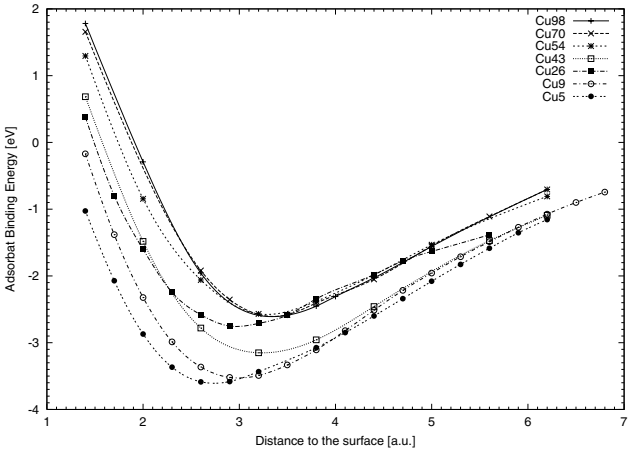


Figure 1: Potential energy curves in rLDA-approximation for all calculated systems.

After extensive calculations we are able to give the results for the potential energy curves as function of the distance of the adatom to the surface for system Cu_5 up to Cu_{99} in Fig.1.

As can be seen from these curves the results are the same for Cu_{54} and larger systems, so that the binding energy in the rLDA-approximation is -2.70 eV. This number can be compared to the best solid-state slab-calculations of Scheffler *et al.* [11] who got -2.74 eV.

This result is the first step towards a calculation of atoms respectively molecules of superheavy elements on realistic solids which will be needed in thermochromatography experiments.

References

[1] T. Baştuğ *et al.*, Phys. Rev. B **55**, 5015 (1997)
[2] T. Jacob, PhD thesis, Universität Kassel (2001)
[3] D. Geschke *et al.*, Phys. Rev. B, in press
[4] R. Stumpf *et al.*, Phys. Rev. B **53**, 4958 (1996)
[5] T. Jacob *et al.*, Surf. Sci. **486 (3)**, 194 (2001)
[6] W. Kohn *et al.*, Phys. Rev. A **140(4B)**, 1133 (1965)
[7] S. H. Vosko *et al.*, Can. J. Phys. **58**, 1200 (1994)
[8] E. Engel *et al.*, Phys. Rev. A **53**, 1367 (1996)
[9] A. D. Becke, Phys. Rev. A **38(6)**, 3098 (1988)
[10] J. P. Perdew *et al.*, Phys. Rev. B **33(12)**, 8800 (1986)
[11] Y. Shin, M. Scheffler, private communications

Theoretical Predictions of Hydrolysis and Complex Formation of Element 104, Rf, in HF and HCl Solutions

V. Pershina[1] and J. V. Kratz[2]
[1] GSI, Darmstadt
[2]Institut für Kernchemie, Universität Mainz, 55099 Mainz

The accumulated results on the extraction behaviour of element 104, Rf, from HF and HCl solutions have revealed quite a number of surprises and disagreements between separate measurements (for a review, see ref. [1]). Another open question was that of hydrolysis of Rf, where two types of experiments [2,3] revealed different trends for Zr, Hf and Rf. To clear those points, our theoretical research has been extended to the consideration of the above mentioned processes. Thus, we present here results of the calculations of the electronic structures of various hydrated, hydrolyzed and fluoride/chloride complexes of Zr, Hf, and Rf. On their basis, we predict stability and extraction of these complexes under the experimental conditions.

For the calculations, the fully relativistic density-functional (DFT) method [4] was used. For predictions of hydrolysis and complex formation, the model described in ref. [5] was utilized. It allows for predicting free energies of a reaction by calculating changes in the electrostatic, ΔE^C, and covalent interactions, (overlap population, OP), separately using Mulliken numbers. Results of the calculations of E^C are shown in Table 1.

Table 1. Coulomb part of the binding energy, E^C (in eV), for various complexes of Zr, Hf and Rf.[a]

Complex	Zr	Hf	Rf
$M(H_2O)_8^{4+}$	-53.36(8.93)	-52.09(9.03)	-50.93(9.11)
$MOH(H_2O)_7^{3+}$	-58.05(8.10)	-56.70(8.21)	-55.04(8.29)
$MF(H_2O)_7^{3+}$	-53.36	-52.07	-50.53
$MF_2(H_2O)_6^{2+}$	-50.40[b]	-49.14[b]	-47.38[b]
	-49.77[c]	-48.56[c]	-46.79[c]
$MF_3(H_2O)_5^{+}$	-45.44	-44.20	-42.32
$MF_4(H_2O)_4$	-37.50	-36.25	-34.41
MF_4 (T_d)	-12.79	-12.36	-11.61
MF_6^{2-}	-2.59	-1.18	0.23
MCl_4 (T_d)	-5.37	-4.26	-3.28
MCl_6^{2-}	-1.21	0.41	2.13

[a] some OP are given in the parentheses; [b] *cis*-position, [c] *trans*-position of F atoms.

On the basis of the data of Table 1, ΔE^C defining free energies of reactions, or complex formation constants, were determined. Thus, for the first hydrolysis step

$$M(H_2O)_8^{4+} \Leftrightarrow MOH(H_2O)_7^{3+},$$

the values of ΔE^C give the following trend in hydrolysis of group 4 elements: Zr > Hf > Rf in agreement with conclusions of ref. [3]. The first hydrolysis constant $\log K_{11}$(Rf) ≈ -4 was defined using ΔE^C, ΔOP and log K_{11} for Zr and Hf, similarly as it is shown in ref. [5].

For the fluorination process

$$M(H_2O)_8^{4+} \Leftrightarrow MF(H_2O)_7^{3+} \ \ldots \ \Leftrightarrow \ \ldots MF_5(H_2O)^{-} \Leftrightarrow \ MF_6^{2-},$$

the ΔE^C data of Table 1 give different sequences for Zr, Hf and Rf depending on whether the fluorination process starts from the non-hydrolyzed, or hydrolyzed (fluorinated) species (i.e., depending on pH). Thus, in the first case, the trend is Zr > Hf > Rf for all types of complexes, while in the second case, the trend for the formation of the cationic complexes is the same, Zr > Hf > Rf, but it becomes reversed for the formation of the anionic MF_6^{2-}: Rf ≥ Zr > Hf. The obtained sequences are in agreement with the cation exchange separations (CIX) of group 4 elements from 0.1 M $HNO_3/10^{-3}$ – 10^{-1} M HF solutions [6], while for the anion exchange separations (AIX), the experimental sequence depends on the competition of the counter ion NO_3^- for the binding sites.

For the following chlorination process

$$M(H_2O)_8^{4+} + 6HCl \Leftrightarrow MCl_6^{2-},$$

i.e., for the AIX separations at 4-8 HCl, the trend will definitely be Zr > Hf > Rf, so that the sequence obtained in experiments [7] cannot be explained on the basis of the calculated data.

It is interesting to note here, that for the formation of the tetrahedral species, MF_4 or MCl_4, which could be extracted, for example, by TBP, the trend is totally reversed in the group: Rf > Hf > Zr. Nevertheless, to predict the sequences in the extraction of these elements by TBP, the calculations of E^C for $ML_4(TBP)_2$ would be desirable.

References

[1] J. V. Kratz, In *Heavy Elements and Related New Phenomena*, Ed. Greiner, W. and Gupta, Raj K., World Scientific: Singapore, 1999, p. 129-193.
[2] A. Bilewicz, *et al.*, *Radiochim. Acta*, **75**, 121 (1996).
[3] K. R. Czerwinski, *Studies of Fundamental Properties of Rutherfordium (Element 104) Using Organic Complexing Agents*, Thesis, Lawrence Berkeley Laboratory, April 1992.
[4] T. Bastug, *et al.*, *Chem. Phys. Lett.* **211**, 119 (1993).
[5] V. Pershina and J. V. Kratz, *Inorg. Chem.* **40**, 776 (2001).
[6] E. Strub, *et al.*, *Radiochim. Acta* **88**, 265 (2000).
[7] Y. Nagame, presentation at the ASR2001, Tokai, 2001.

ACCELERATOR-EXPERIMENTS AND -DEVELOPMENT

Operation Report of UNILAC and SIS 189
D. Wilms, U. Scheeler

Ion Source Development and Operation 191
P. Spädtke, J. Bossler, M. Galonska, F. Heymach, R. Hollinger, R. Iannucci, R. Lang, K.D. Leible, K. Tinschert

UNILAC Status and Developments 193
W. Barth, L. Dahl, J. Glatz, L. Groening, J. Klabunde, S. Richter

SIS Status Report 195
K. Blasche, U. Blell, O. Boine-Frankenheim, H. Damerau, H. Eickhoff, M. Emmerling, P. Forck, B. Franczak, P. Hülsmann, G. Hutter, K. Kaspar, H.G. König, B. Langenbeck, G. Moritz, P. Moritz, C. Mühle, E. Mustafin, A. Peters,H. Reich-Sprenger, R.Rojko, U. Scheeler, G. Schreiber, P. Spiller, W. Vinzenz, D. Wilms

ESR Operation and Development 197
K. Beckert, P. Beller, W. Bourgeois, B. Franczak, B. Franzke, F. Nolden, U. Popp, A. Schwinn, M. Steck

Fast Pulsed Superconducting Magnets 198
J. Kaugerts, G. Moritz, C. Mühle, G. Walter

Simulation of the Nuclotron Dipole Magnet by a Hybrid 2D Finite-Element, Spectral-Element Discretization 199
H. De Gersem, M. Clemens, Y. Jing, M. Wilke, T. Weiland

Mismatch and Halo in High Intensity Accelerators 201
G. Franchetti, I. Hofmann

Selfconsistent Study of the Montague Resonance applied to the SIS100 203
I. Hofmann, O. Boine-Frankenheim

The Transition from Finite to Infinite Spherical Coulomb Crystals 205
R.W. Hasse

Superconducting CH-Cavities for Low- and Medium Beta Ion and Proton Accelerators 207
R. Eichhorn, C. Peschke, U. Ratzinger

RFQ Development for an Injector Linac for Therapy Facilities 209
A. Bechtold, U. Ratzinger, A. Schempp, B. Schlitt

Operation Report of UNILAC and SIS

U. Scheeler, D. Wilms GSI

This report describes the operation statistics of the accelerator facility of the year 2001. The data were collected with the help of the program **PROST** [1]. Accelerator development and experiments are the topic of separate contributions [2], [3] and [4] to this annual report.

1. General overview

The operation started at the begin of March after a longer shutdown, which was used to resume the maintenance of the Alvarez section (started in September 2000) and for the check and correction of beamline alignment of many sections along the accelerator. An upgrade of the power supplies between the pion target and the rear experimental stations now allows the fast change of polarity for the transport of negative pions and the pulse to pulse operation at all target stations. Altogether there were again 4 beam periods in this year. The first one lasted over almost 3 months until end of May and the three following beam periods had a length of almost 2 months.

Table 1: Overall beam time of the accelerator facility

	Total beam time 2001	Target time 2001	Target time 2000
UNILAC experiments	5569 h	4595 h	4854 h
SIS experiments	6695 h	5350 h	5118 h
ESR experiments		734 h	1031 h

The total beam time and the achieved target time is given in table 1 for the different experimental areas. The reduction of operation time of the accelerator facility (number of working hours), 5944 h in 2001, 6 days less than in the last year, is one reason for the lower values of target time at the UNILAC. Technical problems at the High Charge State Injector (vacuum leak of a drift tube quadrupol) led to a reduced operation time of this injector connected with the reduction and the shifting of beam time for a few experiments. In general the down times could be reduced by providing an alternative beam (if possible) with appropriate quality. The increase of beam time at the SIS shows that the main focus of operation was directed to the SIS experiments. The decrease of the ESR target time results from its use for reinjection. An Au-beam was redirected to the SIS after stripping in front of the ESR and there accelerated to 1.5 GeV/u for about four weeks.
Ion beams of 19 different isotopes from hydrogen to uranium were accelerated. They were delivered to 18 low energy experiments at the UNILAC and to 33 high energy experiments behind the SIS. As shown in Figure 1 the medium heavy elements were delivered to UNILAC experiments and the light

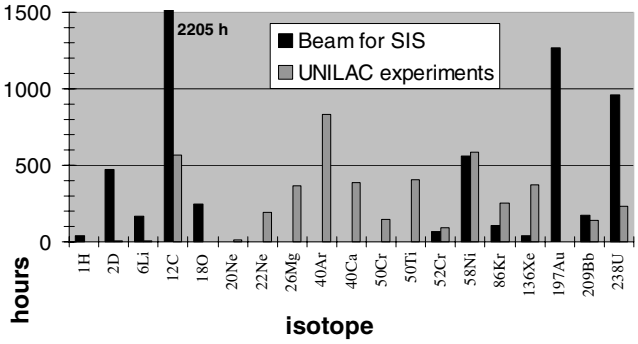


Figure 1: Accelerated isotopes in 2001

and heavy ones were mostly used at the SIS. This separated use of ion sources for different experiments allows a comfortable operation and the optimum realization of experimental requirements concerning intensity and duty cycle.

2. UNILAC Operation

The beam time for the UNILAC experiments is summarized in table 2. The column “fraction” contains the ratio (in percent) between the corresponding number of hours and the total beam time. It indicates the efficiency of the accelerator operation. The difference between operation time and total beam time results from beam periods, when the UNILAC was only used for SIS injection.

Table 2: Beam delivered to UNILAC experiments in 2001

	(h)	Fraction
Target time for experiment runs	4562	81,9%
Beam for experiment tests	36	0,6%
Accelerator development	66	1,2%
Accelerator tune-up	430	7,8%
Ion source replacement	103	1,8%
Unscheduled down time	283	5,1%
Retuning	53	1,0%
Stand-by	36	0,6%
Total beam time	5569	

The percentage of beam time for experiment (including tests) is slightly higher than in 2000. We tried to organized tune up and development times in parallel to running experiments, which led to a reduction of their percentage. The 66 hours for

accelerator development were used to a large fraction for the optimization of settings of the High Current Injector and the Alvarez section at High Current conditions.
The unscheduled down time was due to failures of injectors (45h), rf-amplifiers (100h), magnet power supplies (50h), beam diagnostics (2h), vacuum system (31h), computer control (22h) and others (33h). The 100 h of down time for rf-amplifiers result mainly from problems with the electrical strength of rf generator components of the High Current Injector.

Table 3: UNILAC beam delivered to SIS in 2001

	(h)	Fraction
Beam available for SIS injection	6630	89,9%
Accelerator development	22	0,3%
Ion source replacement	91	1,2%
Accelerator tune-up	259	3,5%
Unscheduled down time	339	4,6%
Retuning	33	0,5%
Total beam time	7374	

Table 3 displays the provided beam time of the UNILAC for SIS injection.

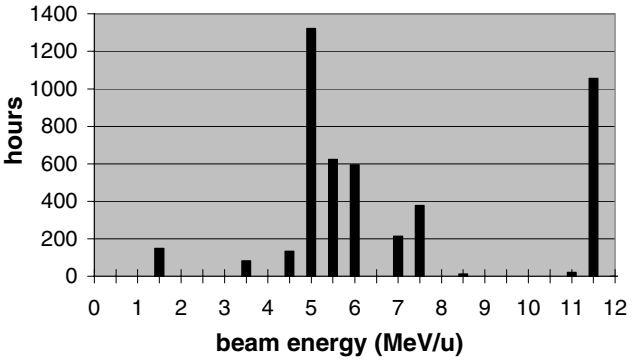


Figure 2: Beam energies of the UNILAC experiments

In Figure 2 the target time of the UNILAC experiments (without beam injected into SIS) is displayed versus beam energy. The new phase control units of the buncher cavities in the poststripper section allow phase changes from pulse to pulse. Therefore they can be used for beams with different energies. The beam energies in the range from 4 to 6 MeV/u mainly result from the experiments for super heavy element synthesis and nuclear physics. Energies around 8 MeV/u were used for nuclear chemistry experiments and above 10 MeV/u for material science and for the plasma physics experiments.

3. SIS Operation

In table 4 the operating statistics for the SIS is given. Compared to last year the total target time remains nearly constant.
The loss in beam time due to technical failures distributes to power supplies (59h), rf-amplifiers (66h), beam diagnostics

Table 4: SIS operation time in 2001

	(h)	Fraction
Beam for target area	4032	60,2%
Therapy	1313	19,6%
Beam delivered to ESR	729	10,9%
Beam for experiment tests	5	0,1%
Total target time	6079	90,8%
Accelerator development	226	3,4%
Accelerator tune-up	124	1,9%
Unscheduled down time	266	3,9%
Total beam time	6695	

(7h), computer control (17h), vacuum system (53h) and others (64h). A burn down of a transformer of the main power supply of the rf-amplifier caused a longer interruption and is mainly responsible for the long down time of rf cavities.

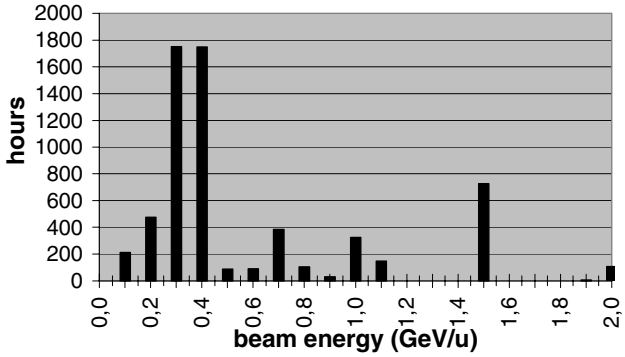


Figure 3: Beam energies delivered to the SIS experiments

Figure 3 shows the beam time versus energy for the SIS experiments. The high fraction of target time at about 400 MeV/u results from the acceleration of ^{12}C beam for the cancer therapy like in the last year. Beam at the lower energy range was also provided to the ESR and the fragment separator. The reinjection beam time of a gold beam provides the main part at 1.5 Gev/u. The remaining hours at this energy results from carbon beam for the pion production. 35 hours of hydrogen beam at 4.7 GeV/u are not displayed due for clearness.

References

[1] **PR**ogramm für **O**perating und **ST**atistik
[2] W. Barth et. al. UNILAC Status and Developments
[3] K. Blasche et. al. SIS Status Report
[4] M. Steck et. al. ESR Operation and Development

Ion Source Development and Operation

P. Spädtke, J. Bossler, M. Galonska, F. Heymach, R. Hollinger,
R. Iannucci, R. Lang, K.D. Leible, K. Tinschert

High Current Ion Sources

During the commissioning of the high current injector (HSI) in 1999 a result was that the ion currents are limited behind the acceleration system although the extracted ion currents from the ion source are even higher. In the acceleration gap the ion beam is inevitably decompensated for a few centimeters. As a result the space charge forces have to be compensated by the focusing strength of the gap. To investigate the optical properties of the acceleration system and the influence of a solenoid between ion source and acceleration gap on the brilliance of the ion beam, emittance measurements were made [1].

The ion source was a MUCIS [2] using deuterium, helium, argon and xenon. The emittance of the ion beam for different settings was measured as function of the following parameters: flux density of the solenoid, aspect ratio and aperture diameter of the acceleration system, and ratio of extraction voltage and acceleration voltage. Emittance measurements have shown how fundamental the solenoid is for the matching of the ion beam to the acceleration gap. This concerns the beam quality as well as the beam intensity exemplified by a comparison between an 88 keV argon beam (85 % $^{40}Ar^{1+}$) without and with solenoid. The aperture of the high voltage electrode is 40 mm in diameter and the aspect ratio S is 0.5. All the parameters (ion source parameters, aspect ratio, ratio of extraction voltage to acceleration voltage) have been optimized with the goal to extract a highly brilliant ion beam.

The extracted ion current was 120 mA and the the accelerated ion current was only 9 mA because of the small aperture of the HV-electrode. The absolute emittance for 90 % of the beam is 145 mm mrad with divergence angles less than 25 mrad. Using the solenoid the accelerated ion current increases by a factor of two and the ion beam is more brilliant although the emittance is a little bit larger. In the second case the solenoid has the maximum flux density. This is also the optimal condition for a highly brilliant 88 keV argon beam. The solenoid used for this experiment was limited in flux density, able to focus a beam up to a mass-to-charge ratio of 40 for the applied extraction voltage.

The emittance measurements pointed out that the solenoid is a very important instrument to match the ion beam to the acceleration system. For every ion species there exists an optimum solenoid flux density depending on the intensity and energy of the ion beam. To avoid too strong space charge forces in the acceleration gap a smooth injection of the ion beam into the acceleration system is favorable. It is very important to have a balance between the space charge forces and the focusing strength of the acceleration system to avoid large divergence angles. Furthermore, there exists an optimal aspect ratio of the acceleration gap for each ion species. For argon the aspect ratio is 0.5. The geometry of the acceleration gap has been optimized for a highly brilliant ion beam. The diameter of the high voltage electrode has been increased for that reason. For argon we reached the space charge limit of the acceleration system with an accelerated ion current of 45 mA at a voltage of 88 kV. The next optical element behind the acceleration gap has to accept the emittance for the optimized case (with solenoid). This would be either a quadrupole with a large aperture or a magnetic solenoid for a better matching of the ion beam to the LEBT section.

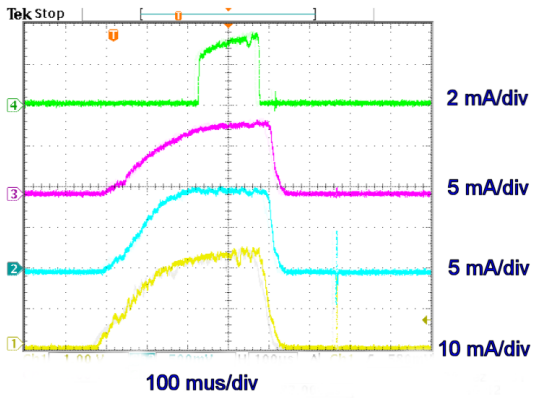


Figure 1: Ion beam currents along the beam line. From bottom to top: total current (24 mA), analyzed beam (10 mA), in front of the RFQ (8 mA) and behind the RFQ (3 mA).

A high current uranium beam was provided by the high current injector HSI using the MEVVA ion source in long time operation over four weeks. Since the design ion for the HSI is $^{238}U^{4+}$ efforts have been made to increase the fraction of $^{238}U^{4+}$ reaching a rate of 67 % of the total beam current. Beam quality could be improved concerning pulse stability, noise reduction and availability of the source by using robust meshes, increasing the arc current and changing the bonding technique of the cathodes.

Modification of the extraction system concerning geometry and electrode material enhanced the extracted beam current and decreased the number of high voltage breakdowns to 2 per day and thus increased the availability of the ion source tremendously. The ion source is delivering a total beam current of 55 mA at 30 kV extraction voltage. Fluctuation of the full beam current amounts to 6 % (see Fig. 1). These improvements made it possible to provide a current of up to 10 mA $^{238}U^{4+}$ in front of the RFQ. Typical ion beam currents along the beam line, starting behind the post acceleration system (see Fig. 1): total current (24 mA), analyzed beam (10 mA), in front of the RFQ (8 mA) and behind the RFQ (3 mA).

ECR Ion Source (ECRIS)

The long shut down period at the beginning of the year was used to upgrade the low energy beam line at the high charge state injector (HLI) between ECRIS and dipole spectrometer by implementing a solenoid lens which generates an intermediate focus of the ion beam after extraction from the ECRIS. Furthermore two pairs of horizontal and vertical steerers were placed in front of this focus and behind. Beam transport from the ECRIS to the entrance of the RFQ was investigated with MIRKO [3] calculations defining the positions of the lenses. Furthermore a longitudinal adjustment of solenoid (± 100 mm) and quadrupole singlet (± 50 mm) is provided allowing for a change of ion optical conditions without breaking the vacuum. The beam line is now identical to the one of the ECR injector test setup (EIS) [4] which proved its functionality and reliability during the past four years. The technical environment of the ECRIS was also upgraded with an improved interlock system and a new vacuum control system.

The good results obtained in a test run of the ECRIS before the first beam time were confirmed during the regular beam time periods of the year showing improved beam transport through the spectrometer for selected ion species like H_2^+, $^{22}Ne^{5+}$, $^{26}Mg^{5+}$ and $^{136}Xe^{19+}$ (e.ġ. an enhancement factor of 1.4 for $^{136}Xe^{19+}$).

The beams delivered from the ECRIS to the accelerator were dominated by cancer therapy which used 56 % of the whole beam time with C^{2+} ions. Ions from gases were routinely produced from Ar and enriched ^{22}Ne and ^{136}Xe. A H_2^+ ion beam was delivered to an experiment for the first time. With respect to a short accelerator test run in December 2000 the average level of intensity could be increased by 30 %.

The analyzed beam intensity of $^{26}Mg^{5+}$ could be improved by 40 % with respect to the run of the preceding year. The beam time at the HLI could profit from several test runs at the EIS which provided more experience in optimization of the ion source parameters. The long term stability was much better giving an increased average level of intensity. Beams of $^{50}Cr^{8+}$ which required enriched isotope material and of $^{58}Ni^{9+}$ were produced by evaporation with the standard oven.

A new challenge arose from the request for a ^{6}Li beam. At GSI good experience was gained using natural LiF for evaporation which can be handled more easily than Li metal. For ^{6}Li it was necessary to use enriched material which could only be obtained as ^{6}LiF powder. As powder cannot be used directly it was pressed into small pellets in the GSI target laboratory as it is also done for ZnO. The pellets were enclosed in a tantalum crucible which was heated with the ECR standard oven. After a series of tests at the EIS a successful run could be performed at the HLI providing a stable beam of moderate intensity (typ. 20 μA of $^6Li^{1+}$).

Besides preparatory work for the development of beams for the accelerator various experimental investigations were performed at the test stands. The use of compounds for evaporation (e. g. ZnO) can be an alternative if the vapor pressure of the pure metal is not matching the capabilities of the oven (e. g. Mo, W). WO_3 was expected to have a suitable vapor pressure and was chosen for an experiment. It was possible to produce a W ion beam with a still low level of intensity but with a charge state distribution that is suitable for the accelerator by running the standard oven at a temperature of about 1150°C. The development of the high temperature oven was continued and concentrated on tests of new materials for critical parts of the oven in order to improve performance and lifetime. To approach the design temperature of 2000°C step by step under real operating conditions vanadium was chosen as a further candidate which requires 1800°C to attain an appropriate vapor pressure. The test run was very successful and resulted in charge state distributions peaking around V^{8+} which is suitable for HLI operation. Intensities of up to 160 eμA could be obtained.

In the framework of an european collaboration for research and technical development experiments were started to do systematic investigations of the afterglow operation with our ECRIS. The dependence of shape, intensity and stability of the afterglow pulse on the ion source parameters and on pulsing conditions are subject of the present investigations.

Penning Ion Source

Beside the regular operation of the PIG source with neon, argon, calcium, titanium, nickel, krypton, gold, bismuth, and uranium systematic measurements at the PIG test bench have been made to investigate an accel-decel extraction system instead of the regularly used diode system. Such extraction systems are well known from high current ion sources where they are used to trap secondary electrons within the extracted beam. For the PIG source however, such a system is used to increase the extraction field strength to provide the possibility to extract higher currents [5, 6], as long as the extraction is not emission limited. A substantial increase of the intensity by a factor of two could be observed at the test bench. Planned emittance measurements behind the acceleration column at the PIG terminal will show, whether the intensity increase can be a benefit at the injector.

References

[1] R. Hollinger et al., Beam Emittance Measurements at the High Current Injector at GSI, Proceedings of the 9th International Conference on Ion Sources, Oakland, 2001.

[2] R. Keller, Multi Charge Ion Production with MUCIS, GSI- Scientific Report 1987-1.

[3] B. Franczak, MIRKO, Proceedings of the Europhysics Conference on Computing in Accelerator Design and Operation, Berlin (1983)

[4] K. Tinschert et al., Rev. Sci. Instrum. **69**, (1998) 709

[5] P. Spädtke et al., An Accel-Decel Extraction System for the PIG Ion Source, GSI report, to be published.

[6] P. Spädtke et al., Accel-Decel Extraction System for PIG sources, Proceedings of the 9th International Conference on Ion Sources, Oakland, 2001.

UNILAC Status and Developments

W. Barth, L. Dahl, J. Glatz, L. Groening, J. Klabunde, S. Richter, GSI

Status of Operation

In 2001 both injectors, the high current injector HSI and the high charge state injector HLI, were used extensively for operation routinely [1]. Carbon from the HLI for the cancer therapy was accelerated for a long period with very high efficiency like in former reporting periods. For different UNILAC-experiments the beam from the ECR source with its excellent stability and low consumption rate - especially for rare isotopes - was accelerated in the HLI and postsripper (^{12}C, ^{22}Ne, ^{26}Mg, ^{50}Cr, ^{136}Xe, ^{58}Ni). Nevertheless a multitude of ion species from the HSI was delivered to the experimental hall (^{20}Ne, ^{40}Ar, ^{40}Ca, ^{50}Ti, ^{58}Ni, ^{86}Kr, ^{209}Bi, ^{238}U). ^{40}Ar, ^{50}Ti and ^{50}Cr were provide for the SHIP experiment. Two octupole magnets were installed in the beam-line to generate a homogeneous beam shape on the target – more details will be reported. Beside hydrogen and ^{6}Li (from the HLI) the beam for SIS-injection was accelerated in the HSI. In doing so PIG (^{58}Ni, ^{132}Xe, ^{197}Au, ^{238}U), MUCIS and MEVVA sources were in operation. For low mass numbers (^{18}O) up to 10^{11} particles per spill were reached in the SIS. New results for the highest intensities with ^{40}Ar from MUCIS will be discussed in this report. The experiences within the first operation period with a high intense Uranium beam from the MEVVA for SIS injection will be presented.

High Current Machine Experiments

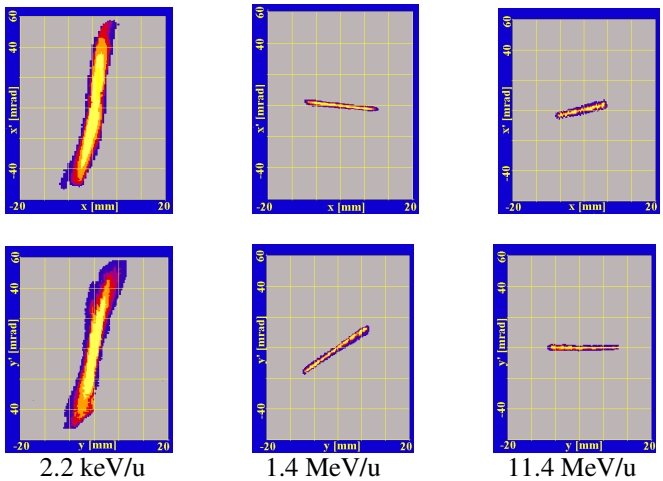


Fig 1: Measured horizontal (top) and vertical (bottom) emittance; 10 emA Ar^{1+} (2.2keV/u), 7 emA Ar^{10+} (1.4 MeV/u, after stripping and 11.4 MeV/u).

All the measurements were carried out with an intense argon beam, while the HSI worked at the design intensity limit. The horizontal and vertical emittance for the several energy steps of the HSI (and at 11.4 MeV/u) was measured exclusively with a slit-grid device for short pulses. As an example Fig. 1 shows the measured transverse emittance for three different UNILAC energies. The measured emittance data for an Ar^{1+} beam with 10 emA at RFQ injection, 7 emA at the HSI exit, and an Ar^{10+} current (after stripping and charge state analysis) of 7 emA agree well with the calculation, when a measuring error of about ±15 % is taken into account.

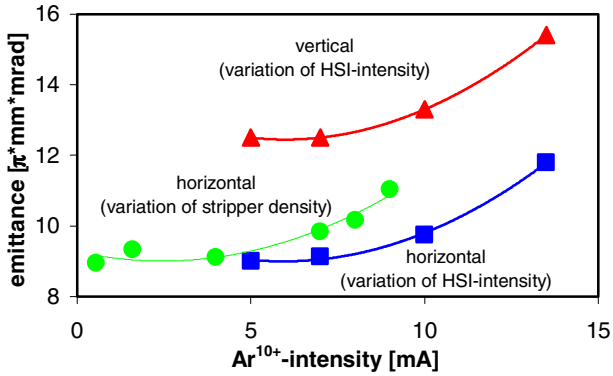


Fig. 2: Measured Emittance growth after stripping at 1.4 MeV/u as a function of beam intensity.

As shown in Fig. 2 the emittance after the gas stripper at 1.4 MeV/u increases significantly as a function of the Ar^{10+}-intensity. At the design intensity of 6 emA an emittance growth of less than 10% was observed, in contrast to 40% as expected from calculations – the explication is still open, probably space charge compensation, due to electron capture, is responsible. If the intensity attenuation is achieved by decreasing the stripper gas density only emittance blow up due to space charge effects in the HSI accelerator takes place. The emittance growth effects are mainly caused by the strong space charge forces after stripping. The different emittance values in the transverse planes are predicted by calculation [2].

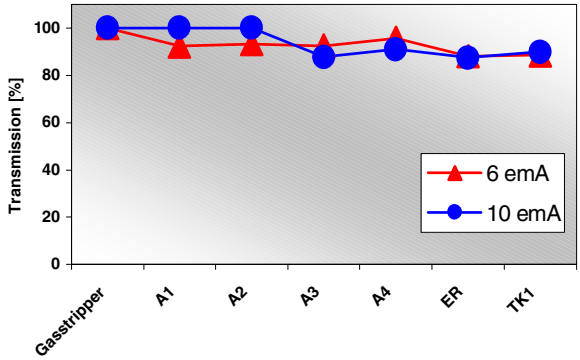


Fig.3 Measured particle transmission in the Alvarez, single gap resonators and transfer channel for a high intense Ar^{10+} beam.

Optimization of the particle transmission in the poststripper, single gap resonator section and in the transfer line was performed for the highest Ar^{10+} intensities. As shown in Fig. 3 the transmission for 6 emA (design current) and 10 emA (responding to 21 emA U^{4+}) is close to 90%.

Operation with a MEVVA-U^{4+} -Beam

In December 2001 a FRS experiment required 10^9 Uranium ions per spill, corresponding to a U^{73+} current of 0.2 emA at the injection into the SIS. In order to meet this request the MEVVA ion source was used for the first time in routine operation providing Uranium for a physics experiment. The rf-field levels for Uranium were achieved in the HSI due to simultaneous rf-conditioning during preceding experiments. In December several experiments were served simultaneously and the time for machine optimization with respect to highest Uranium intensities was reduced considerably. The MEVVA ion source provided an average U^{4+} current of 5.5 emA at the entrance to the RFQ. At maximum 8.5 emA were achieved. The RFQ transmission was about 55% for routine operation and up to 75% after extensive optimization. However, a RFQ transmission of 85% and smaller transverse beam emittances at the entrance to the RFQ were measured in previous machine experiments. The overall HSI transmission ranged from 50% (routine) to 70% (optimized). A considerably low and unstable gas stripping efficiency of about 9.5% was found in December. Usually 13% were obtained easily. The observed reduction is not understood so far. The beam passed the ALVAREZ with an efficiency close to 100% but the transmission through the subsequent section of 15 single gap resonators was only 60% mainly caused by four missing focusing lenses in this section. The further transport through the transfer line and the foil stripper to the SIS was straightforward. The transmissions achieved during routine operation are displayed together with the design values in Fig. 4. The limiting factors for beam intensities indicated by the December beam time are addressed in upcoming machine experiments. At the beginning of 2002 the number of single gap resonators will be reduced to 10 and the beam focusing in this section is significantly simplified now. Finally, a new RFQ design providing higher transmissions is currently under discussion.

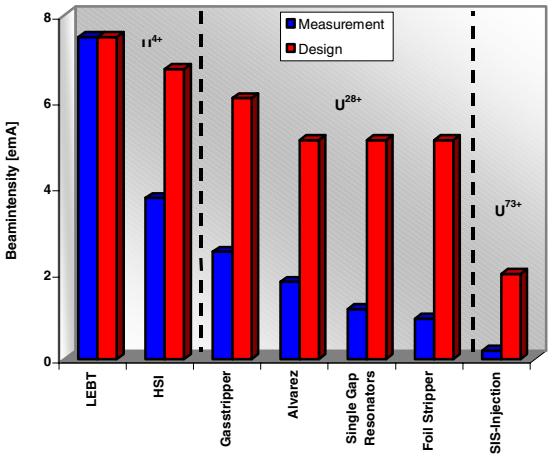


Figure 4: Transmissions for first operation and the design transmissions from the MEVVA source to the SIS injection for an intense Uranium beam. The design values are based on a U^{4+} current of 7.5 emA at the entrance to the RFQ.

Upgrade of the Beamline to SHIP

Two octupole magnets were installed in the beam-line to the experimental setup for super heavy element production (SHIP). The tolerable beam intensity is very low due to the almost Gaussian beam shape that induced very high thermal stress on the center of the target. The addition of octupoles in the beamline allows to generate a homogeneous beam shape and thus to increase the number of particles on the target roughly by a factor of 3. The transformation of the Gaussian beam profile to a flatter rectangular one is shown in Fig.5. The underlying effect of these highly non-linear devices is that they influence beam far away from axis. Thus the mainly transverse phase space distribution is tilted at its ends towards the center of the beam.

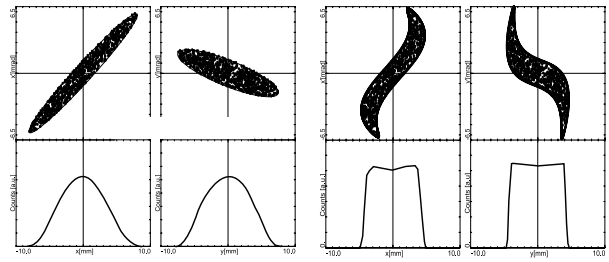


Fig. 5: The calculated horizontal and vertical phase space distributions are shown on top, whereas on the bottom the beam profile in the corresponding axes is displayed (left: no octupoles used; right: octupoles employed.

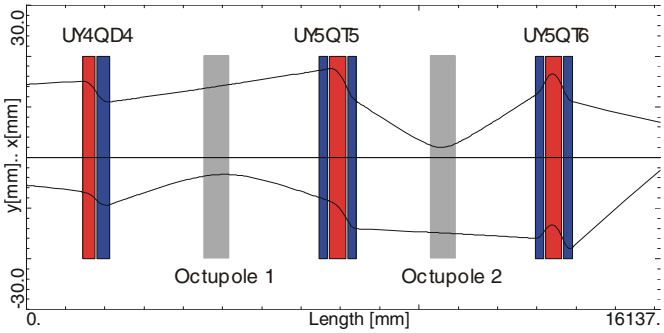


Fig. 6: Theoretical determined envelope in the beam-transport line UY4 to UY7. For the MIRKO-simulation the octupoles are approximated by a short multipole with the order of 3.

Due to the strong coupling of the horizontal and vertical plane a dedicated matched beam-line setting is enforced to ensure a proper behavior. To reduce this coupling the beam is focused in y-plane in the center of the 1st octupole and expanded in the x-plane. This setup is inverted for the 2nd octupole. The first octupole acts on the horizontal plane and the second one on the vertical plane. First experiences with the beamline set-up have been gained during the last beam period in 2001. The functionality of the new beamline could show as a matter of principal; more machine experiments are necessary to improve the performance.

References

[1] U. Scheeler, D. Wilms, Operation of the Unilac and SIS, (this report)

[2] W. Barth, et. al., Beam measurements at the GSI high current injector, proceedings/PAC2001, Chicago (U.S.A.)

SIS Status Report

K.Blasche, U.Blell, O.Boine-Frankenheim, H.Damerau, H.Eickhoff, M.Emmerling, P.Forck, B.Franczak, P.Hülsmann, G.Hutter, K.Kaspar, H.G.König, B.Langenbeck, G.Moritz, P.Moritz, C.Mühle, E.Mustafin, A.Peters, H.Reich-Sprenger, R.Rojko, U.Scheeler, G.Schreiber, P.Spiller, W.Vinzenz, D.Wilms

GSI Darmstadt

1. Status of Operation

In 2001 twelve different ion species – ^{1}H, ^{2}D, ^{6}Li, ^{12}C, ^{18}O, ^{52}Cr, ^{58}Ni, ^{86}Kr, ^{136}Xe, ^{197}Au, ^{209}Pb, and ^{238}U – were accelerated in the SIS. Altogether 6079 h of beam time were provided for experiments, often with one or more high-energy target experiments and the ESR running in a pulse-to-pulse time-sharing operation mode. Another 350 h were used for accelerator tune-up and development. The total down-time of 266 h (4 % of the total operation time) was to a large part caused by technical failures in the power supplies (59 h), the rf accelerating system (66 h), and in the vacuum system (53 h).

The total user time of 6079 h was distributed to radiotherapy with carbon ions (1313 h or 21.6 %), to production runs for target experiments (4032 h or 66.4 %), and to the ESR (729 h or 12 %).

SIS intensities for heavy ions like U^{73+}-ions were still restricted, since the new high current injector HSI at the front end of the UNILAC has not yet reached the design injection current of 2 to 4 mA. With the available current of 150 to 200 µA the SIS provided about $2\cdot10^{9}$ U^{73+}-ions per machine cycle. A comparable beam intensity is available for much lower injection currents using beam accumulation with a series of multi turn injections based on electron cooling.

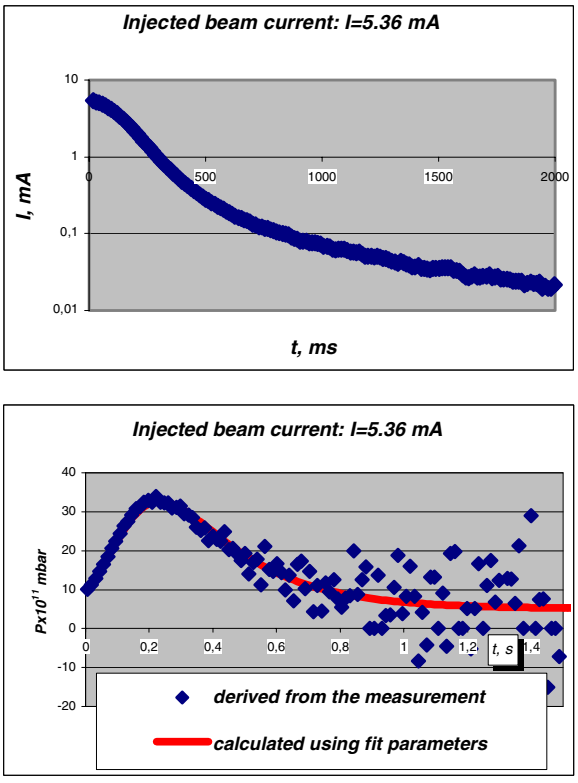


Fig. 1: SIS high intensity operation with $6\cdot10^{9}$ U^{28+} ions. The upper diagram shows the current decay and the lower diagram the equivalent pressure bump, which was derived from the intensity curve.

A new record beam intensity of $1\cdot10^{10}$ U^{28+}-ions was achieved with an injection current of about 800 µA. However, the first run with high-intensity U^{28+} beams showed strong beam losses immediately after multiturn-injection (Fig. 1). The equivalent beam lifetime was about 200 ms, while for lower beam intensities up to about $2\cdot10^{9}$ ions the measured beam lifetime was 3 s. These results correspond to similar observations for the storage of Pb^{29+} ions in the LEIR storage ring at CERN [1]. There it has been shown that one single heavy ion hitting the vacuum chamber can set free about 10^{4} atoms. The desorption of wall atoms leads to a pressure rise, which in case of the SIS experiment with $1\cdot10^{10}$ U^{28} ions resulted in an average pressure rise up to $3\cdot10^{-10}$ mbar and a corresponding decrease of beam life time.

A new test-facility for the study of wall desorption effects has been designed. In addition, further studies are underway to reduce injection losses as far as possible, to improve local control of beam losses with well-designed collimator systems and with high local pumping efficiency.

2. Development of SIS Machine Operation

It is obvious that the development of high-intensity beams for U^{28+} and U^{73+} ions will play a key role in the future development of SIS machine operation. The beam intensity must be raised to $2\cdot10^{10}$ or even $4\cdot10^{10}$ U^{73+} ions and to more than $1\cdot10^{11}$ U^{28+} ions per machine cycle.

In addition, it will be necessary to develop SIS operation in the SIS12 mode with a ramp rate of 10 T/s for the dipole magnets to approach the high mean intensity of $1\cdot10^{12}$ U^{28+} ions per second [2]. In June 2001 a new test run for the SIS12 mode took place. During the test run the effect of the 25 MW GSI pulse load at industrial customers was studied carefully. As shown before in 1988, the results showed again that the high pulse load cannot be tolerated by the power company. The test run was also used to check for the first time beam acceleration at a high ramp rate. Within the short test run of 2 h it could be shown that beam acceleration at a ramp rate of 5 T/s is feasible.

It is planned to provide a connection of the GSI pulse load via a separate 110 kV line to the 380 kV line at the nearby Urberach transformer station for two days in 2002 to further develop SIS12 operation at 10 T/s.

Negotiations with the power companies are under way to check, if a separate 110 kV line can be installed for permanent operation at the high pulse load of 50 to 60 MW that will be required for the SIS12 mode operation and for the proposed New Accelerator Facility.

A newly developed extraction system with an rf-noise-synthesizer locking into the revolution frequency, power amplifiers and the integration in the SIS control system is now ready for routine operation. In this scheme a transverse rf noise voltage is used to knock out ions by excitation of large radial oscillations, which lead into resonance [3]. In comparison to the usual slow-extraction scheme with two fast extraction quadrupoles, which gradually shift the horizontal tune towards the

resonance at Q_h = 4 1/3 the new scheme provides excellent position stability for the extracted beam and also an easy way to interrupt the spill and to proceed with slow extraction after a short pause.

The new transverse feedback system will be used to damp coherent transverse instabilities observed during operation with cooled ion beams, e.g. with $2 \cdot 10^9$ U^{73+} ions. It is planned to extend the range for stable operation with cooled beams to about $5 \cdot 10^9$ ions. This system with two of the existing position monitor probes as pickup-system, a new feedback kicker, a new DSP processing stage (100 MHz, 12 bit), new power amplifiers, and a closed orbit suppressor system, was tested in coasting beam operation with a low intensity gold beam. Coherent horizontal beam oscillations were induced by the knock out extraction system and then damped by the new feedback system (Fig. 2). The integration of the TFS into the computer control system is underway. The vertical part of the TFS for coasting beam operation and the operation with bunched beams have to be tested.

3. New SIS Machine Components

For the control of coherent longitudinal instabilities a fast feedback in the power amplifiers of the two rf acceleration stations was developed to reduce the impedance from $R_p \simeq$ 3 kOhm to values below 1 kOhm per rf station. These studies have been continued on the test cavity. With a new design of the grid input circuit, the power amplifiers can be driven alternatively via the old low pass solution or the tuneable ferrite grid resonator. Measurements at fixed frequencies showed that the existing driver amplifiers allow reduction of the gap impedance to a value slightly below 1 kOhm. The present feedback concept is being revised to check if vacuum tube feedback amplifiers will be included for safe operation at a high radiation level.

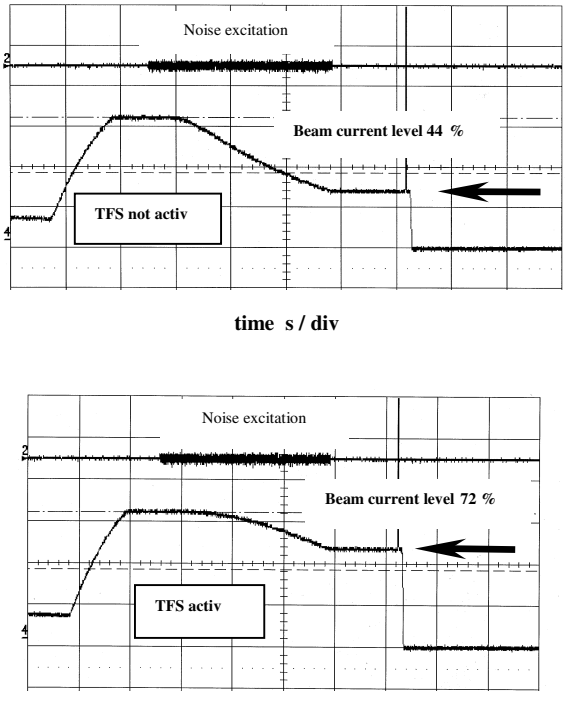


Fig. 2: Slow resonance extraction using a transverse rf noise voltage to knock out ions by excitation of large radial oscillations, which lead into resonance (top) and damping of horizontal beam oscillations by the new transverse feedback system (bottom).

The production of the set of correction coils was delayed by the manufacturer. Meanwhile the first coils arrived and installation in the SIS will start soon. All necessary power supplies are ready for commissioning. Fig. 3 shows schematically the layout of the correction unit with a three-layer coil arrangement: a skew sextupole on a printed circuit and a skew sextupole in the inner layer and a regular correction quadrupole in the outer layer.

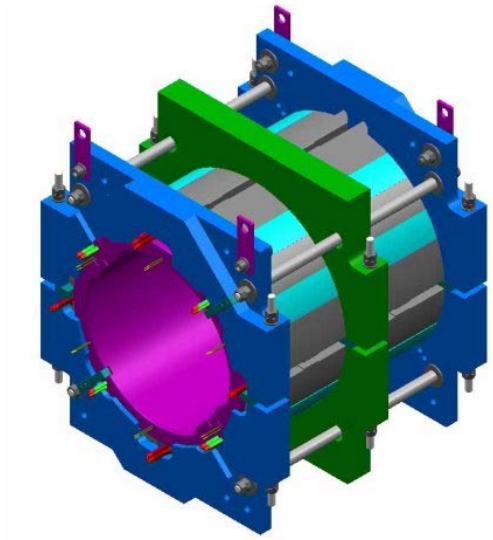


Fig. 3: Schematic layout of the new SIS correction units with a three layer coil arrangement: a skew sextupole on printed circuit board combined with skew quadrupole coils in the inner layer and a correction quadrupole in the outer layer.

For the SIS vacuum system an upgrade program is underway. The vacuum diagnostic system was improved by replacement of extractor gauges and by installation of new residual gas analysers (RGA) to provide precise information on the composition of the residual gas with good time resolution. All ion getter pumps and titanium evaporator pumps were carefully checked in a complete maintenance service.

The four bunch compressor cavities will be installed to produce a short high intensity bunch before fast extraction, e.g. a bunch with up to $2 \cdot 10^{11}$ U^{28+} ions of 50 ns or 10 m pulse width [4]. Each compressor cavity has an inductive load of twelve cores made of metallic alloy. Measurements on prototype cores, VITROVAC 6030 F from Vakuumschmelze and FINEMET FT-3L from Hitachi showed rf-losses twice as high as shown in the data sheets. Therefore the submission for the complete set of 48 cores had to be postponed. Meanwhile several sets of different small test cores have been developed by Allied Signal (Honeywell) using carefully selected production techniques, which seem to fulfill the requirements. GSI measurements will be available soon. In addition, the production of further test cores is being discussed with the RTI in Moscow and with the AMET Company in St. Petersburg.

References

[1] M.Channel et al., CERN/PS 2001-040 (2001)
[2] An International Accelerator Facility for beams of Ions and Anti Protons. Conceptual Design Report, GSI 2001.
[3] K.Hiramoto and M.Nishi; Resonant beam extraction scheme with constant separatrix**;** NIM A, 1992, pp. 154-160
[4] K.Blasche et al., Proceedings of the 6th EPAC, (1998) 1347

ESR Operation and Development

K. Beckert, P. Beller, W. Bourgeois, B. Franczak, B. Franzke, F. Nolden,
U. Popp, A. Schwinn, M. Steck, GSI Darmstadt

After a nine months' shutdown period ESR operation started in June 2001. During the shutdown the internal target section has been modified and new pressurized air actuators have been installed which allow fast (within 1 s) positioning of charged particle detectors. These detector drives have already been successfully employed in physics experiments. Their motion is fully computer controlled and triggered by events from the accelerator timing system thus avoiding any dead time between beam manipulations and data acquisition for experiments. A new zero degree electron spectrometer has been installed about 1 m downstream the interaction point with the gas jet. Magnets and vacuum system of the electron spectrometer section are ready for operation, commissioning with beam is foreseen for the first beam time period in 2002. All pick up electrodes of the stochastic cooling system have been equipped with individual low noise pre-amplifiers in order to improve the signal to noise ratio and thus the cooling time. The improved performance has been tested and confirmed with beam and is available for use in experiments.

During June and July the ESR was operated together with the SIS in the reinjection mode for five weeks providing bare gold ions in Cave C at nearly 1.5 GeV/u. A typical beam intensity of $2-3\times10^8$ bare gold ions was injected into the ESR at an energy of 350 MeV/u. By application of an electron current of 0.7 A the cooling time was 5 s only. After reinjection into the synchrotron SIS the ions were accelerated to 1.499 GeV/u and slowly extracted over 5 s. Compared to previous beam times the cooling time in the ESR was considerably reduced thus the processing time in the ESR contributed less than 30 % to the total cycle time. The efficiency of beam transportation from the ESR to the SIS could be continuously increased in the course of the beam time. More than 70 % of the ions circulating in the ESR were transfered to the SIS resulting in $1-2\times10^8$ bare gold ions supplied to the experiment in one cycle of 20-30 s. Most of the losses between ESR and SIS can be attributed to down charged ions which are produced during the cooling period in the ESR and which can not be transfered due to their difference in magnetic rigidity.

Bismuth ions in the hydrogen- and lithium-like charge state were stored at energies of 415 and 393 MeV/u, respectively, for measurements of the hyperfine splitting with a collinear laser. For efficient production of incompletely stripped ions at this energy carbon foils recently installed in the beam line in front of the ESR were employed. Energies around 415 MeV/u correspond to the highest electron energy in the cooler used for an experiment. Experience showed that reliable cooler operation near the current maximum energy requires careful conditioning of the electron cooling system over several days.

The transfer of ions through the fragment separator to the ESR was studied with a nickel beam at 390 MeV/u. Beyond general optimization of the optical setting of the transfer line the test revealed an unintentional transposition of a quadrupole dublett which is, at least partially, accountable for beam losses.

Decelerated heavy ion beams have been provided for various atomic physics experiments. Bare uranium was decelerated from 300 to 43 MeV/u for the investigation of x-rays emitted during recombination of the ions with electrons in the cooling section. The use of a decelerated beam allowed a considerable reduction of the background originating from Bremsstrahlung of electrons lost in the electron cooler. Up to 3×10^7 ions were decelerated to the energy of 43 MeV/u and stored for several minutes. Later during this beam time the decelerated uranium beam was also used for tests of the beam line to Cave A.

In the final beam time of 2001 uranium ions decelerated to 20 MeV/u had to be transported to Cave A for channeling experiments. Unfortunately the total beam time had to be cut short due to problems in the Unilac accelerator section. Nevertheless the machine cycle could be successfully established and also the beam line from the ESR to Cave A equipped with new diagnostics for low energy beams could be commissioned. The decelerated uranium beam with an energy of 20 MeV/u was extracted with extraction times on the order of minutes by charge changing of the bare uranium beam. Electron capture in the electron cooler was chosen as the process providing hydrogen-like ions at a rate not exceeding 10^4 ions/s. The required extraction rate was accomplished by a reduction of the electron current to 100 mA with a total extraction times of 2 minutes per cycle. Figure 1 shows some essential parameters of the machine cycle in this operation mode. After a cooling time of about 15 s the beam is decelerated in 8 s to an intermediate energy of 30 MeV/u and after 6 s of cooling within 2 s to the final energy of 20 MeV/u.

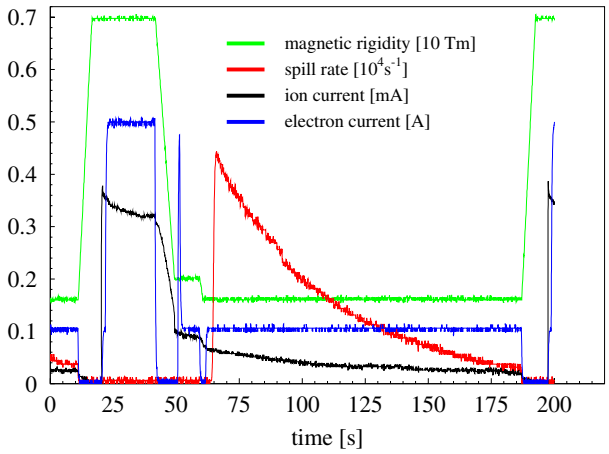


Figure 1: Typical deceleration cycle for a bare uranium beam from 300 MeV/u injection energy to an energy of 20 MeV/u with slow extraction. The curves show dipole field, ion and electron current and spill rate at the experiment in the units indicated in the plot as a function of time.

Fast pulsed superconducting Magnets

J. Kaugerts, G. Moritz, C. Mühle, G. Walter
GSI – Darmstadt

To reach the desired high average intensities of ions and protons in the proposed new accelerator facilities at GSI (Ref. 1), fast pulsing magnets will be required. An investment and operating costs comparison has shown that a superconducting, rather than resistive, magnet solution is less expensive.
A two synchrotron ring design has been chosen, one ring with magnets that will ramp up to 2 T, at a ramp rate of up to 4 T/s , the other ring with magnets that will ramp up to 4 T, at a ramp rate of 1 T/s.
The existing large storage rings of today, which employ superconducting magnets, operate at relatively low ramp rates
(0.07 T/s for RHIC at BNL- Fig. 1)

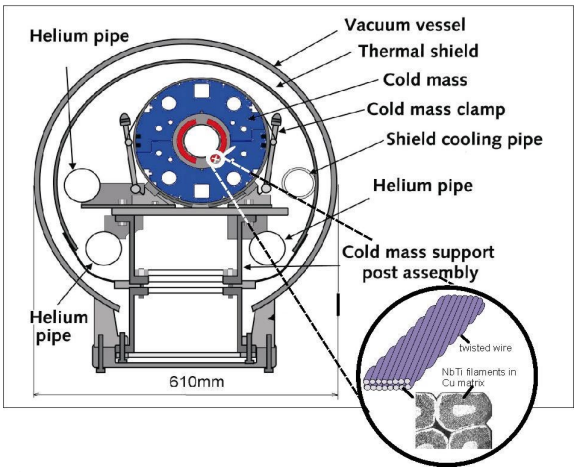


Fig. 1 RHIC magnet

An attempt to build a fast-ramping synchrotron was pursued at JINR, Dubna, where the Nuclotron ring , with 4T/s superferric dipoles (Fig. 2), was built and operated.

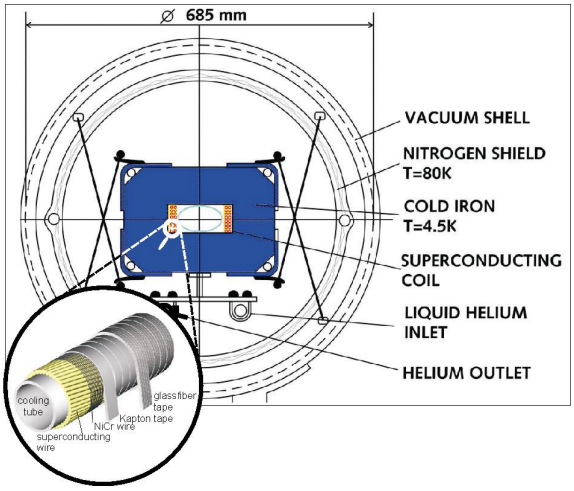


Fig. 2 Nuclotron magnet

In order to reduce development time and project costs, these two magnet designs have been adopted as starting points for the magnets of the two synchrotron rings.
The goals for the Nuclotron superferric magnet design are to reduce its AC losses, improve the magnetic field quality, and improve the mechanical restraint of the superconductor. Progress has been made in meeting the first two of these goals
(Refs. 2 &3) and the third will be the subject of work, to be undertaken during 2002.
The RHIC magnet design requires a substantial reduction of AC losses in the superconductor, in order to be viable at the required 1 T/s ramp rate. To achieve such a reduction, the superconducting cable has been redesigned (Fig. 3), by the insertion of a stainless steel tape (core) and the coating of the strands of the cable with staybrite solder.

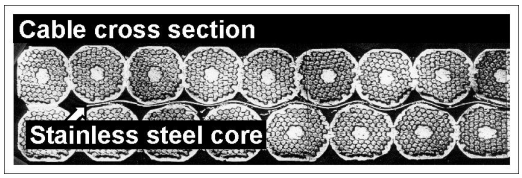


Fig. 3 Low AC loss cable conductor for RHIC-type magnet

Design studies of such conductors (Ref.4) have shown that the cooling must also be improved, in order to keep the superconductor well below its critical temperature (at which it reverts to the normal resistive state). A novel laser technique is being considered (Fig.4) to cut cooling holes into the Kapton insulation of the cable.

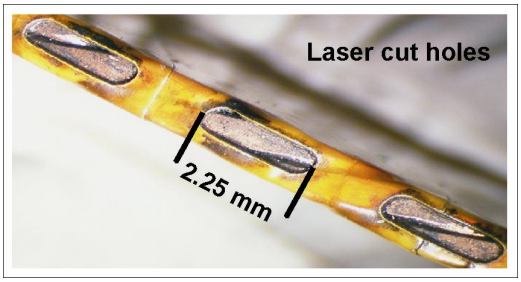


Fig. 4 Improved cable cooling (edge view)

References

[1] G. Moritz et al, Towards Fast-Pulsed Superconducting Synchrotron Magnets, PAC 2001, Chicago, June 2001
[2] G. Moritz et al, Optimization of a Superferric Nuclotron Type Dipole for the GSI Fast Pulsed Synchrotron, MT17, Geneva, 2001
[3] N. Agapov et al, Magnet with Iron at T = 80 K for the GSI Fast Cycling Synchrotron, MT17, Geneva, 2001
[4] M.N. Wilson et al, Design Studies on Superconducting Cosθ Magnets for a Fast Pulsed Synchrotron, MT17, Geneva, 2001

Simulation of the Nuclotron Dipole Magnet by a Hybrid 2D Finite-Element, Spectral-Element Discretization

Herbert De Gersem*, Markus Clemens, Jing Yuan, Markus Wilke, Thomas Weiland†

1 Introduction

To reduce investment and operation costs, superconductive magnets are preferred over conventional magnets for the new GSI accelerator facilities [1]. The eddy current and hysteresis losses caused by the fast ramping of the magnets have to be reduced as far as possible. In order to account for both the eddy current losses in the cables and the losses due to hysteresis in the superconductive filaments, transient simulation has to be performed. Even 2D models may suffer from excessive computation times if inappropriate discretization schemes are selected. In this paper, a hybrid discretization is constructed for the Nuclotron dipole magnet (Fig. 1). The hybrid approach turns out to require less computation time compared to standard discretization techniques.

2 Hybrid FE-SE Discretization

The magnetic field in the Nuclotron dipole magnet is computed using a 2D formulation based on the magnetic vector potential. To account for the ferromagnetic saturation of the iron core and the hysteresis of the superconductive filaments, a Newton linearization is applied. Finite elements (FEs) enable the convenient simulation of model parts with non-linearities, arbitrary geometries and complicated local effects, whereas spectral elements (SEs) offer small and accurate models in case of homogeneous materials and simple geometries [2]. A hybrid FE-SE discretization combines the advantages of both approaches. The FE model part contains the superconductive coils, the iron yoke and a part of the aperture and the surroundings. A circular part of the aperture and the infinite domain outside a circle surrounding the magnet are discretized by SEs. The corresponding coupled system of equations

$$\begin{bmatrix} K & B^H \\ B & -C \end{bmatrix} \begin{bmatrix} u \\ c \end{bmatrix} = \begin{bmatrix} f \\ 0 \end{bmatrix} \tag{1}$$

contains the FE stiffness matrix K, the FE load vector f, the SE stiffness matrix C and the coupling terms $B = ZFQ$ where Q is an operator selecting the nodes at the circular interface Γ, F the discrete Fourier transform and Z a symmetrizing diagonal matrix [3]. The FE mesh is assumed to be equidistant at Γ. This particular form of FE-SE coupling is only applicable to circular inclusions and far field domains. For SE inclusions with a floating constant component, a slightly modified formulation is used.

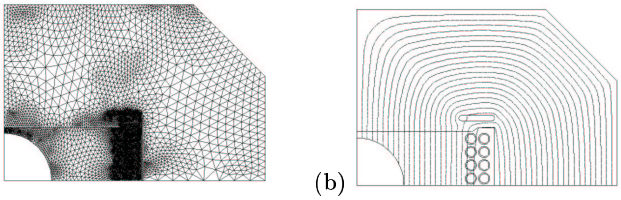


Figure 1: (a) FE mesh and (b) magnetic flux lines of the nuclotron dipole magnet.

3 Specialized Solution Techniques

The most efficient approach is solving the positive definite, reduced system

$$\left(K + B^H C^{-1} B\right) u = f \tag{2}$$

by the preconditioned Conjugate Gradient method [4]. The explicit construction of B, C and $K + B^H C^{-1} B$ is not recommended. Instead, only the matrix-vector multiplication with the system of (2) is defined. The Fast Fourier Transform (FFT) algorithm is used for F and F^H. Although the SE model parts constitute 10% of the entire model, only 1% of the overall computation time is spent for the FFTs. Hence, apart from a better converging discretization error, SEs offer favourable solution times, even when coupled to FEs.

4 Conclusions

The numerical experiments for a magnetostatic Nuclotron dipole model taking ferromagnetic saturation into account, indicates that the hybrid FE-SE model requires less computation time than a full FE approach [4]. This property will enable the efficient simulation of transient phenomena including hysteresis and temperature effects while retaining acceptable solution times. The hybrid FE-SE discretization technique is planned for 3D models as well.

References

[1] G. Moritz and et al., "Towards fast-pulsed superconductive synchrotron magnets," in *PAC'2001*, Chicago, Illinois, USA, June 2001.

[2] B. Fornberg, *A Practical Guide to Pseudospectral Methods*, Cambridge University Press, Cambridge, 1996.

[3] H. De Gersem, M. Clemens, and T. Weiland, "Coupled finite element - spectral element discretization for models with circular inclusions and far field domains," accepted for presentation at CEM2002, 8-11 April, 2002, Bournemouth, United Kingdom.

[4] H. De Gersem, M. Clemens, and T. Weiland, "Iterative solution techniques for hybrid finite-element, spectral-element models," Submitted to CEFC2002, 16-19 June, 2002, Perugia, Italy.

* Herbert De Gersem is working in the cooperation project "DA-WE1 (TEMF/GSI)" with the "Gesellschaft für Schwerionenforschung (GSI)", Darmstadt.

† All authors are with the Technische Universität Darmstadt, Computational Electromagnetics Laboratory (TEMF), Schloßgartenstraße 8, D-64289 Darmstadt, Germany; phone: +49 6151 162361; fax: +49 6151 164611; email: degersem/clemens/yuan/wilke/weiland@temf.tu-darmstadt.de.

Mismatch and Halo in High Intensity Accelerators

G. Franchetti and I. Hofmann, GSI

We study the conversion of free energy from rms mismatch of anisotropic beams into rms emittance growth of a halo and find that for Gaussian beams the growth of rms emittances is quite anisotropic. Our findings can be applied to initially mismatched beams injected into linear as well as circular accelerators.

Most of the halo studies so far have considered round (isotropic) beams with axi-symmetric focusing (see the review by Wangler [1]). The new aspects caused by anisotropy – with the ratio of focusing strengths and/or emittances as additional free parameters – were first discussed for 2D beams by Ikegami [2]. In our more systematic study we focus on the rms properties of halo and show that conversion of free energy from mismatch into rms emittance growth takes place with a significant modification accounting for 2D anisotropy. We use the 2D particle-in-cell simulation code MIMAC[3] for a constant focusing transport system with 50.000 simulation particles on a 128x128 grid with selfconsistent space charge calculation. As an example, we consider in Fig. 1 a beam with relatively weak space charge and equal emittances in the two transverse directions, z and x. The tune depression in x is assumed to be $Q_x/Q_{0x} = 0.95$, which is typical for high-current rings. The tune ratio, Q_z/Q_x, is scanned from 0.9 to 1.1 in small steps , which includes the region of maximum growth. Each marker indicates a simulation run over 190 betatron periods, which is found sufficient to reach practically saturation of the rms emittance growth effect. The mismatch factor, defined as ratio of mismatched to matched envelopes, is chosen equal for both directions ($M = M_z = M_x$). The rms emittance growth curve rises steeply in the direction for which the focusing strength increases, i.e. in z for $Q_z/Q_x > 1$, and in x for $Q_z/Q_x < 1$. The strongly anisotropic response is confined primarily to a region around $Q_z/Q_x = 1$ of a width comparable with the relative tune depression (0.05 here). The *averaged* rms emittance growth (over z and x) is found surprisingly constant at 24%, to within less than $\pm 0.2\%$ variation. Comparing this value with the analytical expression in Reiser's model of mismatch induced free energy conversion in axi-symmetric beams [4], we find better than 1% agreement. For axi-symmetric beams such nearly 100% conversion – somewhat less for higher space charge – was already shown by Cucchetti et al. [5]. We have found that the Gaussian tails play an important role in this full energy conversion – truncated Gaussians lead to only partial conversion of the free energy and reduced emittance growth. We can now use the fact that the *averaged* growth factor is independent of Q_z/Q_x to plot it as function of M in Fig. 2. The agreement with Reiser's theoretical curve is equally good for all M. In Fig. 2 we also show the maxima and minima of growth factors found in the interval $0.9 < Q_z/Q_x < 1.1$. The pronounced anisotropy of the reponse is in contrast with a simple picture of thermalization

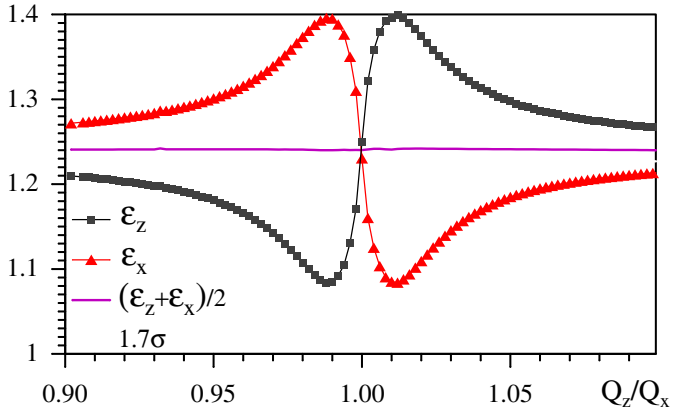


Figure 1: Final rms emittance growth factors $\Delta\epsilon/\epsilon$ in z, x, and *averaged* over z and x as function of tune ratio Q_z/Q_x ($Q_x/Q_{0x} = 0.95$, $\epsilon_z/\epsilon_x = 1$ and $M = 1.4$) for Gaussian distribution.

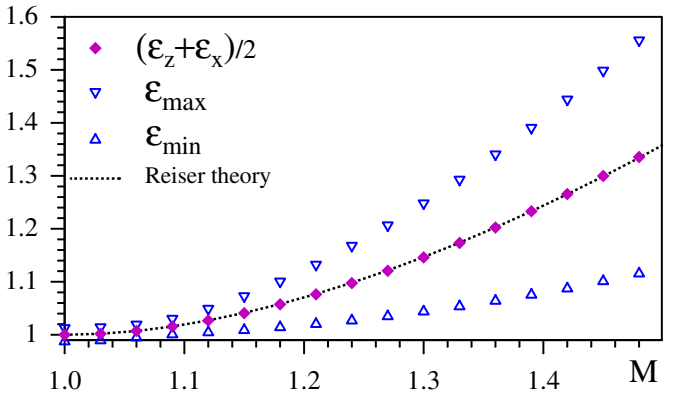


Figure 2: Maximum, minimum and averaged rms emittance growth factors compared with Reiser theory, as function of M for Gaussian beams ($\epsilon_z/\epsilon_x = 1$, $Q_x/Q_{0x} = 0.95$).

and should be seen as result of the underlying resonance behaviour. In practical terms these results suggest that single turn injection into a ring needs to avoid mismatch exceeding a few percent due to the rms emittance growth; as this is accompanied by a halo halo extending to typically 5σ, beam loss might exceed the tolerable level.

References

[1] T.P. Wangler, *Phys. Rev. ST-AB* **1**, 084201 (2000).

[2] M. Ikegami, *Nucl. Instr. and Meth.* **A**, 454, 289 (2000).

[3] G. Franchetti, I. Hofmann, and G. Turchetti *AIP Conf. Proc.* **448**, 233 (1998); ed. A.U.Luccio and W.T. Weng.

[4] M. Reiser *J. Applied Phys.* **70**, 1919 (1991).

[5] A. Cucchetti, M. Reiser and T.P. Wangler, in *Proceedings of the Particle Accelerator Conference* San Francisco, 1991, edited by IEEE, Piscataway, NJ, p. 251 (1991).

Selfconsistent Study of the Montague Resonance applied to the SIS100

I. Hofmann and O. Boine-Frankenheim, GSI

Emittance coupling in the space charge dominated regime is of increasing interest in connection with the new project of a high-current synchrotron at GSI (SIS100). An important case of a resonance driven by space charge only is the well-known "Montague resonance", a fourth order difference resonance of the type $2Q_x - 2Q_y \approx 0$, which we study self-consistenly here. It is driven by the zero-th harmonic of a quartic term in the space charge potential. In machines with noticeably larger horizontal than vertical emittance it may lead to an exchange of emittances and possibly loss due to vertical acceptance limitation, if the tune split is not chosen sufficiently large. The original analysis by Montague was based on a single particle approach using a "frozen" space charge force defined by the initial distribution [1]. It neglects, however, the effect of the additional time-varying (collective) space charge force resulting from the resonance crossing.

While details on the analytically calculated stopband for the self-consistent KV-model and comparison with simulation are presented elsewhere (see Ref. [2]) we apply the results here to the SIS100 and discuss the restrictions resulting for the choice of the working point. We note that the self-consistent analytical description of collectively driven resonances has been proposed in Ref. [3] using a Vlasov perturbation approach to the anisotropic 2D Kapchinskij-Vladimirskij (KV) distribution. To explore the significance of this resonance we have employed a standard 2D particle-in-cell code with 10^5 simulation particles in a rectangular conducting boundary sufficiently far away from the beam. We have carried out simulations with initial KV as well as rms (but not intrinsically) matched waterbag distributions (WB) for $\epsilon_x/\epsilon_y = 2$ and the relatively large normalized space charge tune shift $\Delta Q_y/Q_{0y} = 0.2$ in order to reduce the simulation time. We note that for both cases the exchange of emittances is as fast as 10-20 betatron periods; this time is roughly inversely proportional to $\Delta Q_y/Q_{0y}$. Hence, this type of space charge driven resonant exchange can be found in a similar way for a broad class of distribution function. It is completely dominated by exponential coherent instability for the KV-distribution (where the driving term for this fourth order resonance is only present as noise initially), whereas for the more realistic waterbag distribution it is a combination of single particle and coherent effect. Results for the saturated rms emittance growth for the $y-$plane are given in Fig. 1 as function of the tune ratio, which controls the condition of resonance. The emittance of the $x-$plane is seen to shrink correspondingly. Effective exchange only occurs in the vicinity of a specific tune ratio, which is shifted from the single particle condition $2Q_x - 2Q_y \approx 0$ due to space charge. We found that growth rates as well as the width of the stopband are roughly proportional to ΔQ. The maximum growth of ϵ_y and the growth profile are nearly independent of ΔQ. This enables us to construct a stopband for the working

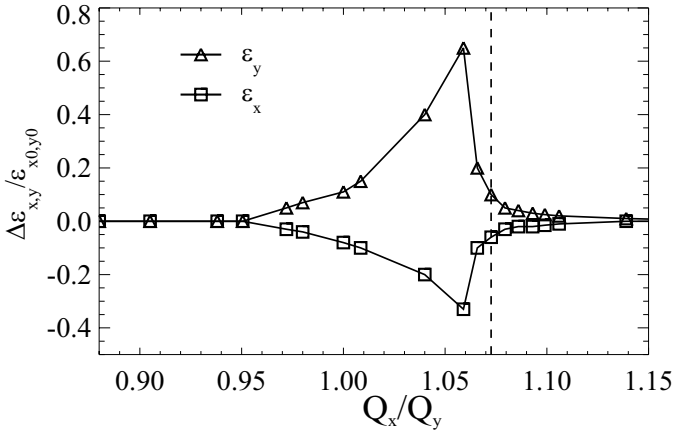


Figure 1: Simulation results for initial WB distribution ($\Delta Q_y/Q_{0y} = 0.2$, $\epsilon_x/\epsilon_y = 2$) as function of the tune ratio (dashed vertical line: symmetric focusing $Q_{0x}/Q_{0y} = 1$).

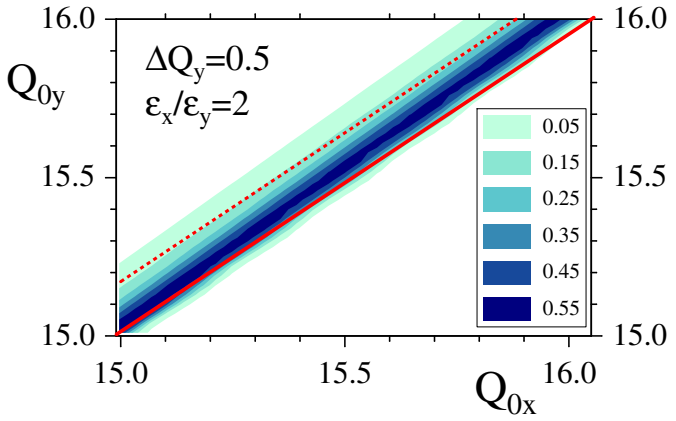


Figure 2: Stopband of selfconsistent Montague resonance for SIS100. Colour scale indicating growth of originally smaller emittance in units of $\Delta\epsilon_y/\epsilon_y$.

diagram of the SIS100 based on the profile of Fig. 1 for the waterbag case.

This is related to the SIS100 tune diagram in Fig. 2 assuming $\Delta Q_y = 0.5$ and $\epsilon_x/\epsilon_y = 2$. The asymmetry of the stopband around the diagonal is due to space charge and $\epsilon_x > \epsilon_y$. The strongest growth of ϵ_y occurs near $Q_{0x} - Q_{0y} = 0$ and *not* near $Q_x - Q_y = 0$ (dotted line). Note the asymmetry of the stopband with respect to the line $Q_{0x} - Q_{0y} = 0$. Also, we found that the width of this stopband is proportional to ΔQ as well as $\epsilon_x/\epsilon_y - 1$.

References

[1] B.W. Montague, CERN-Rep. 68-38, CERN, 1968.

[2] I. Hofmann and O. Boine-Frankenheim, *Phys. Rev. Lett.* **87**, 034802 (2001).

[3] I. Hofmann, *Phys. Rev.* **E 57**, 4713 (1998).

The Transition from Finite to Infinite Spherical Coulomb Crystals

Rainer W. Hasse, GSI Darmstadt, Germany

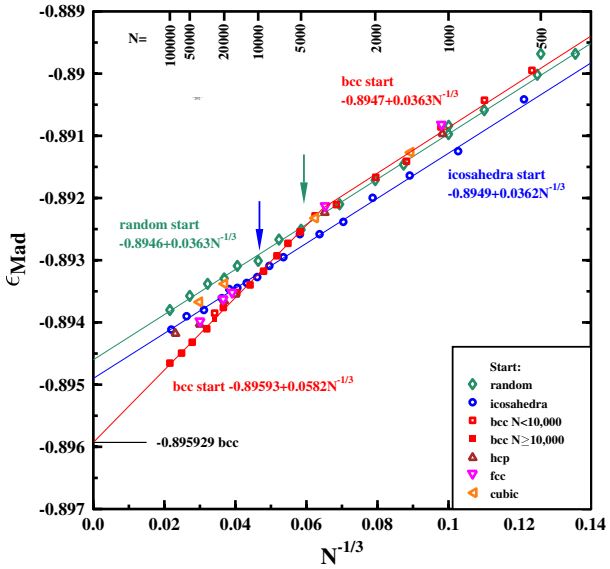


Figure 1: Madelung energies of Coulomb crystals with different starting configurations indicated in the key. The lines are fits explained in the text.

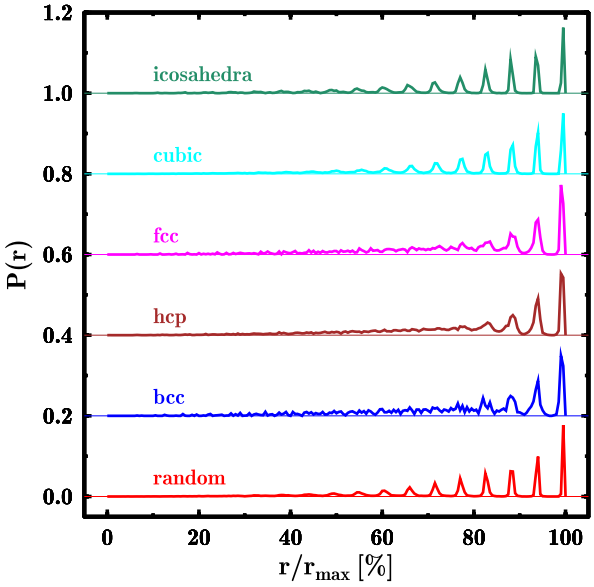


Figure 2: Radial distributions of large spherical Coulomb crystals with different starting configurations

In the framework of our studies to the possible existence of crystalline beams in heavy ion storage rings we also investigate the properties of finite Coulomb crystals which can be generated experimentally in ion traps. Here it has been shown [1] that *semiinfinite* Coulomb matter exhibits different structures in a few layers at the surface as in the interior. We verify this effect in very large *finite* spherical Coulomb crystals. Moreover, we find the critical number of particles where in the interior a phase transition happens from the multilayered icosahedral lattice in small crystals to the bcc lattice of infinite Coulomb matter.

As in ref.[2], we perform Molecular Dynamics calculations for systems of charged ions with particle numbers up to about 100,000 under their mutual Coulomb repulsion and under constant radial focussing. As initial conditions random, bcc, fcc, hcp, or cubic configurations in a sphere are used or multilayer Mackay icosahedra or rounded multilayer Mackay icosahedra [3] and the systems are cooled down to plasma parameters (the ratio of mutual Coulomb energy of two ions to their kinetic energy) up to $\Gamma = 10^{12}$ until the Madelung (or excess or cohesive) energy stayed constant up to 10^{-8}. Here the Madelung energy is defined as the total, i.e. Coulomb plus focussing energies, per particle minus the one of the homogeneous system,

$$\epsilon_{\rm Mad} = \epsilon_{\rm total} - \frac{9}{10} N^{2/3},$$

i.e. the energy gained by crystallization.

The results are shown in Fig.1. Relatively small systems with icosahedral start configurations always relax into icosahedral shells with a surface energy (coefficient of 0.0362) and with a Madelung energy of -0.8949 (energies are measured in units of the pair Coulomb energy). Those with random or bcc start configurations have about the same surface energy but a larger Madelung energy of -0.8946 ... -0.8947. For particle numbers $N < 5,000$, however, the surface energy of bcc start configurations becomes essentially higher, 0.0582, and at the same time their Madelung energy approaches the low value of infinite Coulomb matter, -0.89593 [4]. At $N \approx 10,000$ this line crosses the line of the icosahedral start configurations, thus becoming absolutely lowest in energy. Hence for particle numbers smaller than about 10,000, pentagonal icosahedra which do not exist in nature as crystalline structures, rounded by the Coulomb force, are lowest in energy, above 10,000 bcc crystals are lower in energy.

This phase transition from pentagonal to hexagonal structures can be seen in Fig.2 where the radial distribution of systems with about 10,000 particles and different start configurations is shown: The fcc, hcp and bcc systems exhibit no shell structure in the interior, the particles rather remain in flat layers.

The graphical Windows program traps can be downloaded from the webpage http:/www.gsi.de/~hasse/.

[1] D.H.E. Dubin and T.M. O'Neil, Rev. Mod. Phys. **A71** (1999) 87

[2] R.W. Hasse and V.V. Avilov, Phys. Rev. **A44** (1991) 4506

[3] A.L. Mackay, Act. Crystallogr. **15** (1962) 916

[4] S.G. Brush, H.L. Salin and E. Teller, J. Chem. Phys. **A45** (1966) 2102

Superconducting CH-Cavities for Low- and Medium Beta Ion and Proton Accelerators

R. Eichhorn, GSI Darmstadt,
C. Peschke und U. Ratzinger, IAP Frankfurt

The CH cavity is a multi-gap drift tube structure operated in H_{210} mode currently under development in a collaboration between IAP Frankfurt and GSI. Like the IH cavity (H_{110} mode) used at different places now for the acceleration of ions, this structure provides a high shunt impedance and allows the acceleration of intense beams at high accelerating gradients. The dedicated KONUS beam dynamics used for H-mode cavities results in long lens free sections (like the High Current Injector at GSI), making the design of a superconducting CH resonator possible. First ideas were presented in [1]. An other aspect of the investigations started at GSI and IAP Frankfurt is to extend the attractive velocity range of H-mode cavities up to β=0.5 by these actual developments.

Many future projects (the Accelerator Driven Transmutation Project ADTP, the European Spallation Source ESS or Spallation Neutron Source SNS in the US) are based on the availability of efficient accelerating cavities with properties like mentioned above. Other applications as envisaged within future projects are cw operation of proton or ion accelerators.

It is commonly accepted that above an energy of 200 MeV/u superconducting cavities are superior to room temperature structures at duty cycles around or above a few percent. By combining the advantages of CH-mode cavities with the benefits of superconductivity, effective ion acceleration at high duty cycle and at low injection energies will become possible. For high current proton beams the injection energy will be around 10 MeV, while for heavy ions the injection energy may become as low as 1 MeV/u.

The results gained from numerical simulations show that the CH cavity can be a multi-gap alternative to the spoke-type or reentrant cavities currently under investigation in other labs up to beam energies around 150 MeV/u. The key parameters have been calculated for different prototype cavities (see tab. 1) and have been compared to other cavities [2].

Table 1: Parameters and expected performance of the different prototype CH-cavities

Frequency (MHz)	352	433	700
Particle velocity (v/c)	0.17	0.17	0.5
Gap number	18	18	10
Accel. gradient (MV/m)	6.7		
Length of the cavity (m)	1.43	1.01	1.07
Tank radius (mm)	185	130	105
E_{max}/E_{acc}	4.1	3.9	5.2
B_{max}/E_{acc} (mT/(MV/m))	5.8	3.7	8.8
R/Q_0 (kΩ/m)	2.7	4.7	2.6
Q-factor (4K,Nb)	$4.3\cdot10^9$	$2.7\cdot10^9$	$1.4\cdot10^9$
Diss. power (4K,Nb) (W)	6.5	4.0	13.8
Stored energy (J)	12.6	4.1	4.3

A copper model of one prototype cavity (352 MHz, β=0.17, shown in fig. 1) was built at the IAP Frankfurt to study the low-level rf behavior of the resonator.

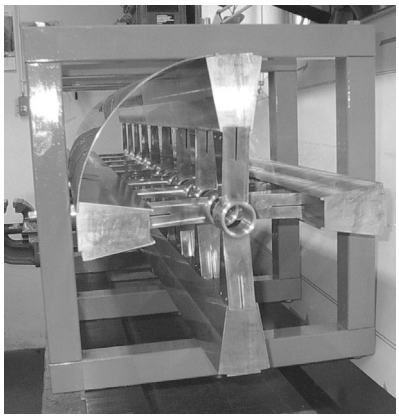


Figure 2: Photo of the CH copper model cavity. The end cells and part of the tank housing is removed

The resonant frequency was found to be 350 MHz, which is less than 1 % below the predicted value. The on axis field distribution for the cavity was measured with a bead pull setup. The yielded field distribution after the first tuning procedure is shown in fig. 2, where the gap length of the 2nd and 17th gap was reduced by 25 %, leading to a field enhancement in this gap. This tuning principle is fully developed and has been found to be adequate. Further tuning steps towards a flat field distribution will take place soon.

Our investigations indicate that CH-mode cavities are well suited to design sc resonators. The results of the numerical simulation and the first measurements of a room temperature model cavity are very promising. Using state of the art technology the fabrication of a superconducting CH-mode cavity will be possible. A design study in cooperation with industry will be available soon.

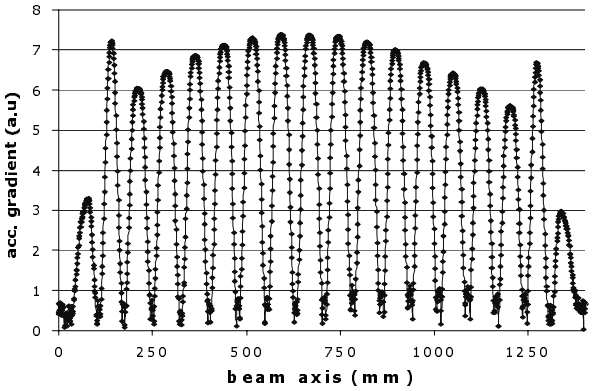


Figure 2: Accelerating on-axis field distribution of the 350 MHz CH model cavity where the gap length of the second and the 17th gap was decreased from 38 mm to 28

References

[1] R. Eichhorn and U. Ratzinger, Proc. of the Workshop on RF Superc., Santa Fe (1999) 462.
[2] R. Eichhorn and U. Ratzinger, Proc. of the Lin. Acc. Conf., Monterey SLAC-R-561 (2000) 926.

RFQ Development for an Injector Linac for Therapy Facilities*

A. Bechtold, U. Ratzinger, A. Schempp, IAP, Johann Wolfgang Goethe-Universität, Frankfurt am Main
B. Schlitt, GSI

The design of a compact 7 MeV/u, 217 MHz carbon injector linac for therapy facilities [1] has been presented already in earlier reports [2,3]. In the last year the RFQ design has been further improved leading to the structure parameters as presented in Fig. 1 [4].

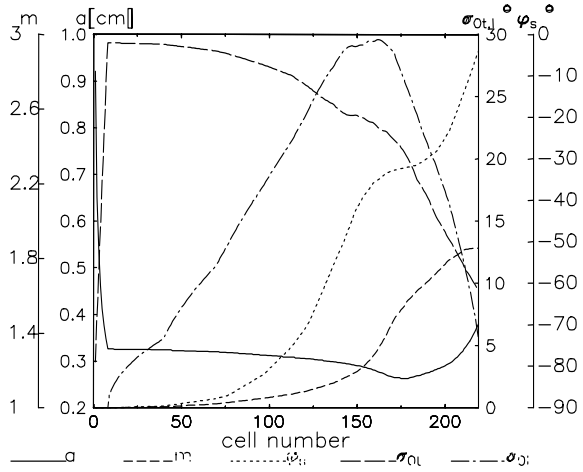


Fig. 1: Design parameters of the RFQ.

A new RF model has been investigated. It comprises the last section of the RFQ structure followed by two drift tubes, which shall be integrated into the RFQ tank as a buncher (Fig. 2). Bead-perturbation measurements have been performed on the model set up in good accordance with MAFIA simulations and resulted in a voltage ratio between electrodes and buncher gaps of 1.23 [4], corresponding to a total bunching voltage of 86.1 kV with 70 kV at the RFQ electrodes. This is very close to the optimum for a minimum phase spread at the entrance of the subsequent IH-type drift tube linac (Fig. 3). Fig. 3 shows the 95 % phase spread at the DTL entrance for different total bunching voltages resulting from beam dynamics simulations along the RFQ and the complete matching section using a modified PARMTEQ code. The required phase spread of ≤ ±15° can be achieved with a total bunching voltage between about 75 kV and 100 kV.

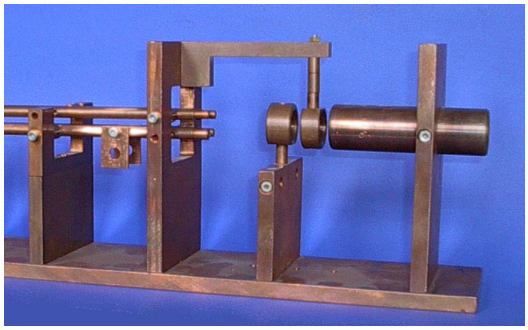


Fig. 2: Model set up of the RFQ drift tube combination.

Further beam dynamics simulations have been performed taking into account the distortions of the field distribution between the RFQ electrodes and the subsequent drift tubes. A new subroutine for the IAP version of the PARMTEQ code has been written to simulate the particle dynamics in an arbitrary potential distribution. The generation of the potential has been done externally by solving the Poisson equation with the method of successive overrelaxation [4]. These simulations have shown only negligible effects on the beam dynamics in comparison to simulations using a field-free drift section between RFQ electrodes and drift tubes.

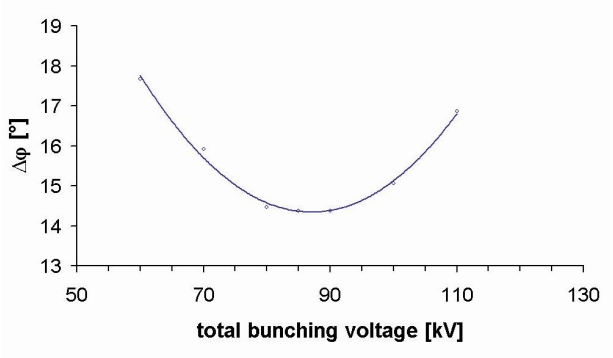


Fig. 3: Simulated phase width at the entrance of the IH-DTL versus buncher voltage at RFQ exit.

Presently, first components including the RFQ tank (Fig. 4), stems and ground plate of the RFQ have been manufactured at NTG in Gelnhausen. The manufacturing of the electrodes is still in process at NTG. The tank has been copper plated at GSI already. Alignment and tuning of the RFQ are planned for the first half of 2002.



Fig. 4: RFQ tank for the injector linac for therapy facilities.

References:

[1] B. Schlitt, A. Bechtold, U. Ratzinger, A. Schempp, in: *Proc. LINAC 2000*, p. 226.
[2] A. Bechtold, A. Schempp, U. Ratzinger, B. Schlitt, in: *GSI Scientific Report 1999*, p. 198.
[3] B. Schlitt, A. Bechtold, U. Ratzinger, A. Schempp, in: *GSI Scientific Report 2000*, p. 191.
[4] A. Bechtold, U. Ratzinger, A. Schempp, B. Schlitt, in: *Proc. PAC 2001*, p. 2485.

* Work supported by the BMBF

NEW INSTRUMENTS AND METHODS

Estimation of Carbon-Ion-Caused Radiation Levels by Calculating the Transport of the Produced Neutrons Through Shielding Layers 205
G. Fehrenbacher, F. Gutermuth, T. Radon

New Possibilities in the Preparation of Heavy-Ion Targets by Sputtering Deposition 206
W. Hartmann, B. Kindler, J. Klemm, B. Lommel, J. Steiner

LabVIEW Control Applications for Cave A and SHIPTRAP 207
D. Beck, H. Brand, K. Poppensieker, K. Wunderle

MBS Version 4.2 New Features 208
H.G. Essel, N. Kurz

Go4: Status 209
J. Adamczewski, M. Al-Turany, D. Bertini, H.G. Essel

Towards Spectroscopy of ^{100}Sn: Selective ISOL of Short-lived Sn (and Ge) Isotopes 211
R. Kirchner

R3B: A Next-Generation Experimental Setup for Reaction Studies with Relativistic Radioactive Beams 212
T. Aumann, R3B Coll.

Calorimetric Low Temperature Detectors for Mass Identification of Heavy Ions 213
S. Kraft, A. Bleile, P. Egelhof, R. Golser, O. Kisselev, W. Kutschera, V. Liechtenstein, H.J. Meier, A. Priller, A. Shrivastava, P. Steier, C. Vockenhuber, M. Weber

Diamond Detectors 2001 - Applications for Minimum-Ionizing Particles 214
E. Berdermann, K. Blasche, W. de Boer, H. Bol, G. Caragheorgheopol, H.W. Daues, E. Grigoriev, F. Hauler, P. Moritz, M. Petris, M. Petrovici, H. Stelzer, B. Voss, J. Wieser

Development of Multistrip Glass Resistive-Plate Counters (GRPC) 216
M. Petrovici, N. Herrmann, K.D. Hildenbrand, G. Augustinski, M. Ciobanu, I. Cruceru, M. Duma, O.N. Hartmann, Y.J. Kim, P. Koczon, T. Kress, M. Marquardt, D. Moisa, M. Petris, C. Schröder, A. Schüttauf, V. Simion, G. Stoicea, Z. Tyminski, J. Weinert

The New Readout Electronics for TAPS 217
P. Drexler, U. Thöring, W. Bonn, H.A.P. van der Duin, R. Holzmann, G. van der Kruk, B. Krusche, H. Löhner, V. Metag, T.W. Nijboer, J.G. Messchendorp, R. Novotny, C. Salz, S. Schadmand, M. Steinacher, M. Thiel, H. Vorenholt, TAPS Coll.

Test of the New Preamplifier for the ALICE TRD 218
I. Rusanov, J. Stachel, V. Catanescu, M. Ciobanu

New Front-End Electronics for the ALICE TPC-Detector 219
H.K. Soltveit, J. Stachel, P. Glässel, I. Rusanov

Position Resolution with Prototypes for the ALICE TRD 220
A. Andronic, H. Appelshäuser, C. Blume, P. Braun-Munzinger, D. Bucher, O. Busch,
A. Castillo-Ramirez, G. Catanescu, M. Ciobanu, H. Daues, A. Devismes, C. Garabatos,
N. Herrmann, M. Ivanov, T. Lister, T. Mahmoud, T. Peitzmann, M. Petrovici, K. Reygers,
R. Santo, R. Schicker, S. Sedykh, R.S. Simon, J. Stachel, H. Stelzer, G. Tsiledakis,
B. Vulpescu, J. Wessels, O. Winkelmann, B. Windelband, C. Xu, ALICE Coll.

Lorentz Angle Measurements with ALICE TRD Prototypes 221
O. Busch, A. Andronic, H. Appelshäuser, C. Blume, P. Braun-Munzinger, D. Bucher,
A. Castillo-Ramirez, G. Catanescu, M. Ciobanu, H. Daues, A. Devismes, C. Garabatos,
N. Herrmann, M. Ivanov, T. Lister, T. Mahmoud, T. Peitzmann, M. Petrovici, K. Reygers,
R. Santo, R. Schicker, S. Sedykh, R.S. Simon, J. Stachel, H. Stelzer, G. Tsiledakis,
B. Vulpescu, J. Wessels, O. Winkelmann, B. Windelband, C. Xu, ALICE Coll.

Development of the Radiator for the TRD of the ALICE Experiment 222
A. Andronic, V. Angelov, H. Appelshäuser, C. Blume, P. Braun-Munzinger, D. Bucher,
O. Busch, A. Castillo-Ramirez, V. Catanescu, M. Ciobanu, S. Chernenko, V. Chepurnov,
H. Daues, A. Devismes, O. Fateev, C. Finck, P. Foka, C. Garabatos, R. Glasow,
M. Gutfleisch, N. Herrmann, M. Ivanov, F. Lesser, V. Lindenstruth, T. Lister, T. Mahmoud,
A. Marin, D. Miskowiec, Yu. Panebratsev, T. Peitzmann, V. Petracek, M. Petrovici, C. Reichling,
K. Reygers, A. Sandoval, R. Santo, R. Schicker, R. Schneider, S. Sedykh, S. Shimanski,
R.S. Simon, L. Smykov, J. Stachel, H. Stelzer, H. Tilsner, G. Tsiledakis, I. Rusanov, B. Vulpescu,
J. Wessels, B. Windelband, O. Winkelmann, C. Xu, V. Yurevich, Yu. Zanevsky, O. Zaudtke

ALICE TPC Readout Chambers 223
P. Braun-Munzinger, C. Garabatos, J. Fiess, U. Frankenfeld, P. Glässel, M. Ivanov,
R. Renfordt, H. Sann, H.R. Schmidt, H. Stelzer, D. Vranic, B. Windelband

Estimation of carbon-ion-caused radiation levels by calculating the transport of the produced neutrons through shielding layers

G. Fehrenbacher, F. Gutermuth, T. Radon
GSI Darmstadt, Germany

An important aspect to be considered when designing the GSI future project will be the radiation protection of both the staff and the environment. One of the prerequisites for a permission for the operation of a high-energy accelerator is a careful planning of the necessary radiation shielding equipment. In order to give recommendations for the amount of concrete needed for adequate radiation shielding one has to calculate the transport of the primary produced radiation through the shielding walls.

Here we report on using the radiation transport code FLUKA [1] for the evaluation of the shielding design of a medical radiation treatment unit [2]. As an example the irradiation room of the planned heavy-ion cancer therapy facility in Heidelberg is subject to an radiation protection analysis. Neutrons of a wide energy range mainly constitute the radiation impact behind the shielding walls. The production of neutrons by a 400 MeV/u carbon beam in tissue-equivalent material has been measured at the HIMAC in Chiba [3]. Using the computer program FLUKA these *primary* neutrons are further transported through the shielding geometry by Monte-Carlo techniques. For comparison a conventional *line-of-sight* model is applied, too.

The shielding equipment of the treatment rooms in Heidelberg will consist of two main components, one solid iron block placed directly behind the patient and a thick wall made of concrete surrounding the room. The geometrical arrangement of the design is illustrated in figure 1.

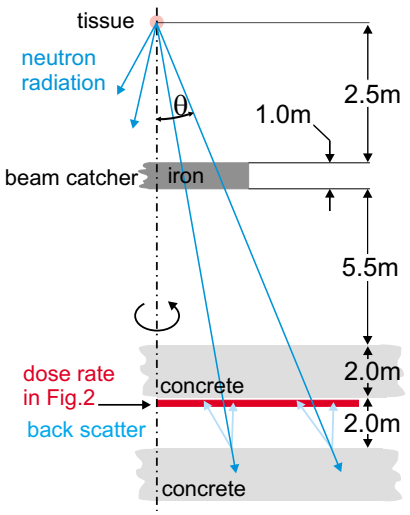


Figure 1: Principle geometry of the irradiation setup in the planned cancer treatment unit. Carbon ions are absorbed in the tissue. The resulting secondary radiation is absorbed by a solid iron beam catcher and a thick concrete wall subsequently. A second wall may cause back-scattering of neutrons.

At the moment there is no computer code available which is capable of transporting heavy ions through dense matter. As a work-around one can measure primary neutron production of heavy ions in thick targets and take these neutron spectra as an input for further radiation transport calculations. Here the neutron spectra measured by Kurosawa *et al.* [3] are used in a simulation of the treatment chamber with FLUKA. The results are compared with calculations made according to the so-called *line-of-sight* method. In this approach one assumes that the fluence of particles decreases with the square of the distance *(line-of-sight)*. The absorption of particles follows an exponential function of the path-length inside the shielding material.

Figure 2 shows the dose rate behind the wall of the irradiation chamber. The lowest line represents the results obtained with the *line-of-sight* model. A steep increase in dose rate is evident for angles higher than 26.5 degree, where the *line-of-sight* does not cross the iron beam catcher. In contrast the results of the FLUKA simulations do not show this pronounced change in dose rate. This difference can be explained by the lack of scattering in the *line-of-sight* model which moderates the transition from regions with and without shielding in the direct *line-of-sight*. Another phenomenon which the *line-of-sight* method does not account for is the neutron albedo.

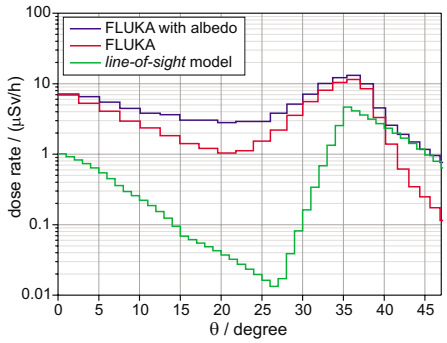


Figure 2: Dose rates behind the first shielding wall (see line in figure 1) as calculated according to the *line-of-sight* method and with the radiation transport code FLUKA [1].

In figure 1 a second wall of concrete is indicated which can be part of a mash for example. The upper line in figure 2 shows the results of a second FLUKA simulation including the second wall. The back-scattering of neutrons from the second wall causes an additional radiation exposure.

It can be concluded that radiation transport codes employing Monte-Carlo technique are superior to the conventional *line-of-sight* model. Particularly scattering and albedo effects are taken into account which can contribute significantly to the expected neutron dose rates.

References

[1] A. Fasso *et al.*, Proc. 3rd SARE Workshop, KEK, Tsukuba (Japan) 7-9 May 1997. Ed. H. Hirayama, KEK Proceedings 97-5 (1997)
[2] G. Fehrenbacher *et al.*, GSI-Report 2001-05 (2001)
[3] T. Kurosawa *et al.*, Intern. confer. Nucl. data f. Science a. Technology; Ed. G. Reffo; A. Ventura; C. Grandi; Trieste, May, (1997)

New Possibilities in the Preparation of Heavy-Ion Targets by Sputtering Deposition

W. Hartmann, B. Kindler, J. Klemm, B. Lommel, J. Steiner
Gesellschaft für Schwerionenforschung mbH, Planckstrasse 1, 64291 Darmstadt, Germany

Introduction: Sputtering is a ballistic process which allows to deposit layers of very different materials: low melting metals as well as refractory materials, elements and compounds, and with an rf-sputter source even dielectrics and insulators can be sputtered. Additionally it is possible to sputter in presence of an reactive gas or a gas mixture so that for example oxides can be created directly during the deposition. At large sputtered layers have a higher adhesive strength on a substrate than evaporated layers. All these properties make sputtering deposition a powerful tool in preparation of heavy-ion targets.

Sputtering in the target laboratory: Until recently we used the sputtering technique solely with a focused ion beam sputtering apparatus from Danfysik [1]. There, a beam of Ar-ions is extracted from a duoplasmatron ion source and is focused to a diameter of about 2 mm on a sputter cathode made of the wanted target material. This method has a very high efficiency so that one can work with extremely small amounts of material. This is essential especially for rare and expensive isotopes. But because of the limited power (10 keV, 1 mA) and the close set up only small-size targets can be produced in a justifiable time and with a reasonable homogeneity.

In the end of 2000 the target laboratory purchased a new sputter coater from BOC Edwards which is equipped with two 1" and one 3" magnetron sputtering sources like the one depicted in principle in figure 1. They can be operated in the DC as well in the RF mode. After the installation of the machine and a rather short running-in period we began in 2001 with the test and the first production of targets with this equipment.

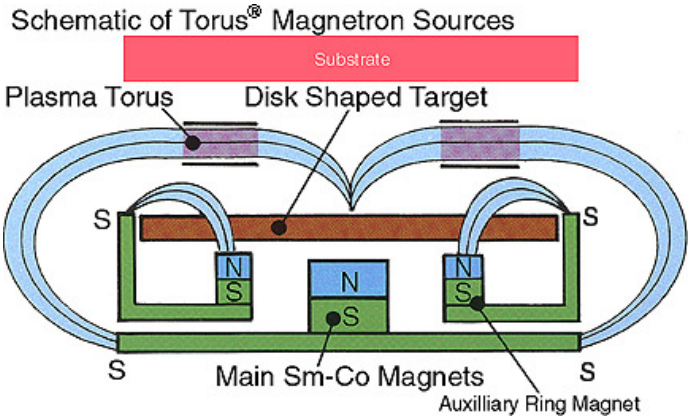
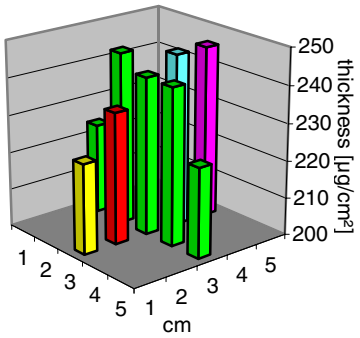


Figure 1: Principle of a Magnetron Source [2]. The magnetic fields depicted above in combination with a vertical **E**-field confine the low-pressure plasma to a torus above the target.

Gold is a material that sputters well. We deposited Au-layers in a wide thickness range on glass substrates coated with betain-saccharose and detached them easily. By depositing Au directly on glass plates one gets durable mirror layers. We also deposited Au-layers on thin Cr-layer on diamond substrates for the detector laboratory.

We made some tests of producing free standing C-layers with DC sputtering as well as with RF-sputtering but the sputtering rate of C is rather poor and the results are not convincing until now.

We also had the task to produce layers of cobalt, of chromium, of nickel, and of niobium on tantalum plates respectively which had to have an high adhesive strength. In the case of Cr and Nb the sputtering was rather easily and straight forward and the homogeneity of the layers is satisfactory as you can see in figure 2. But for the magnetic materials of Co and Ni we ran into problems. The inner magnetic field of Co respectively Ni interfered with the magnetic field of the Sm-Co magnets situated below the sputtering target (see figure 1). They are meant to confine the plasma to a stable a toroidal zone burning right above the sputtering target. With standard sputtering targets out of Cr or Ni of thickness between 3 mm to 5 mm it was not possible to ignite a stable plasma. We finally succeeded with those layers anyhow in stacking several thin foils of a thickness not higher than 250 to 300 µm and replacing the upper one after some time.



average 237 µg/cm²
deviation ± 9.94 µg/cm²
± 4.19 %

Figure 2: Distribution of the weight per area of a sputtered Ni-layer and the corresponding tolerances.

For the heavy-element program at SHIP we produced large-area targets of tantalum on a C-backing. Ta is a refractory material so that thermal evaporation - which is the standard method for the SHIP-wheels - was not possible in this case. Ta could only be evaporated with an electron beam gun but for the banana-shaped SHIP-targets with an active target area of about 18.5 cm² one would need a very large distance between the crucible and the target to get at least a tolerable homogeneity of the layer. This was no real alternative. Since ^{181}Ta has a natural abundance of 99,988 % it was possible to make a first try for the production of SHIP-targets because one could use a pure standard plate of Ta as sputtering target. In other cases this would possibly be not so easy since for experiments with low reaction cross-sections it is necessary to use highly enriched material. To get highly enriched isotopes in the form of a metal sheet of 1 inch in diameter and a sufficient thickness will be a difficult task for some isotopes. But nevertheless this new method opens up a new perspective for heavy-ion targets out of materials categorized until now as impossible.

References:

[1] H. Folger, J. Klemm, and M. Müller, IEEE, Vol. NS-30, No.2 April 1983.

[2] http://www.lesker.com

LabVIEW Control Applications for Cave A and SHIPTRAP

Dietrich Beck, Holger Brand, Klaus Poppensieker and Kai Wunderle, DVEE, GSI

1 Stepper Motor Control for Cave A

A control system is required to operate up to 16 stepper motors in Cave A. These are needed for experiments performed by the Atomic Physics Division. All stepper motors have to be controlled at the same time from outside the Cave.

A first system has been set up that is able to control six axes[1]. The hardware is based on FlexMotion PCI cards from National Instruments[2] and an amplifier built by Movtec[3]. The software is written using LabVIEW from National Instruments. Although this system has been successfully used in a couple of beam-times, it is not intended to extend it to 16 axes. The reasons for that are the following. First, the design of the system is not suitable for a distributed system that is controlled remotely. The main limitation here is the length of cables and a missing modularity. Second, quite a few hardware bugs were found and had to be cured before that system was operational. Third, some hardware components are especially built for this set-up and not available off the shelf.

A couple of products of different companies have been evaluated. As a result, it was decided to use components from another company, IEF Werner[4]. The quality of these components has industry standard, can be used without modification and can be controlled from outside Cave A via a Profibus interface (see below). The control software is presently implemented with LabVIEW.

2 Using Profibus from LabVIEW

Profibus is an field bus with an open specification and frequently used and supported by industry [5]. Profibus master cards for PCs are available by various suppliers together with so called OPC servers. The input and output parameters of Profibus are represented by process variables, so called tags, on the OPC server. They can easily be accessed by other PC applications like LabVIEW.

Three combinations of Profibus master card and OPC server were evaluated.

- Comsoft[6]: The OPC server and Profibus master are the ones which can be used most easily. Unfortunately, no fiber optics but only RS485 connectors are supported.

- Siemens[7]: Presently, Siemens is the only manufacturer supporting the RS485 as well as fiber optics connectors. Unfortunately, the configuration of the OPC server is less user friendly than for the ones of Comsoft and Beckhoff.

- Beckhoff[8]: The OPC server from Beckhoff gives access not only to Profibus but to all common field busses like CANopen, Interbus, Modbus and others. Moreover, intelligent and non intelligent bus terminals with Ethernet connections are supported as well. In addition, the configuration of the OPC server is still fairly easy. Profibus master cards with fiber optics are not yet available but will be during this year.

To summarize, it is recommended to use the Profibus master card and software from Beckhoff.

3 The Control System for SHIPTRAP

SHIPTRAP is a facility that is tailored to slow down, cool and purify short lived trans-uranium isotopes delivered by SHIP. Experiments will be done either with SHIPTRAP itself or with other set-ups that are placed behind SHIPTRAP and which require cooled, purified and low-energy ions. The design and implementation of the control system for such a facility is challenging [9]. About 1000 process variables have to be controlled. The experimental procedures require timing sequences to control actions with a precision of about 100ns. The different operational modes that will be used require the control system to be highly flexible. The control system will consist of two parts. First, there is a general control software package that can be used as a framework for other experiments as well. Second, there are SHIPTRAP specific add-ons. The general part of the system will be implemented in collaboration with other trap experiments.

Presently, the first version of the general part of the control system is finished. For the implementation, an object oriented approach, that is made possible by a toolkit from Vogel Automatisierungstechnik[10], has been used together with LabVIEW. During spring 2002, the SHIPTRAP specific add-ons will be implemented. The commissioning of the first version of the overall system is planned for summer 2002.

[1] http://www-wnt.gsi.de/steppercavea
[2] http://www.ni.com
[3] http://www.movtec.de
[4] http://www.ief-werner.de
[5] http://www.profibus.com
[6] http://www.comsoft.de
[7] http://www.siemens.de
[8] http://www.beckhoff.de
[9] http://www-wnt.gsi.de/shiptrap
[10] http://www.objectview.de/english/index.htm

MBS Version 4.2 New Features

H. G. Essel, N. Kurz
DVEE, GSI Darmstadt

Lynx and MBS Status
All Lynx nodes are still running LynxOS 2.5 except the RIO3 which runs LynxOS 3.1. LynxOS version 3.0 is ready for CVC and E7. The nodes will be upgraded soon. RIO2 and PC will be upgraded to LynxOS 4.x when available.
Figure 1 shows the increasing number of MBS installations. Since 1999 only "active" installations are included. In addition there are more than 10 "roaming" systems used occasionally.

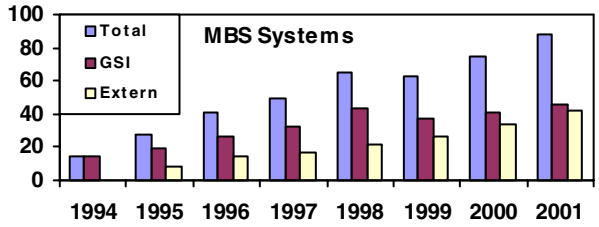


Figure 1: MBS Installations.

Besides by the names `prod`, `old`, and `deve` the MBS version can be selected by vnm, i.e. v42. By alias `mbslogin <version>` one can switch. A new script `/mbs/login <version>` should be used in the `.login` script. The MBS file system has been changed slightly to enable the distribution of a single version.

New User IDs on Lynx
All user and group IDs on the Lynx machines have been changed to fit into the Linux ID space. The file systems of Lynx are mounted on the Linux cluster machines to `/lynx/Lynx/<group>`. The MBS file system is mounted to `/lynx/Mbs`.

Delayed Event Building
A mechanism has been implemented to optimize the data throughput with a pulsed beam like SIS. The data readout is slowed down by the event building because both tasks access the sub-event pipe. If they are running on the same node, they must share the CPU in addition. This conflict is reduced by delaying the event building into the beam pauses. Triggers 12 and 13 are used to signal spill on and off, respectively, to the MBS. These signals must be provided by cabling.
The delayed event building can be enabled/disabled by commands. In delay mode the MBS collectors read the data from the sub-event pipes only if spill is off, or if the pipes are filled up to an adjustable upper limit. When the collectors are forced to start reading the pipes during the spill, they stop when the pipe filling goes below a lower limit.
The lower and upper limits can be set by commands as well. The lower limit must be less than 50%, because a pipe has two buffers. The readout needs exclusive write access to one buffer. After a readout blocking due to a full pipe the readout has to wait until the collector emptied one buffer. Table 1 shows sustained data rates for a best suited example. All measurements have been done with 100% dead time and variable event size (1 to 4000 long words). Of cause, the benefit depends on many parameters. The optimal enhancement is achieved if the pipes are big enough to keep the data of one spill, and if the collectors can empty the pipes during the spill pause.

RIO3 and PC	Delayed off	Delay on
Spill 4 sec on/off	3.6 MB/sec	5.3 MB/sec
Spill 2 sec on / 4 sec off	2.4 MB/sec	5.3 MB/sec

Table 1: Performance of delayed event building.

Optimized Mapping of Sub-event Pipes.
On RIO2 and RIO3 the sub-event pipe memory can now be mapped directly instead through a shared segment. Because of the caching mechanisms enabled with direct mapping the read/write from/to the pipes is enhanced considerably. MBS systems running in this mode gain between 20% and 45% data throughput (last row in table 2).
In combination with delayed event building data rates can be increased in best suited cases by a factor of two without hardware investments (compare tables 1 and 2).

RIO3 and PC	Delayed, segment	Delayed, direct map
Spill 4 sec on/off	5.3 MB/sec	7.5 MB/sec
	segment	direct map
DC, no delayed	6.6 MB/sec	9.3 MB/sec

Table 2: Performance with direct mapping.

Direct mapping is enabled by a new parameter in the user setup files.

Writing to Disk
Instead of writing to a directly attached tape it is now possible to write the raw data to disk. It is mandatory to use an experiment group server as fileserver to provide the disk space. Data rates up to 3 MB/sec sustained can be achieved (RIO3, Fast Ethernet).

New VME Trigger Modules
A redesigned version of the VME Trigger Module is available. Functional identical to the old one it allows now the connection of trigger modules over longer distances via the trigger bus. A system with 7 modules and a 200m trigger bus length has been successfully tested .The usage of new bus driver chips with better common mode rejection will reduce possible problems in electrical unclean conditions. A programmable gate generator has been implemented on free output pins. Apart from a minor change, the user interface is backwards compatible.

Actual information on further developments can be found on http://daq.gsi.de

Go4: Status

J. Adamczewski, M. Al-Turany, D. Bertini, H. G. Essel
DVEE, GSI Darmstadt

The GSI analysis system GO4 is a multi-threaded analysis based on the ROOT framework [1]. Figure 1 shows the overall software structure.

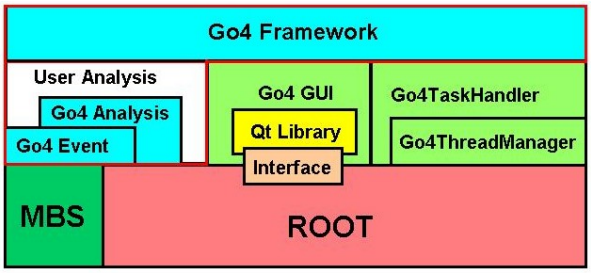


Fig.1 Go4 software layers.

The kernel classes have been implemented and are in a testing phase by several users. The main starting entries to use Go4 are 1. use the event IO package (MBS, lmd input). 2. use Go4 event and analysis classes, 3. use the Go4 non-blocking GUI. The GUI can be used with any ROOT based analysis with little effort as demonstrated with the standard Hades on-line analysis. Figure 2 gives an overview of the Go4 functional packages and the adaptations required for extending to the next level of usage.

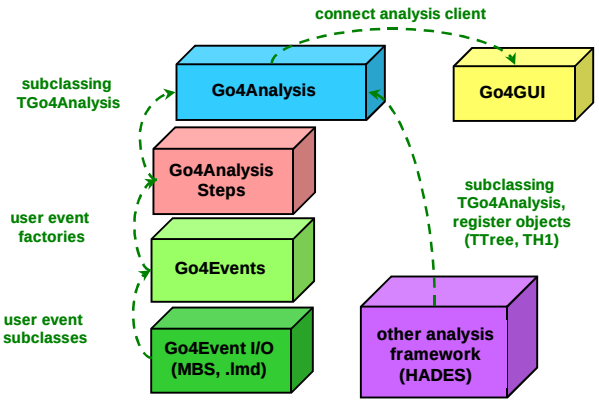


Fig.2 Go4 functional components.

In the following we describe the analysis loop and the GUI in more detail.

Go4 Event IO

The Go4 concept consists in interface classes which can be implemented by subclasses. For the event IO, Go4 offers framework plug-ins of the base classes TGo4EventSource and TGo4EventStore, e.g. TGo4MbsFile, TGo4MbsEventServer, TGo4FileSource, and TGo4FileStore.
These classes provide the event input from all GSI standard sources like MBS, event servers, and raw data files (lmd), and from ROOT files. Event output is implemented using the ROOT tree/branch mechanism. Other event IO can be added using inheritance from the base classes.

Go4 Analysis Framework

In the Go4 framework, a user analysis consists of analysis steps. Each analysis step has at least an input event object, an output event object, and an event processor object. Additionally, it can have an event source and an event store instance, and an event processor calibration object.
Go4 uses the mechanism of an abstract factory design pattern [2] to create the instances for each analysis step: the user specified event factory defines the properties of the analysis step on initialization.
The actual framework consists of the TGo4Analysis class which keeps and organizes the analysis objects (e.g. histograms) and which initializes the analysis steps. The user analysis is defined in a subclass of TGo4Analysis which inherits all methods. Constructor and destructor of the user class, in addition with the overridden virtual methods UserEventFunc(), UserPreLoop(), UserPostLoop(), allow to implement user specific functions.
The Go4 framework may run the analysis in batch mode or in multi-threaded, GUI controlled mode. The current settings of the analysis steps and all framework parameters are presented and controlled on the GUI. This makes a generalized run control possible.

Object Organisation

All objects, which should be visible on the GUI side, have to be registered at the analysis side to the Go4 framework, i.e. they are put in a ROOT TFolder structure, which can be browsed in the GUI. Moreover, the registered objects are kept persistent by the framework, i.e. the Go4 folder structure is saved automatically.

Go4 Inter-task Communication

Go4 uses separate system tasks for the analysis and the controlling GUI. The communication between these tasks is done by the Go4 Task Handler, which is described in [3], [4]. Through the Go4 browser, which is part of the GUI, one can access analysis objects like histograms for display. The objects are sent on demand from the analysis task to the GUI task for processing. Vice versa, analysis commands are sent from the GUI to the analysis for execution.

Qt-ROOT Interface

Because of the free availability of the powerful and well documented Qt graphics library including the Qt Designer [5] the Go4 GUI is based on Qt. A Qt-ROOT interface has been developed following the standard ROOT GUI implementation mechanism. Therefore no changes in the ROOT sources were needed. There is no limitation in the ROOT functionality when used with Qt.

GUI Kernel

The heart of the Go4 GUI package is a static singleton that acts as a window registry and an object dispatcher. Each window of Go4 consists of three separate objects: status-, slots- and wid-

gets-object. The communication inside a widget (Qt-widget) is done via a signal-slot mechanism [5].
When created, each window will register its slot and status objects by the registry. Thus, if a window is closed and re-opened again, it will be reconnected to its status and slots objects through the registry. It will look like before. The registry is also responsible for dispatching the incoming objects (from the analysis) to the corresponding windows.

Go4 GUI
The current Go4 GUI is a first version and will of cause be extended in the future.

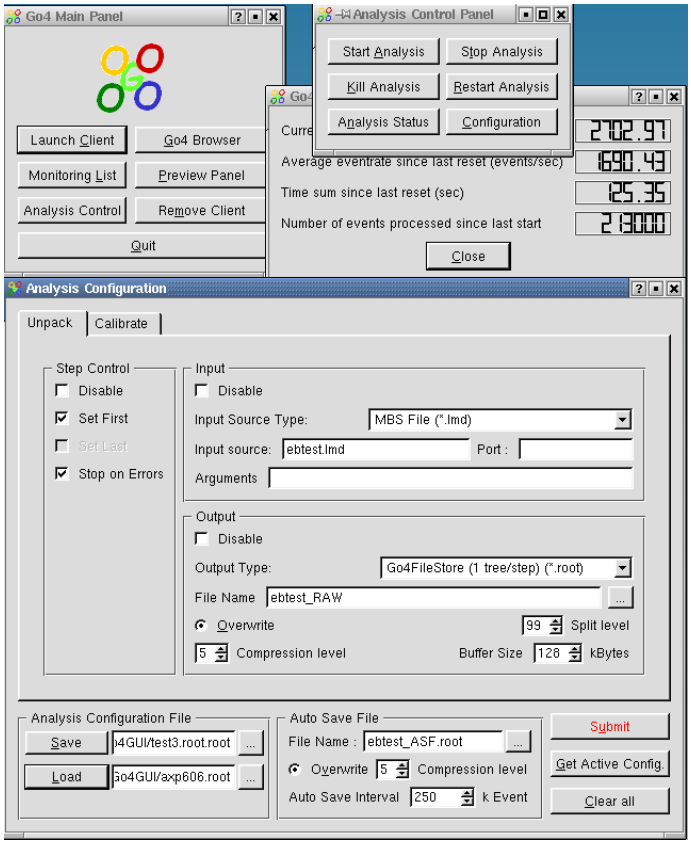


Fig.3 Go4 control panels

The main functionality is

1. Run control: Start/stop analysis task, setup analysis steps.
2. Object browsing: Get objects like histograms for visualization. Store objects in ROOT files.
3. Monitoring: cyclic display of monitored histograms and analysis status.
4. Histogram handling: as provided by ROOT with some GUI extensions.

Figure 3 shows the control panels. The upper left is the startup window. From here the analysis task is controlled and the other panels are started, i.e. the analysis control panel (up right) and the status display (below). The bottom window is for setting up the analysis steps, i.e. data input specs etc..
Figure 4 shows the Go4 object browser that combines the functionality of a remote/local browser and tree viewer. On the left side are the objects of the analysis side (remote), on the right side the local ones (GUI and disk). At the bottom, ROOT commands might be passed to the CINT interpreter.

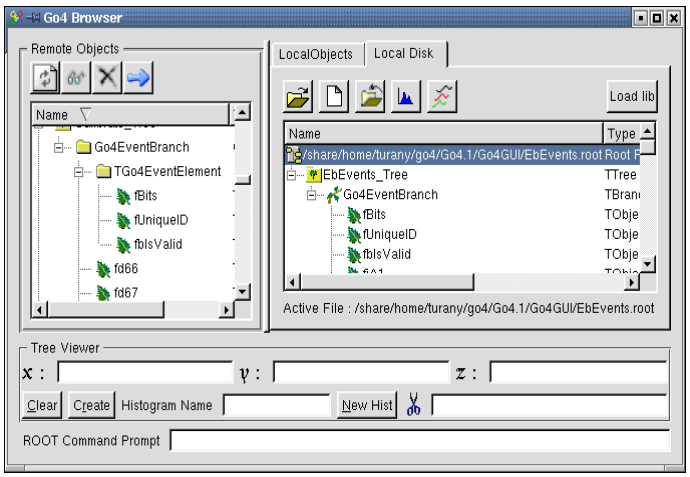


Fig.4 Go4 object browser

Figure 5 shows examples of ROOT graphics. Besides the standard ROOT functionality there are additional buttons with shortcuts for frequently used functions.

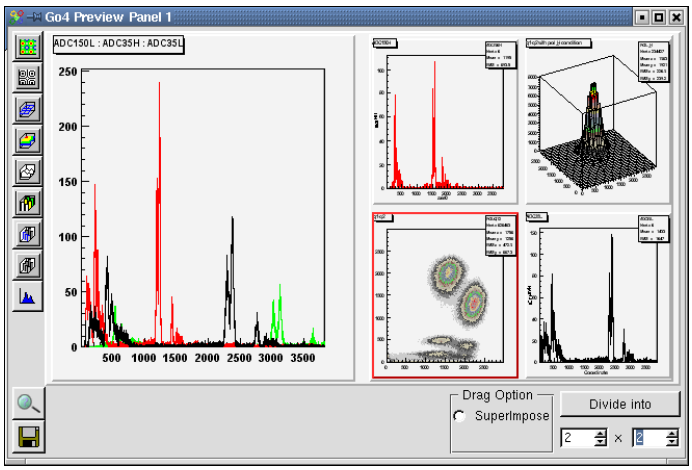


Fig.5 Some canvases with ROOT graphics.

Conclusion
After the first phase of prototypes the second phase of implementation has been finished. Beta releases of Go4 v1.0 are running in user test beds. The results and the feed back of these tests will be taken into account for the first production release in 2002.
Documentation of Go4 can be found at *http://go4.gsi.de.*

References

[1] R.Brun and F.Rademakers, “ROOT - An object oriented data analysis framework” *Nucl. Inst. Meth. in Phys. Res.* vol. A 389, pp. 81-86, 1997. See also http://root.cern.ch/.

[2] E.Gamma, R.Helm, R.Johnson, J.Vlissides “Design Patterns: Elements of Reusable Object Oriented Software”,Addison-Wesley 1999

[3] J.Adamczewski, M.Al-Turany, D.Bertini, H.G.Essel, M.Hemberger, N.Kurz, M.Richter, "Go4 Multi-tasking Class Library with ROOT", accepted by IEEE Trans. NS (2002)

[4] J.Adamczewski, M.Al-Turany, D.Bertini, H.G.Essel, "Go4: Multithreaded Inter-Task Communication with ROOT - writing non-blocking GUIs", Proceedings of CHEP 2001, September, 2001, Beijing, P.R.China

[5] Qt 2.30 Tutorial and Reference, Troll Tech AS, http://www.trolltech.com/

Towards Spectroscopy of ^{100}Sn: Selective ISOL of Short-lived Sn (and Ge) Isotopes

R. Kirchner, GSI

In isotope separation on-line (ISOL), the detailed spectroscopic investigation of short-lived isotopes of tin, e.g. of ^{100,102}Sn, was so far always hindered by the dominance of the simultaneously produced isobaric indium, cadmium, and silver isotopes. Initiated by the recent www-release [1] from Oak Ridge that the formation of SnS molecules permits a powerful separation of Sn from Sb and Te, we found in off-line test experiments [2] that this on-line tin chemistry also suppresses effectively In, Ag, and Cd. It also works for Ge (the homologue to Sn) and its respective contaminants. The formation of SnS molecules, which was performed in Oak Ridge utilizing the emanation of sulphur contaminating the targets, was tested to work reliably with vapours of either gaseous H_2S, liquid CS_2, or from solid sulphur powder. The figures below show that, depending on the operation mode of the FEBIAD-B2-C [3] ion source, the ions of Sn (or Ge, both subsequently referred to as X) coming out of the ion source appear with high probability in the sulfide sideband, at $^{32}S^+$ ion currents that do not obstruct the ion-source operation. At 1830K and $^{32}S^+$ currents of 700-900 nA, i.e. where the sulfide-ion formation probability $\beta=XS^+/(X^+{+}XS^+)$ is sufficiently well in saturation, the suppression of contaminations in the sulfide sideband was measured with isotopes of stable tracers to be

$SbS^+/Sb^+ \le 5*10^{-3}$	$AsS^+/As^+ \le 3*10^{-2}$
$InS^+/In^+ \le 3*10^{-3}$	$GaS^+/Ga^+ \le 1.4*10^{-3}$
$CdS^+/Cd^+ < 3*10^{-4}$	$ZnS^+/Zn^+ < 10^{-4}$
$AgS^+/Ag^+ < 10^{-4}$	$CuS^+/Cu^+ < 10^{-4}$

The measurements from Oak Ridge [1] indicated that the transport of SnS is faster than for Sn in the absence of sulphur. This conclusion could be confirmed by measurements of the characteristic current variations, operating a heatable cold-trap in the ion source („bunching technique“ [3]) which yield the mean wall sticking times. These are (per wall collision) of the order of milliseconds for Sn, and around 1s for Ge [3] in the absence of sulphur and turned out to be negligible (order of µs) for SnS and GeS. Also the formation time for SnS (and probably also for GeS) is short and estimated to be of the order of 1ms (at ~ 1µA sulphur current) from the slope of β in Fig. 1 and the known mean sticking time of Sn atoms. The gain in separation speed is best illustrated by an on-line test with the 31s isotope ^{65}Ge, the rate of which increased by a factor of 37, when separating $^{65}GeS^+$ with sulphur addition instead of $^{65}Ge^+$ without. The comparatively long wall sticking times for Sb [3] also become negligible in the presence of sulphur, even though the SbS^+ *molecular ion* hardly shows up; for a fast migration it is sufficient that the SbS *molecule* is stable enough.

The “speed” measurements and the dependencies of the measured β values, shown below as function of the $^{32}S^+$ ion current (i. e. the sulphur concentration in the source) and vs. the mean temperature of the ion source enclosure, support the following interpretation of the underlying processes:

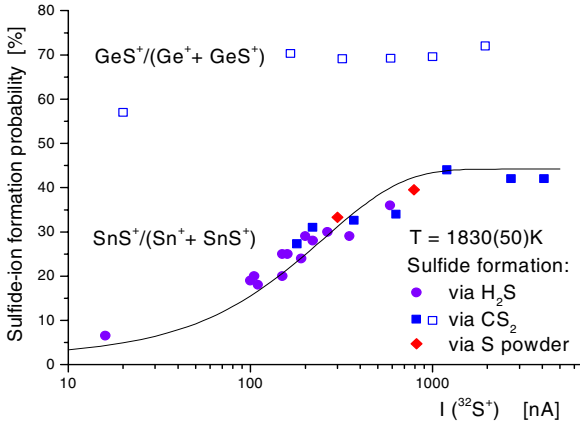
a. The formation of XS molecules happens on the surfaces of the ion source, since the wall sticking times of X are long compared to the mean flight time between two wall collisions. $\beta = f\{I(^{32}S^+)\}$ is well fitted by the typical (1-exp(-ax)) dependence, the slope reflecting the competition of desorbing X and XS particles. The saturation level indicates that here essentially only XS migrates in the ion source. XS is ionized with high efficiency (probably similar to the 40-50% for X^+ [4]) to XS^+ in the ionizing volume. The ions XS^+ are thermally less stable than neutral XS molecules and partly dissociate into X^+ and S. This is why β does not reach 100%, even though in saturation the conversion into XS at the walls is complete. This interpretation is supported by both the temperature dependence of β (which shows decreasing stability of the molecular ions with increasing temperature) and the “bunching” measurements which show no difference in the release characteristics of X^+ and XS^+ under saturation conditions [2].

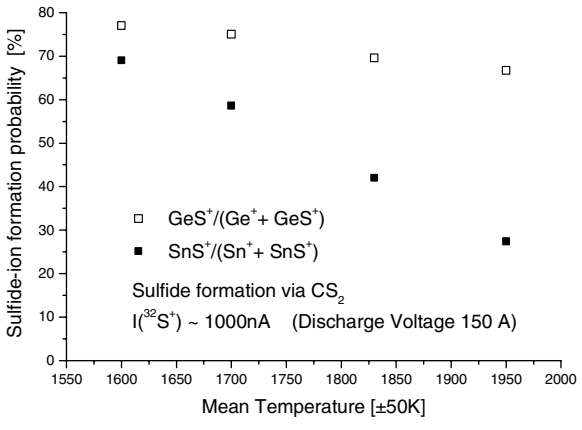
b. The saturation value of β is higher for Ge than for Sn and less sensitive to temperature variation, thus indicating that the molecular ion GeS^+ is more stable than SnS^+.

c. The saturation of β is reached for Ge at much lower sulphur concentration than for Sn, since the probability for sulfide-formation during adsorption is much higher for Ge due to the considerably longer surface sticking times of Ge atoms compared to Sn atoms [3].

References

[1] www.phy.ornl.gov/hribf/usersgroup/news/spring2_01.html
[2] www-aix.gsi.de/~msep/isol.html, chapter Ion Sources
[3] R. Kirchner, Nucl. Instr. Meth. B26 (1987) 204
[4] R. Kirchner, Nucl. Instr. Meth. B70 (1990) 186





R^{3}B: A next-generation experimental setup for Reaction studies with Relativistic Radioactive Beams

T. Aumann[1)] for the R^{3}B collaboration[1,2)]

[1)] *GSI,* [2)]*GANIL, Chalmers University, Uni Giessen, Uni Krakow, CEA Saclay, TU Muenchen, Uni Santiago de Compostela*

The objectives of the R^{3}B project [1] are to design and partly implement an advanced experimental setup for **R**eaction studies with **R**elativistic **R**adioactive ion **B**eams (R^{3}B) at GSI. The European Community funded this RTD project [2] with 0.8 MEuro for the period from 1st March 2000 to 31st August 2002. The project consists of several sub-projects, for which the major achievements are listed below: 1) A design study for a super-conducting fragment separator ("Super-FRS") with much larger acceptance for secondary beams than the present FRS has been carried out. This involves a new ion-optical design that guarantees the necessary purity and efficiency. 2) Detailed temperature-profile calculations were performed, which are essential for the technical design of a high-power production target that can withstand short pulses with high intensities of relativistic heavy ions available from the upgraded SIS synchrotron. 3) Layout of a large-acceptance magnetic spectrometer for momentum analysis and mass identification of the reaction products with a gap width that allows the observation of both neutrons and fission fragments behind the magnet. 4) Construction of a liquid-hydrogen reaction target adapted in size to the dimensions of the secondary beams from Super-FRS. 5) Construction of a ring-imaging Cerenkov detector (RICH) for velocity measurements of reaction products. 6) A new concept for a data-acquisition (DAQ) system and front-end electronics that facilitates the read out of the detectors installed in the R^{3}B setup. 7) Definition, planning, and simulation of key experiments, in the domains of both light nuclei (e.g. nuclear halos) and heavy nuclei (e.g. fission studies).

A schematic view of the reaction setup is shown in Figure 1. The task is to achieve a kinematically complete measurement of all reaction products after scattering exotic beams off secondary targets. The experiments to be performed cover a large variety of reaction types such as knockout reactions, electromagnetic and nuclear excitations, fission studies, in-beam γ-ray spectroscopy, multifragmentation, as well as charge exchange reactions. A zero-degree superconducting dipole magnet was designed within the R^{3}B project, which fulfills all requirements dictated by the various types of experiments mentioned above. The main parameters of the spectrometer are: (i) A large vertical gap allowing a cone with an angular range of ±80 mrad for neutrons to be covered. (ii) A horizontal acceptance, which allows a maximum bending angle of 40^0. This ensures an acceptance close to 100% even for experiments involving proton emission, or in general for experiments with very different magnetic rigidities for the beam and fragments. (iii) A high field integral of 5 Tm is required, which allows a bending angle of 18^0 for a 15 Tm beam (e.g. 1 GeV/u ^{132}Sn or 500 MeV/u ^{8}He). The required momentum resolution of up to 10^{-3} can be achieved by tracking the particles with high resolution. The design includes four super-conducting coils, shown in Figure 2, which are tilted to match the required acceptance angle for the particles of interest. The side coils are optimized to reduce the fringe field, and guarantee a low magnetic field in the target region, where detectors have to be placed.

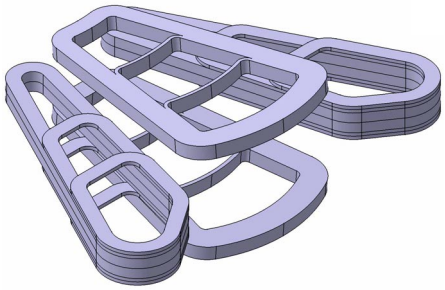


Figure 2. Layout of the four supersonducting coils. The side coils are optimized to reduce the fringe fields. The field integral amounts to about 5 Tm.

References

[1] http://www-land.gsi.de/r3b/

[2] Improving Human Potential Programme, Contract ID HPRI-CT-1999-50010

Supported by the European Community

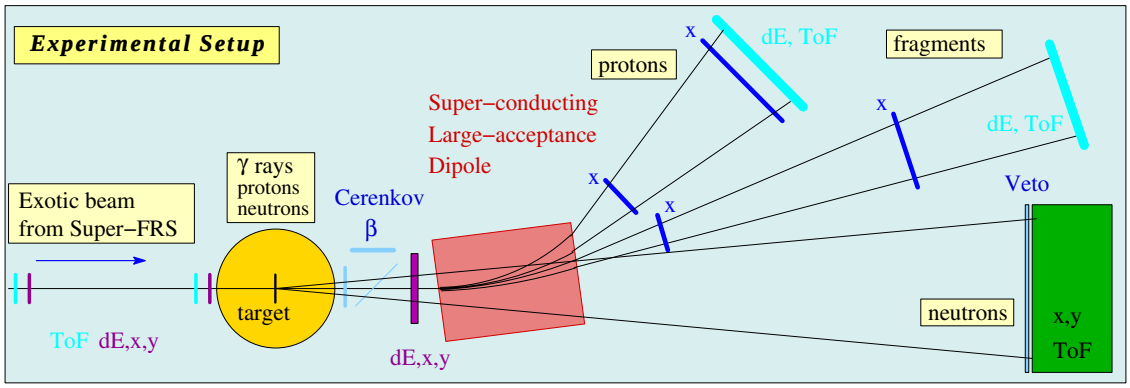


Figure 1. Schematic drawing of the experimental setup (not to scale). The incoming secondary beam is identified by measuring magnetic rigidity, energy loss dE and time-of-flight ToF. Behind the target, the kinematically forward focused reaction products are identified and momentum analyzed. The distance between target and neutron detector is typically 12 m.

Calorimetric Low Temperature Detectors for Mass Identification of Heavy Ions

S. Kraft[1,2], A. Bleile[1,2], P. Egelhof [1,2], R. Golser[3], O. Kisselev[1], W. Kutschera[3], V. Liechtenstein[3], H. J. Meier[1,2], A. Priller[3], A. Shrivastava[1,2], P. Steier[3], C. Vockenhuber[3], M. Weber[1,2]

[1]GSI, Darmstadt, Germany, [2]Institut für Physik, Universität Mainz, Germany, [3]Institut für Isotopenforschung und Kernphysik, Universität Wien, Austria

In many experiments, e.g. on synthesis of super-heavy elements, in accelerator mass spectrometry (AMS) or in nuclear spectroscopy, the mass of an isotope is to be determined directly via a combined kinetic energy and time of flight (TOF) measurement. Such measurements are limited by the energy resolution of conventional heavy ion detectors. Calorimetric low temperature detectors based on a superconducting Al meander structure as thermistor (T_C = 1.4 – 1.5 K) and sapphire absorbers have been demonstrated to provide an excellent relative energy resolution of 1 – 2 x 10^{-3} for energetic heavy ions in a wide range of ion species and energies (E = 5 – 1000 MeV/amu) [1]. Such detectors measure the temperature rise of an absorber due to the energy deposited by the incident heavy ion. In contrast, conventional heavy ion detectors such as semiconductor detectors and ionization chambers which operate on a charge collection principle, provide a relative energy resolution of $\Delta E/E \geq 10^{-2}$ for heavy ions in this energy range and becoming substantially worse for even lower energies. They are limited by incomplete energy detection due to charge recombination and short lifetimes of the detectors due to radiation damage, etc.

Due to their excellent performance, calorimetric low temperature detectors bear a large potential for various applications in basic and applied heavy ion research: In combination with a time of flight measurement of comparable precision, it should be possible to distinguish neighboring isotopes even for the heaviest ions. In accelerator mass spectrometry, calorimetric low temperature detectors are expected to provide considerable advantage over conventional detectors with respect to detection efficiency and energy resolution, allowing background reduction and therefore determination of very small isotope ratios.

Systematic investigations on the response of calorimetric low temperature detectors on the impact of heavy ions have recently been extended to the energy range of E = 0.1 – 1 MeV/amu, commonly used for AMS. The detectors used for the present investigations consist of a superconducting thin aluminum film thermometer operated at T ≈ 1.5 K, which is evaporated onto a sapphire substrate serving as absorber with a thickness of 330 µm and an active area of 2.5 × 2.5 mm^2. The thermal signal decay time of τ = 285 µs obtained for this detector allowed for count rates up to about 0.5 kHz. Experiments were performed using various beams (^{12}C, ^{197}Au, ^{238}U) provided by the Vienna 3 MV Tandem accelerator VERA and, in addition, a ^{241}Am α–source. For ^{197}Au at E = 17.8 MeV (≈ 0.1 MeV/amu), an absolute energy resolution ΔE_{FWHM} = 104 keV has been achieved corresponding to $\Delta E/E$ = 5.8 x 10^{-3}. This result already represents a considerable improvement compared to conventional ionization detectors, in particular for such relatively slow heavy ions. For comparison, the relative energy resolution for a conventional Si surface barrier detector under the same experimental conditions amounted to $\Delta E/E$ = 62 x 10^{-3}. In addition, a relatively fast decrease of the energy resolution of the silicon detector throughout several hours of measuring time was observed, most probably due to radiation damage, whereas the calorimetric detector showed no evidence of such behavior.

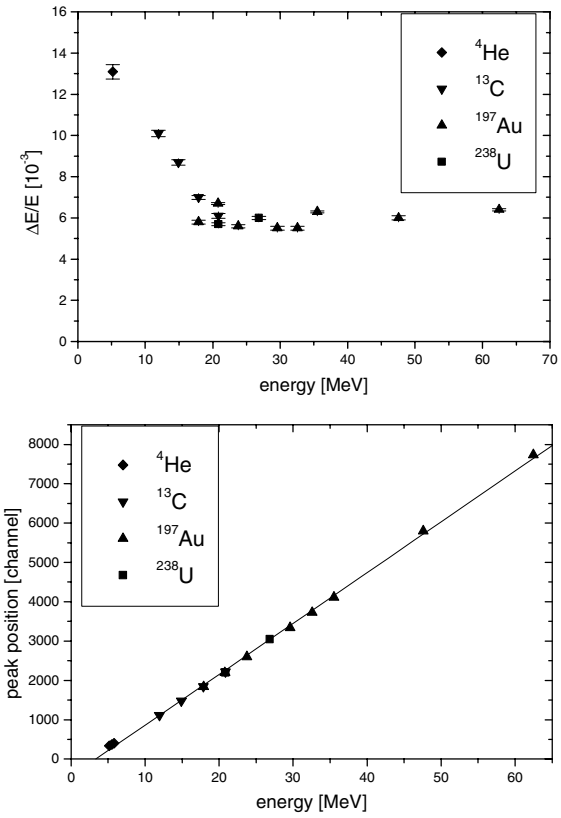


Fig. 1: Summary of a systematic study of detector performance for various ions and energies: relative energy resolution (upper part) and linearity of energy response (lower part) obtained for various ions in an energy range E = 5 – 60 MeV. The solid line represents a linear fit to the data.

In fig. 1 (upper part), results on the relative energy resolution obtained for all ions and energies investigated are summarized. The increase at low energies (E ≤ 20 MeV) may be explained by a lack of detector sensitivity due to their relatively large heat capacity. This problem may be solved by using substantially thinner absorbers. For the same data set, the energy response is displayed in fig. 1 (lower part). A perfectly linear behaviour is obtained, independent of the ion species, spanning the entire range of elements from ^4He up to ^{238}U. Hence, no evidence for pulse height defects is observed. In contrast, the measurements performed with the conventional silicon detector showed substantial pulse height defects up to more than 50% when comparing ^{13}C and ^{238}U.

References

[1] P. Egelhof, Advances in Solid State Physics **39** (1999) 61, and references therein.

Diamond Detectors 2001 – Applications for Minimum-Ionizing Particles

E. Berdermann[1], K. Blasche[1], W. de Boer[2], H. Bol[2], G. Caragheorgheopol[3], H. W. Daues[1], E. Grigoriev[2], F. Hauler[2], P. Moritz[1], M. Petris[3], M. Petrovici[3], H. Stelzer[1], B. Voss[1], J. Wieser[1]
[1] GSI Darmstadt, [2] Institut für Experimentelle Kernphysik Uni Karlsruhe, [3] Nat. Inst.for Nuclear Physics and Engeneering Bukarest

Last year the development of diamond detectors at GSI has been extended to applications for minimum-ionizing particles (mip's). Due to the extensive work of the RD42 Collaboration [Appendix, this report] a significant improvement of the CVD-diamond material has been achieved and radiation hard diamond strip- and pixel tracking prototypes for the innermost shells of the ATLAS and the CMS detectors (LHC, CERN) have been already developed. A position resolution below 20 µm is measured and further improvement is possible [1]. We have started to test the suitability of this material for mip timing below 100 ps [2] and for beam-diagnostics applications.

1. Time-Zero Detectors for Minimum Ionizing Particles

Highest quality diamond films have to be used. The so called 'detector grade' CVD diamond (DG) is produced from wafers of 'electronic grade' (EG) grown thicker than 1 mm and treated by polishing from the nucleation side to the required thickness, not thinner as 300 µm. It is characterized by a longer charge-carrier lifetime and homogeneity than 'as grown' (AG) material and a mean mip signal of about 10 000 e^-.
We have installed a characterisation station in order to measure the charge-collection distance d_{CD} [3] of the samples which is determined by the relations given in (1)

$$d_{CD} = (\mu \cdot \tau) \cdot E_D = \frac{Q_C}{Q_G} d_D \text{ where } Q_G^{mip} = \frac{36e^-}{\mu m} \cdot d_D \qquad (1)$$

with Q_C the collected resp. Q_G the particle generated charge in the detector, d_D the detector thickness, $(\mu \cdot \tau)$ the mobility-weighted carrier lifetime and E_D the electric field applied.
It is expected that DG material with a significantly larger $(\mu \cdot \tau)$ combines both, a higher Signal-to-Noise ratio (S/N) and a higher velocity of the charge carriers in the diamond bulk. The d_{CD} measurements are being performed using electrons from a collimated ^{90}Sr source (E_{max} = 2.4 MeV). Directly behind the diamond a plastic scintillator detector is placed in order to provide an independent trigger signal and the selection of the minimum-ionizing electrons from the high-energy tail of the β spectrum. A charge-sensitive (CS) amplifier and a main amplifier with a shaping time of 2 µs are used to amplify the diamond signals. Plot 1 in Fig. 1a) shows the full range of the d_{CD} measurement of a DG sample with a thickness of 500 µm. The hysteresis is a typical behaviour caused by polarisation and memory effects due to deep trap levels existing in CVD-diamond. Plots 2 and 3 show a limited range of data obtained from EG-AG samples of larger thickness produced in 1995. Assuming a linear increase of d_{CD} [3] the results of plot 2 and 3 are normalized to d_1. The enormous profit of collection distance (more than a factor of 2) is not only due to the post treatment but also due to a continuous improvement of the production process over the past years.

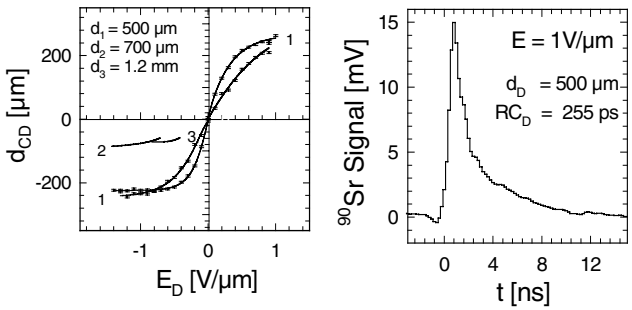


Fig. 1: a) Charge-collection distance of various diamond films measured with CS electronics as a function of the electric field. b) Average of 1000 single pulses from ^{90}Sr electrons amplified with broadband electronics (DG sample of Fig. 1a), plot 1).

The average signal of about 1000 ^{90}Sr electrons measured with a broadband amplifier and a Digital Sampling Oscilloscope (DSO) is plotted in Fig. 1b). The rise time of less than 600 ps is in the same range as measured with the thinnest EG-AG material [4] and thus suitable for fast timing. An intrinsic ToF resolution of σ_i=93 ps is measured using two DG CVD-diamond detectors of a thickness of 500 µm. However, due to the equivalent noise charge of 12000 e^- of the broadband amplifiers the coincidence efficiency was limited to a few percent. At low particle rates and using CS electronics a significantly higher efficiency of 80% is achieved. Hence, although new charge-sensitive fast amplifiers based on high electron-mobility transistors are currently in preparation, a further improvement of the diamond material is still desirable.

2. Beam-Loss Monitors

In order to control the beam transmission from the SIS to the experimental area two diamond detectors are placed after the septum magnet at both sides outside the beamline. For the first tests existing diamonds of EG-AG quality produced in 1995 of a thickness of 1.2 mm resp. 1 mm have been used. They will be replaced by two DG detectors with a thickness of 500 µm. To be noted is that at SIS energies the projectiles traversing the 2 mm thick stainless steel beam lines undergo fragmentation. Due to a position at an angle greater than 5 degrees to the beam direction the beam-loss particles to be measured are mainly protons of projectile velocity and a few pions, in other words all of them are mip's.
Slow- and fast extraction can be recorded. The aim is to develop a fast and easy-to-handle instrument for the operators in order to optimize the beam transmission by minimizing the rates on both diamonds. The detector signals are transmitted to the main control room (HKR) via glas-fiber transmission lines. Fig. 2 shows ^{238}U beam-loss spills of different intensity and pulse-duration time recorded with a DSO. Overlayed to the diamond signal is the corresponding beam-current transformer signal. The DSO is externally triggered by the spill-extraction trigger pulse delivered by the accelerator. It is already successfully tested that the diamond monitors have a higher

sensitivity for this application than all other beam diagnostics detectors. Even minimal changes of the beam focusing can be determined [5].

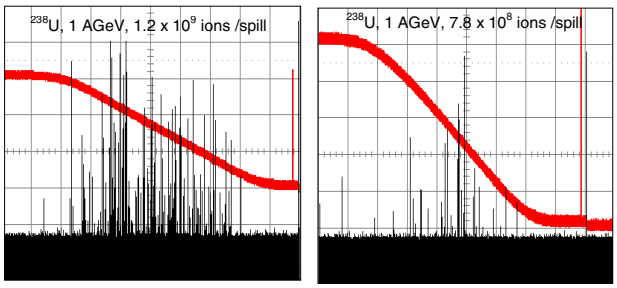


Fig. 2: Beam-loss spills from ^{238}U of 1 GeV/amu measured outside the beam lines (i.e. mainly proton and pion events) with a 1.2 mm thick EG-AG diamond detector. The corresponding beam current signal is overlayed and its slope is given by $t_{extraction}$. The time scales are set to 500 ms/div.

Interesting internal bunch-structure variations are obtained recording beam-loss signals of fast extracted ^{58}Ni spills bunched to 100 ns. Fig. 3 shows two of the most frequently measured patterns. Certainly, the measuring system

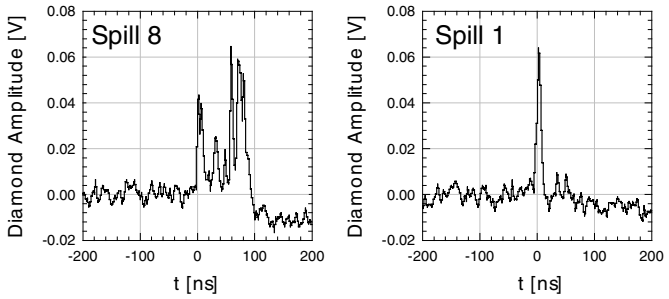


Fig. 3: Beam-Loss ^{58}Ni bunches (E/A = 300 MeV) measured with the same diamond detector and DSO as those of Figure 2.

is not able to identify single particles out of such bursts. Nevertheless, due to the good intrinsic time resolution of CVD-diamond detectors [4] high-frequency inter-bunch-structure studies become possible.

3. High-Intensity Bunch Monitors

Radiation hard and fast bunch monitors of good time- and position resolution are required for Heavy-Ion (HI) induced plasma physics experiments as well as for the future facilities for physics with radioactive beams and antiprotons at GSI and the high-luminosity colliders at DESY (TESLA) and CERN (LHC). Stimulated by a proposal for TESLA [6] we have started the development of diamond micro-strip bunch monitors able to measure the beam-intensity and the beam-profile burst by burst. This is a requirement which cannot be fulfilled by the well known wire scanners used at present.

We have tested the strength of CVD-diamond detectors to withstand beam conditions by which materials become disintegrated by the Coulomb forces working between the completely ionized atoms in the lattice. The interaction of such short ion bunches with matter is that way that thermal conductivity is strongly suppressed and becomes negligible at bunch times shorter than 50 ns. It was the hope that the strong diamond lattice, characterized by a high Debye Temperature of 2000 K (and corresponding Debye Frequency of $4x10^{13}$ Hz) would be able to cope with the shock-waves produced in the material under such irradiation conditions.

Thinnest EG-AG diamond material has to be used for this application. In September 2001, a first test with ^{18}O ions of 300 MeV/amu has been performed. An existing sample of a thickness of 168 µm was placed perpendicular to the beam axis in a vacuum chamber filled with Argon gas. The beam was bunched to bursts of 300 ns and the beam intensity has been tuned from 10^5 to 10^{10} ions/bunch corresponding to 1 GeV resp. 100 TeV energy deposit per bunch in the detector. The beam spot of 4 mm in diameter was optionally focused to a spot < 1 mm in diameter. In order to reduce thermal gradients in the interface diamond-metallisation, sandwitch dot-electrodes made of evaporated pure Aluminum (instead of Cr-Au or Ti-Cr-Au) were applied. One side was connected to ground, while the other side was directly connected to a fast DSO using AC coupling and 50 Ω input impedance.

The first milestones are achieved: neither a removal of the electrodes from the diamond surface occured nor any makro-

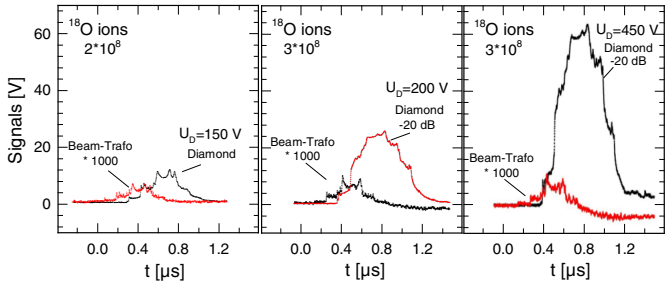


Fig. 4: ^{18}O bunches as seen from the diamond detector increasing the electric field and/or the beam intensity (higher signals, atten. by 20 dB in b) and c)) and from the beam-current transformer (lower signals, multiplied by 1000 in all plots).

scopic damage of the 'diamond target' was visible after the experiment. Moreover, up to $3x10^8$ ions/bunch both are found: the expected signal rise increasing the bias and a linear increase of the signal proportional to the beam intensity. Fig. 4 shows the very first test results. The electric field applied was E_D=0.9V/µm in (a), E_D=1.2 V/µm in (b) and E_D=2.7 V/µm in (c). Note that the diamond signals shown in (b) and (c) are attenuated by 20 dB, whereas the corresponding beam-current transformer pulses are multiplied by a factor of 1000 before being overlayed for comparison. In order to keep a significant drift field in the detector and to extend the linear dynamic range of the monitors a small variable load resistor parallel to the diamond and the 50 Ω impedance of the DSO is forseen. A first test of the new circuit performed recently at the TESLA testbeam facility was very satisfying.

References

[1] The RD42 Collaboration, "A CVD Diamond Telescope for Charged Particle Tracking", Proc. of the IEEE, San Diego, 2001
[2] M. Petrovici et al., IFIN-HH Scientific Report 1999, p60
[3] D. Meier, PhD Thesis, University of Heidelberg, 1999
[4] E. Berdermann et al., "The use of CVD Diamond for Heavy-Ion Detection", Diamond and Related Materials 10 (2001)1770-1777
[5] B. Franczak, private communication
[6] Wim de Boer, private communication

Development of Multistrip Glass Resistive-Plate Counters (GRPC)

M. Petrovici[1,2], N. Herrmann[3], K.D. Hildenbrand[2], G Augustinski[2], M. Ciobanu[1,2], I. Cruceru[1], M. Duma[1], O. Hartmann[2], Y. Kim[2], P. Koczon[2], T. Kress[2], M. Marquardt[2], D. Moisa[1], M. Petriş[1], C. Schroeder[2], A. Schüttauf[2], V. Simion[2], G. Stoicea[1], Z.Tyminski[2], J. Weinert[2]
[1]NIPNE-Bucharest, [2]GSI-Darmstadt, [3]Univ. of Heidelberg

Glass resistive-plate counters (GRPC) with multistrip anodes are possible candidates as ToF detectors for FOPI [1, 2]. Here we present further results obtained with protons of 1.5 GeV at the SIS. All counters have center anodes with strips read out at both ends and altogether six 1 mm thick plates and four gaps of 0.3 mm. Both outermost plates are connected to the HV; the inner electrodes are floating. Further details are given in Table 1. As electronics we used fast GSI amplifiers [3] and different types of discriminators. Fig. 1 shows various quantitites measured with prototype P I as function of the HV.

The position dependence along counter P II is shown in Fig. 2. Parts a) and b) show resolution and mean time at the measured 7 positions. The resolutions lie within 15 ps, however the mean value shows varations of about 100 ps with irregularities in certain regions. These are presumably due to nonuniform gaps (bent/deformed plates). This should be avoided by a better mechanical structure which we have used already in P III. In principle such dependences can be corrected: Part c gives the integrated time spectrum after linearizing the gross dependence with a resolution of 77 ps.

With an incident-particle angle of 55 °, a realistic value for a possible setting in FOPI, the resolution in P III improved to 65 ps (from 80 ps at normal incidence); the efficiency increased by 2%. All results presented so far were obtained with CES-510 discriminators. Double-Threshold Discriminators built at GSI [4] or a discriminator module developed by the HADES Collaboration [5] yielded about the same resolutions.

These results support our previous conclusion [2] that these multistrip GRPCs are a promising new development. Their multihit performance remains to be studied.

Proto-type	L [mm]	W [mm]	strip [mm]	gap [mm]	no. of strips
P I, P II	900	41	2.30	1.14	12
P III	200	189	2.0	1.0	60

Table 1: Active sizes of the GRPC prototypes and strip lay-out (width of the strips, gap in between and number of strips); P I and P II differ by their cathodes (bulk aluminum plate and copper plated glass, respectively).

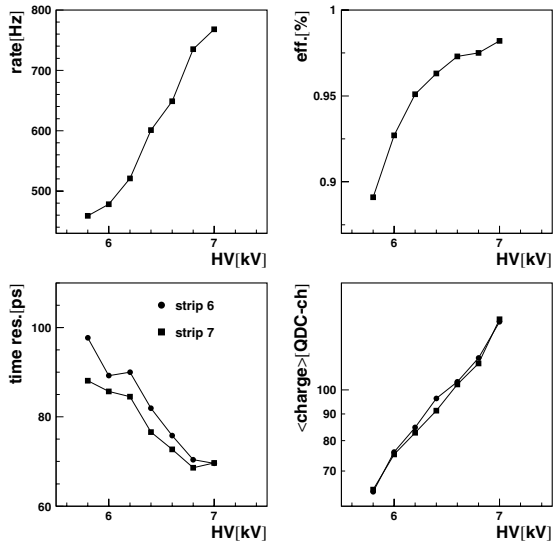


Figure 1: Dark rate (on an active area of 125 cm^2), efficiency, time resolution and average charge as a function of high voltage for prototype P I.

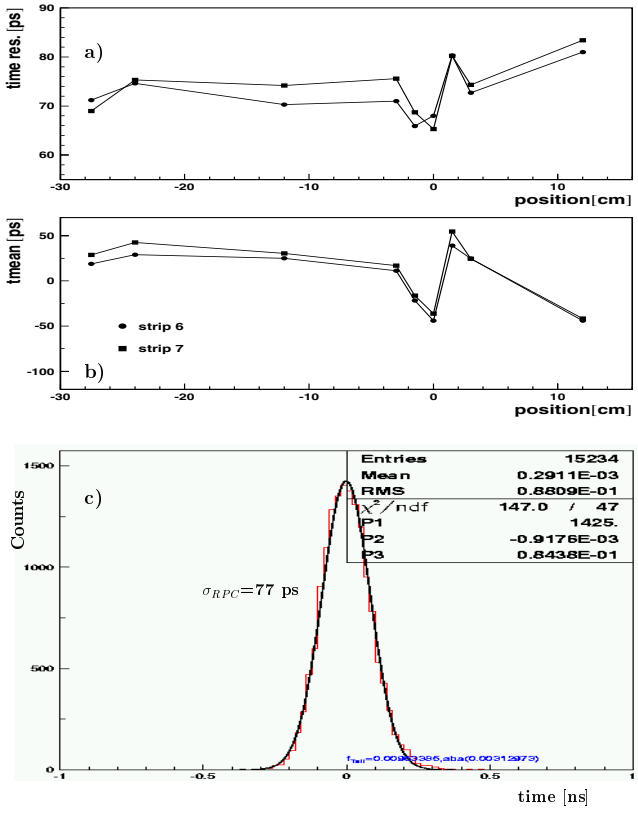


Figure 2: Timing performance as a function of position along the counter for prototype P II.

References

[1] M. Petrovici, et al., NIPNE Scient. Report 1999 p. 59
[2] M. Petrovici, et al., NIM A, in print
[3] E. Berdermann, P. Moritz et al., Nucl. Phys. B(Proc.Suppl.) 78 (1999) 533
[4] Ch. Neyer, Proc. Workshop on Electronics for LHC Experiments, Lisbon (1995) 383
[5] C. Lichtblau, Diplomarbeit, Univ. Giessen, 1999

The New Readout Electronics for TAPS*

P.Drexler[2], U.Thöring[2], W.Bonn[2], H.A.P.van der Duin[3], R.Holzmann[1], G.van der Kruk[3], B.Krusche[4], H.Löhner[3], V.Metag[2], T.W.Nijboer[3], J.G.Messchendorp[2], R.Novotny[2], C.Salz[2], S.Schadmand[2], M.Steinacher[4], M.Thiel[2], H.Vorenholt[3] *for the TAPS collaboration*

[1] GSI, Darmstadt

[2] II. Physikalisches Institut, Universität Gießen

[3] KVI, Groningen, The Netherlands

[4] Department of Physics and Astronomy, University of Basel, Switzerland

The new readout electronics for the electromagnetic calorimeter TAPS [1] was developed by members of the TAPS collaboration at Gießen, KVI and Basel.

The concept of the 4 channel readout module is a 4-fold integration of the BaF_2 signal to provide the separate information of the long and short scintillation components in two different dynamic ranges. A CFD optimizes the timing information obtained by the TAC and guarantees accurate integration gates necessary for pulseshape analysis. 2 LEDs allow more sophisticated trigger conditions. A PLD provides the slow control. These combined analog and digital functions are implemented on a piggyback residing on a commercial VME motherboard, developed by the HADES collaboration (CAEN V874).

A prototype version (4 boards comprising only 2 channels each on two-layer boards assembled with several plugins) was tested in a parasitic experiment at the MAMI tagged photon facility at Mainz to study the achievable energy and time resolutions [2].

The test has shown the functionality of the new electronics, but the detailed analysis of the response of the individual modules has revealed a non-linearity of the measured energy towards higher energies. Laboratory tests with test pulses, simulating the shape of BaF_2 signals, have been performed. Covering a maximum attenuation factor of

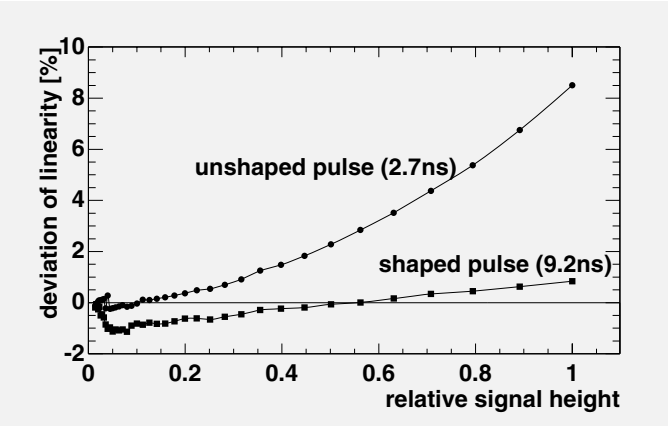


Figure 1: *The measured deviation from linearity shown for an unmodified and a shaped BaF_2 signal, respectively, as a function of relative signal amplitude.*

52dB (0.25% of the signal height), a non-linearity in case of the long integration component of approx. 8% over the full range has been determined with the piggyback used in the MAMI experiment (figure 1).

After a series of detailed investigations the strong nonlinearity could be traced to the fast rise time of the BaF_2-signal, which can not be handled by the used QAC chip. When applying a signal shaping circuit increasing the rise time to 9.2ns, in contrast to the original value of 2.7ns - measured at the input stage of the QAC - the maximum nonlinearity is limited to a value as low as 1.1% over the full range.

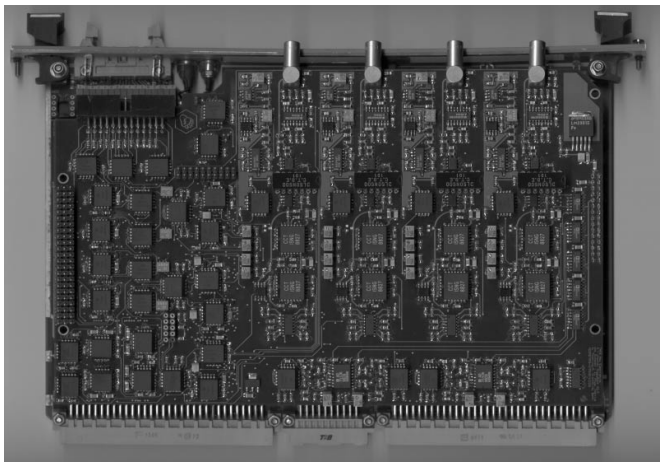


Figure 2: *The new 4 channel piggyback mounted on a HADES motherboard. Each channel consists of a CFD, 2 LEDs, 4 QACs and a TAC.*

Based on that experience, a true 4 channel multilayer piggyback prototype was designed and manufactured as shown in fig. 2. First tests regarding slow control (adjustments of pedestrals and thresholds) and logic settings (CFDs controlling gates and first level trigger decisions) have been completed successfully. Further measurements with a 19 crystal array regarding the linearity and the resolution of the energy integration and the time readout are in progress.

The mass production of the TAPS piggybacks, comprising 144 VME modules, should be started soon.

⋆ supported by BMBF, GSI, SNF, and FOM

References

[1] GSI Scientific Report (1999)
[2] GSI Scientific Report (2000) 209

Test of the new preamplifier for the ALICE TRD

I. Rusanov, J. Stachel, V. Catanescu, M. Ciobanu
University of Heidelberg

One of the major components of the ALICE TRD front-end electronics is a charge sensitive preamplifier/shaper with differential outputs. A general description of this circuit can be found in [1]. In this report we briefly review results from the test of the new prototype chip and the method for measuring the input-output characteristics of this type of amplifiers. The outputs of the preamplifier are designed for high impedance load (R=170 kΩ and C=7 pF). Therefore we have used a test circuit, shown in Fig. 1. With this setup it is possible to measure directly output signals. Another advantage is that on the output of the buffer we measure only the differential noise of the preamplifier.

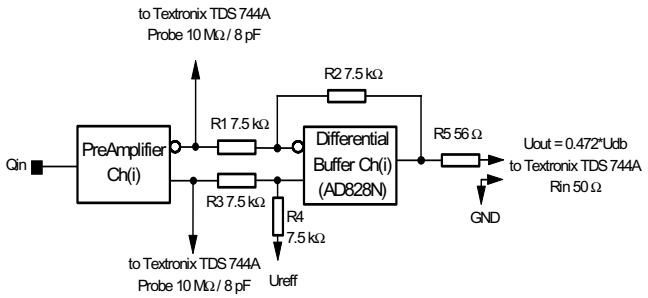


Figure 1: Test circuit

The layout requirement. The first requirement is a good solid ground plane. The length of the wire between GND-pin and ground plane should be kept as short as possible. This will minimize crosstalk and noise. The power supply pins should be bypassed close to the device to the nearby ground plane, therefore ground plane should cover as much of the board area around the preamplifier as possible. On the test-board the bypassing is done with a capacitance value of 1 μF and 0.1 μF. Another requirement concerns to the routing of the input signals. The wires should be short with a minimum spacing between them of about 200 μm because each 1 pF parasitic capacitance between input wires gives 20-30 mV in amplitude of crosstalk signal.

For the test of the TRD preamplifier we use a PCB layout with two layers. The board includes 16-differential buffers (one per channel) and power supply sources with the possibility to change values. The operating voltage range is from 3.0 to 3.6 V.The *charges-generating circuit* is outside of the test board. The reason to use separate *charges-generating circuit* is to remove back-current of the pulse generator. The rise time of input pulses is 12 ns and the amplitude ranges 35 mV to 160 mV.

Measured characteristics. Fig. 2 shows the typical input-output characteristic of the preamplifier. The typical conversion gain is 11.5 mV/fC with integral non-linearity of 1.39%. Dispersion of the gain between channels is about 5 %, which depends on the type of common-bias circuit. Therefore in a new version of the preamplifier we will use a separate-bias network for each channel. Another advantage of changing the bias circuit is a decrease in the feedthrough between channels.

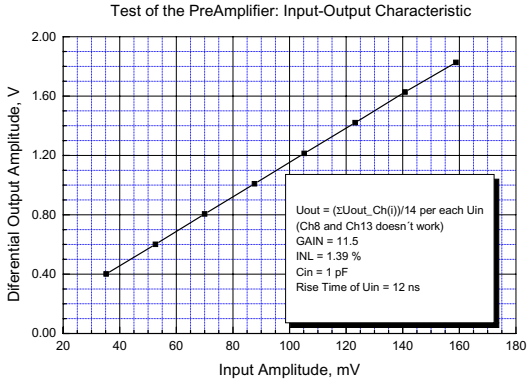


Figure 2: Input-Output Characteristic

One of the main characteristics of the preamplifier is noise. For its measurement we used a digital scope Tektronix TDS 744A. The noise is 1100e for 25 pF capacitance to GND (Fig. 3). The shaping time is 95 ns, the total power consumption is 10 mW per channel.

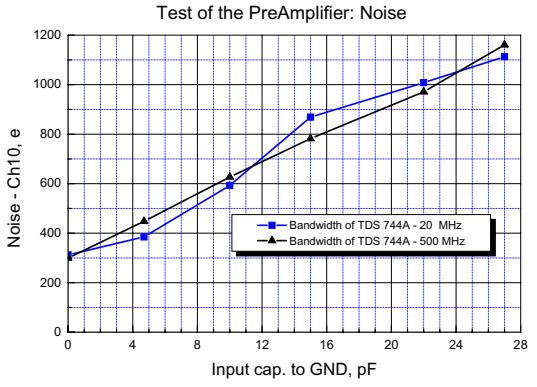


Figure 3: Noise

References

[1] ALICE TRD Technical Design Report, CERN/LHCC, October 2001.

New Front-end Electronics for the ALICE TPC-Detector

H. K. Soltveit, J. Stachel, P. Glässel and I. Rusanov
University of Heidelberg

The first prototype preamplifier-shaper for the ALICE-TPC Front-end Electronic has been evaluated at CERN. In this report we briefly review the results of the performance of the first prototype chip and we describe the new circuit. A general description of the first prototype circuit can be found in [1,2]. A summary of the main parameters can be found in Tab.1. All the values obtained in tests are well within the specifications that are found in [3] except for a lower shaping time (now understood) that converted into higher noise.

Parameter	specific.	Simulated	Tested
Noise	$<$ 1000e	$\approx$ 500e	666-699e
Shaping time [ns]	200	180	$\approx$ 135
Non-linearity	$<$ 1%	0.25%	0.46%
Baseline variation	-	-	2mV
Conv. gain [mV/fC]	12	7.8	$\approx$ 8.3
Powercon.[mW/ch]	$<$ 20	8	7.25

Table 1: Main specifications of the preamplifier - shaper. The simulated and tested values are also given.

Due to changes in the ADC requirements, namely going from a single-ended to a differential input signal, a new version of the preamplifier/shaper circuit has been developed [Figure. 1].
The main part consist of a preamplifier, Pole-Zero network, one single-ended second-order T-bridge filter, one fully-differential second order T-bridge filter, a Common-mode feedback network, and two parallel connected non-inverting stages.
The main modifications concern:

- Migration from a N-channel input stage to a P-channel input stage.
- Replacement of the last buffer-stage in the preamplifier with a voltage divider to increase the output swing.
- Optimization of the design to fulfil the new ADC requirements.
- Addition of a second order filter and its common-mode feedback network to generate a differential output swing.
- Migration from common bias-network to separate the bias-network.
- Addition of two non-inverting amplifiers to split the output signal VREFN and VREFP from the differential amplifier (1V) to 0.5V and 1.5V respectively.

The second second-order shaper is built around a fully-differential folded cascode circuit. A common-mode compensation is necessary to assure common-mode stability. This is done with a CMFB (Common-Mode FeedBack)-network. The common-mode amplifier related to the output of the non-inverting stages and the fully-differential amplifier are used to compensate for offset.

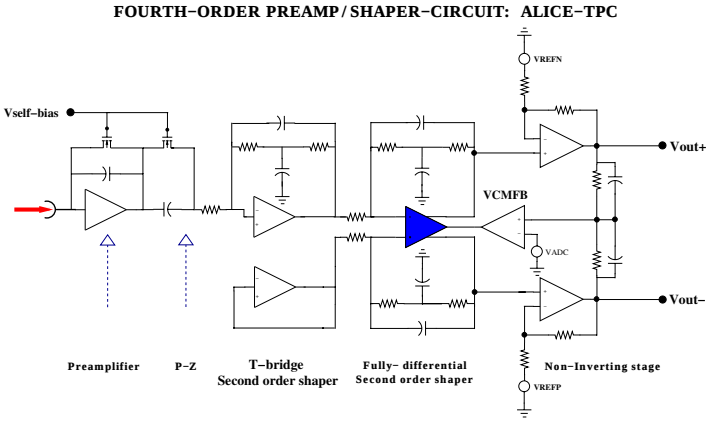


Figure 1: Schematic of the preamplifier chain with shapers, common-mode feedback and the two non-inverting stages

The common-mode voltage (1V) is the same for the fully-differential amplifier, the non-inverting stages and the ADC. The two DC-level splitters are built around a Miller-OTA. The circuit require three different reference voltages VCM (Common-Mode voltage, 1V), VREFN (0.5V) and VREFP (1.5V). These are the same voltages that are used to generate the common-mode voltages and dynamic range for the ADC. With this arrangement it is possible to track the process variations (amplitude/baseline) generated in the preamplifier/shaper circuit and also in the ADC. This solution will also increase the yield.
The reason to change from common-bias to separate-bias is to decrease the feedthrough between channels. This could be in the area of tenths of mV, but within the μV area with separate bias-network.
The new prototype has just been recieved and the first tests looks very promising.
The simulated results of this prototype are as follows:
In terms of noise requirements, the new ALICE preamplifier/shaper fulfills the requirement with an ENC of less than 400 electrons for input capacitances between 3 pF and 14 pF. The response is linear ($<$ 0.25%) up to an dynamic range of 2 V with a peaking time around 120 ns. The gain of the preamplifier/shaper is about 12mV/fC with a total power consumption of 11 mW/channel.
The analog front-end electronics for the read-out for the TPC has been designed and fabricated with the AMS 0.35 μm CMOS process. The area of the chip including scribeline is 16.7mm^2.

References

[1] H.K.Soltveit, J.Stachel GSI Annual Report 2000
[2] G.Gramegna, P. O'Connor, P. Rehak, S.Hart, Nucl. Instr. and Meth., **A390 (1997), 241-250.**
[3] ALICE Technical Design Report, Cern/LHCC, January 2000

Position resolution with prototypes for the ALICE TRD

A. Andronic[1], H. Appelshäuser[2], C. Blume[1], P. Braun-Munzinger[1], D. Bucher[3], O. Busch[1], A. Castillo Ramirez[1], G. Cătănescu[4], M. Ciobanu[4], H. Daues[1], A. Devismes[1], C. Garabatos[1], N. Herrmann[2], M. Ivanov[1], T. Lister[3], T. Mahmoud[2], T. Peitzmann[3], M. Petrovici[4], K. Reygers[3], R. Santo[3], R. Schicker[2], S. Sedykh[1], R.S. Simon[1], J. Stachel[2], H. Stelzer[1], G. Tsiledakis[1], B. Vulpescu[2], J. Wessels[2], O. Winkelmann[3], B. Windelband[2], C. Xu[2]
[1]GSI Darmstadt, [2]Universität Heidelberg, [3]Universität Münster, [4]NIPNE Bucharest (for the ALICE Collaboration)

In addition to electron identification [1], an important aspect of the performance of the ALICE Transition Radiation Detector (TRD) is its capability to provide a trigger for high momentum electrons [2]. A good position resolution of the drift chamber (DC) of about 400 μm is necessary in oder to achieve the challenging tasks of the TRD trigger [2].

We present results on the position reconstruction performance using a single drift chamber with chevron pad readout, tested using pion and electron beams of 1 GeV/c at GSI. The drift region of 3 cm is sampled in 14 time bins of 100 ns each. The displacement along the anode wire direction is calculated for each time bin using a center of gravity method. The angle of incidence with respect to the drift field, α, is extracted from a straight line fit of the displacements as a function of drift time. This reconstructed angle is biased by the Landau fluctuations of the energy deposit along the track. We use two methods to correct the data: i) the correlation of the reconstructed angle with the drift time position of the average signal, $t_{\langle Q \rangle}$; ii) a tail cancellation (TC) algorithm.

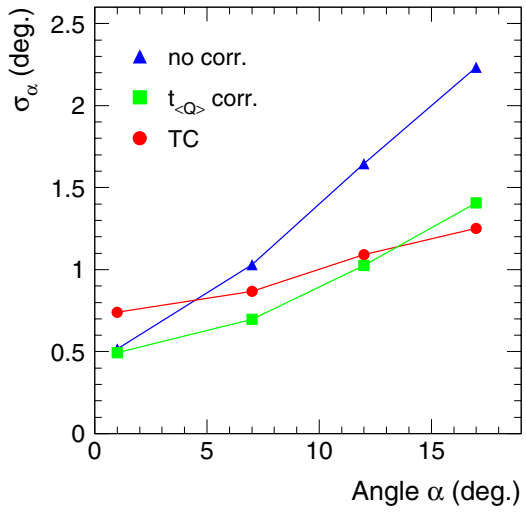


Figure 1: Angular resolution as a function of the incident angle.

In Fig. 1 we present the angular resolution, σ_α, as a function of the incident angle. The uncorrected data (triangles) are compared to the values with the $t_{\langle Q \rangle}$ correction (squares) and with the tail cancellation (dots). Both methods improve the angular resolution drastically and in addition remove the strong dependence of the angular resolution on the incident angle exhibited by the uncorrected values.

In Fig. 2 we show the point resolution, σ_R (variance of the residuals of the fit) and the angular resolution, σ_α, as a function of signal-to-noise ratio, S/N, at the incident angle of 17°. The different methods discussed above are compared. The dashed line in the upper panel is a $1/\sqrt{S/N}$ function, arbitrarily normalized. In the lower panel, the dashed and the dotted curves are the expected angular resolutions derived from the point resolutions under the assumption of 14 and 8 independent fit points, respectively.

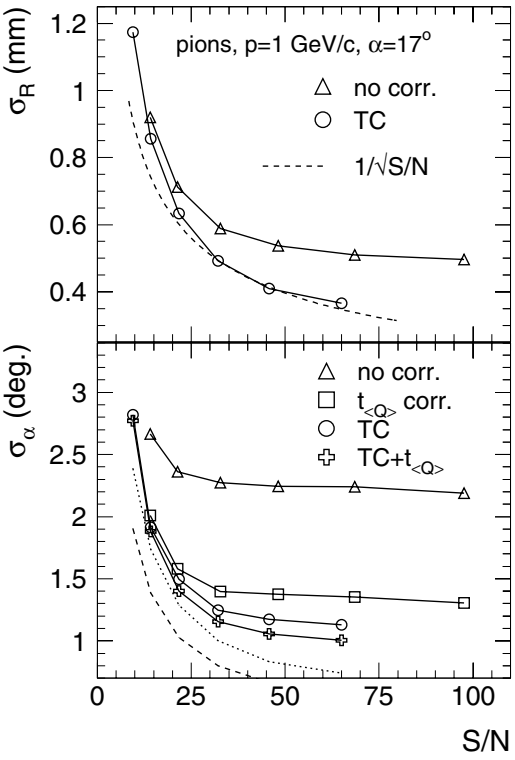


Figure 2: Position resolution as a function of signal-to-noise ratio, S/N. Upper panel: point resolutions, lower panel: angular resolution. The different methods are discussed in the text.

Obviously, the $t_{\langle Q \rangle}$ correction cannot improve the point resolution, but improves only the angular resolution. The crosses in the lower panel indicate the case of tail cancellation to which an additional $t_{\langle Q \rangle}$ correction is applied. One can notice that the saturation towards large values of S/N is different for the various cases presented. The corrected values have a more pronounced dependence of S/N, as expected after removing the systematic contributions.

References

[1] A. Andronic et al., IEEE Trans. Nucl. Sc., vol. 48, 1259 (2001) [nucl-ex/0102017]

[2] ALICE TRD Technical Design Report, CERN/LHCC 2001-021 (2001), *http://www.gsi.de/∼alice/trdtdr*

Lorentz angle measurements with ALICE TRD prototypes

O. Busch[1], A. Andronic[1], H. Appelshäuser[2], C. Blume[1], P. Braun-Munzinger[1], D. Bucher[3], A. Castillo Ramirez[1], G. Cătănescu[4], M. Ciobanu[4], H. Daues[1], A. Devismes[1], C. Garabatos[1], N. Herrmann[2], M. Ivanov[1], T. Lister[3], T. Mahmoud[2], T. Peitzmann[3], M. Petrovici[4], K. Reygers[3], R. Santo[3], R. Schicker[2], S. Sedykh[1], R.S. Simon[1], J. Stachel[2], H. Stelzer[1], G. Tsiledakis[1], B. Vulpescu[2], J. Wessels[2], O. Winkelmann[3], B. Windelband[2], C. Xu[2]
[1]GSI Darmstadt, [2]Universität Heidelberg, [3]Universität Münster, [4]NIPNE Bucharest (for the ALICE Collaboration)

The study of rare probes via their (semi-)leptonic decays in the ALICE experiment requires dedicated triggers. The TRD provides the necessary capabilities to trigger on high p_t (>3 GeV) electrons by means of track reconstruction in a magnetic field and TR signature.

TRD prototype tests were carried out in August 2001 at the GSI secondary pion beam with a momentum of 1 GeV/c. A drift chamber (DC), operated with Xe,CO_2(15%) mixture was placed in magnetic fields of up to 0.3 T, produced by two coils in a Helmholtz configuration. We used a prototype equipped with chevron pad plane with FADC readout. The detector provides information on the position of ionization electrons in the gas volume, which can be used to reconstruct the trajectory of an incident particle. Exploiting this feature, we performed a first direct measurement of the Lorentz angle (the angle of drifting electrons with respect to the electric field lines) for a Xe,CO_2 mixture (see [1] for other mixtures). This quantity is very important for the final detector, as it has implications on track reconstruction at the trigger level.

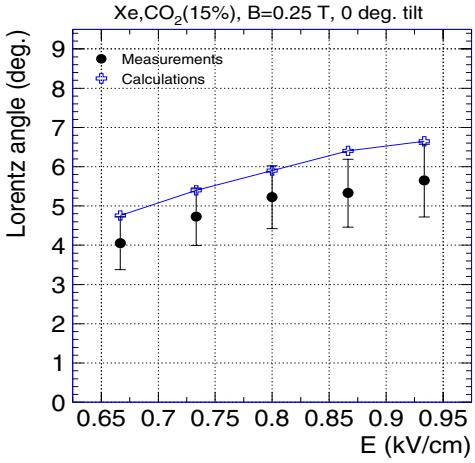


Figure 1: Lorentz angle in Xe,CO_2(15%) mixture as a function of the applied drift field for B=0.25 T.

Fig. 1 shows the measured Lorentz angle as a function of the drift field for B=0.25 T. Two correction were taken into account: i) the chamber tilt (due to positioning imprecision), which is determined in B=0 runs; ii) the deflection of the beam in the magnetic field, which is measured by two silicon sicrostrip detectors, placed before and after the DC. The errors on our results have two sources: i) the inaccuracy to distinguish between the drift region and the amplification region of the detector; ii) the angular spread of the beam. We compare our results to GARFIELD/MAGBOLTZ [2, 3] calculations. We find overall agreement with the calculations, but the measured Lorentz angles are systematically lower than the calculated ones. In Fig. 2 we present the Lorentz angle as function of the magnetic field for a drift field of 0.66 kV/cm. In this case too, there is a similar agreement with the calculations.

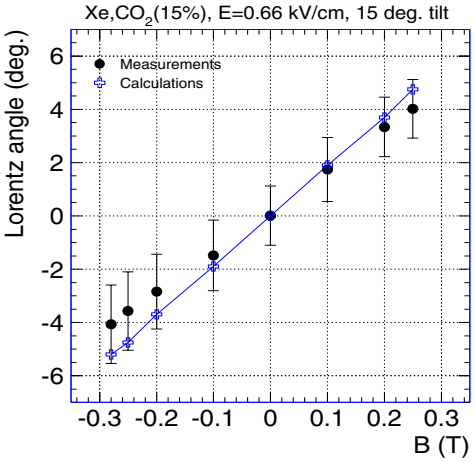


Figure 2: Lorentz angle in Xe,CO_2(15%) mixture as a function of the external magnetic field B.

In November 2001 we performed similar measurements using a 4 GeV/c pion beam at the CERN PS. This time we operated two chambers with rectangular pads in a dipole magnet. As drift gas we used a neon-based mixture, Ne,CO_2(13%). The results are presented in Fig. 3 in comparison to GARFIELD calculations. Taking into account the errors of the method, our results are in a similar agreement with the calculations for the Ne,CO_2 mixture as in the case of Xe,CO_2 mixture.

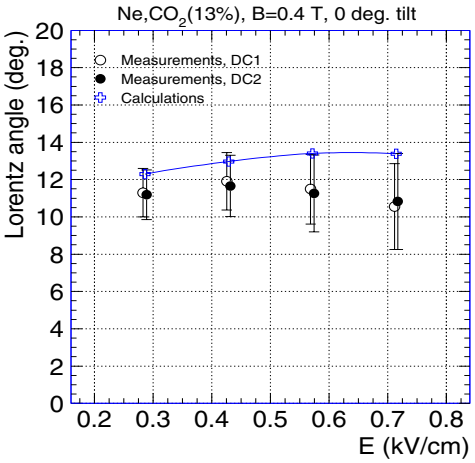


Figure 3: Lorentz angle in Ne,CO_2(13%) mixture as a function of the drift field for B=0.4 T.

References

[1] U. Becker et al., Nucl. Instr. Meth. A421 (1999) 54.
[2] R. Veenhof, Nucl. Instr. Meth. A419 (1998) 726.
[3] S. Biaggi, Nucl. Instr. Meth. A421 (1999) 234.

Development of the Radiator for the TRD of the ALICE Experiment*

A. Andronic[1], V. Angelov[2], H. Appelshäuser[3], C. Blume[1], P. Braun-Munzinger[1], D. Bucher[4], O. Busch[1], A. Castillo-Ramirez[1], V. Catanescu[5], M. Ciobanu[5], S. Chernenko[6], V. Chepurnov[6], H. Daues[1], A. Devismes[1], O. Fateev[6], C. Finck[1], P. Foka[1], C. Garabatos[1], R. Glasow[4], M. Gutfleisch[2], N. Herrmann[3], M. Ivanov[1], F. Lesser[2], V. Lindenstruth[2], T. Lister[4], T. Mahmoud[3], A. Marin[1], D. Miskowiec[1], Yu. Panebratsev[6], T. Peitzmann[4], V. Petracek[3], M. Petrovici[5], C. Reichling[2], K. Reygers[4], A. Sandoval[1], R. Santo[4], R. Schicker[3], R. Schneider[2], S. Sedykh[1], S. Shimanski[6], R.S. Simon[1], L. Smykov[6], J. Stachel[3], H. Stelzer[1], H. Tilsner[3], G. Tsiledakis[1], I. Rusanov[3], B. Vulpescu[3], J. Wessels[3], B. Windelband[3], O. Winkelmann[4], C. Xu[3], V. Yurevich[6], Yu. Zanevsky[6] and O. Zaudtke[4]

[1] Gesellschaft für Schwerionenforschung, Darmstadt, Germany
[2] Kirchhoff Institut für Physik, Heidelberg, Germany
[3] Physikalisches Institut der Universität Heidelberg, Germany
[4] Institut für Kernphysik, Universität Münster, Germany
[5] NIPNE Bucharest, Romania
[6] JINR Dubna, Russia

The Transition Radiation Detector (TRD) of the ALICE experiment has the purpose to extend the capabilities to measure electrons of high transverse momenta[1]. By this the sensitivity to measure hard processes, in particular charm and beauty production is increased. In addition, the TRD will be used as a trigger detector on high p_T-electrons. With this the measurement of jets with high transverse momenta will be possible.
Transition radiation is produced, if a highly relativistic particle traverses the boundary between two media of different dielectric constants[2]. As the average energy of the emitted photon is related to the γ of the particle, this provides a means to discriminate electrons and pions. However, since the emission probability is small, a large number of boundaries have to be combined to obtain a reasonable efficiency. Commonly used are foil stacks of a few hundred polypropylene foils. However the layout and the mechanical constraints of the ALICE TRD excludes the usage of foils so that other materials have to be used. For this purpose extensive studies of different materials (foils, foams, fibre mats) were carried out. During several tests with electron/pion beams at the GSI various radiator candidates have been investigated and their TR production was studied. Based on this knowledge a fibre mat radiator was chosen to be the best candidate for the ALICE TRD radiator. It can be regarded as an approximation to foil stacks, but compared to foils they have an irregular structure.

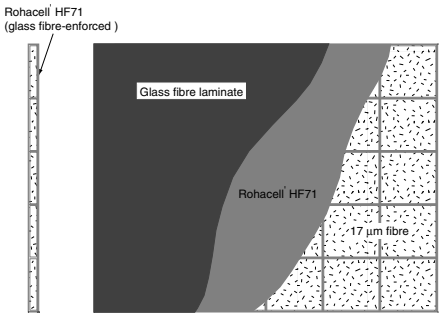


Figure 1.: Principal design of the ALICE TRD sandwich radiator.

Besides the TR production the radiator is intended to mechanically support the front window of the chambers, which also serves as the cathode for the drift field of the readout drift chamber. The radiator has to keep the window below the maximum tolerated deflection of 1mm to avoid large distortions of the drift field. To achieve this a combination of the already mentioned fibre mats with a carbon fibre reinforced foam (ROHACELL) was developed. Using a sandwich like structure we achieve under the given load a deflection of below 0.8mm for the largest planned radiator, which is about 1.6*1.2m^2. A sketch of the radiator design is shown in figure 1.

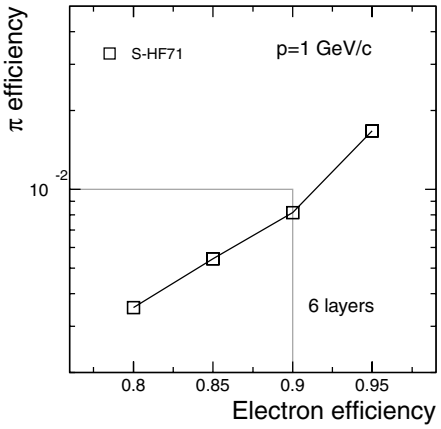


Figure 2.: Pion efficiency as a function of the electron efficiency of the sandwich radiator *S-HF71* extrapolated to 6 detector layers for a particle momentum of 1 GeV/c.

The TR production was measured for the sandwich radiator in comparison to the pure materials (fibres and foams). The results were extrapolated to a stack of 6 TRD chambers as foreseen in the experiment. The extracted pion efficiency is plotted vs. the electron identification efficiency in figure 2. The dotted line marks the requested performance of the detector (a factor of 100 pion rejection at 90% electron efficiency), which is met with the current radiator design.
For a more comprehensive discussion and the detailed results see ref. [1].

References

[1] ALICE TRD Technical Design Report, CERN/LHCC 2001-021

[2] V.L. Ginzburg and I.M. Frank, Zh.Esko.Teor.Fiz. 16 (1946) 15

* Supported by BMBF and GSI

ALICE TPC Readout Chambers

P. Braun-Munzinger[1], C. Garabatos[1], J. Fiess[2], U. Frankenfeld[1], P. Glässel[3], M. Ivanov[1], R. Renfordt[2], H. Sann[1], H.R. Schmidt[1], H. Stelzer[1], D. Vranic[1], B. Windelband[3]

[1]GSI Darmstadt, [2]University of Frankfurt, [3]University of Heidelberg

A major component of the CERN-LHC ALICE detector is the central barrel, contained in the large L3 magnet and composed of detectors devoted mainly to the study of hadronic signals [1] and dielectrons [2]. The main tracking devices are the silicon based Inner Tracking System (ITS) and the Time Projection Chamber (TPC). Within their acceptance ($-0.9 \leq \eta \leq 0.9$) about 12000 tracks will be recorded, yielding information about particle type and momentum.

The readout planes at the two sides of the TPC field cage are subdivided into 18 segments each. The segments are split into an inner and an outer readout chamber (ROC). The ROCs are conventional multiwire proportional chambers with cathode pad readout as used in many TPCs before.

After successful testing of prototypes [3], the series production has started in August 2001. A detailed production plan has been set up, in which the complete production of a chamber has been split into 32 steps, ranging from checking the mechanical accuracy of the parts delivered by the workshops up to the testing of the finished chamber. The goal of the planning to produce one chamber within five working days has been reached after a short startup phase.

All the pad planes with their 5504 pads have been checked with a semi-automatic device for a good contact to one and only one connector on the backside of the plane. About 10 % of the pad planes had to be rejected. The gluing of the pad plane onto the aluminium body and some machining has been done at the Physikalische Institute in Heidelberg. During production, several quality controls were applied to ensure the same performance for all the chambers. The planarity of the pad plane and its distance to the reference points on the backside was measured with a high-precision X-Y-Z measuring table. On each wire plane, the mechanical tension of each wire was measured and documented. The resistance of all the wire planes to each other and to ground was measured. The acceptance tests consisted of the check of the gas tightness (typically 10-5 mbar·l/s) (Fig. 1), the determination of the gas gain by counting the pulses of a ^{55}Fe source and measuring the anode current (Fig. 2), a check of the homogeneity across the active area and, finally, a long term test, where the chamber was operated with a strong ^{55}Fe source at a gain of about 20000 for 50 hours minimum.

All the 18 chambers built up to now have passed these tests. Two more will be completed by the end of February 2002. The other 20 chambers are being built in Bratislava.

A total of 512 out of the 5504 pads in one ROC have been equipped with CERES preamplifier-shapers. This chip, used in the CERES TPC, is the basis of the ALICE PASA chip and thus comparable in its properties. In order to answer the question whether the ALICE readout chambers operate stably both at high gain and high particle load, i.e., the LHC conditions, the chamber has

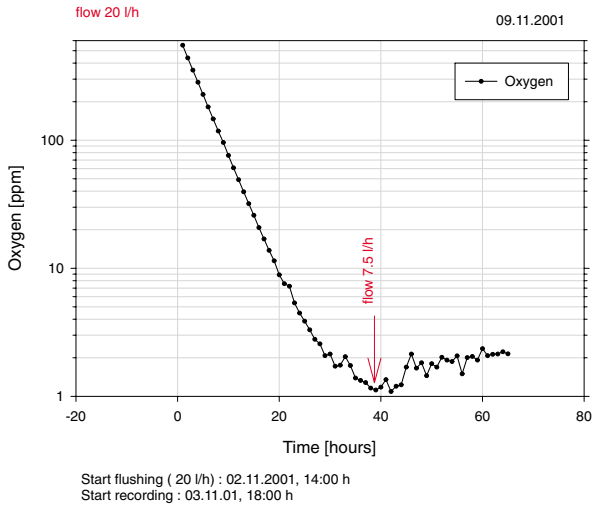


Figure 1: Dependence of the oxygen content at the chamber exhaust as funtion of time as indicator of the leak rate.

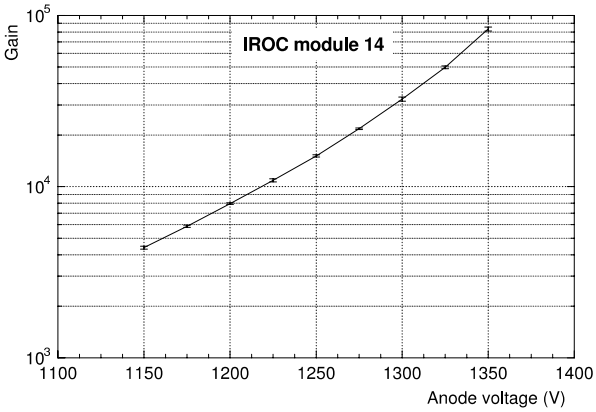


Figure 2: Gas gain of one of the Inner ROCs as a function of the applied high voltage in a Ne-CO_2 [90-10] gas mixture.

been exposed to secondary particles from a GSI heavy-ion beam (^{12}C, 800 AMeV). The particle rate – controlled by varying the target thickness and/or the beam intensity – was adjusted to recreate typical ALICE conditions, i.e, an occupancy in pad-time up to 50% and an average anode currrent $\geq 10\,\mu$A. The chamber under test demostrated a very stable operation at the nominal gas amplification of $2{\cdot}10^4$ and up to the maximum average current investigated of $80\,\mu$A.

References

[1] ALICE Collaboration, Technical Proposal, CERN/LHCC/95-71

[2] ALICE Collaboration, Technical Proposal, Addendum 2, CERN/LHCC/99-13

[3] GSI Scientific Report 2000, GSI 2001-1

ANNEX

Publications	225
GSI-Reports and Preprints	248
Invited Talks at Conferences, Sympos., Workshops	251
Invited Talks at other Institutes	257
Lectures and Courses	261
Seminars, Workshops at GSI	263
Theses, Diploma	270
Beamtime at GSI	271
Collaborations	274

Author Index

Internal Organisation

Availability of GSI-Publications

GSI Reports and Preprints

GSI reports and preprints are distributed, on exchange, to other libraries and institutions working in the field of heavy ion physics. Individual copies are made available free of charge, as long as stock lasts.

Written requests should be made to: GSI-Bibliothek, Planckstr. 1, D-64291 Darmstadt, Germany or e-mail can be send to U.Grundinger@gsi.de

Other Papers

For copies of papers published in periodicals, books or conference proceedings, please contact your local Library or one of the authors. **GSI provides no centralized distribution of reprints.**

Publications

Adam, W.; E. Berdermann, P. Bergonzo, G. Bertuccio, F. Bogani, E. Borchi, A. Brambilla, M. Bruzzi, C. Colledani, J. Conway, P. D'Angelo, W. Dabrowski, P. Delpierre, A. Deneuville, J. Doroshenko, W. Dulinski, B. van Eijk, A. Fallou, F. Fizzotti, J. Foster, F. Foulon, M. Friedl, K.K. Gan, E. Gheeraert, B. Gobbi, G.P. Grim, G. Hallewell, S. Han, F. Hartjes, J. Hrubec, D. Husson, H. Kagan, D. Kania, J. Kaplon, R. Kass, T. Koeth, M. Krammer, R. Lander, A. Logiudice, R. Lu, L. mac Lynne, C. Manfredotti, D. Meier, M. Mishina, L. Moroni, A. Oh, L.S. Pan, M. Pernicka, L. Perera, S. Pirollo, R. Plano, M. Procario, J.L. Riester, S. Roe, C. Rott, L. Rousseau, A. Rudge, J. Russ, S. Sala, M. Sampietro, S. Schnetzer, S. Sciortino, H. Stelzer, R. Stone, B. Suter, R.J. Tapper, R. Tesarek, W. Trischuk, D. Tromson, E. Vittone, R. Wedenig, P. Weilhammer, C. White, W. Zeuner, M. Zoeller:
Diamond Pixel Detectors
Nucl. Instr. and Meth. in Phys Res.A465,88(2001)

Adla, A.; Buschmann, V.; H. Fuess, C. Trautmann:
Investigation of Heavy Ion Tracks in Polymers by Transmission Electron Microscopy
Nucl. Instr. and Meth. in Phys. Res.B185,210(2001)

Andreyev, A.N.; M. Huyse, P. van Duppen, L. Weissman, D. Ackermann, J. Gerl, F.P.Heßberger, S. Hofmann, A. Kleinböhl, G. Münzenberg, C. Schlegel, H. Schaffner, P. Cagarda, M. Matos, S. Saro, A. Keenan, C.J. Moore, C.D. O'Leary, R.D. Page, M.J. Taylor, H. Kettunen, M. Leino, A. Lavrentiev, R. Wyss, K. Heyde:
The Discovery of a Prolate-Oblate-Spherical Shape Triple of Spin 0^+ States in the Atomic Nucleus ^{186}Pb
Nucl. Phys. A682, 482c (2001)
(Proc. of the Conf. on Nuclear Structure 2000, East Lansing, USA, Aug. 15-19, 2000)

Andreyev, A.N., D. Ackermann, P. Cagarda, J. Gerl, F.P. Heßberger, S. Hofmann, M. Huyse, A. Keenan, H. Kettunen, A. Kleinböhl, A. Lavrentiev, M. Leino, B. Lommel, M. Matos, G. Münzenberg, C.J. Moore, C.D. O'Leary, R.D. Page, S. Reshitko, S. Saro, C. Schlegel, H. Schaffner, M.J. Taylor, P. Van Duppen, L. Weissman, R. Wyss:
New Microsecond Isomers in ^{189,190}Bi
E. J. of Phys. A 10, 129 (2001)

A. Andronic, G. Stoicea, M. Petrovici, V. Simion, P. Crochet, J.P. Alard, R. Averbeck, V. Barret, Z. Basrak, N. Bastid, A. Bendarag, G. Berek, R. Caplar, A. Devismes, P. Dupieux, M. Dzelalija, M. Eskef, Ch. Finck, Z. Fodor, A. Gobbi, Y. Grishkin, O.N. Hartmann, N. Herrmann, K.D. Hildenbrand, B. Hong, J. Kecskemeti, Y.J. Kim, M. Kirejczyk, M. Korolija, R. Kotte, T. Kress, R. Kutsche, A. Lebedev, K.S. Lee, Y. Leifels, V. Manko, H. Merlitz, W. Neubert, D. Pelte, C. Plettner, F. Rami, W. Reisdorf, B. de Schauenburg, D. Schüll, Z. Seres, B. Sikora, K.S. Sim, K. Siwek-Wilczynska, V. Smolyankin, M.R. Stockmeier, M. Vasiliev, P. Wagner, K. Wisniewski, D. Wohlfarth, I. Yushmanov, A. Zhilin (FOPI Collaboration) :
Transition from in-Plane to out-of-Plane Azimuthal Enhancement in Au+Au Collision
Nucl. Phys. A679, 765 (2001)

Andronic, W. Reisdorf, J.P. Alard, V. Barret, Z. Basrak, N. Bastid, A. Bendarag, G. Berek, R. Caplar, P. Crochet, A. Devismes, P. Dupieux, M. Dzelalija, Ch. Finck, Z. Fodor, A. Gobbi, Y. Grishkin, O.N. Hartmann, N. Herrmann, K.D. Hildenbrand, B. Hong, J. Kecskemeti, Y.J. Kim, M. Kirejczyk, P. Koczon, M. Korolija, R. Kotte, T. Kress, R. Kutsche, A. Lebedev, Y. Leifels, W. Neubert, D. Pelte, M. Petrovici, F. Rami, B. de Schauenburg, D. Schüll, Z. Seres, B. Sikora, K.S. Sim, V. Simion, K. Siwek-Wilczynska, V. Smolyankin, M.R. Stockmeier, G. Stoicea, P. Wagner, K. Wisniewski, D. Wohlfarth, I. Yushmanov, A. Zhilin (FOPI Collaboration) :
Differential Directed Flow in Au+Au Collisions
Phys. Rev. C64, 041604 (2001)

Angelis, G. de; T. Martinez, A. Gadea, N. Marginean, E. Farnea, E. Maglione, S. Lenzi, W. Gelletly, C.A. Ur, D.R. Napoli, Th. Kroell, S. Lunardi, B. Rubio, M. Axiotis, D. Bazzacco, A.M. Bizzeti Sona, P.G. Bizzeti, P. Bednarczyk, A. Bracco, F. Brandolini, F. Camera, D. Curien, M. De Poli, O. Dorvaux, J. Eberth, H. Grawe, R. Menegazzo, G. Nardelli, J. Nyberg, P. Pavan,

Publications

B. Quintana, C. Rossi Alvarez, P. Spolaore, T. Steinhart, I. Stefanescu, O. Thelen, R. Venturelli:
Coulomb Energy Differences between Isobaric Analogue States in ^{70}Br and ^{70}Se – Identification of Excited States of the $T_z = 0$ Nucleus ^{70}Br
E. Phys. J. A12, 51 (2001)

Apel, P.Yu; Yu.E. Korchev, Z. Siwy, R. Spohr, M. Yoshida:
Diode-Like Single-Ion Track Membrane Prepared by Electro-Stopping
Nucl. Instr. and Meth. in Phys. Res.B184,337(2001)

Apel, P.Yu; I.V. Blonskaya, V.R. Oganessian, O.L. Orelovitch, C. Trautmann:
Morphology of Latent and Etched Heavy Ion Tracks in Radiation Resistant Polymers Polyimide and Poly(Ethylene Naphtalate)
Nucl. Instr. and Meth. in Phys. Res.B185,216(2001)
(Proc. of the '4th. Int. Conf. on Ionizing Radiation and Polymers (IRAP2000)', Gouvieux-Chantilly, France, Sept. 2000)

Armbruster, P.:
Lise Meitner (1878-1968) "Mother of Nuclear Structure Physics"
Ricerca Scientifica ed Educazione Permanente, Suppl. No. 117, p.1 (2001)
(Proc. 'XXXIX Int. Meet. on Nucl. Phys.', Bormio, Italy, 22-27. Jan. 2001, eds.: I. Iori, A. Moroni)

Ashrafi, S.; M. Lipoglavek, A. Likar, J. Cederkall, C. Fahlander, H. Grawe, A. Johnson, S. Mitarai, L. -O. Norlin, J. Nyberg, M. Palacz, J. Persson, D. Seweryniak, T. Shizuma, G.Sletten, T. Vidmar:
Monte-Carlo Simulation of the Charged Particle Detector Used in the NORDBALL Gamma-Ray Spectrometer
Nucl. Instr. and Meth. in Phys. Res.A458,690(2001)

Aumann, T.; A. Leistenschneider, U. Datta Pramanik, K. Boretzky, D. Cortina, J. Cub, W. Dostal, Th.W. Elze, H. Emling, H. Geissel, A. Grünschloß, M. Hellström, R. Holzmann, S. Ilievski, N. Iwasa, M. Kaspar, A. Kleinböhl, J.V. Kratz, R. Kulessa, Y. Leifels, E. Lubkiewicz, G. Münzenberg, P. Reiter, M. Rejmund, C. Scheidenberger, Ch. Schlegel, H. Simon, J. Stroth, K. Sümmerer, E. Wajda, W. Walus, S. Wan:
Measurements of the Dipole Response with Radioactive Beams
Nucl. Phys. A687, 103 (2001)
(Proc. of the 7th Int. Topical Conf. on Giant Resonances, Osaka, Japan, 12-15 June, 2000, eds.: T. Wasaka, M. Fujiwara, M. Nomachi, H. Ejiri)

Back, B.B.; R.R. Betts, J. Chang, W.C. Chang, C.Y. Chi, Y.Y. Chu, J.B. Cummings, J.C. Dunlop, W. Eldredge, S.Y. Fung, R. Ganz, E. Garcia, A. Gillitzer, G. Heintzelman, W. Henning, D.J. Hofman, B. Holzman, J.H. Kang, E.J. Kim, S.Y. Kim, Y. Kwon, D. McLeod, A. Mignerey, M. Moulson, V. Nanal, C.A. Ogilvie, R. Pak, A. Ruangma, D. Russ, R. Seto, J. Stanskas, G.S.F. Stephans, H. Wang, F. Wolfs, A.H. Wuosmaa, H. Xiang, G. Xu, H. Yao, C. Zou:
Strangeness Production in Au+Au Collisions at AGS Energies.
J. of Phys. G27, 301(2001)

Back, B.B.; R.R. Betts, J. Chang, W.C. Chang, C.Y. Chi, Y.Y. Chu, J.B. Cumming, J.C. Dunlop, W. Eldredge, S.Y. Fung, R. Ganz, E. Garcia, A. Gillitzer, G. Heintzelman, W.F. Henning, D.J. Hofman, B. Holzman, J.H. Kang, E.J. Kim, S.Y. Kim, Y. Kwon, D. McLeod, A.C. Mignerey, M. Moulson, V. Nanal, C.A. Ogilvie, R. Pak, A. Ruangma, D.E. Russ, R.K. Seto, P.J. Stanskas, G.S.F. Stephans, H.Q. Wang, F.L.H. Wolfs, A.H. Wuosmaa, H. Xiang, G.H. Xu, H.B. Yao, C.M. Zou:
Baryon Rapidity Loss in Relativistic Au+Au Collisions.
Phys. Rev. Lett. 86, 1970 (2001)

Basset, M.; G. Jakob, G. Wirth, H. Adrian:
Patterned Irradiation of $YBa_2 Cu_3 O_{7-x}$ Thin Films
Phys. Rev. B64, 024525 (2001)

Bechtold, A.; U. Ratzinger, A. Schempp, B. Schlitt:
Design Studies of an RFQ-Injector for a Medicine Synchrotron
IEEE Cat. No. 01CH37268, p. 2485 (2001),
ISBN: 0-7803-7191-7
(Proc. of the 2001 Particle Acc. Conf., Chicago, June 2001)

Publications

Beck, D.; F. Ames, M. Beck, G. Bollen, B. Delauré, P. Schuurmans, S. Schwarz, P. Schmidt, N. Severijns, O. Forstner:
Space Charge Effects in a Gas Filled Penning Trap
Hyperfine Interactions 132, 469 (2001)
(Proc. of the APAC2000, Cargèse, Frankreich)

Beckert, K.; P. Beller, O. Boine-Frankenheim, A. Dolinski, B. Franzke, F. Nolden, M. Steck:
An Accelerator Complex for Antiprotons at GSI
Structure of Hadrons, GSI, Darmstadt, p.304 (2001)
(Proc. of the Int. Workshop XXIX on Gross Properties of Nuclei and Nuclear Excitation, Hirschegg, Austria, 14-20 Jan 2001, eds: H. Feldmeier, J. Knoll, W. Nörenberg, J. Wambach)

Bednarz, G.; A. Warzcak, P. Swiat, Th. Stöhlker, H. Beyer, F. Bosch, R.W. Dunford, S. Hagmann, E.P. Kanter, C. Kozhuharov, A. Krämer, D. Liesen, T. Ludziejewski, X. Ma, P.H. Mokler, Z. Stachura:
Double Electron Capture in Relativistic U^{92+} Collisions Observed at the ESR Gas Jet Target
Physica Scripta T92, 429 (2001)
(Proc. of the 10th Int. Conf. on the Phys. of Highly Charged Ions, Berkeley, USA, July30-Aug3, 2000)

Beier, T.; A.N. Artemyev, G. Plunien, V.M. Shabaev, G. Soff, V.A. Yerokhin:
Vacuum-Polarization Screening Corrections to the Low-Lying Energy Levels of Heliumlike Ions
Hyperfine Interactions, 132, 369 (2001)
(Proc. of the APAC2000, Cargèse, Frankreich)

Beier, T.; I. Lindgren, H. Persson, S.O. Salomonson, P. Sunnergren:
The G_j Factor of an Electron Bound in Hydrogenlike Carbon: Status of the Theoretical Predictions
in: The Hydrogen Atom, Springer Verlag, Berlin, p.605 (2001) (eds.: S.G. Karshenboim, F.S. Pavone, F. Bassini, M. Induscio, T.W. Hänsch)

Benlliure, J.; P. Armbruster, M. Bernas, A. Boudard, J.P. Dufour, T. Enqvist, R. Legrain, S. Leray, B. Mustapha, F. Rejmund, K.-H. Schmidt, C. Stephan, L. Tassan-Got, C. Volant:
Isotopic Production Cross Sections of Fission Residues in ^{197}Au-on-Proton Collisions at 800 AMeV
Nucl. Phys. A683, 513 (2001)

Berdermann, E.; K. Blasche, P. Moritz, H. Stelzer, B. Voss:
The use of CVD-Diamond for Heavy-Ion Detect.
Diamond and Related Materials 10 (2001) 1770
(Proc. of the 7th Int. Conf. on New Diamond Science and Technology (ICNDST-7))

Bertulani, C.A.; M.S. Hussein, G. Münzenberg
Physics of Radioactive Beams
Nova Publishers, Inc.; Huntington, N.Y. 2001
ISBN: 1-59033-141-9

Boer, F.W.N. de; K. Bethge, H. Bokemeyer, R. van Dantzig, J. van Klinken, V. Mironov, K.A. Müller, K.E. Stiebing:
Further Search for a Neutral Boson with a Mass around 9 MeV/c^2
J. of Phys. G 27, L29 (2001)

Boccanfuso, M.; A. Benyagoub, M. Toulemonde, C. Trautmann, K. Schwartz, C. Dufour:
Heavy-Ion Induced Damage in Fluorite Nanopowder
Nucl.Instr.+ Math.in Phys.Res.B175-177,590(2001)

Boccanfuso, M.; A. Benyagoub, K. Schwartz, M. Toulemonde, C. Trautmann:
Study of Ion Beam Induced Swelling in Fluorite as an Inert Matrix Model
Prog. Nucl. Energy, 38, 271 (2001)

Bock, R.; S. Borneis, Ch. Bruske, J. Caird, D. Habs, D. Hoffmann, H.-J. Kluge, Th. Kühl, D. Marx, P. Nickles, M. Perry, M. Roth, W. Sandner, P. Seelig, A. Tauschwitz:
PHELIX – A Petawatt High-Energy Laser for Heavy-Ion Experiments
in: Inertial Fusion Sciences and Applications 99, p. 703 (2001), Elsevier Publ., eds.: C. Labaune, W.J. Hogan, K.A. Tanaka

Boine-Frankenheim, O.; I. Hofmann:
Vlasov Simulation of the Microwave Instability
Nucl. Instr. + Meth. in Phys. Res.A464,351(2001)

Publications

(Proc. of the 13th Int. Symp. on HIF, San Diego, USA, March 13.-17, 2000)

Bollen, G.; F. Ames, G. Audi, D. Beck, J. Dilling, O. Engels, S. Henry, F. Herfurth, A. Kellerbauer, H.-J. Kluge, A. Kohl, E. Lamour, D. Lunney, R.B. Moore, M. Oinonen, C. Scheidenberger, S. Schwarz, G. Sikler, J. Szerypo, C. Weber, (ISOLDE Collaboration):
Mass Measurements on Short-Lived Nuclides with ISOLTRAP
Hyperfine Interactions, 132, 215 (2001)
(Proc. of the APAC2000, Cargèse, Frankreich)

Borcea, R.; J. Äysö, E. Caurier, P. Dendooven, J. Döring, M. Gierlik, M. Gorska, H. Grawe, M. Hellström, Z. Janas, A. Jokinen, M. Karny, R. Kirchner, M.LaCommara, K. Langanke, G. Martinez-Pinedo, P. Mayet, A. Nieminen, F. Nowacki, H. Penttilä, A. Plochocki, M. Rejmund, E. Roeckl, C. Schlegel, K. Schmidt, R. Schwengner, M. Sawicka:
Beta Decay of ^{56}Cu
Nucl. Phys. A695, 69 (2001)

Botvina, A.S.; I.N. Mishustin:
Statistical Evolution of Isotope Composition of Nuclear Fragments
Phys. Rev. C63, 061601 (2001)

Bräuning, H.; P.H. Mokler, D. Liesen, F. Bosch, B. Franzke, A. Krämer, C. Kozhuharov, T. Ludziejewski, X. Ma, F. Nolden, M. Steck, Th. Stöhlker, R.W. Dunford, E.P. Kanter, G. Bednarz, A. Warzcak, Z. Stachura, L. Tribedi, T. Kambara, D. Dauvergne, R. Kirsch, C. Cohen:
Strong Evidence for Enhanced Multiple Electron Capture From Surfaces in 46 MeV/u Pb^{81+} Collisions with Tin Carbon Foils
Phys. Rev. Lett. 86, 991 (2001)

Bräuning, H.; P.H. Mokler, D. Liesen, F. Bosch, B. Franzke, A. Krämer, C. Kozhuharov, T. Ludziejewski, X. Ma, F. Nolden, M. Steck, Th. Stöhlker, R.W. Dunford, E.P. Kanter, G. Bednarz, A. Warzcak, Z. Stachura, L. Tribedi, T. Kambara, D. Dauvergne, R. Kirsch, C. Cohen:
Multiple Electron Capture by 46 MeV/u Pb^{81+} Ions from Solid Targets
Physica Scripta T92, 43 (2001)
(Proc. of the 10th Int. Conf. on the Phys. of Highly Charged Ions, Berkeley, USA, July30-Aug3, 2000)

Braun-Munzinger, P.:
Chemical Equilibration and the Hadron QGP Phase Transition
Nucl. Phys. A681, 119c (2001)
(Proc. of the 3rd Catania Relativistic Ion Study, Acicastello, Italy, May 22-26, 2000)

Braun-Munzinger, P.; J. Stachel:
On Charm Production near the Phase Boundary
Nucl. Phys. A690, 119c (2001)
(Proc. of the Int. Symp. on the occasion of Achim Richter's 60th birthday, Darmstadt, Germany, Oct. 11-13, 2000)

Brinzanescu, O.; Th. Stöhlker:
Radiative Recombination Rate Coefficients
Physica Scripta T92, 275 (2001)
(Proc. of the 10th Int. Conf. on the Phys. of Highly Charged Ions, Berkeley, USA, July30-Aug 3, 2000)

Burkhard, J.:
Schnelle, lokale CDKN14A(p21) Akkumulation in menschlichen Zellkernen als Marker von Schwerionenspuren
in: Ganzkörperbestrahlung – Strahlexposition in der Diagnostik, p.17 (2001), Urban und Fischer, Hrsg.: D. Gottschild, Chr. Reiners (Proc. of the "42. Jahrestagung der Vereinigung Deutscher Strahlenschutzärzte e.V.", Jena, Germany, 10.-12.05.2001)

Caamano, M.; P.M. Walker, P.H. Regan, C.J. Pearson, Zs. Podolyak, P. Mayet, J. Gerl, Ch. Schlegel, M. Hellström, M. Mineva, P. Pfützner:
Isomeric Decays in ^{200}Pt
Acta Phys. Pol. B32, 763 (2001)
(Proc. of the 'XXXV Zakopane School of Physics, Trends in Nuclear Physics', 5.-13.09.2000)

Caamano, M.; P.H. Regan, Zs. Podolyak, C.J. Pearson, P. Mayet, J. Gerl, Ch. Schlegel, M. Pfützner, M. Hellström, M. Mineva (GSI ISOMER Coll.):
Nuclear Structure of Heavy Neutron-Rich Systems: Fragmentation Spectroscopy with a1 GeV per Nucleon ^{208}Pb Beam
Nucl. Phys. A682, 223c (2001)

Publications

(Proc. of the Conf. on Nuclear Structure 2000,
East Lansing, USA, Aug. 15-19, 2000)

Chang, W.C.; B.B. Back, R.R. Betts, J. Chang, W.C. Chang, C.Y. Chi, Y.Y. Chu, J.B. Cumming, J.C. Dunlop, W. Eldredge, S.Y. Fung, R. Ganz, E. Garcia, A. Gillitzer, G. Heintzelman, W.F. Henning, D.J. Hofman, B. Holzman, J.H. Kang, E.J. Kim, S.Y. Kim, Y. Kwon, D. Mcleod, A.C. Mignerey, M. Moulson, V. Nanal, C.A. Ogilvie, R. Pak, A. Ruangma, D.E. Russ, R.K. Seto, P.J. Stanskas, G.S.F. Stephans, H.Q. Wang, F.L.H. Wolfs, A.H. Wuosmaa, H. Xiang, G.H. Xu, H.B. Yao, C.M. Zou:
E917 Results on Strangeness Production in Au+Au Collisions at AGS.
Singapore: World Scientific, p.573 (2001)
(Proc. of the 30th Int. Conf. on High Energy Physics, Osaka, Japan, 27.06.-02.08.2000,
eds: C.S. Lim, T. Yamanaka)

Chulkov, L.; E. Roeckl:
Rätsel um überschweren Wasserstoff
Phys. Bl. 57, 22 (2001)

Cortina-Gil, D., T. Baumann, H. Geissel, H. Lenske, K. Sümmerer, L. Axelsson, U.Bergmann, M.J.G. Borge, L.M. Fraile, M. Hellström, M. Ivanov, N. Iwasa, R. Janik, B.Jonson, K. Markenroth, G. Münzenberg, F: Nickel, T. Nilsson, A. Ozawa, K. Riisager, G. Schrieder, W. Schwab, H. Simon, C. Scheidenberger, B. Sitar, T: Suzuki, M. Winkler:
One-Nucleon Removal Cross-Sections for ^{17,19}C and ^{8,10}B
E. J. of Phys. A 10, 49 (2001)

Czanta, M.; C. Strietzel, H.J. Besch, H.F. Beyer, F. Bosch, R. Deslattes, F. Förster, A. Gumberidze, G. Hölzer, P. Indelicato, C. Kozhuharov, O. Klepper, A. Krämer, D. Liesen, T. Ludziejewski, X. Ma, B. Manil, G. Menzel, N. Pavel, A. Simionovici, M. Steck, T. Stöhlker, S. Toleikis, J. Tschischgale, A.H. Walenta, O. Wehrhan:
Spectroscopy of Ly-f Lines at Storage Rings by Crystal Spectrometry and Absorption Edge Technique
Hyperfine Interactions, 132, 491 (2001)
(Proc. of the APAC2000, Cargèse, Frankreich)

Datta Pramanik, U.; T. Aumann, D. Cortina. H. Emling, H. Geissel, M. Hellström, R. Holzmann, N. Iwasa, Y. Leifels, G. Münzenberg, M. Rejmund, C. Scheidenberger, K. Sümmerer, A. Leistenschneider, Th.W. Elze, A. Grünschloss, S. Ilievski, K. Boretzky, J.V. Kratz, R. Kulessa, E. Lubkiewicz, E. Wajda, W. Walus, P. Reiter, H. Simon:
Structure Studies of Light Neutron-Rich Nuclei
Pramana-Journal of Physics 46, 285 (2001)

Datta Pramanik, U.; T. Aumann, D. Cortina. H. Emling, H. Geissel, M. Hellström, R. Holzmann, N. Iwasa, Y. Leifels, G. Münzenberg, M. Rejmund, C. Scheidenberger, K. Sümmerer, A. Leistenschneider, Th.W. Elze, A. Grünschloss, S. Ilievski, K. Boretzky, J.V. Kratz, R. Kulessa, E. Lubkiewicz, E. Wajda, W. Walus, P. Reiter, H. Simon:
Structure Studies of Light Neutron-Rich Nuclei
World Scientific, Singapore, p.261, 2001,
eds.: R. Casten et al.
(Proc. 'Int. Symp. on Nuclear Structure Physics', Göttingen, Germany, 2001)

Diehl, A.; H. Bräuning, R. Trassl, D. Hathiramani, A. Theiss, H. Kern, E. Salzborn, I. Hofmann:
Charge Transfer and Ionization in Collisions between Multiply Charged Noble Gas Ions
J. Phys. B34, 4073 (2001)

Dilling, J.; G. Audi, D. Beck, G. Bollen, F. Herfurth, A. Kellerbauer, H.-J. Kluge, D. Lunney, R.B. Moore, C. Scheidenberger, S.Schwarz, G. Sikler, J. Szerypo:
Mass Measurements of $^{114\text{-}124,130}$Xe with the ISOLTRAP Penning Trap Spectrometer
Hyperfine Interactions, 132, 331 (2001)
(Proc. of the APAC2000, Cargèse, Frankreich)

Dilling, J.; D. Ackermann, F.P. Heßberger, S. Hofmann,H.-J. Kluge, G. Marx, G. Münzenberg, Z. Patyk, W. Quint, D. Rodriguez, C. Scheidenberger, J. Schönfelder, G. Sikler, A. Sobiczewski, C. Toader, C. Weber:
A Physics Case for SHIPTRAP: Measuring the Masses of Transuranium Elements
Hyperfine Interactions, 132, 495 (2001)
(Proc. of the APAC2000, Cargèse, Frankreich)

Publications

Dobrev, D.; J. Vetter, N. Angert, R. Neumann:
Growth of Iron Single Crystals in the Etched Ion Tracks of Polymer Foils
Appl. Phys. A72, 729 (2001)

Dobrev, D.; J. Vetter, R. Neumann, N. Angert:
Conical Etching and Electrochemical Metal Replication of Heavy-Ion Tracks in Polymer Foils
J. Vac. Sci. Technol. B19, 1385 (2001)

Döring, J.; C. Plettner, M. Axiotis, R. Borcea, J. Eberth, A. Gadea, M. Gorska, H. Grawe, Z. Janas, R. Kirchner, M. La Commara, C. Mazzocchi, E. Nacher Gonzalez, A. Plochocki, E. Roeckl, K. Schmidt, R. Schwengner, T. Steinhardt, J. Zylicz:
Study of Medium-Mass Odd-Odd Nuclei Close to the N=Z Line
in: Nuclear Structure, World Scientific, Singapore, p.121, 2001, eds. G.C. Bonsignori et al.
(Proc. 'Structure of the Nucleus at the Dawn of the Century', Bologna, Italy, May 2000)

Egelhof, P.; IKAR Coll.:
Nuclear Matter Distributions of Neutron-Rich Halo Nuclei from Intermediate Energy Elastic Proton Scattering in Inverse Kinematics
Progr. Part. Nucl. Phys. 46, 307 (2001)

Emling, H.:
Nuclear Structure Experiments with Unstable Fragment Beams at GSI
Progr. in Part. and Nucl. Phys. 46, 285 (2001)

Engels, O.; L. Beck, G. Bollen, D. Habs, G. Marx, J. Neumayr, U. Schramm, S. Schwarz, P. Thirolf, V. Varentsov:
First Measurements with the Gas Cell for SHIPTRAP
Hyperfine Interactions, 132, 501 (2001)
(Proc. of the APAC2000, Cargèse, Frankreich)

T. Enqvist, W. Wlazlo, P. Armbruster, J. Benlliure, M. Bernas, A. Boudard, S. Czajkowski, R. Legrain, S. Leray, B. Mustapha, M. Pravikoff, F. Rejmund, K. -H. Schmidt, C. Stéphan, J. Taieb, L. Tassan-Got, C. Volant:
Isotopic Yields and Kinetic Energies of Primary Residues in 1 *A* GeV ^{208}Pb+p Reactions
Nucl. Phys. A686, 481 (2001)

Fahlander, C.; M. Palacz, D. Rudolph, D. Sohler, J. Blomqvist, J. Kownacki, K. Lagergren, L.-O. Norlin, J. Nyberg, A. Algora, C. Andreoiu, G. de Angelis, A. Atac, D. Bazzacco, L. Berglund, T. Bäck, J. Cederkäll, B. Cederwall, Zs. Dombradi, B. Fant, E. Farnea, A. Gadea, M. Gorska, H. Grawe, N. Hashimoto-Saitoh, A. Johnson, A. Kerek, W. Klamra, S.M. Lenzi, A. Likar, M. Lipoglavsek, M. Moszynski, D. Napoli, C. Rossi-Alvarez, H.A. Roth, T. Saitoh, D. Seweryniak, Ö. Skeppstedt, M. Weiszflog, M. Wolinska:
Neutron Single Particle Energies with Respect to the ^{100}Sn Core Determined from Excited States in ^{103}Sn
Phys. Rev. C63, 021307 (2001)

Feili, D.; Ph. Bosselmann, K.-H. Schartner, P.H. Mokler, X. Ma, A.E. Livingston, F. Folkmann, E. Träbert:
Access to Two-Photon QED Contributions via 2s $^2S_{½}$ - 2P $^2P_{½}$ Transitions in Heavy Li-Like Ions
Physica Scripta T92, 362 (2001)
(Proc. of the 10th Int. Conf. on the Phys. of Highly Charged Ions, Berkeley, USA, July30-Aug 3, 2000)

Feldmeier, H.:
Liquid-Gas Phase Transition in Fermionic Molecular Dynamics
Nucl. Phys. A281, 398c (2001)
(Proc. of the 3rd Catania Relativistic Ion Study, Acicastello, Italy, May 22-26, 2000)

Fertig, N.; Ch. Meyer, R.H. Blick, Ch. Trautmann, J.C. Behrends:
Microstructure Glass Chip for Ion-Vhannel Electrophysiology
Phys. Rev. E64, 040901

Finck, Ch.; and the FOPI Collaboration:
A New Time of Flight System for the FOPI Detector
Ricerca Scientifica ed Educazione Permanente, Suppl. No. 117, p.287 (2001)
(Proc. 'XXXIX Int. Wint. Meet. on Nucl. Phys.', Bormio, Italy, 22-27. Jan. 01,eds.: I.Iori, A.Moroni)

Publications

Fischer, B.E.; M. Cholewa, H. Noguchi:
Some Experiences on the Way to Biological Single Ion Experiments
Nucl. Inst. and Meth. in Phys. Res. B181, 60 (2001)
(Proc. of the '7th Int. Conf. on Nuclear Microprobe Technology + Applications, Bordeaux,France,2000)

Fournier, C.; M. Scholz, W.K. Weyrather, H.P. Rodemann, G. Kraft :
Changes of Fibrosis-Related Parameters after High- and Low-LET Irradiation of Fibroblasts
Int. J. Rad. Biol. 77, 713 (2001)

Franchoo, S.; M. Huyse, K. Kruglov, Y. Kudryavtsev, W.F. Mueller, R. Raabe, I. Reusen, P. Van Duppen, J. Van Roosbroeck, L. Vermeeren, A. Wöhr, H. Grawe, K.-L. Kratz, B. Pfeiffer, W.B. Walters:
Monopole Migration in ^{69,71,73}Cu Observed from Beta-Decay of Laser-Ionized $^{68-74}$Ni
Phys. Rev. C64, 054308 (2001)

Fritzsche, S.; Th. Stöhlker:
High-Z Projectile Ionization: Studies on the Validity of First-Order Perturbation Theory
Physica Scripta T92, 311 (2201)
(Proc. of the 10th Int. Conf. on the Phys. of Highly Charged Ions, Berkeley, USA, July30-Aug 3, 2000)

Galindo, E.; M. Hausmann, A. Jungclaus, D. Kast, K.P. Lieb, G.A. Müller, O. Yordanov, S. Brant, D. Vretenar, A. Algora, F. Brandolini, G. de Angelis, M. De Poli, C. Fahlander, A. Gadea, T. Martinez, D. R. Napoli , A. Dewald, R. Peusquens, H. Tiesler, M. Górska, H. Grawe, P.G. Bizzeti, P. Sona, G. Bonsignori:
Lifetime Measurements of High-Spin States in ^{101}Ag and their Interpretation in the Interacting Boson Fermion plus Broken Pair Model
Phys. Rev. C64, 034304 (2001)

Galindo, E.; M. Hausmann, A. Jungclaus, K.P. Lieb, G.A. Müller, O. Yordanov, A. Algora, G. de Angelis, P.G. Bizzeti, F. Brandolini, A. Dewald, C. Fahlander, A. Gadea, M. Górska, H. Grawe, T. Martinez, D. R. Napoli, R. Peusquens, M. De Poli, H. Tiesler:
Coincidence Lifetime Measurements in ^{101}Ag
World Scientific, Singapore, p.355, 2001,
eds.: R. Casten et al.
(Proc. 'Int. Symp. on Nuclear Structure Physics', Göttingen, Germany, 2001)

Geissel, H.; F. Attallah, K. Beckert, F. Bosch, M. Falch, B. Franzke, M. Hausmann, Th. Kerscher, O. Klepper, H.-J. Kluge, C. Kozhuharov, Yu. Litvinov, K.E.G. Löbner, G. Münzenberg, N. Nankov, F. Nolden, Yu. Novikov, T. Ohtsubo, Z. Patyk, T. Radon, C. Scheidenberger, J. Stadlmann, M. Steck, K. Sümmerer, H. Weick, H. Wollnik:
Progress in Mass Measurements of Stored Exotic Nuclei at Relativistic Energies
Nucl. Phys. A685, 115c (2001)
(Proc. of the 7th Int. Conf. on Nucleus-Nucleus Collisions, Strasbourg, France, 03.-07.07.2000 eds.: W. Nörenberg, D. Guerreau, V. Metag)

Geissel, H.; H. Wollnik:
Mass Measurements of Stored Exotic Nuclei
Nucl. Phys. A693, 19 (2001)
(Special Issue on Research Oppertunities with Accelerated Beams of Radioactive Ions)

Golubev, A.; V. Turtikov, A. Fertman, I. Roudskoy, B. Sharkov, M. Geissel, U. Neuner, M. Roth, A. Tauschwitz, H. Wahl, D.H.H. Hoffmann, U. Funk, W. Süß, J. Jacoby:
Experimental Investigation of the Effective Charge State of Ions in Beam-Plasma Interaction
Nucl. Instr. + Meth. in Phys. Res.A464,247 (2001)
(Proc. of the 13th Int. Symp. on HIF, San Diego, USA, March 13.-17, 2000)

Georgiev, G.; D.L. Balabanski, C. Bingham, C. Borcea, N. Coulier, R. Coussement, J.M. Daugas, G. Defrance, F. de Oliveira Santos, G. Goldring, M. Górska, H. Grawe, R. Grzywacz, M. Hass, C. O'Leary. M. Lewitowicz, H. Mach, I. Macovei, R. Page, M. Pfützner, Yu.E. Penionzkevich, Zs. Podolsyak, P.H. Regan, K. Rykaczewski, M. Sawicka, N.A. Smirnova, Yu.G. Sobolev, M. Stanoiu, S. Teughels, K. Vyvey, G. Neyens:
Measurement of the g-Factors of Isomers near the Proposed N=40 Subshell Closure
Phys. Atomic Nuclei, 64, 1181 (2001);
Yad Fiz. 64, No. 7, 1258 (2001)

Publications

Georgiev, G.; D.L. Balabanski, C. Bingham, C. Borcea, N. Coulier, R. Coussement, J.M. Daugas, G. Defrance, F. de Oliveira Santos, G. Goldring, M. Górska, H. Grawe, R. Grzywacz, M. Hass, C. O'Leary. M. Lewitowicz, H. Mach, I. Macovei, R. Page, M. Pfützner, Yu.E. Penionzkevich, Zs. Podolsyak, P.H. Regan, K. Rykaczewski, M. Sawicka, N.A. Smirnova, Yu.G. Sobolev, M. Stanoiu, S. Teughels, K. Vyvey, G. Neyens:
Gyromagnetic Factors of Isomers in the Neutron-Rich N=40 Region: The Case of ^{69}Cu
World Scientific, Singapore, p.357, 2001, eds.: R. Casten et al.
(Proc. 'Int. Symp. on Nuclear Structure Physics', Göttingen, Germany, 2001)

Grawe, H.; M. Gorska, J. Döring, C. Fahlander, M. Palacz, F. Nowacki, E. Caurier, J.M. Daugas, M. Lewitowicz, M Sawicka, M. Pfützner, R. Grzywacz, K. Rykaczewski, O. Sorlin, S. Leenhardt, F. Azaiez, M. Rejmund, K. Hauschild, J. Uusitalo:
Nuclear Structure in the Vicinty of Shell Closures far from Stability
AIP, CP 561, p. 287 (2001), Tours Symp. on Nuclear Physics IV (eds.: M. Arnold et al.)

Grawe, H.; M. Lewitowicz:
Shell Structure of Nuclei far from Stability
Nucl. Phys. A693, 116 (2001)
(Special Issue on Research Oppertunities with Accelerated Beams of Radioactive Ions)

Grigorenko, L.G.; R.C. Jonson, I.G. Mukha, I.J. Thompson, M.V. Zhukov:
Two-Proton Radioactivity and Three-Body Decay: I. General Problems and Theoretical Approach
Phys. Rev. C64, 054002 (2001)

Gudowska-Nowak, E.; A. Kleczkowski, G. Kraft, E. Nasonova, S. Ritter, M. Scholz:
Mathematical Models of Radiation-Induced Mitotic Delay: Time Course Analysis and Statistics of Lesions
Phys. Med. XVII, Suppl. 1, 161 (2001)

Gupta, R.K; M. Balasubramaniam, G. Münzenberg, W. Greiner, W. Scheid:
Cold ^{86}Kr Valley in Superheavy Z = 104-120 Nuclei
J. of Phys. G 27, 867 (2001)

Hannawald, M.; V.N. Fedoseyev, U. Köster, K.-L. Kratz, V.I. Mishin, W.F. Müller, H.L. Ravn, J. Van Roosbroeck, H. Schatz, V. Sebastian, W.B. Walters, and the ISOLDE Collaboration:
Deacy Properties of N=82 to 84 Cadmium R-Process Nuclides
Nucl. Phys. A688, 578 (2001)
(Proc. of the 6th Int. Conf. on Nuclei in the Cosmos, Aarhus, Denmark, 27.6.-01.07.2000, eds.: J. Christensen-Dalsgaard, K. Langanke)

Hasse, R.W.:
Multiple Coulomb Ordered Strings of Ions in a Storage Ring
Phys. Rev. Lett. 86, 3028 (2001)

Hauschild, K.; M. Rejmund, H. Grawe, E. Caurier, F. Nowacki, F. Becker, Y. Le Coz, W. Korten, J. Döring, M. Górska, K. Schmidt, O. Dorvaux, K. Helariutta, P. Jones, R. Julin, S. Juutinen, H. Kettunen, M. Leino, M. Muikku, P. Nieminen, P. Rahkila, J. Uusitalo, F. Azaiez, M. Belleguic:
Isomer Spectroscopy in $^{216}_{90}Th_{126}$ and the Magicity of $^{218}_{92}U_{126}$
Phys. Rev. Lett. 87, 072501 (2001)

Hausmann, M.; J. Stadlmann, F. Attallah, K. Beckert, P. Beller, F. Bosch, H. Eickhoff, M. Falch, B. Franzcak, B. Franzke, H. Geissel, Th. Kerscher, O. Klepper, H.-J. Kluge, C. Kozhuharov, Yu.A. Litvinov, K.E.G. Löbner, G. Münzenberg, N. Nankov, F. Nolden, Yu.N. Novikov, T. Ohtsubo, T. Radon, F. Schatz, C. Scheidenberger, M. Steck, Z. Sun, H. Weick, H. Wollnik:
Isochronous Mass Measurements of Hot Exotic Nuclei
Hyperfine Interactions, 132, 291 (2001)
(Proc. of the APAC2000, Cargèse, Frankreich)

Publications

Hawkes, S.; J. Collier, C. Hooker, C. Reason, C. Edwards, C. Herandez-Gomez, C. Danson, I. Ross, C. Häfner:
Adaptive Optics Trials on Vulcan
Central Laser Facility Annual Report 2000/2001, RAL-TR-2001-030, p. 153, ISBN 0902376160

Hees, H. van; J. Knoll:
Finite Pion Width Effects on the Rho-Meson
Nucl. Phys. A683, 369 (2001)

Heinz, A.; T.L. Khoo, P. Reiter, I. Ahmad, P. Bhattacharyya, J. Caggiano, M.P. Carpenter, J.A. Cizewski, C.N. Davids, W.F. Henning, R.V.F. Janssens, G.D. Jones, R. Julin, F.G. Kondev, T. Lauritsen, C.J. Lister, D. Seweryniak, S. Siem, A.A. Sonzogni, J. Uusitalo, I. Wiedenhover:
Entry Distribution of ^{220}Th: a Method to Determine the Fission Barrier of an Unstable Nucleus.
Nucl. Phys. A682, 458 (2001)
(Proc. Nuclear Structure 2000 Conf. East Lansing, USA, 15-19 Aug 2000)

Henning, W.F.
Hadrons and Nuclei: Concept for the Future GSI-Facility
Structure of Hadrons, GSI, Darmstadt, p.300 (2001)
(Proc. of the Int. Workshop XXIX on Gross Properties of Nuclei and Nuclear Excitation, Hirschegg, Austria, 14-20 Jan 2001, eds: H. Feldmeier, J. Knoll, W. Nörenberg, J. Wambach)

Herfurth, F.; J. Dilling, A. Kellerbauer, G. Audi, D. Beck, G. Bollen, S. Henry, H.-J. Kluge, D. Lunney, R.B. Moore, C. Scheidenberger, S. Schwarz, G. Sikler, J. Szerypo:
Towards Shorter-Lived Nuclides in ISOLTRAP Mass Measurements
Hyperfine Interactions, 132, 309 (2001)
(Proc. of the APAC2000, Cargèse, Frankreich)

Herfurth, F.; J. Dilling, A. Kellerbauer, G. Bollen, S. Henry, H.-J. Kluge, E. Lamour, D. Lunney, R.B. Moore, C. Scheidenberger, S. Schwarz, G. Sikler, J. Szerypo:
A Linear RF Ion Trap for Accumul., Bunching, and Emitt. Improv. of Radioactive Ion Beams
Nucl. Instr. and Meth. in Phys. Res.A469,254(2001)

Herfurth, F.; J. Dilling, A. Kellerbauer, G. Audi, D. Beck, G. Bollen, H.-J. Kluge, D. Lunney, R.B. Moore, C. Scheidenberger, S. Schwarz, G. Sikler, J. Szerypo, ISOLDE Coll.:
Breakdown of the Isobaric Multiplet Mass Equation (IMME) at A=33, T=3/2
Phys. Rev. Lett. 87, 142501 (2001)

Hessberger, F.P.; S. Hofmann, D. Ackermnn, V. Ninov, M. Leino, G. Münzenberg, S. Saro, A. Lavrentev, A.G. Popeko, A.V. Yeremin, Ch. Stodel:
Decay Properies of Neutron-Deficient Isotopes ^{256,257}Db, ^{255}Rf, ^{252,253}Lr
Eur. Phys. J. A12, 57 (2001)

Hoffknecht, A.; C. Brandau, T. Bartsch, C. Böhme, H. Knopp, S. Schippers, A. Müller, C. Kozhuharov, K. Beckert, F. Bosch, B. Franzke, A. Krämer, P.H. Mokler, F. Nolden, M. Steck, Th. Stöhlker, Z. Stachura:
Recombination of Bare Bi $^{83+}$ Ions with Electrons
Phys. Rev. A63, 012702 (2001)

Hoffknecht, A.; C. Brandau, T. Bartsch, C. Böhme, H. Knopp, S. Schippers, A. Müller, C. Kozhuharov, K. Beckert, F. Bosch, B. Franzke, A. Krämer, P.H. Mokler, F. Nolden, M. Steck, Th. Stöhlker, Z. Stachura:
Recombination of Bare Bi $^{83+}$ Ions with Electrons
Physica Scripta T92, 398 (2001)
(Proc. of the 10th Int. Conf. on the Phys. of Highly Charged Ions, Berkeley, USA, July30-Aug 3, 2000)

Hofmann, I.:
Heavy Ion Inertial Fusion in Europe
Nucl. Instr. + Meth. in Phys. Res.A464,24(2001)
(Proc. of the 13th Int. Symp. on HIF, San Diego, USA, March 13.-17, 2000)

Hofmann, I.; J. Qiang, R. Ryne:
Collective Resonance Model of Energy Exchange in 3D Nonequipartitioned Beams
Phys. Rev. Lett. 86, 2313 (2001)

Publications

Hofmann, I.; O. Boine-Frankenheim:
Resonanz Emittanz Transfer Driven by Space Charge
Phys. Rev. Lett. 87, 034802 (2001)

Hofmann, S.; F.P. Heßberger, D. Ackermann, S. Antalic, P. Cagarda, S. Cwiok, B. Kindler, J. Kojouharova, B. Lommel, R. Mann, G. Münzenberg, A.G. Popeko, S. Saro, H.J. Schött, A.V. Yeremin:
The New Isotope ^{270}110 and its Decay Products ^{266}Hs and ^{262}Sg
E. J. of Phys. A 10, 5 (2001)

Hofmann, S.:
Synthesis of Superheavy Elements Using Radioactive Beams and Targets
Progr. in Part. and Nucl. Phys. 46, 293 (2001)

Hofmann, S.:
Advances in the Search for Superheavy Elements at GSI
EP Systema Bt., Publisher, Debrecen, Hungary, p.171,2001 (ed.: W. Greiner)
(Proc. of the Symp. on "Fundamental Issues in Elementary Matter", in Honor and Memory of Michael Danos)

Hu, Z.:
Nuclear Data Sheets for ^{97}Pd
Nucl. Data Sheets 92, 253 (2001)

Ilievski, S.; T. Aumann, K. Boretzky, J. Cub, W. Dostal, B. Eberlein, Th. W. Elze, H. Emling, A. Grünschloß, J. Holeczek, R. Holzmann, C. Kozhuharov, J. V. Kratz, R. Kulessa, Y. Leifels, A. Leistenschneider, E. Lubkiewicz, T. Ohtsuki, P. Reiter, H. Simon, K. Stelzer, J. Stroth, A. Surowiec, E. Wajda, W. Walus, (LAND Collaboration):
Multi-Phonon Giant Resonances and Coulomb Fission of ^{238}U
Nucl. Phys. A687, 178 (2001)
(Proc. of the 7th Int. Topical Conf. on Giant Resonances, Osaka, Japan, 12-15 June, 2000, eds.: T. Wasaka, M. Fujiwara, M. Nomachi, H. Ejiri)

Indelicato, P.; E. Lindroth, T. Beier, J. Biero, A.M. Costa, I.Lindgren, J.P. Marques, A.-M. Martensom-Pendrill, M.C. Martins, M.A. Oudane, F. Parente, P. Patté, G.C. Rodrigues, S. Salomonson, J.P. Santos:
Relativistic Calculations for Trapped Ions
Hyperfine Interactions, 132, 349 (2001)
(Proc. of the APAC2000, Cargèse, Frankreich)

Ivanov, Yu.B.; J. Knoll, H. van Hees, D.N. Voskresensky:
Soft Modes, Resonances and Quantum Transport
Phys. Atom. Nucl. 64, 652 (2001)

Jäkel, O.; M. Krämer, C.P. Karger, J. Debus:
Treatment Planning for Heavy Ion Therapy: Clinical Implementation and Application
Phys. Med. Biol. 46, 1101 (2001)

Janas, Z.; M. Karny, Y. Fujita, L. Batist, D. Cano-Ott, R. Collatz, P. Dendooven, A. Gadea, M. Gierlik, M. Hellström, Z. Hu, A. Jokinen, R. Kirchner, O. Klepper, F. Moroz, M. Oinonen, H. Penttilä, A. Plochocki, E. Roeckl, B. Rubio, M. Shibata, J.L. Tain, V. Wittman:
Total Absorption Spectroscopy of ^{58}Cu Decay
Eur. Phys. J A12, 143 (2001)

Jungclaus, A.; D. Kast, K.P. Lieb, C. Teich, M. Weiszflog, T. Härtlein, C. Ender, F. Köck, D. Schwalm, J. Reif, R. Schwengner, I.P. Johnstone, A. Dewald, J. Eberth, R. Peusquens, H.G. Thomas, M. Gorska, H. Grawe:
Electromagnetic Properties of Particle-Hole Excitations in Nuclei near N=50
in: Nuclear Structure, World Scientific, Singapore, p.286, 2001, eds. G.C. Bonsignori et al.
(Proc. 'Structure of the Nucleus at the Dawn of the Century', Bologna, Italy, 2000)

Jurado, B.; A. Heinz, A. Junghans, K.-H. Schmidt, J. Benlliure, T. Enqvist, F. Rejmund:
New Results on Dissipation in Fission
Ricerca Scientifica ed Educazione Permanente, Suppl. No. 117, p.238 (2001)
(Proc. 'XXXIX Int. Wint. Meet. on Nucl. Phys.', Bormio, Italy, 22-27. Jan. 01,eds.: I.Iori, A.Moroni)

Publications

Karny, M.; L. Batist, B. A. Brown, D. Cano-Ott, R. Collatz, A. Gadea, R. Grzywacz, A. Guglielmetti, M. Hellström, Z. Hu, Z. Janas, R. Kirchner, F. Moroz, A. Piechaczek, A. Plochocki, E. Roeckl, B. Rubio, K. Rykaczewski, M. Shibata, J. Szerypo, J. L. Tain, V. Wittmann, A. Wöhr:
Determination of the Gamow Teller Strength Function for the Neutron-Deficient Isotopes $^{104-107}$In
Nucl. Phys. A690, 367 (2001)

Kellerbauer, A.; G. Bollen, J. Dilling, S. Henry, H.-J. Kluge, E. Lamour, D. Lunney, R.B. Moore, C. Scheidenberger, S. Schwarz, G. Sikler, J. Szerypo:
Improvement of the Applicability, Efficiency, and Precision of the Penning Trap Mass Spectrometer ISOLTRAP
Hyperfine Interactions, 132, 511 (2001)
(Proc. of the APAC2000, Cargèse, Frankreich)

Kindler, B.; S. Antalic, H.-G. Burkhard, P. Cagarda, D. Gembalies-Datz, W. Hartmann, S. Hofmann, J. Kojouharova, J. Klemm, B. Lommel, R. Mann, S. Saro, H.-J. Schött, J. Steiner:
Status of the Target Development for the Heavy Element Programm
AIP 576, 5 (2001)
(Proc. of the 16th Int. Conf. 'Application of Accelerators in Research and Industry', Denton, USA, Nov. 2000)

Klempt, T.; S. Schweizer, K. Schwartz, O. Kanert, D. Suter, U. Rogulis, J.-M. Späth:
Magnetic Resonance Investigation of the Dynamics of F Centers in LiF
Solid State Commun., 119, 453 (2001)

Knau, H.L.; T. Beier, M. Sönnecken:
Iron Works and Water Power. The Development of Mechanical Hammer Works in the "Südergebirge"
Acta Metallurgica Slovaca 7, 127 (2001)

Knoll, J.; Yu.B. Ivanov, D.N. Voskresensky:
Exact Conservation Laws of the Gradient Expanded Kadanoff-Baym Equations
Ann. Phys. 293, 126 (2001)

Kojima, M.; K. Nishigori, M. Yoshida, A. Sakumi, J. Hasegawa, U. Funk, U. Neuner, Y. Oguri M. Ogawa:
WP.II-13 Laser Plasma Induced from Solid Hydrogen for Beam-Plasma Interaction
Nucl. Instr. + Meth. in Phys. Res.A464,262(2001)
(Proc. of the 13th Int. Symp. on HIF, San Diego, USA, March 13.-17, 2000)

Kotomin, E.A.; V. Kashcheyevs, V.N. Kuzovkov, K. Schwartz, C. Trautmann:
Modeling of Primary Defect Aggregation in Tracks of Swift Heavy Ions in LiF
Phys. Rev. B64, 144108 (2001)

Krämer, A.; A. Kritzer, H. Reich, Th. Stöhlker:
Commissioning of a Hydrogen Cluster Target at the Experimental Storage Ring
Nucl. Instr. and Meth. in Phys. Res.B174,205(2001)

Krämer, M.:
Treatment Planning for Heavy-Ion Radiotherapy: Biological Optimization of Multiple Beam Ports
J. Radiat. Res., 42, 39 (2001)

Krammer, M.; W. Adam, E. Berdermann, P. Bergonzo, G. Bertuccio, F. Bogani, E. Borchi, A. Brambilla, M. Bruzzi, C. Colledani, J. Conway, P. D'Angelo, W. Dabrowski, P. Delpierre, A. Deneuville, W. Dulinski, B. van Eijk, A. Fallou, F. Fizzotti, F. Foulon, M. Friedl, K. K. Gan, E. Gheeraert, G. Hallewell, S. Han, F. Hartjes, J. Hrubec, D. Husson, H. Kagan, D. Kania, J. Kaplon, R. Kass, T. Koeth, A. Logiudice, R. Lu, L. MacLynne, C. Manfredotti, D. Meier, M. Mishina, L. Moroni, A. Oh, L. S. Pan, M. Pernicka, A. Peitz, L. Perera, S. Pirollo, M. Procario, J. L. Riester, S. Roe, L. Rousseau, A. Rudge, J. Russ, S. Sala, M. Sampietro, S. Schnetzer, S. Sciortino, H. Stelzer, R. Stone, B. Suter, R. J. Tapper, R. Tesarek, W. Trischuk, D. Tromson, E. Vittone, A. M. Walsh, R. Wedenig, P. Weilhammer, M. Wetstein, C. White, W. Zeuner, M. Zoeller:
CVD Diamond Sensors for Charged Particle Detection
Diamond and Related Materials 10 (2001) 1778
(Proc. of the 7th Int. Conf. on New Diamond Science and Technology (ICNDST-7))

Publications

Krause, H.F.; C.R. Vane, S. Datz, P. Grafström, H. Knudsen, U. Mikkelsen, C. Scheidenberger, R.H. Schuch, Z. Vilakazi:
Electron Capture and Ionization of 33TeV Pb Ions in Gas Targets
Phys. Rev. A 63, 032711 (2001)

Kühl, T.; S. Borneis, A. Dax, T. Engel, S. Faber, M. Gerlach, C. Holbrow, G. Huber, D. Marx, P. Merz, W. Quint, F. Schmitt, P. Seelig, M. Tomaselli, H. Winter, M. Wuertz, K. Beckert, B. Franzke, F. Nolden, H. Reich, M. Steck:
Ground-State Hyperfine Structure of Heavy Hydrogen-Like Ions
Lecture Notes in Physics, 570, 672 (2001)
(Proc. of the 'Conf. Hydrogen II, Castiglione delle Pescaia, Italy, June 2000, eds.: S. Karshenboim, F. Pavone)

Kumagai, H.; A. Ozawa, N. Fukuda, K. Sümmerer, I. Tanihata:
Delay-Line PPAC for High-Energy Light Ions
Nucl. Instr. and Meth. in Phys. Res.A470,562(2001)

Labzowsky, L.N.; A.V. Nefiodov, G. Plunien, G. Soff, R. Marrus, D. Liesen:
Parity-Violation Effect in Heliumlike Gadolinium and Europium
Phys. Rev. A63, 054105 (2001)

Lavaud, F.; G. Auger, Ch.O. Bacri, M.L. Begemann-Blaich, N. Bellaize, R. Bittiger, F. Bocage, B. Borderie, R. Bougault, B. Bouriquet, Ph. Buchet, J.L. Charvet, A. Chbihi, R. Dayras, D. Doré, D. Durand, J.D. Frankland, E. Galichet, D. Gourio, D. Guinet, S. Hudan, B. Hurst, Ph. Lautesse, J.L. Laville, Ch. Leduc, A. Le Fèvre, R. Legrain, O. Lopez, J. Lukasik, U. Lynen, W.F.J. Müller, L. Nalpas, H. Orth, E. Rosato, A. Saija, C. Schwarz, W. Seidel, C. Sfienti, J.C. Steckmeyer, G. Tabacaru, B. Tamain, W. Trautmann, A. Trczinski, K. Turzo, E. Vient, M. Vigilante, C. Volant, B. Zwieglinski (ALADIN and INDRA Coll.):
Multifragmentation and Radial Flow in Au+Au Central Collisions between 40 and 100 AMeV
Ricerca Scientifica ed Educazione Permanente, Suppl. No. 117, p.160 (2001)
(Proc. 'XXXIX Int. Wint. Meet. on Nucl. Phys.', Bormio, Italy, 22-27. Jan. 01,eds.: I.Iori, A.Moroni)

Leistenschneider, A.; T. Aumann, K. Boretzky, D. Cortina, J. Cub, U. Datta Pramanik, W. Dostal, Th.W. Elze, H. Emling, H. Geissel, A. Grünschloss, M. Hellström, R. Holzmann, S. Ilievski, N. Iwasa, M. Kaspar, A. Kleinböhl, J.V. Kratz, R. Kulessa, Y. Leifels, E. Lubkiewicz, G. Münzenberg, P. Reiter, M. Rejmund, C. Scheidenberger, C. Schlegel, H. Simon, J. Stroth, K. Sümmerer, E. Wajda, W.Walus, S. Wan(LAND-FRS-CB Coll.)
Electromagnetic Excitation of Neutron-Rich Oxygen Nuclei $^{17-22}$O
Acta Phys. Pol. B32, 1095 (2001)
(Proc. of the 'XXXV Zakopane School of Physics, Trends in Nuclear Physics', 5.-13.09.2000)

Leistenschneider, A.; T. Aumann, K. Boretzky, D. Cortina, J. Cub, U. Datta Pramanik, W. Dostal, Th. W. Elze, H. Emling, H. Geissel, A. Grünschloß, M. Hellström, R. Holzmann, S. Ilievski, N. Iwasa, M. Kaspar, A. Kleinböhl, J. V. Kratz, R. Kulessa, Y. Leifels, E. Lubkiewicz, G. Münzenberg, P. Reiter, M. Rejmund, C. Scheidenberger, C. Schlegel, H. Simon, J. Stroth, K. Sümmerer, E. Wajda, W. Walús, S. Wan:
Photoneutron Cross Sections for Unstable Neutron-Rich Oxygen Isotopes
Phys. Rev. Lett. 86, 5442 (2001)

Lenzi, S.M.; N. Marginean, D.R. Napoli, C.A. Ur, A. P. Zuker, G. de Angelis, A. Algora, M. Axiotis, D. Bazzacco, N. Belcari, M. A. Bentley, P.G. Bizzeti, A. Bizzeti-Sona, F. Brandolini, P. von Brentano, D. Bucurescu, J.A. Cameron, C. Chandler, M. De Poli, A. Dewald, H. Eberth, E. Farnea, A. Gadea, J. Garces-Narro, W. Gelletly, H. Grawe, R. Isocrate, D. T. Joss, C. A. Kalfas, T. Klug, T. Lampman, S. Lunardi, T. Martínez, G. Martínez-Pinedo, R. Menegazzo, J. Nyberg, Zs. Podolyak, A. Poves, R. V. Ribas, C. Rossi Alvarez, B. Rubio, J. Sánchez-Solano, P. Spolaore, T. Steinhardt, O. Thelen, D. Tonev, A. Vitturi, W. von Oertzen, M. Weiszflog:
Coulomb Energy Differences in T=1 Mirror Rotational Bands in ^{50}Fe and ^{50}Cr
Phys. Rev. Lett. 87, 122501 (2001)

Lewitowicz, M.; B. Blank, J.M. Daugas, H. Grawe, R. Grzywacz, G. Neyens, M. Pfützner, P.H. Regan, K. Rykaczewski:

Publications

Nuclear Structure Studies by Means of Short-Lived Isomers at Intermediate Energies
Nucl. Phys. A682, 175c (2001)
(Proc. of the Conf. on Nuclear Structure 2000, East Lansing, USA, Aug. 15-19, 2000)

Lieb, K.P.; D. Kast, A. Jungclaus, I.P. Johnstone, G. de Angelis, C. Fahlander, M. de Poli, P.G. Bizzeti, A. Dewald, R. Peusquens, H. Tiesler M. Górska, H. Grawe:
Proton Versus Neutron Excitations in High-Spin Spectrum of ^{102}Cd
Phys. Rev. C63, 054304 (2001)

Lieb, K.P.; D. Kast, A. Jungclaus, I.P. Johnstone, G. de Angelis, C. Fahlander, M. de Poli, P.G. Bizzeti, A. Dewald, R. Peusquens, H. Tiesler M. Górska, H. Grawe:
Proton Versus Neutron Excitations in High-Spin Spectrum of ^{102}Cd
World Scientific, Singapore, p.371, 2001, eds.: R. Casten et al.
(Proc. 'Int. Symp. on Nuclear Structure Physics', Göttingen, Germany, 2001)

Litvinov, Yu.N.; F. Attallah, K. Beckert, F. Bosch, M. Falch, B. Franzke, H. Geissel, M. Hausmann, Th. Kerscher, O. Klpper, H.-J. Kluge, C. Kozhuharov, K.E.G. Löbner, G. Münzenberg, F. Nolden, Yu.N. Novikov, Z. Patyk, W. Quint, T.Radon, C. Scheidenberger, M. Steck, L. Vermeeren, H. Wollnik:
Schottky Mass Measurements of Cooled Exotic Nuclei
Hyperfine Interactions, 132, 283 (2001)
(Proc. of the APAC2000, Cargèse, Frankreich)

Liu, J.; R. Neumann, C. Trautmann, C. Müller:
Tracks of Swift Heavy Ions in Graphite Studied by Scanning Tunneling Microscopy
Phys. Rev. B64, 184115 (2001)

Liu, W.-P.; M. Hellström, R. Collatz, J. Benlliure, L. Chulkov, D. Cortina Gil, F. Farget, H. Grawe, Z. Hu, N. Iwasa, M. Pfützner, A. Piechaczek, R. Raabe, I. Reusen, E. Roeckl, G. Vancraeynest, A. Wöhr:
Precise Determination of ^{40}Ti Mass by Measuring the ^{40}Sc Isospin Analogue State
Chin. Phys. Lett. 18, 1449 (2001)

Lukasik, J.; A.S. Botvina, G. Auger, Ch.O. Bacri, M.L. Begemann-Blaich, N. Bellaize, R. Bittiger, F. Bocage, B. Borderie, R. Bougault, B. Bouriquet, Ph. Buchet, J.L. Charvet, A. Chbihi, R. Dayras, D. Doré, D. Durand, J.D. Frankland, E. Galichet, D. Gourio, D. Guinet, S. Hudan, B. Hurst, G. Immé, Ph. Lautesse, F. Lavaud, J.L. Laville, Ch. Leduc, A. Le Fèvre, R. Legrain, O. Lopez, J. Lukasik, U. Lynen, W.F.J. Müller, L. Napas, H. Orth, E. Plagnol, E. Rosato, A. Saija, C. Schwarz, C. Sfienti, J.C. Steckmeyer, G. Tabacaru, B. Tamain, W. Trautmann, A. Trczinski, K. Turzo, E. Vient, M. Vigilante, C. Volant, B. Zwieglinski (ALADIN and INDRA Coll.):
Some Gross Features of Non-Central Heavy Ion Collisions (First Results of the Indra GSI Campaign)
Ricerca Scientifica ed Educazione Permanente, Suppl. No. 117, p.278 (2001)
(Proc. 'XXXIX Int. Wint. Meet. on Nucl. Phys.', Bormio, Italy, 22-27. Jan. 01,eds.: I.Iori, A.Moroni)

Lutz, M.F.M., E.E. Kolomeitsev:
Covariant meson-baryon scattering with chiral and large N_c constraints
Found. Phys. 31, 1671 (2001)

Ma, X.; Th. Stöhlker, F. Bosch, O. Brinzanescu, S. Fritzsche, C. Kozhuharov, T. Ludziejewski, P.H. Mokler, Z. Stachura, A. Warczak:
State-Selective Electron Capture into He-Like U^{90+} Ions in Collisions with Gaseous Targets
Phys. Rev. A 64, 012704 (2001)

Ma, X; Th. Stöhlker, O. Brinzanescu, S. Fritzsche, C. Kozhuharov, P.H. Mokler, T. Ludziejewski, A. Warzcak:
Subshell Differential Cross Sections for Electron Capture Occurring in Collisions between U^{90+} Ions and Gaseous Targets
Physica Scripta T92, 362 (2001)
(Proc. of the 10th Int. Conf. on the Phys. of Highly Charged Ions, Berkeley, USA, July30-Aug3, 2000)

Mach, H.; M. Lewitowicz, M. Stanoiu, F. Becker, J. Blomqvist, M.J.G. Borge, R. Boutami, B. Cerdewall, Z. Dlouhy, B. Fogelberg, L.M. Fraile, G. Georgiev, H. Grawe, R. Grzywacz, P.I. Johansson, W. Klamra, S. Lukyanov, M. Mineva, J. Mrazek, G. Neyens, F. de Oliveira

Publications

Santos, M. Pfützner, Yu.E. Penionzhkevich, E. Ramström, M. Sawicka:
Structure of the Exotic Nuclei near ^{70}Ni Probed by Advanced Time-Delayed Coincidence Methods: The Interpetation of the 1.76 μs Isomer in ^{72}Cu
World Scientific, Singapore, p.379, 2001, eds.: R. Casten et al.
(Proc. 'Int. Symp. on Nuclear Structure Physics', Göttingen, Germany, 2001)

Malmbeck, R.; C. Apostolidis, R. Carlos, J.-P. Glatz, R. Molinet, A. Morgenstern, A. Nicholl, G.Pagliosa, K. Römer, M. Schädel, B. Sätmark, N. Trautmann:
Separation of ^{248}Cm from a ^{252}Cf Neutron Source for Production of Cm Targets
Radiochim. Acta 89, 543 (2001)

Markenroth, K., M. Meister, B. Eberlein, D. Aleksandrov, T. Aumann, L. Axelsson, T. Baumann, M.J.G. Borge, L.V. Chulkov, W. Dostal, Th.W. Elze, H. Emling, H. Geissel, A. Grünschloß, M. Hellström, J. Holeczek, B. Jonson, J.V. Kratz, R. Kulessa, A. Leistenschneider, I. Mukha, G. Münzenberg, F. Nickel, T. Nilsson, G. Nyman, M. Pfützner, V. Pribora, A. Richter, K. Riisager, C. Scheidenberger, G. Schrieder, H. Simon, J. Stroth, O. Tengblad, M.V. Zhukov:
^{8}He – ^{6}He: a Comparative Study of Nuclear Fragmentation Reactions
Nucl. Phys. A679, 462 (2001)

Marx, G.; D. Ackermann, J. Dilling, F.P. Heßberger, S. Hofmann, H.-J. Kluge, R. Mann, G. Münzenberg, Z. Qamhieh, W. Quint, D. Rodriguez, M. Schädel, J. Schönfelder, G. Sikler, C. Toader, C. Weber, O. Engels, D. Habs, P. Thirolf, H. Backe, A. Dretzke, W. Lauth, W. Ludolphs. M. Sewtz:
Status of the SHIPTRAP Project: A capture and Storage Facility for Heavy Radionuclides from SHIP
Hyperfine Interactions, 132, 463 (2001)
(Proc. of the APAC2000, Cargèse, Frankreich)

Mazzocchi, C.; Z. Janas, J. Döring, M. Axiotis, L. Batist, R. Borvcea, D. Cano-Ott, E. Caurier, G. de Angelis, E. Farnea, A. Faßbender, A. Gadea, H. Grawe, A. Jungclaus, M. Kapica, R. Kirchner, J. Kurcewicz, S.M. Lenzi, T. Martinez, I. Mukha, E. Nacher, D.R. Napoli, E. Roeckl, B. Rubio, R. Schwengner, J.L. Tain, C.A. Ur:
First Measurement of Beta-Decay Properties of the Proton Drip-Line Nucleus ^{60}Ga
Eur. Phys. J. A12, 269 (2001)

Mercik, S.; Z. Siwy, R. Spohr, K. Weron:
Characterization of the Asymmetric Action of a Single Pore in Track-Etched Membrane
Acta Phys. Pol.. B32, 1605 (2001)

Milne, W.I.; K.B.K. Teo, M. Chhowalla, G.A.J. Amartunga, J. Yuan, J. Robertson, P. Legagneux, G. Pirio, D. Pribat, K. Bouzehouane, W. Brünger, C. Trautmann:
Carbon Films for Use as the Electron Source in a Parallel e-Beam Lithography System
New Diamond + Front. Carbon Techn.11,235(2001)

Mineva, M.N., M. Hellström, M. Bernas, J. Gerl, H. Grawe, M. Pfützner, P.H. Regan, M. Rejmund, D. Rudolph, F. Becker, C.R. Bingham, T. Enqvist, B. Fogelberg, H. Gausemel, H. Geissel, J. Genevey, M. Górska, R. Grzywacz, K. Hauschild, Z. Janas, I. Kojouharov, Y. Kopatch, A. Korgul, W. Korten, J. Kurcewicz, M. Lewitowicz, R. Lucas, H. Mach, S. Mandal, P. Mayet, C. Mazzocchi, J.A. Pinston, Zs. Podolyàk, H. Schaffner, Ch. Schlegel, K. Schmidt, K. Sümmerer, H.J. Wollersheim:
A New μs Isomer in ^{136}Sb Produced in the Projectile Fission of ^{238}U
E. J. of Phys. A 11, 9 (2001)

Mokler, P.H.:
Relativistic Effects in Collisions of High-Z Ions
The Phys. of Electr. + Atomic Collisions 463 (2001)

Mokler, P.H., R.W. Dunford:
The Two-Photon Decay of 1s2s $^{1}S_{0}$-like States in Heavy Atomic Systems
Fizika A10, 105 (2001)

Moritz, P.; E. Berdermann, K. Blasche, H. Stelzer, B. Voss:
Broadband Electronics for CVD-Diamond Detectors
Diamond and Related Materials 10 (2001) 1765

Publications

(Proc. of the 7th Int. Conf. on New Diamond Science and Technology (ICNDST-7))

Müller, G.A.; A. Jungclaus, O. Yordanov, E. Galindo, M. Hausmann, D. Kast, K.P. Lieb, S. Brant, V. Krstic, D. Vretenar, A. Algora, F. Brandolini, G. de Angelis, M. De Poli, C. Fahlander, A. Gadea, T. Martinez, D. R. Napoli, A. Dewald, R. Peusquens, H. Tiesler, M. Górska, H. Grawe, P. G. Bizzeti:
High-Spin Structure and Electromagnetic Transition Strengths in ^{104}Cd
Phys. Rev. C64, 014305 (2001)

Müller, G.A.; A. Jungclaus, O. Yordanov, E. Galindo, M. Hausmann, D. Kast, K.P. Lieb, S. Brant, V. Krstic, D. Vretenar, A. Algora, F. Brandolini, G. de Angelis, M. De Poli, C. Fahlander, A. Gadea, T. Martinez, D. R. Napoli, A. Dewald, R. Peusquens, H. Tiesler, M. Górska, H. Grawe, P. G. Bizzeti:
Competing Collective and Quasiparticle Structures in the Transitional Nucleus ^{104}Cd
World Scientific, Singapore, p.385, 2001,
eds.: R. Casten et al.
(Proc. 'Int. Symp. on Nuclear Structure Physics', Göttingen, Germany, 2001)

Münzenberg, G.:
Nuclear Structure Physics at GSI – Results and Perspectives
Nucl. Phys. A682, 88c (2001)
(Proc. of the Conf. on Nuclear Structure 2000, East Lansing, USA, Aug. 15-19, 2000)

Münzenberg, G.:
Superheavy Elements – Discoveries + Challenges
Nucl. Phys. A690, 175c (2001)
(Proc. of the Int. Symp. on the Occasion of Achim Richter's 60th Birthday, Darmstadt, Germany, Oct. 11-13, 2000)

Münzenberg, G.:
Cold Fusion of Heavy Ions Paving the Way to Superheavy Elements
Nucl. Phys. A693, 207 (2001)
(Special Issue on Research Oppertunities with Accelerated Beams of Radioactive Ions)

Münzenberg, G.:
Radioactive Beams
Progr. Part. Nucl. Phys. 46, 335 82001)

Nagaraja, H.S.; R. Neumann, P. Mohan Rao:
Ion-Induced Craters on the Surface of Benzoyl, Glycine Single-Crystals Studied by Scanning Force Microscopy
Nucl. Instr. and Meth. in Phys. Res. B185, 66(2001)

Nagel, R.; K. Weyrich, D.H.H. Hoffmann, A.G. Balogh:
Heavy Ion Induced Intermixing of Metal/SiC Interfaces
Nucl. Instr. + Meth. in Phys. Res.B178, 315 (2001)

Napiorkowski, P.J.; J. Srebrny, T. Czosnyka, J. Gerl, Ch. Schlegel, H-J. Wollersheim, D. Cline, C.Y. Wu, R. Teng, K. Vetter, A. Macchiavelli, M. Devlin, J. deBoer, J. Iwanicki, J. Kownacki, M. Loewe, M. Wuerkner:
Coulomb Excitation of the $K^{\pi} = 8^-$ Isomeric Band in ^{178}Hf
Acta Phys. Pol. B32, 861 (2001)
(Proc. of the 'XXXV Zakopane School of Physics, Trends in Nuclear Physics', 5.-13.09.2000)

Nasonova, E.; E. Gudowska-Nowak, S. Ritter, G. Kraft:
Analysis of Ar-Ion and X-Ray-Induced Chromoatin Breakage and Repair in V79 Plateau-Phase Cells by the Premature Chromosome Condensation Technique
Int. J. Radiat. Biol., 77, 59, (2001)

Neumayer, P. ; J. Alvarez, B. Becker de-Mos, S. Borneis, K. Brück, E.W. Gaul, C. Häfner, T. Kühl, D. Marx, I. Reinhard, M. Tomaselli, P.V. Nickles, W. Sandner, W. Seelig :
X-Ray Laser Spectroscopy on Lithium-Like Ions
Soft X Ray Lasers and Applications 4, 326 (2001)
(Proc. of SPIE)

Neuner, U.; R. Bock, C. Constantin, E. Dewald, U.N. Funk, M. Geissel, D.H.H. Hoffmann, J. Jacoby, A. Kozyreva, D. Penache, P. Pirzadeh, F.B. Rosmej, O. Rosmej, M. Roth, W. Süß, N.A. Tahir, A. Tauschwitz, S. Udrea, D. Varentsov, H. Wahl:

Publications

Experiments Using the High Current Upgrade of the GSI Accelerators: Response of Converters to Heating by Intense Heavy Ion Beams
Nucl. Instr. + Meth. in Phys. Res.A464,326(2001)
(Proc. of the 13th Int. Symp. on HIF, San Diego, USA, March 13.-17, 2000)

Neuner, U.; R. Bock, C. Constantin, E. Dewald, U.N. Funk, M. Geissel, S. Hakuli, D.H.H. Hoffmann, J. Jacoby, A. Kozyreva, M. Roth, P. Spiller, N.A. Tahir, A. Tauschwitz, S. Udrea, D. Varentsov, J. Wieser:
High Density Neon-Plasma Created by Intense Gold Beams
Contributions to Plasma Phys. 41, 123 (2001)
(Proc. of the 10th Int. Workshop on the Phys. of Nonideal Plasmas, Greifswald, Sept. 3-8, 2000)

Neuner, U.; R. Bock, M. Roth, H. Wahl, C. Constantin, E. Dewald, U.N. Funk, M. Geissel, S. Hakuli, D.H.H. Hoffmann, J. Jacoby, R. Knobloch, A. Kozyreva, D. Penache, P. Pirzadeh, F.B. Rosmej, O. Rosmej, N.A. Tahir, A. Tauschwitz, S. Udrea, D. Varensov, Y. Maron, M. Sarfaty:
Response of Converters to Heating by Intense Heavy Ion Beams
Proc. of 13th Int. Conf. on High-Power Particle Beams (BEAMS 2000), Nagaoka, June 25-30, 2000, p. 817

Niemann, C.; D.M. Ponce, S.S. Yu, G. Dahlbacka, T.J. Fessenden, W. Leemans, A. Tauschwitz, D.H.H. Hoffmann
Development of a Faraday Polarimeter for Magnetic Field Measurements in a Discharge Channel for Ion Beam Transport
Nucl. Instr. + Meth. in Phys. Res.A464,339(2001)
(Proc. of the 13th Int. Symp. on HIF, San Diego, USA, March 13.-17, 2000)

Nolden, F.; K. Beckert, P. Beller, O. Boine-Frankenheim, A. Dolinskii, B. Franzke, M. Steck, H. Weick:
Planned New Cooler/Storage Ring Complex for Radioactive Beams and Antiprotons at GSI
IEEE Cat. No. 01CH37268, p.569 (2001), ISBN: 0-7803-7191-7
(Proc. of the 2001 Particle Acc. Conf., Chicago, June 2001)

Ozawa, A.; O. Bochkarev, L. Chulkov, D. Cortina, H. Geissel, M. Hellström, M. Ivanov, R. Janik, K. Kimura, T. Kobayashi, A.A. Korsheninnikov, G. Münzenberg, F. Nickel, Y. Ogawa, A.A. Ogloblin, M. Pfützner, V. Pribora, H. Simon, B. Sitár, P. Strmen, K. Sümmerer, T. Suzuki, I. Tanihata, M. Winkler, K. Yoshida:
Measurements of Interaction Cross Sections for Light Neutron-Rich Nuclei at Relativistic Energies and Determination of Effective Matter Radii,
Nucl. Phys. A691, 599 (2001)

Palacz, M.; C. Fahlander, D. Sohler, D. Rudolph, J. Blomqvist, J. Kownacki, K. Lagergren, L.O. Norlin, J. Nyberg, A. Algora, C. Andreoiu, G. de Angelis, A. Atac, D. Bazzacco, L. Berglund, T. Bäck, J. Cederkäll, B. Cederwall, Zs. Dombradi, B. Fant, E. Farnea, A. Gadea, M. Gorska, H. Grawe, N. Hashimoto-Saitoh, A. Johnson, A. Kerek, W. Klamra, S.M. Lenzi, A. Likar, M. Lipoglavsek, M. Moszynski, D. Napoli, C. Rossi-Alvarez, H. Roth, T. Saitoh, D. Seweryniak, Ö. Skeppstedt, M. Weiszflog, M. Wolinska:
Investigations of Neutron Deficient Nuclei Close to ^{100}Sn with EUROBALL
Acta Phys. Pol. B32, 999 (2001)
(Proc. of the 'XXXV Zakopane School of Physics, Trends in Nuclear Physics', 5.-13.09.2000)

Pape Moller, S.; V. Biryukov, S. Datz, P. Grafström, H. Knudsen, H.F. Krause, C. Scheidenberger, U.I. Uggerhoj, C.R. Vane:
Random and Channeled Energy Loss of 33.2TeV Pb Nuclei in Silicon Single Crystals
Phys. Rev. A 64, 032902 (2001)

Paula, D.T. de; T. Aumann, L.F. Canto, B.V. Carlson, H. Emling, M.S. Hussein:
Anharmonicities of Giant Dipole Excitations
Phys. Rev. C64, 064605 (2001)

Peräjärvi, K.; P. Dendooven, M. Gorska, J. Huikari, A. Jokinen, V.S. Kolhinen, M. La Commara, G. Lhersonneau, A. Nieminen, S. Nummela, H. Penttilä, E. Roeckl, J.C. Wang, J. Äystö:
The $1^+ \rightarrow 0^+$ Gamow-Teller Strength of the $^{58}Cu_{g.s.} \rightarrow {}^{58}Ni_{g.s.}$ Transition
Nucl. Phys. A696, 233 (2001)

Publications

Perez, G.E.; D. Sohler, A. Algora, Zs. Dombradi, B.M. Nyako, J.Timar, L. Zolnai, R. Wyss, J. Cederkäll, A. Johnson, A. Kerek, W. Klamra, L. - O. Norlin, M. Lipoglavsek, C. Fahlander, A. Likar, M.Palacz, A. Atac, J. Nyberg, J. Persson, A. Gizon, J. Gizon, A.J. Boston, E.S. Paul, H. Grawe, R. Schubart, D.T. Joss, S. Juutinen, E. Mäkelä, J. Kownacki, M. de Poli, P. Bednarczyk, G. de Angelis,, D. Seweryniak, D. Foltescu, H.A. Roth, Ö. Skeppstedt D. Jerrestam, T. Shizuma, G. Sletten, S. Törmänen:
Structure of high spin states in ^{100}Pd
Nucl. Phys. A686, 41 (2001)

Pershina, V.; J.V. Kratz:
Solution Chemistry of Element 106: Theoretical Predictions of Hydrolysis of Group 6 Cations Mo, W, and Sg
Inorg. Chem. 40, 4, 776 (2001)

Pershina, V.; T. Bastug, B. Fricke, S. Varga:
The Electronic Structure and Properties of Group 8 Oxides MO_4 , where M=Ru, Os and Element 108, Hs
J. Chem. Phys. 115 792 (2001)

Pershina, V.; T. Bastug, J.V. Kratz:
Quantum Chemical Predictions of Properties and Experimental Behaviour of Elements 106, 107 and 108
Radiochim. Acta 89, 729 (2001)

Pochodzalla, J.; W. Trautmann:
Chem. Equilibrium and Isotope Temperatures
in: Isospin Physics in Heavy-Ion Collisions at Intermediate Energies, Nova Science Publ., p. 451 (2001), eds: Bao-An Li, W.U. Schröder, ISBN 1-56072-888-4

Ponce, D.M.; C. Niemann, S.S. Yu, W.P. Leemans, T.J. Fessenden, G. Dahlbacka, W.M. Sharp, A. Tauschwitz:
Diagnostics of Plasma Channel for HIF Transport
Nucl. Instr. + Meth. in Phys. Res.A464,331(2001)
(Proc. of the 13th Int. Symp. on HIF, San Diego, USA, March 13.-17, 2000)

Pop, A.; A. Andronic, I. Berceanu, M. Duma, D. Moisa, M. Petrovici, V. Simion, A. Bonasera, G. Immé, G. Lanzanò, A. Pagano, G. Raciti, N. Colonna, G. d'Erasmo, A. Pantaleo, H. Feldmeier, J. Schnack:
Global Features of Dissipative Processes in Light Heavy-Ion Collisions
Nucl. Phys. A679, 793 (2001)

Protic, D.; Th. Stöhlker, H.F. Beyer, J. Bojowald, G. Borchert, A. Hamacher, C. Kozhuharov, T. Ludziejewski, X. Ma, I. Mohos:
A Micro-Strip Germanium Detector for Position Sensitive X-Ray Spectroscopy
IEEE Trans. Nucl. Scie. 48, 1048 (2001)

Quint, W.; and the g-Factor Coll.:
The g-Factor of the Bound Electron in Hydrogenic Ions
Atomic Physics 17, AIP 551, 269 (2001)
(Proc. XVII Int. Conf. on Atomic Physics, ICAP2000, Florence, Italy, 04.-09.06.2000)
(eds.: E. Arimondo, P. DeNatale, M. Inguscio)

Quint, W.; J. Dilling, S. Djekic, H. Häffner, N. Hermansphan, H.-J. Kluge, G. Marx, R. Moore, D. Rodriguez, J. Schönfelder, G. Sikler, T. Valenzuela, J. Verdu, C. Weber, G. Werth:
HITRAP: A Facility for Experiments with Trapped Highly Charged Ions
Hyperfine Interactions, 132, 457 (2001)
(Proc. of the APAC2000, Cargèse, Frankreich)

Quint, W.; T. Beier, H. Häffner, N. Hermanspahn, S. Karshenboim, H.-J. Kluge, G. Marx, T. Valenzuela, J. Verdu, G. Werth:
The Magnetic Moment Anomaly of the Electron Bound in Hydrogenic Ions
AIP 564, 144 (2001)
(Proc of the Conf. QED2000, ed.: G. Cantatore)

Rahkila, P.; T. Grahn, K. Eskola, J. Gerl, P.T. Greenless, P. Jones, D.T. Joss, R. Julin, S. Juutinen, H. Kankaanpää, A. Keenan, H. Kettunen, I. Kjouharov, P. Kuusiniemi, M. Leino, A. Melarangi, C.J. Moore, M. Muikku, P. Nieminen, R.D. Page, C. Scholey, J. Uusitalo:
Characteristics of Segmented Super Clover Detector in Close Geometry Decay Measurements

Publications

Acta Phys. Pol. B32, 773 (2001)
(Proc. of the 'XXXV Zakopane School of Physics, Trends in Nuclear Physics', 5.-13.09.2000)

Ratzinger, U.:
Commissioning of the New GSI High Current Linac and HIF Related RF Linac Aspects
Nucl. Instr. + Meth. in Phys. Res.A464,636(2001)
(Proc. of the 13th Int. Symp. on HIF, San Diego, USA, March 13.-17, 2000)

Reber, N.; A. Küchel, R. Spohr, A. Wolf, M. Yoshida:
Transport Properties of Thermo-Responsive Ion Track Membranes
J. Membr. Sci. 193, 49 (2001)

Rejmund, F.; B. Mustapha, P. Armbruster, J. Benlliure, M. Bernas, A. Boudard, J.P. Dufour, T. Enqvist, T. Legrain, S. Leray, K.-H. Schmidt, C. Stephan, J. Taieb, L. Tassan-Got, C. Volant:
Measurement of Isotopic Cross Sections of Spallation Residues in 800 A MeV ^{197}Au+p Collisions
Nucl. Phys. A683, 540 (2001)

Ricciardi, M.V.; K.-H. Schmidt, J. Benlliure, T. Enqvist, F. Rejmund, P. Armbruster, F. Ameil, M. Bernas, A. Boudard, S. Czajkowski, R. Legrain, S. Lary, B. Mustapha, M. Pravikoff, C. Stephan, L. Tassan-Got, C. Volant:
Light Nuclides Observed in the Fission and Fragmentation of ^{238}U
Ricerca Scientifica ed Educazione Permanente, Suppl. No. 117, p.224 (2001)
(Proc. 'XXXIX Int. Wint. Meet. Nucl.Phys.', Bormio, Italy, 22-27. Jan.01, eds.:I.Iori,A.Moroni)

Roeckl, E.;
Decay Experiments on N~Z Nuclei: The Role of Masses, Q Values and Separation Energies
Hyperfine Interactions, 132, 153 (2001)
(Proc. of the APAC2000, Cargèse, Frankreich)

Rosmej, F.B.; D.H.H. Hoffmann, W. Süß, M. Geissel, O.N. Rosmej, A.Ya. Faenov, T.A. Pikuz, T. Auguste, P.D'Oliveira, S. Hulin, P. Monot, J.E. Hansen, G. Verbookhaven:
High-Resolution X-Ray Imaging Spectroscopy Diagnostic of Hollow Ions in Dense Plasmas
Nucl. Instr. + Meth. in Phys. Res.A464,257(2001)
(Proc. of the 13th Int. Symp. on HIF, San Diego, USA, March 13.-17, 2000)

Rosmej, F.B.; D. H. H. Hoffmann, M. Geißel, M. Roth, P. Pirzadeh, A. Ya. Faenov, T. A. Pikuz, I. Yu. Skobelev, A. I. Magunov:
Advanced X-Ray Diagnostics Based on an Observation of High-Energy Rydberg Transitions from Autoionizing Levels in Dense Laser-Produced Plasmas

Rosmej, F.B., D.H.H. Hoffmann, W. Süß, M. Geißel, A.Ya. Faenov, T.A. Pikuz:
Direct Observation of Forbidden X-Ray Transitions from Autoionizing Levels in Dense Laser-Produced Plasmas
Phys. Rev. A 63, 032716 (2001)

Roth, M.; T. Cowan, A. Hunt, J. Johnson, C. Brown, W. Fountain, S. Hatchett, E. Henry, M. Key, Th. Kühl, T. Parnell, D. Pennington, M. Perry, T. Sangster, M. Singh, R. Snavely, M. Stoyer, Y. Takahashi, S. Wilks:
Laser-Driven Nuclear Fusion, Positron Creation and Electron Acceleration in Ultra-Intense Laser-Solid Experiments on the Petawatt
in: Inertial Fusion Sciences and Applications 99, p. 1010 (2001), Elsevier Publ., eds.: C. Labaune, W.J. Hogan, K.A. Tanaka

Ruzicka, J.; A. Hrmo, L. Krupa, S. Saro, V. Fajnor, K. Jesenak, L. Kuchta, H. Geissel, H. Irnich, C. Kozhuharov, A. Magel, G. Münzenberg, F. Nickel, C. Scheidenberger, H.J. Schött, A. Schwab, Th. Stöhlker, B. Voss, V.P. Zrelov, P.V. Zrelov, E.D. Pachik:
Vavilov-Cherenkov Radiation Emitted by Heavy Ions Near the Threshold
Vacuum 63, 591 (2002)

Schädel, M.:
Aqueous Chemistry of Transactinides
Radiochim. Acta, 89, 721 (2001)

Scheidenberger, C.; F. Attallah, A. Casares, U. Czok, A. Dodonov, S.A. Eliseev, H. Geissel, M. Hausmann, A. Kholomeev. V. Kozlovski, Yu.A. Litvinov, M. Maier, G. Münzenberg,

Publications

N. Nankov, Yu.N. Novikov, T. Radon, J. Stadlmann, H. Weick, M. Weidnmüller, H. Wollnik, Z. Zhou:
A New Concept for Time-of-Flight Mass Spectrometer with Slowed-Down Short-Lived Isotopes
Hyperfine Interactions, 132, 531 (2001)
(Proc. of the APAC2000, Cargèse, Frankreich)

Schlegel, Ch., P. von Neumann-Cosel, J. de Boer, J. Gerl, M. Kaspar, I. Kozhoukharov, M. Loewe, H.J. Maier, P.J. Napiorkowsky, I. Peter, M. Rejmund, A. Richter, H. Schaffner, J. Srebrny, M. Würkner, H.J. Wollersheim, EBGSI96 Coll.:
Depopulation for the $J^{\pi} = 9^{-}$ Isomer in ^{180}Ta to the $J^{\pi} = 1^{+}$ Ground State by Coulomb Excitation
E. J. of Phys. A 10, 135 (2001)

Schlegel, Th.; J. Meyer-ter-Vehn, D.H.H. Hoffmann, J. Ramirez, R. Ramis:
EOS Investigations by Low Entropy Compression of Matter
Contr. to Plasma Physics, 41, 167 (2001)
(Proc. of the 10th Int. Workshop on the Phys. of Nonideal Plasmas, Greifswald, Sept. 3-8, 2000)

Schmidt, K.; R. Borcea, J. Döring, S. Galanoupoulos, M. Gorska, H. Grawe, S. Harissopulos, M. Hellström, Z. Janas, R. Kirchner, G. Kriembardis, M. La Commara, C. Mazzocchi, A.N. Ostrowski, G. Rainovski, E. Roeckl:
Decay Properties of N~Z Nuclei Below ^{100}Sn
in: Nuclear Structure, World Scientific, Singapore, p.125, 2001, eds. G.C. Bonsignori et al.
(Proc. 'Structure of the Nucleus at the Dawn of the Century', Bologna, Italy, 2000)

Schmidt, K.-H.; J. Benlliure, C. Böckstiegel, H.-G. Clerc, A. Grewe, A. Heinz, A.V. Ignatyuk, A.R. Junghans, M. de Jong, J. Müller, M. Pfützner, F. Rejmund, S. Steinhäuser, B. Voss:
New Results on Structure Effects in Nuclear Fission
Nucl. Phys. A685, 60c (2001)
(Proc. of the 7th Int. Conf. on Nucleus-Nucleus Collisions, Strasbourg, France, 03.-07.07.2000 eds.: W. Nörenberg, D. Guerreau, V. Metag)

Schmidt, K.-H.; J. Benlliure, A.R. Junghans:
Fission of Nuclei far from Stability
Nucl. Phys. A693, 169 (2001)
(Special Issue on Research Oppertunities with Accelerated Beams of Radioactive Ions)

Scholz, M.; B. Jakob, G. Taucher-Scholz:
Direct Evidence for the Spatial Correlation Between Individual Particle Traversals and Localized CDKN1A (p21) Response Induced by High-LET Radiation
Rad. Res. 156, 558 (2001)

Schwartz, K.; C. Trautmann:
Heavy-Ion Induced Damage and Modifications of Insulating Materials
Proc. of SPIE, 4415, 248 (2001)

Schwarz, C.; S. Fritz, R. Bassini, M. Begemann-Blaich, S.J. Gaff-Ejakov, D. Gourio, C. Gross, G. Imme, I. Iori, U. Kleinevoss, G.J. Kunde, W.D. Kunze, U. Lynen, V. Maddalena, M. Mahi, T. Möhlenkamp, A. Moroni, W.F.J. Müller, C. Nociforo, B. Ocker, T. Odeh, F. Petruzzelli, J. Pochodzalla, G. Raciti, G. Riccobene, F.P. Romano, S. Saija, H. Sann, M. Schnittker, A. Schüttauf, W. Seidel, V. Serfling, C. Sfienti, W. Trautmann, A. Trzcinski, G. Verde, A. Wörner, Hongfei, Xi, B. Zwieglinski:
Time Scale in Spectator Fragmentation
Nucl. Phys. A681, 279c (2001)
(Proc. of the 3rd Catania Relativistic Ion Study, Acicastello, Italy, May 22-26, 2000)

Schwarz, S.; F. Ames, G. Audi, D. Beck, G. Bollen, J. Dilling, F. Herfurth, H.-J. Kluge, A. Kellerbauer, A. Kohl, D. Lunney, R.B. Moore, H. Raimbault-Hartmann, C. Scheidenberger, G. Sikler, J. Szerypo:
Accurate Mass Determination of Neutron-Deficient Nuclides Close to Z=82 with ISOLTRAP
Hyperfine Interactions, 132, 337 (2001)
(Proc. of the APAC2000, Cargèse, Frankreich)

Schwarz, S.; F. Ames, G. Audi, D. Beck, G. Bollen, C. De Coster, J. Dilling, O. Engels, R. Fossion, J.-E. Garcia Ramos, S. Henry, F. Herfurth, K. Heyde, A. Kellerbauer, H.-J. Kluge, A. Kohl, E. Lamour, D. Lunney, I. Martel, R.B. Moore, M. Oinonen,

Publications

H. Raimbault-Hartmann, C. Scheidenberger, G. Sikler, J. Szerypo, C. Weber and ISOLDE Coll.:
Accurate Masses of Neutron-Deficient Nuclides Close to Z=82
Nucl. Phys. A693, 533 (2001)

Senger, P.:
Strange Mesons in Dense Nuclear Matter
Nucl. Phys. A685, 312c (2001)
(Proc. of the 7th Int. Conf. on Nucleus-Nucleus Collisions, Strasbourg, France, 03.-07.07.2000 eds.: W. Nörenberg, D. Guerreau, V. Metag)

Senger, P.:
Strangeness and Charm Production in Nucleus-Nucleus Collisions at Beam Energies near the Thresholds
Structure of Hadrons, GSI, Darmstadt, p.259 (2001)
(Proc. of the Int. Workshop XXIX on Gross Properties of Nuclei and Nuclear Excitation, Hirschegg, Austria, 14-20 Jan 2001, eds: H. Feldmeier, J. Knoll, W. Nörenberg, J. Wambach)

Seyboth, P.; J. Bächler, D. Barna, L.S. Barnby, J. Bartke, R.A. Barton, L. Betev, H. Bialkowska, A. Billmeier, C. Blume, C.O. Blyth, B. Boimska, J. Bracinik, F.P. Brady, R. Brun, P. Buncic, L. Carr, D. Cebra, G.E. Cooper, J.G. Cramer, P. Csato, V. Eckardt, F. Eckhardt, D. Ferenc, H.G. Fischer, Z. Fodor, P. Foka, P. Freund, V. Friese, J. Ftacnik, J. Gal, R. Ganz, M. Gazdzicki, E. Gladysz, J. Grebieszkow, J.W. Harris, S. Hegyi, V. Hlinka, C. Höhne, G. Igo, M. Ivanov, P. Jacobs, R. Janik, P.G. Jones, K. Kadija, V.I. Kolesnikov, M. Kowalski, B. Lasiuk, R. Lednicky, P. Levai, A.I. Malakhov, S. Margetis, C. Markert, B.W. Mayes, G.L. Melkumov, J. Molnar, J.M. Nelson, G. Odyniec, M.D. Oldenburg, G. Palla, A.D. Panagiotou, A. Petridis, M. Pikna, L. Pinsky, A.M. Poskanzer, D.J. Prindle, F. Pühlhofer, J.G. Reid, R. Renfordt, W. Retyk, H.G. Ritter, D. Röhrich, C. Roland, G. Roland, A. Rybicki, T. Sammer, A. Sandoval, H. Sann, A.Y. Semenov, E. Schäfer, N. Schmitz, P. Seyboth, F. Sikler, B. Sitar, E. Skrzypczak, R. Snellings, G.T.A. Squier, R. Stock, P. Strmen, H. Ströbele, T. Susa, I. Szarka, I. Szentpetery, J. Sziklai, M. Toy, T.A. Trainor, S. Trentalange, T. Ullrich, D. Varga, M. Vassiliou, G.I. Veres, G. Vesztergombi, S. Voloshin, D. Vranic, F. Wang, D.D. Weerasundara, S. Wenig, C. Whitten, N. Xu, T.A. Yates, I.K. Yoo, J. Zimanyi:
Correlations and Fluctuations in Pb+Pb Collisons
Nucl. Phys. B91, 7 (2001)

Shevelko, V.P.; I.Yu. Tolstikhina, Th. Stöhlker:
Stripping of Fast Heavy Low-Charged Ions in Gaseous Targets
Nucl. Instr. and Meth. in Phys. Res.B184,295(2001)

Shi, W.; S. Böhm, C. Böhme, C. Brandau, A. Hoffknecht, S. Kieslich, S. Schippers, A. Müller, C. Kozhuharov, F. Bosch, B. Franzke, P.H. Mokler, M. Steck, Th. Stöhlker, Z. Stachura:
Recombination of U^{92+} Ions with Electrons
Eur. Phys. J. D15, 145 (2001)

Shi, W.; T : Bartsch ; S. Böhm, C. Böhme, F. Bosch, C. Brandau, B. Franzke, N. Grün, A. Hoffknecht, S. Kieslich, H. Knopp, C. Kozhuharov, A. Krämer, P.H. Mokler, A. Müller, F. Nolden, W. Scheid, S. Schippers, Z. Stachura, M. Steck, T. Steih, Th. Stöhlker, T. Winkler:
Dielectronic Recombination and Spectroscopy of the Heaviest Li-Like Ions
Physica Scripta T92, 191 (2001)
(Proc. of the 10th Int. Conf. on the Phys. of Highly Charged Ions, Berkeley, USA, July30-Aug3, 2000)

Siegmann, B. U. Werner, H.O. Lutz, R. Mann:
Multiple Ionization and Fragmentation of H_2O in Collisions with Fast Highly Charged Ions
J. Phys. B34, L587 (2001)

Siegmann, B.; U. Werner, R. Mann, Z. Kalimann, N.M. Kabachnik, H.O. Lutz:
Orientation Dependence of Multiple Ionization of Diatomic Molecules in Collisions with Fast Highly Charges Ions
Phys. Rev. A65, 010704 (2001)

Sobiczewski, A.; I. Muntian, Z. Patyk:
Problem of "Deformed" Superheavy Nuclei
Phys. Rev. C63, 034306 (2001)

Publications

Soff, G.; I. Bednyakov, T. Beier, F. Erler, I.A. Goidenko, U.D. Jentschura, L.N. Labzowsky, A.V. Nefiodov, G. Plunien,R. Schützhold, S. Zschocke:
Effects of QED and Beyond from the Atomic Binding Energy
Hyperfine Interactions, 132, 75 (2001)
(Proc. of the APAC2000, Cargèse, Frankreich)

Spädtke, P.:
U^{4+} MEVVA Source & Outlook for HIF Sources
Nucl. Instr. + Meth. in Phys. Res. 464,388(2001)
(Proc. of the 13th Int. Symp. on HIF, San Diego, USA, March 13.-17, 2000)

Spielberger, B.; M. Scholz, M. Krämer, G. Kraft:
Experimental Investigations of the Response of Films to Heavy-Ion Irradiation
Phys. Med. Biol. 46, 2889 (2001)

Steck, M.:
Extremely Cooled Ion Beams with Evidence of Ordering
IEEE Cat. No. 01CH37268, p.137 (2001),
ISBN: 0-7803-7191-7
(Proc. '2001 Part. Acc. Conf.', Chicago, June 2001)

Stöhlker, Th.:
Lamb-Verschiebung im wasserstoffartigem Uran
Physik in unserer Zeit 32, 6 (2001)

Stöhlker, Th.; X. Ma, T. Ludziejewski, H.F. Beyer, F. Bosch, O. Brinzanescu, R.W. Dunford, J. Eichler, S. Hagmann, A. Ichihara, C. Kozhuharov, A. Krämer, D. Liesen, P.H. Mokler, Z. Stachura, P. Swiat, A. Warzcak:
Radiative Electron Capture Studied for Bare, Decelerated Uranium Ions
Physica Scripta T92, 432 (2001)
(Proc. of the 10th Int. Conf. on the Phys. of Highly Charged Ions, Berkeley, USA, July30-Aug3, 2000)

Stöhlker, Th.; X. Ma, T. Ludziejewski, H.F. Beyer, F. Bosch, O. Brinzanescu, R.W. Dunford, J. Eichler, S. Hagmann, A. Ichihara, C. Kozhuharov, A. Krämer, D. Liesen, P.H. Mokler, Z. Stachura, P. Swiat, A. Warczak:
Near-Treshold, Photoionization of Hydrogenlike Uranium Studied in Ion-Atom Collisions via the Time-Reversed Process
Phys. Rev. Lett. 86, 983 (2001)

Sturm, C.; I. Böttcher, M. Debowski, A. Förster, E. Grosse, P. Koczon, B. Kohlmeyer, F. Laue, M. Mang, L. Naumann, H. Oeschler, F. Pühlhofer, E. Schwab, P. Senger, Y. Shin, J. Speer, H. Ströbele, G. Surowka, F. Uhlig, A. Wagner, W. Walus:
Evidence for a Soft Nuclear Equation-of-State from Kaon Production in Heavy-Ion Collisions
Phys. Rev. Lett. 86, 39 (2000)

Sudowe, R.; P. Vater, R. Brandt, J. Vetter, W. Ensinger:
Filters with < 100nm Radius Pores for Gas Separation Formed by High-Energy Ion Irradiation of Polymers
Nucl.Instr.+Meth. in Phys.Res.B175-177,564(2001)

Surzhykov, A.; S. Fritzsche, Th. Stöhlker:
Photon Polarization in the Radiative Recombination of High-Z, Hydrogen-Like Ions
Phys. Lett. A289, 213 (2001)

Tahir, N.A.; A. Kozyreva, D.H.H. Hoffmann, A. Shutov, P. Spiller, U. Neuner, A. Tauschwitz, J. Jacoby, M. Roth, J.A. Maruhn, R. Bock, H. Juranek, R. Redmer:
Metallization of Hydrogen Using Heavy Ion Imploded Multi-Layered Cylindrical Targets
Contr. to Plasma Physics, 41, 287 (2001)
(Proc. of the 10th Int. Workshop on the Phys. of Nonideal Plasmas, Greifswald, Sept. 3-8, 2000)

Tahir, N.A.; D.H.H. Hoffmann, A. Kozyreva, A. Shutov, J.A. Maruhn, U. Neuner, A. Tauschwitz, P. Spiller, R. Bock:
Designing Future Heavy-Ion –Matter Interaction Experiments for The GSI Darmstadt Heavy Ion Synchrotron
Nucl. Instr. + Meth. in Phys. Res.A464,211(2001)
(Proc. of the 13th Int. Symp. on HIF, San Diego, USA, March 13.-17, 2000)

Publications

Tahir, N.A.; A. Kozyreva, P. Spiller, D.H.H. Hoffman, A. Shutov:
Influence of Hydrodynamic Expansion on Specific Power Deposition by a Heavy Ion Beam in Matter
Phys. of Plasmas 8, 611 (2001)

Tahir, N.A.; D.H.H. Hoffmann, A. Kozyreva, A. Tauschwitz, A. Shutov, J.A. Maruhn, P. Spiller, U. Neuner, J. Jacoby, M. Roth, R. Bock, H. Juranek, R. Redmer:
Statistical, Nonlinear, and Soft Matter Physics
Phys. Rev. E63, 016402 (2001)

Tahir, N.A.; A. Kozyreva, P. Spiller, D.H.H. Hoffmann, A. Shutov:
Necessity of Bunch Compression for Studies of Heavy Ion Induced Hydrodynamics and Beam Fragmentation in Solid Targets
Phys. Rev. E63, 036407 (2201)

Toimil Molares, M.E.; V. Buschmann, D.Dobrev, R. Neumann, R. Scholz, I. Schuchert, J. Vetter:
Single-Crystalline Copper Nanowires Produced by Electrochemical Deposition in Polymeric Ion Track Membranes
Adv. Mater. 13, 62 (2001)

Toimil Molares, M.E.; J. Brötz, V. Buschmann, D.Dobrev, R. Neumann, R. Scholz, I.U. Schuchert, C. Trautmann, J. Vetter:
Etched Heavy Ion Tracks in Polycarbonate as Template for Copper Nanowires
Nucl. Instr. and Meth. in Phys. Res.B185,192(2001)
(Proc. of the '4th. Int. Conf. on Ionizing Radiation and Polymers (IRAP2000)', Gouvieux-Chantilly, France, Sept. 2000)

Tomaselli, M.; S. Fritzsche, A. Dax, P. Egelhof, C. Kozhuharov, T. Kühl, D. Marx, M. Mutterer, S.R. Neumaier, W. Nörteshäuser, H. Wang, H. -J. Kluge:
Microscopic Model for Charge and Matter Distributions of Nuclei
Nucl. Phys. A690, 298c (2001)
(Proc. of the Int. Symp. on the occasion of Achim Richter's 60th Birthday, Darmstadt, Germany, Oct. 11-13, 2000)

Tomaselli, M.; H.-J. Kluge, T. Kühl, S. Fritzsche:
Properties of Many-Particle Systems in the Dynamic-Correlation Model: Recent Progress in Many-Body Theories
UMIST/Manchester, RPMBT-11, 131 (2001)

Toneev, V.D., J. Cleymans, E.G. Nikonov, K. Redlich, A.A. Shanenko:
Dynamical Interpretation of Chemical Freeze-Out in Heavy-Ion Collisions
J. of Phys. G 27, 827 (2001)

Toulemonde, M.; S.M.M. Ramos, H. Bernas, C. Clerc, B. Canut, J. Chaumont, C. Trautmann :
MeV Gold Irrad. Induced Damage in Alpha-Quartz: Compet. betweenNucl.+Electr. Stopping
Nucl. Instr. and Meth. in Phys. Res.B178,331(2001)

Trassel, R.; H. Bräuning, K.v. Diemar, F. Melchert, E. Salzborn, I. Hofmann:
Ion-Ion Charge Exchange Cross-Sections for Heavy Ion Fusion
Nucl. Instr. + Meth. in Phys. Res.A464,80(2001)
(Proc. of the 13th Int. Symp. on HIF, San Diego, USA, March 13.-17, 2000)

Trautmann, W.:
Hot Fragmentation of Nuclei
Nucl. Phys. A685, 233c (2001)
(Proc. of the 7th Int. Conf. on Nucleus-Nucleus Collisions, Strasbourg, France, 03.-07.07.2000 eds.: W. Nörenberg, D. Guerreau, V. Metag)

Tryggestad, E.; T. Aumann, D. Bazin, J.R. Beene, Y. Blumenfeld, M. Chartier, M.L. Halbert, P. Heckman, J.F. Liang, D.C. Radford, D. Shapira, B.M. Sherrill, M. Thoennessen, R.L. Varner:
Dipole Strength Function in ^{20}O
Nucl. Phys. A687, 231 (2001)
(Proc. of the 7th Int. Topical Conf. on Giant Resonances, Osaka, Japan, 12-15 June, 2000, eds.: T. Wasaka, M. Fujiwara, M. Nomachi, H. Ejiri)

Turchetti, G.; A. Bazzani, F. Bergamini, S. Rambaldi, I. Hofmann, L. Bongini, G. Franchetti:
Frequency Map Analysis of Resonances in a Nonlinear Lattice with Space Charge
Nucl. Instr. and Meth. in Phys. Res.A464,551(2001)

Publications

Turzo, K.; G. Auger, Ch.O. Bacri, M.L. Begemann-Blaich, N. Bellaize, R. Bittiger, F. Bocage, B. Borderie, R. Bougault, B. Bouriquet, Ph. Buchet, J.L. Charvet, A. Chbihi, R. Dayras, D. Doré, D. Durand, J.D. Frankland, E. Galichet, D. Gourio, D. Guinet, S. Hudan, B. Hurst, G. Immé, Ph. Lautesse, F. Lavaud, J.L. Laville, Ch. Leduc, A. Le Fèvre, R. Legrain, O. Lopez, J. Lukasik, U. Lynen, W.F.J. Müller, L. Napas, H. Orth, E. Plagnol, G. Raciti, E. Rosato, A. Saija, C. Schwarz, W. Seidel, C. Sfienti, J.C. Steckmeyer, G. Tabacaru, B. Tamain, W. Trautmann, A. Trczinski, E. Vient, M. Vigilante, C. Volant, B. Zwieglinski (ALADIN and INDRA Coll.):
Spectator Fragmentation Induced by Relativistic ^{12}C Projectiles
Ricerca Scientifica ed Educazione Permanente, Suppl. No. 117, p.152 (2001)
(Proc. 'XXXIX Int. Wint. Meet. on Nucl. Phys., Bormio, Italy,22-27. Jan. 01, eds.: I.Iori, A.Moroni)

Varentsov, D.; P. Spiller, U.N. Funk, D.H.H. Hoffmann, A. Kozyreva, N. Tahir, C. Constantin, E. Dewald, J. Jacoby, U. Neuner, S. Udrea, R. Bock:
Time-Resolved Energy Loss Spectroscopy of Energetic Heavy Ion Beams Generating a Dense Plasma
Nucl. Instr. and Meth. in Phys. Res.B174,215(2001)

Werth, G.; H. Häffner, N. Hermanspahn, H.-J. Kluge, W. Quint, J. Verdu:
The g-Factor of Hydrogenic Ions: A Test of Bound State QED
Lecture Notes in Physics 570, 207 (2001)
(Proc. of the 'Conf. Hydrogen II, Castiglione delle Pescaia, Italy, June 2000, eds.: S. Karshenboim, F. Pavone)

Werth, G.; H. Häffner, H.-J. Kluge, W. Quint, T. Valenzuela, J. Verdu:
A Possible New Value, for the Electron Mass from g-Factor Measurements on Hydrogen-Like Ions
Hyperfine Interactions, 132, 209 (2001)
(Proc. of the APAC2000, Cargèse, Frankreich)

Wirtz, Ch.; J.V. Kratz, W. Brüchle, M. Schädel:
Excitation Energy Division in ^{51}V+^{197}Au Collisions 75MeV above the Barrier
Radiochim. Acta 89, 689 (2001)

Wiss. T.; H. Matzke, V.V. Rondinella, T. Sonoda, W. Assmann, M. Toulemonde, C. Trautmann:
Damage Produced in Magnesium Aluminate Spinel by High Energy Heavy Ions Including Fission Products of Fission Energy: Microstructure Modifications
Prog. Nucl. Energy, 38, 281 (2001)

Wrzesinski, J.; K.H. Maier, R. Broda, B. Fornal, W. Krolas, T. Pawlat, D. Bazzacco, S. Lunardi, C. Rossi Alvarez, G. de Angelis, A. Gadea, J. Gerl, M. Rejmund:
High-Spin States in ^{208}Pb
Eur. Phys. J. A10, 259 (2001)

Yerokhin, V.A.; V.M. Shabaev, T. Beier, J. Eichler:
Calculation of the Interelectronic-Interaction Correction to Radiative Recombination of an Electron with a Heavy He-Like Ion
Hyperfine Interactions, 132, 393 (2001)
(Proc. of the APAC2000, Cargèse, Frankreich)

Zwieglinski, B.; T. Odeh, C. Gross, C. Schwarz, R. Bassini, M. Begemann-Blaich, S. Fritz, S.J. Gaff-Ejakov, D. Gourio, G. Imme, I. Iori, U. Kleinevoss, G.J. Kunde, W.D. Kunze, U. Lynen, V. Maddalena, M. Mahi, A. Moroni, T. Möhlenkamp, W.F.J. Müller, C. Nociforo, B. Ocker, F. Petruzzelli, J. Pochodzalla, G. Raciti, G. Riccobene, F.P. Romano, S. Saija, H. Sann, M. Schnittker, A. Schüttauf, W. Seidel, V. Serfling, C. Sfienti, W. Trautmann, A. Trzcinski, G. Verde, A. Wörner, Hongfei, Xi:
Interplay of Equilibrium and Nonequilibrium Phenomena in the Nuclear Liquid-Gas Phase Transition
Nucl. Phys. A681, 275c (2001)
(Proc. of the 3rd Catania Relativistic Ion Study, Acicastello, Italy, May 22-26, 2000)

GSI-Reports and Preprints

Reports

2001-01
Grundinger, U.(ed.):
Scientific Report 2000

2001-02
Hollinger, R.; L. Dahl, F. Heymach, P. Spädtke:
Transversale Emittanzmessungen am Injektor Nord

2001-03
A. D'Elia
Study and Realization of a Digital Notch Filter for the TFS in the SIS

2001-04
Weyrich, K. (ed.):
High Energy Density in Matter Produced by Heavy Ion Beams
(Annual Report 2000)

2001-05
Fehrenbacher, G.; F. Gutermuth, T. Radon:
Berechnungen zum baulichen Strahlenschutz für die geplante Schwerionentherapieanlage in Heidelberg

2001-06
Radon, T.; Yu.N. Novikov, H. Geissel, G. Münzenberg, F. Attallah, K. Beckert, T. Beha, F. Bosch, H. Eickhoff, M. Falch, B. Franzke, Y. Fujita, M. Hausmann, F. Herfurth, H. Irnich, H.C. Jung, Th. Kerscher, O. Klepper, H.-J. Kluge, C. Kozhuharov, Yu.A. Litvinov, K.E.G. Löbner, F. Nickel, F. Nolden, Z. Patyk, H. Reich, C. Scheidenberger, W. Schwab, B. Schlitt, M. Steck, K. Sümmerer, A.H. Wapstra, Th. Winkler, H. Wollnik:
Schottky Mass Measurements of Cooled Nuclei and Mass Landscape of the New Area of Neutron-Deficient Sub-Uranium Nuclides

Preprints

2001-01
Stöwe, S.; U. Neuner, R. Bock, M. Dornik, V.E. Fortov, U.N. Funk, M. Geissel, S. Golubev, D.H.H. Hoffmann, M. Kulish, V. Mintsev, M. Roth, B. Sharkov, A. Shutov, P. Spiller, M. Stetter, W. Süss, N.A. Tahir, A. Tauschwitz, V. Yakushev:
Heavy Ion Induced Hydrodynamic Motion in Lead Targets

2001-02
Reinhard, P.-G., M. Bender, J.A. Maruhn:
Mean-Field Models and Superheavy Elements

2001-03
Bender, M.:
Extrapolation of Mean-Field Models to Superheavy Nuclei

2001-04
Jurado, B.; A. Heinz, A. Junghans, K.-H. Schmidt, J. Benlliure, T. Enqvist, F. Rejmund:
New Results on Dissipation in Fission
Ricerca Scientifica ed Educazione Permanente, Suppl. No. 117, p.238 (2001)
(Proc. 'XXXIX Int. Wint. Meet. on Nucl. Phys.', Bormio, Italy, 22-27. Jan. 01,eds.: I.Iori, A.Moroni)

2001-05
Armbruster, P.:
Lise Meitner (1878-1968)
"Mother of Nuclear Structure Physics"
Ricerca Scientifica ed Educazione Permanente, Suppl. No. 117, p.1 (2001)
(Proc. 'XXXIX Int. Meet. on Nucl. Phys.', Bormio, Italy, 22-27. Jan. 2001, eds.: I. Iori, A. Moroni)

2001-06
Mukha, I.G.; G. Schrieder:
Two Proton Radioactivity of ^{19}Mg as a Genuine Three-Particle Decay
(Proc. of the Int. Conf. on Phys. with Radioact. Ion Beams ISOL '01, Oak Ridge, USA, March 2001)

GSI-Reports and Preprints

2001-07
Borcea, R.; J. Äystö, E. Caurier, P. Dendooven, J. Döring, M. Gierlik, M. Gorska, H. Grawe, M. Hellström, Z. Janas, A. Jokinen, M. Karny, R. Kirchner, M. La Commara, K. Langanke, G. Martinez-Pinedo, P. Mayet, A. Nieminen, F. Nowacki, H. Penttilä, A. Plochocki, M. Rejmund, E. Roeckl, C. Schlegel, K. Schmidt, R. Schwengner, M. Sawicka:
Beta Decay of ^{56}Cu
Nucl. Phys. A695, 69 (2001)

2001-08
Ricciardi, M.V.; K.-H. Schmidt, J. Benlliure, T. Enqvist, F. Rejmund, P. Armbruster, F. Ameil, M. Bernas, A. Boudard, S. Czajkowski, R. Legrain, S. Leray, B. Mustapha, M. Pravikoff, C. Stephan, L. Tassan-Got, C. Volant:
Light Nuclides Observed in the Fission and Fragmentation of ^{238}U
Ricerca Scientifica ed Educazione Permanente, Suppl. No. 117, p.224 (2001)
(Proc. 'XXXIX Int. Wint. Meet. Nucl.Phys.', Bormio, Italy, 22-27. Jan.01, eds.:I.Iori,A.Moroni)

2001-09
Bender, M.; W. Nazarewicz, P.-G. Reinhard:
Shell Stabilization of Super- and Hyperheavy Nuclei without Magic Gaps

2001-10
Jeon, S.; V. Koch, K. Redlich, X.-N. Wang:
Fluctuations of Rare Particles as a Measure of Chemical Equilibration

2001-11
Leistenschneider, A.; T. Aumann, K. Boretzky, D. Cortina, J. Cub, U. Datta Pramanik, W. Dostal, Th.W. Elze, H. Emling, H. Geissel, A. Grünschloß, M. Hellström, R. Holzmann, S. Ilievski, N. Iwasa, M. Kaspar, A. Kleinböhl, J.V. Kratz, R. Kulessa, Y. Leifels, E. Lubkiewicz, G. Münzenberg, P. reiter, M. Rejmund, C. Scheidenberger, C. Schlegel, H. Simon, J. Stroth, K. Sümmerer, E. Wajda, W. Walus, S. Wan:
Photo-Neutron Cross Sections for Unstable Neutron-Rich Oxygen Isotopes
Phys. Rev. Lett. 86, 5442 (2001)

2001-12
Lutz, M.F.M.; E.E. Kolomeitsev:
Relativistic Chiral SU(3) Symmetry, Large N_c Sum Rules and Meson-Baryon Scattering

2001-13
Lutz, M.F.M.; E.E. Kolomeitsev:
Covariant Meson-Baryon Scattering with Chiral and Large N_c Constraints
Found. Phys. 31, 1671 (2001)

2001-14
Redlich, K.:
Strangeness Production in Heavy Ion Collisions

2001-15
Braun-Munzinger, P.; D. Magestro, K. Redlich, J. Stachel:
Hadron Production in Au-Au Collisions at RHIC

2001-16
Redlich, K. ; A. Tounsi:
Strangeness Enhancement in Heavy Ion Collisions

2001-17
Redlich, K.; J. Cleymans, H. Oeschler, A. Tounsi:
Conservation Laws and Particle Production in Heavy Ion Collisions

2001-18
Lutz, M.F.M.; C.L. Korpa:
Self Consistent Propagation of Hyperons and Antikaons in Nuclear Matter Based on Relativistic Chiral SU(3) Dynamics

2001-19
Jurado, B.; K.-H. Schmidt, K.-H. Behr:
Application of a Secondary-Electron Transmission Monitor for High-Precision Intensity Measurements of Relativistic Heavy-Ion Beams

2001-20
Geissel, H.; H. Gilg, A. Gillitzer, R.S. Hayano, S. Hirenzaki, K. Itahashi, M. Iwasaki, P. Kienle, M. Münch, G. Münzenberg, W. Schott, K. Suzuki, D. Tomono, H.Weick, T. Yamazaki, T. Yoneyama:
Deeply Bound 1s and 2p Pionic States in ^{205}Pb and Determination of the s-Wave Part of the Pion-Nucleus Interaction

GSI-Reports and Preprints

2001-21
Hees, van H.; J. Knoll:
Renormalization in Self-Consistent Approxim. Schemes at Finite Temperature I: Theory

2001-22
Chulkov, L.V. for the S135 Collaboration:
What can we Learn from the Fragmentation of Halo Nuclei?

2001-23
Benlliure, J.; P. Armbruster, M. Bernas, A. Boudard, T. Enqvist, R. Legrain, S. Leray, F. Rejmund, K.-H. Schmidt, C. Stephan, L. Tassan-Got, C. Volant:
Signatures of Fission Dynamics in Highly Excited Nuclei Produced in ^{197}Au(800 A MeV) on Proton Collisions

2001-24
Kraft, S.; A. Bleile, P. Egelhof, R. Golser, O. Kisselev, W. Kutschera, V. Liechtenstein, H.J. Meier, A. Priller, A. Shrivastava, P. Steier, C. Vockenhuber, M. Weber:
Calorimetric Low Temperature Detectors for Mass Identification of Heavy Ions

2001-25
Bleile, A.; P. Egelhof, S. Kraft, D. McCammon, H.J. Meier, A. Shrivatava, C.K. Stahle, M. Weber:
Calorimetric Low-Temperature Detectors for High Resolution X-Ray Spectroscopy on Stored Highly Stripped Heavy Ions

2001-26
Meister, M.; K. Markenroth, D. Aleksandrov, T. Aumann, T. Baumann, M.J.G. Borge, L.V. Chulkov, D. Cortina-Gil, B. Eberlein, Th.W. Elze, H. Emling, H. Geissel, M. Hellström, B. Jonson, J.V. Kratz, R. Kulessa, A. Leistenschneider, I. Mukha, G. Münzenberg, F. Nickel, T. Nilsson, G. Nyman, M. Pfützner, V. Pribora, A. Richter, K. Riisager, C. Scheidenberger, G. Schrieder, H. Simon, O. Tengblad, M.V. Zhukov:
^{8}He – ^{6}He: A Comparative Study of Electromagnetic Fragmentation Reactions

2001-27
C. Mazzocchi, Z. Janas, J. Döring, M. Axiotis, L. Batist, R. Borcea, D. Cano-Ott, E. Caurier, G. de Angelis, E. Farnea, A. Faßbender, A. Gadea, H. Grawe, A. Jungclaus, M. Kapica, R. Kirchner, J. Kurcewicz, S.M. Lenzi, T. Martinez, I. Mukha, E. Nacher, D.R. Napoli, E. Roeckl, B. Rubio, R. Schwengner, J.L. Tain, C.A. Ur:
First Measurement of β-Decay Properties of the Drip-Line Nucleus ^{60}Ga
Eur. Phys. J. A12, 269 (2001)

2001-28
Redlich, K.; V. Koch, A. Tounsi:
Chemical Equilibration of U(1) Charged Particles in a Thermal Environment

2001-29
Enqvist, T.; P. Armbruster, J. Benlliure, M. Bernas, A. Boudard, S. Czajkowski, R. Legrain, S. Leary, B. Mustapha, M. Pravikoff, F. Rejmund, K.-H. Schmidt, C. Stéphan, J. Taieb, L. Tassan-Got, F. Vivés, C. Volant, W. Wlazlo:
Primary Residue Production Cross Sections and Kinetic Energies in AGeV ^{208}Pb on Deuteron Reactions

2001-30
Lutz, M.F.M. ; Gy. Wolf, B. Friman:
Scattering of Vector Mesons off Nucleons

2001-31
Hees, van H.; J. Knoll:
Renormalization of Self-Consistant Approximation Schemes at Finite Temperature II: Applications to the Sunset Diagram

2001-32
Bock, R.:
Inertialfusion mit Schwerionenstrahlen

Invited Talks at Conferences

Aarhus, Denmark: APAC, 08.-13.09.2001

T. Beier
Theory of the Electronic g Factor in Hydrogenlike Ions – Towards a Promisiong Tool for Determing Fundamental and Nuclear Constants

F. Bosch
Astrophysical Impact of Beta Decay of Highly Charged Ions

G. Kraft
Tumortherapy with Relativistic Ion Beams Including the Use of Heavy-Ion Storage Rings

W. Quint
The g-Factor of a Bound Electron in Hydrogen-Like Systems

M. Steck
Overview of Machine Developments in Magnetic Storage Rings

Th. Stöhlker
Structure and Dynamics of High-Z Ions Studied in Relativistic Atomic Collisions at the ESR Storage Ring

Aguas de Lindoia, Brazil: XXIV Braz. Workshop on Nucl. Phys., 01.-05.09.2001

H. Emling
Experiments with Radioactive Beams at GSI

Archamps, France: European School of Medical Physics, 08.-11.11.2001

M. Krämer
From Ion Tracks to Ion Radiotherapy

Bad Blankenburg, Germany: Sommerschule über Ionenstrahlen und Nukleare Sonden, 23.-28.09.2001

C. Trautmann
Material Modification Induced by MeV-GeV Ion Beams

Bad Honnef, Germany: Workshop on Beam Cooling and Related Topics, ECOOL 2001, 13-18.05.2001

N. Angert
Proposal for an Accelerator Complex for Energetic Ion Beams of Highest Intensity and Quality

M. Steck
Low Energy Electron Cooling

Bad Honnef, Germany: Symp.on Fundamental Issues in Elementary Matter, 25.-29.09.2001

S. Hofmann
Advances in the Search for Superheavy Elements at GSI

Bad Liebenzell, Germany: Neutrino Workshop 20.01.2001

W. Quint
Precision Measurements of the ^{3}He-Tritium Mass Difference in Penning Traps

Baikal Lake, Russia: Int. Symp. on Exotic Nuclei (EXON-2001), 24.-28.07.2001

S. Hofmann
Superheavy Elements at SHIP – New Results and Technical Developments

G. Münzenberg
GSI – Next Generation Exotic Beam Facility

Belgodere, France: XIIIth Colloque GANIL, 17.-22.09.2001

C. Schwarz
Space Time Extent of Fragmenting Nuclei

Berkeley, USA: Int. Nuclear Physics Conference INPC2001, 30.07.-03.08.2001

T. Haberer
Advances in Charged Particle Therapy

S. Hofmann et al.
Effect of the Entrance Channel on the Synthesis of Superheavy Elements

F. Lavaud (INDRA-ALADIN Coll.)
Nuclear Multifragmentation and the Onset of Radial Flow: a Study of Au+Au Collisions between 40 and 100MeV/A

J. Lukasik
Transverse Velocity Scaling in Au+Au Midrapidity Emissions

Berlin, Germany: 7th Europ. Conf. on Atomic and Molecular Physics (ECAMP7), 02.-06.04.2001

W. Quint
High-Accuracy Determination of the Atomic Mass of the Electron

Bormio, Italy: XXXIX Int. Winter Meeting on Nucl. Phys. 22.-27.01.2001

A.S. Botvina
Statistical Evolution of Fragment Isospin in Nuclear Multifragmentation

F. Lavaud, INDRA-ALADIN Coll.
Multifragmentation and Radial Flow in Au+Au Central Collisions between 40 and 100 AMeV

J. Lukasik
Some Gross Features of Non-Central Heavy-Ion Collisions. First Results of the INDRA@GSI Campaign

Invited Talks at Conferences

K. Turzo
Spectator Fragmentation Induced by Relativistic ^{12}C Projectiles

Casta-Papiernicka, Slovakia: 5th Conf. on 'Dynamical Aspects of Nuclear Fission', 23.-27.10.2001

K. Turzo
Multipfragmentation Processes at GSI

Catania, Italy: Int. Workshop on Multifragmentation and Related Topics 2001 (IWM2001), 28.11.-01.12.2001

A.S. Botvina
Statistical Properties of Fragment Isospin in Multifragmentation

J. Lukasik
Au+Au Collisions at 40-150 MeV/Nucleon: From Peripheral to Central (INDRA@GSI)

Al.H. Raduta
Thermodynamical Properties of Finite Extensive and Nonextensive Systems

Al.H. Raduta
Critical-Like Behaviour in Finite Nuclear Systems

W. Trautmann
Experiments at GSI with ALADIN

Chicago, USA: Particle Accelerator Conference, 18.-22.06.2001

R. Eichhorn
RF Strukture for Linear Acceleration of Radioactive Beams

W. Henning
Nuclear Physics – Future Directions

M. Steck
Extremely Cooled Ion Beams in the ESR with Evidence of Ordering

Chicago, USA: Symp. 'Fast Ion Stopping and Collection in Gas' ACS Meeting, 26./27.08.2001

H.-J. Kluge
The Isoltrap Triple-Trap Mass Spectrometer at ISOLDE and the SHIPTRAP Project at GSI

Copenhagen, Denmark: Radioactive Beam Research – Status in a Fifty-Year Perspective, 23.-24.11.2001

W. Henning
Status of the GSI's RIB Program and Plans for the Upgrade

Darmstadt, Germany: Komitee für Hadronen und Kernphysik, 16.07.2001

S. Hofmann
Superheavy Elements

Darmstadt, Germany: FLNR-GSI Coll. Meeting, 05.12.2001

R. Eichhorn
Dedicated cw Linac for the Synthesis of SHE

Dourdan, France: NuPECC-Workshop on Nuclear Science, 22.11.2001

W. Quint
The Impact of Nuclear Physics on Atomic Physics and Solid-State Physics (and vice versa)

Dresden, Germany: European Radiation Research 01.-04.09.2001

G. Kraft
Unconventional Radiation Quality – Heavy Charged Particles

East Lansing, USA: Workshop on Heavy Ion Reactions and Matter under Extreme Conditions, 16./17.11.2001

W. Traurmann
Isoscaling of Light-Ion Induced Data and Interpretation

W. Trautmann
Transverse Velocities in Au+Au

Frankfurt, Germany: Strange Quarks in Matter, 24.-29.09.2001

F. Bosch
The Experimental Programme at GSI

W. Henning
The Future Physics of GSI

P. Senger
The Compressed Baryonic Matter Experiment at the Future Facility at GSI

Freiberg, Germany: Arbeitstreffen "Forschung mit nuklearen Sonden und Ionenstrahlen (FRI2001)", 03.-05.10.2001

R. Neumann
Neue GSI-Arbeiten zur Ionenspur-Analyse in Halogenidkristallen und Graphit

Geneva, Switzerland: Workshop on Radioactive Antiprotonic and Muonic Atoms, 23.02.2001

H.-J. Kluge
Ion Traps and RFQ's for Radioactive Isotopes

Invited Talks at Conferences

Geneva, Switzerland: ISOLDE, 20-22.09.2001

E. Roeckl
News on N≅Z Nuclei: Recent Results from GSI

Geneva, Switzerland: Eurotraps Network Meeting, 13.10.2001

T. Beier
QED: Theory and Tests

Giessen, Germany: Workshop on Strong Non-Equilibrium Matter, 08.-10.11.2001

P. Danielewicz
Partons in Physe Space

H. van Hees
Renormalization of Selfconsistent Conserving Approximations

J. Knoll
Exact Conservation Laws in Quantum Transport of Particles and Resonances

V. Koch
Fluctuations in Ultrarelativistic Heavy-Ion Collisions

Grenoble, France: 5th Europ. Workshop on Beam Diagnostics and Instrumentation, 13.-15.05.2001

F. Nolden
Instrumentation and Diagnostics Using Schottky Signals

Groningen, The Netherlands: Workshop on Strangeness at KVI, 02./03.11.2001

M. Lutz
Strange Chiral QCD with Large Number of Colors and Meson-Baryon Scattering

P. Senger
The Strangeness Program at GSI

Hämeenlinna, Finland: 3rd Int. Conf. on Exotic Nuclei and Atomic Masses, ENAM 2001, 02.-07.07.2001

T. Beier
The Measurement of the Electronic g Factor in Hydrogenlike Ions – Towards a Promising Tool for Determing Fundamental and Nuclear Constants

P. Egelhof
Exotic Nuclei and Atomic Masses

S. Hofmann
Status and Properties of Synthesizing Superheavy Elements

E. Roeckl
Decay Properties of N≅Z Nuclei

C. Scheidenberger
Direct Mass Measurements of Exotic Nuclei

K.-H. Schmidt
Fission Studies with Relativistic Beams

Hasliberg,Switzerland: 5th Workshop on the Chemistry of the Heaviest Elements, 26.-29.08.2001

S. Hofmann
Investigations of Superheavy Elements at SHIP

M. Schädel
Recoil Separators for Superheavy Element Chemistry

Heidelberg, Germany: Graduierten Kolleg, 15.-19.10.2001

F. Bosch
Nuclear Astrophysics at the ESR

Hirschegg, Austria: Int. Workshop XXIX on Gross Properties of Nuclei and Nuclear Excitations, Structure of Hadrons, 14.-20.01.2001

K. Beckert, P. Beller, O. Boine-Frankenheim, A. Dolinski, B. Franzke, F. Nolden, M. Steck
An Accelerator Complex for Antiprotons at GSI

W. Henning
Hadrons and Nuclei: Concept of the Future GSI-Facilities

P. Senger
Strangeness and Charm Production in Nucleus-Nucleus Collisions at Beams Energies near the Thresholds

Hirschegg, Austria: Physics of High Energy Density in Matter, 28.01.-03.02.2001

W. Henning
The GSI Project

Irkutsk, Russia: Int. Conf. EXON-2001, 23.-27.06.2001

H. Geissel
Experiments with Stored Rare Isotopes

Jaipur, India: Workshop on Surface Modification and Characterization by Energetic Ion Beams, 23./24.11.2001

R. Neumann
Analysis of Heavy Ion Damage in Fluoride Single Crystals and Graphite

Jyväskylä, Finland: Euro Summer School, 24.-30.06.2001

W.K. Weyrather
Medical Applications of Accelerated Ions

Invited Talks at Conferences

Kerkrade, The Netherlands: EURESCO Conf. 'Rel. Effects in Heavy-Element Chemistry and Physics', 21.-26.04.2001

T. Beier
Theory for the g Factor of the Electron in Hydrogen-Like Ions and a New Value for the Electron Mass

V. Pershina
Theoretical Predictions of Chemical Properties of the Heaviest Elements

M. Schädel
Superheavy-Element Chemistry – Where do we Stand Experimentally?

Krzyze, Poland: Masurian School of Physics, 02.-09.09.2001

P. Senger
The Strangeness and Charm of Hot and Dense Matter

Kyoto, Japan: 2nd Int. Conf. on Inertial Fusion Sciences and Applications, 09.-14.09.2001

I. Hofmann
The Potential of Heavy Ion Drivers for Inertial Fusion

Kyoto, Japan: Int. Yukawa Symp. 04.-09.11.2001

H. Geissel
Present and Future Experiments with Stored Exotic Nuclei at Relativistic Energies

Kyoto, Japan: Workshop on Ion Beam Cooling – Towards the Realization of Crystalline Beams, 12.-14.11.2001

R.W. Hasse
Multiple Coulomb Strings in Storage Rings

Lanzhou, China: Int. Workshop on Nuclear Physics with RIB, 28.-31.08.2001

T. Aumann
Nuclear Structure of Light Neutron-Rich Nuclei Investigated via Reactions with Fast Secondary Beams

O. Klepper
Measurements of Nuclear Masses and Half-Lives in the Cooler-Storage Ring ESR

G. Münzenberg
Studies of Exotic Nuclei at GSI – The GSI Program and its Future Perspectives

Legnaro, Italy: Int. Meeting on Gamma Spectroscopy, 02.-03.04.2001

H. Geissel
Atomic Interaction of Heavy Ions with Matter Placed in Optical Systems

Lipari, Italy: Int. Conf. on Nuclear Physics at Border Lines, 21.-24.05.2001

S. Hofmann
Recent Experiments and Plans for the Synthesis of Superheavy Elements at the GSI SHIP

Lisboa, Portugal: XIX Autumn School "New Perspectives with Nuclear Radioactivity", 08.-13.10.2001

S. Hofmann
Superheavy Elements

G. Kraft
Ion Beam Treatment of Cancer

Lyon, France: INDRA Coll. Meeting, 08.12.2001

M.V. Ricciardi
Determination of the Freeze-Out Temperature in the Fragmentation of Relatiovistic ^{238}U Projectiles by Means of the Isospin Thermometer

Manchester, United Kingdom: Int. Proton Therapy Consensus Meeting, 03.09.2001

W.K. Weyrather
Heavy Ion Therapy

Milano, Italy: LXXXVII Congr. Naz. Soc. Ital. di Fisica, 24.-29.09.2001

C. Sfienti
Liquid-Gas Phase Transition in Nuclear Matter: Results and Perspectives

New Dehli, India: Accelerator Based Research in Basic & Applied Sciences, 24.-27.02.2001

W. Henning
Basic and Applied Research with Beams of Unstable Nuclei

Oak Ridge, USA: ISOL 01, 11.-14.03.2001

W. Henning
Keynote Talk on the Physics of Radioactive Ion Beams

E. Roeckl
Deacy Properties of N≅Z Nuclei: Progress Report from the GSI-ISOL-Facility

Invited Talks at Conferences

Odense, Denmark: Int. Meeting STOP01, 18.04.2001

H. Geissel
Slowing-Down Experiments of Heavy Ions in the keV/u to GeV/u Energy Range

Orsay, France: Workshop on Direct Reactions with Exotic Beams, DREB, 27.-29.06.2001

T. Aumann
Dipole Excitations in Exotic Nuclei

P. Egelhof
Elastic Proton Scattering off Halo Nuclei at Intermediate Energies

Paris, France: ICACS 19, 29.07.-03.08.2001

G. Kraft
Hadron Therapy: Ion Beam Interactions with Living Tissue

Pommersfelden, Germany: Arbeitstreffen Hadronen und Kerne,24.-28.09.2001

R. Eichhorn
Beschleunigerentwicklung am Institut für Angewandte Physik Frankfurt

Pula, Croatia: NATO Adv. Research Workshop, The Nuclear Many-Body Problem 2001, 02.-05.07.2001

G. Münzenberg
Superheavy Elements – Results and Challenges

Puri, India: Int. Workshop on 'Production with Rare Isotope Beams', 12.-17.02.2001

H. Emling
Nuclear Reactions with Rare Isotope Beams at GSI

Sandanski, Bulgaria: 2nd East-West Coordination Meeting on Nuclear Science, 05.-09.05.2001

S. Hofmann
Prospects of Synthesizing Superheavy Elements at GSI

G. Münzenberg
Exotic Nuclei from Projectile Fragmentation – The GSI Program and its Future Perspectives

San Diego, USA: 221th ACS Nat. Meeting, 01.-05.04.2001

S. Hofmann
Synthesis of Superheavy Elements at the GSI SHIP

M. Schädel
From "SHE" to "SHE" at GSI – A Historical Perspective of 25 Years of Nuclear Chemistry at GSI

K. Sümmerer
Isospin Effects in the Formation of Heavy Fragments at Relativistic Energies

W. Trautmann
Freeze-Out in Gold on Gold

San Diego, USA: Workshop on Nonneutral Plasmas, 30.07.-02.08.2001

R.W. Hasse
Single and Multiple Coulomb Strings in Heavy Ion Storage Rings

Santa Tecla, Italy: European Summer School, 01.-06.10.2001

G. Münzenberg
Recoil Mass Separators

Schleching, Germany: Expertentreffen, 01.-08.03.2001

P. Senger
Mesonenproduktion in Schwerionenstößen

Semmering, Österreich: Meeting der Österr. Ges. f. Radiobiologie u. med. Radiophysik, 05.10.2001

W.K. Weyrather
Die Relative Biologische Wirksamkeit (RBW)

Snowmass, USA: Summer Study on the Future of Particle Physics, 30.6.-21.07.2001

I. Hofmann
Coulomb Effects in High Intensity Drivers

Strasbourg, France: Workshop on Future of Nuclear Structure and Gamma Spectroscopy with Stable Beams, 07./08.06.2001

S. Hofmann
Present and Future of Superheavy Elements

Strasbourg, France: SFP2001, 11.07.2001

W. Henning
Perspectives and Projects for Heavy Ions

Tokai, Japan: The 2nd Int. Symp. on Advanced Science Research 'Advances in Heavy Element Research', (ASR2001) 13.-15.11.2001

G. Münzenberg
SHE Research at GSI – Achievements and Plans

V. Pershina
Theoretical Study of the Chemistry of the Heaviest Elements: Recent Results

M. Schädel
The Chemistry of Transactinide Elements – Experimental Achievements and Perspectives

Invited Talks at Conferences

M. Schädel
Conference Summary

K.-H. Schmidt
Experiments on Fission Dynamics with Relativistic Heavy-Ion Beams

Trento, Italy: Int. Workshop on Reaction Meachanisms with Exotic Nuclei, 19.02.-02.03.2001

T. Aumann
Exclusive Measurements of Reactions with High-Energy Exotic Beams

Trento, Italy: Rama Workshop at ETC, 22.05.2001

W. Quint
Ion Trap Technology

Trento, Italy: Int. Workshop on Very Heavy Nuclear Systems, 09.-14.07.2001

G. Münzenberg
GSI Future Plans

V. Pershina
Relativistic Atomic and Molecular Electronic Structure Calculations for the Very Heavy Elements

Trento, Italy: ECT Workshop "Current Theoretical and Experimental Investigations of the Nuclear Many-Body Problem and Applications, 24.09.-03.10.2001

H. Grawe
Shell Structure in Exotic Nuclei – An Experimental Status Report

Trento, Italy: Workshop on the Physics of Halo Nuclei, 04.-12.10.2001

T. Aumann
Dipole Excitations of Neutron Halos and Skins

K.L. Jones
Invariant Mass Spectroscopy of the Unbound Nucleus 13 Be

Tsukuba, Japan: Workshop on RF Superconductivity 06.-11.09.2001

R. Eichhorn
Superconducting CH-Cavities for Low- and Medium Beta Ion and Proton Accelerators

Tsukuba, Japan: Int. Conf. on Nuclear Data for Science and Technology (ND2001), 07.-12.10.2001

G. Münzenberg
Frontiers of Heavy-Ion Physics and Superheavy Elements

Uppsala, Sweden: The Svedberg Lab. Workshop on Applied Physics, 03.05.2001

C. Trautmann
Material Modification Induced by MeV-GeV Ion Beams

Victoria, Canada: Canadian Ass. of Physicists Meeting (CAP2001), 17.-20.06.2001

H.-J. Kluge
High-Accuracy Experiments with Ions Confined in Storage Rings and Ion Traps

Washington DC, USA: MENU 2001, 26.-31.07.2001

M. Lutz
The χ-BS(3) Approach

Weimar, Germany: Symposium, Rhön Klinikum, 15.06.2001

G. Kraft
Mit Ionenstrahlen gegen Krebs

Würzburg, Germany: Jahrestagung Chemie 2001, 23.-29.09.2001

G. Münzenberg
Die Physik der schwersten Elemente

Invited Talks at other Institutes

Aumann, T.:

Dipole Excitations of Neutron-Rich Exotic Nuclei
IPN Orsay, Univ. Paris-Sud, France, 20.09.2001
Reaction Studies with Relativistic Radioactive Beams
Serv. de Phys. Nucl., CEA Saclay, France, 17.10.2001

Beier, T.:

Naturwissenschaft enthüllt die Geheimnisse antiker Schönheit: Woher bezog Nofretete ihr Parfum?
University of Kassel, Germany, 29.11.2001

Berdermann, E.:

Radiation-Hard, Ultra-Fast Particle Detectors made of CVD Diamond
University of Karlsruhe, Germany, 15.05.2001

Botvina, A.S.:

Statistical Disintegration of Nuclei
University of Minnesota, USA, 05.04.2001
Statistical and Dynamical Evolution of Fragment Isospin in Nuclear Multifragmentation
Ist. Naz. di Fisica Nucl. Trieste, Italy, 22.05.2001

Datta Pramanik, U.:

Coulomb Dissociation Using Unstable Nuclear Beams
Univ. of Edinburgh, United Kingdom, 31.05.2001
Structure and Reaction Studies of Exotic Neutron-Rich Nuclei at GSI
RIKEN, Tokyo, Japan, 16.11.2001
Structure and Reaction Studies of Exotic Nuclei at GSI
NSC New Dehli, India, 11.01.2001

Egelhof, P.:

Hochaufl. kalorim. Tieftemperaturdetektoren für Anwendungen in der Atom- und Kernphysik
University of Wien, Austria, 25.01.2001
Kalorimetr. Tieftemperaturdetektoren für die Schwerionenphysik – Status und Perspektiven
University of Heidelberg, Germany, 07.05.2001
Anwendungen von bolometrischen Tieftemperaturdetektoren zur direkten Massenbestimmungen von schweren Ionen
University of Wien, Austria, 09.11.2001
Kalorimetr. Tieftemperaturdetektoren für die Schwerionenphysik – Status und Perspektiven
University of Mainz, Germany, 22.11.2001

Eichhorn, R.:

Supraleitende LINAC-Strukturen und ihre Anwendungen
FZ Jülich, Germany, 09.05.2001
Entwicklung eines supraleitenden cw Linacs für GSI
University of Frankfurt, Germany, 07.03.2001
Entwicklung einer surpraleitenden CH Struktur für den mittleren Energiebereich
TU Darmstadt, Germany, 22.10.2001
Entwicklung einer supraleitenden CH Struktur für den mittleren Energiebereich
University of Rostock, Germany, 30.10.2001

Emling, H.:

Nuclear Structure Experiments with Radioactive Ion Beams at GSI
KVI Groningen, The Netherlands, 16.01.2001
Recent and Future experiments with radioactive Ion Beams at GSI
Saha Institute of Nuclear Physics, Calcutta, India, 20.02.2001

Geissel, H.:
Physics with Relativistic Exotic Nuclei
Univ. of Santiago de la Postella, Spain, 18.04.2001
Super-FRS the Next-Generation European In-Flight Facility
MSU, East Lansing, USA, 23.05.2001

Haberer, T.:

Die Schwerionentherapieanlage in Heidelberg
DKFZ, Heidelberg, Germany, 06.06.2001

Häfner, C.:
Current Status of PHELIX-Laser Setup – Design and Modelling of the Laser and the Adaptive Optics
MPQ Garching, ADAPTOOL Meet., 8./9.10.2001
Actual Status and Progress of the PHELIX-Laser Project at GSI Darmstadt
Lab. d'Opt. Appl., Palaiseau, France, 2001

Invited Talks at other Institutes

Hasse, R.W.:

Coulomketten von Ionen
University + TU München, Germany, 25.05.2001
Single and Multiple Chains of Ions in Storage Rings
Okayama University, Japan, 15.11.2001

Henning, W.:

The Structure of Matter: Concept for the Future GSI Facility
III. Nat. Scientific Committee of the INFN, Rom, Italy, 19.04.2001
The Structure of Matter: The Strong-Interaction Regime
University of Padua, Italy, 20.04.2001
Future Plans at GSI
JINR Dubna, Russia, 17.05.2001
Future Plans at GSI
Ires, Strasbourg, France, 31.05.2001
Physik der Strahlen instabiler Kerne
University of Bâle, Switzerland, 15.06.2001
Zukünftige Forschung bei der GSI Darmstadt – Beschleunigeranlage für exotische Strahlen und Antimaterie
University of Frankfurt, Germany, 31.10.2001
Neue Beschleunigerprojekte an der GSI – Perspektiven für Plasmaphysik und QCD
University of Rostock, Germany, 01.11.2001

Hofmann, I.:

Space Charge and Resonances in Non-Equi-partitioned Beams
University of Maryland, USA, 07.05.2001
The Future Project at GSI
University of Naples, Italy, 17.10.2001
Halo and Equipartition in Linacs
University of Frankfurt, Germany, 07.12.2001

Hofmann, S.:

Synthesis and Properties of the Heaviest Elements
Weizmann Institute, Rehovot, Isreal, 24.01.2001
Experimente und Pläne zur Synthese Superschwerer Elemente
LMU München, Germany, 01.06.2001
Die Erweiterung des Periodensystems der Elemente, Atomgewicht 500?
University of Freiburg, Germany, 29.10.2001

Jones, K.L.:

The Halo Nucleus ^{14}Be and the Unbound Nucleus ^{13}Be
Inst. of Nucl. Phys., Krakow, Poland, 19.12.2001

Kausch, C.:

Physikerinnen und Physiker im Beruf: Gleiche Chancen für Männer und Frauen
Inst. f. Metallische Werkstoffe, IFW Dresden, Germany, 01.02.2001

Klepper, O.:

Nuclear Spectroscopy at the On-Line Separator, Fragment Separator and Storage Ring
Shanghai Inst. of Nucl. Res., China, 24.08.2001
Measurements of Nuclear Masses and Half-Lives in the Cooler-Storage Ring ESR
RIKEN, Saitama, Japan, 21.09.2001

Kluge, H.-J.:

Towards Precision by Cooling: Atomic and Nuclear Physics Using Stored Particles
TIFR, Bombay, India, 13.03.2001
Nuclear Physics with Cooled Particles Stored in Ion Traps, Storage Rings and Laser Traps
BARC, Bombay, India, 14.03.2001
Towards Precision by Cooling: Atomic and Nuclear Physics Using Stored Particles
Bangalore, India, 15.03.2001
Das SHIPTRAP Projekt an der GSI
University of Mainz, Germany, 03.05.2001
Precision by Cooling: Atomic and Nuclear Physics in Small and Large Ion Traps
McGill University, Montreal, Canada, 14.09.2001
Atomic Physics at Accelerators
MSU, East Lansing, USA, 30.10.2001
High-Accuracy Atomic Physics Experiments with Stored and Cooled Particles
University of Calgary, Canada, 09.11.2001
Precision by Cooling: Atomic and Nuclear Physics in Small and Large Ion Traps
Argonne Nat. Lab., Batavia, USA, 16.11.2001
GSI Plans for a Future Facility for Physics with Heavy Ions and Antiprotons
TRIUMF, Vancouver, Canada, 20.12.2001

Kraft, G.:

Tumortherapie mit schweren Ionen
Klinikum Aschaffenburg, Germany, 07.02.2001
Clinical Revelance of Carbon Therapy
Belvoir Park Hospital, Belfast, Ireland, 21.03.2001

Invited Talks at other Institutes

Tumor Therapy with Relativistic Ions: Basic Considerations, Technical Realisation and Clinical Results
Queen's University, Belfast, Ireland, 21.03.2001
Tumor Therapy with Ion Beams
University College, Dublin, Ireland, 22.03.2001
Tumor Therapy with Relativistic Ions: Basic Considerations, Technical Realisation and Clinical Results
University College, Cork, Ireland, 23.03.2001
Therapie mit schweren Ionen
University of Stuttgart, Germany, 24.04.2001
The Relevance of High RBE for Therapy – Three Decades of Biological Research with Heavy-Ion Beams
LBNL, Berkeley, USA, 08./09.06.2001
Tumortherapie mit Ionenstrahlen
Physik. Verein, Frankfurt, Germany, 27.06.2001
Grundlagen der Tumortherapie mit schweren Ionen und erste klinische Ergebnisse
Forsch.Zentrum Karlsruhe, Germany, 13.11.2001
Radiobiology of Particles
NuPECC, Dourdan/Paris, France, 21-23.11.2001

Kühl, T.:
Status of the PHELIX Project
CESTA Le Barp, France, 20.03.2001
Adaptive Optics at the PHELIX Project
ADAPTOOL Meeting, UK, 29/30.03.2001

Lutz, M.:
Chiral SU(3) symmetry and strangeness
SQM2001, Frankfurt, 24.-29.09.2001

Neumann, R.:
Survey of Materials Research at GSI
RIKEN, Saitama, Japan, 28.02.2001
Analysis of Ion Tracks in Different Fluoride Crystals and in Highly Oriented Pyrolytic Graphite
JAERI, Tokai, Japan, 01.03.2001
Materials Research with Heavy Ions at GSI
Nucl.Scie.Centre, New Dehli, India, 19.11.2002
Analysis of Heavy-Ion Damage in Fluoride Single Crystals and Graphite
Nucl. Scie.Centre, New Dehli, India, 21.11.2001
Materials Research with Heavy Ions at GSI
Univ. of Mangalore, Mangalore, India, 28.11.2001

Neuner, U.:
The Plasma Lens: A Precision 240 kA z-Pinch and its Applications
University of Nevada, Reno, USA, 23.02.2001
The Plasma Lens: Precision Applications of a Z-Pinch
MPI Plasmaphys., Greifswald,Germany, 09.03.2001
Plasmaphysik im Großprojekt: Beschleuniger-komplex für Ionenstrahlen an der GSI
IPP Garching, Germany, 28.05.2001

Quint, W.:
Messung des magnetischen Moments des gebundenen Electrons in hochgeladenen Ionen: Ein Präzisionstest der Theorie der QED
MPI f. Kernphysik, Heidelberg, 28.06.2001
Präzisionsexperimente an einzelnen Teilchen in Ionenfallen
University of Freiburg, Germany, 19.10.2001

Schädel, M.:
Current Developments in Superheavy-Element Chemistry
JAERI, Tokai, Japan, 01.03.2001

Scheidenberger, C.:
Direkte Massenmessung exotischer Kerne am Experimentierspeicherring ESR
TU Darmstadt, Germany, 14.05.2001

Schmidt, K.-H.:
General Features of Nuclide Production in Fission
DAPNIA Saclay, Gif sur Yvette, France,13. 6. 2001

Scholz, M.:
Modellierung der biologischen Wirkung von Ionenstrahlen: Theorie und Anwendung bei der Bestrahlungsplanung für die Schwerionen-Tumortherapie
TU Dresden, Germany, 19.06.2001
Modelle zur Beschreibung der biologischen Wirksamkeit von Ionenstrahlen und ihr Einsatz in der Schwerionen-Tumortherapie
University of Homburg, Germany, 28.06.2001

Invited Talks at other Institutes

Senger, P.:
Future Experiments at SIS200/GSI
Jagiellonian Univ., Krakow, Poland, 20.05.2001
Strange Particle in Dense Nuclear Matter
Polish Phys. Soc., Krakow, Poland, 10.05.2001
The CBM Exper. at the Future Facility at GSI
University of Frankfurt, Germany, 17.05.2001
The Nucleus-Nucleus Collision Program at the Future Facility at GSI
Topical Meeting, KHuK, GSIDarmstadt, Germany, 19.10.2001
Probing Highly Compressed Baryonic Matter – the Future Facility at GSI
Garduiertenkolleg, Giessen, Germany, 01.11.2001
Seltsame Teilchen in dichter Kernmaterie – Experimente an der GSI
University of Mainz, Mainz, Germany, 17.12.2001

Steck, M.;
Experimente mit gekühlten Schwerionenstrahlen an der Beschleunigeranlage GSI
Hahn-Meitner-Inst., Berlin, Germany, 09.07.2001

Stöhlker, Th.:
Die 1s-Lambverschiebung im wasserstoffartigen Uran: Test der QED in starken elektr. Feldern
Univ. of Frankfurt, Frankfurt, Germany, 25.01.2001
Atomphysik mit gekühlten Schwerionenstrahlen am Speicherring ESR
University of Kassel, Kassel, Germany, 28.06.2001
Precision Studies for Cooled Ions: Atomic Physics at Heavy Ions Storage Rings
Lanzhou University, Lanzhou, China, Oct. 2001
Radiative Recombination in Relativistic Ion-Atom Collisions
IMP Lanzhou, Lanzhou, China, Oct. 2001

Sümmerer, K.:
Coulomb Dissociation of ^{8}B: an Alternative Method to Investigate the Production of ^{8}B in the Sun
University of Bâle, Switzerland, 08.11.2001

Trautmann, C.:
Material Modification Induced by MeV-GeV Ion Beams
University of Stuttgart, Germany, 31.05.2001

Weyrather, W.K.:
Tumortherapie mit Ionenstrahlen – Die Auswahl der Ionensorte aus biophysikalischer Sicht
HMI Berlin, Germany, 18.12.2001

Lectures and Courses

Ackermann, D.; P. Egelhof, G. Münzenberg, G. Huber:

WS2000/2001: Seminar über „Interdisziplinäre Anwendungen der Atom- und Kernphysik“
(University of Mainz, Germany)
WS2001/2002: Seminar über “Anwendungen der Atom- und Kernphysik in der Umwelt- und Medizinforschung”
(University of Mainz, Germany)

Aumann, T.:

WS2001/2002: Exotic Nuclei: From Halo Nuclei up to Superheavy Elements
(University of Mainz, Germany)

Bock, R.; D.H.H. Hoffmann, Th. Kühl, J.A. Maruhn, P. Mulser:

Physik dichter Plasmen mit Schwerionen- und Laserstrahlen
(GSI Darmstadt, Germany)

Bosch, F.:

WS2000/2001: Seminar über aktuelle Fragen der Astrophysik
WS2001/2002: Astronomie und Astrophysik I
(University of Kassel, Germany)

Egelhof, P.:

WS2000/2001: Seminar zum Praktikum für Fortgeschrittene
SS2001: Vorlesung “Kernphysikalische Aspekte der Astrophysik”
WS2001/2002: Seminar zum Praktikum für Fortgeschrittene
(University of Mainz, Germany)

Egelhof, P.; S. Kraft:

SS2001: Übungen zur Vorlesung „Kernphysikalische Aspekte der Astrophysik“
(University of Mainz, Germany)

Egelhof, P.; C. Enss:

SS2001: Seminar über Kalorimetrische Tieftemperaturdetektoren
(Univ. of Mainz and Univ. of Heidelberg, Germany)

Egelhof, P.; G. Münzenberg, Doz./EXAKT:

WS2000/2001: Seminar über „Experimentelle Atom- und Kernphysik“
SS2001: Exp. Atom- u. Kernphys.(Seminar)
WS2001/2002: Experimentelle Atom- und Kernphysik(Seminar)
(University of Mainz, Germany)

Emling, H.:

WS2001/2002: Gruppenunterricht Physik V
SS2001: Gruppenunterricht Physik III
(Univeristy of Heidelberg, Germany)

Friman, B.:

SS2001: Einführ. in die Elementarteichenphysik
WS2001/2002: Theoretische Kernphysik
(Technical University of Darmstadt, Germany)
23./24.09.2001: Hadrons in Matter
(Lec. at the Student Presymp. to Strange Quark in Matter, Univ. of Frankfurt, Germany)

Kluge, H.-J.:

WS2000/2001: Oberseminar über Atomphysik
SS2001: Oberseminar über Atomphysik
(Univ. of Heidelberg, GSI Darmstadt, Germany)
EUROSCHOOL on Exotic Beams: Atomic Physics with Exotic Nuclei
(Jyväskylä, Finland, 25-30.06.2001)
Summer Student Course: Atomic Physics (Techniques) at Accelerators)
(TRIUMF, Vancouver, Canada, 09.-20.07.2001)

Kluge, H.-J.; F. Bosch:

WS2000/2001: PhD Student Seminar
SS2001: PhD Student Seminar
(Univ. Heidelberg, GSI Darmstadt, Germany)

Kraft, G.; D. Schardt:

WS2000/2001: Strahlenphysik
(TU Darmstadt, Germany)

Kraft, G.; G. Taucher-Scholz, C. Wiese:

WS2001/2002: Molekulare Mechanismen der Strahlwirkung: DNA Brüche und Reparatur
(TU Darmstadt, Germany)

Kühl, Th.:

WS2000/2001: Physik der Ultrahochintensitäts-laser
(University of Mainz, Germany)

Lectures and Courses

Liesen, D.:

SS2001: Gruppenunterricht zur Physik IV
WS2001/2002: Oberseminar über Atomphysik
(University of Heidelberg, Germany)

Malzacher, P.:

WS2001/2002 Objektorient. Systementwicklung für Naturwissenschaftler
(University of Frankfurt, Germany)

Mokler, P.H.; N. Grün, A. Müller, E. Salzborn, K.-H. Schartner, W. Scheid:
SS2001: Seminar über Atomphysik (Graduierte)
WS2001/2002:Sem. über Atomphys.(Graduierte)
(University of Giessen, Germany)

Münzenberg, G.:

WS2000/2001: Anwend. d. Atom- u. Kernphys. in d. Umwelt- u. Medizinforschung(Seminar)
(University of Mainz, Germany)

Münzenberg, G.; C. Scheidenberger:

SS2001: Phys. mit Schwerionen – Grundlagen, Forschung u. Anwendung (Blockseminar)
(University of Mainz, Germany)

Münzenberg, G.; K.-L. Kratz, U. Ott:

Aktuelle Themen aus Kosmochemie und Astrophysik(Seminar)
(University of Mainz, Germany)

Neumann, R.:

SS2001: Materialforschung mit energiereicher Strahlung I
WS2001/2001: Materialforschung mit energiereicher Strahlung II
(University of Heidelberg, Germany)

Orth, H.:

SS2001: Struktur der Hadronen
WS20012002: Mechanik und Wärmelehre
WS2001/2002: Tutor. zur Mech. + Wärmelehre
(University of Heidelberg, Germany)

Quint, W.:

WS2000/2001: Exp. Atomphys.: Atome u. Felder
SS2001: Exp. Atomphys.: Atomare Mehrteilchensysteme
WS2001/2002: Exp. Atomphys.: Atome u. Felder
(University of Heidelberg, Germany)

Schädel, M.:

Academic Year 2000/2001: Frontiers in Chem. Research, Distinguished Lect. Series Program: Superheavy Elements – A Nuclear and Chemical Puzzle
(Texas A&M University, College Station, USA)

Scholz, M.; P. Peschke, K.J. Weber:

SS2001;WS2001/2002: Radiologischer Kurs/Strahlenbiologie
(University of Heidelberg, Germany)

Schwarz, C.:

SS2001: Praktikum für Fortgeschrittenen
WS2201/2002: Praktikum für Fortgeschrittene
(Universität Frankfurt, Germany)

Stöhlker, Th.:

WS200/2001: Schlüsselexp. der atom. Stoßphysik
SS2001: Atomphysik II
(University of Frankfurt, Germany)

Trautmann, W.; G. Walter:

WS2001/2002: Kernphysik für Studierende des Lehramtes
(University of Frankfurt, Germany)

Seminars, Workshops at GSI

09.01.
C. Constantin, TU Darmstadt, Germany
Optical Diagnostics on Heavy Ion Beam - Matter Interaction

09.01.
W. Semmler, DKFZ Heidelberg, Germany
Entwicklungen in der Radiodiagnostik: Von der Form zur Funktion

16.01.
T. Löffler, University of Frankfurt, Germany
Erzeugung von Ferninfrarot (THz) Strahlung mittels laser-generierten Plasmen

16.01.
W. Flury, ESOC Darmstadt, Germany
Space Debris - a Hazard to Spaceflight

17.01.
F. Herfurth, GSI/LMU München, Germany
Masses of Short-Lived Nuclides for Fundamental Studies

23.01.
I. Enculescu, Nat. Inst. for Mat. Phys. Bucharest, Romania
Growth of Metal Structures in Quartz Crystals by Electrodiffusion

23.01.
F. Wagner, IPP Greifswald, Germany
Tokamaks and Stellarators – Two Routes to a Fusion Reactor

24.01
C. Schulze-Briese, PSI Villigen, Switzerland
Curved Crystal Optics for Focussing and Imaging of Synchrotron Radiation

26.01
I. Hofmann, GSI Darmstadt, Germany
The (Non-) Equipartition Question in High-Intensity Linacs and Rings

26.01.
T. Barnes, Oak Ridge, USA
Meson Strong Decays

30.01.
Th. Walcher, University of Mainz, Germany
The Hadron is a Relativistic Many Body Problem

31.01.
J.R. Crespo Lopez-Urrutia, Univ. of Freiburg, Germany
Electron Beam Ion Traps: Current Status and Future Development

31.01.
P. Krafft, GSI Darmstadt, Germany
Kohärente Zustände als nicht orthogonale Basis

06.02.
W. Kutschera, University of Vienna, Austria
Ötzi, der prähistorische Eismann

07.02.
A. Voitkiv, University of Freiburg, Germany
Electron Capture in Fast Collisions Assisted by a Laser Field

07.02.
A. Schwenk, Stony Brook, USA
Low Momentum Nucleon-Nucleon Interaction and Fermi Liquid Theory

13.02.
K. Witte, MPQ Garching, Germany
Anwendungen von Femtosekundenpulsen hoher Intensität: Heiße, dichte Plasmen, schnelle Elektronen, Positronen und Neutronen

14.02.
A. Saenz, University of Konstanz, Germany
Molecules in Strong Fields: Bond Softening, Enhanced Ionisation and Coherent Control

14.02.
H. Oeschler, TU Darmstadt, Germany
Strange Particle Production from SIS to RHIC

15.02.
A. Ramirez, Mexico
TPCino Tests for the CERN HARP Experiment

Seminars, Workshops at GSI

22.02.
E. Chapochnikova, CERN Geneva, Switzerland
Studies of Microwave Instability in the CERN SPS

26.02.
V.P. Smirnov, Kurchatov Inst., Moscow, Russia
Problems of IFS

28.02.
A.V. Nefiodov, Nucl. Phys. Inst., St. Petersb., Russia
Experiments on Parity-Violation Effects at Ion Storage Rings

08.03.
J. Kaugerts, BWX Technologies, Germany
Superconductors for Accelerator Applications: The Role of Interstrand Resistance

13.03.
Y. Lashko
Angular and Energy Distributions in the Reaction of ^{6}He Photodisintegration

21.03.
V.M. Shabaev, St. Petersburg, Russia
Towards Tests of QED in Heavy Ions

28.03.
Z.-T. Lu, Argonne Nat. Lab., USA
Ultrasensitive Trace-Isotope Analysis with a Magneto-Optical Trap

28.03.
A. Schäfer, University of Regensburg, Germany
The Status of Higher Twist in Hadron Structure Physics

04.04.
J. Struckmeier, GSI Darmstadt, Germany
Canonical Transformations and Invariances in Time Dependent Classical Hamilton Systems

10.04.
S. Rohr, Steinbeis Stiftung, Stuttgart, Germany
Konzept des wettbewerblichen Technologie-transfers der Steinbeis-Stiftung

18.04
Pengfei Zhuang, Beijing+Heidelberg, China/Germany
Nonthermal Pion Enhancement with Chiral Symmetry Restoration

24.04.
E. Förster, University of Jena, Germany
Laserproduzierte Plasmen: Röntgendiagnose sowie Anwendung als Blitzquelle

24.04.
W. Heil, University of Mainz, Germany
Spin Polarized ^{3}He: from Nuclear Physics to NMR Tomography

27.04.
R. Klingenberg, University of Bern, Switzerland
The NA52 Experiment: Strangelet Search and Particle Production Studies in Pb+Pb Collisions

04.05.
Th. Peitzmann, University of Münster, Germany
Facets of High Energy Heavy Ion Physics: Selected Results of the Exp. WA80/93 and WA98

08.05.
H. Lesch, LMU München, Observatory, Germany
Coherent Radiation from Pulsars

08.05.
G. Soff, TU Dresden, Germany
The Many Facets of Atomic Phyiscs in Strong Fields

10.05.
T. Kambara, RIKEN, Japan
Observation of Elastic Waves Generated by Fast Heavy Ions in Solids – Ion Beam Acoustics

15.05.
R. Stock, University of Frankfurt, Germany
The Parton-Hadron Phase Transition

15.05.
D. Habs, TU München, Germany
Laserbeschleunigung und Lasertransport von Teilchenstrahlen

Seminars, Workshops at GSI

16.05.
Ch. Trautmann, GSI Darmstadt, Germany
Schwerioneninduzierte Materialveränderungen

17.05.
G. Tsiledakis, University of Thessaloniki, Greece
Living Matter as a Detector of Weakly Interacting Radiation

21.05.
Phuong Mai, DINH, Saclay, France
Charmonium Suppression in Central Nucleus-Nucleus Collisions at SPS and RHIC

21.05.
S. Nagaitsev, Fermilab, USA
Fermilab R&D Program in High Energy Electron Cooling

22.05.
O. Pshenichnov, Inst. for Nucl. Res., Moscow, Russia
Electromagnetic Interactions of Ultrarelativistic Heavy Ions: from CERN SPS to RHIC and LHC

22.05.
M. Basko, ITEP Moscow, Russia
Hydrodynamic Instability of Shells Accelerated by Direct Heating with Ion Beams

23.05.
A. & A. Raduta, GSI Darmstadt, Germany
Thermodynamical Aspects of Nuclear Multi-fragmentation

29.05.
S. Atzeni, Univ. of Rome & INFM, Rome, Italy
Inertial Fusion Fast Ignitors: A Review of Studies on Ignition and Burn

29.05.
T. Yamazaki, University of Tokyo, Japan
Deeply Bound Pionic States

30.05.
U. Becker, Fritz-Haber-Inst., Berlin, Germany
Kohärenz in der Photoelektronenemission homonuklearer Moleküle

31.05.
B. Schlitt, GSI Darmstadt, Germany
Ein 7 MeV/u, 217 MHz Injektor-Linac für den Therapiebeschleuniger in Heidelberg

06.06.
J. Schmiedmayer, University of Heidelberg, Germany
Towards Mesoscopic Physics with Cold Atoms

06.06.
M. Urban, TU Darmstadt, Germany
Vector and Axial Vector Correlators in a Chirally Symmetric Model

12.06.
A. Hening, Atom. Phys. Inst. Bucharest, Romania
Laser-Driven X-Ray Sources and Applications

12.06.
F.-K. Thielemann, University of Basel, Switzerland
Supernovae and Galactic Evolution - Indicators of their Nucleosynthesis

12.06.
K. Bugaev, University of Frankfurt, Germany
Critical Indices of the Statistical Multifragmentation Model

13.06.
U. Schramm, LMU München, Germany
Dichte kristalline Ionenstrahlen – der RFQ Speicherring PALLAS

19.06.
A. Schüttauf, MPI f. Physik, München, Germany
A Forward TPC for STAR

19.06.
E. Gaul, GSI Darmstadt, Germany
Lichtwellenleiter in Plasma für hochintensive Laserstrahlführung

19.06.
G. zu Putlitz, University of Heidelberg, Germany
50 Jahre erlebte Physik

Seminars, Workshops at GSI

20.06.
R. Dörner, University of Freiburg, Germany
Von tanzenden Elektronen und zitternden Kernen

27.06.
S.P. Möller, ISA, Univ. of Aarhus, Denmark
The Development of the Electrostatic Storage Ring ELISA; New Possibilities within Atomic Physics and Biology?

28.06.
H. Damerau, GSI Darmstadt, Germany
Entwicklung eines 24MHz Bunch-Kompressions-System für den Dortmunder Elektronen-Booster BoDo bei DELTA

03.07.
A. Kingsep, A. Lobanov, Moscow, Russia
- **Study of High-Current Plasma System Aimed to ICF**
- **Modeling of Fast Z-Pinches and Plasma-Filled Diodes**

03.07.
A. Reinefeld, K. Zuse Zentrum, Berlin, Germany
How to Build a High-Performance Compute Cluster for the Grid

04.07.
Frank Rathmann, FZ Jülich, Germany
Experiments with Polarized Gas Targets in Storage Rings

04.07.
R. Rapp, Stonybrook, USA
J/Psi and Charm Production in High-Energy Nuclear Collisions

05.07.
K.D. Jentsch,
Deutsches Primatenzentrum,Göttingen,Germany
Neue gentherapeutische Ansätze zur AIDS-Therapie

10.07.
H.J. Specht, University of Heidelberg, Germany
Quark Matter – 20 Years and no Finale yet

11.07.
Davor Protić, FZ Jülich, Germany
Aktuelle Entwicklungen auf dem Gebiet ortsempfindlicher Germanium- und Si(Li)-Detektoren

11.07.
H. Wolter/LMU München, Germany
Charge-Asymmetry Effects in Nuclear Fragmentation

12.07.
G. Schreiber, University of Frankfurt, Germany
Entwicklung eines Pulsgenerators für den Subnanosekundenbereich zur Strahlsimulation für einen Beam-Position-Monitor

17.07.
M. Beuve, GSI Darmstadt, Germany
Lectures on Modelling of Electronic Excitations Induced by Swift Heavy Ions in Solids

18.07.
P. Danielewicz, MSU, East Lansing, USA
Nuclear Equation of State

18.07.
T. Kühl, GSI Darmstadt, Germany
Status of the PHELIX Project at GSI

01.08.
X. Cai, Inst. of Mod. Physics, Lanzhou, China
The Cooler Storage Ring Facility for Atomic Physics in Lanzhou

09.08.
M. Galonska, University of Frankfurt, Germany
Untersuchungen zur Ionenwinkelverteilung während der Plasma-Immersions-Ionenim-plantation

15.08.
M. Key, LLNL Livermore, USA
Informal Discussion with M. Key on High Intensity Short Pulse Science at LLNL

Seminars, Workshops at GSI

16.08.
H. Nishimura, ILE, Osaka University, Japan
Ultra-Intensive Laser Plasma Research at ILE: Status and Future Plans

05.09.
H. Rothard, CIRIL-Ganil, Caen, France
Auger-, Binary Encounter and 'Fermi Shuttle' Electron Ejection in Heavy Ion-Solid Collisions

18.09.
S. Panitkin, BNL, USA
Recent Results from STAR at RHIC

04.10.
L. Groening, GSI Darmstadt, Germany
Untersuchung zum Einfluß kohärenter Synchrotron-Strahlung auf Strahlparameter im Rahmen des CLIC-Projektes am CERN

09.10.
S. Damjanovic, University of Heidelberg, Germany
Recent Results from the CERES Electron Data Analysis

17.10.
C. Brandau, University of Gießen, Germany
Messungen zur Photorekombination schwerer, hochgeladener Ionen an Speicherringen

17.10.
L. Alvarez-Ruso, LBL Berkeley, USA
Phi Meson Propagation in a Hot Hadronic Gas

18.10.
D. Hitz, CEA Grenoble, France
Electron Cyclotron Resonance Ion Sources and High Intensity Beam Production

23.10.
I. Hofmann, GSI Darmstadt, Germany
The Potential of Heavy Ion Drivers for Inertial Fusion Energy

23.10.
P. Kienle, TU München, Germany
Buridian's Donkey did not Starve to Death and for the Same Reason Hadrons Acquired Large Masses

24.10.
M. Reicherts, Univ. of Kaiserslautern, Germany
Formation of Weakly Bound Atomic Negative Ions in Slow Collisions with State-Selected Rydberg Atoms

30.10.
A. Kozyreva, TU Darmstadt, Germany
Possibility of Creating High-Energy Density Matter Using Intense Heavy Ion Beams

30.10.
P. Mittelstädt, University of Köln, Germany
EPR-Paradoxon, Nichtlokalität und Überlicht-geschwindigkeit

06.11.
H. Takabe, ILE, Grad. School of Scie., Osaka, Japan
Laser Astrophysics

06.11.
J.-P. Blaizot, CEA Saclay, France
The J/Ψ Meson and the Quark-Gluon-Plasma

07.11.
T. Beier, GSI Darmstadt
Why is the Rain Lighter at Winter Time?

08.11.
S. Richter, GSI Darmstadt
Neues lokales Steuerungssystem für den Darmstädter Elektronenlinearbeschleuniger S-DALINAC

13.11.
C. Weinheimer, University of Bonn, Germany
In Search for the Neutrino Mass: From the Mainz Experiment to KATRIN

14.11.
S. Dreuil, University of Paris, France
Dynamics of Hot Nanoplasmas Induced by Electron-Ion Collisions during Femtosecond Laser Interaction with Clusters

Seminars, Workshops at GSI

14.11.
M. Nowak, Cracow, Poland
Lectures on Chiral Disorder in Quantum Chromodynamics
I: Introduction to Chiral Symmetry

20.11.
H. Abele, University of Heidelberg, Germany
Neutron Beta-Decay, Quark Mixing and the Question of Unitarity

20.11.
A.Ya. Faenov, VNIIFTRI, Meneleevo, Russia
X-Ray Radiation Properties of Different Clusters Under Intensive fs Laser Interaction

21.11.
P. Senger, GSI Darmstadt, Germany
Compressed Baryonic Matter Experiments at the Future GSI Facility

21.11.
M. Block, University of Mainz, Germany
The Lifetime of the $3^2D_{5/2}$ Level of Ca^+ Lifetime-Measurements in a Linear Paul Trap

21.11.
M. Nowak, Cracow, Poland
Lectures on Chiral Disorder in Quantum Chromodynamics
II: Diffusion of the Light Quarks in the QCD Vaccum

22.11.
S. Yaramishev, ITEP, Moscow, Russia
Design and Beam Dynamics Study of High Current Ion Linacs

27.11.
J.-M. Clarisse, CEA/Bruyères-le-Châtel, France
Computing Hydrodynamic Instabilities in ICF : Some Issues and Tentative Answers

27.11.
B. Leibundgut, ESO Garching, Germany
Supernovae and the Accelerated Universe

28.11.
F.P. Heßberger, GSI Darmstadt, Germany
Nuclear Structure Investigations of Transactinide Nuclei

28.11.
S. Zakowicz, University of Giessen, Germany
Dielectronic Recombination into Highly-Charged Heavy Ions with Emission of Two Photons

28.11.
M. Nowak, Cracow, Poland
Lectures on Chiral Disorder in Quantum Chromodynamics
III: Spectral Properties of the Chiral Condensate and Lattice Data

04.12.
U. Schumacher, University of Stuttgart, Germany
Magnetischer Einschluß heißer Plasmen

05.12.
B. Srivastava, Purdue University, USA
A Systematic Study of the Multifragmentation of 1AGeV Au, La and Kr and the Phase Transition

05.12.
A. Lauck, FH Wiesbaden, Germany
Verfahrensentwicklung zur Partialdruck-kalibrierung von Quadrupol-Massenspektro-metern im Hochvakuum

05.12.
M. Möller, TU Darmstadt, Germany
Phänomenologie von kaonischen Atomen

06.12.
A. Jakob, J. Pozimski, Univ. of Frankfurt,Germany
- **Messungen des Strahlionendichteprofils mittels CCD-Kamera**
- **Bestimmung der Korrespondenz zwischen einer Folge von Strahlprofilen und der Emittanz**

11.12.
S. Karsch, MPQ Garching, Germany
Correction of Wave Front Distortions and Fluence Profile Modulations by Closed-Loop Adaptive Optics in a Multi Stage TiS Laser

Seminars, Workshops at GSI

11.12.
G. Iliakis, Universitätsklinikum Essen, Germany
Repair of DNA Double Strand Breaks in Cells of Higher Eukaryotes

12.12.
C. Schwarz, GSI Darmstadt, Germany
Physics with Anti Protons at the Future GSI Facility

12.12.
T. Nandi, NSC Dehli, India
Time Resolved Spectroscopy of He- and Li-Like Ions for Z=20-30 using One- as well as Two-Foil Targets with the 15UD Pelletron at NSC

12.12.
J. Berges, University of Heidelberg, Germany
Quantum Fields far from Equilibrium and Thermalization

12.12.
S. Radomski, Warsaw Univ. of Technology, Poland
Selected Aspects of Software System Integration in the STAR and ALICE Experiments

14.12.
E. Mahner, CERN, Switzerland
Experimental Investigation of Impact-Induced Molecular Desorption by 4.2 MeV/u Lead Ions

18.12.
H. Lesch, LMU München, Germany
Schlagzeilen vom Rand der Wirklichkeit

Workshops, Meetings at GSI

13./14.02.	Fachtagung / Supraleitung
26.03.	The Europ. Network on Ion Track Technology (EuNITT)
27.03.	Granzer Workshop I: Phenomena in Restricted Geometries based on Ion Tracks
03.-04.05.	Symp. on Nuclear Astrophysics
07.-09.05.	Workshop on Atomic Physics and Related Fields at SIS and ESR (http://www-ap.gsi.de/conferences/workshop/AtPhReFi.html)
30.06./01.07.	Gas-Cell Workshop
12./13.07.	NuPECC Subcommittee Meeting
06.08.-28.09.	International Student Program
12.11.	Granzer Workshop II: Phenomena in Restricted Geometries Based on Ion Tracks

Jointly organized Conferences, Workshops, Meetings

14.-20.01.	Int. Workshop XXIX on Gross Properties of Nuclei and Nuclear Excitation, Hirschegg, Austria (TU Darmstadt + GSI)
09.-14.09.	12th Int. Conf. on Surface Modification of Materials by Ion Beams (SMMIB 2001) (Univ. of Marburg + GSI)
25.-29.09.	Strange Quarks in Matter 2001 (Univ. of Frankfurt + GSI)

Thesis, Diploma

PhD Thesis

Berger, S.:
Untersuchung der Wirkung von Schwerionenstrahlen auf menschliche Hautfibroblasten unter besonderer Berücksichtigung chromosomaler Veränderungen
(University of Mainz, Germany, 2001)

Borcea, R.:
Beta Decay of ^{56}Cu
(University of Bucarest, Romania, 2001)

Dilling, J.:
Direkte Massenmessungen an exotischen Kernen mit SHIPTRAP und ISOLTRAP
(University of Heidelberg, Germany, 2001)

Feili, D.:
Access to Two-Photon Exchange QED Contributions via High Precision Measurement of Lamb Shift Transitions in Heavy Li and Be-Like Ions
(University of Giessen, Germany, 2001)

Herfurth, F.:
Ein neuer Ionenstrahlkühler und –pulser für ISOTRAP und Massenmessungen an radioaktiven Argonisotopen
(University of Heidelberg, Germany, 2001)

Jones, K.L.:
The Unbound Nucleus ^{13}Be
(University of Surrey, United Kingdom, 2001)

Kollmus, H.:
Kinematisch vollständige Untersuchung der simultanen Ionisation von Projektil und Target in Stößen von 3,6 MeV/u C^{2+} mit Helium
(University of Frankfurt, Germany, 2001)

Leistenschneider, A.:
Untersuchungen zur Kernstruktur instabiler neutronenreicher Sauerstoff-Isotope
(University of Frankfurt, Germany, 2001)

Schlögl, M.:
Ladungsträgertransportdynamik in CVD Diamantschichten und mikroelektronischen Bauelementen untersucht mit einem fein fokussierten Ionenstahl – Anwendungsmöglichkeiten einer Schwerionenmikrosonde in der Materialforschung
(University of Frankfurt, Germany, 2001)

Stotz, A.:
Untersuchungen des Gamov-Teller-Zerfalls in der Nachbarschaft von ^{100}Sn
(University of Munich, Germany, 2001)

Sturm, Ch.:
K^+-Produktion in Schwerionenreaktionen als Sonde für die Inkompressibilität von Kernmaterie
(TU Darmstadt, Germany, 2001)

Toimil Molares, M.E.:
Fabrication and Characterization of Copper Nanowires Electrochemically Deposited in Etched Ion-Track Membranes
(University of Heidelberg, Germany, 2001)

DIPLOMA

Bank, A.:
Profilmessung durch Restgasleuchten am GSI-UNILAC-Ionenstrahl
(FH Wiesbaden, Germany, 2001)

Lang, M.:
Rasterkraftmikroskopie an natürlichen und Ionen-Induzierten Strahlenschäden in Phlogopit
(University of Heidelberg, Germany, 2001)

Weiss, A.:
Neues Leuchtschirmsystem für hochenergetische Ionenstrahlen
(FH Wiesbaden, Germany, 2001)

Experiments performed at the GSI accelerators in 2001

R. Holzmann, beam time coordinator

1. SIS/ESR experiments

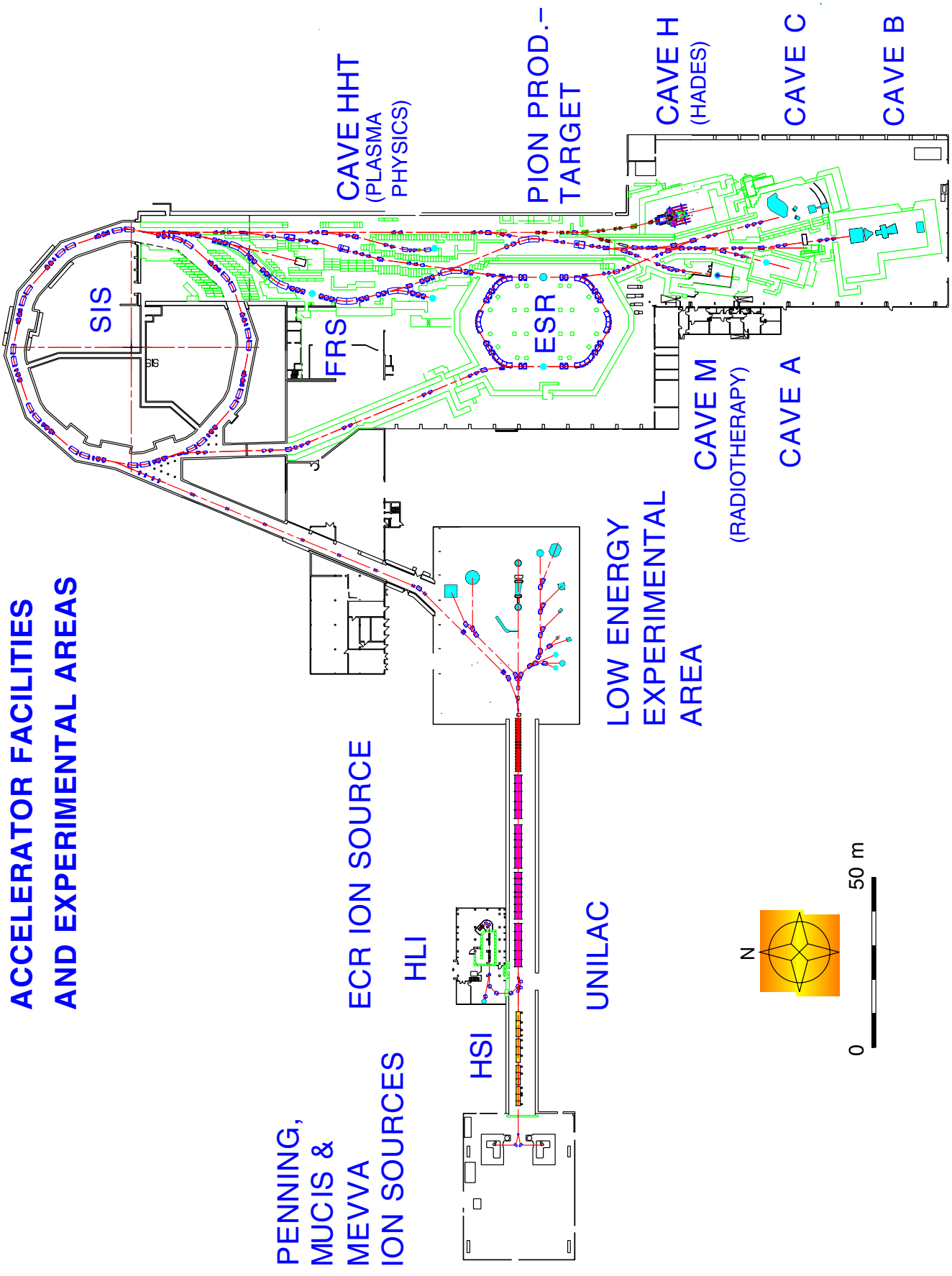
exp. no.	spokesperson	affiliation	short title	beam	exp. area	8h shifts
E000	Franzke, Geissel, Steck	GSI	ESR commissioning	^{18}O, ^{58}Ni, ^{197}Au, ^{238}U	ESR, FRS + ESR	16
E025	Kühl	GSI	hyperfine structure of He-like Bi	^{209}Bi	ESR	22
E027	Poizat	Lyon	electron capture in channeling	^{238}U	ESR + A	9
E038	Warczak	Krakow	radiative double-electron capture	^{238}U	FRS	12
E042	Bräuning	GSI	high-Z multi-electron capture	^{238}U	FRS + A	15
E045	Stöhlker	GSI	2-electron Lamb shift in U^{90+}	^{238}U	ESR	17
S000	Blasche, Blell, Franzke, Spiller	GSI	SIS development	^{6}Li, ^{18}O, ^{197}Au, ^{238}U	SIS, HHT	28
M000	Debus	Heidelberg	tumor therapy	^{12}C	M	164
SBIO	Schardt, Scholz	GSI	SIS biology experiments	^{12}C	A, M	14
SDET	Berdermann	GSI	diamond detector development	^{58}Ni, ^{238}U	FRS	1
S174	Egelhof	GSI	proton scattering off n-rich nuclei	^{2}H	B	1
S198	Neuner	GSI	high energy density in matter	^{238}U	HHT	19
S200	Friese	München	HADES commissioning	^{12}C, ^{50}Cr	HADES	19
S202	Pfützner	Warsaw	search for doubly-magic ^{48}Ni	^{58}Ni	FRS	36
S206	Senger	GSI	K-meson properties in dense nuclear matter	^{197}Au	C	122
S225	Liesen	GSI	lifetime studies in He-like ions	^{238}U	A	12
S227	Benlliure	Santiago	exploring cold fragmentation	^{238}U	FRS	14
S234	Pochodzalla	Mainz	study of hypernuclei	^{1}H	C	3
S235	Schmidt	GSI	proton-decays in heavy nuclei	^{58}Ni	FRS	7
S236	Gillitzer	Jülich	deeply-bound pionic states	^{2}H	FRS	81
S237	Schmidt, Simon	GSI	detector tests for the ALICE exp.	^{12}C, ^{58}Ni	B, C	13
S239	De Pascale	Pisa	longterm effects in astronauts	^{12}C	A	6
S244	Regan	Surrey	FRS gamma campaign	^{238}U	FRS	16
S245	Jonson	Göteborg	study of halo nuclei	^{18}O	FRS + B	22
S246	Hammache	GSI	big-bang nucleosynthesis	^{6}Li	FRS + C	22
S248	Ducret	Saclay	detection of spallation residues	^{12}C, ^{86}Kr	B	14
S249	Vasina	Sarov	stopping-range measurements	^{58}Ni, ^{238}U	HHT	18
S251	Hildenbrand	GSI	FOPI commissioning	^{1}H, ^{58}Ni, ^{86}Kr, ^{238}U	B	12
S254	Trautmann	GSI	mass and spin effects in multifragmentation	^{12}C, ^{86}Kr	B	3
S258	Savard	ANL	development of a gas-catcher system at the FRS	^{58}Ni, ^{136}Xe, ^{197}Au	FRS	24
S260	Ting	MIT	radiation hardness of AMS electronics	^{86}Kr, ^{197}Au, ^{238}U	A, HHT	10
S262	Friese	TUM	dilepton production in C+C	^{12}C	H	16

total: 788 shifts

2. UNILAC experiments

exp. no.	spokesperson	affiliation	Short title	beam	exp. area	shifts (8h)
U000	Barth, Forck, Klabunde, Richter	GSI	UNILAC development	^{1}H, ^{2}H, ^{12}C, ^{40}Ar, ^{238}U	HIS, HLI	3
UBIO	Scholz, Schardt, Rodriguez	GSI	UNILAC biology experiments	^{12}C, ^{50}Ti, ^{58}Ni, ^{136}Xe, ^{238}U	X6	54
UMAT	Fischer, Neumann, Trautmann, Vetter, Wirth	GSI	material science	^{12}C, ^{22}Ne, ^{50}Cr, ^{136}Xe, ^{197}Au, ^{209}Bi, ^{238}U	X0	84
U068	Egelhof	GSI	bolometric detectors	^{209}Bi	X8	8
U083	Rubio	Valencia	Gamov-Teller decay studies	^{58}Ni	Y5	16
U175	Walker	Surrey	long-lived isomers in ^{177}Lu	^{136}Xe	Y5	16
U177	Tauschwitz	Darmstadt	properties of high current discharge channels	^{58}Ni, ^{238}U	Z4	16
U181	Andreyev	Leuven	oblate/prolate competition in Pb and Po nuclei	^{50}Cr	Y7	18
U182	Kratz	Mainz	chemical properties of superheavy elements	^{20}Ne, ^{22}Ne, ^{26}Mg, ^{40}Ca	X1	30
U183	Tabor	Tallahassee	isomer spectr. and β-decay of $^{77-79}$Y	^{40}Ca	Y5	20
U184	Hofmann	GSI	synthesis of superheavy elements	^{40}Ar, ^{50}Ti, ^{50}Cr, ^{86}Kr	Y7	161
U185	Gäggeler	Bern	chemical properties of superheavy elements	^{26}Mg	Y5	38
U188	Zou	Shanghai	lifetimes of highly-charged ions	^{58}Ni	X3	12
U189	Rosmej	GSI	x-ray spectroscopy of swift ions traversing matter	^{50}Ti, ^{58}Ni	Z6	48
U190	Golubev	ITEP Moscow	stopping power in non-ideal plasmas	^{12}C, ^{58}Ni	Z6	15
U192	Savard	ANL	precision half-life measurement of ^{62}Ga	^{40}Ca	Y5	14
U196	Woods	Edinburgh	proton-decay studies	^{58}Ni	Y5	14
U414	Kirchner	GSI	ISOL source developments	^{6}Li, ^{18}O	Y5	1

total: 568 shifts


ACCELERATOR FACILITIES
AND EXPERIMENTAL AREAS
SIS
FRS
ESR
CAVE HHT
(PLASMA
PHYSICS)
PION PROD.-
TARGET
CAVE H
(HADES)
CAVE C
CAVE B
CAVE M
(RADIOTHERAPY)
CAVE A
LOW ENERGY
EXPERIMENTAL
AREA
ECR ION SOURCE
HLI
UNILAC
HSI
PENNING,
MUCIS &
MEVVA
ION SOURCES
N
0
50 m

Collaborations

CERES Collaboration:

D. Adamová[7], G. Agakichiev[3], H. Appelshäuser[6], V. Belaga[4], P. Braun-Munzinger[3], A. Castillo-Ramírez[3], A. Cherlin[8], S. Damjanović[6], T. Dietel[6], L. Dietrich[6], A. Drees[9], S.I. Esumi[6], K. Filimonov[6], K. Fomenko[4], Z. Fraenkel[8], C. Garabatos[3], P. Glässel[6], A. Gnaenski[8], G. Hering[3], J. Holeczek[3], V. Kushpil[7], B. Lenkeit[2], W. Ludolphs[6], A. Maas[3], A. Marín[3], F. Messer[9], J. Milošević[6], A. Milov[8], D. Miśkowiec[3], Yu. Panebrattsev[4], O. Petchenova[4], V. Petráček[6], A. Pfeiffer[2], J. Rak[3], I. Ravinovich[8], P. Rehak[1], H. Sako[3], W. Schmitz[6], J. Schukraft[2], S. Sedykh[3], S. Shimansky[4], J. Slívová[6], H.J. Specht[6], J. Stachel[6]*, M. Šumbera[7], H. Tilsner[6], I. Tserruya[8], J.P. Wessels[6], T. Wienold[6], B. Windelband[6], J.P. Wurm[5], W. Xie[8], S. Yurevich[6], V. Yurevich[4]

[1]Brookhaven Nat. Lab. Upton, USA
[2]CERN, Geneva, Switzerland
[3]GSI Darmstadt, Germany
[4]JINR Dubna, Russia
[5]MPI f.Kernphysik Heidelberg, Germany
[6]Univ. of Heidelberg, Germany
[7]NPI/ASCR Řež, Czech Republic
[8]Weizmann Inst. Rehovot, Israel
[9]SUNY, Stony Brook, USA
*spokesperson

FOPI Collaboration:

A. Andronic[4], Z. Basrak[12], N. Bastid[3], A. Bendarag[3], G. Berek[2], V. Barret[3], R. Caplar[12], P. Crochet[4], A. Devismes[4], P. Dupieux[3], M. Dzelalija[12], Ch. Finck[4], Z. Fodor[2], J. Gasparic[12], A. Gobbi[4], Y. Grishkin[7], O. Hartmann[4], N. Herrmann[6]*, K.D. Hildenbrand[4], B. Hong[9], D. Kang[9], J. Kecskemeti[2], Y.J. Kim[9], M. Kirejczyk[11], P. Koczon[4], M. Korolija[12], R. Kotte[5], M. Kowalczyk[11], T. Kress[4], A. Lebedev[7], Y. Leifels[6], X. Lopez[3], V. Manko[8], M. Merschmeyer[6], D. Moisa[1], W. Neubert[5], D. Pelte[6], M. Petrovici[1], F Rami[10], W. Reisdorf[4], B. de Schauenburg[10], A. Schüttauf [4], Z. Seres[2], B. Sikora[11], K.S. Sim[9], V. Simion[1], K. Siwek-Wilczynska[11], M. Smolarkiewicz[11], V. Smolyankin[7], J. Soliwoda[11], M. Stockmeier[6], G. Stoicea[1], Z. Tyminski[11], P. Wagner[10], K. Wisniewski[6], D. Wohlfarth[5], I. Yushmanov[8], A. Zhilin[7]

[1]NIPNE Bucharest, Romania
[2]CRIP/KFKI Budapest, Hungary
[3]LPC Clermont-Ferrand, France
[4]GSI Darmstadt, Germany
[5]FZ Rossendorf/Dresden, Germany
[6]Univ. of Heidelberg, Germany
[7]ITEP Moscow, Russia
[8]Kurchatov Institute, Moscow, Russia
[9]Korea University Seoul, Korea
[10]IReS Strasbourg, France
[11]Univ. of Warsaw, Poland
[12]RBI Zagreb, Croatia
*spokesperson

HADES Collaboration

G. Agakichiev[3], C. Agodi[6], H. Alvarez-Pol[13], E. Badura[3], A. Balanda[7], R. Bassini[14], G. Bellia[6], D. Bertini[3], J. Bielcik[3], M. Böhmer[12], C. Boiano[14], H. Bokemeyer[3], J. Boyard[4], S. Brambilla[14], P. Braun-Munzinger[3], S. Chernenko[9], R. Coniglione[6], M. Dahlinger[3], H. Daues[3], R. Dressler[2], I. Duran[13], T. Eberl[12], L. Fabbietti[12], O. Fateev[9], P. Finocchiaro[6], J. Friese[12], I. Fröhlich[10], B. Fuentes[13], J. Garzon[13], R. Gernhäuser[12], M. Golubeva[5], E. Grosse[2], F. Guber[5], J. Hehner[3], T. Hennino[4], S. Hlavac[11], J. Hoffmann[3], R. Holzmann[3], J. Homolka[12], I. Iori[14], R. Ispiryan [16], M. Jaskula[7], J. Jourdain[4], M. Kajetanowicz[7], T. Karavicheva[5], K. Kanaki[2], T. Karavicheva[5], A. Kastenmüller[12], P. Kienle[12], I. Koenig[3], W. Koenig[3], H. Körner[12], B.Kolb[3], R. Kotte[2], A. Kugler[1], R. Kulessa[7], A. Kurepin[5], W. Kühn[10], J. Lehnert[10], E. Lins[10], R. Lorenzo[13], D. Magestro[3], P. Maier-Komor[12], C. Maiolino[6], J. Markert[8], V. Metag[10], H. Meunier[15], M. Münch[12], C. Müntz[8], L. Naumann[2], W. Ott[3], J. Otwinowski[7], Y. Pachmayer[8], V. Pechenov[9], M. Petri[10], P. Piattelli[6], J. Pietraszko[7], R. Pleskac[1], M. Ploskon[7], J. Pouthas[4], W. Przygoda[7], B. Ramstein[4], A. Reshetin[5], J. Ritman[10], G. Rodriguez Prieto[13], K. Rosenkranz[8], M. Roy-Stephan[4], J. Sabin Fernandez[13], A. Sadovski[2], B. Sailer[12], P. Salabura[7], M. Sanchez[13], P. Sapienza[6], D. Schäfer[10], C. Schroeder[3], W. Schön[12], J. Seibert[2], P. Senger[3], K. Shileev[5], R. Simon[3], L. Smykov[9], J. Sowa[7], S. Sapataro[6], H. Stelzer[3], H. Stroebele[8], J. Stroth[8], M. Sudol[3], A. Taranenko[1], V. Tiflov[5], A.Titov[9], P. Tlusty[1], A. Toia[10], M. Traxler[10], H. Tsertos[16], I. Turzo[11], A. Vazques[13], V. Wagner[1], W. Walus[7], Y. Wang[8], S. Winkler[12], T. Wojcik[7], J. Wüstenfeld[8], Yu. Zanevsky[9], D. Zovinec[3], P. Zumbruch[3]

Collaborations

[1]Inst. of Nucl. Phy. INP, Řež, Czech. Rep.
[2]FZR Rossendorf, Germany
[3]GSI Darmstadt, Germany
[4]IPN Orsay, France
[5]Inst. for Nucl. Res., Moscow, Russia
[6]INFN-LNS, Depart. di Fisica, Catania, Italy
[7]Jagellonian University Cracow, Poland
[8]Univ. of Frankfurt, Germany
[9]JINR Dubna, Russia
[10]Univ. of Giessen, II. Physik. Inst., Germany
[11]Inst. of Physics IOP Bratislava, Slovakia
[12]TU Munich, Phys. Depart., Garching, Germany
[13]Univ. of Santiago de Compostela, Spain
[14]Dip. di Fisica, Univ. di Milano, Italy
[15]Univ. of Clermont-Ferrand, Aubiere, France
[16]University of Cyprus, Nicosia, Cyprus

IKAR Collaboration:

G.D. Alkhazov[1], M.N. Andronenko[1], A. Bauchet[2], A.V. Dobrovolsky[1], P. Egelhof[2], S. Fritz[2], G.E. Gavrilov[1], H. Geissel[2], C. Gross[2], H. Irnich[2], A.V. Khanzadeev[1], G.A. Korolev[1], G. Kraus[2], A.A. Lobodenko[1], G. Münzenberg[2], M. Mutterer[3], S.R. Neumaier[2], T. Schäfer[2], C. Scheidenberger[2], W. Schwab[2], D.M. Seliverstov[1], T. Suzuki[2], A.A. Vorobyov[1], V.I. Yatsoura[1]

[1]Nucl. Phys. Inst., Petersburg, Russia
[2]GSI Darmstadt, Germany
[3]Inst. f. Kernphysik, TU Darmstadt, Germany

INDRA-ALADIN Collaboration:

G. Auger[1], Ch.O. Bacri[2], M. Begemann-Blaich[6], N. Bellaize[3], R. Bittiger[6], F.Bocage[3], B. Borderie[2], A.S. Botvina[6,] R. Bougault[3], B. Bouriquet[1], Ph. Buchet[4], J.L. Charvet[4], A. Chbihi[1], R. Dayras[4], D. Doré[4], D. Durand[3], J.D. Frankland[1], E Galichet[5], D. Gourio[6], D. Guinet[5], S. Hudan[1], B. Hurst[3], G. Immé[8], P. Lautesse[5], F. Lavaud[2], J.L. Laville[1], C. Leduc[5], A. Levèvre[6], R. Legrain[4], O. Lopez[3], J. Lukasik[6,10], U. Lynen[6], W.F.J. Mueller[6], L. Nalpas[4,] H. Orth[6], E. Plagnol[2], G. Raciti[8], E. Rosato[7], A. Saija[8], C. Sfienti[6], C. Schwarz[6], J.C. Steckmeyer[3], G. Tabacaru[1], B. Tamain[3], W. Trautmann[6]*, A. Trczinski[9], K. Turzo[6], E. Vient[3], M. Vigilante[7,] C. Volant[4], B. Zwieglinski[9]

[1]GANIL, Caen, France
[2]IPN Orsay, Orsay, France
[3]LPC, Caen, France
[4]DAPNIA/SPhN, Saclay, Gif-sur-Yvette, France
[5]IPN Lyon, Villeurbanne, France
*spokesperson
[6]GSI Darmstadt, Germany
[7]INFN, Napoli, Italy
[8]INFN, Catania, Italy
[9]Soltan Inst. for Nucl. Studies, Warsaw, Poland
[10]Niewodniczanski Inst. for Nucl. Phys., Krakow, Poland

KaoS Collaboration:

I. Böttcher[4], A. Förster[2], E. Grosse[6], P. Koczon[1], B. Kohlmeyer[4], S. Lang[2], M. Menzel[4], L. Naumann[6], H. Oeschler[2], M. Ploskon[1], F. Pühlhofer[4],W. Scheinast[6], A. Schmah[2], T. Schuck[3], E. Schwab[1], P. Senger[1], Y. Shin[3], H. Ströbele[3], C. Sturm[2], F. Uhlig[2], A. Wagner[2], W. Walus[5]

[1]GSI Darmstadt, Germany
[2]TH Darmstadt, Germany,
[3]Univ. of Frankfurt, Germany
[4]Univ. of Marburg, Germany
[5]Jagellonian Univ., Cracow, Poland
[6]FZ Rossendorf, Germany

LAND Collaboration:

T. Aumann[2]*, K. Boretzky[3], U. Datta Pramanik[2], Th.W.Elze[1], H.Emling[2]*, A. Grünschloß[1], G. Ickert[2], S. Ilievski[2], K. Jones[2], J.V. Kratz[3], R. Kulessa[5], Le Hong Khiem[3], A. Leistenschneider[1], E. Lubkiewicz[5], R. Palit[1],W. Prokopowicz[2,5], H. Simon[4], K. Sümmerer[2], T. Lange[1], E. Wajda[5], W. Walus[5]

[1]Univ. of Frankfurt, Germany
[2]GSI Darmstadt, Germany
[3]Univ. of Mainz, Germany
[4]TH Darmstadt, Germany,
[5]Jagellonian Univ., Cracow, Poland
*spokesperson

Collaborations

NA49 Collaboration:
S.V. Afanasiev[9], T. Anticic[21], D. Barna[5], J. Bartke[7], R.A. Barton[3], L. Betev[10], H. Bialkowska[19], A. Billmeier[10], C. Blume[8], C.O. Blyth[3], B. Boimska[19], M. Botje[1], J. Bracinik[4], R. Bramm[10], R. Brun[11], P. Buncic[10,11], V. Cerny[4], O. Chvala[17], J.G. Cramer[18], P. Csato[5], P. Dinkelaker[10], V. Eckardt[16], P. Filip[16], H.G. Fischer[11], Z. Fodor[5], P. Foka[8], P. Freund[16], V. Friese[15], J. Gal[5], M. Gazdzicki[10], G. Georgopoulos[2], E. Gladysz[7], S. Hegyi[5], C. Höhne[15], G. Igo[14], P.G. Jones[3], K. Kadija[11,21], A. Karev[16], V.I. Kolesnikov[9], T. Kollegger[10], M. Kowalski[7], I. Kraus[8], M. Kreps[4], M. van Leeuwen[1], P. Levai[5], A.I. Malakhov[9], S. Margetis[13], C. Markert[8], B.W. Mayes[12], G.L. Melkumov[9], A. Mischke[8], J. Molnar[5], J.M. Nelson[3], G. Palla[5], A.D. Panagiotou[2], K. Perl[20], A. Petridis[2], M. Pikna[4], L. Pinsky[12], F. Pühlhofer[15], J.G. Reid[18], R. Renfordt[10], W. Retyk[20], C. Roland[6], G. Roland[6], A. Rybicki[7], T. Sammer[16], A. Sandoval[8], H. Sann[8], N. Schmitz[16], P. Seyboth[16]*, F. Sikler[5], B. Sitar[4], E. Skrzypczak[20], G.T.A. Squier[3], R. Stock[10], H. Ströbele[10], T. Susa[21], I. Szentpetery[5], J. Sziklai[5], M. Toy[2,14], T.A. Trainor[18], D. Varga[5], M. Vassiliou[2], G.I. Veres[5], G. Vesztergombi[5], D. Vranic[8], S. Wenig[11], A. Wetzler[10], C. Whitten[14], I.K. Yoo[15], J. Zaranek[10]J. Zimanyi[5],

[1]NIKHEF, Amsterdam, The Netherlands
[2]Dep. of Physics, Univ. of Athens, Greece
[3]School of Physics, Univ. of Birmingham, UK
[4]University of Bratislava, Slovakia
[5]KFKI Budapest, Hungary
[6]MIT, Cambridge, USA
[7]Inst. of Nuclear Physics, Cracow, Poland
[8]GSI Darmstadt, Germany
[9]JINR, Dubna, Russia
[10]Fachber. Phys., Univ. of Frankfurt, Germany
[11]CERN, Geneva, Switzerland
[12]Univ. of Houston, Houston, USA
[13]Kent State Univ. Kent, USA
[14]Univ. of California, Los Angeles, USA
[15]Fachber. Phys., Univ. of Marburg, Germany
[16]MPI für Physik, München, Germany
[17]University of Prague, Republic of Tschechia
[18]University of Washington, Seattle, USA
[19]Inst. Nucl. Studies, Univ. of Warsaw, Poland
[20]Inst. Exp. Phys., Univ. of Warsaw, Poland
[21]Rudjer Boskovic Inst., Zagreb, Croatia
*spokesperson

R^{3}B Collaboration:
T. Aumann[1]*, L. Axelsson[3], J. Benlliure[8], M. Böhmer[7], P. Chesny[6], P. Chomaz[2], D. Cortina[8], A. Dael[6], J.-E. Ducret[6], H. Emling[1], J. Friese[7], H. Geissel[1], B. Gastineau[6], R. Gernhäuser[7], M. Jacquemet[6], B. Jonson[3], M. Kajetanowicz[5], H.-J. Körner[7], J. Kojouharova[1], K. Korcyl[5], R. Kulessa[5], N. Kurz[1], B. Lommel[1], W. Mittig[2], G. Münzenberg[1], G. Nyman[3], M.F. Ordonez[8], K.H. Schmidt[1], R. Schneider[7], K. Sümmerer[1], N. Tahir[1], V. Vysotsky[6], H. Weick[1], M. Winkler[4], H. Wollnik[4], M. Yavor[1]

[1]GSI, Darmstadt, Germany
[2]GANIL, Caen, France
[3]Chalmers University, Göteborg, Sweden
[4]University of Giessen, Germany
[5]Jagellonski University, Krakow, Poland
[6]CEA Saclay, France
[7]TU München, Germany
[8]University of Santiago de Compostela, Spain
*spokesperson

RD42 Collaboration:
W. Adam[1], E. Berdermann[2], P. Bergonzo[3], W. de Boer[20], F. Bogani[4], E. Borchi[5], A. Brambilla[3], M Bruzzi[5], C. Colledani[6], J. Conway[7], P. D'Angelo[8], W. Dabrowski[9], P. Delpierre[10], W. Dulinski[6], J. Doroshenko[7], M. Doucet[15], B. van Eijk[11], A. Fallou[10], F. Fizotti[12], F. Foulon[3], M Friedl[1], K.K. Gan[13], G. Grigoriev[20], G. Hallewell[10], S. Han[13], F. Hartjes[11], J. Hrubec[1], D. Husson[6], H. Kagan[13]*, D. Kania[13], J. Kaplon[14], R. Kass[13], T. Koeth[7], M. Krammer[1], A. Logiudice[12], R. Lu[12], L. mac Lynne[7], C. Manfredotti[12], D. Meier[14], M. Mishina[16], L. Moroni[8], J. Noomen[11], A. Oh[15], L.S. Pan[13], M Pernicka[1], L. Perera[7], S. Pirollo[5], M. Procario[17], J. L. Riester[6], S. Roe[14], L. Rousseau[3], A. Rudge[14], J. Russ[17], S. Sala[8], M. Sampietro[18], S. Schnetzer[7], S. Sciortino[5], H. Stelzer[2], R. Stone[7], B. Suter[17], W. Trishuk[19], D. Tromson[3], E. Vittone[12], R. Wedenig[1], P. Weilhammer[14]*, M. Wetstein[7], W. Zeuner[15], M. Zoeller[13]

Collaborations

[1]HEPHY, Vienna, Austria
[2]GSI Darmstadt, Germany
[3]LETI-CEA Saclay, Paris, France
[4]LENS, Florence, Italy
[5]Univ. of Florence, Florence, Italy
[6]LEPSI, IN2P3/CNRS-ULP, Strassbourg, France
[7]Rutgers University, New York, USA
[8]INFN, Milano, Italy
[9]UMM, Cracow, Poland
[10]CPPM, Marseille, France
[11]NIKHEF, Amsterdam, Netherlands
[12]Univ. of Torino, Torino, Italy
[13]The Ohio State Univ., Columbus, USA
[14]CERN, Geneva, Switzerland
[15]II. Inst. f. Exp. Physik, Hamburg, Germany
[16]FNAL, Batavia, USA
[17]Carnegie-Mellon Univ. Pittsburgh, USA
[18]Polytechnico di Milano, Milano, Italy
[19]Univ. of Toronto, Toronto, Canada
[20]Inst. f. Exp. Kernphys., Karlsruhe, Germany
*spokesperson

S135 Collaboration:
D. Aleksandrov[1], T. Aumann[2], L. Axelsson[3], T. Baumann[2], M.J.G. Borge[4], L.V. Chulkov[1,2], W. Dostal[5], B. Eberlein[2,5], Th.W. Elze[6], H. Emling[2], C. Forssen[3], H. Geissel[2], A. Grünschloss[6], M. Hellström[2], B. Jonson[3]*, J.V. Kratz[5], R. Kulessa[7], Y. Leifels[2], A. Leistenschneider[6], K. Markenroth[3], M. Meister[3,8], I. Mukha[1,8], G. Münzenberg[2], T. Nilsson[3], G. Nyman[3], A. Richter[8], K. Riisager[9], C. Scheidenberger[2], G. Schrieder[8], H. Simon[8], O. Tenglbad[4], M.V. Zukhov[3]

[1]Kurchatov Institute Moscow, Russia
[2]GSI Darmstadt, Germany
[3]University of Göteborg, Sweden
[4]CSIC Madrid, Spain
[5]University of Mainz, Germany
[6]Univ. of Frankfurt, Germany
[7]Jagellonski University, Krakow, Poland
[8]TU Darmstadt, Germany
[9]University of Aarhus, Denmark
*spokesperson

S174 Collaboration:
F.Aksouh[1], A. Bleile[1], O.V. Bochkarev[2], T. [2], L.V. Chulkov[2], D. Cortina-Gil[3], A.V. Dobrovolsky[4], P. Egelhof[1], H. Geissel[1], M. Hellström[1], N.B. Isaev[4], O.A. Kisselev[1,4], B.G. Komkov[4], M. Matos[1], F.V. Moroz[4], G. Münzenberg[1], M. Mutterer[5], V.A. Mylnikov[4], S.F. Neumaier[1], V.N. Pribora[2], D.M. Seliverstov[4], L.O. Sergueev[4], A. Shrivastava[1], K. Sümmerer[1], H. Weick[1], M. Winkler[1], V.I. Yatsoura[4],

[1]GSI Darmstadt, Germany
[2]Kurchatov Institute Moscow, Russia
[3]Univ. de Santiago de Compostela, Spain
[4]Nucl. Phys. Inst., Petersburg, Russia
[5]TU Darmstadt, Germany

S223 Collaboration
I. Böttcher[3], D. Cortina[1], A. Förster[6], M. Gai[9], H. Geissel[1], U. Greife[2], F. Hammache[1], M. Hellström[1], N. Iwasa[7], P. Koczon[1], B. Kohlmeyer[3], R. Kulessa[4], H. KUmagai[7], N. Kurz[1], M. Menzel[3], T. Motobayashi[8], H. Oeschler[6], A. Ozawa[7], M. Ploskon[4], W. Prokopowicz[4], F. Schürmann[2], E. Schwab[1], P. Senger[1], F. Strieder[2], C. Sturm[1], K. Sümmerer[1], Z. Sun[1], G. Surowka[4], S. Typel[10], F. Uhlig[6], A. Wagner[5], W. Walus[4]

[1]GSI Darmstadt, Germany
[2]Ruhr-University, Bochum, Germany
[3]Philipps-University, Marburg, Germany
[4]Jagellonski University, Krakow, Poland
[5]FZ Rossendorf, Dresden, Germany
[6]TU Darmstadt, Darmstadt, Germany
[7]RIKEN, Saitama, Japan
[8]Rikkyo University, Toshima, Japan
[9]University of Connecticut, Storrs, USA
[10]Michigan State University, East Lansing, USA

Collaborations

SHIPTRAP:

D. Ackermann[3], J. Äystö[1], H. Backe[2], G. Bollen[14], F. Bosch[3], J. Dilling[3], A. Dretzke[2], O. Engels[5], T. Faestermann[4], J. Friese[4], H. Geissel[3], A. Gillitzer[4], H. Grawe[3], D. Habs[5], F.P. Heßberger[3], S. Hofmann[3], M. Huyse[6], A.A. Ignatiev[7], A. Junghans[3], O. Kester[5], P. Kienle[4], H.-J. Kluge[3], H.J. Körner[4], Ch. Kozhuharov[3], J.V. Kratz[8], W. Lauth[2], M. Leino[1], K.E.G. Löbner[5], D. Lunney[9], R. Mann[3], G. Marx[3], R.B. Moore[10], G. Münzenberg[3], M. Mukherjee[3], J. Neumayer[5], J.A. Pinston[11], W. Quint[3], S. Rahaman[3], D. Rodriguez[3], E. Roeckl[3], G. Savard[12], M. Schädel[3], K.-H. Schmidt[3], R. Schneider[5], U. Schramm[5], M. Sewtz[2], G. Sikler[3], A. Steinhof[2], T. Stöhlker[13], M. Tarisien[3], P.G. Thirolf[5], N. Trautmann[8], P. Van Duppen[6], V.L. Varentsov[5], C. Weber[3]

[1]University of Jyväskylä, Finland
[2]University of Mainz, Germany
[3]GSI, Darmstadt, Germany
[4]TU München, Germany
[5]LMU München, Germany
[6]University of Leuven, Belgium
[7]Inst. for Inform. and Automation, St.Petersburg, Russia
[8]Universität of Mainz, Germany
[9]CSNSM-IN2P3-CNRS, Orsay, France
[10]McGill University, Montreal, Canada
[11]ISN, Grenoble, France
[12]Argonne National Laboratory, Argonne, USA
[13]University of Frankfurt, Germany
[14]Michigan State University, USA

TAPS Collaboration

J. Ahrens[7], L. Aphecetche[3,10], R. Averbeck[1], J.C.S. Bacelar[6], F. Ballester[4], R. Beck[7], H. Delagrange[3,10], D. d'Enterrìa[3,10], J. Dìaz[4], K. Föhl[7], V. Hejny[8], S. Hlavac[1], M. Hoek[2], R. Holzmann[1], S. Janssen[2], N. Kalantar-Nayestanaki[6], M. Kotulla[2], B. Krusche[11]*, A. Kugler[5], H. Löhner[6], G. Martínez[3,10], T. Matulewicz[9], J.G. Messchendorp[2], V. Metag[2], R. Novotny[2], V. Olmos de Leòn[7], R. Ortega[3,10], R.W. Ostendorf[6], M. Pfeiffer[2], R. Pleskac[5], K. Römer[2], S. Schadmand[2], Y. Schutz[3,10], R. Siemssen[6], R.S. Simon[1], H. Ströher[8], A. Taranenko[5], P. Tlusty[5], M. Volkerts[6], V. Wagner[5], H.W. Wilschut[5], N. Yahlali[4]

[1]GSI Darmstadt, Germany
[2]II. Phys. Inst., Univ. Giessen, Germany
[3]GANIL Caen, France
[4]IFIC Valencia, Spain
[5]NPI Rez u Prahy, Czech. Republic
[6]KVI Groningen, The Netherlands
[7]Inst. für Kernphysik, Univ. Mainz, Germany
[8]FZ Jülich, Germany
[9]Inst. of Exp. Physics, Warsaw Univ., Poland
[10]present addr.: SUBATECH Nantes, France
[11]University of Basel, Schwitzerland
*spokesperson

VEGA-Collaboration:

J. Döring[1], J. Gerl[1], M. Gorska[1,3], H. Grawe[1], M. Hellström[1], F. Hessberger[1], S. Hofmann[1], I. Kozhoukharov[1], E. Roeckl[1], C. Schlegel[1], H.J. Wollersheim[1],

[1]GSI Darmstadt, Germany
[2]University of Frankfurt, Germany
[3]University of Warsaw, Poland

WA98 Collaboration:

M.M.Aggarwal[1], A.Agnihotri[2], Z.Ahammed[3], A.L.S.Angelis[4], V.Antonenko[5], V.Arefiev[6], V.Astakhov[6], V.Avdeitchikov[6], T.C.Awes[7]*, P.V.K.S.Baba[8], S.K.Badyal[8], A.Baldine[6], L.Barabach[6] C.Barlag[9], S.Bathe[9], B.Batiounia[6], T.Bernier[10], K.B.Bhalla[2], V.S.Bhatia[1], C.Blume[9], R.Bock[11], E. M.Bohne[9], D.Bucher[9], A.Buijs[12], E.-J.Buis[12], Z.Böröcz[9], H.Büsching[9], L.Carlen[13], V.Chalyshev[6], S.Chattopadhyay[3], R.Cherbatchev[5], T.Chujo[14], A.Claussen[9], A.C.Das[3], M.P.Decowski[12], H.Delagrange[10], V.Djordjadze[6], P.Donni[4], I.Doubovik[5], S.Dutt[8], M.R.Dutta Majumdar[3], K.El Chenawi[13], S.Eliseev[15], K.Enosawa[14], P.Foka[4], S.Fokin[5], V.Frolov[6], M.S.Ganti[3], S.Garpman[13], O.Gavrishchuk[6], F.J.M.Geurts[12], T.K.Ghosh[16], R.Glasow[9], S.K.Gupta[2], B.Guskov[6], H.Å.Gustafsson[13], H.H.Gutbrod[10], R.Higuchi[14], I.Hrivnacova[15], M.Ippolitov[5], H.Kalechofsky[4], R.Kamermans[12], K.-H.Kampert[9], K.Karadjev[5], K.Karpio[17], S.Kato[14], S.Kees[19], B.W.Kolb[11], I.Kosarev[6], I.Koutcheryaev[5], T.Krümpel[9], A.Kugler[15], P.Kulinich[18], M.Kurata[14], K.Kurita[14], N.Kuzmin[6], I.Langbein[11], A.Lebedev[5], Y.Y.Lee[11], H.Löhner[16], L.Luquin[10], D.P.Mahapatra[19], V.Manko[5], M.Martin[4], G.Martinez[10], A.Maximov[6], R.Mehdiyev[6], G.Mgebrichvili[5], Y.Miake[14],

Collaborations

D.Mikhalev[6], Md.F.Mir[8], G.C.Mishra[19], Y.Miyamoto[14], D.Morrison[20], D.S.Mukhopadhyay[3], V.Myalkovski[6], H.Naef[4], B.K.Nandi[19], S.K.Nayak[10], T.K.Nayak[3], S.Neumaier[11], A.Nianine[5], V.Nikitine[6], S.Nikolaev[5], P.Nilsson[13], S.Nishimura[14], P.Nomokonov[6], J.Nystrand[13], F.E.Obenshain[20], A.Oskarsson[13], I.Otterlund[13], M.Pachr[15], A.Parfenov[6], S.Pavliouk[6], T.Peitzmann[9], V.Petracek[15], F.Plasil[7], W.Pinganaud[10], M.L.Purschke[11], J.Rak[15], R.Raniwala[2], S.Raniwala[2], V.S.Ramamurthy[19], N.K.Rao[8], F.Retiere[10], K.Reygers[9], G.Roland[18], L.Rosselet[4], I.Roufanov[6], C.Roy[10], J.M. Rubio[4], H.Sako[14],S.S.Sambyal[8], R.Santo[9], S.Sato[14], H.Schlagheck[9], H.-R.Schmidt[11], Y.Schutz[10], G.Shabratova[6], T.H.Shah[8], I.Sibiriak[5], T.Siemiarczuk[17], D.Silvermyr[13], B.C.Sinha[3], N.Slavine[6], K.Söderström[13], N.Solomey[4], S.P.Sørensen[20], P.Stankus[7], G.Stefanek[17], P.Steinberg[18], E.Stenlund[13], D.Stüken[9], M.Sumbera[15], T.Svensson[13], M.D.Trivedi[3], A.Tsvetkov[5], L.Tykarski[17], J.Urbahn[11], E.C.v.d.Pijll[12], N.v.Eijndhoven[12], G.J.v.Nieuwenhuizen[18], A.Vinogradov[5], Y.P.Viyogi[3], A.Vodopianov[6], S.Vörös[4], M.A.Vos[12], B.Wyslouch[18], K.Yagi[14], Y.Yokota[14], G.R.Young[7]

[1]Univ. of Panjab, Chandigarh, India
[2]Univ. of Rajasthan, Jaipur, India
[3]VECC, Calcutta, India
[4]Univ. of Geneva, Switzerland
[5]Kurchatov Inst., Moscow, Russia
[6]JINR, Dubna, Russia
[7]ORNL, Oak Ridge National Laboratory, USA
[8]Univ. of Jammu, Jammu, India
[9]Univ. of Münster, Germany
[10]Subatech, Ecoles des Mines, Nantes, France
[11]GSI Darmstadt, Germany
[12]Univ. of Utrecht, The Netherlands
[13]Univ. of Lund, Lund, Sweden
[14]Univ. of Tsukuba, Ibaraki, Japan
[15]Nucl. Physics Inst., Rez, Czech Republic
[16]KVI, Univ. of Groningen, The Netherlands
[17]Inst. of Nucl. Studies, Warsaw, Poland
[18]MIT, Cambridge, USA
[19]IOP, Bhubaneswar, India
[20]Univ. of Tennessee, Knoxville, USA
[21]CERN, Geneva, Switzerland
*spokesperson

Author Index

Ackermann, D. 3, 12, 14, 15, 109
Adamczewski, J. 209
Aichelin, J. 66
Al-Garni, S.D. 13
Al-Turany, M. 209
Aleksandrov, D. 17
Algora, A. 8, 9
Alvarez Ruso, L. 68
Alvarez, J. 105, 107
Ames, F. 86
Andreev, O.Yu. 120
Andreyev, A.N. 14
Andronic, A. 33, 34, 220, 221, 220
Angelov, V. 222
Angert, R. 181
Antalic, S. 12, 14, 15
Aouissat, Z. 61, 73
Apel, P. 142, 143
Appelshäuser, H. 220, 221, 222
Armbruster, P. 21, 22
Attallah, F. 10
Audebert, P. 130
Audi, G. 86
Augustinski, G. 216
Aumann, T. 17, 19, 20, 212
Axelsson, L. 17

Backe, H. 109
Badura, E. 169
Balogh, A.G. 137
Bardonner, A. 107
Barth, W. 193
Bartsch, T. 95
Basko, M. 133
Bastug, T. 186
Batist, L. 5, 8, 9, 13
Baumann, T. 17
Baur, D. 142, 143
Becher, W. 155, 165, 169
Bechtold, A. 204
Beck, D. 86, 109, 207
Beck, L. 109
Becker, G. 152
Becker-de Mos, B. 105, 107
Beckert, K. 10, 95, 197
Bednarz, G. 89, 91, 98, 103
Bednyakov, I. 117, 120
Behrends, J.C. 145
Beier, T. 85
Beller, P. 10, 197
Bender, M. 29
Benlliure, J. 21, 22, 24
Berdermann, E. 91, 214
Berky, W. 137
Bernas, M. 21, 22
Bertini, D. 209
Bertsch, A. 144
Besch, H.J. 87, 88
Beyer, H.F. 87, 88, 89, 91, 98
Bingham, C. 4
Birkner, R. 127
Blank, B. 4
Blasche, K. 195, 214
Blaschke, D. 75
Blaum, K. 86
Blazevic, A. 130
Blazhev, A. 9, 13
Bleicher, M. 81
Bleile, A. 213
Blell, U. 195
Blick, R.H. 145
Blume, C. 43, 47, 220, 221, 222
Boardman, H.J. 14
Bock, R. 105, 133
Böhm, S. 95
Böhme, C. 95
Boer, W. de 214
Böttcher, I. 30, 37
Bohr, O. 74
Boine-Frankenheim, O. 195, 201
Bol, H. 214
Bollen, G. 86
Bonn, W. 217
Borcea, R. 5, 6, 13
Boretzky, K. 19, 20
Borge, M.J.G. 17
Borisenko, N. 128
Borneis, S. 105, 107
Bosch, F. 10, 87, 88, 89, 91, 95, 98, 102, 103, 109
Bosselmann, Ph. 94
Bossler, J. 191
Botvina, A.S. 23, 53
Boudard, A. 21, 22
Bourgeois, W. 197
Boutin, D. 10
Bräuning, H. 98, 102, 103
Bräuning-Demian, A. 91, 98, 102, 103, 114
Brambrink, E. 105, 130
Bramm, R. 43, 47
Brand, H. 105, 169, 207
Brandau, C. 95
Braun-Munzinger, P. 51, 65, 220, 221, 222, 223
Brons, S. 156

Author Index

Brown, G.E. 25
Browning, D. 105
Brüchle, W. 1, 2, 179, 180, 181
Brück, K. 105, 107
Bruske, C. 105, 107
Bucher, D. 220, 221, 222
Bürvenich, T. 28, 29
Buncic, P. 43, 47
Busch, O. 220, 221, 222

Cagarda, P. 12, 14, 15
Cai, X. 89, 98, 103
Caird, J. 105
Cano-Ott, D. 8, 9
Canto, L.F. 20
Caragheorgheopol, G. 214
Carlson, B.V. 20
Casarejos, E. 22
Cassing, W. 72
Castillo-Ramirez, A. 220, 221, 222
Catanescu, G. 218, 221
Catanescu, V. 220, 222
Chartier, M. 4
Chepurnov, V. 222
Chernenko, S. 222
Chevallier, M. 102
Chimi, Y. 140
Cholewa, M. 146
Chulkov, L.V. 17
Ciobanu, M. 216, 218, 220, 221, 222
Clemens, M. 199
Cleymans, J. 65
Cohen, C. 102, 103
Collatz, R. 8
Constantin, C. 127, 129
Cornelius, T. 28, 29
Cortina, D. 19, 20
Cortina-Gil, D. 17
Cowan, T.E. 130
Crespo
Lopez-Urrutia, J.R. 99
Crespo, P. 170, 173
Cruceru, I. 216
Cullen, D.M. 13
Czajkowski, S. 21, 22
Czanta, M. 87, 88

Dahl, L. 193
Damerau, H. 195
Danielewicz, P. 56
Datta Pramanik, U. 19, 20
Daues, H. 214, 220, 221, 222
Dauvergne, D. 102, 103
Dax, A. 27, 108, 118
De Gersem, H. 199
Debrowski, M. 36
Debus, J. 177, 178
Denisov, V.Yu. 30
Devismes, A. 33, 34, 220, 221, 222
Dewald, E. 105, 128, 129, 133
Dietrich, D.D. 82, 83
Dilling, J. 86, 109
Dinkelaker, P. 43, 47
Djekic, S. 113
Dobrev, D. 149
Dodonov, A.F. 109
Döring, J. 5, 6, 9, 13, 79
Dohrmann, F. 36
Dorn, A. 99
Dostal, W. 17
Dressler, R. 1, 179
Dretzke, A. 109
Dreuil, S. 153
Drexler, P. 217
Duddek, H. 105
Düllmann, Ch.E. 1, 179
Duin, H.A.P. van der 217
Duma, M. 216

Eberhardt, K. 1, 179, 182
Eberlein, B. 17
Egelhof, P. 213
Eichhorn, R. 203
Eichler, B. 1, 179
Eichler, R. 1, 179, 183, 184, 185
Eickhoff, H. 10, 168, 169, 177, 195
El-Masri, H.M. 13
El-Said, A.S. 138
Elisseev, S.A. 109
Elze, Th.W. 17, 19, 20
Emling, H. 17, 19, 20
Emmerling, M. 195
Enculescu, I. 148
Engels, O. 109
Enghardt, W. 170, 171, 172, 173, 175, 176, 177
Enqvist, T. 21, 22, 23
Erler, F. 117, 120
Essel, H.G. 169, 208, 209

Faessler, A. 57, 58, 67
Fästermann, T. 7
Falch, M. 10
Fateev, O. 222

Author Index

Fehrenbacher, G. 205
Feili, D. 93, 94
Feldmeier, H. 26, 116
Fertig, N. 145
Feuerstein, B. 99
Fiess, J. 223
Finck, C. 33, 34, 222
Fischer, B.E. 146
Fischer, D. 99
Fleischer, P. 29
Förster, A. 36, 37
Foka, P. 222
Folkmann, F. 94
Forck, P. 195
Forssén, C. 17
Fortov, V.E. 134
Fournier, C. 156
Franchetti, G. 200
Franczak, B. 10, 169, 195, 197
Frankenfeld, U. 223
Franzke, B. 10, 95, 197
Fricke, A. 158
Fricke, B. 186, 187
Friese, J. 7
Friman, B. 25, 62
Fritsch, S. 55
Fritzsche, S. 27, 97, 118, 122, 187
Froemel, F. 80
Fuchs, C. 58, 67
Fuchs, J. 130
Fujita, M. 16

Gadea, A. 8, 9
Gäggeler, H.W. 1, 2, 179
Galanopoulos, S. 6
Galonska, M. 191
Ganzhur, S. 48
Garabatos, C. 220, 221, 222, 223
Garces Narro, J. 13
Gaul, E.W. 105, 107
Gauthier, J.C. 130
Gazdzicki, M. 43, 47
Geissel, H. 4, 7, 10, 16, 17, 19, 20, 104, 109,
Geißel, M. 130
Geissler, U. 128
Gerl, J. 7, 14
Gerlach, R. 154
Gierlik, M. 9
Gilg, H. 16
Gillitzer, A. 16
Ginter, T.N. 1, 179
Giovinazzo, J. 4
Glässel, P. 219, 223
Glasmacher, U.A. 141
Glasow, R. 222
Glatz, J. 193
Glaus, F. 1, 179
Gobbi, A. 33, 34
Golser, R. 213
Górska, M. 6
Grawe, H. 5, 6, 8, 9, 13
Gregorich, K.E. 1, 179
Greiner, W. 28, 29, 81, 82, 83
Grigorian, H. 75
Grigoriev, E. 214
Grodner, E. 4
Groening, L. 193
Größer, T. 161
Grözinger, S.O. 165
Grosse, E. 36, 37
Grün, N. 95, 121
Grünschloß, A. 19, 20
Grzywacz, R. 4
Gu, Y. 142
Gudowska-Novak, E. 161
Gumberidze, A. 87, 88, 89, 91,97, 98, 102, 103
Gutermuth, F. 205
Gutfleisch, M. 222

Haberer, Th. 165, 168, 169, 172, 177
Habs, D. 109
Haeffner, H. 85
Häfner, C. 105, 107
Hagmann, S. 89, 91, 98, 99, 153
Hahn, T. 105
Hammache, F. 18
Harman, Z. 121
Harrisopulos, S. 6
Hartmann, O.N. 33, 34, 48, 216
Hartmann, W. 206
Hartnack, Ch. 66
Harutyunyan, H. 103
Hasch, B. 164
Hashimoto, T. 140
Hasse, R.W. 202
Hauler, F. 214
Hausmann, M. 10
Hayano, R.S. 16
Heeg, P. 166, 167
Heerlein, C. 123
Hees, H. van 71
Hegelich, M. 130

Author Index

Heinz, S. 109
Heiß, M. 146
Hejny, V. 48
Helariutta, K. 20
Hellström, M. 4, 6, 7, 8, 17, 19, 20
Herfurth, F. 86
Hermanspahn, N. 85
Herrmann, N. 33, 34, 35, 216, 220, 221, 222
Hessel, P. 161
Heymach, F. 191
Heßberger, F.P. 3, 12, 14, 15, 109
Hildenbrand, K.D. 33, 34, 216
Hirenzaki, S. 16
Höhr, C. 99
Hoffknecht, A. 95
Hoffman, D.C. 1, 179
Hoffmann, A.-K. 159
Hoffmann, D.H.H. 105, 127, 128, 129, 131, 132, 133, 134
Hoffmann, J. 169
Hofman-Hüther, H. 160
Hofmann, I. 200, 201
Hofmann, M. 81
Hofmann, S. 3, 12, 14, 15, 109
Hohn, O. 114
Hollinger, R. 191
Holzmann, R. 217, 271
Hu, Z. 8
Hubenthal, F. 157
Hüfner, J. 76
Hülsmann, P. 195
Hüttermann, J. 159
Hussein, M.S. 20
Hutter, G. 195
Hutton, R. 93
Huyse, M. 14

Iannucci, R. 191
Ilievski, S. 19, 20
Indelicato, P. 91
Ionescu, D.-C. 126
Ionescu, R.A. 70
Ishikawa, N. 140
Isselhorst, C. 61
Itahashi, K. 16
Ivanov, M. 220, 221, 222, 223
Iwasa, N. 19
Iwasaki, M. 16
Iwase, A. 140

Jacob, T. 186, 187
Jacoby, J. 127, 129, 131, 132, 133
Jäger, E. 1, 179, 181, 183
Jäkel, O. 164
Jahnke, T. 114
Jakob, B. 151, 152
Janas, Z. 4, 5, 6, 8
Janulewicz, K. 107
Jing, Y. 199
Jones, K.L. 19, 20
Jonson, B. 17
Jost, D.T. 1, 179
Juchem, S. 72
Junghans, A.R. 24
Jurado, B. 24

Kabachnik, N.M. 101
Kaiser, N. 55
Kambara, T. 140
Kamys, B. 36
Kapusta, M. 170
Karlgren, D. 14
Karny, M. 8
Karsch, S. 130
Karshenboim, S.G. 85
Kaspar, K. 195
Katayama, I. 108
Kaugerts, J. 198
Kausch, C. 176
Kavatsyuk, M. 5
Kaza, E. 10
Kellerbauer, A. 86
Kellerer, A.M. 154
Kerscher, Th. 10
Kienle, P. 7, 16
Kieslich, S. 95
Kim, Y.J. 33, 34, 216
Kindler, B. 12, 14, 15, 206
Kirbach, U. 1, 179
Kirchner, R. 5, 6, 8, 9, 13, 108, 211
Kirsch, R. 102, 103
Kisselev, O. 213
Klabunde, J. 193
Kleinheinz, P. 8, 9
Klemm, J. 206
Klepper, O. 10, 87, 88, 89, 98
Kluge, H.-J. 10, 27, 85, 86, 105, 107, 108, 109, 113
Knobloch, R. 127
Knoll, J. 71
Knopp, H. 95
Koch, H. 48

Author Index

Koch, V. 68, 79
Koczon, P. 36, 37, 216
König, H.G. 195
Körner, H.-J. 7
Kohlmeyer, B. 36, 37
Kojouharov, I. 12, 14
Kojouharova, J. 15
Kolb, T. 109
Kolhinen, V. 86
Kolleger, T. 43, 47
Kollmus, H. 99
Kolomeitsev, E.E. 63
Konradt, M. 155
Kopeliovich, B.Z. 76
Korchev, Y.E. 142, 143
Korpa, C.L. 64
Kozhuharov, C. 10, 87, 88, 89, 91, 95, 98, 102, 103, 109
Kozyreva, A. 133
Krämer, M. 164, 169
Kraft, G. 152, 153, 155, 156, 162, 165, 177
Kraft, S. 213
Kratz, J.V. 2, 17, 19, 20, 181, 188
Kraus, I. 43, 47
Kress, T. 33, 34, 216
Krivoruchenko, M.I. 57, 58
Kronenberg, A. 2
Kruk, G. van der 217
Krusche, B. 217
Kube, G. 109
Kuckein, M. 86
Kuczewski, B. 2
Kühl, T. 27, 105, 107, 108, 118
Kühne, M. 158
Kuhn, R. 117, 120
Kulessa, R. 17, 19, 20
Kummermehr, J. 163
Kurcewicz, J. 4
Kurz, N. 169, 208
Kutschera, W. 213

L'Hoir, A. 102
La Commara, M. 6, 13
Labzowsky, L.N. 120
Lacey, R. 56
Lalleman, A.S. 4
Lang, M. 139, 141
Lang, R. 191
Lang, S. 37
Langenbeck, B. 195
Langrock, G. 181
Larionov, A.B. 69
Lauckner, K. 173
Laue, C. 2
Laue, F. 36
Lauth, W. 109
Lawall, J. 87, 88
Le Hong Khiem 20
Le Fèvre, A. 32
Lee, D.M. 1, 179
Legrain, R. 21, 22
Leible, K.D. 191
Leifels, Y. 17, 19, 33, 34
Leino, M. 14
Leistenschneider, A. 19, 20
Lenz, G. 155, 169
Leray, S. 21, 22
Lesser, F. 222
Leupold, S. 69, 80
Li, Q. 165
Liechtenstein, V. 213
Liesen, D. 87, 88, 89, 91, 98, 102, 103, 117
Lindenstruth, V. 222
Lister, T. 220, 221, 222
Litvinov, Yu.A. 10
Liu, L.C. 27
Livingston, A.E. 94
Löbner, K.E.G. 10
Löbrich, M. 158
Löhner, H. 217
Lommel, B. 12, 14, 15, 206
Lomonosov, I.V. 134
Lotz, R. 155
Lubkiewicz, E. 19, 20
Lucke, C. 117, 120
Lukasik, J. 31
Lunney, D. 86
Lutz, H.O. 101
Lutz, M.F.M. 62, 63, 64
Luxenburger, H.M. 159
Lynch, W.G. 56
Lynen, U. 48

Ma, X. 87, 88, 89, 91, 93, 98
Madland, D.G. 28
Mahmoud, T. 220, 221, 222
Maier, L. 16
Manil, B. 87, 88, 91
Mann, R. 12, 15, 99, 101, 109
Marin, A. 222
Markenroth, K. 17
Marquardt, M. 216

Author Index

Marrus, R. 91
Martemyanov, B. 58
Maruhn, J.A. 28, 29
Marx, D. 27, 105, 107, 118
Marx, G. 109, 113
Matos, M. 10, 16
Mazzocchi, C. 4, 5, 6, 13
Meier, H.J. 213
Meister, M. 17
Mendel, M. 181
Menzel, M. 36, 37
Merschmeyer, M. 35
Messchendorp, J.G. 217
Metag, V. 217
Metz, S. 144
Meyer, C. 145
Meyer-ter-Vehn, J. 133
Michikami, O. 140
Mineva, M.N. 7
Mischke, A. 43, 47
Miskowiec, D. 51, 222
Möllers, B. 124
Moisa, D. 216
Mokler, P.H. 89, 91, 93, 95, 95, 98, 102, 103
Moore, C. 14
Moore, R.B. 86
Moritz, G. 195, 198
Moritz, P. 195, 214
Moroz, F. 8
Mosel, U. 60, 69, 80
Moshammer, R. 99
Moszysnki, M. 170
Mühle, C. 195, 198
Müller, A. 95
Müller, C. 138, 139, 140, 143
Müller-Klieser, W. 162
Münch, M. 7
Münzenberg, G. 7, 10, 14, 16, 17, 19, 20, 109
Mukha, I. 4, 5, 9, 13
Mukherjee, M. 109
Mustafin, E. 195
Mustapha, B. 21, 22
Muthig, A. 98
Mutterer, M. 27

Nacher, E. 8, 9
Nähler, A. 2, 181
Nandori, I. 117, 120
Nankov, N. 10
Nasonova, E. 161
Naumann, L. 36, 37
Nayak, G.C. 82, 83
Neacsu, C. 93, 94
Neff, S. 127
Neff, T. 26
Nefiodov, A. 117
Neise, L. 81
Neumaier, S.R. 27
Neumann, R. 138, 139, 140, 141, 147, 149
Neumayer, P. 105, 107
Neumayr, J. 109
Nickles, P.V. 107
Niemann, C. 127, 129
Nijboer, T.W. 217
Nilsson, T. 17
Nitsche, H. 1, 179
Nörenberg, W. 30, 52
Nörtershäuser, W. 27, 108, 118
Nolden, F. 10, 95, 197
Novikov, Yu.N. 10, 109
Novotny, R. 217
Nyman, G. 17

Oeschler, H. 36, 37, 65, 66
Ohtsubo, T. 16
Olson, R.E. 99
Orth, H. 48
Ostrowski, A. 6
Ott, W. 169

Page, R.D. 14
Pal, C. 159
Palit, R. 19, 20
Panebratsev, Yu. 222
Papp, G. 52
Parodi, K. 171, 172
Patin, J.B. 1, 179
Patyk, Z. 10
Pavan, J.R. 5
Pawelke, J. 170
Pearson, C.J. 13
Peitzmann, T. 220, 221, 222
Pelte, D. 35
Penache, C. 114
Penache, D. 127
Penner, G. 60
Perry, M. 105
Pershina, V. 1, 179, 186, 187, 188
Peschke, C. 203
Peters, A. 168, 195
Peters, K. 48

Author Index

Petracek, V. 222
Petris, M. 214, 216
Petrovici, M. 214, 216, 20, 221, 222
Pfützner, M. 4, 17
Piguet, D. 1, 179
Plaß, W.R. 109
Plettner, C. 4, 5, 6, 9, 13
Plochocki, A. 5
Ploskon, M. 37
Plunien, G. 117, 120
Pönisch, F. 175
Poizat, J.-C. 102
Popeko, A.G. 3, 12, 15
Popp, U. 197
Poppensieker, K. 105, 169, 207
Pravikoff, M. 21, 22
Presura, R. 127
Priller, A. 213
Pühlhofer, F. 36, 37

Qin, Z. 1, 179
Quint, W. 10, 85, 109, 113

Radon, T. 10, 205
Raduta, Ad.R. 54
Raduta, Al.H. 54
Ragaller, I. 155, 167
Rahaman, S. 109
Rainovski, G. 6
Ratzinger, U. 113, 203, 204
Rave-Fränk, M. 160
Ray, C. 102
Redlich, K. 65
Reemts, D. 105
Regan, P.H. 13
Reich, H. 10
Reich-Sprenger, H. 195
Reichling, C. 222
Reinhard, I. 105, 107
Reinhard, P.-G. 28, 29
Reisdorf, W. 33, 34, 35
Reiter, P. 19, 20
Rejmund, F. 21, 22
Renaud, P. 144
Renfordt, R. 43, 47, 223
Renk, T. 59
Reygers, K. 220, 221, 222
Ricciardi, M.V. 21, 23
Richter, A. 17
Richter, M. 169
Richter, S. 193
Rieth, U. 2
Rietzel, E. 164, 165, 167, 169
Riisager, K. 17
Ritman, J.L. 48
Ritter, S. 161
Rodríguez, D. 86, 109, 113
Roeckl, E. 4, 5, 6, 8, 9, 13
Rojko, R. 195
Roos, H. 154
Rosmej, F.B. 127
Rosmej, O. 125, 128
Roth, M. 105, 130
Roth, R. 116
Rothard, H. 153
Rozet, J.-P. 103
Rozmej, P. 52
Rubio, B. 8, 9
Ruppert, J. 83
Rusanov, I. 218, 219, 222
Rykaczewski, K. 4, 8

Salvachúa, B. 5
Salz, C. 217
Samek, S. 105
Sanchez, R. 108, 118
Sanchez-Brandelik, R. 163
Sandner, W. 107
Sandoval, A. 43, 47, 222
Sann, H. 43, 47, 223
Santo, R. 220, 221, 222
Saro, S. 3, 12, 15
Sarpe-Tudoran, C. 187
Sato, M. 16
Sauvan, E. 86
Schadmand, S. 217
Schädel, M. 1, 2, 179, 181, 182, 183, 184, 185
Schäfer, A. 76
Schäfer B.-J. 74
Schaller, G. 117, 120
Schardt, D. 166, 167, 169, 177
Schartner, K.-H. 93, 94
Schatz, H. 10
Schaub, H. 155
Schausten, B. 1, 2, 179, 181
Scheeler, U. 189, 195
Scheid, W. 95, 121
Scheidenberger, C. 10, 17, 19, 20, 86, 104, 109
Scheinast, W. 36, 37
Schempp, A. 204
Scherer, S. 81
Schicker, R. 220, 221, 222

Author Index

Schimpf, E. 1, 179, 181, 182, 183
Schippers, S. 95
Schlegel, C. 7, 14
Schlegel, T. 129, 130, 133
Schlitt, B. 204
Schlund, M. 144
Schmah, A. 37
Schmidt, H.R. 223
Schmidt, K. 4, 6, 13
Schmidt, K.-H. 20, 21, 22, 23, 24
Schmidt-Böcking, H. 114
Schmidt-Ott, W.D. 13
Schneider, C. 36
Schneider, R. 222
Schneider, R. 7, 59
Schößler, S. 114
Schött, H.-J. 1, 179
Scholz, M. 151, 152, 155, 162, 163
Schreiber, G. 195
Schrieder, G. 17
Schröder, C. 216
Schroeter, C.D. 99
Schubert, E. 169
Schuchert, I.U. 147
Schuck, T. 37
Schümann, F. 18
Schüttauf, A. 216
Schützhold, R. 117, 120
Schulz, M. 99
Schulz-Ertner, D. 178
Schwab, E. 36, 37
Schwartz, K. 138
Schwarz, C. 48
Schwarz, S. 86
Schweikhard, L. 86
Schwenk, A. 25
Schwinn, A. 197
Sedykh, S. 220, 221, 222
Seelig, W. 105, 107
Senger, P. 36, 37
Sepp, W.-D. 187
Sewtz, M. 109
Shabaev, V.M. 119, 120
Shekhter, K. 58
Shevelko, V.P. 125
Shi, W. 95
Shimanski, S. 222
Shimbara, Y. 13
Shin, Y. 36, 37
Shindo, M. 16
Shrivastava, A. 213
Shutov, A. 131, 132, 133
Siegmann, B. 101
Sierpowski, D. 89, 98
Sikler, G. 86, 109
Simion, V. 216
Simon, H. 17, 19, 20
Simon, R.S. 7, 220, 221, 222
Siwy, Z. 142, 143, 147
Smykov, L. 222
Sörensen, A.H. 104
Soff, G. 117, 120
Soltveit, H.K. 219
Soverna, S. 1, 179
Spädtke, P. 191
Spielberger, B. 114, 168
Spiller, P. 131, 132, 133, 195
Spohr, H.A. 142, 143
Spohr, R. 142, 143, 147, 148
Stöcker, H. 81, 83
Stöhlker, Th. 87, 88, 89, 91, 95, 97, 98, 102, 103, 125, 109, 113, 122
Störmer, J. 166
Stachel, J. 218, 219, 220, 221, 222
Stachura, Z. 89, 91, 95, 98, 103
Stadlmann, J. 10
Stahl, S. 85
Stanoiu, M. 4
Steck, M. 10, 87, 88, 89, 95, 197
Steier, P. 213
Steih, T. 95
Steinacher, M. 217
Steiner, J. 206
Steiner, R. 169
Stelzer, H. 214, 220, 221, 222, 223
Stephan, C. 22
Stiel, E. 181
Stock, R. 43, 47
Stockmeier, M.R. 35
Stoicea, G. 216
Stolz, A. 7
Strietzel, C. 87, 88
Ströbele, H. 36, 37, 43, 47
Strub, E. 2
Sturm, C. 36, 37
Stéphan, C. 21
Sudowe, R. 1, 2, 179
Sümmerer, K. 7, 18, 19, 20
Sulaksono, A. 28
Sun, Z. 10, 18
Surowka, G. 36
Surzhykov, A. 97, 122

Author Index

Suzuki, K. 16
Suzuki, T. 16
Szawlowski, M. 170

Tabor, S.L. 5
Tahir, N.A. 131, 132, 134
Taieb, J. 22
Tain, J.L. 8, 9
Tanihata, I. 27, 108
Tarasov, A.V. 76
Taridien, M. 102
Tarisien, M. 109, 113
Tassan-Got, L. 21, 22
Taucher-Scholz, G. 151, 152, 156
Tauschwitz, A. 105, 127, 129, 133
Tengblad, O. 17
Terasawa, M. 103
Thiel, M. 217
Thilmann, C. 178
Thirolf, P.G. 7, 109
Thöring, U. 217
Thörle, P. 1, 179, 182
Thomas, J.C. 4
Tilsner, H. 222
Timokhin, S.N. 1, 179
Tinschert, K. 191
Toepffer, C. 123, 124
Toimil Molares, M.E. 147
Toleikis, S. 87, 88, 89, 91, 98, 102, 103
Tolstikhina, I.Yu. 125
Tomaselli, M. 27, 107, 108, 118
Topsch, J. 162
Toulemonde, M. 102
Träger, F. 157
Trautmann, C. 138, 144, 145, 147
Trautmann, N. 1, 179, 181, 182
Trautmann, W. 31, 53
Tsigutkin, K. 128
Tsiledakis, G. 220, 221, 222
Türler, A. 1, 2, 179
Tyminski, Z. 33, 34, 216
Typel, S. 18

Udrea, S. 129
Uhlig, F. 18, 36, 37
Ullrich, J. 99
Uusitalo, J. 12, 15

Vahle, A. 1, 179
Valenzuela, T. 113
Valiente, J.J. 9
Van Duppen, P. 14
Van de Vel, K. 14
Varentsov, D. 129, 131, 132, 134
Varentsov, V. 109
Verdú, J. 85, 113
Vermeeren, L. 10
Vetter, J. 149
Vinzenz, W. 195
Virsik-Köpp, P. 160
Vockenhuber, C. 213
Voit, F. 109
Volant, C. 21, 22
Vorenholt, H. 217
Voskresensky, D.N. 75
Voss, B. 155
Voss, B. 169, 214
Voss, K.O. 139
Vranic, D. 223
Vulpescu, B. 220, 221, 222

Wagner, A. 36, 37
Wagner, G.A. 141
Wajda, E. 19, 20
Walenta, A.H. 87, 88
Walker, P.M. 13
Walter, G. 198
Walter, M. 124
Walus, W. 19, 20, 36, 37
Wambach, J. 61, 73, 74
Wang, H. 27, 108, 118
Wang, Z. 109
Wannenmacher, M. 178
Warczak, A. 89, 91, 98, 103
Weber, C. 86, 109
Weber, M. 213
Weber, U. 164, 169
Wefers, E. 7
Weick, H. 7, 10, 16, 104
Weidenmüller, M. 109
Weiland, T. 199
Weinert, J. 216
Weise, W. 55, 59
Weiss, A. 168
Werner, U. 101
Werth, G. 85, 113
Wessels, J. 220, 221, 222
Wetzler, A. 43, 47
Wheldon, C. 13
Wiedeking, M. 5
Wiedner, U. 48
Wiese, C. 156
Wieser, J. 128, 131, 132, 133, 214

Author Index

Wilcox, R. 105
Wilfart, A. 109
Wilk, P.A. 2
Wilke, M. 199
Wilms, D. 189, 195
Windelband, B. 220, 221, 22, 223
Winkelmann, O. 220, 221, 222
Winkler, M. 10, 16
Winkler, T. 10
Wirth, G. 1, 179, 181
Wisniewski, K. 35
Wittman, V. 8
Wlazlo, W. 22
Wolf, Gy. 62
Wolf-Reber, A. 142
Wollnik, H. 10
Wolter, H.H. 70
Wood, R. 13
Wooding, S.C. 13
Wunderle, K. 207

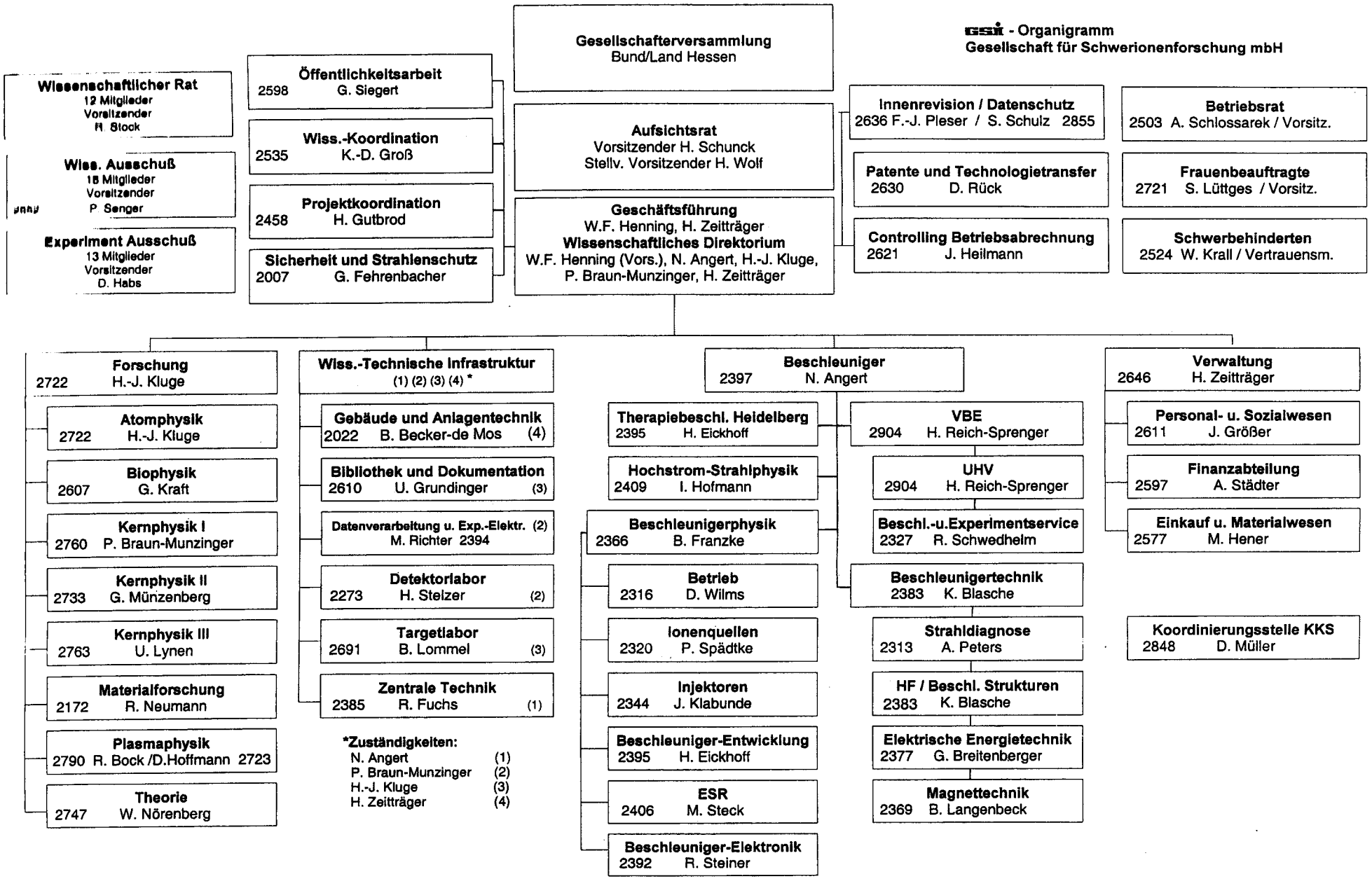
Xu, C. 220, 221, 222

Yakushev, A.B. 1, 179
Yamazaki, T. 16
Yeremin, A.V. 3, 12, 15
Yerokhin, V.A. 119, 120
Yoneyama, T. 16
Yoo, I.-K. 47
Yordanov, O. 21
Yurevich, V. 222

Zabrodin, E. 67
Zakowicz, S. 121
Zanevsky, Yu. 222
Zaranek, J. 43, 47
Zaudtke, O. 222
Zeitelhack, K. 7
Zhao, Y. 157
Zhou, Z. 109
Zhukov, M.V. 17
Zielinski, P. 1, 179
Zimmermann, C. 108
Zou, Y. 89, 93
Zweidorf, A. von 181
Zwicknagel, G. 124

Collaborations

ALICE Coll. 220, 221
ESR Team 104
FOPI Coll. 33, 34, 35
HADES Coll. 39
INDRA-ALADIN Coll. 31, 32
KaoS Coll. 36, 37
NA49 Coll. 43, 47
R3B Coll. 212
S233 Coll. 18
TAPS Coll. 217



Stand: 18.02.2002

Postanschrift: Postfach 11 05 52 64220 Darmstadt
Telefon: 0 61 59/71-0 Telefax: 0 61 59/71-27 85


Frankfurt/M.
A3
S3
A5
A661
B486
Langen
Egelsbach
GSI
DA-Wixhausen
B3
(neu)
Weiter-
stadt
Wiesbaden
Mainz
A67
Darmstadt
Mannheim
Heidelberg